A critical reappraisal of some problems in engineering seismology

A thesis submitted to the University of London

for the degree of Doctor of Philosophy and for the Diploma of the

Imperial College of Science, Technology and Medicine

By

John Douglas

Department of Civil and Environmental Engineering

Imperial College of Science, Technology and Medicine

London, SW7 2BU

October 2001

ABSTRACT

The estimation of strong-motion characteristics is important for engineering design. Such an estimation, often in terms of peak ground acceleration and spectral ordinates, is usually based on the combination of physical models that describe the process with observed ground motions recorded during earthquakes.

A multitude of results have been derived over the past thirty years, based on different models and different quantities and qualities of input data. However, there is still little consensus on their validity and on the associated uncertainties which are important for the estimation of expected ground motions in design.

This thesis describes investigations of whether best use is being made of the strong-motion observations now becoming available, given the assumptions underlying the relationships to estimate ground motions, in the hope that this estimation can be improved. Potential sources of scatter, from each stage of the derivation of attenuation relations are highlighted, and many of these are critically examined to assess their importance. This is achieved by: assessing the inherent uncertainty of the input strong-motion data including that arising from accelerogram processing, examining the importance of independent parameters and the effect of uncertainties and errors in these variables and by investigating the effect of the data distribution with respect to the independent variables.

This thesis presents updated relations for horizontal and vertical near-field strong-motion characteristics including peak ground acceleration and spectral acceleration, examines the assessment of permanent ground displacements in the near field due to faulting and estimates the effect of vertical ground motion on horizontal response. It concludes that any further improvement of the scaling of ground motions with seismological parameters and local site conditions depends primarily on the acquisition of more high-quality observational data.

Acknowledgements

Firstly I must thank my supervisor, Prof. Ambraseys, for taking me on as a PhD student in engineering seismology after doing a mathematics degree. His vast experience in the area and his willingness to impart his knowledge has help me during my three years of research.

Mum, Dad, Martin and Clare have given me much support. Dad carefully proofread the thesis and gave me excellent advice on improvements, especially to the English. I chose not to follow his advice of using ‘speed’ rather than ‘velocity’. Martin also gave some useful suggestions on the presentation of the thesis.

Patrick Smit has been a great help throughout my work. His diligent work in creating the databank and database has made my work easier and more reliable. He has also solved many of my computer problems.

Dr Sarma has been helpful to me during the last three years especially in fixing some computer programs.

Some of my papers and chapters have been read by Dr Bommer who has made constructive comments and has been enthusiastic about the results. He also provided some useful references.

I thank Dr D.M. Boore for the numerous suggestions which he made on my chapter about baseline correction techniques which helped improve the work including noting that the initial velocity needs to be used in calculation of response spectra. Also he provided the computer subroutines to implement causal Butterworth filtering on strong-motion records.

Dr W.H.K. Lee kindly sent me a report giving the measured GPS displacements from the Chi-Chi earthquake.

Dr V. Graizer made some suggestions regarding my chapter on his correction technique.

I have been fortunate to meet Prof. A. Marcellini in Keffalinia and Lisbon where he made some useful suggestions about my baseline correction and pure error work.

The authors of LaTeX, the document preparation program I used for this thesis, deserve a big thank you for helping create such an excellent program, especially as they do the work for free and are always willing to give advice on how to get the most out of it. I have used MikTeX, written by Christian Schenk, pdfLaTeX, written by Han The Thanh, and numerous packages including the ‘thesis’ document class by Wenzel Matiaske, the ‘subfigure’ package by Steven Douglas Cochran and the citation package ‘natbib’ by Patrick W. Daly. The editor I have used is Winshell by Ingo H. de Boer. The physical creation of this thesis has been made much easier by their work.

My fellow PhD students in the section, including Carlos Rodriguez-Pineda, Christiana Dymiotis, Do Hyung Lee, Dominic White, George Cossenas, Iain Tromans and Jorge Prieto-Salazar, and my friends from overseas (Alberto, Alison, Dina, Isabel, Julian and Marco) have helped me through the past three years.

CONTENTS

LIST OF FIGURES

LIST OF TABLES

1. INTRODUCTION

1.1 Background

Engineering seismology is the link between earth sciences and engineering and aims primarily at the design of structures to resist earthquake forces with minimum or controllable damage.

The main input of engineering seismology in engineering design are loading conditions which must satisfy certain conditions regarding their level and frequency of occurrence during the lifetime of a structure. Loading conditions appropriate for a particular type of structure are expressed in terms of ground motion in the frequency and/or time domains. One method for estimating these loading conditions are through equations based on strong ground motion recorded during previous earthquakes. These equations have a handful of independent parameters, such as magnitude and source-to-site distance, and a dependent parameter, such as peak ground acceleration or spectral acceleration, and the coefficients in the equation are usually found by regression analysis. Although the equations are often referred to as attenuation relationships, attenuation relations or attenuation equations, they predict more than how ground motion varies with distance. The equations are vital to probabilistic seismic hazard analysis, as Cornell (1968) shows, and also to deterministic seismic hazard analysis. Hence over the past thirty years attenuation relations have been much studied and many versions published.

Even though the quantity and quality of the input data and the methods of analysis have improved dramatically over the past thirty years these equations are still associated with large uncertainties. Anderson (1991) states:

> Strong motion seismology has the responsibility to neither overestimate nor underestimate the hazard. Everyone is familiar with the most obvious costs of an underestimate of the hazard; these have been graphically displayed in the news reports that show the damage resulting from several recent destructive earthquakes. The cost of an overestimate of the hazard is less familiar: higher costs for seismic resistance in the design of a structure, that divert capital that could have been used otherwise to attack some of the other urgent problems facing our society. Thus there is an urgent need to define and reduce the uncertainties in ground motion predictions.

Knowledge of the precision with which the design motions are assessed will allow the design engineers, if they also know the uncertainties in their structural design, to estimate appropriate factors of safety against failure or excessive damage. Therefore it is important that the uncertainties associated with attenuation relations derived using recorded strong-motion data are assessed. It is hoped that this thesis goes some way to meeting this need.

1.2 Outline of thesis

This thesis has three main themes all of which are important for assessing the uncertainty in strong ground motion estimates. These three themes are outlined individually in the following three sections.

1.2.1 First theme: Standard deviation of individual predictions using attenuation relations

This part of the thesis concerns the accuracy of an individual prediction of the ground motion which would occur at a site given the occurrence of an earthquake. Figure 1.1 outlines the general procedure for deriving attenuation relations and highlights the main sources of inaccuracies in the equations and in their use. The following discussion uses this figure as a basis.

The first stage of the procedure is the recording of strong ground motions using accelerographs. There are two sources of errors in these recordings which can lead to a decrease in the accuracy of the final equation: a non-free-field instrument location and that the accelerograph does not measure the true ground acceleration but actually the transducer response. Both these factors can mean the recorded short-period ground motions are significantly less than the true ground motion. However, errors caused by a non-free-field instrument location can be avoided by using only accelerograms from sites which are thought not to have been affected by the surrounding structure (these are known as free-field sites). The underestimation of the true short-period ground motion caused by the instrument type can be corrected for in the processing stage. These errors, therefore, are not discussed in detail in this thesis.

If the instrument that recorded the strong ground motion is an analogue accelerograph then the film or paper accelerogram has to be converted into digital form by digitising the record. This step, although it can be the source of large errors, is not investigated here because if care is taken over the digitisation, and appropriate processing is used, the errors can be small. For digital instruments, which are being increasingly deployed, this step is not needed and so records from such instruments should be more precise.

A dependent variable must be chosen and calculated for all strong-motion records in the set of selected data. This variable must be useful for engineering design and also must be able to be reliably computed for all records in the set. Errors can be introduced by the method chosen to compute the variable, however, this should not be a problem as long as care is taken; for the main variables used in this study verification of the computer programs used for the calculation of the dependent variables is presented in Appendix B.

Many factors are thought to influence strong ground motions and their effects are complex and

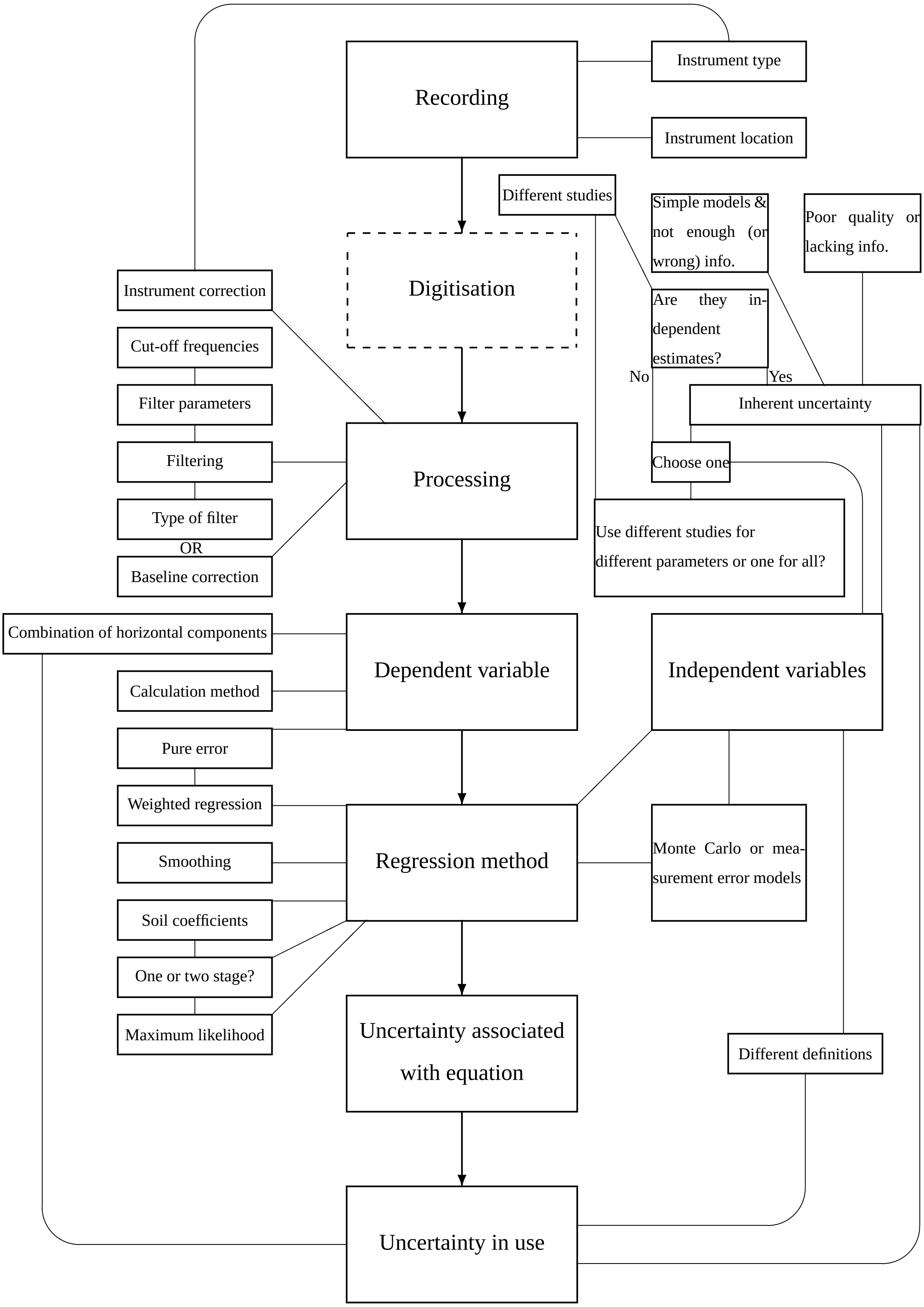

Fig. 1.1: Procedure (large boxes and arrows down centre of diagram) and sources of uncertainties (small boxes) in ground motion prediction using strong-motion records. Dashed box signifies that the digitisation step is not needed for records from digital instruments.

often interrelated; these factors are discussed in Chapter 2. It is perfectly feasible to estimate ground motions if these parameters are known *a priori* which is not the case, and the chief difficulty is establishing reliable methods for the estimation of ground motions with only few of these parameters with their large uncertainties. Attenuation relations are derived using only a handful of independent variables to characterise the source, travel-path and the local site conditions; a review of previous attenuation relations is given in Chapter 3. This leads to large standard deviations in the obtained equations. A detailed example of this is shown in Chapter 7 for the attenuation relations derived in this thesis and in Chapter 8 for attenuation relations derived by other workers. Most accelerographs record acceleration in two mutually perpendicular horizontal directions; how these recordings are combined and its effect on uncertainty is investigated in Chapter 8. Part of the cause of the large standard deviations is the inherent uncertainty (pure error) of strong ground motions; it is impossible to reduce such uncertainty without introducing more independent variables. By using a large set of strong-motion records (see Chapter 5) estimates of this pure error are derived in Chapter 8.

In almost all published attenuation relations the independent variables are assumed to be error free, however, seismological parameters such as magnitude and earthquake location, and consequently source-to-site distance, are not precisely known. Partly this is due to poor quality information, such as the seismic velocity structure, or even due to the complete lack of such information. These problems combine with simple modelling assumptions and the lack of available seismograms to cause inherent uncertainty in the independent variables. The effect of these errors is investigated in Chapter 8. Measurement error models (Fuller, 1987) can be used to derive attenuation relations where the independent variables are assumed to be only imprecisely known; such techniques are not investigated in this thesis.

For some important earthquakes there are many studies which give estimates of the required independent parameters, such as magnitude and earthquake location, which can be used for the derivation of the attenuation relations. However, unless Monte Carlo methods are used, a choice of one set of independent variables needs to be made in order to derive the equations. If the seismological variables given by the different studies are independent estimates of the variables then they yield an estimate of the inherent uncertainty in the variables. Then the means, or similar averages, of the variables can be used in the analysis.

However, because each of the different studies probably used at least some of the same data the estimates given in each study are not fully independent and hence estimating the inherent uncertainty using them is incorrect. Chapter 8 presents investigations into the effect of choosing one study for the independent variables rather than another study.

Derived equations must only contain independent parameters which can be estimated reliably for future earthquakes, otherwise even though the modelling uncertainty has been reduced the parametric uncertainty has risen and so the total uncertainty remains the same. This problem is addressed in Chapter 8.

1.2.2 Second theme: Importance of vertical ground motion

This part of the thesis concerns the importance of vertical ground motion in the near field of large earthquakes. Recently there has been an increase in interest about vertical ground motions because buildings have become more architecturally unique and more structurally complicated, base isolation systems are being increasingly employed which may become unstable if there is uplift at any of the isolation elements and also sensitive equipment mounted on floors may be adversely affected by amplified vertical ground motions.

All previous attenuation relations for spectral acceleration have been developed for the estimation of response spectral ordinates using a simple single-degree-of-freedom (SDOF) system of structures which is only valid for zero-gravity conditions and it ignores the effect of vertical ground motion on horizontal response. In this thesis SDOF models, which include the effect of vertical excitation, are studied. A literature review of the existing studies on this topic is presented in Chapter 4.

A large set of near-field strong-motion records from large earthquakes was collected for this study and the independent parameters reassessed and often recalculated. The characteristics of this construction set is given in Chapter 5. In Chapter 6 these records are used to discuss the general effects of vertical excitation on horizontal response and limits on the models used having first verified the computer programs used, see Appendix B.

There have been few studies which present consistently derived equations for the estimation of horizontal and vertical ground motions in the near field of large earthquakes. Chapter 7 presents new attenuation equations for use in the near field which examine the effect of fault mechanism and local site conditions as well as magnitude and distance and also include the effect of vertical ground motion on horizontal response.

1.2.3 Third theme: Effect of accelerogram correction technique

In the third stage of the procedure the strong-motion records are processed to eliminate errors due to the recording and digitisation steps, see Figure 1.1. These errors are mainly in the high-frequency (short-period) range and in the low-frequency (long-period) range and can be large especially for analogue records. Short-period errors are not discussed in this thesis because they are usually outside the period range of engineering significance ($T \gtrsim 0.1\,\mathrm{s}$). The problem of long-period errors, however, is important for engineering design especially since the advent of displacement-based design and for base-isolated buildings and multi-supported bridges (Gregor, 1995). Therefore correction techniques to remove these long-period errors are investigated in Chapter 9.

2. FACTORS AFFECTING STRONG GROUND MOTION

2.1 Introduction

Many factors are thought to affect strong ground motion and the literature on each of the factors is large. Reviews of these factors have been undertaken in the past by Boore (1983), Joyner (1987), Heaton & Hartzell (1988), Joyner & Boore (1988) and Anderson (1991) all of which contain comprehensive bibliographies. This chapter highlights factors which are currently not explicitly included in equations for estimating strong ground motions but which may explain much of the observed variability in strong-motion records. Definitions of the factors mentioned in this chapter and the symbols used are given in Appendix A.

Traditionally factors are grouped into three categories: those which are source based, those which are travel-path based and those which depend on the local conditions near the site (this also contains the effect of the instrument although this effect is usually removed in the accelerogram correction procedure). Therefore the ground motion at frequency (ω) and time (t), $A(\omega, t)$, is given by:

$$A(\omega, t) = B(\omega, t)C(\omega, t)D(\omega, t)$$

where $B(\omega, t)$, $C(\omega, t)$ and $D(\omega, t)$ are the contributions due to the source, the travel-path and the local site conditions respectively.

This separation of factors is followed here although some factors bridge two categories and because of non-linear effects the different contributions can become confused.

2.2 Source factors

From the static or geological point of view, three independent source parameters (any two from: characteristic dimension, $\tilde{L}$, average slip, $\bar{D}$, and static moment, M_0; and either mean stress, $\bar{\sigma}$, or energy released by faulting or strain energy change, E) are required to describe the statics of faulting (Kanamori & Anderson, 1975). However, to describe the dynamic process of earthquakes many more source parameters are required.

Source effects are thought to be the most important factor controlling strong ground motion in the near field of large earthquakes, for example Irikura *et al.* (1971) state that ‘the seismic spectra near the epicentre depends strongly on the source spectrum'. However, use of source parameters in attenuation relations is difficult because a) consistent, accurate measurements of some source parameters are difficult to find for many earthquakes and b) characteristics of earthquakes are difficult to assess *a priori* so they can be used in hazard analysis.

2.2.1 Size of earthquake

The finiteness and motion of the seismic source cannot be ignored whenever the dimensions of the source are of the order of the wavelength or when the time of rupture is of the order of the period; this was shown using simple models for surface waves by Ben-Menahem (1961) and for body waves by Ben-Menahem (1962).

Finite faults produce starting and stopping phases which contribute most of the high-frequency components (Luco & Anderson, 1983) although such phases are less important than the rupture passage phase close to the fault especially for the fault parallel and vertical components (Anderson & Luco, 1983a). For the fault perpendicular component the constructive interference of the starting and rupture phases for short faults increases peak ground velocity (PGV) for faults less than about $40\,\mathrm{km}$, as the fault length increases separation of these phases leads to decreasing PGV (Anderson & Luco, 1983a).

Fault area, S

Rupture planes are often thought to be circular, $S = \pi r^2$ where r is radius, for small earthquakes and rectangular, $S = LW$, for large earthquakes. However, inversion of seismograms for many earthquakes has shown that often this assumption is false.

Small earthquakes ($M \lesssim 6$) which do not rupture the entire seismogenic zone are geometrically similar but large earthquakes are not geometrically similar because only their length can increase, their width cannot.

Spatial incoherence of strong ground motions for sites close to large earthquakes is partly caused by interference between simultaneous arrivals from different parts of the rupturing fault; however, this is usually smaller than other sources of incoherence (Somerville *et al.*, 1991b).

For sites very close to the causative fault, fault length has been found to have a negligible effect on ground motion (e.g. Aki, 1968).

Scholz (1982) uses fault scaling arguments to find the theoretical scaling of peak ground acceleration (PGA) and PGV with fault length for large earthquakes. He argues that:

$$\begin{aligned} \mathrm{PGA} &= \mathrm{PGA}^* \sqrt{\ln \frac{L}{L^*}} \\ \text{and: } \mathrm{PGV} &= \mathrm{PGV}^* \sqrt{\frac{L}{L^*}} \end{aligned}$$

where superscript $*$ refers to the value of the variable when the length of the rupture, L, equals the width, W.

Seismic moment, M_0

Seismic moment describes the overall change of tectonic state and hence is a static measurement. Often it is thought to determine the intensity of the emitted seismic radiation and therefore it is the best measure of the size of an earthquake in terms of elastic radiation (Gubbins, 1990).

Long-period waves are less affected by structural complexities than short-period waves, which are used for determination of magnitude, therefore seismic moment is one of the most reliably determined instrumental source parameters (Kanamori & Anderson, 1975).

McGarr (1984) argues that PGV should scale with $M_0^{1/3}$ and deviations from this scaling are because of the confounding effects of focal depth and stress state. After removing these two factors McGarr (1984) finds such a scaling holds for $0.4 \leq M_w \leq 7.0$. McGarr (1984) also finds that PGA should be independent of M_0 but that the variation in focal depth and stress state masks this.

Magnitude, M

Magnitude is an empirical measurement of the size of an earthquake which is not directly related to a physical quantity but is calculated from some gross characteristic (usually wave amplitudes) of earthquake seismograms. Magnitude can be approximately related to the energy released during the earthquake but these are *a posteriori* findings. Aki (1967) states that '. . . a single parameter, such as magnitude cannot describe an earthquake even as a rough measure' .

The concept of magnitude was first introduced by Richter (1935), who defined a local magnitude scale for southern California. Since then many different magnitude scales have been introduced to provide magnitude estimates for different sizes of earthquakes and for different regions of the world. These different scales have often been derived so that the magnitude obtained through one procedure approximately equals that obtained through another. However, large differences between magnitudes from different scales do occur and hence the scales are not interchangeable. Different types of magnitude sample different parts of the energy spectrum and cannot be considered as measuring the same physical parameter of the earthquake source (Adams, 1982). Nuttli & Herrmann (1982) note that there was much confusion over differing magnitude scales leading to the mixing up of different scales. A comprehensive review of the multitude of magnitude scales which have been derived in the past is provided by Båth (1981).

Alsaker *et al.* (1991) note that M_L is important for regional distances simply because it is the most consistent and stable and is the easiest magnitude to measure. However, they state that the Lg waves used for calculation of M_L are more dependent upon local geological conditions (especially those relating to different tectonic regimes) than those waves (which penetrate the approximately homogeneous Earth's mantle) used for calculation of M_s or m_b and therefore seismic wave attenuation within each region must be determined for M_L to be consistent worldwide. Distance calibration functions have been derived for different regions of the world by, for example: Haines (1981) (New Zealand), Alsaker *et al.* (1991) (Norway), Kim (1998) (Eastern North America) and Langston *et al.* (1998) (Tanzania). Boore (1989) finds many of these calibration functions are similar within $100\,\mathrm{km}$ of the source but diverge considerably beyond that.

At teleseismic distances the short-period waves measured by Wood-Anderson seismometers, which at local distances are used for the calculation of M_L, are scattered and hence give an unreliable estimate of the size of the earthquake (Gubbins, 1990).

Global formulae can be used for surface-wave magnitude because the long-period waves used for the calculation of M_s are only moderately affected by local geological conditions (Alsaker *et al.*, 1991).

M_L, M_s and m_b all saturate, i.e. above a certain level there is no increase in magnitude with increase in actual earthquake size. For M_L and m_b the maximum magnitude that can be measured is about 7 (Hanks & Kanamori, 1979; Hanks, 1979). The maximum M_s that can be measured is about 8.3 (Hanks, 1979). Saturation occurs because M_L, M_s and m_b are finite bandwidth measurements (M_L and m_b measure the elastic radiation at about $1\,\mathrm{s}$ and M_s measures the elastic radiation at about $20\,\mathrm{s}$). Above the saturation level, all narrow-band time-domain amplitude measurements no longer measure gross faulting characteristics but only limiting conditions on localised failure along crustal fault zones (Hanks & Kanamori, 1979).

Nuttli & Herrmann (1982) state that M_L and $m_{b,Lg}$ are the best magnitude scales to use for earthquake engineering because they measure level of excitation of ground waves in the damaging frequency range. However, as will be shown in Chapter 3 almost all attenuation relations do not use M_L or $m_{b,Lg}$ magnitude scales.

Hanks & Johnson (1976) examine 40 recordings made at rupture distances of about $10\,\mathrm{km}$ from 27 worldwide earthquakes ($3.2 \leq M \leq 7.1$) and find PGA is essentially independent of magnitude for $M \gtrsim 4\frac{1}{2}$ but for $3.2 \leq M \leq 4\frac{1}{2}$ there is a clear increase with magnitude. Some PGAs may reflect chance arrivals of two or more high-frequency pulses with just the right phase coherence to interfere constructively. For large earthquakes there is a higher chance of this coincidental arrival of two waves than for small earthquakes because of a longer rupture duration. The suggestion that it is the rupture duration of earthquakes rather than the amount of energy radiated that controls PGA was was also made by Hanks & McGuire (1981) based on the Brune (1970, 1971) model[1]. For small earthquakes $M \leq 4\frac{1}{2}$ the frequencies for which this coincidence can occur can easily exceed 20–$25\,\mathrm{Hz}$ but amplitudes of such waves are reduced by anelastic attenuation and by the instrument characteristics.

Energy

When faults slip and earthquakes occur strain energy stored in the Earth's crust is released. The total energy released by faulting, E, is used to do work against friction, E_f, and a proportion is radiated as seismic energy, E_s. Therefore $E = E_f + E_s$. For engineering seismology the important quantity is the radiated seismic energy.

Radiated seismic energy, E_s

Adams (1982) states that the unambiguous measure of earthquake size is the total energy integrated over the entire spectrum of radiation, as detected on broad-band instruments. However, such measurements, although they can be made for theoretical and research purposes, involve complex recording equipment and analysis techniques and so magnitude, particularly local magnitude, is the only possible measure of earthquake size for many parts of the world. Choy & Boatwright (1995) state that E_s is a measure of seismic potential for damage.

Radiated seismic energy, E_s, is defined by:

$$E_s = E - E_f = \eta E$$

E_s is approximately related to the more routinely calculated source parameters, M_s and M_0, although the scatter is large, partly because of differences in stress conditions. Kanamori & Anderson (1975) theoretically show that E_s is proportional to $10^{1.5M_s}$ for large earthquakes which Gutenberg & Richter (1956) and Choy & Boatwright (1995) also find empirically and Vassiliou & Kanamori (1982) find that E_s is proportional to $10^{1.81M_s}$. Choy & Boatwright (1995) find that globally $E_s = 1.6 \times 10^{-5} M_0$.

Seismic efficiency, η

Acharya (1979) finds large differences in the dependence of rupture length on magnitude between seven regions of the world. Assuming that stress and stress drop are constant for earthquakes with $M \geq 6$ this difference is interpreted as meaning seismic efficiency varies from region to region. The data also suggests that seismic efficiency is dependent on rupture length or magnitude.

[1] In the rest of this chapter, this model will be known as Brune's model.

Rupture duration, t_c

Trifunac (1994) states that the corner frequency of source spectra is inversely proportional to the rupture duration given by: $t_c = L/v_R + W/(2\beta)$.

2.2.2 Depth of earthquake

The usual measure of the depth of an earthquake is the focal (or hypocentral) depth which is the depth at which the rupture nucleated. For small earthquakes, which do not rupture the entire seismogenic layer, the focal depth is an important parameter but larger earthquakes, which do rupture the entire seismogenic layer, usually nucleate at the base of the seismogenic layer (Das & Scholz, 1983) so focal depth is less important.

McGarr (1984) finds that crustal shear strength is linearly dependent on depth and hence, because this strength is one of the governing factors for PGA and PGV, there is a dependence of PGA and PGV on focal depth. A deep earthquakes recorded at the same hypocentral distance as a shallow earthquake is associated with a higher PGA and PGV. The data of McGarr (1984) shows this dependence once tectonic regime and seismic moment are removed from the analysis. Idriss (1978) states '…the deeper the source the more deficient in surface waves are the generated motions. The converse of this statement is also true (i.e. the shallower the source, the richer in surface waves are the generated motions).' Therefore records from deeper earthquakes contain higher frequencies.

Anderson & Luco (1983a) find, from an infinite fault length model, that the depth to the bottom of the fault, often approximately equal to focal depth, has little effect on simulated ground motions.

The depth to the top of the fault is found to have a significant effect on PGA, PGV and peak ground displacement (PGD) within distances comparable to the depth to the top of fault, by Anderson & Luco (1983a). However, Aki (1968) finds that this depth had a negligible effect on ground motions recorded at Parkfield-Cholame Shandon Array 2W during the Parkfield earthquake (28/6/1966) which was only $80\,\mathrm{m}$ from the causative fault

2.2.3 Rise time, τ

Varying τ in simulations of ground motion has been shown to have a limited effect on short-period ground motion, smaller τ increases short-period amplitudes, and little effect on long-period motions (Kanamori, 1974; Anderson & Luco, 1983a).

2.2.4 Stress

Stress conditions at a fault before, during and after an earthquake play an important role in high-frequency ground motion.

A set of records from earthquakes of a wide range of magnitudes ($0.4 \leq M_w \leq 7.0$), with focal depths between 0.07 and $18\,\mathrm{km}$ and from small hypocentral distances are examined by McGarr (1984). It is found that crustal shear strength is dependent on the tectonic regime (i.e. whether it is extensional or compressional) and that the localised stress drops which give rise to PGAs, and to a lesser extent PGVs, are controlled by crustal strength therefore PGA and PGV should be dependent on crustal shear strength. From the set of records it is found that PGA increases up to a factor of 3 for PGA and PGV increases up to a factor of 2.3 between compressional and extensional regimes. The upper bound on the PGA from extensional regimes is estimated as $0.5\,\mathrm{g}[5\,\mathrm{ms}^{-2}]$ and in compressional regimes as $1.9\,\mathrm{g}[19\,\mathrm{ms}^{-2}]$.

The initial form of the seismic source-time function associated with a fracturing process taking into account the cohesive force in the source function is studied by Ida (1973). It is found that:

$$\begin{aligned} \mathrm{PGA} &\sim \left(\frac{\sigma_0}{\mu}\right)^2 \left(\frac{v_R^2}{D_0}\right) \\ \mathrm{PGV} &\sim \frac{\sigma_0}{\mu} v_R \end{aligned}$$

where σ_0 is the strength of material and D_0 is slip displacement required for the initial formation of crack surface. Therefore near-source strong ground motion is governed by gross strength of rocks. Using $\sigma_0 = 100\,\mathrm{MPa}[1\,\mathrm{kbar}]$, $D_0 = 10\,\mathrm{cm}$, $v_R = 1\,\mathrm{kms}^{-1}$ and $\mu = 100\,\mathrm{GPa}[1\mathrm{Mbar}]$ gives $\mathrm{PGA} \sim 1\,\mathrm{g}[10\,\mathrm{ms}^{-2}]$ and $\mathrm{PGV} \sim 1\,\mathrm{ms}^{-1}$.

Initial stress, σ_0

Radiated energy, E_s, is dependent on the initial stress which does not affect permanent displacements or the seismic moment (Betbeder-Matibet, 1995).

Stress drop, $\Delta\sigma = \sigma_0 - \sigma_1$

Stress drop can be used as a measure of the strength of high-frequency radiation and hence is a useful parameter for engineering seismology. However, due to the number of different definitions and the lack of robust calculation methods its usefulness is limited.

There are two types of stress drop: static and dynamic. Dynamic stress drop is the difference between the applied tectonic stress and the dynamic frictional strength of the fault

Static stress drop is calculated from formulae of the form:

$$\Delta\sigma = C D_{\max} \mu / W$$

where $D_{\max}$ is the maximum fault slip. Brune & Allen (1967) give three expressions for calculating stress drop using various fault parameters observed in the field: C equals $4/3$ for an infinitely long narrow strip in a uniform shear field, $1/2$ for an infinitely long vertical surface fault with strike-slip displacement and $2\pi/3$ for a circular fault in an infinite medium. Therefore $C \approx 1$. It only approaches the actual average of the static stress drop over the rupture area if the stress release varies gradually over the fault surface; for complex faulting it substantially underestimates the mean or r.m.s. static stress drop of the ruptured region (Boatwright, 1984).

Brune's model is often used to provide an estimate of static stress drop. In fact Brune (1970, 1971) uses effective stress, σ_e, in his model which is only equivalent to stress drop, $\Delta\sigma$, if the frictional stress σ_f is equal to the final stress, σ_1. The formula used for the calculation of effective stress for Brune's model is:

$$\sigma_e = \frac{7M_0}{16r^3}$$

where r is the radius of an equivalent circular dislocation surface. The problem with using such a formula is that reliable estimates of r are difficult to obtain and because this radius is cubed small errors in r cause large errors in σ_e. A similar problem occurs when $\Delta\sigma$ is calculated from the cube of the corner period (Kanamori & Anderson, 1975).

There are two measures of dynamic stress drop although sometimes apparent stress is used as a stress drop.

Dynamic stress drop of small earthquakes or individual subevents of large earthquakes can be calculated using the initial slope of velocity waveform: $\Delta\sigma \approx \mu\Delta\dot{u}_0/v_R$, where $\dot{u}_0$ is the asymptotic slip velocity behind the rupture front.

The second type of dynamic stress drop is the a_{rms} stress drop defined by Hanks & McGuire (1981).

Simple models of faulting often demonstrate the importance of stress drop. In Betbeder-Matibet (1995) some theoretical attenuation relations are derived for PGA and PGV using a number of simplified models. In both the velocity and acceleration equations there is a strong dependence on the stress drop (exponents of $\frac{2}{3}$ and $\frac{5}{6}$ respectively). McGarr (1981) presents a simple model of inhomogeneous faulting where the failure of an asperity within an annular faulted region is followed by a broader-scale dynamic readjustment. The newly formed fault zone is associated with a stress drop many times larger than the average stress drop. This model gives these expressions for PGA and PGV:

$$\begin{aligned} \mathrm{PGA} &= \frac{\Delta\sigma}{\rho R}\left[0.30\left(\frac{r_0}{r_i}\right)^2 + 0.45\right] \\ \mathrm{PGV} &= \frac{\beta\Delta\sigma r_0}{\mu R}\left[0.10\left(\frac{r_0}{r_i}\right) + 0.15\right] \end{aligned}$$

where r_0/r_i is the ratio of the radius of the previously faulted annular region and the radius of the circular asperity and is found to be between in the range 1–10 using a set of records from 16 mine tremors and earthquakes with $-0.76 \leq M_L \leq 6.4$. When the effective stress equals the stress drop then Brune's model also shows that stress drop is an important parameter.

However, McGarr (1984) finds stress drop is not related to stress state nor to focal depth and that the localised stress drops that give rise to high frequency ground motion are functions of crustal properties not the overall stress drop.

One major problem with stress drop is the lack of consistency between different estimates of $\Delta\sigma$ for the same earthquake. This is in part because of the different ways stress drop is measured. For example, Boatwright (1984) examines five different measures of stress drop for eight aftershocks of the Oroville earthquake with $3.6 \leq M_L \leq 4.8$. The three measures which are estimates of dynamic stress drop are strongly correlated whereas for the two measures of static stress drop (Brune and average static stress drop) much variability is found and they do not correlate with dynamic stress drop. Hanks & McGuire (1981) find all 15 Californian earthquakes they analyse have $\Delta\sigma$ of about $10\,\mathrm{MPa}[100\,\mathrm{bar}]$ (to a factor of about 2) by fitting Brune's model to a_{rms}, although published $\Delta\sigma$ for these earthquakes are usually much lower than $10\,\mathrm{MPa}[100\,\mathrm{bar}]$ (which they state could be caused by overestimating source dimensions from the aftershock distribution).

Even when stress drop is calculated in the same way large differences can occur between estimates partly because of different assumed sizes of the rupture area. For example, Bent & Helmberger (1989) estimate the stress drop for the Whittier Narrows earthquake (1/10/1987) as $75\,\mathrm{MPa}[750\,\mathrm{bar}]$ whereas the estimate of Douglas (1997) is $0.26\,\mathrm{MPa}[2.6\,\mathrm{bar}]$, a difference of almost 300 times. Hanks & McGuire (1981) estimate $\Delta\sigma$ is accurate to a factor of about 3.

As the estimation of stress drop is associated with a large uncertainty it is difficult to be confident that the apparent differences in stress drops between regions which authors find are true differences, unless the calculation methods are similar. One such study is that by Cocco & Rovelli (1989) who calculate Brune and apparent stress drops of some Friuli shocks and a Montenegro earthquake, which are from regions of compression, and report Brune and apparent stress drops of some Italian earthquakes from regions of extension calculated in a previous study using an identical technique. They find a significant difference (at the 95% confidence level) of roughly a factor of 2 in apparent stress drops and a factor of 3 in Brune stress drops between the two types of earthquake; Friuli and Montenegro earthquakes having the higher stress drops. Kanamori & Anderson (1975) find approximately constant $\Delta\sigma$ for the earthquakes they study. They find large interplate earthquakes have $\Delta\sigma \approx 3\,\mathrm{MPa}[30\,\mathrm{bar}]$ and intraplate earthquakes have systematically larger $\Delta\sigma$ of about $10\,\mathrm{MPa}[100\,\mathrm{bar}]$. Much larger stress drops for intraplate earthquakes are also found by Scholz *et al.* (1986) through an analysis of the ratio of fault length to fault slip.

Atkinson & Beresnev (1997) note that for small earthquakes Brune's model describes simple ruptures reasonably well but for complex ruptures or for large earthquakes for which finite fault effects are significant, deviations from this simple representation become important hence the spectrum becomes complicated and stress drop becomes a highly ambiguous and non-unique parameter, depending entirely on how it is measured. These stress drops may bear no relation to stresses in the real earth or on the fault surface, particularly for complex ruptures.

Although the use of stress drop for strong ground motion estimation is appealing from the presumed theoretical scaling of high-frequency ground motions with stress drop, using stress drop as a parameter in attenuation relations, is at present extremely difficult. There are two main reasons for this. Firstly as shown here there are many definitions of stress drop, some of which are measurable for small earthquakes (dynamic stress drop) and some for large simple earthquakes (static stress drop) which precludes the use of one measure for the entire magnitude range of interest. Also even for one definition of stress drop different studies can give widely different estimates. Determination of stress drop is model dependent (Choy & Boatwright, 1995). Secondly at present there are no known methods of predicting the stress drop of future earthquakes in a region for seismic hazard analysis, such as is done for magnitude through Gutenberg-Richter relations. Trifunac (1976) says neglecting stress drop can be justified from a practical point of view, since data and statistical analyses of magnitude are more complete and reliable than the interpretations of the inferred amplitudes of stress drop.

Currently stress drop is implicitly accounted for in attenuation relations by the use of strong-motion data from tectonically similar regions of the world, such as subduction zones, interplate regions or intraplate regions. Similarly the variation in strong ground motion due to differences in stress drop for earthquakes with different source mechanisms are sometimes accounted for in attenuation relations. As was noted above there seems to be some relationship between the type of tectonic regime and the average stress drop of earthquakes occurring with the region.

Faults with longer repeat times have shorter lengths for the same magnitude, indicating a large average stress drop and, presumably, higher ground motion (Joyner & Boore, 1988).

Average effective stress, $\sigma_e = \sigma_0 - \sigma_f$

The importance of average effective stress was demonstrated by Brune (1970, 1971) who modelled earthquake dislocation as an instantaneous tangential stress pulse applied to the interior of a dislocation surface. After considering the effects of the edges of the dislocation surface becoming felt at the observation point the tangential displacement, u, and the initial particle velocity, $\dot{u}$, close to the fault are given by:

$$\begin{aligned} u &= \frac{\sigma_e}{\mu}\beta\tau[1-\exp(-t/\tau)] \\ \dot{u} &= \frac{\sigma_e}{\mu}\beta\exp(-t/\tau) \end{aligned}$$

where $\tau = O(r/\beta)$ and r is a characteristic distance. Also this model predicts that PGA is proportional to σ_e. For $\sigma_e = 10\,\mathrm{MPa}[100\,\mathrm{bar}]$, $\mu = 3 \times 10^{10}\,\mathrm{Nm}$, $\beta = 3\,\mathrm{kms}^{-1}$ this model gives a PGA of about $20\,\mathrm{ms}^{-2}[2\,\mathrm{g}]$ and PGV of about $100\,\mathrm{cms}^{-1}$. Taking the Fourier transform of the expression for u gives the near-field spectrum:

$$\Omega(\omega) = \frac{\sigma_e}{\mu} \frac{\beta}{\omega\sqrt{\omega^2 + \tau^{-2}}}$$

In the far field allowing for diffraction, spherical spreading and applying conditions so that the long-period part of spectrum agrees with dislocation source moment and high-frequency limit conserves the energy-density flux at large distances gives the r.m.s. far-field spectrum:

$$\langle\Omega(\omega)\rangle = \langle R_{\theta,\phi}\rangle \frac{\sigma_e \beta}{\mu} \frac{r}{R} F(\epsilon) \frac{1}{\omega^2 + \alpha^2}$$

where $\alpha = 2.34\beta/r$, $F(\epsilon)$ is function which modifies the spectrum for fractional stress drop, ϵ, and $R_{\theta,\phi}$ is the radiation pattern function.

These results show that effective stress is an important parameter controlling ground motion.

Effective stress is often thought to be equivalent to stress drop and this is often justified (e.g. Kanamori & Anderson, 1975).

Kanamori & Anderson (1975) note that although constancy of effective stress for all earthquakes is not as well established as that of stress drop it is a reasonable assumption especially because it is even more of a material property than $\Delta\sigma$.

Dynamic shear-stress differences

Hanks & Johnson (1976) argue that PGA is proportional to dynamic shear-stress differences accompanying localised faulting.

Apparent stress, σ_a

Kanamori & Anderson (1975) find that apparent stress is approximately constant for large earthquakes and that for interplate earthquakes σ_a is about $1\,\mathrm{MPa}$ to $2\,\mathrm{MPa}$ [10 to $20\,\mathrm{bar}$] and for intraplate earthquakes σ_a is about $5\,\mathrm{MPa}$ [$50\,\mathrm{bar}$]. Hence $\sigma_a \approx \frac{1}{2}\Delta\sigma$.

Choy & Boatwright (1995) analyse 397 shallow earthquakes with $m_b > 5.8$ and measurements of E_s and find globally that σ_a is $0.47\,\mathrm{MPa}[4.7\,\mathrm{bar}]$, but the scatter is extremely large. Splitting the earthquakes into categories by focal mechanism and by tectonic regime shows that apparent stress is dependent on both focal mechanism and tectonic regime although most of the relations are associated with large scatter, see Table 2.1. Apparent stress is a robust parameter because it does not depend on the assumed rupture geometry or model.

Tab. 2.1: Average apparent stress, σ_a, for different focal mechanisms and tectonic regimes found by Choy & Boatwright (1995).

Focal mechanism	Tectonic regime	Average σ_a (MPa) [bar]
Thrust	All	0.32 [3.2]
	Subduction zones	0.29 [2.9]
	Intraplate continental	0.46 [4.6]
	Near-plate margin	0.95 [9.5]
	Continental collision	0.43 [4.3]
Normal	All	0.48 [4.8]
	Oceanic subduction zones	0.59 [5.9]
	Continental collision	0.46 [4.6]
	Intraplate	0.95 [9.5]
	Rift zones	0.25 [2.5]
Strike-slip	All	3.55 [35.5]
	Oceanic ridge-ridge transform faults	4.48 [44.8]
	Oceanic intraplate	6.95 [69.5]
	Transitional boundary	1–3 [10–30]

2.2.5 Rupture propagation

Large earthquakes of engineering significance have long rupture lengths (e.g. Wells & Coppersmith, 1994). Rupture cannot occur along the whole fault simultaneously therefore this finiteness of the source inevitably means that the source is moving. The movement of the source along the fault creates an effect on the radiation pattern which is commonly known as directivity and also an effect on pulse shapes which is recognized as the Doppler effect (Douglas *et al.*, 1988).

High-frequency radiation (with wavelengths smaller than dimensions of the fault and larger than the non-linear zone near the rupture front) are determined by the slip velocity field near the source, i.e. the motion and intensity of slip velocity concentration (Madariaga, 1977). Therefore radiation is strongest when the rupture velocity changes abruptly as a result of variations in the strength or cohesion of the fault. Hanks & Johnson (1976) and McGarr (1981) suggest PGA is from an isolated and localised faulting event; Boatwright & Boore (1982) estimate the size of the subevents for two Livermore earthquakes to have radii of $1.3 \pm 0.1\,\mathrm{km}$ and $1.5 \pm 0.1\,\mathrm{km}$. McGarr (1982) estimates the size of these subevents as between 0.23 and $1.81\,\mathrm{km}$ for six California earthquakes with $4.0 \leq M_L \leq 6.6$.

Simple transient crack models of the sudden extension of a pre-existing antiplane crack and of an in-plane shear crack are investigated by Madariaga (1977). It is found that in the forward direction there is a strong velocity peak associated with the slip velocity singularity at the rupture front and that this is a near-field effect which only appears in the vicinity of the rupture front.

Many models of earthquake fault motion assume a constant rupture velocity but realistic fault motion is more irregular. Betbeder-Matibet (1995) states that some of the scatter associated with strong-motion data is due to non-uniform rupture of the fault along its length.

As rupture velocity approaches the Rayleigh wave velocity PGA and PGV show large amplifications but PGD is less affected (Anderson & Luco, 1983a). The effects are strongest for parallel and vertical components because they are dominated by P, SV and Rayleigh waves whereas perpendicular components are dominated by SH waves (Anderson & Luco, 1983a). As rupture velocity increases the contribution from the Rayleigh waves increases and so rate of attenuation decreases (Anderson & Luco, 1983a).

Although rupture velocity is important, for most earthquakes it usually lies between 2 and $3\,\mathrm{kms}^{-1}$ (Trifunac, 1994). However, estimates of rupture velocity for one earthquake can differ depending on the calculation method; for example, for the Imperial Valley earthquake (15/10/1979) rupture velocity estimates are 1.80–$1.95\,\mathrm{kms}^{-1}$ (Anderson & Luco, 1983a), 2.5–$2.7\,\mathrm{kms}^{-1}$ (Hartzell & Helmberger, 1982) and 4–$5\,\mathrm{kms}^{-1}$ (Olson & Apsel, 1982), although Olson & Apsel (1982) note that their estimate may be too high.

The rupture velocity up the fault (transverse rupture velocity) has little effect on ground motions (Anderson & Luco, 1983a).

Directivity (Doppler effect)

Directivity is used to describe the general radiation pattern due to the motion of the source and can be thought of as resulting from the destructive interference of waves from different parts of the fault or due to frequency shifts. Directivity of a source depends on more than the Doppler shift of frequency components because it is affected by the amplitude of the source as a function of time and position.

Archuleta & Brune (1975) find PGV at the far ends of the fault is roughly three times that at the middle of the fault (the initiation point), from foam rubber models of earthquakes. The most probable cause of this is focussing of energy in the direction of propagation (Doppler focussing), which is critically dependent on coherence of seismic waves as rupture propagates. A continuously propagating rupture in a homogeneous medium could result in very high particle velocities.

Boatwright & Boore (1982) examine the mainshock (24/1/1980, $M_w = 5.8$) and an aftershock (27/1/1980, $M_w = 5.5$) of the Livermore Valley earthquake both being strike-slip earthquakes with nearly vertical fault planes. The observed PGA is divided by the predicted PGA, using the Joyner & Boore (1981) attenuation relation, to correct for geometrical and anelastic attenuation and this ratio is plotted against azimuth from source to receiver. It is found that the difference in PGA due to azimuthal variation is a factor of 8 for the mainshock and 5 for the aftershock. Also Boatwright & Boore (1982) analyse the ratio of PGA recorded at a single station from the two earthquakes, which are thought to have ruptured in opposite directions but along the same fault plane direction, to minimize errors due to site effects, radiation pattern and the attenuation relation used. The total variation between PGA recorded at a particular site during the two earthquakes is up to a factor of 30. PGV is analysed in a similar way and it is found that the variation due to directivity is a factor of 5 for both events. A good correlation is found between a directivity function (Equation 2.1) and the observed azimuth variation for the mainshock but poorer fit for the aftershock.

$$D^s(\psi) = \left(1 - \frac{\Delta v}{\beta} \cos\psi\right)^{-1} \tag{2.1}$$

where ψ is the angle between direction of rupture and takeoff direction of ray (taken as angle between rupture direction and azimuth to station) and Δv is the change in rupture velocity associated with radiation of acceleration pulse which is found to be $> 0.7\beta$.

The directivity function of Equation 2.1 is an upper bound on expected directivity because neither the takeoff angles nor the direction of rupture are purely horizontal (Boatwright & Boore, 1982).

The 23:19 aftershock ($M_L = 5.0$) of the Imperial Valley earthquake (15/10/1979) was examined by Liu & Helmberger (1985) and they find evidence for directivity affecting the SH velocity pulse width with the stations in the direction of rupture propagation recording a time duration about half that recorded by stations opposite to the direction of rupture. This directivity effect had an influence on the ground motion: producing high-amplitude, high-frequency accelerations at stations in the direction of rupture and low-amplitude, low-frequency acceleration at stations opposite to the direction of rupture.

Niazi (1982) considers the residuals (i.e. difference between observed value and that predicted using an attenuation relation) of PGA and PGV recorded at stations on soil within $50\,\mathrm{km}$ of the rupture of the Imperial Valley earthquake ($M_s = 6.9$). No evidence for directivity is found for PGA but for PGV there is a clear correlation with purely geometrical directivity factor (Equation 2.2).

$$D^g(\psi) = \left(\frac{\beta}{v_R} - \cos\psi\right)^{-1} \tag{2.2}$$

where ψ is the angle subtended between the ray leaving the source and direction of rupture.

Nine 5% pseudo-acceleration response spectra from within $60\,\mathrm{km}$ of the Landers earthquake (28/6/1992, $M_s = 7.6$, $M_w = 7.3$) are examined by Campbell & Bozorgnia (1994a). It is found that the fault-normal component for the five spectra from stations north of the epicentre (in the direction of rupture) are much larger (up to 3 or 4 times) than the fault-parallel components for periods greater than about $1\,\mathrm{s}$ and that the four spectra to the south of the epicentre (in the opposite direction to rupture) do not show such a great difference (only about 1.5 to 2 times) in the fault-normal and fault-parallel directions.

Sirovich (1994) plots PGAs, normalised with respect to radiation pattern, from the Campano Lucano earthquake (23/11/1980, $M_s = 6.9$) (which had a normal mechanism and bilateral rupture) against azimuth and finds what may be a small directivity effect.

Midorikawa (1993) uses a simplified semi-empirical Green's function method to estimate PGAs from theoretical earthquakes. For a $M = 7.2$ earthquake, PGA from a unilateral rupture is approximately 30–40% lower in the direction opposite to the direction of rupture than in other directions but the effects of directivity are not significant in other directions. This finding is almost independent of the dip of the fault.

Benz & Smith (1987) find a frequency shift in simulated seismograms (Doppler effect) for locations at the end of a $45°$ dipping normal fault.

Boore & Joyner (1978) model a unidirectional rupture along a fault subdivided into segments which are triggered sequentially by the rupture front, each segment is an idealised model of rupture with random length, displacement and rupture velocity. It is found that the mean spectrum of this incoherent rupture is made up of a deterministic part and a statistical part and so has two spectral corners: one associated with the rupture over the whole fault length at mean velocity and the other at higher frequencies related to rupture over the coherence length. They note that any incoherence due to variations in rupture will destroy destructive interference so spectral levels and peak motions will, in general, be larger than for smooth rupture. Even random rupture in space and time occurring over a planar source leads to directivity.

2.2.6 Radiation pattern

Since seismic waves do not radiate equally in all directions the expected amplitude of the ground motion at a particular site is a function of the azimuth measured from the strike of the fault. These patterns vary for different fault types, dips, rakes and type of body wave (P, SH and SV). Close to the fault the different waves have not become separated out and so the azimuthal differences are not so important. In the far field the waves are separated but the azimuthal dependence is reduced because the waves have been reflected, refracted and scattered and also surface waves may be present. Note that this effect is not the same as directivity because it occurs even for point sources but directivity effects can often mask the radiation pattern.

Many studies which have looked for azimuthal variation in strong ground motion due to radiation pattern have not found it. Boatwright & Boore (1982) find the predicted SH radiation pattern is significantly obscured in their azimuthal analysis of two Livermore earthquakes ($M_w = 5.8$ and

$M_w = 5.5$). Liu & Helmberger (1985) find that for an aftershock ($M_L = 5.0$) of the Imperial Valley earthquake that there is little evidence that PGAs are affected by the radiation pattern but that for accelerations filtered with passband at $0.5\,\mathrm{Hz}$ or at $1.0\,\mathrm{Hz}$ there is evidence that the radiation pattern does affect accelerations. Vidale (1989) notes that shorter period (0.1–$1\,\mathrm{s}$) ground motions may not show clear radiation pattern effects because of scattering in crust, which is more important for short than long periods because such waves have travelled more wavelengths from source to site, and because the fault plane itself may not be equally smooth on all scales so perhaps short-period radiation pattern is more complex than a double couple. Ohno *et al.* (1993) find that observed PGAs and earthquake intensities do not show the azimuthal variation that is predicted but are constant around the fault. The possible reasons given are: changing mechanism during rupture propagation and slip heterogeneity. However, long-period waves do show the expected variation.

Some studies, however, have found possible dependence of strong ground motion with azimuth. Vidale (1989) examined the ratio of PGAs from the Whittier Narrows main shock (1/10/1987, $M_L = 5.9$) and an aftershock (4/10/1987, $M_L = 5.3$). The ratio of PGAs (found to be associated with waves of between 3 and $6\,\mathrm{Hz}$) from the two shocks was examined because this minimizes the local site effects. Vidale (1989) assumes that in the whole space radiation pattern of S waves dominates over weaker P waves and computes the expected total S-wave vector (square root of sum of squares of SH and SV amplitudes) ratio for each station. A good fit (correlation coefficient 0.63) is found between observed and predicted ratios and that a focal mechanism dependence in the ratios is preferred to a focal mechanism independence. Little evidence is found for P waves or surface waves affecting radiation pattern. Campbell & Bozorgnia (1994a) derive attenuation relations from strong-motion recordings on alluvium sites during the Landers earthquake and examine the residuals with respect to azimuth. It is found that the PGA residuals are significantly different (at the 90% confidence level) in different azimuthal ranges up to an average factor of 1.62 for stations to the northwest which is partly due to the SH radiation pattern although the situation is complicated by directivity and by possible basin and local site effects. Resolved PGAs from 13 stations (not thought to be significantly affected by site effects) which recorded the Campano Lucano earthquake (23/11/1980, $M_s = 6.9$) were investigated by Sirovich (1994) for evidence of the effect of radiation pattern. The recorded PGAs were normalised by a fitted attenuation equation and plotted against azimuth to the epicentre. A match was found between these normalised values and the predicted radiation pattern using a combination of SH waves and the horizontal component of SV waves. Radiated pattern effects are found to be present in the simulations of Anderson & Luco (1983b) but they are not always simply related to the point source patterns.

A special case of the effect of radiation pattern on ground motion are the large amplitude vertical accelerations recorded at five stations during the Imperial Valley earthquake (15/10/1979). They are interpreted by Archuleta (1982) as PP waves which are controlled by the velocity profile. This hypothesis also explains the absence of such large vertical accelerations at stations which are closer to the epicentre than those stations which recorded the large vertical PGAs.

Sirovich (1994) notes that if focal mechanisms and orientations of ruptures are consistent in a region, such as is thought to happen in the southern Apennines, then the inclusion of azimuthal dependence in seismic hazard assessment may be useful.

2.2.7 Focal mechanism

Foam rubber models of a 60° dipping normal fault and a vertical strike-slip fault are used by Brune & Anooshehpoor (1999) to get qualitative results of the difference between normal and strike-slip ground motion. Systematically lower accelerations (between 5 and 10 times smaller) for normal faulting compared with strike-slip faulting are found. A 2D finite element method, including the time-dependence of the normal stress on the fault, is used by Oglesby *et al.* (1996) to investigate how PGV and PGD vary in the near field of reverse and normal earthquakes with dips of 30, 45 and 60°. The model predicts much larger PGV and PGD for thrust earthquakes compared with normal earthquakes and that this difference increases with increasing dip angle. Oglesby *et al.* (2000b) extend this to 3D, and find similar results to the 2D case, and also model strike-slip ruptures of varying dip. It is found that for 30° faults PGV for strike-slip mechanism earthquakes is slightly higher than that for thrust, although few strike-slip earthquakes have dips much different than 90°. Oglesby *et al.* (2000a) find that the difference between PGV and PGD for normal and thrust/reverse faults almost disappears when the fault is buried. The difference between normal and thrust ground motions persists even at large distances. Anderson & Luco (1983b) find using an infinite fault model that rake has relatively small effect on peak amplitudes although dip-slip faults with dips less than 90° can have significantly larger ground motions than vertical strike-slip faults.

Westaway & Smith (1989) report a study where the distances, magnitudes and mechanism of each event in their set of 243 strong-motion records from normal faulting earthquakes are carefully verified. Horizontal PGAs (considering their uncertainties due to instrument calibration, digitization and in baseline fitting) are comparable to those PGAs predicted by attenuation relations of Joyner & Boore (1981) and Campbell (1981) when allowance is made for the uncertainty in distance. It is found that horizontal PGA is well estimated by both equations therefore PGAs from normal earthquakes is similar to that from strike-slip and reverse/thrust earthquakes.

There seems to be three main suggestions for the measured differences in strong ground motion due to differences in the focal mechanism. One explanation is by Vidale (1989) who suggests that the difference in radiation pattern of reverse and strike-slip earthquakes may contribute to the observed large ground motions from reverse shocks because the lobes of reverse-shock radiation patterns occur close to the source whereas lobes in the radiation pattern of strike-slip shocks occur farther from the source.

Oglesby *et al.* (1996, 2000a,b) find that reflected waves from the free surface amplify the motion of thrust faults near the free surface whereas the opposite is true of motion of normal faults because these waves affect the normal stress.

The most accepted explanations are connected to differences in stress conditions between normal, strike-slip and reverse/thrust faults.

McGarr (1982) attempts to calculate upper bounds on near-source PGA using a model of inhomogeneous faulting which involves an annular faulted region surrounding an unfaulted asperity, the failure of which results in the earthquake. This failure is thought to depend on both the level of ambient shear stress above the frictional stress resisting fault slip and the ratio of the outer and inner radii of the prefaulted annulus. By considering the orientation of the maximum principal stress and the minimum principal stress McGarr (1982) estimates that for an extensional stress state (where the maximum principal stress is oriented vertically) $\mathrm{PGA} < 0.4\,\mathrm{g}$, for a compressional stress state (where the minimum principal stress is oriented vertically) $\mathrm{PGA} < 2\,\mathrm{g}$ and for perfect strike-slip faulting (where the vertical stress is the average of the two horizontal principal stresses) $\mathrm{PGA} < 0.7\,\mathrm{g}$.

For normal faults the static normal and shear stresses along the fault must approach zero at the ground surface because the tectonic forces are extensional and the lithostatic forces are zero. At depth the stresses are limited if the fault surface consists of incompetent sediments, since such materials could not maintain permanent stresses. Therefore normal faults are inherently weak in the upper parts of the fault zone and cannot maintain the high levels of shear strain required for high dynamic energy release to be possible unlike strike-slip faults (Brune & Anooshehpoor, 1999).

2.2.8 Dip of fault, δ

Geometrical asymmetry of the fault means the earthquake generated stress field must change to match the stress boundary at the free surface causing variations in the normal stress on the fault. This is because seismic waves radiated by the rupture will reflect off the free surface and hit the fault again modifying the stress field both ahead of and behind the rupture front as it travels towards the surface. These variations affect the friction and hence the dynamic rupture of the earthquake therefore causing asymmetric ground motion in the proximity of the fault (Oglesby *et al.*, 1996). This asymmetry of ground motions was found by Archuleta (1982) for the Imperial Valley earthquake (15/10/1979) which occurred on a fault which dips at approximately $75°$.

Anderson & Luco (1983b) find that dip has a strong effect on peak amplitudes, ground motions from shallow faults are larger than from vertical faults, but this is partly due to decreasing distance to source.

2.2.9 Hanging wall effect

In recent thrust earthquakes, for example San Fernando (Allen *et al.*, 1998), Northridge (Abrahamson & Somerville, 1996) and Chi-Chi (Shin *et al.*, 2000), it has been found that strong ground motion is often larger at stations on the hanging wall compared with stations on the foot wall. Recently computational modelling (Boore & Zoback, 1974; Anderson & Luco, 1983b; Oglesby *et al.*, 1996, 2000a,b; Shi *et al.*, 1998) and foam rubber modelling (Brune, 1996; Brune & Anooshehpoor, 1999) studies have found differences between ground motion on the two sides of the fault. There are at least four proposed reasons for such a difference.

The most obvious reason, and also the easiest to incorporate into attenuation relations, is simply that hanging-wall stations are closer to most of the source than foot-wall stations with the same rupture distance, see Figure 2.1. Therefore stations on the hanging wall will receive more energy, and hence ground motions will be larger, than stations on the foot wall. Using distance to the surface projection of the fault or particularly a distance metric which is an ‘average’ distance to the source, such as equivalent hypocentral distance (see Section 8.4) would approximately model this effect. Abrahamson & Somerville (1996) believe this is the most important reason for the calculated differences. In Abrahamson & Somerville (1996) differences in ground motion between the hanging and foot walls are only seen for PGA and short periods (0.2 and $0.3\,\mathrm{s}$) and for longer periods the hanging-wall and foot-wall ground motions are similar. If the amount of energy reaching the station was the controlling factor in the difference between hanging-wall and foot-wall motions then longer periods ground motions would be the most different, because PGA and short-period ground motions are thought to be caused by small regions of isolated faulting and hence rupture distance is a good distance measure. Abrahamson & Somerville (1996) suggest that motions on the hanging wall and foot wall for longer periods are similar because directivity would affect both hanging wall and foot wall stations equally and such large increases would mask other differences. Anderson & Luco (1983b) find that differences in the ground motions on either side of the fault are slightly reduced by using rupture distance rather than distance to top of fault or distance to surface projection.

Another reasonably simple reason for the apparent difference, proposed by Oglesby *et al.* (1996, 2000a,b), is that the hanging wall wedge is much smaller than the foot wall wedge, near the free surface, so for the same forces on both sides of the fault the hanging wall will experience greater accelerations.

Brune (1996) has found that interface waves associated with the fault, propagate along the thrust plane and on reaching the free surface they temporarily decouple the overlying hanging wall from the foot wall thereby trapping energy in the wedge. This trapped energy breaks out at the toe of the thrust fault with a spectacular increase in motion.

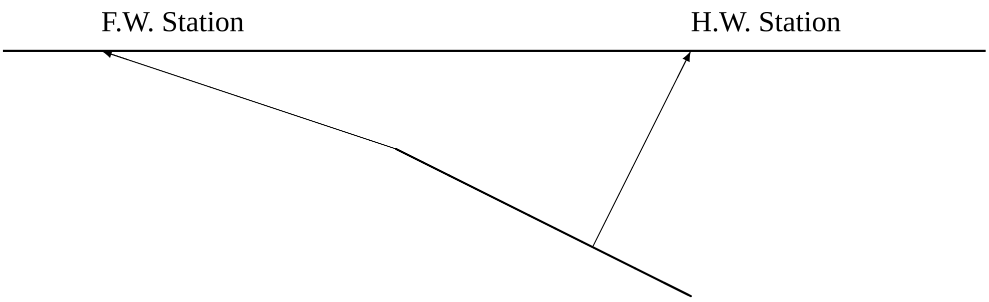

Fig. 2.1: Diagram showing how a hanging-wall station is closer to most of the source than a foot-wall station at the same rupture distance.

On either side of a fault the rock type may be different thus causing a variation in hanging wall and foot wall motions because of differences in the surface geology. These differences are covered in other sections in this chapter.

The main characteristics of the hanging wall effect are:

- All types of earthquakes exhibit an asymmetry in ground motions on either side of the fault (Anderson & Luco, 1983b; Oglesby *et al.*, 2000b).
- Differences between PGV and PGD on either side of the fault increases with decreasing dip (Oglesby *et al.*, 1996).
- Differences in PGV and PGD can reach a factor of over 2 for earthquakes with dip angles of 30° (Oglesby *et al.*, 1996) and both horizontal and vertical PGA and PGV can be about 3–5 times larger on the hanging wall for earthquakes with dip angles of 15 and 30° (Shi *et al.*, 1998). Abrahamson & Somerville (1996) find that for reverse and reverse-oblique earthquakes with $M \geq 6.0$ hanging wall stations at rupture distances 10–$20\,\mathrm{km}$ experience ground motions about 50% larger than the average ground motion for station at a similar distance but not on the hanging wall.
- For 'blind' faults (faults which do not reach the surface) the differences in PGV and, to a lesser extent, PGD between hanging and foot wall stations almost disappear even when the top of the fault is only at depths of 1 or $5\,\mathrm{km}$ (Oglesby *et al.*, 2000a). This is because the fault is farther from the free surface, thus the effect of the free surface is reduced, and also because buried faults are constrained not to move at both its edges whereas the up-dip edge of a fault which intersects the surface may move freely, greatly amplifying motion. However, the Northridge fault did not intersect the surface, in fact it terminated at a depth of about $5\,\mathrm{km}$

(Wald *et al.*, 1996), but differences were found between hanging-wall and foot-wall motions (Abrahamson & Somerville, 1996).

- Differences between hanging and foot wall motions decrease rapidly with distance away from the fault (Abrahamson & Somerville, 1996; Oglesby *et al.*, 2000a).

2.3 Travel-path factors

As the distance of the site from the source increases travel-path effects become more important (e.g. Hasegawa, 1975).

2.3.1 Types of wave and geometrical spreading

Different types of seismic wave (P, S, Lg, surface and others) travel at different velocities through the earth. Figure 2.2 shows well separated P, S and Lg waves on an uncorrected accelerogram.

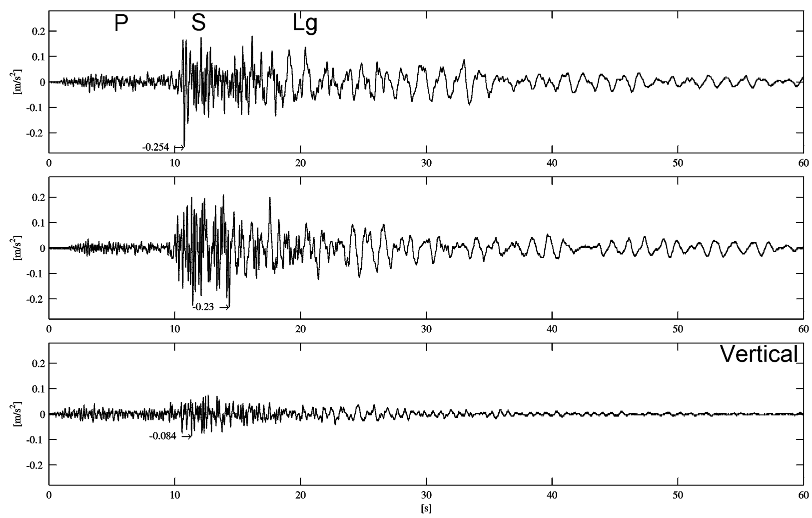

Fig. 2.2: Uncorrected accelerograms from Rieti recorded during Umbro-Marchigiano earthquake (26/9/1997 00:33:16, $M_s = 5.5$) at an epicentral distance of $66\,\mathrm{km}$ displaying separated P, S and Lg waves. On the vertical component record P-wave amplitudes are similar to those on the two horizontal components but S-wave amplitudes are much smaller, this is because S waves are predominately in the horizontal direction.

Theoretically these different types of waves have different rates of decay with distance. Thus body waves, e.g. P and S, decay at a rate r^{-1} and guided S waves and surface-wave phases, e.g. Lg, decay at a rate $r^{-1/2}$ (e.g. Westaway & Smith, 1989). So surface waves should dominate over body waves at distances greater than a few tens of kilometres. Joyner & Boore (1988) find that at distances of about $100\,\mathrm{km}$ and greater, the dominant phase is Lg, a superposition of multiply-reflected S waves trapped in the crust by supercritical reflection, which is an Airy phase and has a decay with distance of $r^{-5/6}$. This effect may be more noticeable for small earthquakes ($M < 6$) because they have simpler waveforms than larger earthquakes (Westaway & Smith, 1989). PGA is found to occur within the direct S-phase of the ground motion (Hanks & McGuire, 1981; Westaway & Smith, 1989) but at greater distances PGV and PGD, long-period strong-motion parameters, are sometimes found to be associated with surface waves (Berrill, 1975; Hanks & McGuire, 1981). Derived attenuation relations from alluvium recordings of the Landers earthquake show a low attenuation rate which is possibly due to the increasing dominance of surface waves compared with body waves at greater distances (Campbell & Bozorgnia, 1994a). However, the development of surface waves is not a simple phenomena and so the distance at which they become dominant is not easily predictable (Gregor, 1995).

Joyner & Boore (1988) state that although the amplitudes of Fourier spectra of surface-wave ground motion do decay as $r^{-1/2}$, time-domain amplitudes do not, because of dispersion. Thus well-dispersed surface waves have a time-domain amplitude decay of r^{-1}, and Airy phases, which correspond to stationary points on the group-velocity dispersion curve, have a decay of $r^{-5/6}$.

2.3.2 Scattering

Scattering contributes to the complexity of observed ground motions and occurs when seismic waves are reflected off inhomogeneities in the crust. It deflects some of the energy from the direct waves distributing it into the seismic coda.

Aki (1980) shows that scattering due to inhomogeneities distributed throughout the lithosphere could cause the apparent dependence of Q on frequency. For tectonically stable areas Q^{-1} seems to be constant or monotonically decreasing with frequency. For tectonically active areas Q^{-1} is characterised by a peak at frequencies around 0.5–$1\,\mathrm{Hz}$. The difference between stable and active areas disappears at about $25\,\mathrm{Hz}$.

2.3.3 Anelastic attenuation (absorption)

Waves attenuate due to internal friction, also called intrinsic attenuation, the effect of which can be summarised by the parameter Q. Strains and stresses occurring within a propagating wave can lead to irreversible changes in the crystal defect structure of the medium, and work may also be done on grain boundaries within the medium if adjacent material grains are not elastically bonded (Aki & Richards, 1980). The elastic energy is converted to heat. Such media are called anelastic because the configuration of material particles is to some extent dependent on the history of the applied stress.

Residuals with respect to azimuth from a derived attenuation relation for horizontal PGA of the Loma Prieta earthquake are examined by Campbell (1991). PGAs are on average 19% higher for azimuths between 320° and 350° and PGAs are an average of 29% lower for azimuths between 350° and 030° compared with the overall average, which are significant at the 90% confidence level. Similar results are found for rock records therefore the cause is probably not a site effect. It is found that the cause of these average differences is different attenuation rates in the two directions compared with the average, due in part to geological structure, and not source directivity or radiation pattern. There is a low attenuation rate for azimuths 320° to 350° because they are parallel to the San Andreas fault whereas travel paths to sites with azimuths between 350° and 030° cross several major fault zones and traverse the down-dropped basins of Santa Clara valley and San Francisco Bay, thus there is more scattering and anelastic attenuation.

Westaway & Smith (1989) find that geometric spreading is more important than crustal anelasticity particularly for large events in determining horizontal PGA for distances up to tens of kilometres from the source. For small earthquakes ($M < 5$) though PGA is associated with higher frequencies above $10\,\mathrm{Hz}$ so anelastic attenuation is more important.

Most studies assume that the value of Q is constant along the whole path of the wave from the source to the site. In fact Q is affected by: pressure, temperature, saturation state of the rock, frequency of the propagating wave and amplitude of propagating strain (Stewart *et al.*, 1983). All of these factors can be assumed to be constant along the path from shallow earthquakes except the amplitude of propagating strain which will vary considerably. Attenuation in rocks generally increases once a certain threshold strain, about 10^{-6}, has been reached and then increases linearly with strain (Stewart *et al.*, 1983). Stewart *et al.* (1983) suggest that this large strain attenuation is due to the frictional work loss from individual asperity contacts therefore large strain attenuation increases linearly with crack density.

Minster & Day (1986) propose this relationship for the local Q value: $Q^{-1}(\omega, \epsilon) = Q_a^{-1}(\omega) + \gamma\epsilon$, where Q_a is the small strain (anelastic) quality factor, γ is a constant for a particular type of rock (and found to be equal to about 3×10^3) and ϵ is the strain amplitude.

Fundamental-mode surface waves are confined to shallow layers and so are subject to greater anelastic attenuation than body waves (Joyner & Boore, 1988).

Arrival of critical reflections ('Moho bounce')

The layered structure of the Earth's crust means that the dependence of ground motion amplitudes on distance may not display a smooth decrease with distance due to the dominance of individual

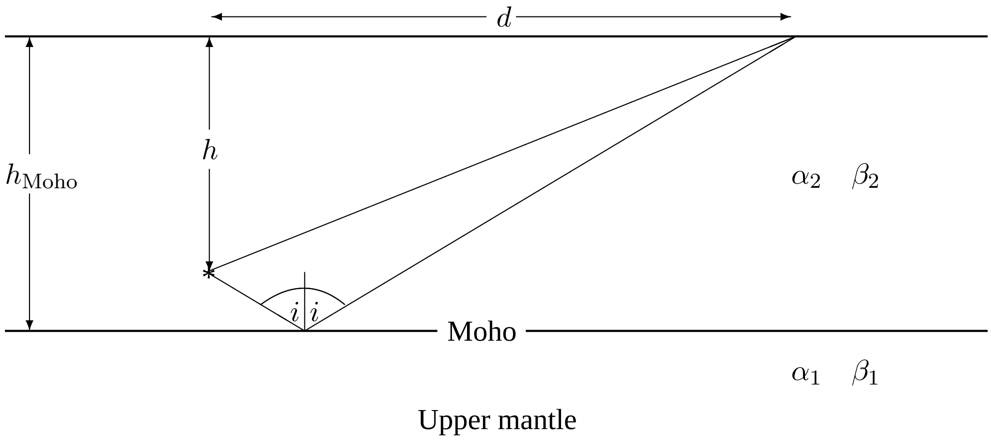

Fig. 2.3: Diagram showing minimum distance at which reflections off the Moho are possible. α_1 and α_2 are P-wave velocities, β_1 and β_2 are S-wave velocities, h_{Moho} is the depth of the Moho, h is the focal depth and d is the epicentral distance.

seismic phases over specific distance ranges. The most important discontinuity in the Earth for engineering seismology is that between the crust and the mantle called the Mohorovičić discontinuity (or Moho). It is at a depth of 20–30 km over most of the Earth. The change in wave velocity at such discontinuities results in the reflection of seismic waves which are incident at greater than the critical angle of incidence. The minimum distance at which critical reflections are possible is shown in Figure 2.3. This distance can be calculated using Snell's law. The critical angle of incidence, $i = \sin^{-1}(\alpha_2/\alpha_1)$, and the critical distance, $d = (2h_{\mathrm{Moho}} - h)\tan i$. For example, if $h = 14\,\mathrm{km}$, $h_{\mathrm{Moho}} = 25\,\mathrm{km}$, $\alpha_2 = 6.15\,\mathrm{kms}^{-1}$ and $\alpha_1 = 8.0\,\mathrm{kms}^{-1}$ then $i = 50^\circ$ and $d = 43\,\mathrm{km}$. However, more complicated velocity profiles occur in practice so the distance at which critical reflections become possible is more difficult to predict than with this simple model.

Critical reflections on strong motions have been increasingly thought of as being important since the Loma Prieta earthquake (18/10/1989) in which such reflections are thought to have been partly responsible for the large ground motions recorded in San Francisco. Somerville & Yoshimura (1990) find that the largest accelerations at each station further than $50\,\mathrm{km}$ from the source of the Loma Prieta earthquake coincides with the arrival time of the critical Moho reflections. The amplification due to the critical reflections at $80\,\mathrm{km}$ was equal to a factor of about 2 which is similar to the amplification due to soft soil. Campbell (1991) examines horizontal PGAs from the Loma Prieta earthquake recorded on 71 alluvial sites and finds that there is a zone of almost constant acceleration for seismogenic distances between 51 and $79\,\mathrm{km}$ which can be attributed to the arrival of critical reflections off the base of the crust. Chin & Aki (1991) calculate synthetic seismograms using a point source model of the Loma Prieta earthquake and the local velocity structure. For hypocentral distances less than about $30\,\mathrm{km}$ the direct S wave is associated with PGV, for distances between about 30 and $50\,\mathrm{km}$ the Conrad reflections are associated with PGV and for distances between 50 and $110\,\mathrm{km}$ the Moho reflections are associated with PGV. However, for hypocentral distances between 0 and $140\,\mathrm{km}$ these differences in wave types do not cause much deviation in a R^{-1} geometrical decay of PGA or spectral periods between 0.5 and $2\,\mathrm{s}$.

Similarly Campbell & Bozorgnia (1994a) suggest that the calculated low attenuation rate found for alluvium recordings of the Landers earthquake could be due to the arrival of critical reflections off the Moho.

The importance of critical reflections in maritime Canada and in central USA is investigated by Burger *et al.* (1987) using recorded and synthetic accelerograms. An examination of the horizontal pseudo-velocities at $1\,\mathrm{s}$ and 5% damping from eastern North American strong-motion records normalised to $m_{b,Lg} = 5$ shows that there is a decrease in amplitudes from 10 to $60\,\mathrm{km}$, constant amplitudes from 60 to $150\,\mathrm{km}$ and a further decrease for distances greater than $150\,\mathrm{km}$. Computed seismograms for the maritime Canada crustal structure (Moho at $25\,\mathrm{km}$) show constant amplitudes at distances between $100\,\mathrm{km}$ and $200\,\mathrm{km}$ whereas computed seismograms for the central USA crustal structure (Moho at $25\,\mathrm{km}$) exhibit constant amplitudes for distances between 60 and $150\,\mathrm{km}$. This difference occurs because the velocity contrast at the Moho is larger in the central USA model than in the maritime Canada model. Burger *et al.* (1987) also find that the most important phases on the San Onofre strong-motion record of the Borrego Mountain earthquake (9/4/1968, $M_w = 6.8$, focal depth $8\,\mathrm{km}$) are from crustal interfaces at 14 and $25\,\mathrm{km}$.

2.3.4 Basin effects

Variations of subsurface topography, particularly basins containing deep soils of lower shear-wave velocities than the surrounding region, can have a large effect on ground motions. Shallow low-velocity subsurface sediments overlying steeply sloping bedrock at the basin edges can generate surface waves which increase long-period ground motions.

One of the most commonly cited examples of where this effect occurs are the basins around Los Angeles. For example, Liu & Heaton (1984) examine ground accelerations and velocities from the San Fernando earthquake along three different profiles. A good correlation of the velocity waveforms with the topography of the deep (2–$5\,\mathrm{km}$) subsurface basins is found. Long-period surface waves (period about $5\,\mathrm{s}$) develop and are trapped in the San Fernando valley and cannot propagate through the Santa Monica mountains into the Los Angeles basin where surface waves again develop. These waves increase the duration of the ground motion and the PGVs in the basins compared with the mountains. Areas of little or no sediments (depth $< 1\,\mathrm{km}$) do not show clear surface waves. High frequencies, as measured by acceleration, are much less affected by the subsurface topography.

Strong ground motion from an earthquake (9/11/1974, $M_s = 7.2$) $100\,\mathrm{km}$ from Lima recorded at two sites (Instituto Geofísico del Peru and La Molina) is analysed by Zahradník & Hron (1987). The record from Instituto Geofísico del Peru, which is on horizontally homogenous layers, is deconvolved using an estimated shear-wave velocity profile. This is then used as the input to a number of models of the sediment-filled valley (about $200\,\mathrm{m}$ deep and $2000\,\mathrm{m}$ wide) underlying La Molina station. The time-history at La Molina is computed using a finite-difference scheme and a good match with the recorded motion is found. The importance of the two-dimensional structure of the underlying valley is shown by the prominent surface waves which are caused by a top layer of low-velocity sediments overlying the steeply sloping bedrock at the edge of the valley and at the local bedrock outcrop inside the valley.

King & Tucker (1984) report a number of experiments in the Chusal valley in Tajikistan, which is a $400\,\mathrm{m}$ wide by $700\,\mathrm{m}$ long (with a maximum depth of $60\,\mathrm{m}$) sediment-filled valley underlain by granitic rocks. The S-wave impedance between the rock and valley sediments is about $5.8 : 1$. All the recorded motions are weak (10^{-5} to $10^{-3}\,\mathrm{g}$). No dependence in the motions with distance along the valley was found. Across the valley though, large amplifications, up to a factor of 10, with respect to a rock site just outside the valley, were found by using smoothed Fourier amplitude spectral ratios. The period at which the peak amplifications occur depends on the width of the valley not just the vertical soil column beneath the site although the size of the amplification is related to the thickness of the sediments and hence its position. One-dimensional models are adequate for predicting amplification at the centre but are poor at edges. The azimuth of the incident waves is not important. Tucker & King (1984) find that the response of this valley for PGAs between 10^{-5} and $0.2\,\mathrm{g}$ is not dependent on amplitude of input motion.

Papageorgiou & Kim (1991) model the 2D response of a valley to the Caracas, Venezuela earthquake (29/7/1967, $M_w = 6.6$) to synthetic time-histories of SH waves. The asymmetric model of the NS cross-section of the valley has sediments with shear-wave velocity of $1000\,\mathrm{ms}^{-1}$ overlying rock with shear-wave velocity of $2300\,\mathrm{ms}^{-1}$ and is about $3.5\,\mathrm{km}$ wide and has a maximum depth of about $400\,\mathrm{m}$. Elastic rock amplification ratios across the valley are computed using the 2D model and a 1D model and it is found that the two ratios are similar although the 2D ratios are more variable and the amplifications are larger. For example, 1D models predict peak amplifications which decrease with increasing incidence angle whereas 2D models can predict increasing amplifications with increasing incidence angle. Incident SH waves induce Love waves which result from overcritical reflections at the inclined bottom of the sediments and propagate between the two edges of the valley. The steeper northern edge is the most efficient generator of such waves. It is found that PGA and PGD are not strongly affected by the valley response (only varying by a maximum of 1.5) but that PGV varies considerably across the valley (up to a factor of 3). Spectral accelerations in the period range 0.6 to $1.4\,\mathrm{s}$ are amplified by factors of up to 3 due to the valley response.

Results of many numerical simulations of valley response have been published, many of which use the method of Aki & Larner (1970). Two classes of parameters define a valley characteristics: geometrical and rheological and only the ratios between certain valley parameters, for example depth and width (h/D), are important for calculating the response of valleys therefore one numerical solution can be used for a number of different real valleys. The case of incident P and SV waves is more complex than incident SH waves and so few studies for incident P and SV waves have been conducted.

Bard & Bouchon (1980a) investigate the response of two types of sediment-filled valleys (one a one-cycle cosine shaped valley and one a plane layer closed on each side by a half-cycle cosine shaped interface) to Ricker wavelet incident waves using the Aki-Larner method. Love waves are generated at the valley edges which propagate across the valley and lead to large amplifications (up to a factor of 5.5) when they constructively interfere usually at the centre of the valley. This means that amplifications due to 1D models are only valid for the early part of the record. For deeper valleys the effect is similar but more energy is reflected by the valley's edges as the steepness of the interface increases and also the waveforms become more complex because of interference between up-and-down reflections and lateral Love waves. For the plane layer valley the largest amplitudes in deep basins are at the centre whereas for shallow basins the largest amplitudes are at the edges. The one-cycle cosine valley has much larger wave amplitudes for same depth-to-width ratio than the plane layer valley because the continuously increasing depth reinforces Love waves over all their travel towards the centre. However, the plane layer valley is better at trapping waves. For lower impedance contrasts the results are similar but less emphasised and Love waves are less well reflected hence some Love wave energy is transmitted into the rock outside the basin and can cause displacements outside the valley. Bard & Gariel (1986b) extend the Aki-Larner method to sediment valleys with inhomogeneous shear-wave velocities in the sedimentary layer. The transition between shallow and deep valley behaviours is much smoother.

Bard & Bouchon (1980b) use the Aki-Larner method to model the response of two types of valley: — one cosine-shaped and one flat bottomed — to low-frequency vertically incident P and SV waves of Ricker wavelet form. Incident P waves generate laterally propagating waves which are shown to be Rayleigh waves but the maximum amplitudes are almost always due to the direct signal or at most the first interface reflection. Incident SV waves also generate Rayleigh waves but whether the fundamental or first higher Rayleigh mode is predominately excited depends partly on the frequency and direction of the incident waves. The peak amplitudes are always due to Rayleigh waves localised in space and time. Even for low velocity contrasts surface waves still occur but they are smaller, because transmission between alluvial valley and underlying bedrock is greater, and the largest amplitudes always occur due to the direct signal. They can still be quite large, however, especially in the centre of the valley. For cosine-shaped valley Rayleigh waves are of higher amplitude because of a larger curved interface and so even for P waves, Rayleigh waves are more important. For SH the response becomes more complicated. For SV waves 'lateral' resonance due to trapping of horizontal propagating P waves inside the layer makes the valley behave grossly as a 1D resonator which implies a complicated reflection and refraction pattern at valley edges with P-SV conversions. The frequency of resonance depends on valley shape and velocity contrast and becomes more important as h/D increases.

The question of whether simplified models can be used to predict ground motion in sediment-filled valleys to incident plane SH waves is addressed by Bard & Gariel (1986a). One shallow valley and two deep valleys (one with large impedance contrast and one with a low impedance contrast), all with linearly increasing shear-wave velocity in the valley are modelled using: a) a 2D model including the change in shear-wave velocity in the sediment; b) a 2D model with an average shear-wave velocity in the sediment; c) a 1D model including the change in shear-wave velocity in the sediment; and d) a 1D model with an average shear-wave velocity in the sediment. It is found that the simplest model (d) underestimates PGA for all three valleys. For the shallow valley and the deep valley with low impedance contrast, PGA may be satisfactorily approximated by model c). However, for sediments with low damping the 2D effects become more important and so this conclusion may not hold. For embanked, high impedance contrast valleys the prevailing effects are geometrical so 2D models are needed.

An important study on the effect of sediment filled valleys on strong motion was conducted by Bard & Bouchon (1985) using the Aki-Larner technique to investigate the response of sine-shaped valleys to incident P, SV and SH waves. A comprehensive parameter study is conducted and it is found that there exists a critical shape ratio (shape ratio is $h/2w$, where $2w$ is the total width over which sediment thickness is more than half its maximum value) below which 1D resonance and lateral wave propagation dominates and above which 2D resonance occurs. Lateral (surface) waves are generated at valley edges regardless of shape ratio. When the valley is shallow these are well separated from vertical resonance because they arrive at the centre after the direct arrival. For deeper valleys these waves have wavelengths comparable to the valley width which results in lateral interferences. These combine with 1D vertical interferences and hence produce 2D resonance. These 2D resonances though are highly dependent on the frequency of the incident wave but because the amplifications are so great they will swamp the real earthquake signals. The critical shape ratio is given by: $(h/2w)_c = 0.65/\sqrt{C_v - 1}$ where C_v is the velocity contrast between the valley and the surrounding rock. From a simple model of a soft rectangular inclusion it is possible to derive an approximate formulae for fundamental frequency of the valley, to incident P, SH and SV waves, which is only dependent on shape ratio and 1D fundamental frequency. It is shown that fundamental frequencies and amplifications predicted using 1D and 2D theory are very different except for shallow valleys and amplifications can be underpredicted by up to 4 times by 1D theory.

The influence of the depth of the alluvial valley is investigated by Dravinski (1982) using a source method for a semi-elliptical valley subjected to incident plane harmonic waves. The shear-wave velocity of the homogeneous, linearly elastic, isotropic material in the valley is 80% of the shear-wave velocity of the surrounding half-space. Two shapes of valley are investigated: one shallow with a ratio of width to depth of 0.75 and one deep with a ratio of width to depth of 2.5, for two frequencies, Ω: ratio of width of valley to wavelength of incident wavefield of 0.4 and ratio of width of valley to wavelength of incident wavefield of 1.0 and one angle of incidence, $30°$. For SH-waves at $\Omega = 1$ the increase in sediment depth produces locally larger displacements. For $\Omega = 0.4$ the depth of valley has little effect and the displacement field does not vary much across the valley. For P waves even at $\Omega = 0.4$ the depth of the valley changes the surface motion pattern significantly; strong amplifications (up to about 2) occur at the edges of the shallow valley and smaller amplifications occur for the deep valley. For SV waves large local amplifications (factor of about 2) occur for the shallow valley and these amplifications decrease with increasing depth. Rayleigh waves are less important than the other types of wave and the shallow valley produces higher amplifications.

The closed-form analytical solution for the response of semi-cylindrical alluvial valleys to incident plane SH waves was found by Trifunac (1971a). It was found that as the incident wavelength decreases the effects of the valley increase and that large amplifications (not necessarily at the centre of the valley) are possible due to focussing of the waves through the discontinuity. Nearly-standing waves are generated. The amplification over the valley displays a complex pattern which increases with increasing frequency of incident waves and it also changes due to the angle of the incident waves. For incident wavelengths longer than 10 to 20 times the radius of the valley the effects of the valley are negligible. However, there are few known geological configurations with cross-sections resembling the semi-cylindrical valley and whose length is sufficiently great to permit 2D analysis. Wong & Trifunac (1974) find the analytical solution for the response of semi-elliptical alluvial valleys to incident plane SH waves. It was found that for $\omega H/V_s < \pi/2$, where ω is the frequency of the incident waves, H is the depth of the equivalent layer and V_s is the shear-wave velocity of the valley, that 1D theory could be used but for deeper valleys 1D and 2D predicted amplifications are much different. Similar results are obtained for sine-shaped and triangular cross sections by Sánchez-Sesma & Esquivel (1979).

Recently, Joyner (2000) has developed a way to incorporate basin effects into strong-motion attenuation relations based mainly on observations in the Los Angeles basin. Joyner (2000) finds that surface waves generated at basin edges by the conversion of S waves behave as through they are from a line source in a 2D medium and thus geometric spreading is zero. However, low-Q basin sediments produce significant anelastic attenuation. Thus the functional form used is:

$y = f(M, R_E) + c + bR_B$ where $f(M, R_E)$ is a general attenuation relation, R_E is distance from the source to the edge of the basin, R_B is distance from edge of basin to the recording site and c is a measure of coupling between incident body waves and surface waves in basin. It is found that surface waves are important for periods 3–$6\,\mathrm{s}$ and can lead to amplifications up to a factor of 3 over the predictions made by the general strong-motion equation not including basin effects.

2.4 Site (near-receiver) effects

The effect of local geological deposits on seismic waves is commonly frequency dependent and strongly influenced by their relative thicknesses and seismic velocities. Although it is usually thought that rock sites do not experience large amplification Rogers *et al.* (1984) find that the response of rock sites is highly variable and some sites can exhibit a strong response.

Idriss (1978) says '…the scatter in recorded peak accelerations on one site condition is comparable to any difference in peak accelerations that may exist because of site conditions' and '[w]hile such general functional relationships are theoretically possible, insufficient data and insufficient knowledge regarding the influence of each factor preclude the development of empirical relationships that contain all these factors.' Rogers *et al.* (1984) find a mean standard deviation of 1.38 in the spectral ratio of records from one site to a base rock site showing the level of predictability in site response.

Peak ground motion parameters may not always reflect the strong amplification effect at a site because the frequency of maximum incoming energy is not coincident with the resonant peak frequency of the site (Rogers *et al.*, 1984).

Faccioli & Resendiz (1976) concluded that '…for strong motions at relatively close distances from the source and under stable soil behaviour, the influence of local soil conditions is often not the most important factor'. If the soil is unstable, i.e. liquefaction is possible, or it contains weak interbedded layers which can liquefy then Faccioli & Resendiz (1976) state that '…the pattern of surface ground motion in the epicentral area of strong earthquakes could be governed by the dynamic behaviour of local soils to a larger extent than by source-mechanism and transmission-path characteristics.'

In a comparison of the amplifications due to local geological conditions Rogers *et al.* (1984) compare the amplification spectra derived using data from explosions and that found using San Fernando data which have different source and path conditions and find that source and path factors have about the same importance in defining the amplification.

Anderson & Brune (1991) state large vertical accelerations are a common feature of large earthquakes on thick sedimentary sequences, however, Suhadolc & Chiaruttini (1987) generate synthetic accelerograms for a variety of different crustal structures and find that vertical PGA is consistently *lower* than the horizontal PGA (a factor of between about 1.5 to 10) for crustal structures with sediments. For crusts with no sediments they find the vertical PGA is larger, by a factor of about 2, than the horizontal.

The water content of soils, which can have a seasonal variation, is an important factor in wave attenuation and ground amplification but there is a lack of evidence for its effect (Bolt, 1970).

2.4.1 High-frequency band-limitation of radiated field, $f_{\max}$

$f_{\max}$ refers to the frequency above by which there is little physically meaningful ground motion (Hanks, 1982).

Hanks (1982) examines one Oroville aftershock (16/8/1975, $M_L = 4.0$) and estimates (noting that this involves some subjective judgment) $f_{\max}$ at 9 stations all from similar hypocentral distances. It is found that those five on Pleistocene or younger, probably water-saturated, gravels and alluvium have $f_{\max} \sim 15\,\mathrm{Hz}$ while those on crystalline bedrock of Mesozoic age or on a thin layer of Tertiary gravels filling a pre-existing drainage in the crystalline rock have $f_{\max} \sim 20$–$30\,\mathrm{Hz}$. Similar $f_{\max}$ values are found for seven aftershock records from the same station showing that $f_{\max}$ is not a source parameter. Hanks (1982) suggests that $f_{\max}$ may be due to an abrupt increase in Q^{-1} in the near-surface layer.

Hanks (1982) states:

$$a_{\max} \sim \sqrt{f_{\max}}\sqrt{\ln(2f_{\max})} \quad \text{for:} \quad f_{\max} \gg 1/t_c$$

Liu & Helmberger (1983) find that at high frequencies (about 2–20 Hz), the Fourier acceleration spectrum of S waves, $a(f)$, decays exponentially in a majority of Californian accelerograms. A model of this decay is $a(f) = A_0\mathrm{e}^{-\pi\kappa f}$ for $f > f_E$. The spectral decay parameter, κ, is thought to be primarily a subsurface geological effect, due to attenuation within the earth, because it is only a weak function of distance and it seems to be smaller on rock sites than on sites with less competent geology.

2.4.2 Impedance contrast amplification

The energy contained in a seismic wave is proportional to $\rho V A^2$ where A is wave amplitude, V is wave velocity and ρ is density. Therefore when a wave is totally transmitted from one material to another (Joyner *et al.*, 1981):

$$A_2 = A_1\sqrt{\frac{\rho_1 V_1}{\rho_2 V_2}}\sqrt{\frac{\cos i_1}{\cos i_2}}$$

where subscript 1 refers to properties of the underlying medium and subscript 2 refers to properties of the surface medium, i is the angle of incidence of the waves and ρV is the impedance of the material. This equation is true only when waves are totally transmitted between two media, such as the case of high-frequency energy passing through a velocity gradient (with no attenuation). At lower frequencies, some energy will be reflected away from the gradient, reducing the amount of transmitted wave energy. At a major velocity discontinuity significant energy is always reflected, and this equation is never applicable. Thus, simple calculations of seismic wave amplifications based on impedance contrasts are only valid in very special circumstances, where material properties vary smoothly and only relatively high frequencies are considered. Joyner & Boore (1988) believe that site amplification due to impedance contrast is the most common type of amplification. When the angle of incidence in the underlying medium is not large $\cos i_1 \approx 1$ and $\cos i_2 \approx 1$ and $\sqrt{\frac{\cos i_1}{\cos i_2}}$ can be neglected (Joyner *et al.*, 1981). Joyner *et al.* (1981) find that this approximation is reasonably good at predicting the observed amplification between the ground motion recorded on a Franciscan rock site, Gilroy #1, and a Quaternary alluvium site, Gilroy #2, during the Coyote Lake earthquake (6/8/1979, $M_L = 5.9$) using a reference depth of one quarter wavelength. Joyner *et al.* (1981) believe this amplification mechanism is most important for the Gilroy #2 record because the velocity trace is simple and so resonant amplification is not likely because this requires multiple reflections in the layer.

2.4.3 Resonant amplification

When a vertical P or SH wave is incident on an undamped surface layer (medium 2) of depth, H, overlying a half-space (medium 1) then the amplification due to multiple reflections within the surface layer creating modes with well-defined resonant frequencies is given by (Shearer & Orcutt, 1987):

$$\frac{A_2}{A_1} = \frac{\rho_1 V_1}{\rho_2 V_2}$$

which occurs at periods, T, given by:

$$T = \frac{4H}{(2n-1)V_2} \quad \text{with} \quad n = 1, \ldots$$

This type of amplification is believed by Joyner & Boore (1988) to be less important than impedance contrast amplification.

Shearer & Orcutt (1987) believe that more complicated structures typical of the real earth are unlikely to lend themselves to simple analyses because the simple equations for prediction of amplifications fail for some of their simple examples.

2.4.4 Focussing

There are two important focussing mechanisms that result in variations in strong ground motion. The first of these occurs when the geometry of the ground surface and substrata focus the rays by reflection or refraction at a curved interface. The second occurs in smoothly inhomogeneous media where the rays are continuously refracted and appear as smooth curves. Jackson (1971) states that in nonuniform or distorted strata focussing may be more effective than resonance in amplifying ground motion.

One of first studies on the importance of the focussing effects of substrata was by Jackson (1971) who examines qualitatively the effect of three different types of nonuniform substrata on ground motion. A simple model of Skopje, former Yugoslavia, is used to examine whether a steep increase in the depth of the alluvium layer was a contributing factor to the anomalously high damage which occurred in a small part of the city due to the earthquake of 26/7/1963. The model showed that this variation in alluvium layer depth helps explain the high damage zone. Variations in the angle of incidence and the velocity parameters of the alluvium layer do not significantly affect the focussing.

Langston & Lee (1983) use a 3D ray-tracing algorithm for plane SH waves with frequencies of $20\,\mathrm{Hz}$ and 2D models of the Duwamish river valley (central Seattle), where postglacial unconsolidated sediment fill a glacially scoured channel 1 to $2\,\mathrm{km}$ wide and at most $100\,\mathrm{m}$ deep. These sediments overlie a complex of compacted preconsolidated Pleistocene sediments. It is found that the curvature of the valley can cause extreme amplification (factors up to 12) of the fourth and fifth S reverberations due to accumulated geometrical spreading effect of several reflections off the centre of the valley. If the basin is too shallow with insufficient curvature then focussing does not occur. Large changes can occur over very short distances (about $25\,\mathrm{m}$ can lead to tripling of amplitudes). Langston & Lee (1983) conclude that focussing is undoubtedly very complex and is strongly dependent on: back azimuth of incident waves, character of the velocity gradients within the structure, scattering from boundaries and scattering from deeper structures, and they note that anelasticity of media could significantly reduce amplifications and that amplifications of approximately two are the maximum that occurs in practice.

37 records from the Lotung Large Scale Seismic Test Array in Taiwan of a $M_L = 6.5$ earthquake were examined by Wen *et al.* (1992). PGAs vary between $0.09\,\mathrm{g}$ and $0.21\,\mathrm{g}$ over the array where the largest distance between two stations is only $4\,\mathrm{km}$. This scatter along with the significant change in wave propagation direction and velocity over the array is attributed to geometrical focussing effects in the 3D basin.

Joyner *et al.* (1981) believe that focussing, due to concave curvature of bedrock, may explain the underprediction (1.25 in PGA and 1.8 in PGV) of the observed ground, calculated (using linear and non-linear models) at Gilroy #2 (Quaternary alluvium site) given the motion at Gilroy #1 (Franciscan rock site).

The possible importance of focussing due to the low-velocity zones surrounding faults is highlighted by Cormier & Beroza (1987). They suggest such focussing could partially explain the five-fold increase in the recorded PGVs at Gilroy #6 (within fault zone) compared with Gilroy #7 (outside fault zone), which are only $4\,\mathrm{km}$ apart and are both hard rock sites, during the Morgan Hill earthquake (24/4/1984). It is found that the rays from the fault are bent due to the low-velocity fault zone and so the ground motion is greater in the fault normal direction than in the laterally homogenous case. Also the lateral heterogeneity strongly affects arrival time, amplitude and polarity of phases recorded at stations within a 2–$3\,\mathrm{km}$ zone centred on the fault trace.

A sedimentary basin, concave upwards, can have a lens-like effect on high-frequency ground motion (1–$30\,\mathrm{Hz}$) collecting and focussing seismic energy and thus leading to local amplifications in isolated pockets where the caustics intersect the surface (Rial, 1984). Such amplitude enhancement may be softened by diffraction, attenuation, medium inhomogeneities and non-linear soil response but caustics are robust features of the wavefield so changes in source location, basin shape and refraction indicies have little influence on their location and strength (Rial, 1984). Only rough basin parameters are required to predict their locations. The areas of high levels of damage in the Caracas earthquake in 1967 matched the predicted areas where focussing would occur for the basin underlying Caracas (Rial, 1984). Rial *et al.* (1986) interpret the extremely large high-frequency accelerations (vertical $\mathrm{PGA} = 1.74\,\mathrm{g}$) at El Centro #6 during the Imperial Valley earthquake (15/10/1979) as caused by the focussing of waves through a wedge-like structure between Imperial Valley and Brawley faults.

Sites on media having strong lateral heterogeneities in seismic velocity, such as folded sedimentary rocks, like the Coalinga anticline (California), can show strong spatial incoherence due to multipathing, caustics and shadows, however, this incoherence does not show a large dependence on station separation or wave frequency (Somerville *et al.*, 1991b). Somerville *et al.* (1991b) use a simplified model of the Los Angeles basin to investigate this phenomenon and find that some arrays within the basin show large spatial incoherence amongst the records whereas the records from other arrays within the basin do not.

2.4.5 Near-site scattering

Sites on flat-lying alluvial sequences, such as Imperial Valley (California) and Lotung (Taiwan), show spatial incoherence that increases smoothly as a function of station separation and wave frequency showing the importance of wave scattering in an otherwise laterally homogeneous seismic velocity structure (Somerville *et al.*, 1991b). The coherence, C, due to this effect can be modelled by the simple function: $C = \exp((-a - b\omega^2)R)$ where ω is the frequency of the waves and R is the separation distance.

2.4.6 Anelastic attenuation

The amplitude of ground motion at sites on thick deposits of young, low-Q, sedimentary rocks will be strongly attenuated at all frequencies $f \gtrsim Q\beta/\pi h$, where Q, β and h are, respectively, the quality factor, shear-wave velocity and thickness of the sedimentary layer, than at sites with little or no such sedimentary cover (Seekins & Hanks, 1978).

Seekins & Hanks (1978) find for the Oroville sequence ($3 \leq M_L \leq 5$) that the PGAs recorded on thin ($< 50\,\mathrm{m}$ thick) Tertiary gravel deposits overlying crystalline basement or on the crystalline basement are higher than those recorded on several hundred metres or more of sedimentary rocks. This finding is attributed to the higher anelastic attenuation of high-frequency ($\gtrsim 10\,\mathrm{Hz}$) ground motion under the sedimentary rock sites. It is also found that the rate of increase of PGA with increasing magnitude is larger for sites on sedimentary rock as compared with the bedrock PGAs which may be due to the frequency of the PGA decreasing with increasing magnitude so that anelastic attenuation is less important.

2.4.7 Non-linear soil behaviour

In the near field the strains generated by earthquakes can be large, of the order of 10^{-4} to 10^{-3} (assuming PGVs of between $10\,\mathrm{cms}^{-1}$ and $100\,\mathrm{cms}^{-1}$ and a wave velocity of $1\,\mathrm{kms}^{-1}$), for example see Berrill (1975). These strains reduce the shear modulus (and consequently the shear-wave velocity) and increase the damping ratio (e.g. Seed & Idriss, 1969; Hardin & Drnevich, 1972). Such non-linear behaviour of soils may explain the difference between expected high amplifications due to site effects and the lower amplifications recorded in large earthquakes (Seed & Idriss, 1969).

Chin & Aki (1991) simulate strong-motion records from the Loma Prieta earthquake. For hypocentral distances less than $50\,\mathrm{km}$ the predicted PGA on soil is overestimated and the predicted PGA on rock is underestimated. This difference is systematic for all stations within $50\,\mathrm{km}$ so it is not due to the radiation pattern, near-source structure or topography but is thought to show that the soil sites behave non-linearly for PGA larger than 0.1–$0.3\,\mathrm{g}$ [$1\,\mathrm{ms}^{-2}$–$3\,\mathrm{ms}^{-2}$] and so the amplification due to the sediment layers is not as great as it is for weak motion.

Records from different sizes of earthquakes from two rock and soil station pairs which are within $2.5\,\mathrm{km}$ of each other are investigated by Darragh & Shakal (1991) using the ratio of smoothed Fourier amplitude spectra of a $10\,\mathrm{s}$ time-window that includes the direct S-wave arrival. The first pair is Treasure Island (manmade island of $11\,\mathrm{m}$ of hydraulic fill over sand and bay mud which underwent liquefaction in the Loma Prieta earthquake) and Yerba Buena Island (Franciscan sandstone and shale) which recorded the Loma Prieta mainshock ($M_L = 7.0$) at about $100\,\mathrm{km}$ and four aftershocks (with M_L between 3.3 and 4.3). Amplification is found at Treasure Island for periods between about 0.14 and $2\,\mathrm{s}$ for all five pairs of records but at about $1\,\mathrm{s}$ the amplification decreases from about a factor of 25 to a factor of about 4 as the amplitude of the input motion increases. Also predominant peaks in the amplification spectra at 0.5 and $1\,\mathrm{s}$ for the weak motion are absent in the spectrum from the mainshock; so the behaviour of the site is non-linear. The second pair is Gilroy #2 (alluvial-fan deposits) and Gilroy #1 (moderately weathered sandstone at surface with thin beds of shale at depth) which recorded the Coyote Lake ($M_L = 5.9$), Morgan Hill ($M_L = 6.1$), Loma Prieta ($M_L = 7.0$) mainshocks and 13 aftershocks ($4.1 \leq M_L \leq 5.4$). Significant amplification at Gilroy #2 is found between about 0.5 and $2\,\mathrm{s}$ which does not depend on the amplitude of the input motion. A significant peak (factor of about 6) at $0.4\,\mathrm{s}$ in the amplification spectra of the aftershock records is absent in the records from the stronger earthquakes. Non-linear behaviour therefore possibly occurs for this site but it is not as clear as for the soft soil-rock pair.

Field *et al.* (1997) compare recordings from 184 aftershocks ($3.0 \leq M \leq 5.6$) of the Northridge (17/1/1994) earthquake with records from the main shock at 21 sites including 15 alluvial sites. A generalised inversion for source, path and site effects using the shear-wave Fourier amplitude spectrum shows that during the aftershocks the amplification at the alluvial sites is about 1.4 at a period of $0.1\,\mathrm{s}$, about 2.5 at a period of $0.3\,\mathrm{s}$ and about 3.1 at a period of $1\,\mathrm{s}$, whereas for the mainshock the amplification is only about 0.8 at $0.1\,\mathrm{s}$, about 1.3 at $0.3\,\mathrm{s}$ and about 1.9 at $1\,\mathrm{s}$. These differences are significant at the 99% confidence level between 0.2 and $1.3\,\mathrm{s}$.

Joyner *et al.* (1981) find no evidence for non-linear behaviour in the Quaternary alluvium underlying Gilroy #2 during the Coyote Lake earthquake ($M_L = 5.9$) even though $\mathrm{PGA} = 0.25\,\mathrm{g}[2.5\,\mathrm{ms}^{-2}]$ and $\mathrm{PGV} = 30\,\mathrm{cms}^{-1}$.

Berrill (1975) estimates the maximum strains measured at stations which recorded the San Fernando earthquake from PGDs and the period of the associated waves. For a few of the closest stations to the hypocentre these strains are larger than the strain at which non-linear effects could be expected to begin but no significant differences between the attenuation at these stations and those where strains are lower are seen. From this result he concludes that ‘material nonlinearity may be very important close to the focus, at hypocentral distances of $20\,\mathrm{km}$ or more it does not seem to be a major factor’.

2.4.8 Pore water pressure

During an earthquake soil is subjected to excess pore water pressures which decrease the effective confining stresses resulting in a reduction of stiffness of the deposits, thereby lengthening the predominant period of ground surface motion. As the excess pore water pressures dissipate the strength increases and the predominant period shortens. Seismic pore water pressures can have a large effect on response of deposits of saturated sands but the effect on the ground surface response of clay deposits is relatively small (Zorapapel & Vucetic, 1994). Zorapapel & Vucetic (1994) study the records from the bottom of sand deposits, the ground surface and of pore water pressure from the Wildlife Liquefaction Array during two earthquakes (24/11/1987, $M_s = 6.2$, 6.6). There was no lengthening of the predominant period for the first earthquake, when liquefaction did not occur. However, for the second earthquake, when liquefaction did occur, there is clear lengthening of horizontal and vertical predominant period even for moderate excess pore water pressures. Excess pore water pressures can lead to significant increases (factors of 3–6) in long-period ground motions and also impose a possible limit on PGA of about $0.2\,\mathrm{g}$.

2.4.9 Directional site resonance

S-wave geophone recordings of ten aftershocks of the Loma Prieta earthquake, with different hypocentres and focal mechanisms, from the ZAYA six station array are examined by Bonamassa *et al.* (1991). Four of the six sites show a frequency-dependent preferred direction of motion which is not easy to correlate with topography or surface geology but could be related to deeper geological features. This preferred direction of motion can change within $25\,\mathrm{m}$. Strong-motion records from nine out of 11 stations, on a wide range of surficial geology, which recorded the Whittier Narrows mainshock and aftershock also show evidence for a preferred direction of motion which does not agree with the directions predicted by the focal mechanisms of the two earthquakes.

2.4.10 Topography

The topography of the area around a recording station can have a large effect on the ground motion. However, even though there has been much analytical, numerical, observational and experimental work in the past thirty years on topographic effects it is still difficult to give quantitative results concerning the effects. The basic mechanisms in causing topographic effects are focussing and scattering of the incident wavefields.

The main qualitative characteristics of the effect of topography are listed below.

- Topographic features only affect waves with wavelengths of the order of the characteristic length of the feature (although waves with wavelengths 6 times the length of the feature can be significantly affected (Boore, 1972)) so short-period ($T \lesssim 1\,\mathrm{s}$) ground motions are most affected by topographic features.
- Amplification usually occurs on convex surfaces, for example mountain tops and valley edges.

- Reduction in amplitudes usually occurs on concave surfaces, for example canyon bottoms.
- Reduction in amplitudes can occur at the base of hills and ridges.
- Certain parts of the feature can be in a shadow zone, where the incident waves cannot reach, causing a reduction in amplitudes. Rayleigh waves can be almost completely blocked by canyons (Kawase, 1988).
- Steeper hills cause higher amplifications at the top and greater reductions at the base than shallower hills.
- Surface motion at a particular site depends on topographic features of a wide area around the site.
- SV waves incident on slopes can generate Rayleigh waves.
- Amplification is usually larger for horizontal components than it is for vertical components.
- Changes in angle of incidence of the incident waves can have a dramatic effect.
- Large variations in the amplitude and phase of ground motion are possible over short distances.
- Type of incident wave does not seriously affect the amplifications in terms of Fourier amplitude spectra (Boore, 1972).

The extensive damage to four and five storey buildings in the Canal Beagle area of Viña del Mar from the Chile earthquake (3/3/1985, $M_s = 7.8$) was interpreted by Çelebi (1987) as an example of topographical amplification. Several aftershocks were recorded at sites on the ridges where the damage occurred and on reference sites. The ridges are about 20–30 m high and about 100–150 m wide and are composed of decomposed granite and alluvial deposits. Repeatable strong amplifications (up to a factor of 10–20 times for smoothed Fourier amplitude spectra) at periods of about $0.125\,\mathrm{s}$ and 0.25–0.5 s are found on the ridges compared with the canyon sites.

Çelebi (1991) gives some further examples of measured topographical amplification during other earthquakes. After the Coalinga earthquake (2/5/1983, $M_s = 6.5$) four stations were set up on an anticline (two on the top and two in gulleys on either side). The difference in height between the gulley and the top was about $30\,\mathrm{m}$ and the instruments were about 100–150 m apart. An analysis of several aftershocks showed amplifications up to a factor of 10 at periods $0.13\,\mathrm{s}$ and 0.17–1 s. Aftershocks of the Superstition Hill earthquake (24/11/1987, $M_s = 6.6$) recorded by a temporary array of three stations (one on top of Superstition Mountain and one on either flank) showed amplifications of up to 20 times for periods 0.08–0.5 s even though the mountain only has a slope of 6%.

A small area of anomalously high damage, on the southern slope of Puente Hills, caused by the Whittier Narrows earthquake (1/10/1987, $M_L = 5.9$) was interpreted by Kawase & Aki (1990) as due to the critical incidence of SV waves at a topographical irregularity. The hill is roughly a circular arc with height about $0.3\,\mathrm{km}$ and width $2.4\,\mathrm{km}$ and the incident waves are from four increasingly complex sources. For all types of sources, amplifications up to about 1.9, over the flat surface motion, were found on the far edge of the hill and reductions up to about a factor of 4, were found on the near edge of the hill. The largest amplification occurs at a period of $0.3\,\mathrm{s}$. Boore (1972) reports evidence of topography amplifying vertical ground motions.

Amplifications due to topography, for weak motion, have been also observed by, amongst others Davis & West (1973), Rogers *et al.* (1974), Griffiths & Bollinger (1979) and Pedersen *et al.* (1994). However, one thing which is common to all such studies is that there is much variability in the amplifications recorded at the same location and that the results do not always match numerical solutions for simple topographical features. Geli *et al.* (1988) find that numerical simulations often underestimate observed effects because the models used are not complex enough.

Studies on the effect of topography on strong ground motion are almost entirely based on numerical simulations for simple topographical features, such as: semi-elliptical or triangular canyons or hills, and for simple incident waves such as plane SH. There are a number of computational methods for assessing the effect of topography on ground motion, see for example Sánchez-Sesma (1987) and Geli *et al.* (1988).

Numerical studies are usually based on non-dimensional variables, such as the shape ratio (h/l where h is the height of the feature and l is half the width of the feature), therefore the results can be scaled for predictions on any size of hill or depression. However, numerical studies have been conducted using a few characteristic models of topographic features which means they are unlikely to lead to detailed predictions of the effect of arbitrary features (Boore, 1972).

There are few studies using recorded strong motion which demonstrate the effect of topography. However, there are two sites, Pacoima Dam and Tarzana, where topographical amplification has been suggested as the cause of the extremely large ground motions recorded.

During the San Fernando earthquake (9/2/1971, $M_w = 6.6$) recorded ground motions at Pacoima Dam (PGA of $1.1\,\mathrm{g}[11\,\mathrm{ms}^{-2}]$) were much higher had been recorded anywhere before. The local topography around the Pacoima Dam instrument is a sharp ridge but this ridge is in a steep canyon, the effect of this local and regional topography (the ridge is thought to amplify the motion and the canyon to reduce it) makes estimating the importance of the topography extremely difficult.

Using a finite difference method for incident SH waves Boore (1973) finds that the ridge amplifies the short-period range (0.1 to $0.3\,\mathrm{s}$) by about two times but for longer periods the canyon becomes more important and could slightly reduce the motions. Deconvolving the effect of the topography from the recorded ground motion the PGA decreases to $0.73\,\mathrm{g}[7\,\mathrm{ms}^{-2}]$ but the PGV does not change by much.

A much more complicated 3D finite element model of the surrounding topography, including the dam itself, was used by Reimer *et al.* (1973) to construct the transfer function of the topographic amplification. The site response was then deconvolved from the record. The PGA of the record decreased to $0.4\,\mathrm{g}[4\,\mathrm{ms}^{-2}]$ and similarly large reductions in the spectral accelerations of short periods ($T < 0.5\,\mathrm{s}$) are found but the long-period ($T > 1\,\mathrm{s}$) spectral accelerations are not significantly changed.

Bouchon (1973) investigates the effect of topography on the Pacoima Dam strong-motion record using the Aki-Larner method. The local ridge topography dominates for short periods ($\sim 0.1\,\mathrm{s}$) and leads to an increase of about 30–50% relative to flat surface, thus the PGA is reduced to less than $1\,\mathrm{g}$. For longer periods ($\sim 0.4\,\mathrm{s}$) the regional canyon topography becomes important and it is difficult to decide its effect.

Trifunac (1973) roughly models the Pacoima canyon by semi-cylindrical surface. It is found that first few seconds of motion are reduced by 20–30% due to the topography and last part of record are amplified by a similar amount and so overall there is about a 10–20% difference due to topography.

Anooshehpoor & Brune (1989) came to the exact opposite conclusion to most authors by using a highly detailed 3D foam rubber model of the topography surrounding Pacoima Dam including the dam itself. It was found that the amplifications due to the topography are highly dependent on the angle of the incident SH waves, for some angles the amplitudes were reduced (due to shadowing from the canyon) while for others, amplitudes are increased by up to 130% for frequencies about $6\,\mathrm{Hz}$ (due to the ridge). Also the S14W component was much less affected by the topography than was the N74W component which is roughly normal to the ridge axis. For frequencies greater than about $9\,\mathrm{Hz}$ significant reduction in amplitudes is predicted. No clear evidence that topographic amplification was significant is found and they conclude that if anything the recorded PGA could be about 10% *less* than the PGA at the same site but without the surrounding topography.

During both the Northridge (17/1/1994, $M_s = 6.8$) and the Whittier Narrows (1/10/1987, $M_s = 5.9$) earthquakes the station on a small hill at Tarzana recorded unexpectedly high ground motions. During the Northridge earthquake the PGA recorded was $1.78\,\mathrm{g}[17.5\,\mathrm{ms}^{-2}]$. The hill at Tarzana is about $18\,\mathrm{m}$ high, more than $500\,\mathrm{m}$ long and about $130\,\mathrm{m}$ wide.

Bouchon & Barker (1996) construct a 3D numerical model of the small hill at Tarzana. For vertically incident S waves large amplifications were found despite the gentleness of the slope; the hill has a resonant period of about $0.3\,\mathrm{s}$ and experiences an amplification on the top of the hill of about 45%. As the input frequency increases the areas of greatest ground motion amplification (up to 100% at a period of $0.07\,\mathrm{s}$) are the north and south edges especially at the steepest parts of the hill. Higher amplifications occur when the incident waves are polarised transverse to the length of the hill. It is concluded that the accelerations at Tarzana during the Northridge earthquake were amplified by between 30 and 40%.

Spudich *et al.* (1996a) deployed a dense array of geophones on Tarzana hill to record aftershocks of the Northridge earthquake and found that most of the records are polarized in a direction roughly transverse to the hill. The transverse resonant period is about $0.3\,\mathrm{s}$ and the maximum amplification is a factor of about 4.5 although this is in a narrow band (0.2–$0.3\,\mathrm{s}$). The effect of the irregular ground is correlated with the effect of the internal structure of the hill. Although the largest amplification due to topography is measured and is predicted to occur transverse to the hill; the largest ground motions during the Northridge earthquake were *parallel* to the hill so its response is complicated.

2.4.11 Structure surrounding instrument

The desired motion to be predicted using attenuation relations is the free-field ground motion. However, this is not necessarily the input into the structure because the proposed structure will affect the incident ground motion.

Soil-structure interaction (SSI)

The structure in which the accelerometer is located affects the recorded ground motion. There are two types of soil-structure interaction (SSI):

Inertial interaction Waves are assumed to be propagating vertically upward causing all points on the surface over an area greater than the foundation of any proposed structure to move in unison. Consequently a massless foundation on the ground surface would move with this free-field ground motion. The addition of a structure to the massless foundation changes this free-field motion due to the stresses generated by the motion of the structure and exerted on the foundation. This leads to an amplification of the foundation-level motion relative to the free-field motion.

Kinematic interaction There are three types of kinematic interaction which tend to decrease the foundation-level motions relative to the free-field motion, an effect which tends to get greater with increasing frequency (Stewart, 2000).

1. For foundations with dimensions, in the direction of propagation of a wave, that are of the order of a wavelength or greater then there is a differential motion of the ground over the shape of the foundation and a rigid foundation would move with some average value of the ground displacement which can be much less than the free-field motion. This is known as base-slab averaging.

2. Embedded foundations are subject to ground motion filtering associated with variation in ground motion with depth.

3. Seismic waves are scattered off corners of the foundation.

Most recent strong-motion studies only use records from sites described as 'free-field' because the structure containing the instrument is thought not to have affected the ground motions in the period range of interest unlike records from larger structures such as normal buildings. Small purpose-built instrument shelters away from other structures are used to provide protection for the instruments recording 'free-field' ground motions and Crouse *et al.* (1984) believe that nearly all accelerograms recorded in such shelters are not significantly influenced by the interaction between the shelter and the ground. There are two main reasons for this view:

1. the base dimensions of such stations (usually less than $2\,\mathrm{m}$) are much smaller than the wavelengths of the seismic waves (for frequencies of $< 15\,\mathrm{Hz}$ and a near-surface shear-wave velocity of $> 150\,\mathrm{ms}^{-1}$ these wavelengths are $> 10\,\mathrm{m}$);

2. the natural frequency of the station-ground system (usually $> 15\,\mathrm{Hz}$) is greater than the frequencies of the seismic waves (usually $< 15\,\mathrm{Hz}$).

There have been a number of detailed studies of SSI for typical instrument shelters which confirm these conclusions.

Two typical designs of accelerograph instrument shelters are investigated by Bycroft (1978) who finds that significant magnifications up to a factor of about 1.6 are possible for high frequencies ($> 20\,\mathrm{Hz}$) from such installations if they are on soft soil (shear-wave velocity of about $120\,\mathrm{ms}^{-1}$) due the inertial SSI. For kinematic SSI and the special case of horizontally incident SH-waves an attenuation of 0.7 is found for one of the typical instrument shelters at $20\,\mathrm{Hz}$ and much larger attenuations for bigger structures. Approximate equations for calculating the possible amplification due to the first type of SSI and the possible attenuation due to the second type of SSI for horizontally incident waves are also provided.

Crouse *et al.* (1984) thoroughly investigate the dynamic behaviour of a wooden instrument shelter (which is $1.5\,\mathrm{m}$ high) at Jenkinsville, South Carolina, which is mounted on a concrete pad of dimensions $1.20 \times 1.20 \times 0.6\,\mathrm{m}$ and its probable effect on the recorded ground motion. The site is on a layer of Saprolite soil about $18\,\mathrm{m}$ thick, with a shear-wave velocity of about $150\,\mathrm{m}$, overlying granite. The soil-pad-hut system has natural frequencies of $11\,\mathrm{Hz}$ (damping 0.06) and $48\,\mathrm{Hz}$ (damping 0.20) in one horizontal direction and $17\,\mathrm{Hz}$ (damping 0.04) and $50\,\mathrm{Hz}$ (damping 0.21) in the perpendicular horizontal direction. The computed true free-field ground motions show a reduction in PGA from $0.36\,\mathrm{g}$ (recorded) to $0.27\,\mathrm{g}$ and spectral accelerations for 5% damping reduced by up to 38% for periods $< 0.03\,\mathrm{s}$ but also a significant reduction (7–38%) in spectral acceleration for longer periods (up to $1\,\mathrm{s}$).

Four Californian strong-motion stations on soft to moderately stiff alluvial deposits (shear-wave velocities about 100–$200\,\mathrm{ms}^{-1}$ in top $10\,\mathrm{m}$) are analysed by Crouse & Hushmand (1989). Three of the stations (Parkfield Fault Zone 3, Cholame 1E and El Centro #6) are small (about $1.2 \times 1.2\,\mathrm{m}$) reinforced concrete pads covered with lightweight fibreglass huts. From impulse response and forced harmonic experiments resonant frequencies of these stations were found to be about 25–$40\,\mathrm{Hz}$ and the peak amplifications (factors of 1.25–1.4) were for periods 0.03–$0.05\,\mathrm{s}$; for periods greater than $0.07\,\mathrm{s}$ no amplification was found. One station (El Centro Differential Array) was a heavy masonry block structure with a plywood roof on a concrete foundation $2.44 \times 2.44\,\mathrm{m}$. The resonant frequency of the station was found to be $12\,\mathrm{Hz}$ with: significant amplification (factor of 1.5) at a period of $0.08\,\mathrm{s}$; reductions in amplitudes for periods 0.04–$0.07\,\mathrm{s}$; and large amplification (factor of 2.3) at $0.03\,\mathrm{s}$. Therefore the records are only a crude approximation of true free-field motions.

Italian accelerographs are mostly based in MV/LV substations which are solid brick buildings ($0.20\,\mathrm{m}$ thick walls) on concrete foundations $0.30\,\mathrm{m}$ thick. The instruments are bolted to a circular concrete pillar embedded in soil and isolated from the substation floor. Berardi *et al.* (1991) investigate the effect of the pillar and structure on the recorded ground motions. It is found that the soil-pillar system has a natural frequency of about $80\,\mathrm{Hz}$ and so amplification due to the pillar for periods greater than $0.1\,\mathrm{s}$ is less than 2%. The surrounding structure has natural frequencies at $3.8\,\mathrm{Hz}$, $13.56\,\mathrm{Hz}$ and $20.3\,\mathrm{Hz}$ so the structure only has a significant effect (5–10% amplification or reduction) for very soft soils and periods less than about $0.3\,\mathrm{s}$.

A parametric study of the effect of instrument shelters is conducted by Luco *et al.* (1990). They model a general instrument shelter which consists of a lightweight superstructure modelled as a cylindrical shell with basal radius $50\,\mathrm{cm}$ and height of $110\,\mathrm{cm}$ and mass $55\,\mathrm{kg}$. The instrument is firmly attached to the foundation which is a rigid cylindrical foundation of radius, a, embedded to depth, h, protruding from soil a distance, δ. It is found on soils with very low shear-wave velocities ($< 200\,\mathrm{ms}^{-1}$) in the top 2–$3\,\mathrm{m}$ that significant amplifications occur for very short periods (about $0.025\,\mathrm{s}$) especially when the radius of the foundation is small, the pillar protrudes a long way from the foundations, and the shelter is not greatly embedded. Strong-motion records of three earthquakes in the Cape Mendocino area from two stations only $6.25\,\mathrm{m}$ apart but with two different types of shelter are reported. In one shelter the instrument is bolted to the top of a $40 \times 40 \times 40\,\mathrm{cm}$ concrete pedestal on a reinforced concrete pad ($1\,\mathrm{m} \times 1\,\mathrm{m} \times 12\,\mathrm{cm}$) covered by a $1\,\mathrm{cm}$ thick boiler plate. The other instrument is on a $10\,\mathrm{cm}$ high $50\,\mathrm{cm}$ diameter pedestal connected to a reinforced concrete pad ($1.25\,\mathrm{m} \times 1.25\,\mathrm{m} \times 10\,\mathrm{cm}$) covered by a lightweight fibreglass transformer housing. In one earthquake (6/10/1978, $M_s = 4.2$, epicentral distance $7.7\,\mathrm{km}$) the instrument in the first shelter recorded PGAs of 0.22, 0.16 and $0.05\,\mathrm{g}$ while the second instrument recorded PGAs of 0.11, 0.10 and $0.04\,\mathrm{g}$. Plotting spectral amplitude ratios of acceleration for the three earthquakes reveals that the horizontal components of records from the first instrument were 1.8–2.5 higher in the period range $0.07\,\mathrm{s}$–$0.13\,\mathrm{s}$ but other factors such as amplitude, azimuth, topography and shear-wave velocity could also contribute to the differences.

The removal of the effect of SSI on recorded ground motions is difficult and time-consuming (Crouse *et al.*, 1984), however, as these examples show for the period range of normal engineering interest, i.e. periods greater than $0.1\,\mathrm{s}$, SSI effects of instrument shelters is negligible.

Stewart (2000) is an excellent recent paper on the variations in ground motion between foundation-level motions in buildings and free-field motions. An examination of 64 records from 16 earthquakes at 45 buildings with foundation-level and free-field instruments revealed the importance of a number of factors on SSI. It is found that the number of embedded storeys, the embedded depth and the number of storeys are not good parameters for representing SSI effects. Campbell (1991) found that horizontal PGAs from the Loma Prieta earthquake recorded at embedded and unembedded sites are not significantly different.

The embedment ratio, e/r where e is the embedment depth and r is the radius of equivalent circular foundation, turns out to be a good parameter to represent SSI. Recorded amplitudes from buildings with $e/r \geq 0.5$ are significantly reduced by the building (Stewart, 2000).

A good index of base-slab averaging is found to be a normalised frequency, $\tilde{a}_0$, which is the product of radial frequency and foundation radius normalised by shear-wave velocity. Recorded amplitudes from buildings with $\tilde{a}_0 > 0.2$ are significantly reduced by the building (Stewart, 2000).

The ratio of structure-to-soil stiffness, $1/\sigma_s$, is a reasonable index of SSI but the effects are fairly small (Stewart, 2000).

Stewart (2000) finds that spectral ordinates for periods greater than $1\,\mathrm{s}$ are almost unaffected by SSI once the records from buildings with $e/r \geq 0.5$ are removed.

SSI affects vertical PGAs more than horizontal PGAs because vertical ground motions are often of higher frequency than horizontal motions and vertical motions near shear walls can be significantly influenced by rocking (Stewart, 2000).

3. LITERATURE REVIEW OF ATTENUATION RELATIONS

There are many methods for strong ground motion prediction, for example: attenuation relations based on actual recorded accelerograms; stochastic source models (e.g. Joyner & Boore, 1988; Atkinson & Boore, 1990); synthetic accelerograms generated by superposition of Rayleigh modes (e.g. Suhadolc & Chiaruttini, 1987); and hybrid methods based on the summation of recorded small earthquakes (empirical Green's functions) (e.g. Hadley & Helmberger, 1980). This thesis concentrates on attenuation relations based on observed accelerograms because they are still the most commonly used ground motion prediction method. This chapter is a review of such relations.

3.1 Reviews of attenuation relations

A number of reviews of attenuation studies have been published which provide a good summary of the methods, the results and the problems associated with such relationships. Trifunac & Brady (1975, 1976) provide a brief summary and comparison of published relations. Idriss (1978) presents a comprehensive review of published attenuation relations, including a number which are not easily available. Boore & Joyner (1982) provide a review of attenuation studies published in 1981 and comments on empirical prediction of ground motion in general. Campbell (1985) contains a full survey of attenuation equations. Joyner & Boore (1988) give an excellent summary of ground motion prediction methodology in general, and attenuation relations in particular; Joyner & Boore (1996) update this including more recent studies. Ambraseys & Bommer (1995) provide an overview of relations which are used for design in Europe although they do not provide details on the methods used.

Since these surveys of published attenuation relations were completed and because data selection and processing, forms of equation used, and regression methods were not fully covered by the authors of these studies, a review of such procedures is undertaken here. Douglas (2001) provides a summary of all relations studied for this thesis. Uncertainties associated with the relations are investigated in Section 8.1.

3.2 Types of attenuation relationships

Draper & Smith (1981) define three main types of mathematical models used by scientists:

Functional When the true functional relationship between response (the value to be predicted) and the predictor variables is known and is used.

Control When the independent effects of each of the control variables (the predictor variables) can be estimated through designed experiments.

Predictive When neither functional or control models can be used and within the data much inter-correlation exists, so called ‘problems with messy data’. They do not need to be functional.

Most published attenuation relations have some physical basis, hence some aspects of functional models are present. Since all the physical aspects associated with seismic ground motion are not known in detail and even if they were it would be impossible to express them in the form of one simple equation, attenuation relations are predictive models. Trifunac (1980) notes that attenuation relations should be based on a functional form from the physical nature of phenomena but because of lack of data this cannot be achieved; Caillot & Bard (1993) also state that the form of the equation must have some physical basis. Controlled experiments cannot obviously be performed with ground motion caused by earthquakes because no two earthquakes are the same, nor are the travel paths to station or the local site conditions and hence there is no repeatability. Therefore control models are not possible.

3.3 Data selection criteria

Early attenuation studies (e.g. Milne & Davenport, 1969; Esteva, 1970; Ambraseys, 1975) give little or no information on the data selection criteria adopted, probably because at that time few strong-motion records were available and to ensure that the number of records used was not too small no selection was made. This section concerns what criteria have been applied in the past for the selection of records; in Section 3.8 selection based on site conditions is discussed.

A major choice made is: data from which country, region or seismotectonic regime will be used. Most often authors only use data from one country (or part of the country), for example western North America (mainly California) (e.g. Milne & Davenport, 1969; Esteva, 1970; Joyner & Boore, 1981; Crouse & McGuire, 1996; Chapman, 1999) or Japan (e.g. Iwasaki *et al.*, 1980; Kawashima *et al.*, 1984; Kamiyama *et al.*, 1992; Molas & Yamazaki, 1995; Kobayashi *et al.*, 2000). For these two regions there are many time-histories from a wide distribution of magnitudes, distances and other seismological parameters such as source mechanism so the coefficients derived through regression are stable and not controlled by a few data points. Trifunac (1976) does not use data from regions, other than western USA, because attenuation varies with geological province and magnitude determination is different in other countries. Even for those authors who use a criteria based on a particular region, differences can still occur, for example Crouse & McGuire (1996) and Sadigh *et al.* (1997) both develop equations for use in California but Crouse & McGuire (1996) exclude data from the Mammoth Lakes area (which is an active volcanic region) because it is atypical of the rest of California whereas Sadigh *et al.* (1997) include 65 records from the Mammoth Lakes area.

Others have also limited their data to those recorded within one country, for example Italy (Sabetta & Pugliese, 1987; Mohammadioun, 1991; Tento *et al.*, 1992; Caillot & Bard, 1993). Such criteria though is artificial because each country is not a single seismotectonic regime and nor are earthquakes from one country completely different to those in another. To limit the data by such criteria can lead to a small suite of records with a limited spread of independent parameters, for example Sabetta & Pugliese (1987) use 95 records from 17 earthquakes with magnitudes between 4.6 and 6.8. This means the equation may be controlled by a few data points and for independent variables outside this limited range predictions could be incorrect, a problem which Sabetta & Pugliese (1987) themselves note. Some areas, for example Iceland (Sigbjörnsson & Baldvinsson, 1992) and Hawaii (Munson & Thurber, 1997), seem to have much different attenuation properties than non-volcanic regions which means developing equations based solely on data from these small areas may be justified although again there is a lack of data. Zhao *et al.* (1997) exclude some New Zealand records which may have been affected by different attenuation properties in volcanic regions.

To overcome the lack of records some authors supplement their data with accelerograms from other regions of the world which are felt to be tectonically similar. For example, Campbell (1981) uses eight records from outside western USA (from shallow tectonic plate boundaries) because they make an important contribution to understanding near-source ground motion and this outweighs differences which may exist due to tectonics and recording practice. Differences in anelastic attenuation between the different areas are minimized by using only near-source records and he uses only data from instruments with similar dynamic characteristics to avoid problems due to recording practice. This increases the distribution of the data space so that the derived equations have a greater applicability. McCann Jr. & Echezwia (1984) also use data from outside western N. America, even though tectonics and travel paths may be different, because additional information in the near field is considered more important. Theodulidis & Papazachos (1992) supplement their Greek data with 16 records from other regions (Japan and Alaska) to increase the number of records from large ($7.0 \leq M \leq 7.5$) shallow earthquakes which can occur in Greece but for which no Greek strong-motion records exist. Fukushima *et al.* (1988) use 200 records, from distances 0.1–$48\,\mathrm{km}$, from western USA to constrain the near-source behaviour of the attenuation equation because Japanese data from this distance range are lacking.

Attenuation relations have been derived for particular tectonic regimes and not simply based on a country's borders. Dahle *et al.* (1990b) present a study using records from worldwide intraplate areas, defined as tectonically stable and geologically more uniform than plate boundaries, although due to lack of data they choose data from ‘reasonably’ intraplate areas. Spudich *et al.* (1996b, 1999) find equations for extensional regimes (where lithosphere is expanding ‘areally’) using worldwide data. Crouse (1991) includes data from any zone with strong seismic coupling, such as younger subduction zones, unless there are compelling reasons to exclude data. This is done because there are not enough data available from Cascadia, which is his area of interest. A number of workers (Abrahamson & Litehiser, 1989; Ambraseys & Bommer, 1991; Ambraseys, 1995; Ambraseys *et al.*, 1996; Sarma & Srbulov, 1996; Campbell, 1997; Bozorgnia *et al.*, 2000) derived equations for shallow crustal earthquakes using data from wide regions, including the whole Earth, because, it is felt, such earthquakes and regions are similar worldwide. Campbell (1997) includes shallow subduction interface earthquakes in his mainly shallow crustal set of records, because previous studies have found that their near-source ground motion is similar to that from shallow crustal earthquakes. The distance calibration functions of regional local magnitude scales for different parts of the world are examined by Boore (1989) and it is found that they are similar to distances of about $100\,\mathrm{km}$ but differ beyond that. Boore (1989) thinks that this is because differing anelastic attenuation and wave propagation effects in different crustal structures should not play a large role at close distances. Therefore within the range where ground motions have engineering significance (about $100\,\mathrm{km}$) data from different parts of the whole could be combined as far as distance dependence is concerned.

Criteria based on source depth have been used as an earthquake selection criterion, see Table 3.1.

A minimum magnitude criterion is often applied, see Table 3.2. Blume (1977) and Ambraseys (1995) study the effect of different minimum magnitude cut-offs; Ambraseys (1995) finds that the cut-off used has little effect on ground motion estimates. Selection based on accuracy of the magnitudes is used by Campbell (1981) and Sabetta & Pugliese (1987), who use only earthquakes with magnitudes accurate to within 0.3 units, and Ambraseys & Bommer (1991), who require the standard deviation of M_s to be known.

Minimum and maximum distance criteria are sometimes applied for a variety of reasons. Blume (1977) investigates the effect of using different distance cut-offs. McGuire (1977) excludes records with epicentral or rupture distance smaller than one-half the estimated length of rupture to exclude those records from the near-source region which are governed by different physical laws than those far from the source. A minimum distance criterion, of $2\,\mathrm{km}$, was applied by Wang *et al.* (1999) because $2\,\mathrm{km}$ is the minimum error in epicentral locations and hence including records from smaller distances may give errors in the results. Lack of far-field data motivates Molas & Yamazaki (1995) to exclude records from greater than $200\,\mathrm{km}$ and Crouse *et al.* (1988) to remove data with distances or magnitudes well outside the range of most selected records. Campbell (1981, 1997) uses only near-source records to avoid complex propagation effects observed at longer distances. Only records associated with reliable distances are used by Campbell (1981) and Sabetta

Tab. 3.1: Examples of selection criteria based on source depth in past attenuation relations.

Criterion	Reference	Reasons
Maximum depth	$20\,\mathrm{km}$ (Boore *et al.*, 1993) and $30\,\mathrm{km}$ (Ambraseys *et al.*, 1996)	To restrict to shallow crustal earthquakes
	$60\,\mathrm{km}$ (Iwasaki *et al.*, 1980; Fukushima *et al.*, 1995) (Japan)	Definition of M_{JMA} is different for deeper shocks
	$< 91\,\mathrm{km}$ (Sharma, 1998)	Two deeper earthquakes caused large errors in regression coefficients
Reliable estimates of focal depth	Ambraseys & Bommer (1991)	
Exclude deep slab earthquakes	McVerry *et al.* (2000)	There is high attenuation in the mantle
Exclude deep subduction shocks	Campbell (1981)	There are differences in travel path and stress condition compared with shallow crustal earthquakes

& Pugliese (1987) by including only earthquakes with locations (epicentres or rupture distance) known to within $5\,\mathrm{km}$ or less. Other studies use previously published attenuation relations to impose magnitude dependent distance limits. Fukushima & Tanaka (1990) remove records with predicted $\mathrm{PGA} < 0.1\,\mathrm{ms}^{-2}$ (the assumed trigger level) to avoid biasing the attenuation rate, Fukushima *et al.* (1995) exclude records with predicted $\mathrm{PGV} < 0.1\,\mathrm{cms}^{-1}$ so precise attenuation is found and Kobayashi *et al.* (2000) exclude data from distances with predicted $\mathrm{PGA} < 0.02\,\mathrm{ms}^{-2}$.

Previous studies have tried to reduce possible bias due to using records from large distances which may not be typical of the attenuation rate, through two alternative procedures. Joyner & Boore (1981) exclude records from distances greater than or equal to shortest distance to an instrument which did not trigger. This has been made more strict by Boore *et al.* (1993) who exclude records from distances greater than the distance to the first record triggered on the S wave and for spectral ordinates exclude records from distances greater than the distance to the first non-digitised record (which is assumed to be of smaller amplitude than the digitised records). Boore *et al.* (1994a) conclude that this criterion may be over strict because it is independent of geology and azimuth. Ambraseys & Bommer (1991) and Spudich *et al.* (1996b, 1999) do not use such a criterion because their sets of records are non-homogeneous and from irregularly spaced networks with different and unknown trigger levels, thus making such a criterion difficult or impossible to apply. Crouse (1991)

Tab. 3.2: Examples of minimum magnitude selection criteria in past attenuation relations.

Reason	Minimum magnitude
Restrict data to earthquakes with engineering significance	$M_s = 4$ (Ambraseys *et al.*, 1996) and $M = 5$ (Campbell, 1981; Iwasaki *et al.*, 1980)
Restrict data to earthquakes with smaller errors in the independent parameters	$M = 5$ (Fukushima *et al.*, 1995)
Interested in long-period motions	$M_s = 5.5$ (Bommer *et al.*, 1998)
Restrict to data with high signal-to-noise ratio	$M_s = 5.5$ (Bommer *et al.*, 1998)

also does not apply this criterion but considers his sample adequate for regression and although it may overestimate smaller distant motion it would properly estimate larger motions which are of greater concern for design. Although this is true the attenuation equation obtained would not predict the median hazard at all distances and therefore the use of it in seismic hazard analysis, for example, which requires the 50% hazard curve would bias the results. The other method for removing bias due to non-triggered instruments is the regression based method of Campbell (1997) and Chapman (1999) which uses all the available strong-motion data to derive attenuation relations to predict the non-triggering cut-off distance.

Exclusion of records based on minimum PGA has been proposed as a selection criteria, see Table 3.3. Blume (1977) studies effect of different PGA cut-offs but Blume (1980) does not employ a PGA cut-off because it is, by itself, a poor index of damage in most cases.

Time-history quality is also a criterion used by some authors. Campbell (1981) only includes records which triggered early enough to capture the strong phase of shaking and hence the ground motion is not underestimated. Dahle *et al.* (1990b) exclude records which are not available unprocessed and without sufficient information on instrument natural frequency and damping. Lee (1995) only uses records with high signal-to-noise ratio. Youngs *et al.* (1997) remove poor quality time-histories and those which do not contain the main portion of shaking from their set of data. Records of short duration terminating early in the coda are not including in the analysis of Chapman (1999). Sabetta & Pugliese (1987) use only the first shock of a record if it is a well separated multiple shock record and magnitude and focal parameters apply only to first shock. All these criteria are valid and would help to reduce some of the scatter in the ground motion but less subjective methods are required if records are not simply rejected because they do not seem to match the rest of the data.

Tab. 3.3: Examples of minimum PGA selection criteria in past attenuation relations.

Minimum PGA (ms^{-2})	Reference	Reasons
0.01	Molas & Yamazaki (1995)	Weaker records are not reliable because of resolution of instruments
0.10	Iwasaki *et al.* (1980)	
0.15	Chiaruttini & Siro (1981)	To avoid possible bias
0.20	Campbell (1981)	
0.50	Xu *et al.* (1984)	To avoid too much contribution from far field
Near triggering level	Ambraseys (1995)	Processing errors can be large

Cousins *et al.* (1999) retains data from clipped seismograms.

It is common to use only those records which are not significantly affected by soil-structure interaction although many alternative suggestions have been made on how to select such records, see Tables 3.4 and 3.5.

Ohsaki *et al.* (1980b), Campbell (1981) and Crouse & McGuire (1996) remove records thought to be affected by high topographical relief.

Criteria are sometimes used to achieve a set of data which will not lead to biased results simply because of its distribution. McGuire (1978) uses no more that seven records from the same earthquake and no more than nine from a single site to minimize underestimation of variance and he retains records to give a large distance and magnitude range. Campbell (1981) and Devillers & Mohammadioun (1981) do not use all data from San Fernando to minimize bias due to the large number of records. This problem is also noted by Trifunac (1976) who screens the data to minimize possible bias due to uneven distribution of data amongst different magnitude ranges and soil conditions and from excessive contribution to the database from several abundantly recorded earthquakes. Boore *et al.* (1993) do not use data from more than one station with the same site condition within a circle of radius $1\,\mathrm{km}$ so that the underestimation of variance is minimized. Niazi & Bozorgnia (1991) select earthquakes to cover broad range of magnitude, distance and azimuth and to ensure thorough coverage of whole SMART-1 array (at least 25 stations recorded each shock). Other criteria for the minimum number of records per earthquake used are 3 or more (Atkinson, 1997) and 2 or more (Abrahamson & Litehiser, 1989), both to improve ability of regression to distinguish between magnitude and distance dependence. Caillot & Bard (1993) selects records so mean and standard deviation of magnitude and hypocentral distance in each site category are equal.

Tab. 3.4: Types of strong-motion stations included in past attenuation relations.

Include records from	Reference	Comments
Free-field	Faccioli (1978)	
Free-field and basements of buildings	McGuire (1978)	
Free-field and small structures	Campbell (1981)	Effects of site geology, building size, instrument location and mechanism are found to be extensively interrelated
Buildings	Crouse (1991)	Notes that PGA could be underestimated
Buildings with four stories or less	McVerry *et al.* (2000)	
Buildings with more than three storeys	Zhao *et al.* (1997)	Finds no significant difference to those from free-field
Buildings with up to eight stories	Theodulidis & Papazachos (1992)	
Four and six storey buildings	Crouse & McGuire (1996)	Included because of lack of data in site and distance range where these records are and because structure is thought not to have affected ground motion too much.
Abutments of dams	Ambraseys (1995); Campbell (1997)	Campbell (1997) includes records from dam abutments because they comprise a significant number of rock records and because stiff foundations are not thought to be significantly affected by dam.
Dams and special structures	McCue *et al.* (1988)	Included because of lack of available data
Tunnel portals	Ambraseys (1995)	

Tab. 3.5: Types of strong-motion stations excluded in past attenuation relations.

Exclude records from	Reference	Comments
Basements	Kawashima *et al.* (1986)	
Buildings with three or more storeys	Joyner & Boore (1981)	
Buildings with more than two storeys	Campbell (1997)	For sites on soil or soft rock
Buildings with more than five storeys	Campbell (1997)	For sites on hard rock
First floor	Kawashima *et al.* (1986)	
Abutments of dams	Joyner & Boore (1981)	
Tokyo-Yokohama	Yamabe & Kanai (1988)	They conclude they are affected by nearby buildings

One other selection criterion is that based on the intensity measured at the recording site (Devillers & Mohammadioun, 1981; Mohammadioun, 1991, 1994b). They group their data by single intensities (from V to VIII and higher) and by ranges of intensities and perform the analysis separately on each of these subsets. Therefore even though they do not include site intensity as an independent parameter explicitly, to use their equations still requires a prediction of the intensity which will occur at the site, along with choosing the magnitude and distance. Hence they require the user to make a choice for a parameter, site-intensity, which if known would mean there would be little reason for using an attenuation relation to predict the response spectrum at the site. Mohammadioun (1994b) highlights another problem with the technique because the recording site intensities may be average intensities within the area of the site and hence would neglect possible microzoning effects. A more technical problem is mentioned by Mohammadioun (1991), who does not use intensity-based selection for his derivation of spectral equations for Italy because of the risk of creating a data population which is not statistically significant.

3.4 Correction techniques

As with data selection procedures, early attenuation studies do not state how their strong-motion records were corrected (e.g. Milne & Davenport, 1969; Esteva, 1970; Ambraseys, 1975), thus either uncorrected records were used or standard correction procedures were employed. Since the paper of Trifunac (1976) who gives frequencies between which the accelerations used are thought to be accurate, details of correction techniques used for deriving attenuation relations have often been reported, but again, like data selection procedures, there is little agreement about the best method to use. However, because time-histories from different types of accelerographs have been used and because of the wide variety of levels of ground motion that have been used in different studies, there is no general best procedure. Tento *et al.* (1992) state that correction procedure plays a relevant role in analysis and that it introduces inhomogeneities and errors due to the subjective choice of low frequency filter limits.

Almost all studies, where details are given, have filtered their strong-motion records using a variety of passbands and types of filter. The cut-off frequencies used either have been the same for all records or have been chosen for each record individually using a number of different techniques. Table 3.6 summarises the methods for individually selecting low and high cut-off frequencies and the frequencies chosen.

Some authors have applied standard filter cut-offs to their records apparently irrespective of the quality of time-histories. Gaull (1988) bandpass filters his records to get the PGA associated with periods between 2 and $10\,\mathrm{Hz}$, because high frequency PGA from uncorrected records is not of engineering significance. Although this is true, because the PGA is often used to anchor a response spectrum at zero period, using the PGA not associated with high frequencies to estimate the spectrum is incorrect. Dahle *et al.* (1990b) use an elliptical filter with passband 0.25 to $25\,\mathrm{Hz}$. Niazi & Bozorgnia (1992a) use a trapezoidal filter with corner frequencies 0.07, 0.10, 25 and $30.6\,\mathrm{Hz}$. Kamiyama *et al.* (1992) filter with passband 0.24 and $11\,\mathrm{Hz}$. Molas & Yamazaki (1995) use a low-cut filter with cosine shaped transition from 0.01 to $0.05\,\mathrm{Hz}$. For long records (more than $10\,\mathrm{s}$ duration) and some shorter records (between 5 and $10\,\mathrm{s}$ duration) Ambraseys *et al.* (1996) use a passband 0.20 to $25\,\mathrm{Hz}$. Sarma & Srbulov (1996) employ a low pass elliptical filter. Caillot & Bard (1993) use cut-offs 0.5 and $30\,\mathrm{Hz}$. The application of the same cut-off frequencies for all accelerograms used is justified for those studies which use a homogeneous set of records recorded on the same type of instrument and digitised in the same way (e.g. Niazi & Bozorgnia, 1992a; Molas & Yamazaki, 1995). For those authors who use strong-motion records from a wide variety of sources which have been recorded on different types of instrument and have different digitisation qualities (Dahle *et al.*, 1990b; Ambraseys *et al.*, 1996; Sarma & Srbulov, 1996) using such a general procedure is probably not justified. Bommer *et al.* (1998) show, however, that the choice of the cut-off frequencies does not significantly affect spectral ordinates for periods within the range of main engineering interest (about 0.1 to $2\,\mathrm{s}$), therefore a common correction may not affect the results.

Tab. 3.6: Examples of record-dependent low (f_l) and high (f_h) cut-off frequencies used for filtering in past attenuation relations.

f_l (Hz)	f_h (Hz)	Selection method	Reference
		Chosen to account for length and mean sampling rate of records and response characteristics of accelerographs used	Faccioli (1978)
0.2–0.4	25–35	Visual inspection in order to maximise signal-to-noise ratio within the passband	Sabetta & Pugliese (1987)
0.13–1.18			Tento *et al.* (1992)
	25–30	Site dependent	Fukushima *et al.* (1995)
0.2–0.7	20–35	Compare the Fourier spectrum of signal to that of fixed trace	Sabetta & Pugliese (1996)
		Visual inspection of the Fourier amplitude spectrum and doubly integrated displacement.	Spudich *et al.* (1996b)
0.15–0.5	25	Compare the Fourier amplitude spectrum of signal to that of noise spectrum	Cousins *et al.* (1999)
		Use Fourier amplitude spectrum to choose the high cut-off frequency and integrated displacements to choose low-frequency cut-off.	Abrahamson & Silva (1997)
0.1 upwards		Use a time-consuming method where the low cut-off frequency is selected by visual inspection of velocity and displacement time-histories, selecting the cut-off which they feel eliminates the noise	Bommer *et al.* (1998)
		Visual inspection of the displacements (found using the Fast Fourier Transform method) in prefixed and appended $5\,\mathrm{s}$ sections	Kobayashi *et al.* (2000)
0.15, 0.20 and 0.33		Use noise level in each record	Si & Midorikawa (2000)

Since the paper of Trifunac (1976), removal of the transducer response (instrument correction) from the time-history is often performed (e.g. Sabetta & Pugliese, 1987; Spudich *et al.*, 1996b; Cousins *et al.*, 1999). The need to correct records from Japanese instruments to yield reliable PGAs, because they substantially suppress high frequencies, is noted by Kawashima *et al.* (1986). Data from seismographs also needs to be instrument corrected because of their different frequency response compared with accelerographs (Cousins *et al.*, 1999). Instrument correction requires, at least, the natural frequency and damping of the accelerograph, information which is sometimes lacking and hence such corrections cannot be applied (Ambraseys *et al.*, 1996). Chiaruttini & Siro (1981) do not correct their Friuli records for instrument response but find this does not substantially alter PGA and Bommer *et al.* (1998) do not employ instrument correction because it is not important for displacement spectra.

Whether the corrected or uncorrected PGAs should be included is another topic of debate. Campbell (1981) uses PGA from unprocessed accelerograms because fully processed PGAs are generally smaller due to decimation and filtering of records. Uncorrected PGAs are also used by Munson & Thurber (1997). Other studies, it is supposed, use corrected PGAs. Ambraseys & Bommer (1991) and Ambraseys (1995) use PGAs from accelerograms which have undergone a wide variety of different processing techniques, including no correction, for their studies. They find that most differences (which they can check) are small (below 4 or 5%) but for some records the differences may be larger (up to 10%). Munson & Thurber (1997) also find small differences between uncorrected and corrected PGA. Sabetta & Pugliese (1987) find their correction technique provides reliable estimates of PGA and hence uncorrected PGA values do not need to be used. Accelerogram correction procedures are used to find the *actual* ground motion which occurred at the site therefore uncorrected PGA values are not the real PGAs. There is an inconsistency between using uncorrected estimates of PGA but correcting the records to find spectral ordinates which leads to the PGA attenuation equation not matching the spectral ordinate equations at high frequencies. However, such differences are probably small enough to be neglected when compared with other assumptions made.

A few studies have included other sources of PGA values apart from those given on accelerograms. Chiaruttini & Siro (1981) use some PGA estimates from velocity time-histories. Garcia-Fernandez & Canas (1995) only use PGA values derived from Fourier amplitude spectra at $5\,\mathrm{Hz}$ from short-period analogue time-histories. Cousins *et al.* (1999) differentiate seismograms to yield PGA estimates. Such techniques to supplement a limited set of records, particularly in the far field where accelerographs may not be triggered, are useful but estimates of PGA from the transformation of measurements from instruments with much different characteristics than accelerographs must be verified to be consistent with those from accelerographs.

The choice of correction method strongly affects the range of periods within which the spectral ordinates calculated can be assumed to be correct and not significantly affected by the correction procedure. This question has started to be discussed recently because seismic design is becoming more interested in long-period ground motion which is the range most affected by noise and hence by the correction technique, which seeks to remove this noise but in the process also removes information on the actual ground motion. Mohammadioun (1991) provides no attenuation equations for periods greater than $2\,\mathrm{s}$ because he uses uncorrected time-histories which it is felt contain long-period noise. The $2\,\mathrm{s}$ limit on the acceptability of the derived equations is also noted by Tento *et al.* (1992), who find that the record dependent correction procedure they adopt significantly affects the results for periods greater than $2\,\mathrm{s}$. Boore *et al.* (1993) also only provide spectral ordinate equations for periods between 0.1 and $2\,\mathrm{s}$ because of the low sampling rate of older time-histories, low signal-to-noise ratios and filter cut-offs affecting spectral ordinates for periods outside this range. Lee (1995) believes his records are not adequate for response spectrum calculation outside the period range 0.04 to $2\,\mathrm{s}$. An even shorter period range for acceptable spectral ordinates is stated by Theodulidis & Papazachos (1994), who believe that for periods greater than $0.5\,\mathrm{s}$ the different digitisation (manual or automatic) and correction (baseline fitting or filtering) techniques they have used means longer period values are significantly affected. Niazi & Bozorgnia (1992a) believe their low frequency cut-off may be too low for records from small earthquakes but choosing a higher frequency for this cut-off would remove information on long-period ground motion. If they adopted a record dependent correction procedure and then in deriving long-periods equations use only those records which did not require a higher frequency cut-off, this problem would be overcome. Such a method has been adopted by a number of recent workers (Spudich *et al.*, 1996b, 1999; Abrahamson & Silva, 1997; Bommer *et al.*, 1998). Spudich *et al.* (1996b) use spectral values only from the passband of the filter. Abrahamson & Silva (1997) use spectral values only within frequency band $1.25f_h$ to $0.8f_l$ (where f_h is the high-pass corner frequency and f_l is the low-pass corner frequency). Spudich *et al.* (1999) uses a similar criteria of only using spectral ordinates within $1.25f_h$ and $0.75f_l$ and for eight records which were processed in a different way the acceptable range was 0.1 to $1\,\mathrm{s}$. Bommer *et al.* (1998) use each record's spectral ordinates for regression up to $0.1\,\mathrm{s}$ less than the period of the filter cut-off used for that record. These techniques mean that the number of records and distribution of records used for the regression analysis changes with period and hence it must be checked that for each period the number and distribution of data points is adequate to derive reliable coefficients. There may be a problem of consistency between spectral estimates, derived from the attenuation relations, for short periods, for which probably most of the records were used, compared with long periods, for which the stronger ground motions are probably more represented.

3.5 Separation of attenuation relations into source, path and site dependence

Traditionally discussion of ground motion from earthquakes has been split into three sections: source, travel path and site, upon which the ground motion at the site depends. This separation is somewhat simplistic, because the boundaries between each part are not clearly defined and because the source affects the path's properties and path properties affect site conditions. This separation though will be followed here because it makes reviewing previous attenuation relationships easier but it is complicated by the previously described problems and by the use of non-linear equations in which source, path and site parameters are not separated.

The following discussion is in terms of the untransformed ground motion, y, as opposed to $\log y$ on which the regression is almost always performed.

3.6 Characterisation of source

Earthquake magnitude, M, has been almost the only parameter used to characterise the earthquake source in attenuation relations, although many different magnitude scales and combinations of scales have been used. Recently parameters associated with the source mechanism have also been included although again there are a number of alternative methods for including this information in the equation.

Early studies (e.g. Esteva, 1970; Donovan, 1973), did not state which magnitude scale they use. Many authors use local magnitude (also called Richter magnitude), M_L, to derive their attenuation relations (e.g. McGuire, 1977; Campbell, 1989; Tento *et al.*, 1992; Mohammadioun, 1994b). This may be because these are the only magnitude estimates available for the chosen earthquakes. Chiaruttini & Siro (1981) use M_L because it is determined at short distances, it is homogeneously determined for small earthquakes up to saturation at about $M_L = 7.0$ and because it is determined at about $1\,\mathrm{Hz}$ which is close to the accelerometer band. Mohammadioun (1994b) uses M_L because it is generally available and is uniformly determined but states that it may not be the best choice. Ambraseys (1995) does not use M_L because there are no M_L estimates for many of the earthquakes in his set and many estimates of M_L are unreliable. Boore (1989) states that M_L is difficult to predict for design earthquakes because catalogues of historical earthquakes often contain unreliable M_L estimates.

Another magnitude scale which is commonly used is surface-wave magnitude, M_s (Dahle *et al.*, 1990b; Ambraseys & Bommer, 1991; Ambraseys, 1995; Ambraseys *et al.*, 1996; Crouse & McGuire, 1996; Bommer *et al.*, 1998). Dahle *et al.* (1990b) use M_s because it is reasonably unbiased with respect to source dimensions and there is a globally consistent calculation method. Theodulidis & Papazachos (1992) mainly use M_s but for the foreign earthquakes in their set they use M_w or M_{JMA} which they state to be equivalent between 6.0 and 8.0. Ambraseys (1995) states that the conversion of M_L to M_s should not be done because of uncertainty in conversion which should be retained. This holds for all conversions between magnitude scales but because only M_w can be found for all size earthquakes conversion from one scale to another is often necessary at small and large magnitudes, for example Dahle *et al.* (1990b) and Ambraseys *et al.* (1996) use some M_s converted from other magnitude scales (M_L, m_b, coda length magnitude). Japanese Meteorological Agency magnitude, M_{JMA}, has been employed in many Japanese attenuation relations (e.g. Kawashima *et al.*, 1984; Kamiyama *et al.*, 1992; Fukushima *et al.*, 1995) although Kawashima *et al.* (1984) notes that it may not necessarily be the most suitable parameter to represent magnitude but it is the only one which exists for all earthquakes in their set of records. Peng *et al.* (1985) use Chinese surface-wave magnitude but also use m_b and M_s and find larger residuals.

Recently most equations have been derived using moment magnitude, M_w, (e.g. Boore *et al.*, 1993; Lawson & Krawinkler, 1994; Sadigh *et al.*, 1997; Kobayashi *et al.*, 2000) which is directly related to the size of the source and the slip along the fault, unlike other magnitude scales which are empirically derived and have no physical meaning. The other major advantage of M_w is that it does not saturate for large magnitudes, and can be calculated for small magnitudes, and hence provides a good measure of the energy released over the entire magnitude range. The size and slip of historical earthquakes can be found using geological data which can then be directly related to M_w for use in assessing the design earthquake; this is more difficult to do for other magnitude scales (Boore, 1989). However, M_w is not usually calculated for earthquakes with magnitudes less than about 5 and also it has only been uniformly calculated since 1977 and hence for earlier earthquakes estimates of M_w are more difficult, if not impossible, to find. To overcome these difficulties some authors (e.g. Joyner & Boore, 1981; Xu *et al.*, 1984; Crouse, 1991; Dahle *et al.*, 1995) have used magnitudes from other scales (e.g. M_L, M_s) as estimates of M_w for those earthquakes which do not have a published M_w value. If only a few earthquakes in the set of data do not have a M_w value, if the magnitude scale chosen to supplement M_w is equivalent to moment magnitude for that size of earthquake and if the number of records associated with these earthquakes is small then this method is satisfactory.

The other main technique for providing a homogeneous magnitude scale for all sizes of earthquakes is to use one magnitude scale for small earthquakes, usually M_L and one scale for larger earthquakes, usually M_s. Campbell (1981) introduced this idea to develop magnitude estimates that are generally consistent with M_w. He tried different division points, for the change from M_L to M_s, between 5.5 and 6.5 and found that the magnitude is quite insensitive to choice, but he uses 6.0 as do Abrahamson & Litehiser (1989). Sabetta & Pugliese (1987) use 5.5 as the change-over point from M_L to M_s and find that this combined magnitude scale assures a linear relationship between logarithm of PGA and magnitude and avoids saturation effects of M_L. Niazi & Bozorgnia (1991) use 6.6 as the division point. Lee (1993) uses M_L for $M \lesssim 6.5$ and other different (unspecified) magnitude scales for $M > 6.5$. He does this because seismic hazard analysis often uses catalogues which do not specify magnitude scale and often the estimates are nonhomogeneous. Even though this may be so, increasing the uncertainty, associated with the attenuation relation, by using a mixture of magnitude scales means that it can never be correctly used for seismic hazard analysis because there is no correct magnitude scale and the uncertainties are then increased unnecessarily.

Almost all studies include a factor which has an exponential dependence on magnitude, $\exp aM$, this is because the energy released by an earthquake is exponentially dependent on magnitude (Richter, 1958).

It has been proposed that strong ground motion does not increase without bound for increasing magnitudes and that as magnitude increases ground motion does not increase at a constant rate. This is known as magnitude saturation. Bolt & Abrahamson (1982) split their data into four broad magnitude groups and fit an equation which has no magnitude-dependent factors to the ground motion within each group. They find no systematic increase in near-source PGA as a function of magnitude although the derived equations predict lower PGA for larger magnitudes which, as Joyner & Boore (1983) point out, is not realistic. Hence this study may be biased by a lack of data for large magnitudes. Trifunac (1976) was the first to include a factor to model magnitude saturation, by using a factor that is exponentially dependent on the magnitude squared, i.e. $\exp bM^2$, in addition to the normal factor $\exp aM$. For a positive coefficient, a and a negative coefficient b it predicts a maximum ground motion which could occur however great the magnitude. Such factors have been included by Trifunac (1980), Joyner & Fumal (1984), Huo & Hu (1991), Boore *et al.* (1993), Lee (1995), Lawson & Krawinkler (1994), Chapman (1999) and Abrahamson & Silva (1997). Other authors (Joyner & Boore, 1981; Kawashima *et al.*, 1984; Crouse *et al.*, 1988; Crouse, 1991) incorporate factors like $\exp bM^2$ into their equations but find that the coefficient b is not statistically significant or that it does not improve the adjusted multiple correlation coefficient so remove the factor. Modelling quadratic dependence on magnitude requires records from large magnitude earthquakes that are often lacking (Trifunac, 1976). To overcome this lack of data Spudich *et al.* (1996b, 1999) adopt coefficients, a and b, from Boore *et al.* (1993). Lee (1995) uses only records with $M \geq 4.25$ so that a and b have the correct sign to give magnitude saturation for large magnitudes. Needing to apply such methods to force physically realistic coefficients suggests that magnitude saturation is not supported by the data used and that excluding the factor, $\exp bM^2$, would be preferable.

Factors which are exponentially proportional to higher powers of magnitude have been incorporated into equations by Sadigh *et al.* (1997), who includes a factor $\exp k_1 M^{2.5}$, and Youngs *et al.* (1997), who includes a factor $\exp k_2 M^3$, for the prediction of spectral acceleration. Campbell (1997) uses a non-linear magnitude dependent term, $\exp k_3 \tanh M$.

Kamiyama *et al.* (1992) take the idea of magnitude saturation to its extreme by modelling PGA as completely independent of magnitude up to a distance which is exponentially dependent on magnitude. For distances greater than this near-source zone the predicted ground motion is exponentially dependent on magnitude.

An alternative method for modelling different magnitude dependence for small and large earthquakes is to derive separate equations for $M_w < 6.5$ and for $M_w \geq 6.5$ (Sadigh *et al.*, 1997; Sadigh & Egan, 1998). This technique relies on a large set of data that is well distributed in terms of magnitude so that there is enough data to derive reliable equations for the separate subsets, although Sadigh *et al.* (1997) constrain the predictions to be the same at $M_w = 6.5$.

Ambraseys (1995) notes that because the conversion of M_s to M_w is non-linear there is a non-linear relationship between M_w and ground motion prediction using an equation derived using M_s. Hence some degree of magnitude saturation is implicit in attenuation relations based on M_s, even if only a factor $\exp aM_s$ is included, because M_s saturates at large magnitudes and so the equation does not predict constantly increasing ground motion for increasing earthquake size (as measured by M_w).

Some studies may implicitly account for source mechanism by including many shocks from the same area which have a similar mechanism, for example Trifunac (1976) notes that the large proportion of data from the San Fernando earthquake he uses may bias the results.

Campbell (1981) examines residuals from regression and finds reverse faulting PGA values are systematically higher (significant at the 10% level) than other motions but concludes this may be due to data from outside western N. America and so does not model the effect. Niazi & Bozorgnia (1991) also find evidence, by examining residuals, of higher ground motion from reverse faulting and lower motion from normal faulting as compared with the mean, but it is not modelled because the mechanisms of four earthquakes are unknown. Crouse *et al.* (1988) split data by fault mechanism and find no significant differences between thrust, normal and strike-slip. Spudich *et al.* (1999) find no significant difference between strike-slip and normal ground motions in extensional regimes.

Abrahamson & Litehiser (1989) include a simple multiplicative factor to model difference in ground motion between reverse (and reverse-oblique) and other source mechanisms. Boore *et al.* (1994a) find marginal statistical significance for the difference between strike-slip and reverse-slip ground motion, which they later model as a multiplicative factor (Boore *et al.*, 1994b). Sadigh *et al.* (1997) also model this difference using a multiplicative factor (they include normal faulting ground motion in the strike-slip group because it was not found to be significantly different than strike-slip motion). Zhao *et al.* (1997) and Cousins *et al.* (1999) include a multiplicative factor to account for the difference between crustal reverse motion and other motions. Bozorgnia *et al.* (2000) incorporate factors to model difference between strike-slip (including normal), reverse and thrust ground motions. McVerry *et al.* (2000) include factors, in their crustal earthquake equation, to model differences between normal, reverse-oblique and reverse ground motions. Crouse & McGuire (1996) try a multiplicative factor, to predict the difference between reverse and strike-slip motion, in their equation but they find it is not significant and the inconsistency of the result between soil classes means it is difficult to attach significance to fault type.

More complex factors to model the differences in ground motion caused by different fault mechanisms have recently been included in attenuation relations. Abrahamson & Silva (1997) include magnitude dependent fault mechanism factors and Campbell (1997) includes distance and magnitude dependent factors.

Sadigh & Egan (1998) provides different equations for reverse and strike-slip (including normal faulting) ground motion. This can incorporate complex multiplicative factors (dependent on magnitude, distance and soil category) relating ground motion associated with reverse faulting to that from strike-slip faulting but it requires much data to ensure that the predictions are realistic for all combinations of magnitude and distance.

Sharma (1998) does not attempt to include source mechanism factors because source mechanisms are not well defined for all earthquakes in the set of records and including too many coefficients and a small amount of data may lead to errors.

Recent attempts have been made to model differences in ground motion due to the general tectonic setting of the earthquake. Chiaruttini & Siro (1981) were the first to explicitly consider the tectonic setting (characterised by the earthquakes' geographical location) by developing separate equations for three different areas (Friuli, Italy; Ancona, Italy; and the rest of the Alpide belt) and also one equation which models the differences by a multiplicative factor. Fukushima & Tanaka (1990) allow different magnitude scaling for western N. American earthquakes than for Japanese shocks. Youngs *et al.* (1997) include a multiplicative factor to predict the significant difference between ground motion from interface and intraslab subduction zone earthquakes. Zhao *et al.* (1997) also include a factor to account for the difference between ground motion from interface subduction zone shocks and other types of earthquake. McVerry *et al.* (2000) include factors, in their subduction zone equation, to predict the difference between ground shaking from interface and deep slab shocks. Si & Midorikawa (2000) include two factors to model the difference between crustal, interplate and intraplate Japanese earthquakes.

Kobayashi *et al.* (2000) find their equation over predicts ground motion from interface earthquakes compared with intraslab motions. Crouse *et al.* (1988) find some differences between ground motion in different subduction zones but do not model them, partly because some differences may be because of site effects. Crouse *et al.* (1988) also try to find correlations between seismotectonic information (age, convergence, dip, contact width, maximum subduction depth, maximum historical earthquake, maximum rupture length, stress drop and seismic slip) and ground motion in each zone. They find weak correlations for stress drop and the maximum historical earthquake but lack confidence in the results because of uncertainty in stress drop estimates.

Other studies have found that the difference between strong ground motion in different seismotectonic regions is not significant. Sabetta & Pugliese (1987) exclude records from different seismotectonic and geological regions and repeat their analysis and find predicted PGA is similar. No significant difference is found between Guerrero (Mexico) ground motion and other Central American motion nor between subduction and shallow crustal strong ground motion by Dahle *et al.* (1995). Sharma (1998) neglects tectonic type because of a small set of records and because only small differences are expected. Atkinson (1997) checks for differences in ground motion between crustal, interface and intraslab shocks and finds no dependence on tectonic type.

Azimuthal dependence of ground motion has been investigated in three studies. Sabetta & Pugliese (1987) find that some of their PGA values show azimuthal dependence although this is not modelled because it would require more coefficients and the direction of the azimuthal effect is different from region to region. Lungu *et al.* (1994, 1995) split data into separate quadrants and find attenuation equations for each subset; they find azimuthal dependence. The conclusions of this study are based on limited strong-motion data in each quadrant coming from only four earthquakes and hence special characteristics of these four earthquakes may explain the azimuthal dependence. This azimuthal dependence may also be partly due to differences in travel-paths.

3.6.1 Characterisation of depth

Incorporation of depth through selection criteria has been discussed in Section 3.3, this section describes how depth is included in the attenuation equation.

The use of distance measures which contain information on the depth of the source, i.e. hypocentral distance, rupture distance, seismogenic distance, centroid distance, energy centre distance, equivalent hypocentral distance or surface projection distance with focal depth [as used by Ambraseys & Bommer (1991), Sigbjörnsson & Baldvinsson (1992) and Ambraseys (1995)] forces deeper earthquakes to predict smaller ground motions than shallower shocks. This is actually a path effect.

For sets of earthquakes with depths up to about $250\,\mathrm{km}$ (for example those from subduction zones) a factor which is exponentially dependent on depth is often included as well as using a distance measure which includes depth (hypocentral, centroid, energy centre or rupture distance) (Crouse, 1991; Lungu *et al.*, 1994, 1995; Molas & Yamazaki, 1995; Atkinson, 1997; Youngs *et al.*, 1997; Zhao *et al.*, 1997; Shabestari & Yamazaki, 1998; Cousins *et al.*, 1999; Shabestari & Yamazaki, 2000; Si & Midorikawa, 2000). Annaka & Nozawa (1988), Molas & Yamazaki (1995) and Youngs *et al.* (1997) find it significantly increases coefficients of determination, R^2, or alternatively decreases the standard deviation. Kamiyama & Yanagisawa (1986) use such a factor but employ epicentral distance. Definitions of depth used to characterise the source have been focal depth (e.g.

Atkinson, 1997), depth to top of fault (e.g. Molas & Yamazaki, 1995), centroid depth (e.g. Zhao *et al.*, 1997) and average depth of fault plane (e.g. Si & Midorikawa, 2000).

Some studies (Kawashima *et al.*, 1986; Crouse *et al.*, 1988) have included such factors but have found that they do not significantly reduce errors associated with the equation. Campbell (1989) includes a factor exponentially dependent on depth and alternatively one linearly dependent on depth but although prediction is improved, and the residual plots no longer show a dependence on focal depth, he does not recommend the use of the equations because focal depths are associated with (possibly large) errors and hence the dependence may be false. Campbell (1989) uses a set of earthquakes with a limited range of focal depths (1.8 to $24.3\,\mathrm{km}$) over which focal depth dependence may not exist. Ambraseys (1995) also notes that focal depths are poorly determined and revises many focal depths using time between P and S-wave arrivals. This uncertainty in focal depths means that focal depth dependence is difficult to test unless the range of depths is much greater than the errors associated with each depth estimate. Si & Midorikawa (2000) find that magnitude and depth are positively correlated so their associated coefficients may be incorrectly determined, especially when using rupture distance.

More complex depth dependent terms are tried by Kawashima *et al.* (1986), including factors which are dependent on depth and magnitude and depth and distance, but find there is no significant increase in the adjusted multiple correlation coefficient. A depth dependent anelastic attenuation factor is included and retained by Atkinson (1997).

Lungu *et al.* (1994, 1995) find faster attenuation for deeper earthquakes compared with shallower shocks (this is based on attenuation rates for a few individual earthquakes) whereas Molas & Yamazaki (1995) group earthquakes by depth and find similar predictions for each group and for all the data together.

3.7 Characterisation of path

The distance travelled from the source to the site, d, is the parameter used in all attenuation relations to characterise the path, although many different definitions of this distance are used (see Section 8.4).

The most common form of decay term is a power law decay (which corresponds to geometric decay due to the spreading of waves from a source) using a modified distance, R, therefore the decay term is $R^{-\alpha}$. Distance is often modified through the addition of a constant, i.e. $R = d + \beta$ (e.g. Esteva, 1970), or by assuming that the source is at some depth, h, and then using the slant distance, $R = \sqrt{d^2 + h^2}$ (e.g. Joyner & Boore, 1981). The actual distance, d, is not usually used, except when hypocentral distance (e.g. Caillot & Bard, 1993) or mainly far-field data (e.g. Singh *et al.*, 1987) is used, because for small d unrealistically high values of ground motion are predicted.

The form $R = d+\beta$ does not correspond to a physical situation (even though Donovan & Bornstein (1978) suggest it does), unlike the form $R = \sqrt{d^2 + h^2}$, and hence relating the decay rate, α, found using this form to the real decay rate of different types of seismic waves is not correct. Often the calculated decay rate using $R = d + \beta$ as opposed to $R = \sqrt{d^2 + h^2}$ is greater, for example McCann Jr. & Echezwia (1984) use one set of PGA values and fit both forms of distance dependence and find using the first form (with $\beta = 25\,\mathrm{km}$ assigned) $\alpha = -1.915$ whereas using the second form (with $h = 3.852\,\mathrm{km}$ found through regression) $\alpha = -0.913$. Only in the far field, $d \gg \beta$, does $(d + \beta)^{-\alpha}$ actually give a decay rate α against d and hence only the decay rates where there is much data (usually $d \sim \beta$) should be compared.

The power, α, which controls the decay rate is either fixed or found during the regression. Joyner & Boore (1981) constrain α to unity because this is the decay rate for body waves which they assume cause the peak ground acceleration; this choice of α has been followed by many other authors (e.g. Ambraseys & Bommer, 1991; Munson & Thurber, 1997). Garcia-Fernandez & Canas (1995) constrain α to $\frac{1}{2}$ because they assume their peak acceleration is associated with Lg waves. Ambraseys & Bommer (1991) also use $\alpha = 0.83$ because they assume PGA is associated with the Airy phase. Campbell (1981) constrains α to 1.75 which he says is representative of far-field decay of PGA, although note this is for $R = d + \beta$ and hence it may be larger than if $R = \sqrt{d^2 + h^2}$ was used. Kamiyama *et al.* (1992) and Kamiyama (1995) constrain the decay rate to -1.64 using results from other studies. Often though α is found during the regression which is better, since the equation would fit the data more closely, but requires a well distributed set of data in terms of distance and not too many other coefficients to find. Joyner & Boore (1983) state that they constrain α to 1 in Joyner & Boore (1981) because they believe their data did not permit a physically meaningful, simultaneous determination of a spreading coefficient *and* a coefficient of anelastic attenuation. If the data is insufficient then nonphysical coefficients can be found which although apparently match the data well, predict unrealistic ground motions at the edges of the data space.

Campbell (1981) introduces the concept of magnitude dependent β or h, which means that the part of the attenuation curve (roughly the near field) with smaller decay rate than that in the far field is not constant for all sizes of earthquakes. This is known as distance saturation. Usually β and h are of the form $A\exp(BM)$, where M is the magnitude, because this makes the flattened region of the curve proportional to the size of the fault rupture zone which has been found to be exponentially dependent on magnitude (e.g. Ambraseys & Jackson, 1998). Kamiyama *et al.* (1992) and Kamiyama (1995) give a model where PGA is completely independent of distance within a zone which is exponentially dependent on magnitude. Joyner & Boore (1981), Sabetta & Pugliese (1987), Boore *et al.* (1994a) and Ambraseys (1995) find no evidence for magnitude dependent h for their data and distance definition (distance to surface projection of rupture), although Sabetta & Pugliese (1987) state that their experiment is not conclusive due to the distribution of data (there are only a few near-field records from large magnitude earthquakes in their set of records). Joyner & Boore (1981) prefer a magnitude independent h because fewer coefficients need to be found.

Campbell (1997) models different decay for thrust(-oblique) and reverse(-oblique) faults than that for other source mechanisms (strike-slip and normal). This effect must be due to different seismic waves being predominant in accelerograms from earthquakes with different source mechanisms because the travel path is independent of the source mechanism.

Trifunac & Lee (1989) and Lee (1993) use an attenuation term that is dependent on focal depth, magnitude and correlation radius of source function (which can be approximated by shear-wave velocity).

Campbell (1997), Youngs *et al.* (1997) and Bozorgnia *et al.* (2000) model different decay rates for sites in different soil categories. This idea, although it may be supported by their data, only has a physical meaning (different local site amplifications) as a site effect and not as a path effect because although locally the soil may be known this does not mean such geology is constant along the travel path. Gaull (1988) and Yamabe & Kanai (1988) present models with magnitude dependent decay rates even in the far field. In the far field all earthquakes are seen by the site as point sources and hence the far-field decay rate should be independent of magnitude.

Recorded strong ground motion is composed of many types of seismic waves (P, S, Lg and surface waves), see Section 2.3.1. These wave attenuate with individual rates, therefore different waves dominate at different distances, making the decay of peak ground motion complex. Trifunac & Brady (1975, 1976) and Trifunac (1976) model this by using the distance calibration function used for the calculation of M_L, derived by Richter (1958), which has a change of slope at $d = 75\,\mathrm{km}$ because for $d < 75\,\mathrm{km}$ body waves predominate, with decay $\sim d^{-1}$, where as for $d > 75\,\mathrm{km}$ surface waves predominate, with decay $\sim d^{-1/2}$. Dahle *et al.* (1990b,a) also incorporate a change of slope into their decay term (although it is not a smooth transition from one decay rate to another) which models the change from spherical spreading, i.e. d^{-1}, of S waves to cylindrical spreading, i.e. $d^{-5/6}$, of Lg waves at $100\,\mathrm{km}$, although they note that the point where the slope changes depends on crustal structure and focal depth. McCann Jr. & Echezwia (1984) consider an expression of the near-field response of an elastic whole space which incorporates the first and second order geometrical spreading terms through an expression, $(A/d^2 + B/d)^C$, which allows the peak ground motions to come from the combined effect of two different types of wave.

Joyner & Boore (1981) introduce a term, of form $\exp kR$, to model anelastic decay. This has been adopted by a number of subsequent authors (e.g. Ambraseys & Bommer, 1991; Sigbjörnsson & Baldvinsson, 1992) although often the geometrical decay power, α, is fixed at unity so that a realistic, i.e. negative, anelastic coefficient is found. If α is not fixed then k is often found to be positive (e.g. Ambraseys *et al.*, 1996), which predicts increasing ground motion for increasing distance at large distances.

Abrahamson & Litehiser (1989) only include an anelastic term for interplate earthquakes. Atkinson (1997) includes a depth dependent anelastic decay term. Cousins *et al.* (1999) and McVerry *et al.* (2000) include a term to account for the higher anelastic decay due to the waves travelling through a volcanic region. Lee (1995) includes an anelastic decay term which becomes the only decay term for distances greater than a distance dependent on focal depth, magnitude and correlation radius of source function. Trifunac (1976) states that because the representative frequency of peak amplitudes varies with distance and because the relative digitisation noise also changes with distance it is difficult to include an anelastic decay term.

Abrahamson & Silva (1997) include a term, which is dependent on distance, for sites on the hanging wall of a fault rupture. Their term probably accounts for a site on the hanging wall seeing more of the rupture plane than a site on the foot wall but their complicated form for this term may be not be justified by their limited amount of data.

Donovan & Bornstein (1978) use a complicated distance dependence, involving geometrical decay but also factors which model magnitude and distance-dependent decay. Such a form of distance dependence, although it may be supported by their data, is unnecessarily complex, when it does not reduce the uncertainty associated with ground motion prediction, especially because they fit their non-linear equation, containing 6 coefficients, to only 59 records from 10 earthquakes.

Bolt & Abrahamson (1982) use a form of distance dependence which does not have a physical basis, i.e. they do not try to estimate geometrical decay or anelastic decay coefficients (Bolt & Abrahamson, 1983). Bolt & Abrahamson (1983) state the reason for their choice was to provide a form that will predict accelerations validly, particularly near the source.

3.8 Characterisation of site

Local site conditions at an accelerograph station can dramatically affect the strong ground motion recorded, for example Schenk (1984) relates the great variability in recorded ground motions up to $30\,\mathrm{km}$ to different site conditions. Therefore attempts are made in most attenuation relations to model the effect of different near-surface ground conditions on strong motion. Some publications (e.g. Lungu *et al.*, 1995) however, use data from a wide variety of sites with different properties (ranging from stiff soil to very soft soil sites) and do not try to model or examine any differences.

Data selection criteria, which seek to limit the accelerograms used to those recorded at stations with similar local site conditions, are the simplest techniques which have been employed. Esteva (1970), Faccioli (1978), Ohsaki *et al.* (1980a), Campbell (1989), Dahle *et al.* (1990b), Mohammadioun (1994a) and Xiang & Gao (1994) restrict their data to those from sites comparable to stiff clay or compact conglomerate, soft soil sites, bedrock sites, deep soil (depth greater than $10\,\mathrm{m}$) sites, rock sites, rock sites with $V_s \geq 750\,\mathrm{ms}^{-1}$ and basement rock sites respectively. Some studies do not select records from a homogeneous set of sites but only exclude those which are affected by significant soil amplification or non-linearity (usually soft soil sites) (McGuire, 1977; Campbell, 1981; Ohno *et al.*, 1996; Sadigh *et al.*, 1997; McVerry *et al.*, 2000; Si & Midorikawa, 2000). Other studies (Iwasaki *et al.*, 1980; Ohsaki *et al.*, 1980b; Chiaruttini & Siro, 1981; Kawashima *et al.*, 1986; Huo & Hu, 1991; Caillot & Bard, 1993; Crouse & McGuire, 1996; Sadigh *et al.*, 1997) include data from different site categories but perform the regression on subsets of records with the same site classification. The advantage of this method is that non-linear soil behaviour is implicitly included, because the magnitude and distance scaling for each site category is independent of that for the other categories. Unless there are a lot of records and the distributions within each class are similar, differences between the predicted ground motion on different types of sites may not be significant and may be simply due to the lack of comparable data.

Two studies have taken this idea to its extreme and only used records from a single station (Denham & Small, 1971; Singh *et al.*, 1987). Niazi & Bozorgnia (1991) use records from the SMART-1 array, where the stations have essentially identical site conditions, but find that there is still much uncertainty. Such studies are of limited use for design because structures will not be built on the exact location of the instrument nor is it easy to decide whether another location has similar site conditions to the accelerograph station.

The most commonly used technique to incorporate site effects into an attenuation relation is to use multiplicative factors between ground motion at one type of site and that at another. Trifunac (1976) introduces this method; he uses three site categories and the multiplicative factor between basement rock and intermediate type rock is forced to be half the multiplicative factor between solid hard basement rock and alluvium sites thus limiting the generality of the method. The number of multiplicative factors used is usually one less than the number of site categories used, thus allowing different scalings amongst the site categories (e.g. Boore *et al.*, 1993; Lawson & Krawinkler, 1994; Ambraseys *et al.*, 1996; Sabetta & Pugliese, 1996; Chapman, 1999). Lee (1995) classifies stations into three geological site classes and two local soil classes, although the difference between geological and local scales is not clear, so there are six categories in total but only three factors. All the data is used to derive the magnitude and distance scaling, making the coefficients more robust, and removing bias from the amplification factors between the different site classes due to the distribution of the data. Possible non-linear behaviour though cannot be modelled by these factors because they are equal throughout the dataspace. A combination of this method with the more general method explained above was used by Crouse & McGuire (1996), who compute multiplicative factors for two of their four soil categories because of the lack of data within the two categories. Caillot & Bard (1993) initially derive equations for each of their two site category subsets separately but find that the magnitude and distance coefficients of the two sets of equations are not significantly different so they employ a simple multiplicative factor. This shows that non-linear effects are probably not that important, although Caillot & Bard (1993) use a set of records with many weak motion time-histories so the non-linear effects may be masked.

Some studies have insufficient data to derive adequate site category multiplicative factors so they adopt multiplicative factors from previous studies (e.g. Atkinson, 1997; Spudich *et al.*, 1999). If the site categories used in the two studies are similar enough then this is a valid procedure because true site coefficients should only depend on local site conditions at the stations.

Multiplicative factors between ground motion on different types of site are not always modelled as the same throughout the data space. McGuire (1978) attempts to include a distance dependent multiplicative factor but it is not statistically significant; a magnitude dependent factor, although statistically significant, does not reduce scatter and McGuire (1978) thinks it may be biased due to lack of rock records so it is not adopted. Campbell (1997) incorporates a distance dependent site factor and Cousins *et al.* (1999) and McVerry *et al.* (2000) include distance and magnitude-dependent site factors. Although Youngs *et al.* (1997) develop two separate equations for deep soil and rock sites they employ a joint regression method, because there is not enough data to apply regression to the individual subsets, which forces the soil and rock motion to the same level in the near field. Non-linear soil behaviour is explicitly accounted for in Abrahamson & Silva (1997) through the use of a factor which includes the predicted PGA on rock; a factor also included by McVerry *et al.* (2000) although they adopted the coefficients of Abrahamson & Silva (1997) because they have too few records to give realistic estimates of the coefficients. This problem highlights the main disadvantage of using such complicated factors, namely that a large, well distributed set of records is required to find robust estimates of coefficients in a non-linear equation.

Choices of site categories into which a station is placed is controlled by the quality of available site information. Complex classifications cannot be used, even if desired, unless there is adequate data for all the sites used (Spudich *et al.*, 1999). Thus early studies (e.g. McGuire, 1978; Joyner & Boore, 1981) and some recent studies (e.g. Zhao *et al.*, 1997; Spudich *et al.*, 1999) simply use a binary classification of soil (or alluvium) and rock. Usually a site is classified as soil (or alluvium) if it has soil of more than between 4 (Joyner & Boore, 1981) and $20\,\mathrm{m}$ (Abrahamson & Silva, 1997) thick, because a shallow soil layer is not thought to greatly affect the ground motion. Some studies though have found that shallow soil sites have significantly higher ground motions than rock or stiff soil sites and that rock and deep soil sites have similar ground motion (Campbell, 1981; Sabetta & Pugliese, 1987; Campbell, 1989) although this is for PGA (a high frequency parameter) which is less affected by local site conditions. Ambraseys & Bommer (1991) attribute the apparent small dependence of horizontal PGA on site classification to the lack of available information which compelled them to use a simple binary system. As more site information on strong-motion stations has become available the number of site classes used has grown, so that there are three or more categories of increasing stiffness (roughly increasing shear-wave velocity) (e.g. Trifunac, 1976;

Kawashima *et al.*, 1986; Fukushima & Tanaka, 1990; Lawson & Krawinkler, 1994; Campbell, 1997; Chapman, 1999; Kobayashi *et al.*, 2000). Some studies define the boundaries of the categories in terms of shear-wave velocity (e.g. Boore *et al.*, 1993; Ambraseys *et al.*, 1996) but in fact there are no shear-wave velocity measurements for many of the stations they use, so a rough classification is made. Due to the difficulty of finding site information Theodulidis & Papazachos (1992) examined the PGV/PGA ratio for some of their Alaskan sites to decide whether they were rock or soil, which is based on empirical formulae which find differences in this ratio due to the local site conditions. There is much uncertainty in such formulae, due partly to the variability of ground motion and partly to the accelerogram correction method used to find PGV and hence classification based on PGV/PGA is unreliable. In an attempt to reduce the subjectivity of classifying Greek stations into rock or alluvium categories Theodulidis & Papazachos (1992) use the opinion of seven specialists and then use the average classification; this is a time-consuming process.

Examination of residuals for sites with different soil categories is a useful method for sets of records where site information is not complete, and hence cannot be included explicitly within the equation. This type of analysis was performed by Abrahamson & Litehiser (1989).

To overcome the subjectivity of soil categories some studies have used directly measured properties of the ground beneath the accelerograph station. The most commonly used measurement is the near-surface shear-wave velocity, V_s. Blume (1977) finds that the site impendence, ρV_s (where ρ is the density of the ground which is approximately a constant), is the best measure of site condition and he uses it to derive site factors for his equation although the paper is not entirely clear how this is done. Joyner & Fumal (1984) use the average shear-wave velocity to one-quarter the wavelength of waves of period of concern (although often these shear-wave velocities are extrapolated using geological data); the basis of this choice is energy conservation along ray tubes. Shear-wave velocity is usually only measured down to shallow depths so $30\,\mathrm{m}$ is often used as the reference depth to which to compute the average shear-wave velocity, although Boore *et al.* (1994a) state that ideally they would like to use depth to one quarter wavelength. Boore *et al.* (1994a) and Ambraseys (1995) include site factors based on average shear-wave velocity to $30\,\mathrm{m}$ in their equations. Unlike other formulations to incorporate site conditions into attenuation relations, directly using shear-wave velocity has the advantage of being physically based so the coefficients can be examined to check that they are reasonable. Also it is better because there is no need for subjective categories (Ambraseys, 1995). This has two advantages: firstly no decisions need to be made about the categories to use or which category a particular station is in and secondly when the equation is used for design the shear-wave velocity at the site can be measured and used directly in the formula, removing the need for more subjective judgement on the part of the designer who does not know exactly how site classifications were originally done. The major problem with using V_s is that there are no published measurements at most strong-motion stations, especially those outside California or Japan (Ambraseys, 1995; Spudich *et al.*, 1999). Different choices of the reference depth to compute the average V_s can lead to different results (Ambraseys, 1995) so subjectivity is not completely removed although Boore *et al.* (1994a) believe one-quarter wavelength depth is the best to use but for long periods this is hundreds of metres for which the data is currently unavailable. Another disadvantage of this method is that surface waves could be important (Joyner & Fumal, 1984; Boore *et al.*, 1994a), especially for long periods, and their amplifications are not modelled by using V_s directly in the equation like it is a present (Joyner & Fumal, 1984). Also it does not model the effect of the thickness of attenuating material (Boore *et al.*, 1994a) or resonance effects (Joyner & Fumal, 1984).

Some studies have used site factors based on other measurements which can possibly overcome some of the disadvantages of shear-wave velocity, although not all have a physical basis. Joyner & Fumal (1984) include site factors based on V_s and depth to underlying rock, H, and find correlation for long periods but no correlation for short periods although they state it is inappropriate to use depth to rock at present because the San Fernando strong-motion data does not show any significant correlation. Trifunac (1980) and Trifunac & Lee (1989) include a multiplicative factor which is exponentially dependent on the depth of sedimentary deposit although Trifunac & Lee (1989) note that this is not always known at every location so they also provide an equation using simple site categories. A combination of depth to rock and site categories is employed by Lee (1993) and Campbell (1997) although Campbell uses a complex depth scaling factor. Combinations of depth to rock and site categories are not the most efficient site parameters because they are not strictly independent, for example if a site is classified as rock then the depth to rock must be zero. This correlation could cause problems when coefficients of both these factors are sought.

A single parameter which is a rough combination of shear-wave velocity and depth to bedrock is the natural period of the site, T, which for a single layer equals $4H/V_s$. The need to include a term reflecting explicitly local amplification dependent on natural period of the soil is noted by Benito *et al.* (1992) because they find little correlation between simple soil categories and ground motion. A factor exponentially dependent on natural period is included by Tong & Katayama (1988) and Sun & Peng (1993), although Tong & Katayama (1988) find that it has little effect on estimation. Using natural period explicitly rather than depth to rock and shear-wave velocity reduces generality because if both H and V_s are included there are more coefficients to be determined, allowing modelling of attenuation effects through the soil layer (which depends on depth) and also impedance (which depends on shear-wave velocity).

The most site specific procedure is to use individual coefficients for each station. This idea was introduced by Kamiyama & Yanagisawa (1986) (although Kobayashi & Midorikawa (1982) developed a method which is similar) and has since been adopted in many Japanese studies (Kamiyama *et al.*, 1992; Fukushima *et al.*, 1995; Molas & Yamazaki, 1995; Shabestari & Yamazaki, 1998;

Kawano *et al.*, 2000; Shabestari & Yamazaki, 2000). Its two advantages are that no site information is required about the stations included in the set of records, hence eliminating subjective soil categories or the need to measure shear-wave velocity or similar quantities, and all site effects should be modelled through the use of automatically derived transfer functions. To use this method a large number of records are required for each station, hence its use in Japan where there is an abundance of data, otherwise the station coefficients are not adequately determined. For example, if each station recorded only one earthquake then the standard deviation of the attenuation equation would be zero because the individual site coefficients would equal the residuals from the regression without any site factors. This though would not be correct because the derived coefficients cannot be related to site response but could be due to either source, path or site effects. A number of records at each station are required, with different source and path conditions, before the site coefficients tend to the true values, which gives the correct transfer function for each site. Kamiyama & Yanagisawa (1986) find a good agreement between the site coefficients (transformed to amplification spectra) and the amplification spectra predicted using the shear-wave velocity profiles of the stations. Molas & Yamazaki (1995) find weak correlation between station coefficients and soil categories although there is much scatter. Unless the individual site coefficients can be related to the theoretical transfer function at each station or to some other feature of the site, attenuation relations including these individual factors are impossible to use for the prediction of ground motion at a site which is not within the original set of records. Even if a relation could be found between site characteristics and the coefficients, the use of such equations in seismic hazard analysis, where many sites are considered, would require detailed information on all those under investigation.

The most computational intensive method for including local site effects within an attenuation study is to convert all the recorded time-histories from sites with a variety of properties to time-histories which would have been recorded on a site with given properties. This procedure was adopted by Annaka & Nozawa (1988), who use 1D propagation theory to transform records from sites with $V_s < 300\,\mathrm{ms}^{-1}$ to records from sites with $V_s > 300\,\mathrm{ms}^{-1}$, and Kawano *et al.* (2000), who strip off the effects of the uppermost layers of ground under a station to get a record which comes from a site with $0.5 \leq V_s \leq 2.7\,\mathrm{kms}^{-1}$. Altering the recorded time-history in this way could lead to increased uncertainty because the ground motion is not simply affected by the ground directly under the station (1D effect) but by the ground within an undefined area (2D and 3D effects), see Sections 2.3.4 and 2.4.4.

No published attenuation relation considers topographical effects except those which exclude records believed to be affected by topography, see Section 3.3, and Zhao *et al.* (1997) who include in their rock category records from stations where topographic effects are expected.

3.9 Analysis techniques

The majority of attenuation studies use the ordinary least squares method (or an unspecified procedure) to derive the coefficients of their equation. However, more complex procedures have been developed to overcome problems encountered due to the inhomogeneity, in terms of independent parameters, of most strong-motion sets. These inhomogeneities are listed below.

- In most strong-motion sets, unless they are specially selected, there is a strong correlation between magnitude and distance of the records, because larger earthquakes can be detected at greater distances than smaller earthquakes.
- There is an abundance of accelerograms from large distances (from between about 50 and $200\,\mathrm{km}$) and there still is a lack of near-field data from large earthquakes which are most important for seismic design.
- Some earthquakes (for example San Fernando) occur within a region with a large number of accelerographs so there are many available records.

Regression techniques have been developed to counteract the ill effect on the estimated coefficients (and hence predictions) caused by each of these characteristics.

Donovan (1973) was the first to find that correlation between magnitude and distance leads to changes in the derived coefficients. The regression method most often used to reduce the effect of magnitude and distance correlation is the two-stage technique introduced by Joyner & Boore (1981). In this method, the distance dependent coefficients are derived first, using individual amplitude scaling factors for each earthquake. In the second stage the magnitude-dependent coefficients are derived by fitting a curve to these amplitude scaling factors. Fukushima & Tanaka (1990) conduct simple numerical experiments to show that for sets with a strong correlation between magnitude and distance the distance dependence is reduced, when ordinary least squares is used, compared with the decay associated with an individual earthquake. They find the two-stage method yields distance coefficients similar to those associated with individual earthquakes. This usefulness of the two-stage method has also been demonstrated by Abrahamson & Litehiser (1989), Fukushima *et al.* (1995), Molas & Yamazaki (1995), Sharma (1998) and Sharma (2000) for their highly correlated (correlation coefficients up to 0.63) magnitude and distance values. Sabetta & Pugliese (1987), Boore *et al.* (1994a), Ambraseys (1995), Ambraseys *et al.* (1996) and Sabetta & Pugliese (1996) have found that one-stage and two-stage methods yield similar predictions, especially at intermediate distances where there is most of the data. Ambraseys & Bommer (1991) prefer a one-stage method because more than half the earthquakes in their set of records were only recorded by one instrument and in the second stage these are excluded from the calculation of the magnitude dependence, thereby omitting a large proportion of their data from the regression. Spudich *et al.* (1999) also use a one-stage method because two-stage methods underestimate the earthquake-to-earthquake component of variation for sets of records like theirs with many singly-recorded earthquakes. Caillot & Bard (1993) state that the two-stage method may be misleading because for some spectral periods it does not reduce the variance; they also find significant changes in predictions between one and two-stage methods. A similar technique is applied by Orphal & Lahoud (1974), who use data from the well-recorded San Fernando earthquake to find the distance dependent coefficient and then the rest of the data, from other less well-recorded earthquakes, to define the magnitude scaling. Gaull (1988) applied a variation of this method. This method assumes that the distance decay is the same for all earthquakes; an assumption which is not justified. McCue *et al.* (1988) implemented the reverse of this idea, firstly finding the magnitude dependence by examining PGA for many events recorded at the same distance and then using all data to find the distance dependence.

A more complex procedure to overcome the effect of a strong correlation between magnitude and distance (correlation coefficient 0.84) was developed by Tong & Katayama (1988). It is based on a 'reliability' parameter for each earthquake, it is the product of the number of records from that earthquake and the coefficient of determination of a regression equation, derived for each earthquake individually, which estimates the geometrical decay rate. Using earthquakes with 'reliability' values greater than unity they find that a weighted average, using the 'reliability' values, leads to a distance dependence coefficient which is not affected by the correlation between magnitude and distance.

A method was introduced by Trifunac (1976), where the set of records is split up into 24 different magnitude, site and component (horizontal or vertical) intervals. The magnitude, site, component and confidence interval dependent coefficients are calculated using one PGA value from each interval. This method reduces the possible bias in the coefficients due to a large number of records with similar magnitudes. Another procedure to reduce this bias was used by Blume (1980). The data is divided into distance dependent bands and within each band a regression equation dependent on magnitude is found which is used to calculate the predicted ground motion at a single point within the interval. Each of these points is used to find the overall distance dependent coefficient.

By far the most common technique for minimizing possible bias, due to a many records with similar associated distances and magnitudes, is weighted regression. Huo & Hu (1991) divide their dataspace into magnitude-distance intervals within which each record has a weight equal to the reciprocal of the number of records within that interval and then all subdivisions have equal weight. Similar schemes have been implemented by Caillot & Bard (1993) and Crouse & McGuire (1996). Si & Midorikawa (2000) give near-source records much higher weight than those from large distances. Caillot & Bard (1993) and Munson & Thurber (1997) find that weighting can have a significant effect on the predictions.

To give more weight to near-field PGA values, which are more important for engineering design, Bolt & Abrahamson (1982) use non-linear regression on the untransformed PGA rather than on the logarithm of PGA. They believe that the equation derived by Joyner & Boore (1981) is not strongly affected by the near-field data, limiting its usefulness. The statistical assumption behind the analysis of Bolt & Abrahamson (1982) is that the uncertainty associated with PGA is the same for all levels of ground motion (Draper & Smith, 1981, pp. 237–238). This assumption must be false because otherwise using the standard deviation associated with the equation, to derive predicted ground motion for percentiles less than 50%, would lead to the prediction of negative PGA (by definition a positive quantity).

The problem of well-recorded earthquakes (for example San Fernando and Imperial Valley) having an unwanted strong influence on the regression [as noted by Trifunac (1976)] is also usually reduced through a weighting scheme; an idea first introduced by Campbell (1981). Campbell (1981) divides the dataspace into a number of distance intervals within which each record is weighted by a relative weighting factor equal to the reciprocal of the number of records within that interval from the earthquake with which the record is associated. Variations on this procedure have been adopted by McCann Jr. & Echezwia (1984), Abrahamson & Litehiser (1989), Campbell (1989), Niazi & Bozorgnia (1991), Sun & Peng (1993), Campbell (1997) and Sharma (1998). The two-stage method of Joyner & Boore (1981) also reduces the bias due to well-recorded shocks. The opposite weighting is applied by Si & Midorikawa (2000) who give more weighting to the well-recorded earthquakes. Donovan & Bornstein (1978) find that, although 32% of their data is from one earthquake (San Fernando), no bias is introduced

Campbell (1997) tries to reduce the bias due to a number of recordings being made at close sites during the same earthquake [the same possible bias that Boore *et al.* (1993) reduce by including only one record from similar sites which were less than $1\,\mathrm{km}$ apart] through a weighting scheme.

Ambraseys & Bommer (1991) choose not to apply weights with their regression analysis because it involves assumptions which are difficult to verify. The ordinary least-squares method is applied by Xu *et al.* (1984), who justify its use by the small number of records they employ.

The final reason for not using the ordinary least-squares technique is so that the coefficients obtained are physically realistic. For highly non-linear forms of the equation, where a small change in one coefficient strongly affects another coefficient's value, special techniques need to be employed. Dahle *et al.* (1995) use a Bayesian one-stage method to yield physically possible coefficients. Crouse & McGuire (1996) apply constraints to their coefficients so that predicted ground motion is an increasing function magnitude and decreasing function of distance. Kamiyama *et al.* (1992) obtain one of their coefficients, which controls how far the flat part of the attenuation curve (where there is no decay with distance) extends, by a trial and error process so it is consistent with empirical estimates of fault length. If the unconstrained coefficients are nonphysical then it means that the data used is insufficient for the complexity of equation employed. This is a problem with McVerry *et al.* (2000) who use a very complex functional form for their attenuation relation and then must use many coefficients from Abrahamson & Silva (1997) because their set is insufficient to derive realistic coefficients. Campbell (1997) notes that his adopted functional form has too many coefficients so it is necessary to perform the analysis in many steps finding different sets of coefficients at each stage to ensure a stable result is obtained. Yamabe & Kanai (1988) apply a two-stage regression, which removes the problems caused by products of independent variables because the two stages consist of ordinary linear regression. This method though cannot be used for the vast majority of non-linear functional forms which have been proposed.

The other method for obtaining physically realistic coefficients is by using subsets of the data for different parts of the analysis. This is especially useful for data which is dominated by far-field records but where the adopted equation involves coefficients which are only important in the near field. Donovan & Bornstein (1978) divide their data according to distance and find the equation by least squares (no details of this process are provided in the paper). Abrahamson & Litehiser (1989) group their data into 0.5 magnitude unit intervals and fit simple equations to each subset, the coefficients of which are then used to find the overall functional form and coefficients of their non-linear distance saturation term, which controls the predicted ground motion in the near field. A similar technique is employed by Huo & Hu (1991) and Si & Midorikawa (2000) to find the coefficients of their distance saturation terms although they use the data from a selection of earthquakes rather than magnitude-binned data. Only the earthquakes associated with the most reliable information (those with $M_s > 6.0$) are used by Theodulidis & Papazachos (1992) to find distance coefficients which forces them to adopt a four-stage regression technique to incorporate all the other data.

Schenk (1982, 1984) fits the equation to PGA values by eye and not through regression analysis. Schenk (1982) does this because the least squares method is often highly dependent on marginal observations, meaning that certain points can have a large influence on the derived coefficients. Although this is true, fitting an equation by eye is not an objective method, and so cannot be repeated by another person and get the same result, and it is impossible to use for complicated functional forms where the data cannot be visualised easily.

Only one published attenuation relation (Huo & Hu, 1991) makes the important observation that the independent variables used in attenuation relations (for example magnitude and distance) are associated with their own uncertainties. They develop a method based on weighted consistent least-squares which takes the uncertainties in magnitude and distance into account when deriving the equation.

3.10 Conclusions

From the above discussion it can be seen that little agreement has been reached in the past thirty years of attenuation relation studies, in terms of data selection; characterisation of source, path or site; or regression techniques employed. Workers have chosen their techniques based on the available data, which varies greatly with geographical region. Further comparing Chapter 2, on the factors affecting strong ground motions, and this chapter shows that current attenuation relations use fewer independent variables and simpler functional forms than have been found to describe variations in strong ground motions. Neglecting many factors when predictions using attenuation relations are made leads to large standard deviations as is shown in Chapter 8.

4. EFFECT OF VERTICAL GROUND MOTION ON STRUCTURAL RESPONSE

This chapter contains a summary of published studies of the effect of vertical excitation on the response of structures, concentrating mainly on those about SDOF systems and especially elastic SDOF systems. The derivations of the SDOF equations of motion which model structures' behaviour are given; these equations are used in later chapters.

4.1 Definitions of response quantities

Although the response of a system changes with time, which may be important for some applications, often only the maximum response which a system undergoes is required for design purposes. Consider the structural model illustrated in Figure 4.1 and assume the ground acceleration is $U_{tt}(t)$ and the mass, m, has displacement $u(t)$, velocity $u_t(t)$ and acceleration $u_{tt}(t)$ then the three values of maximum response of interest are:

maximum absolute response acceleration $S_a = \max_t |u_{tt} + U_{tt}|$,

maximum relative response velocity $S_v = \max_t |u_t|$,

maximum relative response displacement $S_d = \max_t |u|$.

Two forces act on the mass one is due to the spring and the other due to the equivalent viscous damping. These forces must resist the total inertial forces of the system, mu_{tt} and mU_{tt} hence, mS_a gives the maximum force acting which must be resisted by the entire system.

From these quantities two 'pseudo' values can be calculated:

maximum absolute pseudo-acceleration $S'_a = (2\pi/T)^2 S_d$,

maximum relative pseudo-velocity $S'_v = (2\pi/T) S_d$,

where T is the natural period of the system.

mS'_a gives the force which must be resisted by the spring (Chopra, 1995) and not the complete system. For small coefficients of critical damping and relatively short periods S_a and S'_a are almost identical (Chopra, 1995).

Maximum relative pseudo-velocity, S'_v, is related to the peak value of strain energy, E_S, stored in the system during the earthquake by the equation: $E_S = mS'^2_v/2$ (Chopra, 1995, p. 200).

4.2 Response spectra

A plot of the quantities defined in Section 4.1 as a function of the natural vibration period, T, and damping, ξ, of the system is called a response spectrum. It provides a convenient means of summarizing the peak response of all possible linear SDOF systems to a particular component of ground motion (Chopra, 1995).

The concept and usefulness of response spectra for earthquake engineering is laid out in Benioff (1934) although no spectra are calculated. He states 'suppose we substitute for the engineering structures a series of undamped pendulum seismometers having frequencies ranging from the lowest fundamental frequency of engineering structures to the highest significant overtones. During an earthquake each component seismometer would write a characteristic seismogram. Plotting the maximum recorded deflection of each pendulum against its frequency, we obtain a curve which may be termed the undamped pendular spectrum of the earthquake.'

4.3 Structural model for zero gravity where vertical acceleration is neglected

4.3.1 Linear elastic model

Consider the SDOF system illustrated in Figure 4.1. This system consists of a mass m, moving on a frictionless surface, driven by a horizontal ground motion with acceleration U_{tt}, with a spring with stiffness k and a dashpot with a coefficient of viscous damping c.

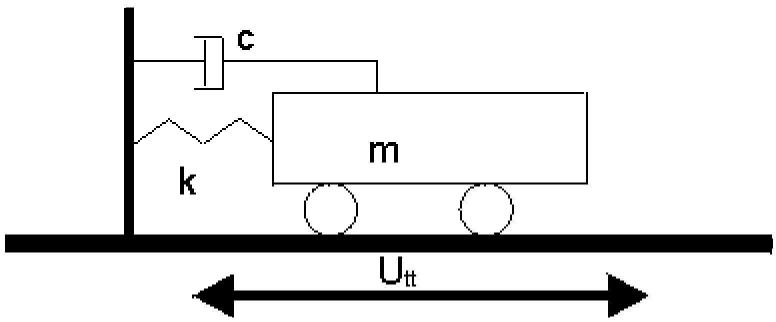

Fig. 4.1: Structural model for zero gravity field where vertical acceleration is neglected.

Let $u(t)$ be the horizontal displacement of the mass at time t. Then using Newton's second law and resolving forces horizontally gives:

$$mu_{tt} + cu_t + ku + mU_{tt} = 0$$

Dividing by m and letting $\omega_0^2 = k/m$ and $\xi_0 = c/2\omega_0 m$ yields the equation of motion:

$$u_{tt} + 2\xi_0\omega_0 u_t + \omega_0^2 u = -U_{tt}. \tag{4.1}$$

Equation 4.1 is usually used to model the response of structures to earthquake excitation, see for example Chopra (1995).

Equation 4.1 is one of the simplest second order differential equations possible and because it models many oscillatory phenomena it has been much studied even before strong-motion records of earthquakes were obtained.

In 1933 the first accelerograms were written during the Long Beach earthquake (11/3/1933) and so the calculation of response spectra became possible.

Biot (1941) used Equation 4.1, with $\xi = 0$, to construct six (one for each horizontal component) undamped response spectra for three western North American strong-motion records. He mentions that undamped and linear elastic models do not really reflect a buildings behaviour implying some damping, i.e. $\xi \neq 0$, and inelastic behaviour, see Section 4.3.2, are required for more realistic results. He mentions that the calculation of one response spectrum took 8 hours and cost $40, this compares with today when a single spectrum takes less than a second to compute and is practically free.

Much of the early work on response spectra computed from strong-motion records, using Equation 4.1, was done by Housner and his co-workers in the 1940s and early 1950s, for example Housner (1941). Damped response spectra were calculated by Alford *et al.* (1951) and published by Housner *et al.* (1953). Again the inelasticity of structures for large strains is noted (see Section 4.3.2).

After the 1950s response spectra became well established as one of the major tools for assessing strong motion and its effect on structures. Almost all compilations of strong-motion observations from earthquakes include response spectra. For example Brady *et al.* (1973) shows response quantities at damping and natural period intervals commonly in use today. Since the advent of faster computers S_a, S_v and S_d are often calculated else well as the pseudo quantities, S'_a and S'_v.

4.3.2 Inelastic model

Structural materials, for example steel and concrete, do not have a linear force-displacement curve for all displacements but behave non-linearly at large displacements which introduces hysteretic damping into the system (Chopra, 1995, p. 242). There are two main types of non-linear behaviour normally assumed for SDOF systems: elastic-perfectly plastic (or elastoplastic) and bilinear force-deformation relations, see Figure 4.2.

The force-deformation relations for both these types of non-linear behaviour are linear until the resisting force reaches F_Y and then a new relationship holds between the displacement and force. Such inelastic systems require at least one extra parameter to describe them fully. For elastoplastic systems the yield force, F_Y, must be given and for bilinear systems both the yield force and the

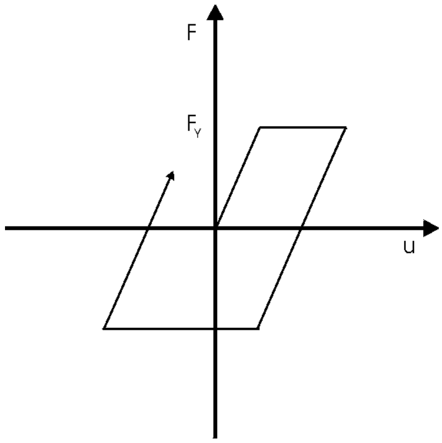

(a) Elastic-perfectly plastic

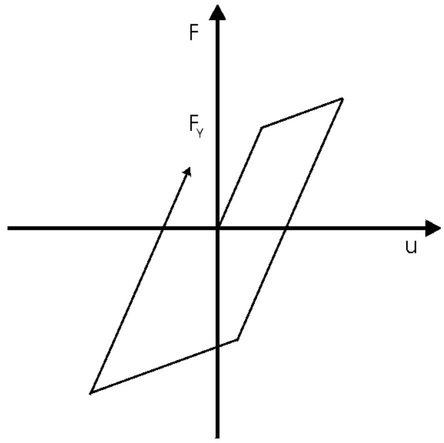

(b) Bilinear (strain hardening)

Fig. 4.2: Two common non-linear force-deformation relations. u signifies the displacement, F is the resisting force and F_Y denotes the force required for yielding to occur.

ratio of the initial stiffness and secondary stiffness, r, must be specified.

Response spectra for inelastic systems can be computed similarly to those for linear elastic systems by replacing ku with the correspond force-deformation relation valid for the system at that time. Normally the inelastic response spectrum for a particular record is plotted as constant-ductility spectrum. Ductility factor, μ, is defined as: $\mu = \max_t |u|/u_Y$, where u_Y is the displacement required for the system to yield. When computing inelastic systems F_Y is chosen not μ hence an iterative procedure is required to find F_Y corresponding to a required μ, see for example Chopra (1995, pp. 259-261).

Approximate methods exist for transforming elastic response spectra into inelastic response spectra by dividing by a number which is dependent on the period and ductility factor (and some times other parameters), called either behaviour factor, q, response modification (or reduction) factor, R (Kappos, 1999). A review of suggestions for such factors is made by Miranda & Bertero (1994).

4.4 Structural models including bending

Structural models in this section behave as if their supporting beam-column bends; hence their failure mechanism is buckling. From now on these SDOF models will be called bending models.

4.4.1 Linear elastic structural model for non-zero gravity where vertical ground motion is neglected

Consider the SDOF system illustrated in Figure 4.3.

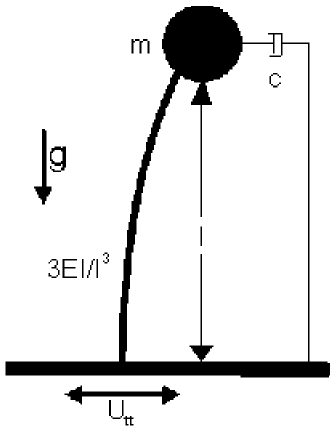

Fig. 4.3: Bending structural model for non-zero gravity field where vertical ground motion is neglected. g denotes acceleration due to gravity.

This is a massless beam-column, clamped in the ground at the lower end, with a concentrated mass at the top. If there is no external force, e.g. ground motion, then the system is governed by (Lin & Shih, 1980; Loh & Ma, 1997):

$$EIx_{yy} = P(u - x) + F(l - y), \tag{4.2}$$

$$mu_{tt} + cu_t = -F, \tag{4.3}$$

where EI is the bending rigidity, c is the damping, m is the mass, $x(y)$ is the horizontal displacement of the column, y is vertical height, u is the horizontal displacement of the mass, F is the shear force and P is the vertical load on the column which is of length l.

Now since the base of the column is rigidly clamped the boundary conditions are: $x(0) = 0$ and $x_y(0) = 0$.

To simplify Equation 4.3 requires F, which can be found by solving Equation 4.2. The solution to Equation 4.2 which satisfies the boundary conditions at $y = 0$ is:

$$x = \frac{F}{P}\sqrt{\frac{EI}{P}}\sin(\sqrt{P/EI}y) - \left[\frac{Fl}{P} + u\right]\cos(\sqrt{P/EI}y) + u + \frac{F}{P}(l - y). \tag{4.4}$$

Now the buckling load of the column, P_{cr}, is given by: $P_{cr} = \pi^2 EI/4l^2$. Define, ν, as:

$$\nu = \pi/2\sqrt{P/P_{cr}}. \tag{4.5}$$

Then Equation 4.4 becomes:

$$x = \frac{Fl}{P\nu}\sin(\nu y/l) - \left[\frac{Fl}{P} + u\right]\cos(\nu y/l) + u + \frac{F}{P}(l - y). \tag{4.6}$$

Now since the mass is attached to the top of the column: $x(l) = u$. Therefore solving Equation 4.6 for the shear force, F, using this boundary condition gives:

$$F = (3EI/l^3)(\nu/\chi(\nu));$$

where

$$\chi(\nu) = [3(\tan\nu - \nu)/\nu^3]. \tag{4.7}$$

Equation 4.3 can be simplified by expansion of $1/\chi(\nu)$ as $P/P_{cr} \leq 1$ so ν is small.
Now:

$$\tan(\nu) = \nu + \frac{1}{3}\nu^3 + \frac{2}{15}\nu^5 + O(\nu^7). \tag{4.8}$$

Substituting Equation 4.8 and Equation 4.5 into Equation 4.7 gives:

$$1/\chi(\nu) \approx 1 - \frac{\pi^2}{10}\frac{P}{P_{cr}}. \tag{4.9}$$

Now $\frac{\pi^2}{10} \approx 1$ so substituting Equation 4.9 into Equation 4.3 gives:

$$mu_{tt} + cu_t + \frac{3EI}{l^3}\left(1 - \frac{P}{P_{cr}}\right)u = 0. \tag{4.10}$$

To get equation of motion into normalised form define the natural frequency and fraction of critical damping of a column not subjected to a vertical load as: $\omega_0^2 = 3EI/(ml^3)$ and $\xi_0 = c/(2m\omega_0)$. Then the equation of motion becomes:

$$u_{tt} + 2\xi_0\omega_0 u_t + \omega_0^2\left(1 - \frac{P}{P_{cr}}\right)u = 0. \tag{4.11}$$

When the column is subjected to a horizontal ground acceleration, U_{tt}, the equation of motion becomes (since $P = mg$):

$$u_{tt} + 2\xi_0\omega_0 u_t + \omega_0^2\left(1 - \frac{mg}{P_{cr}}\right)u = -U_{tt}. \tag{4.12}$$

Letting $\omega_1^2 = \omega_0^2(1-\gamma)$ and $\xi_1 = \xi_0\omega_0/\omega_1$ where $\gamma = mg/P_{cr}$ then have:

$$u_{tt} + 2\xi_1\omega_1 u_t + \omega_1^2 u = -U_{tt}. \tag{4.13}$$

As can be seen by comparing Equation 4.1 with Equation 4.13 gravity loads simply change the natural period of the system and do not alter the size of the response (as long as the correct period is considered). There seem to be no published studies on this model.

This derivation shows one problem with using Equation 4.1 to characterise the response of structures to horizontal seismic loading. If a fundamental period of the structure is found, by using a vibration generator for instance, the structure behaves as if it is in a non-zero gravity field. Consequently the period, $T_1 = 2\pi/\omega_1$, and coefficient of critical damping, ξ_1, found are *non-zero gravity* values. A design spectra, constructed using Equation 4.1, should be consulted for the corresponding zero-gravity period, $T_0 = 2\pi/\omega_0$, and damping, ξ_0, and not for the non-zero gravity values. Thus T_1 and ξ_1 should be converted using $T_0 = T_1\sqrt{1-\gamma}$ and $\xi_0 = \xi_1\sqrt{1-\gamma}$.

In practice though, since the concept of fundamental period and coefficient of critical damping for a complicated structure are already approximations, failure to use the theoretically correct period and damping coefficient is not serious. For $\gamma = 0.33$, i.e. a factor of safety of three, $T_0 = 0.8T_1$ and $\xi_0 = 0.8\xi_1$ thus the discrepancy is not large.

As shown in Section 4.5 the change of fundamental period due to gravity is not the same for bending and hinging models, further complicating the situation.

4.4.2 *Structural model for non-zero gravity where vertical ground motion is considered and vertical stiffness is infinite*

Linear elastic model

Consider the SDOF system illustrated in Figure 4.4. This model assumes that the structure is infinitely stiff vertically so that vertical displacements due to ground motion are constant throughout the whole column therefore the vertical ground motion is the vertical input into the mass at the top of the column, i.e. it is unaffected by the column.

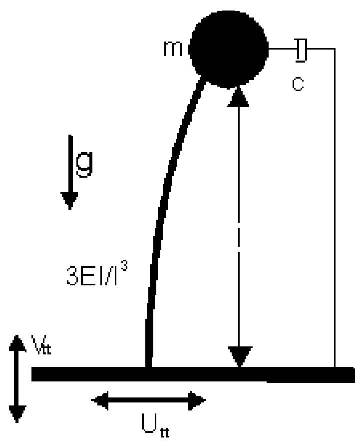

Fig. 4.4: Bending structural model for non-zero gravity field where vertical ground motion is considered and vertical stiffness is infinite.

The derivation of the equation of motion for the system depicted in Figure 4.4 follows the derivation given above for when the vertical ground motion is neglected, but Equation 4.12 becomes:

$$u_{tt} + 2\xi_0\omega_0 u_t + \omega_0^2 \left(1 - \frac{m(g + V_{tt})}{P_{cr}}\right) u = -U_{tt},$$

where V_{tt} is the vertical acceleration (positive downwards). Using the same transformations of variables as before and $\beta = \gamma/g(1-\gamma)$ the equation of motion becomes:

$$u_{tt} + 2\xi_1\omega_1 u_t + \omega_1^2(1 - \beta V_{tt})u = -U_{tt}. \tag{4.14}$$

This model has been studied by a handful of authors to assess the effect of vertical accelerations on the size of the response for elastic systems, namely Lin & Shih (1980), Orabi & Ahmadi (1988), Loh & Ma (1997) and Şafak (2000). Also the stability of Equation 4.14, when the horizontal ground motion is zero, has been much studied, for example Holzer (1970), Wirsching & Yao (1971), Gürpinar & Yao (1973) and Mostaghel (1975), these papers are not of direct relevance to this thesis and so will not be discussed here.

Lin & Shih (1980) use simulated accelerograms of Gaussian white noise modulated by an envelope function using dimensionless variables, through Fokker-Planck equations, in order to compute the expected response. They mention that parametric resonance (see Section 6.6) is possible but that because earthquakes have short durations, such effects will not cause instability. They show that the correlation between vertical and horizontal ground accelerations only has an effect on the structural response if the structure is not initially at rest, hence this correlation can be ignored.

Although the use of dimensionless variables in Lin & Shih (1980) leads to a generalised method for characterising the response of SDOF systems governed by Equation 4.14 it means that the results displayed are not readily useable. They require transformations using realistic structural parameters, such as length of column, natural period and load ratio, before the results can be used for design. Use of Gaussian white noise to simulate the response of SDOF systems to earthquake strong motion is well established, see for example Clough & Penzien (1993). Bycroft (1960) showed that it can be used to derive response spectra which match quite well those from recorded accelerograms. The choices of power spectral density, $\Phi_{11} = 0.0220$ and 0.0314 and $\Phi_{22} = 0.0141$ and 0.0201, made in Lin & Shih (1980) are unrealistically high. Transforming these dimensionless power spectral densities into $\mathrm{m^2s^{-3}}$ yields: $\phi_{11} = l\omega_1^2(1-\gamma)\Phi_{11}$ and $\phi_{22} = \pi^2 l\omega_1^2(1-\gamma)\Phi_{22}/12$. For realistic values of ω_1, l and γ $\phi_{11} \gg \Phi_{11}$ and $\phi_{22} \gg \Phi_{22}$. In Liu & Jhaveri (1969) the power spectral densities given are all less than about $0.009\,\mathrm{m^2s^{-3}}$ and in Orabi & Ahmadi (1988) $0.005544\,\mathrm{m^2s^{-3}}$ is given as the power spectral density of the NS component of the El Centro record (from the El Centro earthquake, 19/5/1940). Therefore Φ_{11} and Φ_{22} are much too high. This means that valid conclusions cannot be drawn from their numerical examples. Lin (2000) noted that the numerical examples given may be unrealistic although the theory is correct. Bycroft (1960) originally proposed the use of white noise due to the dearth of actual recordings close to the source of large earthquakes. Today there are many near-field recordings and these can be used rather than simulating strong motion through white noise.

Orabi & Ahmadi (1988) also use simulated accelerograms of Gaussian white noise modulated using an envelope function and Fokker-Planck equations to evaluate the stochastic response. Also they perform Monte-Carlo simulations directly using segments of white noise in order to check the results. They base the white noise used on the intensities of the NS and vertical components of the El Centro record. The similarity between Monte-Carlo and results using the Fokker-Planck equations is noted for two envelope functions: a constant function (stationary analysis) and an exponential envelope function (nonstationary analysis). Both methods show an increase in response for large load ratios and larger increases for smaller damping ratios. For example for the stationary analysis with $\xi_1 = 0.02$ and $T_1 = 6.3\,\mathrm{s}$ the increase in root-mean-square displacement response as γ increases from 0.5 to 0.9 is about 5% but the increase in response from $\gamma = 0.90$ to 0.95 is about 20%. For the same period but with $\xi = 0.20$ the corresponding increases are 2% and 7%. This shows the important influence of damping and load ratio on the effect of vertical excitations for this model. They also find the relative velocity response spectrum of the El Centro N-S record with and without vertical excitation for different load ratios. They note the similarity between their theoretical results and the computed spectra, their conclusions on the importance of damping and load ratio also hold for this accelerogram.

The study of Orabi & Ahmadi (1988) has a number of limitations. Their results rely on white noise with simple envelope functions to represent the horizontal and vertical ground accelerations which may not model all the characteristics of recorded earthquake strong motion. They also base their input ground intensities on the El Centro record which is no longer one of the most intense ground motions available, thus their results underestimate how much the vertical ground motion may amplify the horizontal response.

Şafak (2000) uses four near-field records, three from the Kocaeli earthquake (17/8/1999, $M_w = 7.4$) (Yarmica, Izmit and Sakarya) and one from the Düzce earthquake (12/11/1999, $M_w = 7.1$) (Düzce), to investigate the response of structures governed by Equation 4.14. Four different load ratios are used, $\gamma = 0$, 0.2, 0.4 and 0.6 and the displacement response spectra for 5% damping for these different γ values are plotted for each fault-normal record. It is found that at long periods, $T = 8.0\,\mathrm{s}$, the spectral displacements from the Sakarya record are 2.5 times higher for $\gamma = 0.6$ than for $\gamma = 0$, which Şafak (2000) suggests is because the amplitudes of the vertical and horizontal accelerations of similar size and that this record has more long-period energy that those from other stations.

The main problem with the analysis of Şafak (2000) is that the displacement spectra are plotted in terms of the non-zero gravity period and damping (see Section 4.4.1) therefore the differences found are almost entirely due to the effect of gravity on the natural period and damping and not because of the vertical ground motion. Plotting the displacement spectra in terms of the non-zero gravity parameters makes it almost impossible to distinguish the effect of the vertical excitation from the effect of gravity.

Loh & Ma (1997) is the only known published study of the response of SDOF systems governed by Equation 4.14 which uses a large number of actual strong-motion records. Two parameters are mentioned as important: the load ratio, γ, and the size of ratio between horizontal and vertical PGA. Thirty[1] Taiwanese records from a hard site are used to develop a uniform hazard response spectrum. Both the horizontal and vertical accelerograms were normalised to have a PGA of $1\,\mathrm{g}$ and $\gamma = 0.5$ was used (it was noted that larger values of γ caused instability although the reason is not given, see Section 6.3) and uniform hazard response spectra were computed which have the same probability of being exceeded at all periods. These can then be scaled by the design level PGA to yield a design spectrum. They conclude that for 5% damping, $\gamma = 0.5$ and horizontal and vertical PGA normalised to $1\,\mathrm{g}$ vertical excitation increases the response by 33% compared with when only horizontal excitation is considered.

Loh & Ma (1997) assume that the importance of vertical ground motion on the response of systems governed by Equation 4.14 is only dependent on PGA and not the other factors known to influence ground motion, e.g. magnitude, distance and local site conditions (see Chapter 2). It also is based on a vertical to horizontal PGA ratio of unity which is larger than other studies have found, see Section 7.5. Therefore it may overestimate the importance of vertical acceleration on bending SDOF systems although the authors do mention that a different choice of this ratio may affect the results (see for example their Figure 12). Also $\gamma = 0.5$ is a higher load ratio than imposed on most buildings.

Inelastic model

Inelastic systems based on Equation 4.14 but with a non-linear force-displacement term have been investigated by Shih & Lin (1982b). Following on from Lin & Shih (1980) they define their equation of motion in terms of nondimensional quantities (although the nondimensional quantities are slightly different to those in Lin & Shih (1980)) which again makes the use of their results difficult. Material non-linearity of the structure is modelled using a function proposed by Hata and Shibata, which is a simple hysteretic function with one parameter, $0 \leq r < 1$, which controls the non-linearity of the system (the system was assumed to have yielded from the beginning). The ground accelerations are modelled as amplitude modulated Gaussian white noise processes and the expected response is found through Fokker-Planck equations (also used in Lin & Shih (1980)

[1] The caption of their Figure 7 says fifty records were used.

although complications arise due to the non-linearity of the system). Numerical results for two different values of r, 0.1 and 0.5, and two levels of spectral density are presented. As for Lin & Shih (1980) the spectral densities chosen, $2\pi\Phi_{11} = 1$, 2 and 3 and $2\pi\Phi_{22} = 0.64\Phi_{11}$ are much too large for earthquake excitation therefore the numerical results are not valid. They do find though (which is probably not dependent on the incorrect spectral densities they use) that one hysteretic system can behave very differently from another system when gravity and vertical accelerations are included. Thus the results are more sensitive to model parameters than is so for linear elastic models.

4.4.3 Linear elastic structural model for non-zero gravity where vertical ground motion is considered and vertical stiffness is finite

Consider the SDOF system illustrated in Figure 4.5. This model assumes that the structure has finite stiffness vertically and that vertically the column responds like a SDOF system governed by an equation of motion like Equation 4.1 although not necessarily with the same damping and natural period as in the horizontal direction. This means that the system is separable into the response vertically and the response horizontally which is affected by the vertical response but not vice versa.

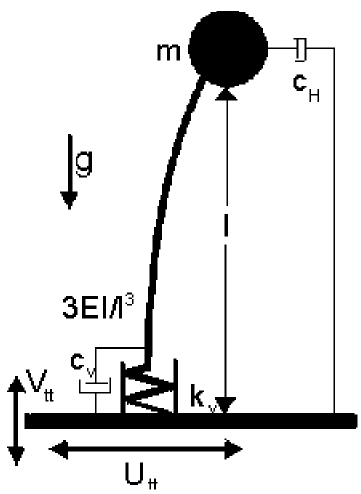

Fig. 4.5: Bending structural model for non-zero gravity field where vertical ground motion is considered and vertical stiffness is finite.

The equation of motion of this system is governed by:

$$u_{tt} + 2\xi_1\omega_1 u_t + \omega_1^2(1 - \beta u_{tt}^v)u = -U_{tt}, \tag{4.15}$$

where $u_{tt}^v = u_{tt}^v(t, T_V, \xi_V)$ is the vertical response acceleration for vertical natural period, T_V, and damping ξ_V, i.e. u_{tt} from Equation 4.1 for $\omega_0 = 2\pi/T_V$, $\xi_0 = \xi_V$ and input acceleration, $V_{tt}(t)$.

No published studies of the response of systems governed by Equation 4.15 could be found.

4.5 Structural models including hinging

Structural models in this section behave as if their supporting beam-column is hinged at the base. From now on these SDOF models will be called hinging models.

4.5.1 Structural model for non-zero gravity where vertical ground motion is neglected

Linear elastic model

Consider an inverted pendulum with an elastic hinge at the base (Figure 4.6).

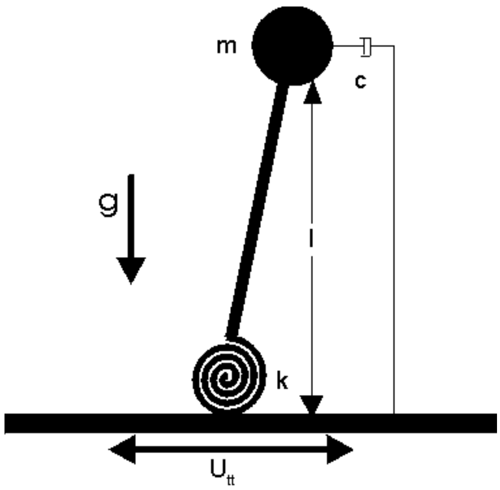

Fig. 4.6: Hinging structural model for non-zero gravity field where vertical ground motion is neglected.

Consider first free oscillations, i.e. no ground acceleration, of this system. Let the pendulum be length l and assume the inverted pendulum has been horizontally displaced from vertical through a distance u, then it will make an angle θ with the vertical.

Resolving forces perpendicular to the pendulum (N.B. not horizontally) in the direction of θ increasing gives (since θ is small):

$$-ml\theta_{tt} - cl\theta_t + mg\sin\theta - kl\sin\theta = 0.$$

Now since θ is small $\sin\theta \approx \theta \approx u/l$ so after dividing by m and defining ω_0 and ξ_0 as in Section 4.4.1 then:

$$u_{tt} + 2\xi_0\omega_0 u_t + (\omega_0^2 - g/l)u = 0.$$

When a horizontal force, mU_{tt}, is applied it needs to be resolved into its components in the direction of θ increasing and in the direction perpendicular to this. The force in the direction of θ increasing is $mU_{tt}\cos\theta$. Now θ is small and $\cos\theta = 1 - \theta^2 + \dots$ so the error caused by not resolving the horizontal force is of the order θ^2 and so is negligible. Consequently the equation of motion of this system is:

$$u_{tt} + 2\xi_0\omega_0 u_t + (\omega_0^2 - g/l)u = -U_{tt}. \tag{4.16}$$

As for the bending case a transformation of variables is useful. If $\omega_0^2 > g/l$ (if this does not hold the system does not oscillate but is unstable) then letting $\omega_1 = \sqrt{\omega_0^2 - g/l}$ and $\xi_1 = \xi_0\omega_0/\omega_1$:

$$u_{tt} + 2\xi_1\omega_1 u_t + \omega_1^2 u = -U_{tt}. \tag{4.17}$$

Requiring $\omega_0^2 > g/l$ gives a limit, i.e. $l > mg/k$, on the smallest l can be for the pendulum simply to withstand gravity loads and so all structures must satisfy this condition, even if they are not designed for earthquake loads.

As for the bending model, see Section 4.4.1, when vertical ground motion is neglected the effect of gravity loading is simply to shift the natural period of the structure. The period, $T_1 = 2\pi/\omega_1$, and coefficient of critical damping, ξ_1, measured from a real structure are *non-zero gravity* values. A design spectra, constructed using Equation 4.1, should be consulted for the corresponding zero-gravity period, $T_0 = 2\pi/\omega_0$, and damping, ξ_0, and not for the non-zero gravity values. Thus T_1 and ξ_1 should be converted using $T_0 = T_1/\sqrt{1 + T_1^2 g/[(2\pi)^2 l]}$ and $\xi_0 = \xi_1/\sqrt{1 + T_1^2 g/[(2\pi)^2 l]}$.

Figure 4.7 shows the factor, $1/\sqrt{1 + T_1^2 g/[(2\pi)^2 l]}$, against T_1 for different lengths of pendula, l. This shows how much the natural period and damping changes when gravity forces are considered. As can be seen the change in natural period and damping is only large for short columns and long periods.

Jennings & Husid (1968), Husid (1969), Sun *et al.* (1973), Bernal (1987) and Fenwick *et al.* (1992) all investigate this model amongst others and conclude the effect of gravity is negligible, which it is if l is reasonably long so that the change in natural period and damping is small.

Inelastic model

Jennings & Husid (1968) and Husid (1969) study a model similar to that specified in Equation 4.17, although not making the assumption that θ is small[2], hence their equation of model is slightly more complex, for elastoplastic and bilinear hysteretic structures. They consider many choices of natural period (0.5, 1.0, 1.5 and $2.0\,\mathrm{s}$) , length of pendulum (1.5, 3.0, 4.5, 6, 7.5 and $9\,\mathrm{m}$) and yield level ($0.05\,\mathrm{g}$ and $0.10\,\mathrm{g}$) each with damping of 2% of critical. Simulated accelerograms of stationary Gaussian random processes of $60\,\mathrm{s}$ duration are used to investigate the time to collapse of such structures. They find that the time to collapse depends hyperbolically on the ratio of earthquake

[2] They verify that there is little difference between predicted responses when this assumption is made and when it is not made.

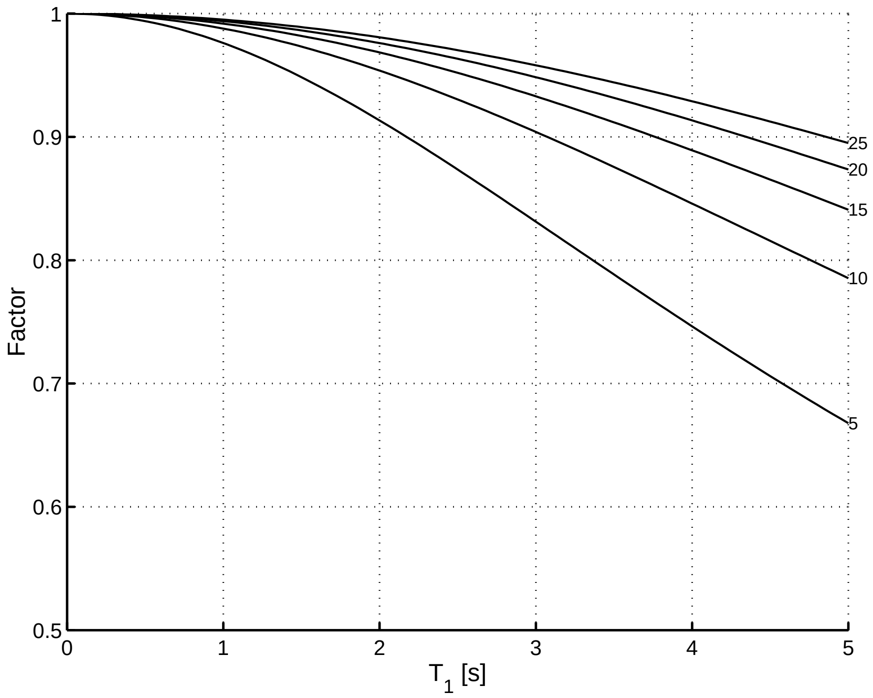

Fig. 4.7: Factor, $1/\sqrt{1+T_1^2 g/[(2\pi)^2 l]}$, against T_1 for length of pendulum, $l = 5$, 10, 15, 20 and $25\,\mathrm{m}$.

strength to yield strength, linearly on length of pendulum and is highly dependent on duration (for longer records less intense motion is required for the structure to collapse), but it is independent of natural period. For the bilinear force-deformation relation, if the ratio of the second slope to the initial slope is sufficiently high collapse is prevented. Results are confirmed using actual accelerograms.

Sun *et al.* (1973) investigate a model similar to that specified in Equation 4.17 but for a force-displacement curve which has ideal elastoplastic behaviour in extension and buckles at zero load in contraction using phase-plane analysis. They find three equilibrium positions using static methods, conditions for when the system will collapse and will suffer a residual displacement after the shaking has stopped. They use the NS El Centro record to illustrate their results. Two design criteria are proposed based on the conditions required for no large residual displacements and for no collapse, in terms of displacement spectra and input energy.

Bernal (1987) compute amplification factors for gravity effects using four strong-motion records (Olympia S86W, El Centro S00E, Taft S69E and Pacoima Dam S16E) in terms of a dimensionless stability coefficient and ductility factor for elastoplastic systems. The amplification factor is the ratio of the displacement response with and without gravity effects. A simple limit on the size of the stability coefficient, $\theta = g/\omega_0^2 l$, is given based on earthquake codes. From this the conclusion is drawn that structures in regions of relatively low seismic coefficients, i.e. low design acceleration, are less protected, by the interstorey drift limitation, against inelastic gravity effects than those in areas of higher design acceleration. Systems with six ductilities (1, 2, 3, 4, 5 and 6), nine stability coefficients (0 to 0.2) and 37 periods (0.2 to $2\,\mathrm{s}$) were investigated for each of the records. No significant correlation was found between period and amplification but an expression for predicting amplification due to gravity based on ductility and stability coefficient is given. This expression was found to give different predictions than those given in codes, some of which are shown to under predict amplification.

Fenwick *et al.* (1992) use a number of strong-motion records, although they base most of their results on an artificial record of about $25\,\mathrm{s}$ duration, to find amplification factors for elastoplastic and bilinear structures. They find that the strain hardening ratio (the ratio between the gradient of the first and second slope of the bilinear force-deformation relation) is not significant for amplification but that viscous damping does make a large difference. They use the Cholame Shandon Array 2W N65E record (from Parkfield earthquake, 28/6/1966), which has a short duration of strong shaking, and compare the amplification factors with those for the El Centro record and the artificial record and find they are much lower. Hence duration has a large effect. They also find that for some records amplifications are not independent of period over its entire period range. Equations are given for amplification factors in terms of ductility and period for firm and flexible subsoils.

4.5.2 Structural model for non-zero gravity where vertical ground motion is considered and vertical stiffness is infinite

Linear elastic model

Consider the SDOF system illustrated in Figure 4.8.

The derivation of the equation of motion for this system follows that given in Section 4.5.1 but Equation 4.16 becomes (since vertical ground acceleration, V_{tt}, acts like an additional gravity force):

$$u_{tt} + 2\xi_0\omega_0 u_t + (\omega_0^2 - (g + V_{tt})/l)u = -U_{tt}. \tag{4.18}$$

Defining ω_1 and ξ_1 as before and letting $\beta = 1/(\omega_0^2 l - g) = 1/\omega_1^2 l$ yields:

$$u_{tt} + 2\xi_1\omega_1 u_t + \omega_1^2(1 - \beta V_{tt})u = -U_{tt}. \tag{4.19}$$

There appear to be no published studies on systems governed by Equation 4.19.

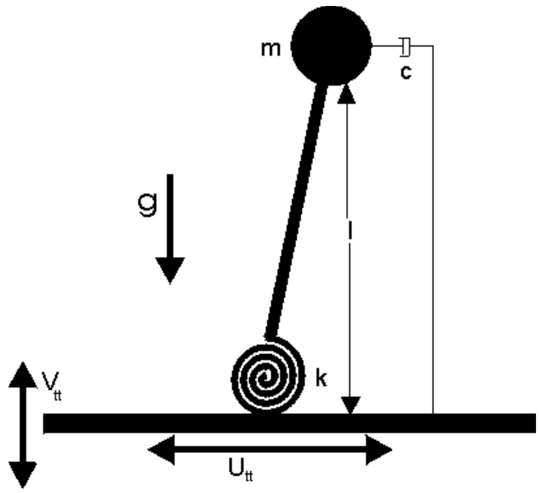

Fig. 4.8: Hinging structural model for non-zero gravity field where vertical ground motion is considered and vertical stiffness is infinite.

Inelastic model

Jennings & Husid (1968) and Husid (1969) as part of their studies also apply vertical ground motion as well as gravity loads and horizontal motion and find that vertical ground motion is relatively unimportant in controlling the time to collapse.

4.5.3 Structural model for non-zero gravity where vertical ground motion is considered and vertical stiffness is finite

Linear elastic model

Consider the SDOF system illustrated in Figure 4.9. As for the bending case, see Figure 4.5, this model assumes that the structure is finitely stiff vertically and that vertically the column responds like a SDOF system governed by an equation of motion like Equation 4.1 although with not necessarily the same damping and natural period as in the horizontal direction. This means that the system is separable into the response vertically and the response horizontally which is affected by the vertical response but not vice versa.

The equation of motion of this system is:

$$u_{tt} + 2\xi_1\omega_1 u_t + \omega_1^2(1 - \beta u_{tt}^v)u = -U_{tt}, \tag{4.20}$$

where $u_{tt}^v = u_{tt}^v(t, T_V, \xi_V)$ is the vertical response acceleration for vertical natural period, T_V, and damping ξ_V, i.e. u_{tt} from Equation 4.1 for $\omega_0 = 2\pi/T_V$, $\xi_0 = \xi_V$ and input acceleration V_{tt}.

No published studies on systems governed by Equation 4.20 could be found in the literature.

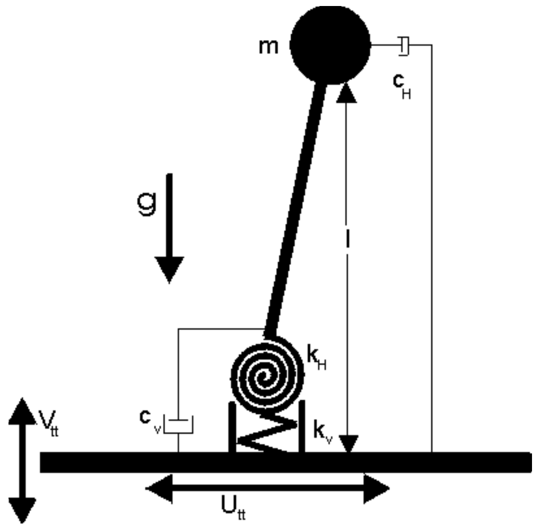

Fig. 4.9: Hinging structural model for non-zero gravity field where vertical ground motion is considered and vertical stiffness is finite.

Inelastic model

Tani & Soda (1977) present an investigation using a similar model to Equation 4.20 although using a bilinear force-displacement relationship, with positive stiffness ratio, similar to that used by Shih & Lin (1982b). They assume the structure continues to behave elastically in the vertical direction even when plastic deformation takes place in the horizontal direction. Horizontal ground motion is assumed to be quasi-nonstationary white noise and vertical excitation is stationary white noise. Statistical mean square response of the system is expressed by a Voltera type integral equation and solved using Laplace transforms. An equivalent linearization method is used to model the bilinear hysteresis which they find to be accurate. Numerical results are given for ten models with different stiffness ratios, r, heights, H, yield displacements and natural periods and for the three conditions: horizontal excitation only, horizontal and gravity loads and horizontal and vertical excitation and gravity loads. All of their models have vertical natural periods equal to a tenth of the the horizontal period, vertical damping equal to 10% and horizontal damping equal to 2%. They conclude that gravity loads can be important, increasing the displacement more than 10%, for tall structures and especially those with small stiffness ratio. They find vertical excitation can be ignored due to its small effect.

The study of Tani & Soda (1977) is small scale, only a few models are considered which do not cover different combinations of horizontal and vertical natural period and damping which could occur in structures. They also do not subject their models to particularly large excitations, the PGA of their most intense white noise excitation is $6\,\mathrm{ms}^{-2}$ and the power spectral density of the vertical excitation of all of their simulations is a quarter of the horizontal density.

4.6 Other studies related to the effect of vertical acceleration on response

4.6.1 Infinite degrees of freedom (IDOF) models

Ruge (1934) studies a vertical cantilever using static theory with a qualitative description of how the system's behaviour will change under the influence of gravity. He concludes the effect of gravity can be important.

Iyengar & Shinozuka (1972) study three elastic vertical cantilevers, which are taken to approximate tall structures, under combined horizontal and vertical ground excitation. They use a bivariate stationary Gaussian process to generate horizontal and vertical ground motions, with power and cross spectra which are frequency dependent. It is found that the vertical acceleration and self-weight affects the two tallest cantilevers more than the short one. It is also concluded that self-weight and vertical motion can decrease or increase the response and that these differences are usually considerable. In fact their Figures 9, 10 and 11 show maximum increases in deflection, bending moment and shear force of about 10%.

Iyengar & Saha (1977) investigate two vertical cantilevers subjected to six pairs of horizontal plus vertical accelerations (El Centro, 19/5/1940; Taft, 21/7/1952; and Eureka, 21/12/1954) and compute their deflections, bending moments and shear forces at various heights. They conclude that vertical ground motion does not always increase or decrease the response of vertical cantilevers but that it needs to be considered because it can have a large effect. Their Figure 5 shows that the bending moment at the top of one of their cantilevers increases by about 60% when vertical acceleration is considered but usually the increase is less than 10%. Figure 4 of Iyengar & Saha (1977) shows that the shear force only changes by a maximum of about 4% when vertical acceleration is included.

4.6.2 Multiple degrees of freedom (MDOF) models

Cheng & Oster (1976) study two steel frames, one with one bay and two storeys and the other with one bay and three storeys, assuming bilinear material behaviour. The two storey frame is subjected to harmonic ground acceleration in horizontal and vertical directions with varying dead loads and dynamic load combinations and the region of instability is investigated. The three storey frame is subjected to a lateral impulse and vertical component of the El Centro accelerogram and an increase in the horizontal response was noted compared with when only the impulse is applied. Also the NS and vertical component are applied to the frame and the displacement response is shown to increase and decrease for certain periods compared with when only the horizontal component is applied.

Shih & Lin (1982a) investigate N-storey buildings modelled as a MDOF system with N differential equations similar in form to Equation 4.14. The vertical acceleration at each storey is equal to the ground acceleration because the vertical motion is assumed to be transmitted almost instantaneously from the bottom to the top, because of the much greater rigidity of the columns to resist dilational than flexural deformations. As in their other work (Lin & Shih, 1980; Shih & Lin, 1982b) nondimensionalised variables are used which again makes interpreting their results for realistic structural parameters difficult. The method of using amplitude modulated Gaussian white noise to model horizontal and vertical ground accelerations and solving stochastic differential equations presented in Lin & Shih (1980) and Shih & Lin (1982b) is again followed although it is slightly more complex due to the use of matrices. A numerical example is given for a six storey building which is a reasonable representation of an actual structure. The model is subjected to two levels of excitation corresponding to power spectral densities $\Phi_{11} = 0.0000444$, 0.000277 and $\Phi_{22} = 0.64\Phi_{11}$ and the nondimensional mean square shear force at the base and displacement at the roof are found for the three cases: horizontal excitation only, horizontal and vertical excitation, and horizontal and vertical excitation and gravity loads. Unlike their other two studies (Lin & Shih, 1980; Shih & Lin, 1982b) the choices of power spectral densities made are reasonable for earthquake excitation so their conclusions are valid. They find that for the less intense excitation gravity and vertical excitation has little effect, increasing the displacement of the roof by about 1% each and the shear force by about 10% for vertical excitation and about 1% for gravity loads. For the more intense excitation both vertical excitation and gravity loads can have a large effect, vertical excitation increasing the displacement by about 20% and the shear force by about 40%. Gravity loads increase both displacement and shear force by about 5%. They mention though that for such large excitations linear behaviour of the structure is probably unrealistic.

Papazoglou & Elnashai (1996) report analysis of lumped parameter MDOF structural models employing bilinear stiffness characteristics in tension and compression applicable to RC column behaviour, which indicates that strong vertical motion can lead to column tension. Intermediate and top storeys are more likely to undergo tensile deformations.

4.6.3 Models of real structures

Over the past thirty years the response of buildings has been modelled, under the combined action of horizontal and vertical ground shaking, by a number of different authors. Results of some of these studies are presented here including some of the most recent investigations.

Anderson & Bertero (1973) study an unbraced single bay frame of ten storeys subjected to two observed accelerograms[3]. They find little difference in the displacement or relative storey displacements when gravity and/or vertical accelerations are considered. Girder and column ductility requirements are significantly increased especially on upper stories (in some places more than 100%)

[3] First 11 s of vertical and S74W components of Pacoima Dam, from San Fernando earthquake (9/2/1971), multiplied by 0.4 and first 14 s of vertical (multiplied by 3) and S69E (multiplied by 2) components of Taft, from Kern County earthquake (21/7/1952).

due to the action of gravity and vertical ground accelerations. Vertical excitations increases upper column plastic hinge rotation requirement and gravity increases lower column plastic hinge rotation requirement compared with when only horizontal excitations are considered. Thus they conclude vertical ground motion and gravity need to be taken into account when analysing buildings.

Cheng & Oster (1977) study three frames under combined horizontal and vertical excitation. First frame is one bay, three storey with strong columns with no plastic rotation excited by the modified Taft accelerogram used by Anderson & Bertero (1973). The other two frames (a three bay, four storey rigid frame where the columns undergo plastic deformations and a one bay, ten storey frame) are subjected to the NS and vertical components of the El Centro record. Vertical motion is found to increase ductility and excursion ratios significantly in all three frames.

Papaleontiou (1992) and Papaleontiou & Roesset (1993) analyse four steel frames, with 4, 10, 16 and 20 storeys, and three spans, which approximate real structures. They use the Capitola record, from the Loma Prieta earthquake (18/1/1989), and find the horizontal and vertical displacement at roof level and the axial force and bending moments in the top and bottom columns of the frames. Axial forces in the top columns are found to increase significantly (360% for the 16 storey structure but less for other frames) when horizontal and vertical acceleration are included to when only horizontal ground motion is applied. Axial forces in the bottom columns are also shown to increase although not by as much (33% for the 16 storey frame). Also bending moments in the upper storey also increase (by up to 75% for one of the frames) when vertical excitation is included to when it is not, but bending moments in the bottom storey are unaffected by the vertical ground motion.

Chouw & Hirose (1999) investigate a three storey one bay frame with and without vertical acceleration using the accelerogram recorded at 17645 Saticoy Street during the Northridge earthquake (17/1/1994). They find that axial forces increase by up to 100% when vertical accelerations are included to when only horizontal shaking is applied.

Reyes-Salazar & Halder (2000) model three steel frames, with partially restrained connections, subjected to 13 actual strong-motion time-histories (El Centro and 12 from the Northridge earthquake). The frames studied are three bay with three, eight and fifteen storeys and the maximum lateral displacement at the top of the frame and the maximum bending moments and axial loads at the ground level for the interior and exterior columns. The results obtained from the simulations are compared with the displacements, forces and moments specified such loading in the Recommended Provisions for Seismic Regulations for New Buildings (National Earthquake Hazard Reduction Program, 1994) and the Mexico City Seismic Code (Comision Federal de Electricidad, 1993). It is found that displacements at the top of the frames and bending moments at the bottom are almost unaffected by the inclusion of vertical ground acceleration and that the National Earthquake Hazard Reduction Program (1994) provisions predict the responses well but the Comision Federal de Electricidad (1993) code over predicts the response by about 17%. Axial forces in the bottom columns are found to be under predicted by both codes when vertical excitation is included, by up to 50% for National Earthquake Hazard Reduction Program (1994) and 70% for Comision Federal de Electricidad (1993) and that the error is not correlated with height of frame but is positively correlated with the ratio of PGA_v to PGA_h.

Yamazaki *et al.* (2000) study the effect of vertical ground motions upon the horizontal response of steel beam-columns which they say are more affected by vertical excitation than frame models. Horizontal natural period of the column is set at 1.0 and $2.0\,\mathrm{s}$ and the vertical natural period is varied between 0.1 and $1\,\mathrm{s}$. Three strong-motion records, El Centro (NS and vertical), Taft (EW and vertical) and JMA-Kobe (NS and vertical) from the Hyogo-Ken Nan-Bu earthquake (16/1/1995), are used as input and the horizontal displacement and shear force are measured and calculated. It is found that when the ratio of vertical to horizontal natural period is higher than 0.5 the maximum displacement changes significantly from when the vertical acceleration is neglected. The phase difference between horizontal and vertical ground motions is also investigated and it is found that for a few conditions the maximum response displacements change by a large amount due to this difference. They conclude, because the ratio of vertical to horizontal period in ordinary high-rise buildings is approximately 0.1 to 0.2, that the effect of vertical ground motion upon horizontal responses of steel high-rise buildings is small.

Kikuchi *et al.* (2000) investigate a three span, five storey, reinforced concrete, moment resisting frame designed to the current Japanese seismic building. The frame was subjected to the El Centro #6 record, from the Imperial Valley earthquake (15/10/1979), and the JMA-Kobe record. Under El Centro #6 loading the column axial force was shown to be increased significantly from when only horizontal ground motion is applied but due to the time lag between the main shaking in the vertical and horizontal directions the damage arises mainly from the horizontal motion. Under JMA-Kobe loading the vertical ground motion is shown to be relatively insignificant in altering the column axial force or the response in general due to the vertical acceleration being much lower than that in the horizontal direction. It is concluded that vertical ground motion has little influence on the damage to the building.

Abdelkareem & Machida (2000) analyse bridge piers subjected to the ground motion recorded at Nishinomya City from the Hyogo-Ken Nan-Bu earthquake for the two conditions: horizontal ground motion only; and combined horizontal and vertical excitation. It was found that the peak response acceleration is significantly increased (up to 80%), compared to when horizontal motion alone is applied, when both horizontal and vertical shaking is used as input and that this increase is less when more shear reinforcement is used. Also it was found that the ratio of maximum axial compression load on the pier when horizontal and vertical excitation is included to when only horizontal motion is applied, is roughly linearly proportional to the ratio of PGA_v to PGA_h. Increases of about 40% in maximum axial compression load are found for $\mathrm{PGA}_v/\mathrm{PGA}_h = 0.8$. It is also found that the ductility level decreased significantly (by up to 20%) when the pier is subjected to the vertical ground motion in addition to the horizontal motion. Vertical motion also increases base shear (by up to 65%), lateral strain (of up to 421% for maximum tensile strain) and axial strain (by up to 216% for maximum compressive strain). They conclude that inclusion of vertical ground motion changed the failure mode of piers from flexural to severe diagonal shear failure.

Three buildings (a two to three storey concrete parking garage, a four storey building and a 16 storey steel building) are analysed in Kehoe & Attalla (2000). It was found that the forces on the structural elements induced by vertical acceleration are often much less than the effects of dead load and overturning effects are more due to horizontal than vertical accelerations. They also found for some structural elements, primarily long span concrete girders, vertical accelerations may be of the same order as the dead load.

Diotallevi & Landi (2000) analyse a five storey, three bay moment resisting RC frame which was designed with aseismic criteria. The frame was subjected to five strong-motion records (three from Northridge, one from San Fernando and one from Imperial Valley) which differ in frequency and time lag between the peak vertical and horizontal accelerations. It is found that the vertical motion contributes a significant additional axial force (by up to 76%) over when only horizontal motion is considered, especially in the columns in the upper floors. Also noted is the important effect of vertical acceleration, for two of the strong-motion records, on displacement (total and interstorey drift), length of plastic zones, size of plastic deformations, amount of energy dissipated and maximum moment and shear values. The authors conclude that vertical motion is important in seismic analysis and that the characteristics of vertical motion should be studied further.

Papazoglou & Elnashai (1996) report instances of damage to buildings and bridges during the Kalamata (13/9/1986), Northridge and Hyogo-Ken Nan-Bu earthquakes, for which they find convincing evidence that the damage was caused by axial overstressing. It was found that net tensile forces and displacements occur and total axial forces increase (by up to 82% compared with when only horizontal ground motion is included) in an eight storey, three bay moment resisting RC frame, designed according to UBC, subjected to the El Centro #6 record, from the Imperial Valley earthquake. The behaviour factor of another eight story, three bay frame designed according to EC-2/EC-8 for an acceleration of $0.15\,\mathrm{g}$ is reduced by up to 50% when vertical ground motion is included, compared with when only horizontal excitation is included. The transverse response parameters, e.g. interstorey drift, of a six storey, three bay moment resisting steel frame subjected to Santa Monica-City Hall and the Arleta Fire Station records (from the Northridge earthquake) were not found to be significantly affected by vertical excitation but for long span structures vertical beam vibration modes may experience significant amplifications.

4.6.4 Other studies

Elnashai & Papazoglou (1997) report results concerning vertical bilinear spectra, i.e. systems with unequal tensile and compressive stiffnesses, for an elastoplastic SDOF system based on 35 vertical strong-motion records. Various ratios between the tensile and compressive stiffnesses, scaled peak ground accelerations and axial force factors are employed. It is found that for large vertical PGA and small axial load factors tensile forces and displacements can occur. Also investigated is the ductility demand spectrum, for 10 of the records, assuming an overall safety factor against static compressive failure of 2.5. It is found that the vertical component alone can lead to dramatic column compression failure accompanied by large ductility demand in compression.

4.7 Conclusions

This chapter shows that although some work has been completed on how vertical ground motion affects structural response, many of these studies are too small scale for their conclusions to be general. Hence there is a need for a more general approach using a range of structural models, structural parameters and ground motion inputs to derive some general conclusions on the importance of vertical ground motion to design.

Models of buildings have been investigated under the combined action of horizontal and vertical ground motion using observed accelerograms and the conclusions drawn from most of these studies is that vertical ground acceleration needs to be included otherwise axial forces in the columns and other structural responses are significantly underestimated. Although this approach yields accurate answers for a particular type of structure (for example steel frames and reinforced concrete buildings) it is difficult to generalise the results for other types of buildings and for seismic code requirements. The rest of this thesis will concentrate on the response of SDOF systems, which although they do not accurately model actual structures they provide results which are more general, since various parameters can be varied to examine their effect, and they can be codified.

Many of the SDOF system studies do not base their results on actual strong-motion recordings but on white noise representation of ground shaking. Although white noise representation may yield adequate estimates of the importance of vertical excitation for most earthquake ground motions which occur, Newmark & Rosenblueth (1971, p. 302) state '[a]dditional confirmation of the orders of magnitude of Monte Carlo results should in general be obtained from spotchecks using records of actual earthquakes'. When white noise was first used to simulate strong-motion records, in the 1960s, there were few records of actual earthquakes especially those from the near field of large earthquakes. Now though there are thousands of strong-motion recordings are available of which a large fraction are from the near field of reasonably large earthquakes, thus no longer do studies on the response of structures to simultaneous horizontal and vertical excitation need to be solely based on white noise approximations.

Those studies which do use actual accelerograms often use only a handful and often they only use the El Centro record, although many other records exist which are more reliable (due to better recording and processing) and contain more intense motion. Thus a large suite of time-histories needs to be utilised to give reliable conclusions which are based on ground motions which have actually occurred.

Linear elastic SDOF systems are investigated here rather than inelastic system because are characterised using less parameters, making the task of examining their response easier. Newmark & Hall (1987) note that ‘it is still difficult to construct mathematical models that lead to satisfactory results and that are not complicated to the point of becoming impractical for analysis of complex structures’. Shih & Lin (1982b) noted, specifically for combined horizontal and vertical excitation, that two inelastic SDOF systems can behave very differently under the same seismic action. Therefore an understanding the response of simple models is needed before complex models can be studied.

5. CHARACTERISTICS OF STRONG-MOTION DATA USED

Two main suites of records were used in this study, a near-field set and a set of records from the near, intermediate and far fields for use in the pure error section.

5.1 Near-field set of records

Vertical ground motion is thought only to be important in the near field of an earthquake, therefore it was decided to use only near-field records.

5.1.1 Definition of near field

The boundary of the near field for an earthquake is defined in terms of magnitude and distance and many different definitions of this boundary have been given (Figure 5.1).

Clearly there is little consensus about the definition of 'near field'. Martínez-Pereira & Bommer (1998) give a rigourous definition of the 'near field' by examining different strong-motion parameters for predicting damage (damage potential parameters) against distance and magnitude. They define the near field as that part of magnitude-distance space in which specific damage potential parameters are above given thresholds. Unfortunately they do not give equations, in terms of magnitude and distance, for this space but note that it is similar to that of Krinitzky & Chang (1987)[1]. Martínez-Pereira (1999) continues this work and does give an expression for the upper bound of this space which is shown in Figure 5.1.

For this thesis the definition of 'near field' of Ambraseys & Simpson (1996) is used, except that the lower limit on PGA is removed and the lower magnitude limit reduced to $M_s = 5.8$. The PGA lower limit was removed for two reasons, firstly the PGA at a site cannot be known before hand and so it will not be known whether the attenuation equations given by Ambraseys & Simpson (1996) apply and secondly this limit introduces a bias with the result that the accelerations are overestimated. Reducing the lower magnitude limit from $M_s = 6.0$ to $M_s = 5.8$ has increased the set of suitable records especially those from Europe[2].

[1] The definition given by Krinitzsky *et al.* (1993) is thought to be similar.

[2] Ambraseys & Simpson (1996) used a number of records from the Whittier Narrows earthquake (1/10/1987) for which they assigned $M_s = 6.00$. For this study the magnitude was recalculated and it was found to be equal to $M_s = 5.94$. Hence the difference in criteria is, in fact, minimal.

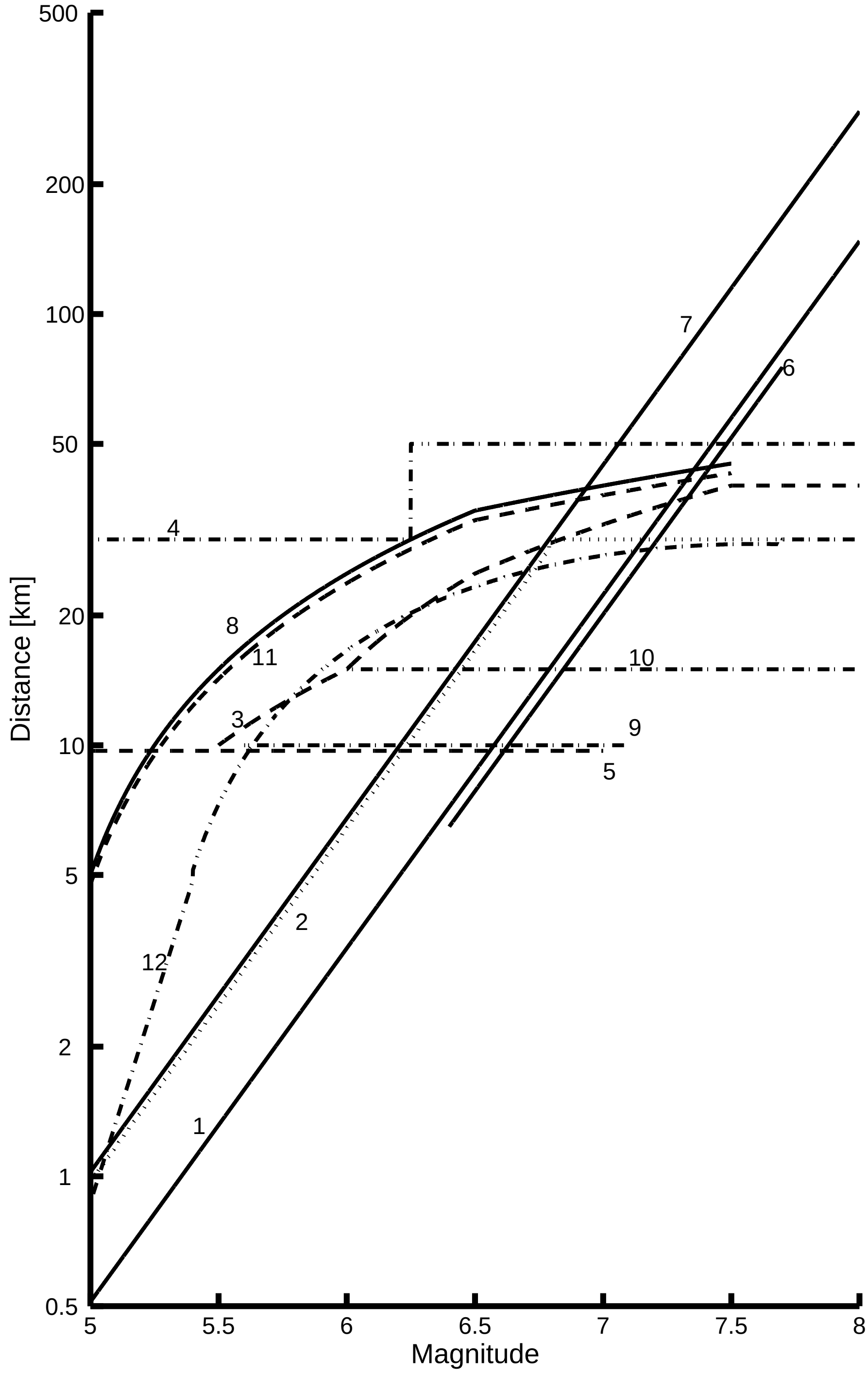

Fig. 5.1: Graph showing definition of 'near field' by different authors. 1) Berrill (1975) 2) Tocher *et al.* (1977) 3) Shteinburg *et al.* (1980) 4) Campbell (1981) and Campbell & Bozorgnia (1994b) (Use expression 'near-source') 5) Bolt & Abrahamson (1982) 6) Ambraseys & Menu (1988) 7) Hudson (1988) (Uses expression 'near-source') 8) Krinitzsky *et al.* (1993) 9) Nisar & Golesorkhi (1995) 10) Ambraseys & Simpson (1996), 11) Hu *et al.* (1996) & 12) Martínez-Pereira (1999). Some authors are not explicit in their definition and so an approximate distance bound was found using the fault length, L, expression ($\log L = -4.09 + 0.82 M_s$) from Ambraseys & Jackson (1998).

A magnitude dependent definition was not employed for two reasons. Firstly as was noted above there is no commonly accepted definition of near field therefore choosing one over another may lead to results inconsistent with other near-field studies where another definition is used. The Ambraseys & Simpson (1996) definition (which is being followed here) is one of strictest of all those published (see Figure 5.1), thus although its use may exclude some records which have the characteristics of a near-field record it should not include records which do not have these characteristics. This is thought to be better than a more relaxed definition in which some of the selected time-histories are not actually from the near field. The second reason is more technical. If the upper bound on the highest allowable fault distance increased with increasing magnitude then the associated magnitudes and distances of the selected set of data would be positively correlated. This can lead to problems with the one-stage regression method (Section 3.9).

Since attenuation relations are found in this study different severities of shaking can be accommodated within the suite of accelerograms used and these differences between them modelled by the attenuation equations found. This differs from the method of Nisar & Golesorkhi (1995) and Elnashai & Papazoglou (1997) where a mean is taken for all records. Taking the mean requires all the records in the set to have roughly the same level of shaking therefore the selection criteria used should be more strict.

5.1.2 Selected records

From the ESEE strong-motion database 186 free-field[3], mainly triaxial[4], strong-motion records from 42 earthquakes were selected using the criteria: surface-wave magnitude $M_s \geq 5.8$, distance to surface projection of fault $d_f \leq 15\,\mathrm{km}$ and focal depth $h \leq 20\,\mathrm{km}$. The chosen records are listed in Table D.1. The majority came from western North America (133 or 72 %), the rest were from Europe (40 or 22%) or from other parts of the world (Canada, Nicaragua, Japan and Taiwan) (13 or 7%). The distribution with earthquake mechanisms is: thrust (98 or 53%), strike-slip (72 or 39%) and normal (16 or 9%). Figures 5.2 to 5.5 show the distribution of the data with magnitude, distance and mechanism.

The records are well distributed in magnitude and distance (Figure 5.2) so the equations obtained based on this set of data are well constrained and representative of the entire dataspace ($0 \leq d \leq 15\,\mathrm{km}$ and $5.8 \leq M_s \leq 7.8$). Figures 5.3 and 5.4 also show reasonably uniform distribution of records. Figure 5.5 shows the lack of near-field recordings of earthquakes with normal mechanisms and also the upper limit on the size of such earthquakes (about $M_s = 6.9$), the result

[3] The definition of free-field used by Joyner & Boore (1981) was adopted, i.e. records from instruments in buildings of three or more storeys and from abutments were excluded unless the structures were thought not to have affected the records within the period range of interest.

[4] Seven of the records had only one or two components of usable time-histories.

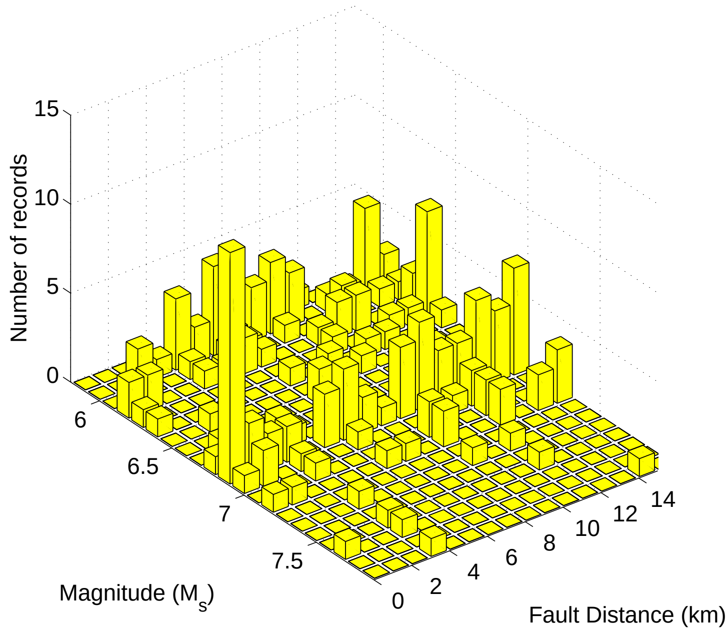

Fig. 5.2: Distribution of all records in near-field set with respect to magnitude and distance.

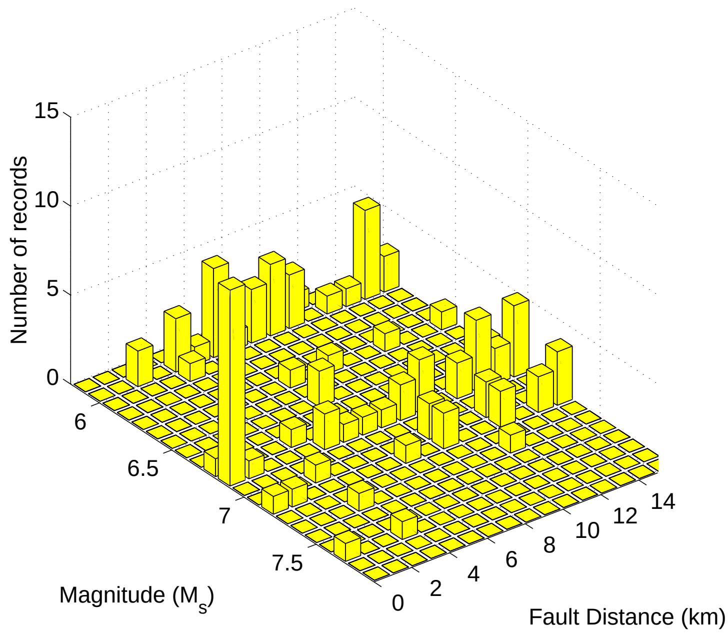

Fig. 5.3: Distribution of records associated with thrust earthquakes in near-field set with respect to magnitude and distance.

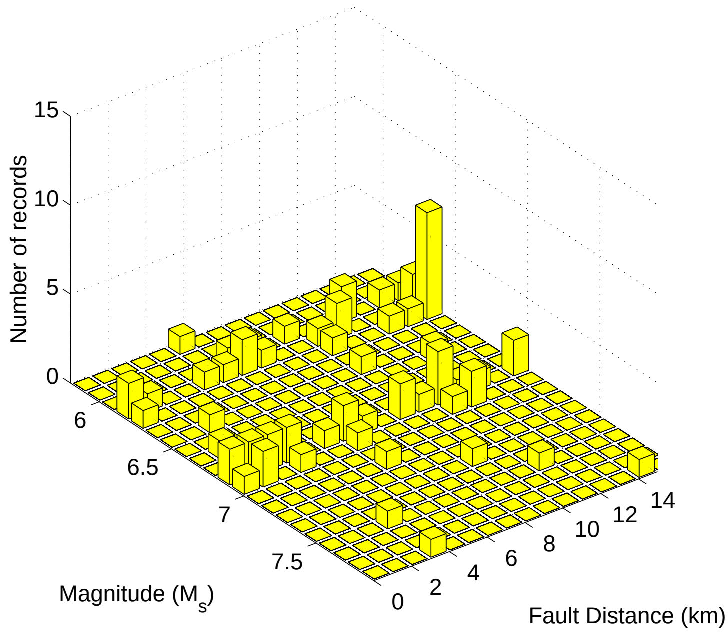

Fig. 5.4: Distribution of records associated with strike-slip earthquakes in near-field set with respect to magnitude and distance.

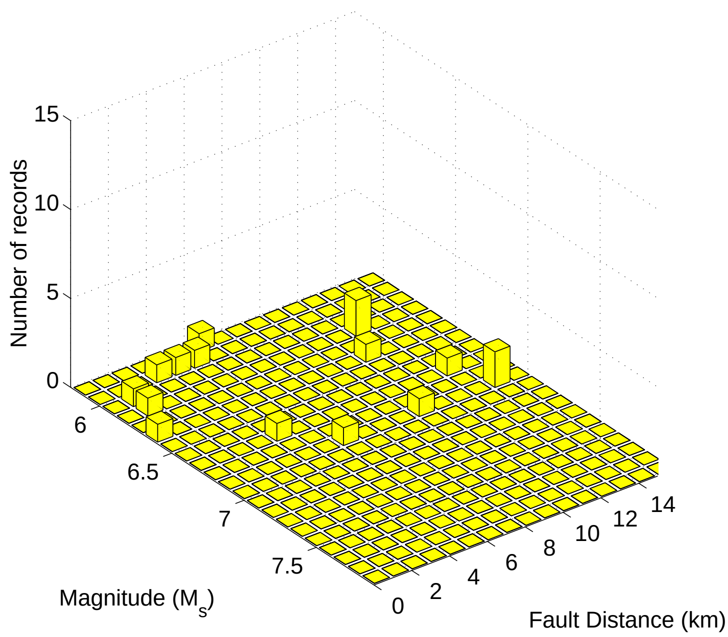

Fig. 5.5: Distribution of records associated with normal earthquakes in near-field set with respect to magnitude and distance.

of fault segmentation.

Site conditions at the stations are also given in Table D.1 using the categorisation proposed by Ambraseys *et al.* (1996) and Ambraseys & Simpson (1996), i.e. L: $V_{s,30} < 180\,\mathrm{ms}^{-1}$, S: $180 \leq V_{s,30} < 360\,\mathrm{ms}^{-1}$, A: $360 \leq V_{s,30} < 750\,\mathrm{ms}^{-1}$ and R: $V_{s,30} \geq 750\,\mathrm{ms}^{-1}$. For many of the Californian stations and European stations soil profiles were found, from which $V_{s,30}$ is found directly. Site conditions at other stations were converted from other workers' site categories. The site conditions for 178 of the 186 records have been classified and there are 4, 83, 68 and 23 records in the L, S, A and R categories respectively.

5.1.3 Correction procedure

Ideally all of the records within this set would have been processed in a uniform way, but this to be possible the time-histories must be available in uncorrected format. Unfortunately some of the records (19) could only be obtained in corrected format. Since these records are from large earthquakes (Petrolia/Cape Mendocino, Landers, Big Bear, Northridge and Hyogo-Ken Nan-Bu) it was thought better to incorporate them in the study. The short period range of interest for this study (0.1–2 s) means that any differences in the correction procedure should make little difference. The 19 records corrected in a different way are labelled with 'C' in Table D.1.

The unprocessed records were corrected using an elliptical filter (Menu, 1986) with pass band $0.2 - 25\,\mathrm{Hz}$. For this study the values of these parameters used were: roll-off frequency: $1.001\,\mathrm{Hz}$, sampling interval: $0.02\,\mathrm{s}$, ripple in pass-band: 0.005 and ripple in stop-band: 0.015. An instrument correction was applied if the necessary characteristics were known for a particular record. Most have the required characteristics. This pass band was chosen because some of the records which could not be obtained in uncorrected form were corrected with a similar pass band. Also because of difference in record quality between the different accelerograms used means that a narrower pass band should be used than when all the records are high-quality. The correction procedure is not expected to affect the results within the period range of interest.

5.2 Set of records for pure error calculations

As will be shown in Section 8.3 the set of records used for estimating pure error does not need to be well distributed with magnitude and distance. Therefore all the free-field records in the Imperial College archive can be used for the estimation of pure error. The definition of free-field proposed by Joyner & Boore (1981) was adopted. Therefore records from base of buildings with three or more storeys and from abutments of dams were excluded. Also only records from earthquakes with focal depths less than or equal to $30\,\mathrm{km}$ were included.

5.2.1 Quality of selected records

All of the 3642 records in Imperial College strong-motion database were examined on the screen before being corrected to answer the following questions.

- Did the accelerograph trigger on the S wave?
- Are there two distinct shocks present on the record?
- Quality is assessed with the following questions:
  - Are there enough points to adequately represent the waveform?
  - Are there serious problems with the baseline which cannot be corrected by a linear function?
  - Are there spikes in the record which are not realistic?
  - Does the record finish while significant ground motion is still continuing?
  - Did the instrument have insufficient resolution to record the acceleration which causes steps in the acceleration time-history?

The records which were found to have possible problems were then re-examined by Patrick Smit who assessed whether these problems were likely to affect the PGA and the spectral acceleration in the period range 0.2 to $1\,\mathrm{s}$.

The records which were deemed to be of sufficient quality were retained in the set and the others were removed.

In total there are 1484 mainly triaxial[5] records from 285 earthquakes in the set. Many of the records were taken from the recently released high-quality CD-ROM of strong-motion records produced by Ambraseys *et al.* (2000). The chosen records are listed in Table D.3. The total number of records within the set from each country are given in Table 5.1.

5.2.2 Magnitude

Moment magnitude, M_w, is the preferred magnitude scale to use (see Section 2.2.1). However, since M_w is not routinely calculated for small ($M_w \lesssim 5.5$) earthquakes it cannot be used for this study which includes many records from small earthquakes. Thus surface-wave magnitude, M_s, is used for which reliable and homogeneous determinations were known for many of the small earthquakes in the database. This was done rather than using conversion formulae from one magnitude scale to another because of the uncertainty associated with such equations which may increase the scatter in the results.

[5] 14 records only had one horizontal component, four records had no vertical component and two records had only one horizontal component and no vertical component. These are indicated in Table D.3.

Tab. 5.1: Distribution of records in pure error set with respect to country where the earthquake occurred

Country	Number of Records	Country	Number of records
USA	497	Spain	10
Taiwan	341	Canada	5
Italy	264	Germany	3
Greece	90	Liechtenstein	3
Turkey	71	El Salvador	2
Mexico	43	Portugal	2
(Former) Yugoslavia	34	Costa Rica	1
Georgia	33	France	1
Armenia	28	New Zealand	1
Iran	25	Nicaragua	1
Japan	17	Uzbekistan	1
Algeria	11		

The magnitude of the smallest earthquake is 2.6 and the largest earthquake has a magnitude of 7.9.

5.2.3 Distance

Many of the selected records large earthquakes are from large earthquakes which means that point-source distance measures are likely to lead to larger scatter compared with line- or surface-source distance measures (see Section 8.4). Therefore the distance to the surface projection of the rupture (referred to here as fault distance) is used for those earthquake for which an estimate of the rupture plane could be found and epicentral distance is used for those earthquakes with no published rupture estimates. Generally there were published estimates of the rupture planes for those earthquakes with $M_s \gtrsim 5.5$ and so fault distances were calculated using Flt_Dis (see Appendix B.5) for those earthquakes which did not already have such measurements in the database. Rupture planes for earthquakes with $M_s < 5.5$ are not usually known so epicentral distance was used for most such earthquakes. The rupture length of earthquakes with $M_s < 5.5$ is less than about $5\,\mathrm{km}$ which means a point-source assumption is unlikely to introduce much error.

The shortest distance is $0\,\mathrm{km}$ (i.e. on the surface projection of the rupture) and the longest distance is $485\,\mathrm{km}$.

Tab. 5.2: Distribution of records in pure error set with respect to site category

Site category	Number of records
Very soft soil (L)	19
Soft soil (S)	322
Stiff soil (A)	392
Rock (R)	211
Unknown	540

Tab. 5.3: Distribution of records in pure error set with respect to source mechanism

Source mechanism	Number of records
Normal	427
Thrust	203
Strike-slip	628
Unknown	226

5.2.4 Site category

Currently the Imperial College strong-motion database uses the site categories of Ambraseys *et al.* (1996), namely very soft soil (L): $V_{s,30} < 180\,\mathrm{ms}^{-1}$, soft soil (S): $180 \leq V_{s,30} < 360\,\mathrm{ms}^{-1}$, stiff soil (A): $360 \leq V_{s,30} < 750\,\mathrm{ms}^{-1}$ and rock (R): $V_{s,30} \geq 750\,\mathrm{ms}^{-1}$. For many of the sites which recorded small earthquakes the local geology was not known therefore a literature search was undertaken to categorise such sites. However, there still remains a large proportion of the used data without an assigned site category. Table 5.2 gives the number of records in each site category; as can be seen there are a large number of records in each site category except for very soft soil (L) so these records are combined with those in the soft soil (S) category in the analysis.

5.2.5 Source mechanism

Currently the database uses three source mechanisms, namely: normal, thrust and strike-slip. For many of the earthquakes the source mechanism was not known therefore a literature search and a search of online catalogues (ISC, Harvard CMT) was undertaken to categorise such earthquakes. However, for a large proportion of the earthquakes particularly those of small magnitude no source mechanism is available. Table 5.3 gives the number of records in each source mechanism category and it shows there are a large number of records in each source mechanism category.

5.2.6 Correction procedure

Some (104) records were only available in an already corrected form[6] which were used as given. However, almost all the records were available in an unprocessed form. All the uncorrected records were corrected using an elliptical filter (Menu, 1986) with pass band $0.5 - 25\,\mathrm{Hz}$. For this study the values of these parameters used were: roll-off frequency: $1.001\,\mathrm{Hz}$, sampling interval: $0.02\,\mathrm{s}$, ripple in pass-band: 0.005 and ripple in stop-band: 0.015. An instrument correction was applied if the necessary characteristics were known for a particular record. The low quality of some of the records from small earthquakes meant that a strict low frequency cut-off of $0.5\,\mathrm{Hz}$ was used so that there is little chance of long–period noise in the records. The correction procedure though should not significantly affect the results within the period range of interest which was restricted to PGA and response spectral parameters in the range 0.2 to $1.0\,\mathrm{s}$.

5.2.7 Distribution with respect to magnitude, distance and soil type

Figure 5.6 shows the distribution of records in the pure error set with respect to magnitude, distance and soil type. From this figure it can be seen that the distribution of the records is good except for small magnitudes ($M_s < 4$) and large distances ($d > 100\,\mathrm{km}$) both of which have low engineering significance. The distribution of the records, with respect to magnitude and distance, for each of the site categories is similar.

[6] These are indicated in Table D.3 by (C).

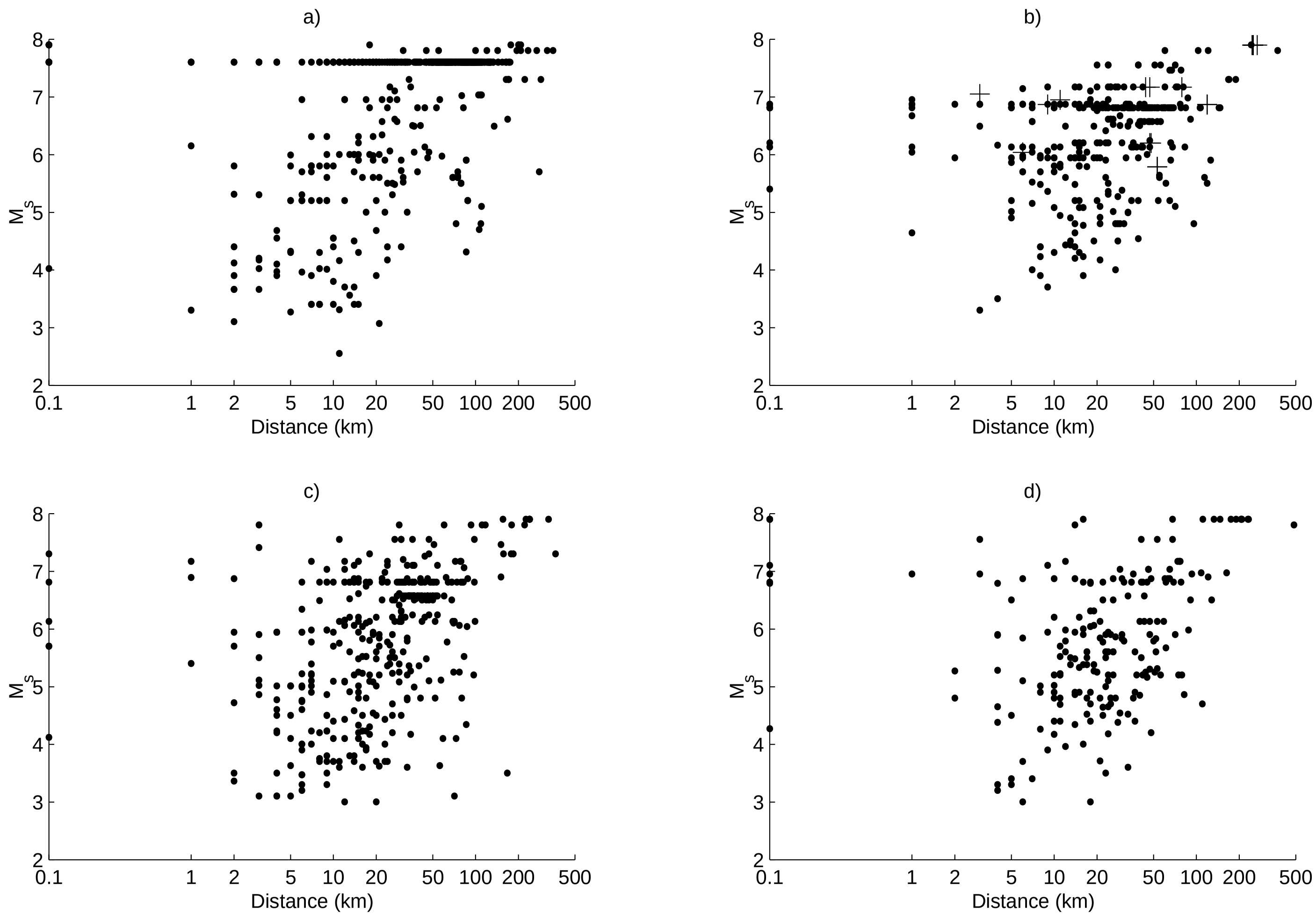

Fig. 5.6: Distribution of records in pure error set with respect to magnitude, distance and site category. a) records with unknown site category, b) records from soft or very soft soil (crosses), c) records from stiff soil and d) records from rock. Records with distance equal to 0 km are plotted at 0.1 km.

6. GENERAL EFFECTS OF VERTICAL GROUND MOTION

This chapter discusses aspects of the effect of vertical ground motions on horizontal response for structures governed by Equations 4.14, 4.15, 4.19 & 4.20. From these equations limits on the structural parameters are found which can be used to characterise the systems.

The effects of vertical ground motions are studied assuming the models of Chapter 4 apply to engineering structures subjected to strong ground motions from earthquakes. Therefore choices of the structural parameters: natural period (horizontal and vertical), damping (horizontal and vertical), load ratio (γ) and column length (l) will be realistic for engineering structures (see Appendix C) and the input excitations (horizontal and vertical) will be acceleration time-histories of real earthquakes.

In the following discussion V_{tt}, vertical ground acceleration, can be replaced by u^v_{tt}, the vertical response acceleration.

6.1 Connection with Mathieu-Hill equation

If $U_{tt} = 0$, $V_{tt} = \cos(\Omega_V t)$ equations 4.14 & 4.19 become:

$$u_{tt} + 2\xi_1\omega_1 u_t + \omega_1^2[1 - \beta\cos(\Omega t)]u = 0 \tag{6.1}$$

The following derivation comes from Bolotin (1964, p. 33) although the notation has been changed for consistency with earlier chapters. Look for solution of form: $u = xy$ then have $u_t = x_t y + x y_t$ and $u_{tt} = x_{tt} y + 2x_t y_t + x y_{tt}$. Substituting into Equation 6.1 gives:

$$y x_{tt} + 2(y_t + \xi\omega_1 y)x_t + [y_{tt} + 2\xi\omega_1 y_t + \omega_1^2(1 - \beta\cos\Omega_V t)y]x = 0$$

Want coefficient of x_t to equal zero so must have:

$$y_t + \xi\omega_1 y = 0$$

Hence $y = Ce^{-\xi\omega_1 t}$. Thus get:

$$x_{tt} + \omega_1^2(1 - \xi^2 - \beta\cos\Omega_V t)x = 0 \tag{6.2}$$

Then the solution is $u = Ce^{-\xi\omega_1 t}x$, where x is solution of Equation 6.2. Equation 6.2 is in the form of a Mathieu-Hill equation on which there is a vast literature (e.g. Lubkin & Stoker, 1943; Bolotin, 1964).

6.2 Assumptions made in derivation of bending model

When deriving Equations 4.14 & 4.15 it is assumed that the top of the pendulum is always at a height $y = l$ whatever the horizontal displacement of the top of the column. In reality because of bending the mass at the top of the column moves down.

The length of the column, $L(h)$, up to a height h can be found from:

$$L(h) = \int_0^h \sqrt{\left(\frac{\mathrm{d}x}{\mathrm{d}y}\right)^2 + 1\mathrm{d}y};$$

where: $\frac{\mathrm{d}x}{\mathrm{d}y} = F\cos(\nu y/l)/P + \nu(F/P + u/l)\sin(\nu y/l) - F/P$ with $F = (3EI/l^3)(\nu/\chi(\nu))$, $P = mg$, $\nu = \pi/2\sqrt{P/P_{cr}}$ and $1/\chi(\nu) \approx 1 - \frac{\pi^2}{10}\frac{P}{P_{cr}}$. Then want to find h when $L(h) = l$. Since this integral cannot be solved exactly and the inaccuracies are small the current method is assumed to be adequate.

Also when the horizontal earthquake force, mU_{tt}, is applied to the mass it is not resolved although really the force should be multiplied by $\cos(\theta)$ where θ is equal to the angle that the column makes with the vertical at the top. For $l = 10\,\mathrm{m}$, $EI = 2.3 \times 10^5\mathrm{Nm}^2$, $\gamma = 0.3$ and $u = 1\,\mathrm{m}$ this angle equals 10.1°, thus $\cos(\theta) = 0.985$. Consequently this assumption does not lead to large inaccuracies.

6.3 Breakdown of bending model for large γ

Consider the homogenous Equation 4.14, i.e. $U_{tt} = 0$, and let $\alpha = (1 - \beta V_{tt})$ be constant for a given period of time. Then the equation of motion becomes:

$$u_{tt} + 2\xi_1\omega_1 u_t + \alpha\omega_1^2 u = 0. \tag{6.3}$$

Looking for solutions of Equation 6.3 of the form $u = Ke^{pt}$ leads to the equation:

$$p = \omega_1(-\xi_1 \pm \sqrt{\xi_1^2 - \alpha}). \tag{6.4}$$

Solutions of Equations 4.1, 4.13 & 4.17 correspond to $\alpha = 1$, ω_1 replaced by ω_0 and ξ_1 replaced by ξ_0 and for both solutions p has a negative real part therefore the amplitude of the motion decays with time. This is not so in equation 6.4. If $\xi_1^2 - \alpha > 0$ and $\sqrt{\xi_1^2 - \alpha} > \xi_1$ then one solution of equation 6.4 will be positive. This means that one of the solutions of equation 6.3 has the form $u = Ke^{p_+ t}$ where $p_+ > 0$, a solution which rapidly tends to ∞ as $t \to \infty$. Therefore if $\beta V_{tt} > 1$ for a reasonable length of time then the displacements of the mass can become very large. This inequality is equivalent to:

$$\begin{aligned} V_{tt} &> \frac{g(1-\gamma)}{\gamma}; \\ \text{or}\gamma &> \frac{1}{V_{tt}/g+1}. \end{aligned} \tag{6.5}$$

Once the column is displaced horizontally from the vertical gravity and positive vertical accelerations mean it is easier for displacements of the mass horizontally to continue. As the displacement increases the equivalent stiffness of the column decreases and so the mass continues to be deflected by more and more. Only the application of a large negative vertical acceleration will counteract this process. Inequality 6.5 simply means that bending model cannot withstand forces (gravity plus vertical ground accelerations) greater than its Euler buckling load, P_{cr}. This limit on the size of vertical ground motion which can cause instabilities was found by Mostaghel (1975) by considering Liapunov functions of the input vertical time-history. Note that this upper limit on γ holds for all non-zero horizontal input motion.

6.3.1 Example of breakdown for large γ

All the records, with vertical components, used for the derivation of the near-field attenuation relations were used to study the onset of instability for increasing γ. The response spectrum, for 0, 2, 5, 10 and 20% damping, of each horizontal component was calculated for γ between 0 and the γ which yields $\mathrm{SA} > 1000\,\mathrm{ms}^{-2}$ at one or more periods, increasing in 0.01 unit intervals, or $\gamma > 0.96$[1]. From each spectrum the largest SA for any period, $\mathrm{SA}_{\max}(\gamma)$ was found. Figure 6.1 shows $\mathrm{SA}_{\max}(\gamma)/\mathrm{SA}_{\max}(\gamma=0)$, i.e. amplification in response due to vertical excitation, against γ for one component for 5% damping. Dashed line marks the boundary between values of γ where the system is stable and γ where Inequality 6.5 holds ($\gamma = 0.58$ for this record), i.e. the system could be unstable if the amplitude of vertical acceleration was sustained.

Figure 6.1 shows that only for values of γ close to the region of instability, around $\gamma > 0.4$, does SA significantly increase. It also shows that SA does not become unrealistically large, i.e. high amplifications, until γ is slightly larger, about $\gamma > 0.65$, than the smallest value where Inequality 6.5 holds. This is because the stability condition of the SDOF system is only violated for a short time and large responses are not able to build up.

For each record it is found that the ratio of critical damping used does not strongly affect the value of γ above which instability occurs. For example, for the Tabas N74E component instability occurs when γ exceeds 0.50, 0.62, 0.65, 0.68 and 0.75 for 0, 2, 5, 10 and 20% damping respectively. The curves of amplification due to the vertical excitation against γ for each damping ratio are similar

[1] For $\gamma > 0.96$ the time to calculate the response became extremely long even for records with small vertical accelerations.

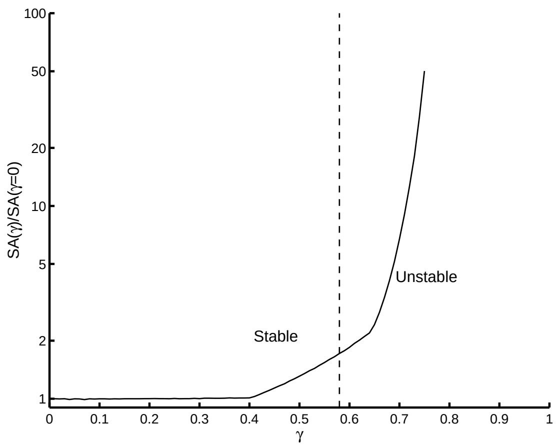

Fig. 6.1: Amplification in maximum spectral acceleration, for 5% damping, due to vertical excitation against γ for Tabas N74E component (from Tabas earthquake, 16/9/1978) (bending model).

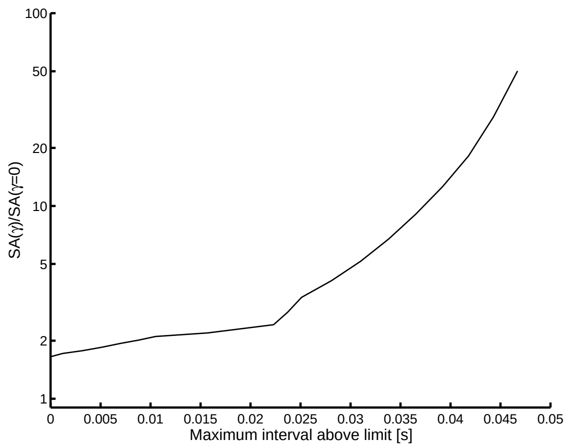

Fig. 6.2: Amplification in maximum spectral acceleration, for 5% damping, due to vertical excitation against maximum interval above limit acceleration for Tabas N74E component (bending model).

to that for 5% shown in Figure 6.1 but shifted slightly to the left for smaller damping ratios and to the right for larger damping ratios.

For each value of γ the minimum acceleration (limit acceleration) which satisfies Inequality 6.5 was calculated and the maximum length of time, in the records, for which accelerations higher than this were sustained. Note this is not the total amount of time for which the recorded acceleration is above a threshold but the maximum interval where accelerations are above a threshold. These intervals are also a function of γ. To calculate this the records were linearly interpolated. Figure 6.2 shows $\mathrm{SA}_{\max}(\gamma)/\mathrm{SA}_{\max}(\gamma = 0)$ against these calculated intervals for one component.

Figure 6.2 shows that the SDOF system is still stable if the interval for which the ground acceleration satisfies Inequality 6.5 is sufficiently small, less than about $0.025\,\mathrm{s}$, but for longer intervals the system's responses can become extremely large, i.e. it is unstable.

6.3.2 General results on the breakdown of the model due to large γ

All examined records show similar behaviour although the length of the interval, during which the ground acceleration is above the limit acceleration, required for instability to occur varies (Table 6.1).

The interval lengths vary because the vertical ground acceleration is a dynamic force and not static and also because of the effect of the combination of horizontal and vertical excitation on the system.

As the load ratio, γ, increases the period of the peak response decreases because vertical ground motion is usually of a higher frequency than the corresponding horizontal ground motion. For load

Damping ratio (%)	Min. and max. interval lengths (s)	Most common interval lengths (s)
0	0 and 0.05	0 to 0.03
2	0 and 0.06	0 to 0.04
5	0.005 and 0.08	0.02 to 0.06
10	0.01 and 0.08	0.02 to 0.07
20	0.01 and 0.13	0.04 to 0.09

Tab. 6.1: Minimum and maximum length of intervals, for which the vertical acceleration is above the limit that causes instability, and the most common length of intervals, for which the vertical acceleration is above limit which causes instability. Bending model.

ratios large enough to increase the response significantly (i.e. close to the unstable region or within the unstable region) the horizontal period at which the largest response occurs is usually between 0.1 and $0.2\,\mathrm{s}$ which reflects the high frequency nature of vertical ground motion. Therefore Table 6.1 shows that instability occurs if the length of the interval when Inequality 6.5 holds is greater than some fraction (usually about an eighth to a quarter for realistic damping levels) of the horizontal period for which the instability occurs.

Table 6.1 shows that damping does not have a strong influence on the onset of instability due to too large a load ratio, γ.

6.3.3 Discussion and conclusions

The analysis shows that the SDOF systems governed by Equation 4.14 or 4.15 become unstable, i.e. the response of the system is unphysically large, for earthquake loading when the vertical ground acceleration is above a limit, given by simple Inequality 6.5, for longer than between 0 and $0.13\,\mathrm{s}$ and that the ratio of critical damping present in the SDOF system does not have a large influence on this.

The limit on the length of the interval that produces unrealistically large responses is related to the natural horizontal period of the system, T_h. For systems with extremely short natural horizontal periods ($T_h < 0.1\,\mathrm{s}$) the critical length of interval approaches zero, i.e. if Inequality 6.5 holds for any length of time during the earthquake then the system will become unstable. For systems with extremely long natural horizontal periods ($T_h > 10\,\mathrm{s}$) then the critical interval tends to the longest interval within the acceleration time-history between zero crossings. This is shown in Table 6.2 using the Tabas N74E component. Due to the correction technique there is little energy in the period range of the records 0 to $0.04\,\mathrm{s}$ and beyond $5\,\mathrm{s}$ thus results for natural horizontal periods within these ranges may be unreliable.

T_h (s)	Length of interval (s)	T_h (s)	Length of interval (s)
0.01	0.01	1.0	0.11
0.02	0.02	2.0	0.22
0.05	0.025	5.0	0.48
0.1	0.03	10.0	0.50
0.2	0.05	20.0	0.50
0.5	0.07	50.0	0.50

Tab. 6.2: Horizontal natural period of system against length of interval over the critical acceleration defined by Inequality 6.5 required to cause instability for the Tabas N74E component and 5% damping.

Table 6.2 shows that limits on the critical interval mentioned above hold, i.e. for extremely short periods the critical interval is also short and as period increases so does the critical interval reaching an upper limit equal to the maximum time between zero crossings of acceleration (in this case $0.50\,\mathrm{s}$).

This result shows that the breakdown of the SDOF systems governed by Equation 4.14 or 4.15 is more likely to occur for short-period than long-period systems because the high vertical acceleration which induces instability only needs to be sustained for an extremely short time. For long period systems the high vertical acceleration needs to be sustained for a longer time but this cannot be longer than the maximum time between zero crossings.

For each record in the near-field set the maximum load ratio, γ, which can be used without Inequality 6.5 holding was calculated for both infinite and finite vertical stiffness (for natural vertical periods between 0.1 and $2\,\mathrm{s}$ and 2, 5, 10 and 20% damping). This was done without considering the time the vertical input acceleration is above the critical level. Figure 6.3 shows the maximum load ratio against the cumulative total of records for which instability may occur for infinite and finite vertical stiffness.

Figure 6.3 shows that for realistic load ratios of 0.3 to 0.5 most vertical acceleration time-histories will not induce instability for systems with infinite vertical stiffness. In fact for load ratios less than 0.34 the infinite-vertical-stiffness SDOF system will definitely not become unstable for any vertical time-history in the set of records which includes the most intense vertical accelerations yet recorded (Nahanni 1 (Nahanni earthquake, 23/12/1985), vertical $\mathrm{PGA} = 19.4\,\mathrm{ms}^{-2}$ [$2\,\mathrm{g}$]; El Centro 6 (Imperial Valley earthquake, 15/10/1979), vertical $\mathrm{PGA} = 15.5\,\mathrm{ms}^{-2}$ [$1.6\,\mathrm{g}$]; Victoria (Victoria earthquake, 9/6/1980), vertical $\mathrm{PGA} = 14.7\,\mathrm{ms}^{-2}$ [$1.5\,\mathrm{g}$] and Tarzana (Northridge earthquake, 17/1/1994), vertical $\mathrm{PGA} = 10.3\,\mathrm{ms}^{-2}$ [$1.0\,\mathrm{g}$])). It is therefore unlikely that for realistic

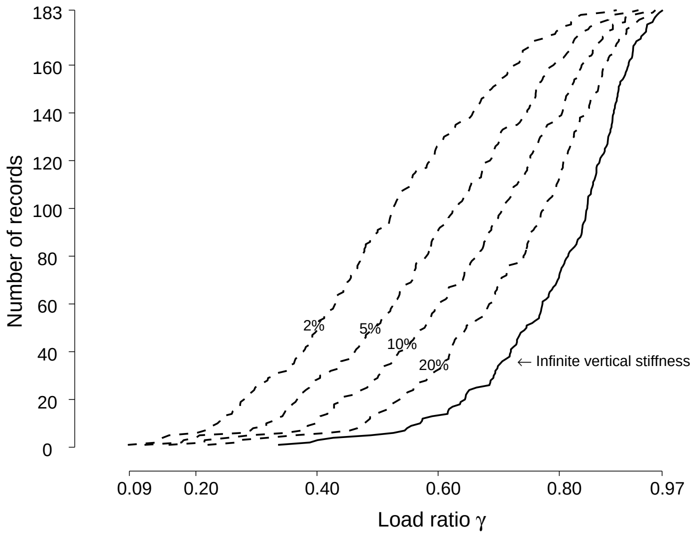

Fig. 6.3: Maximum load ratio against cumulative number of records for which Inequality 6.5 holds, i.e. maximum load ratio which can be used in analysis without instability possibly occurring for infinite vertical stiffness (solid line) and finite vertical stiffness for natural vertical periods between 0.1 and $2\,\mathrm{s}$ and 2, 5, 10 and 20% damping (dashed lines).

load ratios vertical acceleration will result in the failure of such systems through instability.

However, Figure 6.3 shows that for systems with finite vertical stiffness a number of vertical time-histories will induce instability for realistic load ratios of 0.3 to 0.5 even for large vertical damping. Figure 6.3 shows that the maximum load ratio which can be used for an analysis of all the records in the near-field set using the bending model and finite vertical stiffness is about 0.1 for 2 and 5% damping, for 10% damping it is about 0.15 and for 20% damping it is about 0.22. Thus for certain natural vertical periods and realistic choices of γ (0.3 to 0.5) the bending SDOF system will yield unrealistically large responses (due to the system breaking down) for some of the near-field records. This precludes a general analysis. Therefore spectra using the bending model for finite vertical stiffness are not calculated and hence attenuation relations for such spectra are not derived.

6.4 Breakdown of hinging model for small l

In the same way that a rough upper limit can be found for the bending equation of motions, a lower limit on l can be found for the hinging Equations 4.19 & 4.20.

If the coefficient of the third term in Equations 4.19 or 4.20 becomes negative then the solution of the equation of motion is the sum of two real exponentials (see Section 6.3). This occurs when $1 - \beta V_{tt} < 0$, therefore a large response may occur if:

$$
\begin{aligned}
l &< \frac{V_{tt}}{\omega_1^2} \\
\text{or: } V_{tt} &> l\omega_1^2 \\
\text{or: } V_{tt} &> l\omega_0^2 - g
\end{aligned} \tag{6.6}
$$

If this inequality holds then the response of the hinging structure can become large. Since $T_1 = \frac{2\pi}{\omega_1}$ this means that for structures with long natural periods l has to be large for the structure to remain stable. Inequality 6.6 is the same constraint as that placed on l, during the derivation of the equation of motion when vertical ground acceleration is neglected (see Section 4.5.1), modified due to the presence of vertical ground motion.

6.4.1 Example of breakdown for small l

All the records, with vertical components, used here for the derivation of the near-field attenuation relations were also used to study the onset of instability for decreasing l. The response spectrum, for 5% damping, of each horizontal component was calculated for l between $5\,\mathrm{m}$ (for l this large, and for the period range of interest, the vertical excitation has no effect) and the l which yields $\mathrm{SA} > 1000\,\mathrm{ms}^{-2}$ at one or more periods, decreasing by a factor of 0.95 each loop. From each spectrum the largest SA for any period, $\mathrm{SA}_{\max}(l)$ was found. Figure 6.4 shows $\mathrm{SA}_{\max}(l)/\mathrm{SA}_{\max}(l = 5\,\mathrm{m})$, i.e. amplification in response due to vertical excitation, against l for one component. Inequality 6.6 involves frequency (and hence period) thus the boundary between the stable and unstable regions depends on period. The largest period, $2\,\mathrm{s}$, gives the smallest critical l and this is used. In Figure 6.4 the dashed line marks the boundary between values of l where the system is stable and l where Inequality 6.6 holds ($l = 0.74\,\mathrm{m}$ for this record and natural period of $2\,\mathrm{s}$), i.e. the system could be unstable if the amplitude of the vertical acceleration was sustained.

Figure 6.4 shows that Inequality 6.6 is extremely over conservative in its prediction of the stable region, predicting that for $l < 0.74\,\mathrm{m}$ stability could be a problem whereas in fact the response only increases for $l < 0.07\,\mathrm{m}$ and large responses indicative of instability only occur for $l < 0.05\,\mathrm{m}$. The reason for the large difference is that vertical peak ground acceleration is usually associated with high frequency waves which do not affect long period systems which are the ones for which instability is predicted using Inequality 6.6. Unless a vertical strong motion record contains large amplitude long period accelerations then instability is not a problem for realistic choices of l nor does any amplification due to the vertical acceleration occur for realistic l values.

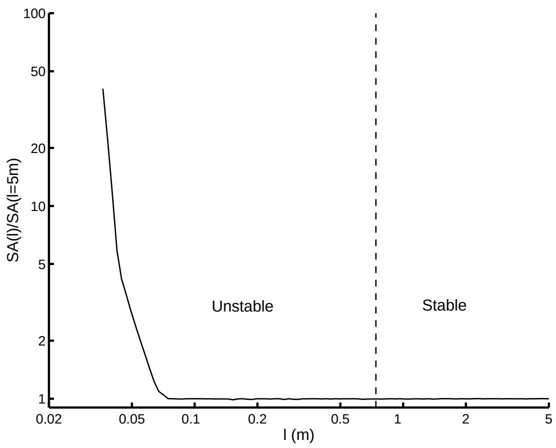

Fig. 6.4: Amplification in maximum spectral acceleration, for 5% damping, due to vertical excitation against l for Tabas N74E component (hinging model).

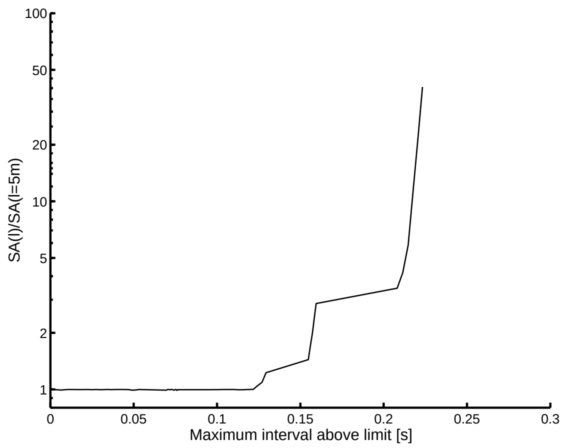

Fig. 6.5: Amplification in maximum spectral acceleration, for 5% damping, due to vertical excitation against maximum interval above limit acceleration for Tabas N74E component (hinging model).

6.4.2 General results on the breakdown of the model due to small l

For each record it was found that the ratio of critical damping used did not strongly affect the value of l below which instability occurs. For example, for the Tabas N74E component the value of l below which instability occurs is 0.07, 0.06, 0.05, 0.05 and $0.04\,\mathrm{m}$ for 0, 2, 5, 10 and 20% damping respectively. The curves of amplification due to the vertical excitation against γ for each damping ratio are similar to that for 5% shown in Figure 6.4 although slightly shifted to the right for smaller damping ratios and to the left for larger damping ratios.

For each value of l the minimum acceleration (limit acceleration) which satisfies Inequality 6.6 was calculated and the maximum time the records show sustained accelerations higher than this. Note this is not the total amount of time in the records which the acceleration was above a threshold but the maximum interval where accelerations above a threshold were recorded. Also note that these intervals are a function of l and natural period. To calculate this the records were linearly interpolated. Figure 6.5 shows $\mathrm{SA}_{\max}(l)/\mathrm{SA}_{\max}(l = 5\,\mathrm{m})$ against these calculated intervals for one component.

Figure 6.5 shows that the SDOF system is still stable if the interval for which the ground acceleration satisfies Inequality 6.6 is sufficiently small, less than about $0.2\,\mathrm{s}$, but for intervals longer than a certain length of time the system's responses are extremely large, i.e. it is unstable.

All examined records show similar behaviour although there is a range of intervals, during which the ground acceleration is above the limit, required for instability (Table 6.3).

The variation occurs because the vertical ground acceleration is a dynamic force and not static

Damping ratio ($\%$)	Min. and max. interval lengths (s)	Most common interval lengths (s)
0	0.05 to 0.9	0.1 to 0.2
2	0.05 to 1.0	0.1 to 0.25
5	0.1 and 1.2	0.15 to 0.25
10	0.1 and 1.2	0.15 to 0.3
20	0.1 and 1.3	0.15 to 0.3

Tab. 6.3: Minimum and maximum length of intervals, for which the vertical acceleration is above limit which causes instability, and the most common length of intervals, for which the vertical acceleration is above limit which causes instability. Hinging model.

and also because of the effect of the combination of horizontal and vertical excitation on the system. The situation is further complicated because Inequality 6.6 is a function not only of l but also the natural period of the system.

6.4.3 Discussion and conclusions

This analysis shows that the SDOF systems governed by Equation 4.19 or 4.20 become unstable, i.e. the response of the system is unphysically large, for earthquake loading when the vertical ground acceleration is above a limit acceleration, given by simple Inequality 6.6, for longer than about 0.05 to $1.3\,\mathrm{s}$. Note that the lengths of the column, l, for which instability can be a problem ($l < 0.07\,\mathrm{m}$ for Tabas N74E component, see Figure 6.4) are much less than occur in practice especially in long period systems where Inequality 6.6 may be violated. Also the length of the intervals for which vertical accelerations satisfying Inequality 6.6 are much longer than those for the bending model. Both these findings mean that large amplification of horizontal response from vertical accelerations is extremely unlikely to occur in practice for structures that can be modelled by the elastic hinging SDOF model.

For each record in the near-field set the minimum length of column, l, which can be used before Inequality 6.6 holds is calculated for both infinite and finite vertical stiffness (for natural vertical periods between 0.1 and $2\,\mathrm{s}$ and 2, 5, 10 and 20% damping). This was done without considering how long the vertical input acceleration is above the critical level. The calculation for infinite vertical stiffness assumes that the wave associated with vertical PGA is of sufficient period to cause instability in a system with natural horizontal period of $2\,\mathrm{s}$. For finite vertical stiffness the vertical spectral acceleration at each period was used to calculate the minimum length of column and then the minimum length from all periods was chosen. Figure 6.6 shows the minimum length of column against the cumulative total of records for which instability may occur for infinite and finite vertical stiffness.

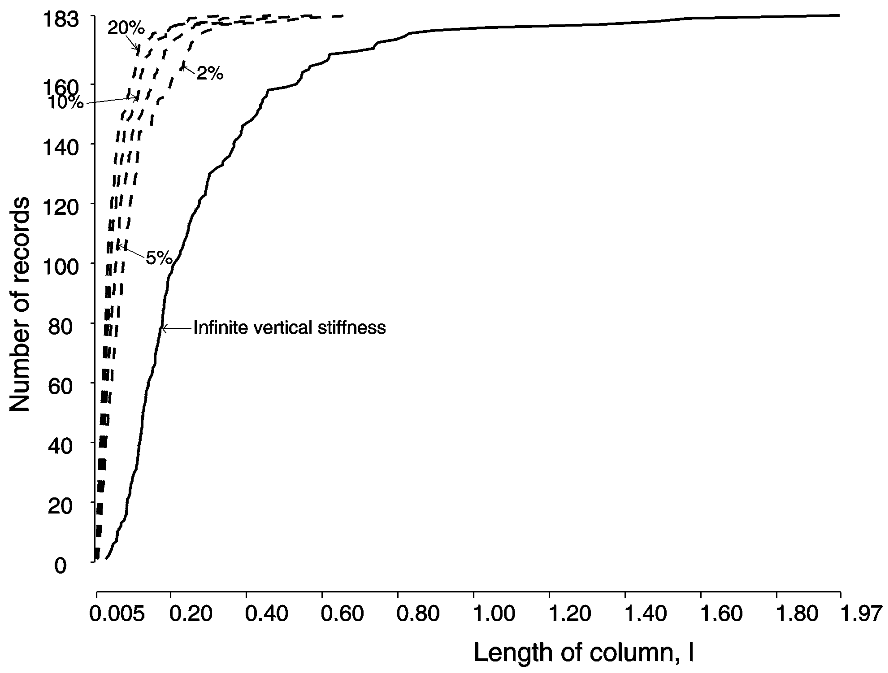

Fig. 6.6: Minimum length of column against cumulative total number of records for which Inequality 6.6 holds, i.e. minimum length of column which can be used in analysis without instability possibly occurring for infinite vertical stiffness (solid line) and finite vertical stiffness for natural vertical periods between 0.1 and $2\,\mathrm{s}$ and 2, 5, 10 and 20% damping (dashed lines).

Figure 6.6 shows that for columns longer than $2\,\mathrm{m}$ no vertical acceleration time-histories will induce instability for systems with infinite vertical stiffness or finite vertical stiffness. In fact since vertical PGAs are associated with high frequencies the situation for infinite vertical stiffness is much different than Figure 6.6 suggests. This is because instabilities only occurs if accelerations over the critical level of vertical acceleration are sustained for more than about $0.1\,\mathrm{s}$, as shown above, which will not be so for the wave associated with vertical PGA. Thus this limit on the minimum length of column which can be used is probably much less than $1\,\mathrm{m}$ for both finite and infinite vertical stiffness. The records used for this analysis includes the most intense vertical ground motions yet recorded so this means it is extremely unlikely that hinging systems with a realistic length of column will fail through instability for any vertical acceleration.

In Chapter 7 some attenuation relations are derived using choices of column length, l, for the hinging model. This can be done for this model because unlike for the bending model instability never occur.

6.5 Perturbation theory

Perturbation theory provides a method for deriving approximate solutions to nonlinear differential equations (McLachlan, 1951). It can be used to find combinations of horizontal and vertical frequencies which lead to large responses in the SDOF system described by Equations 4.14, 4.15, 4.19 & 4.20 (Hara, 1984, 1985). The following analysis is based on Hara (1984) although his notation has been changed for consistency with that presented above.

Consider periodic horizontal and vertical excitation. Let:

$$\begin{aligned} U_{tt} &= -A_H \sin \Omega_H t; \\ \text{and } V_{tt} &= A_V \cos \Omega_V t. \end{aligned}$$

Then Equations 4.14 & 4.19 become:

$$u_{tt} + 2\xi_1 \omega_1 u_t + \omega_1^2 (1 - \beta A_V \cos \Omega_V t) u = A_H \sin \Omega_H t. \tag{6.7}$$

Assume that (since β is small) $u = u^{(0)} + \beta u^{(1)} + \beta^2 u^{(2)} + \ldots$, then consider terms with the same power of β.

Firstly consider terms of degree 1:

$$u_{tt}^{(0)} + 2\xi_1 \omega_1 u_t^{(0)} + \omega_1^2 u^{(0)} = A_H \sin \Omega_H t.$$

The steady state solution of this equation, for $\Omega_H \neq \omega_1$, can be written as:

$$\begin{aligned} u^{(0)} &= R^{(0)} \sin(\Omega_H t - \phi^{(0)}); \\ \text{where } R^{(0)} &= \frac{A_H}{\omega_1^2 \sqrt{[1 - (\Omega_H/\omega_1)^2]^2 + 4\xi_1^2 (\Omega_H/\omega_1)^2}}; \\ \text{and } \tan \phi^{(0)} &= \frac{2\xi_1 (\Omega_H/\omega_1)}{1 - (\Omega_H/\omega_1)^2}. \end{aligned} \tag{6.8}$$

When $\Omega_H = \omega_1$ resonance (called regular resonance by Hara (1984, 1985)) occurs.

Now consider terms of degree β then:

$$u_{tt}^{(1)} + 2\xi_1 \omega_1 u_t^{(1)} + \omega_1^2 u^{(1)} = (\omega_1^2 A_V \cos \Omega_V t) u^{(0)}. \tag{6.9}$$

Substituting Equation 6.8 into Equation 6.9 then:

$$u_{tt}^{(1)} + 2\xi_1 \omega_1 u_t^{(1)} + \omega_1^2 u^{(1)} = A_V R^{(0)} \omega_1^2 \cos \Omega_V t \sin(\Omega_H t - \phi^{(0)}).$$

Now since $\sin A \cos B = [\sin(A+B) + \sin(A-B)]/2$ $u^{(1)}$ can be found for the steady state solution, when $\Omega_H + \Omega_V \neq \omega_1$, $\Omega_H - \Omega_V \neq \omega_1$ and $\Omega_V - \Omega_H \neq \omega_1$, thus:

$$\begin{aligned} u^{(1)} &= R^{(1,1)} \sin[(\Omega_H + \Omega_V)t - \phi^{(0)} - \phi^{(1,1)}] \\ &\quad + R^{(1,2)} \sin[(\Omega_H - \Omega_V)t - \phi^{(0)} - \phi^{(1,2)}]; \qquad (6.10) \\ \text{where } R^{(1,1)} &= \frac{R^{(0)} A_V}{2\sqrt{[1 - (\Omega_H/\omega_1 + \Omega_V/\omega_1)^2]^2 + 4\xi_1^2(\Omega_H/\omega_1 + \Omega_V/\omega_1)^2}}, \\ R^{(1,2)} &= \frac{R^{(0)} A_V}{2\sqrt{[1 - (\Omega_H/\omega_1 - \Omega_V/\omega_1)^2]^2 + 4\xi_1^2(\Omega_H/\omega_1 - \Omega_V/\omega_1)^2}}, \\ \tan\phi^{(1,1)} &= \frac{2\xi_1(\Omega_H/\omega_1 + \Omega_V/\omega_1)}{1 - (\Omega_H/\omega_1 + \Omega_V/\omega_1)^2}, \\ \text{and } \tan\phi^{(1,2)} &= \frac{2\xi_1(\Omega_H/\omega_1 - \Omega_V/\omega_1)}{1 - (\Omega_H/\omega_1 - \Omega_V/\omega_1)^2}. \end{aligned}$$

When $\Omega_H + \Omega_V = \omega_1$, $\Omega_H - \Omega_V = \omega_1$ or $\Omega_V - \Omega_H = \omega_1$ resonance (called combined resonance by Hara (1984, 1985)) occurs.

The form of the solution for terms of degree β^2 is (by using $\sin A \cos B = [\sin(A + B) + \sin(A - B)]/2$ again) is:

$$\begin{aligned} u^{(2)} &= R^{(2,1)} \sin[(\Omega_H + 2\Omega_V)t - \phi^{(0)} - \phi^{(1,1)} - \phi^{(2,1)}] \\ &\quad + R^{(2,2)} \sin[\Omega_H t - \phi^{(0)} - \phi^{(1,1)} - \phi^{(2,2)}] \\ &\quad + R^{(2,3)} \sin[\Omega_H t - \phi^{(0)} - \phi^{(1,2)} - \phi^{(2,3)}] \\ &\quad + R^{(2,4)} \sin[(\Omega_H - 2\Omega_V)t - \phi^{(0)} - \phi^{(1,2)} - \phi^{(2,4)}]. \qquad (6.11) \end{aligned}$$

Therefore the solution exhibits resonance at $\Omega_H + 2\Omega_V = \omega_1$, $\Omega_H = \omega_1$, $\Omega_H - 2\Omega_V = \omega_1$ and $2\Omega_V - \Omega_H = \omega_1$. As shown in Section 6.5.1 these types of resonance do occur. Solutions for higher degree terms, such as β^3, are not important as β is small.

6.5.1 Numerical example

Let $\omega_H = \Omega_H/\omega_1$ and $\omega_V = \Omega_V/\omega_1$, $\beta = 0.1$, $A_H = 1$, $A_V = 1$ and $\xi = 0.01$. Figure 6.7(a) shows a contour plot of $\alpha = u\omega_1^2/A_H$, where u is the perturbation theory solution using the first two terms, $u^{(0)}$ and $u^{(1)}$. α is what Hara (1985) calls response-multiplication factor. On the plot both regular and combined resonance can be clearly seen but parametric resonance cannot.

Comparison with results from Hara (1984, 1985)

Hara (1984, 1985) provides contour plots of the response-multiplication factor, α, against ω_H and ω_V (see Section 6.5.1) for harmonic horizontal and vertical excitation. β in this study is equal to ϵ in Hara (1984, 1985) and the normalisation which Hara performs does not affect the graphs he gives.

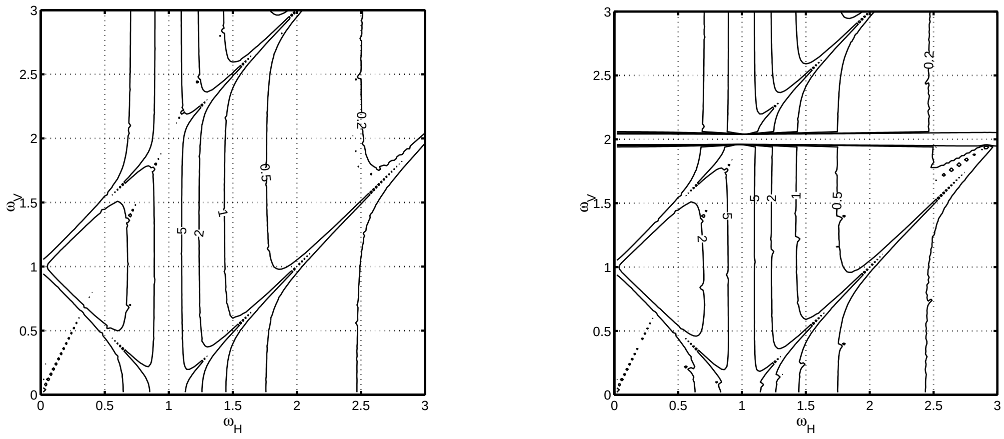

(a) Using perturbation theory

(b) Using HVSPECTRA.

Fig. 6.7: Contour plot of response-multiplication factor, α, from steady-state solution of Equation 6.7.

Since the plots of Hara are for the steady-state response the solution was computed, using HVSPECTRA, for times up to $500\,\mathrm{s}$ and the maximum response from the last $250\,\mathrm{s}$ plotted. This was done so that the transient part of the solution had died away. As in Section 6.5.1 and Figure 2 of Hara (1984, 1985), $\omega_H = \Omega_H/\omega_1$ and $\omega_V = \Omega_V/\omega_1$, $\beta = 0.1$, $A_H = 1$, $A_V = 1$ and $\xi = 0.01$. Figure 6.7(b) shows the computed contour plot.

Comparing Figure 6.7(b) with Figure 2 of Hara (1984, 1985) it is noted that the graphs are almost identical, except in the region around $\omega_V = 2$; this difference is discussed in Section 6.6. Figure 6.7(b) is also almost identical to the solution from perturbation theory shown in Figure 6.7(a) except for area around $\omega_V = 2$.

As was noted in 6.5 the resonance from the terms of degree β^2 can be seen. In Figure 6.7(b) three small increases in the response-multiplication factor are visible along lines $\omega_H + 2\omega_V = 1$, $\omega_H - 2\omega_V = 1$ and $2\omega_V - \omega_H = 1$. None of the higher order resonances due to terms β^3, β^4, … can be seen.

6.6 Parametric resonance

For certain combinations of vertical driving frequency, Ω_V, and the natural *horizontal* frequency ω_1, systems governed by Equations 4.14, 4.15, 4.19 & 4.20 become dynamically unstable and *horizontal* vibrations occur; the amplitude of these vibrations rapidly become large. The frequencies at which a system approaches such a resonance (so called parametric resonance) differs from that for ordinary forced vibrations. For sufficiently small values of the longitudinal force this relationship is $\Omega_V = 2\omega_1$ (Bolotin, 1964).

The region of instability can be determined by finding the conditions under which Equations 4.14, 4.15, 4.19 & 4.20 have periodic solutions with period $2T$. The following calculation is from Bolotin (1964) although the notation has been changed for consistency with above.

Assume that the displacement, u, of the mass can be expressed in a Fourier series (only odd k are possible because the period is $2T$):

$$u(t) = \sum_{k=1,3,5,\ldots}^{\infty} \left(a_k \sin \frac{k\Omega_V t}{2} + b_k \cos \frac{k\Omega_V t}{2} \right). \tag{6.12}$$

Substituting Equation 6.12 into Equation 4.14 or 4.19 with $V_{tt} = A_V \cos \Omega_V t$ and $U_{tt} = 0$ gives:

$$\begin{aligned} &\sum_{k=1,3,5,\ldots}^{\infty} -a_k \left(\frac{k\Omega_V}{2}\right)^2 \sin \frac{k\Omega_V t}{2} - b_k \left(\frac{k\Omega_V}{2}\right)^2 \cos \frac{k\Omega_V t}{2} \\ &+ 2\xi\omega_1 \sum_{k=1,3,5,\ldots}^{\infty} a_k \left(\frac{k\Omega_V}{2}\right) \cos \frac{k\Omega_V t}{2} - b_k \left(\frac{k\Omega_V}{2}\right) \sin \frac{k\Omega_V t}{2} \\ &+ \omega_1^2 (1 - A_V \beta \cos \Omega_V t) \sum_{k=1,3,5,\ldots}^{\infty} a_k \sin \frac{k\Omega_V t}{2} + b_k \cos \frac{k\Omega_V t}{2} \quad = \quad 0. \end{aligned}$$

Equating coefficients of $\sin(k\Omega_V t)/2$ and $\cos(k\Omega_V t)/2$ using $\sin A \cos B = [\sin(A+B) + \sin(A-B)]/2$, $\cos A \cos B = [\cos(A+B) + \cos(A-B)]/2$, $\sin(-A) = -\sin A$ and $\cos(-A) = \cos A$ gives:

$$\begin{aligned} -\left(\frac{A_V\beta}{2}\right) a_3 + \left[1 + \frac{A_V\beta}{2} - \left(\frac{\Omega_V}{2\omega_1}\right)^2\right] a_1 - \left(\frac{\xi\Omega_V}{\omega_1}\right) b_1 &= 0; \\ \left(\frac{\xi\Omega_V}{\omega_1}\right) a_1 + \left[1 - \frac{A_V\beta}{2} - \left(\frac{\Omega_V}{2\omega_1}\right)^2\right] b_1 - \left(\frac{A_V\beta}{2}\right) b_3 &= 0; \\ \left[1 - \left(\frac{k\Omega_V}{2\omega_1}\right)^2\right] a_k - \left(\frac{A_V\beta}{2}\right)(a_{k-2} + a_{k+2}) - \left(\frac{\xi k\Omega_V}{\omega_1}\right) b_k &= 0; \\ \left(\frac{\xi k\Omega_V}{\omega_1}\right) a_k - \left(\frac{A_V\beta}{2}\right)(b_{k-2} + b_{k+2}) + \left[1 - \left(\frac{k\Omega_V}{2\omega_1}\right)^2\right] b_k &= 0. \end{aligned}$$

Now for this system of equations to have a non-trivial solution a_1, b_1, a_3, b_3, $\ldots$ its determinant must equal zero. Therefore:

$$\begin{vmatrix} \cdots & \cdots & \cdots & \cdots & \cdots & \cdots \\ \cdots & 1-\left(\frac{3\Omega_V}{2\omega}\right)^2 & -\frac{A_V\beta}{2} & 0 & \frac{-3\xi\Omega_V}{\omega_1} & \cdots \\ \cdots & \frac{-A_V\beta}{2} & 1+\frac{A_V\beta}{2}-\left(\frac{\Omega_V}{2\omega_1}\right)^2 & -\frac{\xi\Omega_V}{\omega_1} & 0 & \cdots \\ \cdots & 0 & \frac{\xi\Omega_V}{\omega_1} & 1-\frac{A_V\beta}{2}-\left(\frac{\Omega_V}{2\omega_1}\right)^2 & \frac{-A_V\beta}{2} & \cdots \\ \cdots & \frac{3\xi\Omega_V}{\omega_1} & 0 & \frac{-A_V\beta}{2} & 1-\left(\frac{3\Omega_V}{2\omega_1}\right)^2 & \cdots \\ \cdots & \cdots & \cdots & \cdots & \cdots & \cdots \end{vmatrix} = 0. \tag{6.13}$$

Only the four central elements of this determinant need to be considered to find the principal region of instability. Therefore require:

$$\left[1+\frac{A_V\beta}{2}-\left(\frac{\Omega_V}{2\omega_1}\right)^2\right]\left[1-\frac{A_V\beta}{2}-\left(\frac{\Omega_V}{2\omega_1}\right)^2\right]+\left(\frac{\xi\Omega_V}{\omega_1}\right)^2=0.$$

Rearranging this equation for Ω_V yields the equations defining the boundary of the unstable region:

$$\Omega_V = 2\omega_1\sqrt{1-2\xi^2 \pm \sqrt{4\xi^4-4\xi^2+\left(\frac{A_V\beta}{2}\right)^2}}. \tag{6.14}$$

For $\Omega_V = 2\omega_1$ this simplifies to $A_V\beta = 4\xi$, which is about the largest $A_V\beta$ can be before parametric resonance occurs. Figure 6.8 shows the regions of instability predicted by Equation 6.14 for different damping levels, ξ against $A_V\beta$.

6.6.1 Parametric resonance from strong-motion records

Although parametric resonance is important for periodic horizontal and vertical excitations of long durations whether it can occur for non-periodic earthquake strong motions of relatively short duration (usually less than about $30\,\mathrm{s}$ of strong shaking) needs to be investigated. This is the subject of this section.

Finite vertical stiffness

Consider Equations 4.15 & 4.20:

$$u_{tt}+2\xi_1\omega_1 u_t+\omega_1^2(1-\beta u_{tt}^v)u=-U_{tt}. \tag{6.15}$$

Clough & Penzien (1993, pp. 522–525) show, from the power spectral density function, that SDOF systems with reasonably low ratios of critical damping ($\xi < 0.1$) can be classified as narrow-band systems. This means that the response of such systems to excitation will locally appear as a slightly distorted sine function with a frequency near the natural frequency of the system with

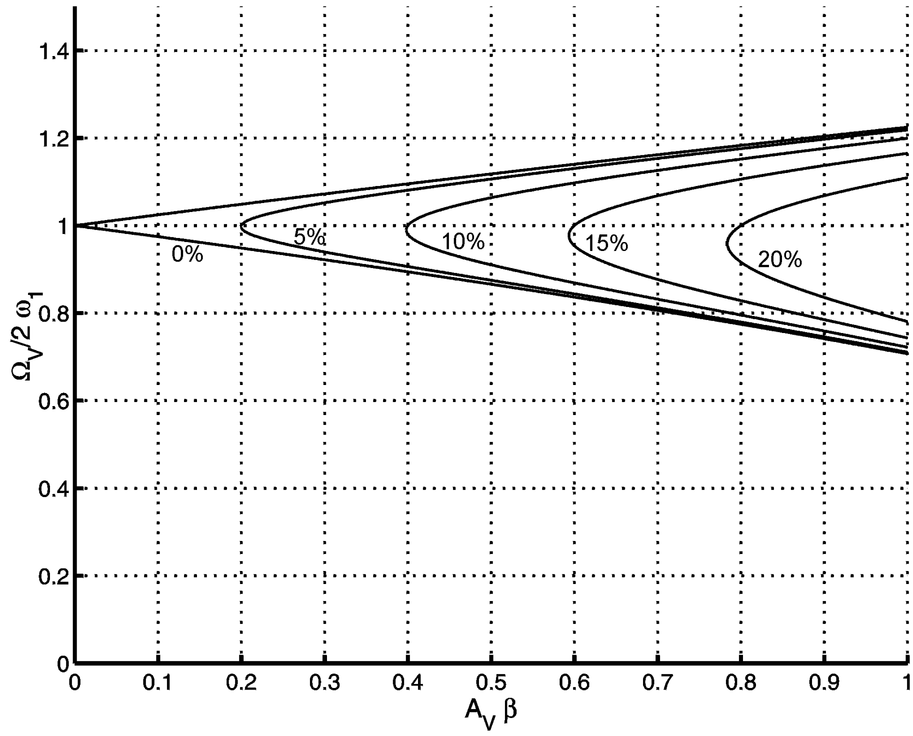

Fig. 6.8: Graph showing regions of instability where parametric resonance occurs, for 0%, 5%, 10%, 15% and 20% damping in terms of the amplitude of the vertical acceleration, $A_v\beta$, and the ratio of the frequency of the vertical acceleration, Ω_V, and twice the natural horizontal frequency of the system, $2\omega_1$. Parametric resonance occurs within the region to the right of each line.

amplitudes that vary slowly in a random fashion. Therefore the response, u^v_{tt}, of a vertical SDOF system to a strong-motion record can be approximated by $u^v_{tt} = A_v\cos(\omega_v t)$, where A_v is the amplitude and ω_v is the natural angular frequency of the system. Hence Equation 6.15 becomes:

$$u_{tt} + 2\xi_1\omega_1 u_t + \omega_1^2[1 - \beta A_v\cos(\omega_v t)]u = -U_{tt}.$$

Therefore parametric resonance is possible if $\beta A_v > \beta_c$, where $\beta_c = A_V\beta$ for the critical value of $A_V\beta$ for ω_v from Equation 6.14. Hence if:

$$A_v > \beta_c/\beta, \tag{6.16}$$

then parametric resonance (leading to large amplification of the horizontal response) can occur if such vertical accelerations are sustained for a long enough time.

An upper bound on A_v is the maximum spectral acceleration at the period and damping of interest for the vertical strong-motion record; this can be found from acceleration response spectra.

The Tabas N74E and vertical components are used as an example of the importance of parametric resonance with $\xi = 0.05$ (5% critical damping in both horizontal and vertical directions) and $\gamma = 0.25$. For $\xi = 0.05$ have $\beta_c = 0.2$ (using Figure 6.8) and for $\gamma = 0.25$ have $\beta = 0.034$ and therefore for $A_v > 0.2/0.034 = 5.9\,\mathrm{ms}^{-2}$ parametric resonance is possible.

For each of the 46 periods between 0.1 and $2\,\mathrm{s}$ and for 5% damping the response of the normal SDOF model to the vertical ground motion was calculated and stored. Figure 6.9 shows the acceleration response spectrum for the vertical component and 5% damping. Also marked is the period range for which parametric resonance is possible using Inequality 6.16. This shows that parametric resonance is possible but only for vertical periods shorter than $0.44\,\mathrm{s}$.

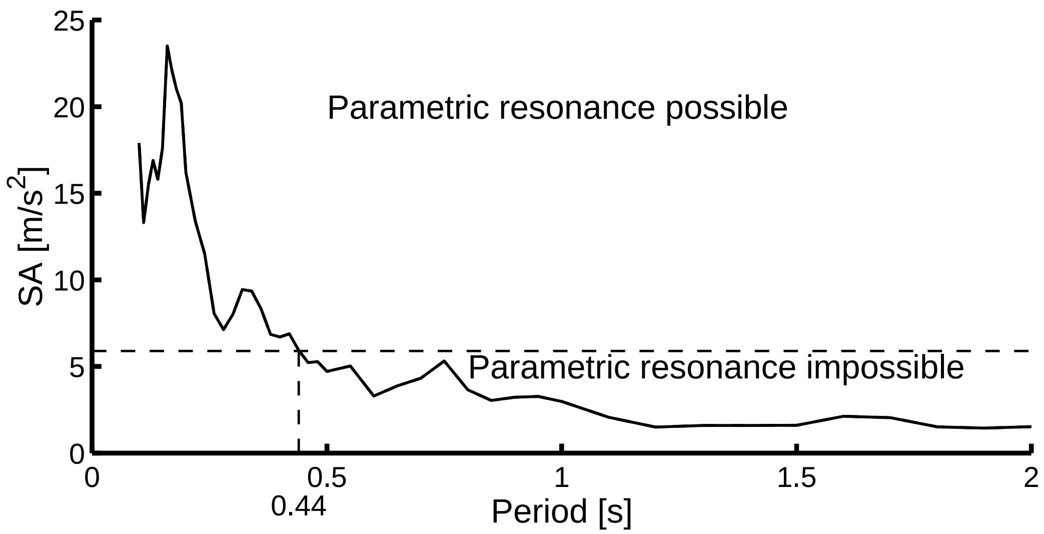

Fig. 6.9: Absolute acceleration response spectrum of the vertical component of the Tabas record for 5% damping. The dashed line marks the lowest amplitude of vertical acceleration required for parametric resonance for $\xi = 0.05$ (5% horizontal damping) and load ratio, $\gamma = 0.25$.

The calculated vertical responses are used as the input to HVSPECTRA to calculate the response spectrum, for 5% damping, of the N74E component using the bending model for $\gamma = 0.25$, i.e. solving Equation 4.15 with u^v_{tt} equal to the vertical response accelerations and $-U_{tt}$ equal to the horizontal ground acceleration. Figure 6.10 shows the percentage increase in spectral acceleration due to the vertical ground motion for the response spectrum of the N74E component and the normal SDOF model.

As can be seen parametric resonance does occur for this record and it leads to an large increase (over 700%) in the horizontal spectral acceleration for horizontal and vertical natural periods 0.36 and $0.18\,\mathrm{s}$ respectively.

To assess the importance of parametric resonance generally the same system was subjected to another strong-motion record. To make the comparison valid a search was made of the near-field records to find a vertical time-history with an acceleration spectrum for 5% damping close to that

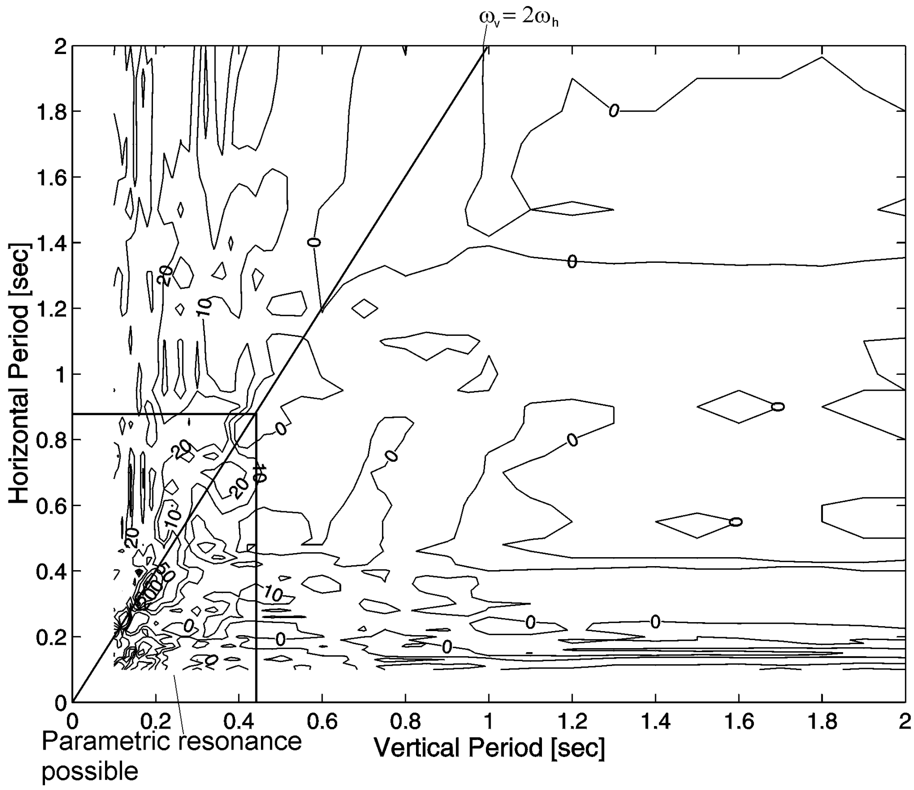

Fig. 6.10: Percentage increase in spectral acceleration due to the vertical ground motion for finite vertical stiffness, 5% damping and $\gamma = 0.25$ (i.e. $100(\mathrm{SA}^V/\mathrm{SA} - 1)$ where SA^V is the spectral acceleration for the bending model and SA is the spectral acceleration for the normal model) for the N74E component of the Tabas strong-motion record. Line of $\omega_v = 2\omega_h$ along which parametric resonance would occur is shown along with lines marking the range of horizontal and vertical periods within which the vertical input accelerations are large enough to possibly cause parametric resonance.

of the vertical spectrum of the Tabas record (Figure 6.9). This means that differences in the effect of the vertical excitation are not due simply to the amplitude of the vertical excitation. The vertical time-history which is the closest match, in terms of the acceleration spectrum for 5% damping, is that from 17645 Saticoy Street from the Northridge earthquake (17/1/1994, $M_s = 6.8$). Figure 6.11 shows the acceleration spectrum which can be compared with that of the Tabas record (Figure 6.9).

The same γ (0.25) was used as for the Tabas record and the horizontal response spectrum for each vertical period between 0.1 and $2\,\mathrm{s}$ was computed. Figure 6.12 shows the percentage increase in spectral acceleration due to the vertical ground motion calculated for the response spectrum of the $180°$ component of the 17645 Saticoy Street record and the normal SDOF model.

As can be seen parametric resonance does occur for this record and it leads to an large increase (over 300%) in the horizontal spectral acceleration for horizontal and vertical natural periods 0.30

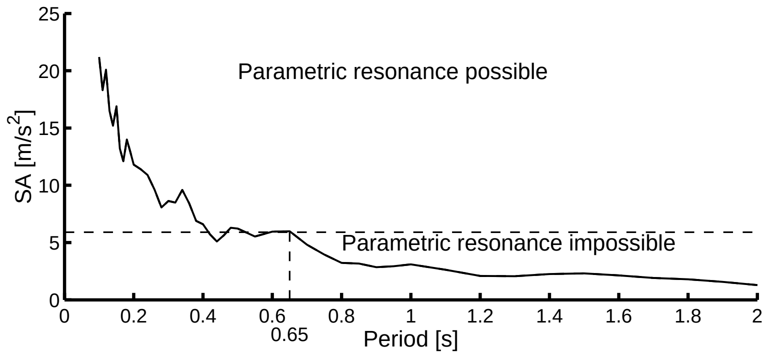

Fig. 6.11: Absolute acceleration response spectrum of the vertical component of the 17645 Saticoy Street record, from the Northridge (17/1/1994) earthquake, for 5% damping. The dashed line marks the lowest amplitude of vertical acceleration required to cause parametric resonance for $\xi = 0.05$ (5% horizontal damping) and load ratio, $\gamma = 0.25$.

and 0.15 s respectively. Comparing Figures 6.10 and 6.12 shows that although parametric resonance does occur for the 17645 Saticoy Street record, as predicted, it does not greatly increase the response as it does for the Tabas record. This is probably due to the shorter duration of large amplitude motion in the 17645 Saticoy Street record compared with the Tabas record. This difference in duration is shown in Figure 6.13 where the vertical acceleration time-histories of these two records are compared.

The strong ground motion in the Tabas record lasts longer than that in the 17645 Saticoy Street record because the Tabas earthquake ($M_s = 7.3$) is larger than the Northridge earthquake ($M_s = 6.8$). Therefore because the large amplitude vertical responses required for parametric resonance do not occur for as long in the 17645 Saticoy Street record there is less chance of such resonance causing large increases in the horizontal response compared with the Tabas record. Therefore whether parametric resonance causes large increases in the horizontal response for a particular record is not simply due to the amplitude of the vertical excitation acceleration being large enough so that Inequality 6.16 holds but also that these large excitations last for a sufficiently long time.

Figures 6.10 & 6.12 also show that when parametric resonance does not occur the amplifications due to vertical ground motion are small (less than about 10 or 20%). Hence if parametric resonance does not occur then vertical ground motion does not have a large effect on horizontal response.

Figure 6.14 shows the regions in which parametric resonance can occur in terms of vertical input acceleration, horizontal damping, ξ, and load ratio, γ, using Inequality 6.16 for the bending model. For example, this graph shows that for a constant harmonic input vertical acceleration with

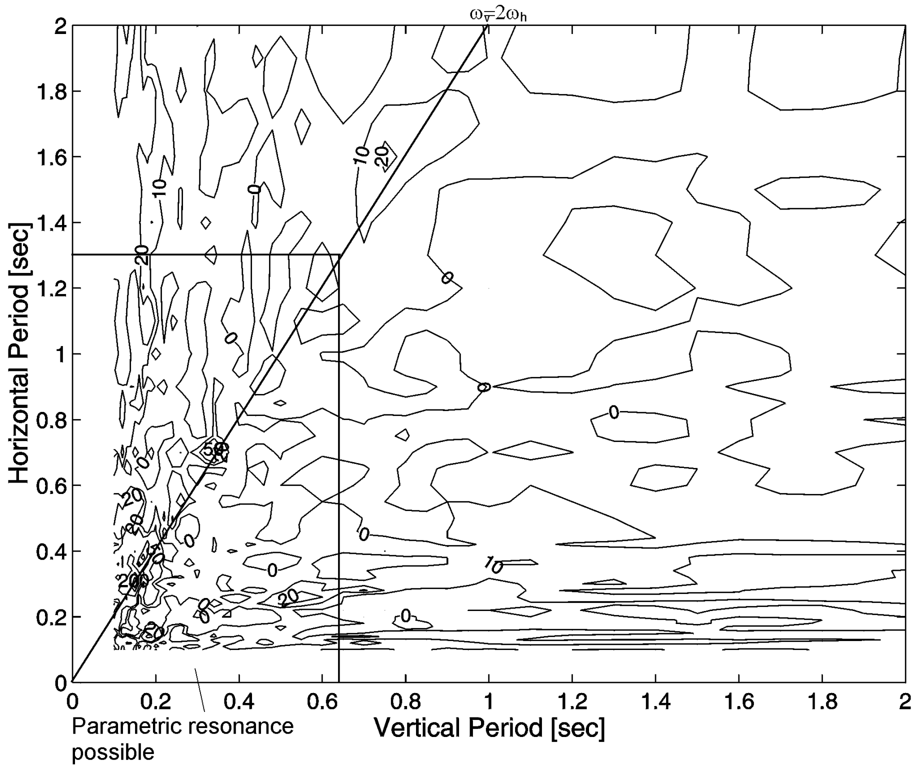

Fig. 6.12: Percentage increase in spectral acceleration due to the vertical ground motion for finite vertical stiffness, 5% damping and $\gamma = 0.25$ (i.e. $100(\mathrm{SA}^V/\mathrm{SA} - 1)$ where SA^V is the spectral acceleration for the bending model and SA is the spectral acceleration for the normal model) for the $180°$ component of the 17645 Saticoy Street strong-motion record from the Northridge earthquake (17/1/1994). Line of $\omega_v = 2\omega_h$ along which parametric resonance would occur is shown along with lines marking the range of horizontal and vertical periods within which the vertical input accelerations are large enough to possibly cause parametric resonance.

amplitude $5\,\mathrm{ms}^{-2}$ parametric resonance will occur for a horizontal natural period equal to twice the period of the vertical acceleration if the horizontal damping is equal to 5% and the load ratio is greater than about 0.3. If the horizontal damping is increased to 10% then the load ratio needs to be increased to about 0.45 for parametric resonance to occur.

The situation for the hinging model is more complicated because β is dependent on the natural horizontal period of the system and also the length of the column.

Figure 6.15 shows the acceleration response spectrum for the vertical component of the Tabas record for 5% damping. Also marked is the period range for which parametric resonance is possible using Inequality 6.16 with $l = 0.5\,\mathrm{m}$ and horizontal damping of 2%. This shows that for vertical periods longer than $0.65\,\mathrm{s}$ parametric resonance is possible but that for shorter periods than $0.65\,\mathrm{s}$

it is impossible.

The calculated vertical responses are used as the input to HVSPECTRA to calculate the response spectrum, for 2% damping, of the N74E component using the hinging model for $l = 0.5\,\mathrm{m}$, i.e. solving Equation 4.20 with u^v_{tt} equal to the vertical response accelerations and $-U_{tt}$ equal to the horizontal ground acceleration. Figure 6.16 shows the percentage increase in spectral acceleration due to the vertical ground motion calculated using the response spectrum of the N74E component using the normal SDOF model.

As can be seen parametric resonance does occur for this record and it leads to an large increase (almost 400%) in the horizontal spectral acceleration for horizontal and vertical natural periods 1.9 and $0.95\,\mathrm{s}$ respectively. Also for short vertical periods (about $0.2\,\mathrm{s}$), corresponding to the peak in the vertical response spectrum there is also a large increase in horizontal response for long horizontal periods which is not caused by parametric resonance.

To assess the importance of parametric resonance generally the same system was subjected to another strong-motion record. Figure 6.17 shows the acceleration spectrum of the 17645 Saticoy Street record and the curve showing the period ranges where parametric resonance is possible for $l = 0.5\,\mathrm{m}$, vertical damping 5% and horizontal damping 2%, which can be compared with that of the Tabas record (Figure 6.15).

The same l ($0.5\,\mathrm{m}$) was used as for the Tabas record and the horizontal response spectrum for each vertical period between 0.1 and $2\,\mathrm{s}$ was computed for 2% damping. Figure 6.18 shows the percentage increase in spectral acceleration due to the vertical ground motion calculated using the response spectrum of the $180°$ component of the 17645 Saticoy Street record using the normal SDOF model.

As can be seen parametric resonance does occur for this record and it leads to an large increase (almost 300%) in the horizontal spectral acceleration for horizontal and vertical natural periods 1.70 and $0.85\,\mathrm{s}$ respectively. Comparing Figures 6.16 and 6.18 shows that although parametric resonance does occur for the 17645 Saticoy Street record, as is predicted, it does not greatly increase the response as does the Tabas record. This is probably due to the smaller duration of large amplitude motion in the 17645 Saticoy Street record compared with the Tabas record. The 17645 Saticoy Street record increases the horizontal response for short vertical periods and long horizontal periods (Figure 6.18) in the same way as the Tabas record (Figure 6.16). Note however that this choice of length of column, $l = 0.5\,\mathrm{m}$, is unrealistic for normal structures.

Figure 6.19 shows the regions in which parametric resonance can occur in terms of vertical input acceleration, horizontal damping, ξ, natural horizontal period and length of column, l, using Inequality 6.16 for the hinging model. For example, this graph shows that for a constant harmonic input vertical acceleration with amplitude $5\,\mathrm{ms}^{-2}$ parametric resonance will occur for a horizontal natural period equal to twice the period of the vertical acceleration if the horizontal damping is equal to 5%, the length of the column is equal to $1\,\mathrm{m}$ and the natural horizontal period is greater than about $1.3\,\mathrm{s}$. If the length of the column is increased to $5\,\mathrm{m}$ then the horizontal damping needs to be decreased to about 1% for parametric resonance to occur.

In Chapter 7 it is shown that most vertical strong-motion records , even in the near field, do not contain enough energy in the long period range for parametric resonance (defined by the regions of Figure 6.19) to occur. Figure 6.19 shows that parametric resonance is most likely for long vertical periods ($T > 1\,\mathrm{s}$), very few structures though have such a vertical period (see Appendix C) and hence it is unlikely that parametric resonance will lead to large increases in the horizontal response of structures that can be modelled by SDOF systems with hinging.

Infinite vertical stiffness

Equation 6.16 can be used to get a lower limit on the amplitude of the vertical ground acceleration required for parametric resonance. However because ground motions are non-harmonic this is a poor estimator of whether parametric resonance will occur.

Figure 6.20 shows that parametric resonance can occur for infinite vertical stiffness and bending models. Figure 6.20(a) clearly shows three peaks of large amplifications (up to about 600%) due to the vertical ground acceleration. These peaks occur at natural horizontal periods: 0.12, 0.36 and $0.42\,\mathrm{s}$, which are double the periods at which the largest vertical accelerations occur (see Figure 6.9) showing that these amplifications are due to parametric resonance. These large amplifications though are not present if the damping is increased to 2% (see Figure 6.20(b)) even though Figure 6.14 shows that parametric resonance is still possible (the graph should be considered for a vertical input acceleration equal to vertical PGA which is $7.3\,\mathrm{ms}^{-2}$ for this record).

Hjelmstad & Williamson (1998) state for the hinging model '[i]t is evident from the preceding discussion [about parametric resonance leading to unbounded responses] that parametric resonance associated with vertical motions, could be a concern in earthquake response of structures if the input motion exhibits near periodicity, as was true in the 1985 earthquake, experienced in the the Mexico City lake bed region. One should note that the values of η [here called β] in building structures are typically rather small, thereby limiting the troublesome range of frequencies associated with parametric resonance.'

This idea was tested using a record of the Michoacán (19/9/1985) from Mexico City (CDAF de Abastos Oficia) which is on very soft soil ($V_{s,30} = 61\,\mathrm{ms}^{-1}$) and exhibits sinusoidal (see Figure 6.21) ground motion with period about 2 to $3\,\mathrm{s}$. Figure 6.22 shows the percentage increase in the horizontal spectral acceleration due to the vertical ground motion for this record with $l = 0.25\,\mathrm{m}$, 5% vertical damping and 0% horizontal damping. From Figure 6.22 it can be seen that there is an increase in the horizontal response due to parametric resonance at periods greater than about $3\,\mathrm{s}$.

However, the length of column required to cause this increase is not realistic.

6.7 Conclusions

The two elastic SDOF models studied for this thesis, the bending and the hinging models, both have three main types of behaviour: normal, parametric resonance and instability. The type of behaviour the system exhibits is controlled by the combination of system parameters and the vertical input acceleration.

The systems are unstable when the multiplier of horizontal displacement in the equation of the motion is negative for a sufficiently long period of time so that exponential solutions of the equation are possible and the systems collapse because the displacement (and velocity and accelerations) tend to infinity. This limit is simply the stability criterion that the system must obey in the static case modified due to vertical ground motion. The following are the main findings on stability.

- The length of interval above the critical acceleration required to induce instability is related to the horizontal natural period of the system: short period systems require shorter intervals than long period systems.
- The length of interval of above critical accelerations required for instability in bending systems with periods between 0.1 and $2\,\mathrm{s}$ is about $0.05\,\mathrm{s}$.
- The length of interval of above critical accelerations required for instability in hinging systems with periods between 0.1 and $2\,\mathrm{s}$ is greater than that for the bending model and is equal to about $0.2\,\mathrm{s}$
- Size of horizontal damping of either system has little effect on the length of time that is required to cause instability.
- A number of vertical records do induce instability in SDOF models with bending and finite vertical stiffness for realistic load ratios of about 0.3 to 0.5. Therefore such a failure mechanism is possible for structures that can be modelled by such SDOF models.
- No recorded vertical ground motions induce instability in SDOF systems with hinging for realistic length of columns (greater than $1\,\mathrm{m}$) and horizontal and vertical damping and period. Therefore such a failure mechanism is not possible for structures that can be modelled by such SDOF models.

The systems exhibit parametric resonance when the amplitude of the vertical acceleration is greater than a limit acceleration and the period of this vertical acceleration is half the natural horizontal period. This limit acceleration depends on the structural parameters: horizontal damping and length of column (for the hinging model) or load ratio (for the bending model). The main findings on parametric resonance are:

- parametric resonance can lead to large increases (up to 700%) in the horizontal response of bending systems with realistic structural parameters;
- although parametric resonance can lead to large increases (up to 300%) in the horizontal response of hinging systems these increases are for unrealistic structural parameters, i.e. extremely short columns with large horizontal and vertical periods so parametric resonance is not likely to occur in structures that approximate to hinging models;
- the duration of the strong motion affects the size of the increase in horizontal response due to parametric resonance so longer durations of strong motion lead to large increases in response because parametric resonance can build up;
- for infinite vertical stiffness parametric resonance can occur but this is only for structural parameters which are unlikely to occur in practice.

When the combination of system parameters and vertical input accelerations means that instability and parametric resonance do not occur then the system behaves almost the same as the ordinary zero-gravity system defined by Equation 4.1. The amplifications due to the vertical excitation are small as is shown in Chapter 7. For most vertical ground motions and realistic choices of system parameters this is the type of behaviour which will occur.

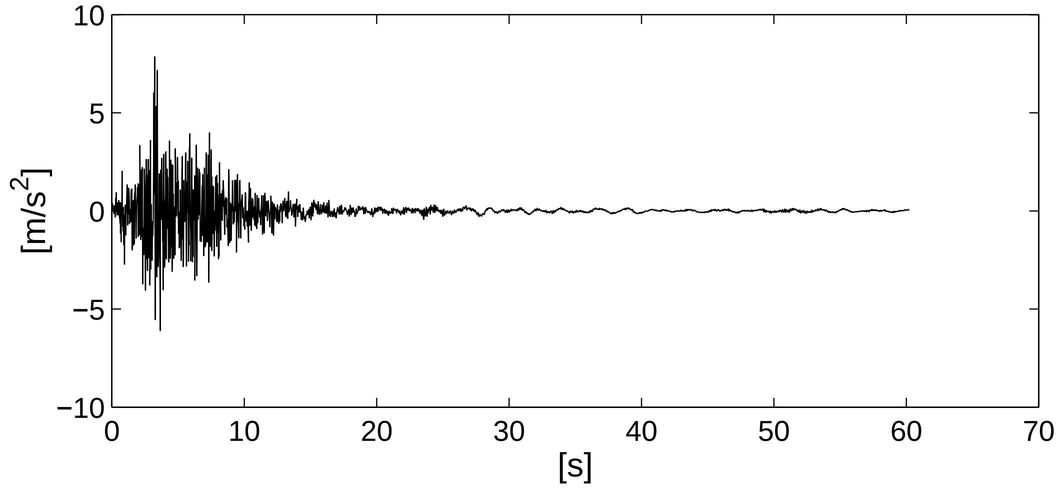

(a) 17645 Saticoy Street ($M_w = 6.7$, $M_s = 6.8$)

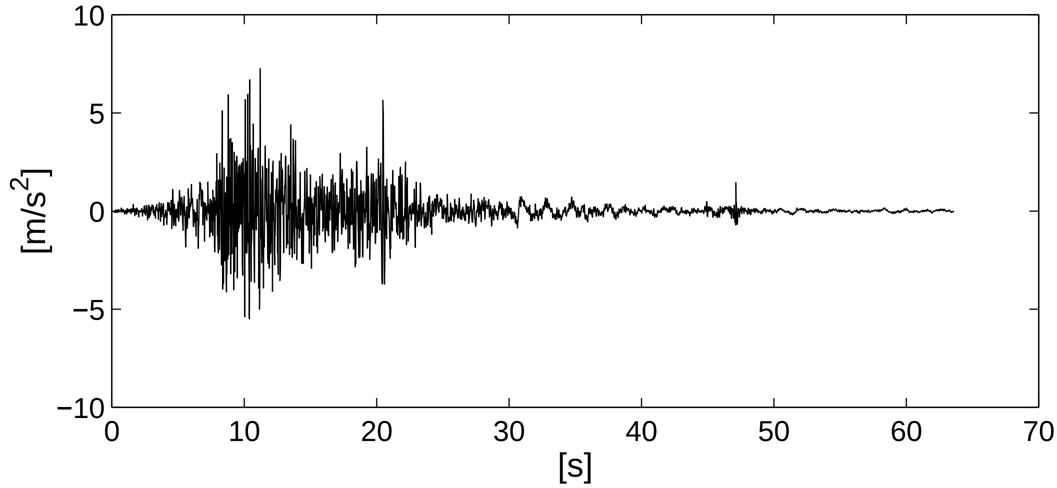

(b) Tabas ($M_w = 7.4$, $M_s = 7.3$)

Fig. 6.13: Vertical acceleration time-histories from 17645 Saticoy Street from the Northridge earthquake (17/1/1994, $M_s = 6.8$) and Tabas from the Tabas earthquake (16/9/1978, $M_s = 7.3$). Note the difference in duration of the strong motion.

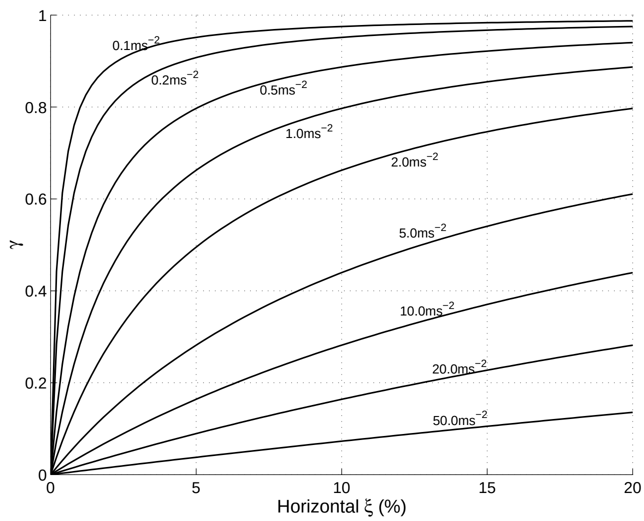

Fig. 6.14: Regions of possible parametric resonance for the bending model in terms of vertical input acceleration (0.1, 0.2, 0.5, 1.0, 2.0, 5.0, 10.0, 20.0 and $50\,\mathrm{ms}^{-2}$), horizontal damping, ξ, in percentage of critical and load ratio, γ. Parametric resonance can occur for combinations of horizontal damping and load ratio which are above line corresponding to the vertical input acceleration.

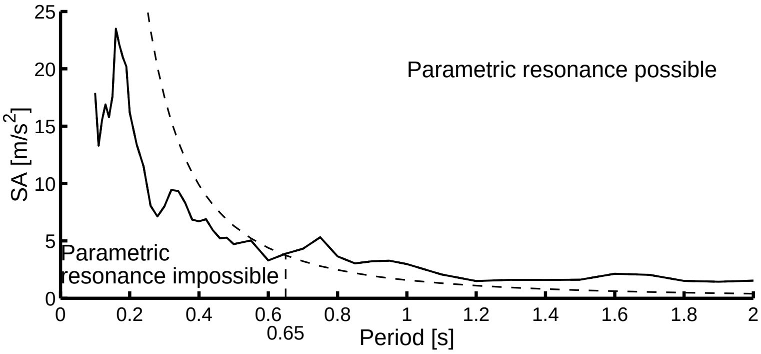

Fig. 6.15: Absolute acceleration response spectrum of the vertical component of the Tabas record for 5% damping. The dashed line marks the lowest amplitude of vertical acceleration required to cause parametric resonance for $\xi = 0.02$ (2% horizontal damping) and length of column, $l = 0.5\,\mathrm{m}$. Note that in contrast to bending model the amplitude of vertical acceleration required to induce parametric resonance is dependent on the natural horizontal period (which is here assumed to equal the natural vertical period).

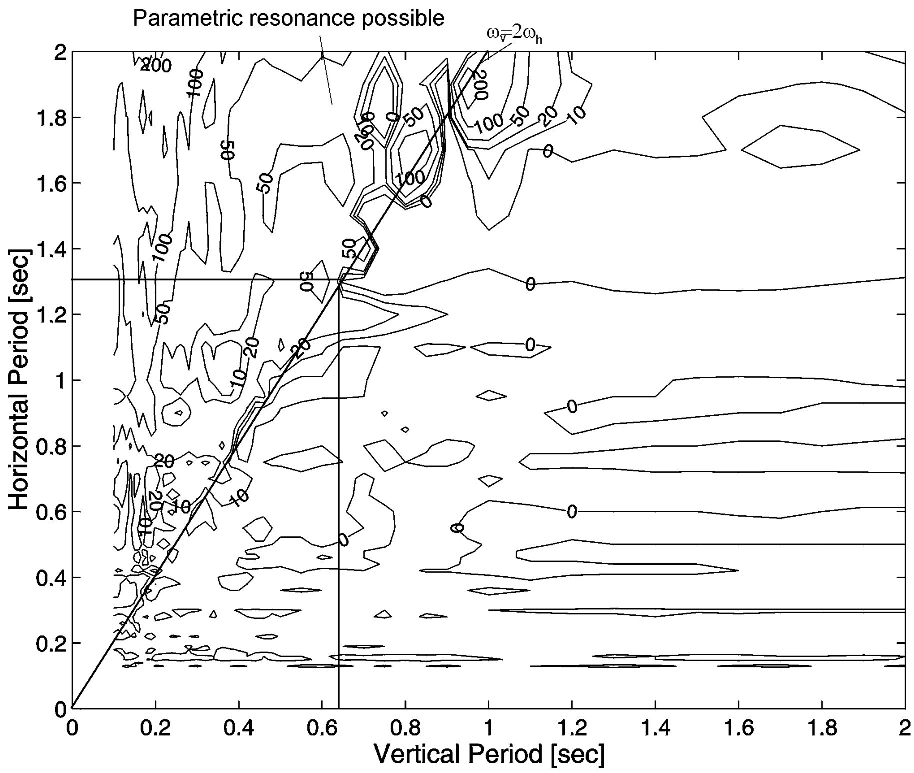

Fig. 6.16: Percentage increase in spectral acceleration due to the vertical ground motion for finite vertical stiffness, 5% damping vertically and 2% damping horizontally and $l = 0.5\,\mathrm{m}$ (i.e. $100(\mathrm{SA}^V/\mathrm{SA} - 1)$ where SA^V is the spectral acceleration for the hinging model and SA is the spectral acceleration for the normal model) for the N74E component of the Tabas strong-motion record. Line of $\omega_v = 2\omega_h$ along which parametric resonance would occur is shown along with lines marking the range of horizontal and vertical periods within which the vertical input accelerations are large enough to possibly cause parametric resonance.

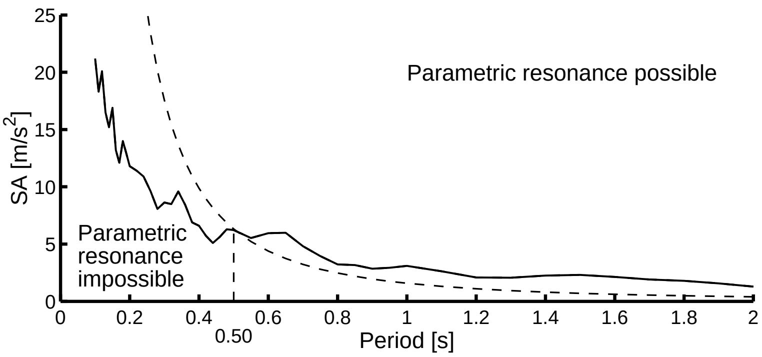

Fig. 6.17: Absolute acceleration response spectrum of the vertical component of the 17645 Saticoy Street record, from the Northridge (17/1/1994) earthquake, for 5% damping. The dashed line marks the lowest amplitude of vertical acceleration required to cause parametric resonance for $\xi = 0.02$ (2% horizontal damping) and length of column, $l = 0.5\,\mathrm{m}$. Note that in contrast to bending model the amplitude of vertical acceleration required to induce parametric resonance is dependent on the natural horizontal period (which is here assumed to equal the natural vertical period).

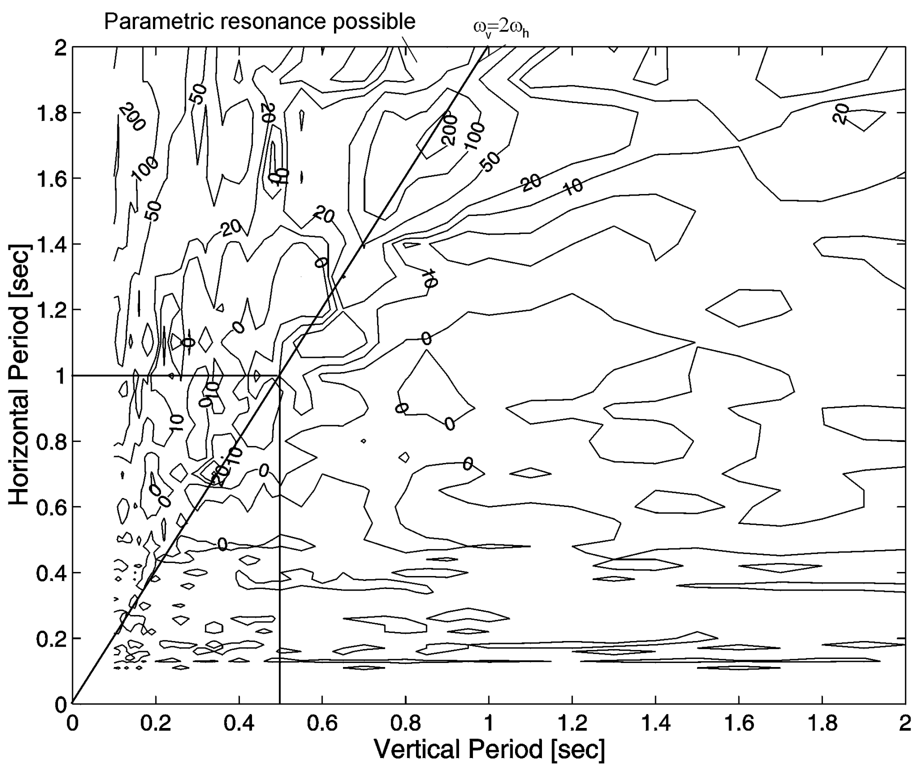

Fig. 6.18: Percentage increase in spectral acceleration due to the vertical ground motion for finite vertical stiffness, 5% damping vertically, 2% damping horizontally and $l = 0.5\,\mathrm{m}$ (i.e. $100(\mathrm{SA}^V/\mathrm{SA} - 1)$ where SA^V is the spectral acceleration for the hinging model and SA is the spectral acceleration for the normal model) for the $180°$ component of the 17645 Saticoy Street strong-motion record from the Northridge earthquake (17/1/1994). Line of $\omega_v = 2\omega_h$ along which parametric resonance would occur is shown along with lines marking the range of horizontal and vertical periods within which the vertical input accelerations are large enough to possibly cause parametric resonance.

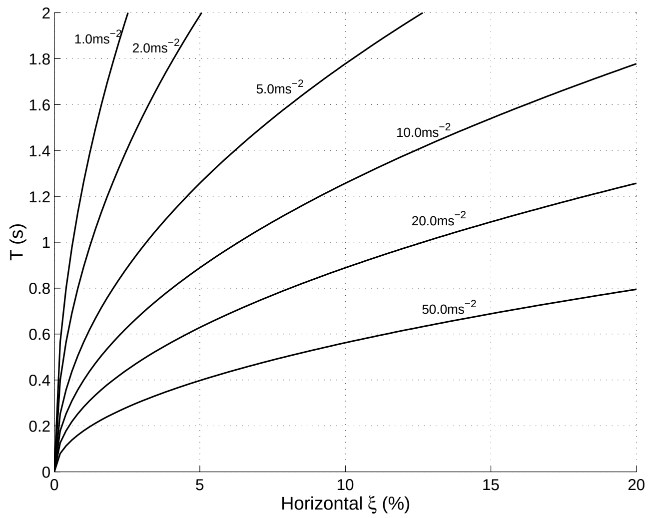

(a) $l = 1\text{m}$

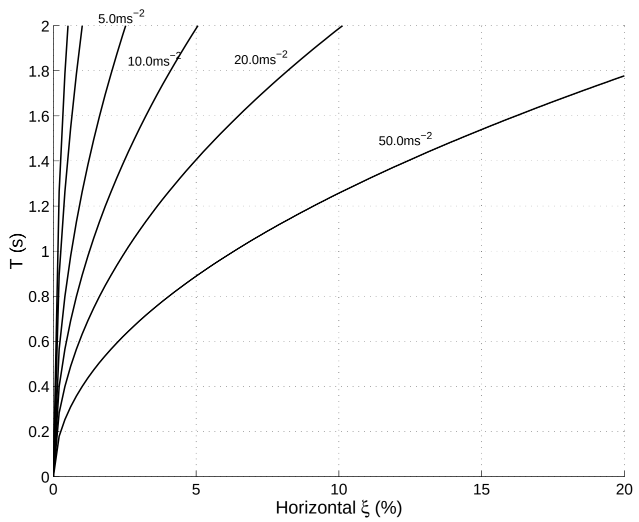

(b) $l = 5\text{m}$

Fig. 6.19: Regions of possible parametric resonance for the hinging model in terms of vertical input acceleration (1.0, 2.0, 5.0, 10.0, 20.0 and $50\,\mathrm{ms}^{-2}$), horizontal damping, ξ, in percentage of critical, natural horizontal period, T, and length of column, l. Parametric resonance can occur for combinations of horizontal damping, natural horizontal period and length of column which are above line corresponding to the vertical input acceleration.

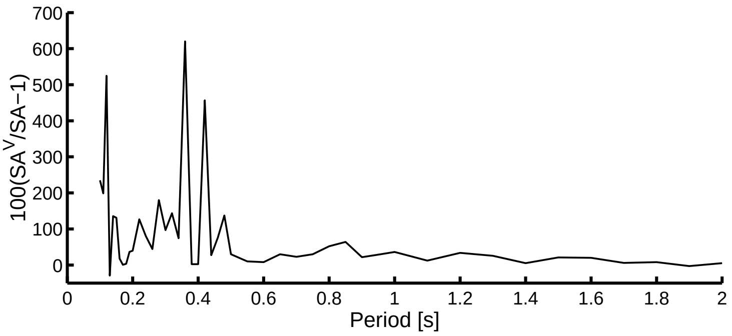

(a) $\xi = 0$ (undamped)

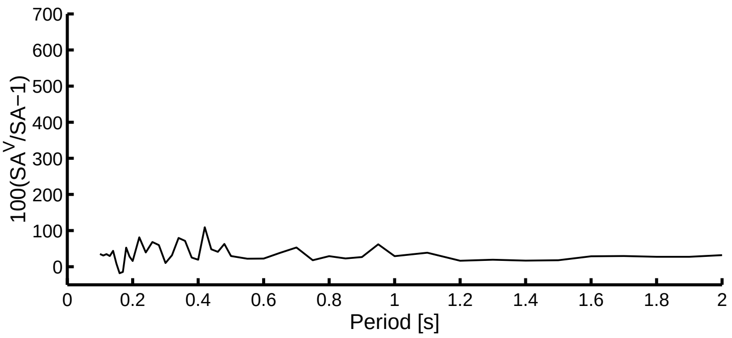

(b) $\xi = 0.02$ (2% damping)

Fig. 6.20: Percentage increase in spectral acceleration due to the vertical ground motion for infinite vertical stiffness, 0% and 2% damping and $\gamma = 0.5$ (i.e. $100(\mathrm{SA}^V/\mathrm{SA} - 1)$ where SA^V is the spectral acceleration for the bending model and SA is the spectral acceleration for the normal model) for the N74E component of the Tabas strong-motion record.

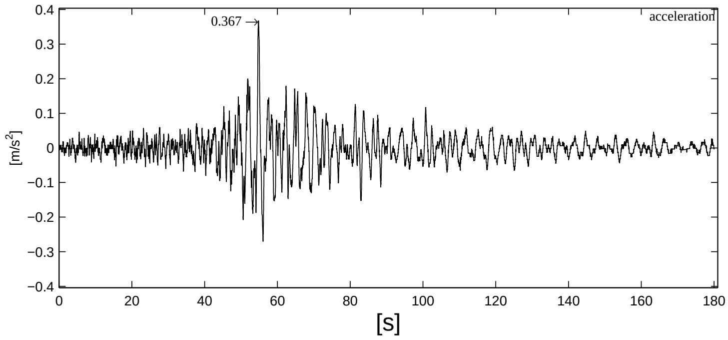

Fig. 6.21: Vertical acceleration time-history from Mexico City (CDAF de Abastos Oficia) of the Michoacán earthquake (19/9/1985) recorded on very soft soil ($V_{s,30} = 61\,\mathrm{ms}^{-1}$). Note that the record is approximately harmonic with period about 2 to $3\,\mathrm{s}$.

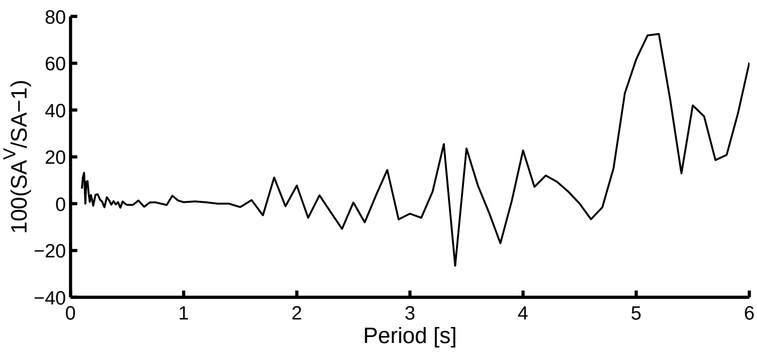

Fig. 6.22: Percentage increase in spectral acceleration due to the vertical ground motion for infinite vertical stiffness, 5% vertical damping, 0% horizontal damping and $l = 0.25\,\mathrm{m}$ (i.e. $100(\mathrm{SA}^V/\mathrm{SA}-1)$ where SA^V is the spectral acceleration for the hinging model and SA is the spectral acceleration for the normal model) for the N000 component of the Mexico City (CDAF de Abastos Oficia) strong-motion record.

7. GROUND MOTION PREDICTION RESULTS

This chapter contains results obtained using the near-field set of records, the characteristics of which were given in Chapter 5.

7.1 Ground motion model used

The ground motion model assumed has the form:

$$\log y = b_1 + b_2 M_s + b_3 d + b_A S_A + b_S S_S$$

where M_s is surface-wave magnitude and d is distance to the surface projection of the rupture plane. If the site is classified as stiff soil (A) S_A is unity otherwise it is 0. Similarly if the site is classified as soft soil (S) S_S is unity otherwise it is 0.

The distance dependence is not defined in terms of $r = \sqrt{d^2 + h^2}$ because if a h term is included it is almost indistinguishable from zero and hence can be dropped. Decay is assumed to be associated with anelastic effects due to large strains, which is reasonable in the near-field of large earthquakes. The geometrical decay term of the form $\log d$ and the anelastic term of the form d are highly correlated within the short distance range used in this study so they cannot be found simultaneously.

The equation for the prediction of horizontal PGA assuming geometrical attenuation derived here is:

$$\log a_h = -0.431 + 0.195 M_s - 0.436 \log \sqrt{d^2 + 2.3^2} + 0.022 S_A + 0.030 S_S \tag{7.1}$$

with $\sigma = 0.212$. Figure 7.1 compares PGA predicted by Equation 7.1 and that predicted by Equation 7.2, the equation which assumes anelastic attenuation. As can be seen both equations predict almost identical PGA and have almost identical standard deviations. Therefore the type of attenuation assumed is unimportant.

The largest horizontal component is used for deriving the attenuation relations in this chapter for consistency with previous work by Ambraseys & Bommer (1991), Ambraseys (1995) and Ambraseys *et al.* (1996).

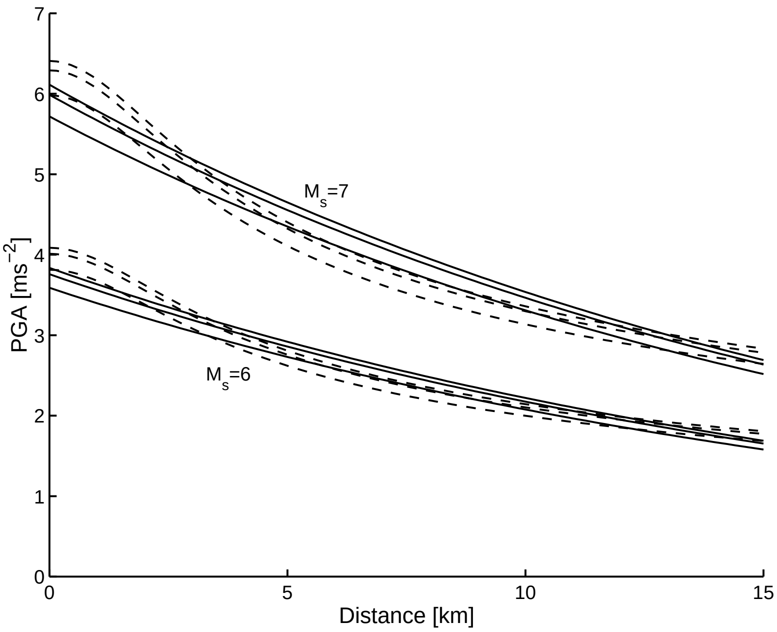

Fig. 7.1: Comparison of near-field horizontal PGA for $M_s = 6$ and $M_s = 7$ predicted using equation which assumes geometric attenuation (Equation 7.1) (dashed lines) and that predicted assuming anelastic attenuation (Equation 7.2) (solid lines). The three lines for each magnitude are for the three different site types (S, A, R).

7.2 Regression methods

There are a number of regression methods for deriving attenuation relations, which one is used can affect the equations obtained and hence the predicted accelerations.

Two main types of regression technique are used: one-stage and two-stage. In one-stage the magnitude and distance coefficients are estimated simultaneously whereas in the two-stage method first distance coefficients and then magnitude coefficients are found. Within these categories there are also two further subdivisions: ordinary least squares estimation and random-effects (or maximum-likelihood) models (Brillinger & Preisler, 1984, 1985). The first of these simply finds the coefficients which minimize the sum of squares of the residuals assuming the errors in each record are independent. The coefficients are estimated and the standard deviation is determined from the error about the line. In the random-effects technique the error is assumed to consist of two[1] parts: an earthquake-to-earthquake component, which is the same for all records from the same earthquake and a record-to-record component, which expresses the variability between each record not expressed by the earthquake-to-earthquake component. The standard deviation of these

[1] Joyner & Boore (1993) give an algorithm assuming the error consists of three parts: an earthquake-to-earthquake component, a site component and a record component, but this is not usually employed due to the limited number of records from each site.

two errors is found along with the coefficients. This method allows for the possibility that records from the same earthquake are not strictly independent.

Most authors find, if they consider the problem at all, that the regression technique used does not affect the results obtained within the range of distance and magnitude that are of engineering interest (Ambraseys & Bommer, 1991; Ambraseys *et al.*, 1996).

There have been some authors though who find, that due to a high correlation between a record's magnitude and distance, the one-stage method gives biased results (Fukushima *et al.*, 1988; Fukushima & Tanaka, 1990) and that the two-stage technique eliminates this bias.

Both these studies are based on Japanese recordings where the depths and distances of the earthquakes are much larger than for this near-field study. In this study the magnitudes and distances used are not strongly correlated, in fact the correlation coefficient $r_{M_s,d} = -0.10$. Consequently in this study d and M_s are assumed to be independent.

The chief advantage of the one-stage method is its simplicity. The two main disadvantages are that if magnitude and distance are correlated then it can yield incorrect coefficients and results are biased in favour of well-recorded earthquakes.

The two advantages of the two-stage method are that the amplitude factors of each earthquake can be examined for linear or nonlinear scaling and also that well-recorded shocks have less effect than when a one-stage method is used. The main disadvantage of the method is that an arbitrary assumption has to be introduced in the weighting in the second stage of the regression.

Before deciding which regression method to use for this study, both one-stage and two-stage ordinary least squares were used to derive equations for peak ground acceleration and spectral ordinates for horizontal and vertical components. A comparison of the results shows almost identical distance dependence terms but quite large differences in the magnitude terms. For one-stage regression horizontal peak ground acceleration (a_h) is given by:

$$\log(a_h) = -0.634 + 0.202M_s - 0.0238d$$

with $\sigma = 0.21$ and vertical peak ground acceleration (a_v) is given by:

$$\log(a_v) = -0.914 + 0.226M_s - 0.0312d$$

with $\sigma = 0.27$.

From a two-stage regression:

$$\log(a_h) = -0.311 + 0.151M_s - 0.0228d$$

with $\sigma = 0.25$, and:

$$\log(a_v) = -0.372 + 0.141M_s - 0.0316d$$

with $\sigma = 0.31$.

Figure 7.2 shows the predicted horizontal PGA from both the one- and two-stage regressions.

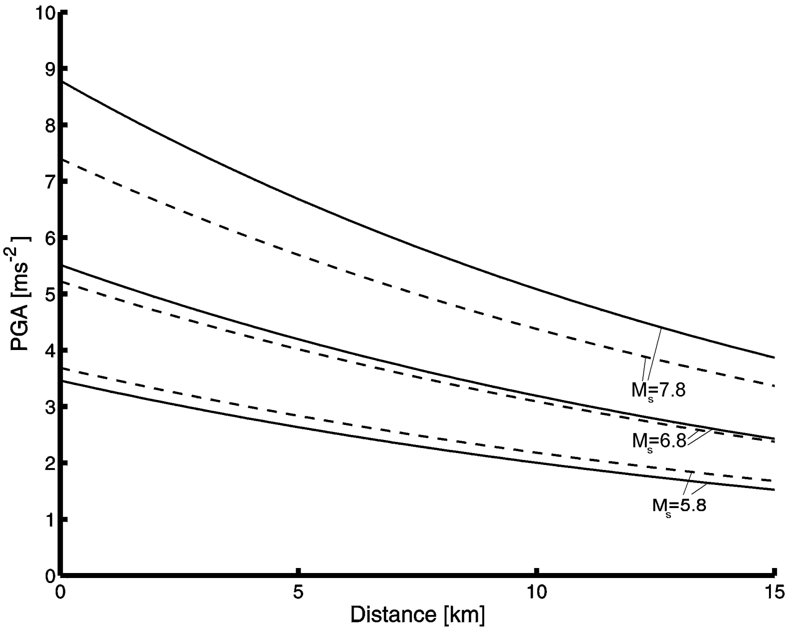

Fig. 7.2: Comparison of predicted horizontal PGA using one-stage and two-stage regression methods for $M_s = 5.8$, 6.8 & 7.8. Solid line is for one-stage equation and dashed line is for two-stage equation.

For $M_s = 6.8$ the predicted PGA from the equations derived using the two different methods are similar, diverging for higher and lower magnitudes (Figure 7.2). The two-stage regression predicts higher accelerations for smaller magnitudes and lower accelerations for larger magnitudes than the one-stage regression. This is also observed for vertical PGA, and for horizontal and vertical spectral ordinates.

Figures 7.3(a) and 7.3(b) show the cumulative frequency distribution for the magnitude scaling of both the one-stage and two-stage methods. The graphs show that the magnitude scaling of the two-stage method is based on a more evenly distributed set of magnitudes than the one-stage method; for example, about 25% of the points for the two-stage method are associated with earthquakes with $M_s > 7.0$, whereas only about 15% of the one-stage are. This seems to imply that the two-stage method gives a better representation over the entire magnitude range.

To investigate this point further, the amplitude factors, a_i, which are used to find the magnitude dependence in the second stage, were plotted against magnitude. As can be seen from Figure 7.4 there is much scatter in amplitude factors although a linear trend with magnitude can be seen. From this graph is is noticeable that a_i, from the Kocaeli earthquake ($M_s = 7.8$) falls well below the

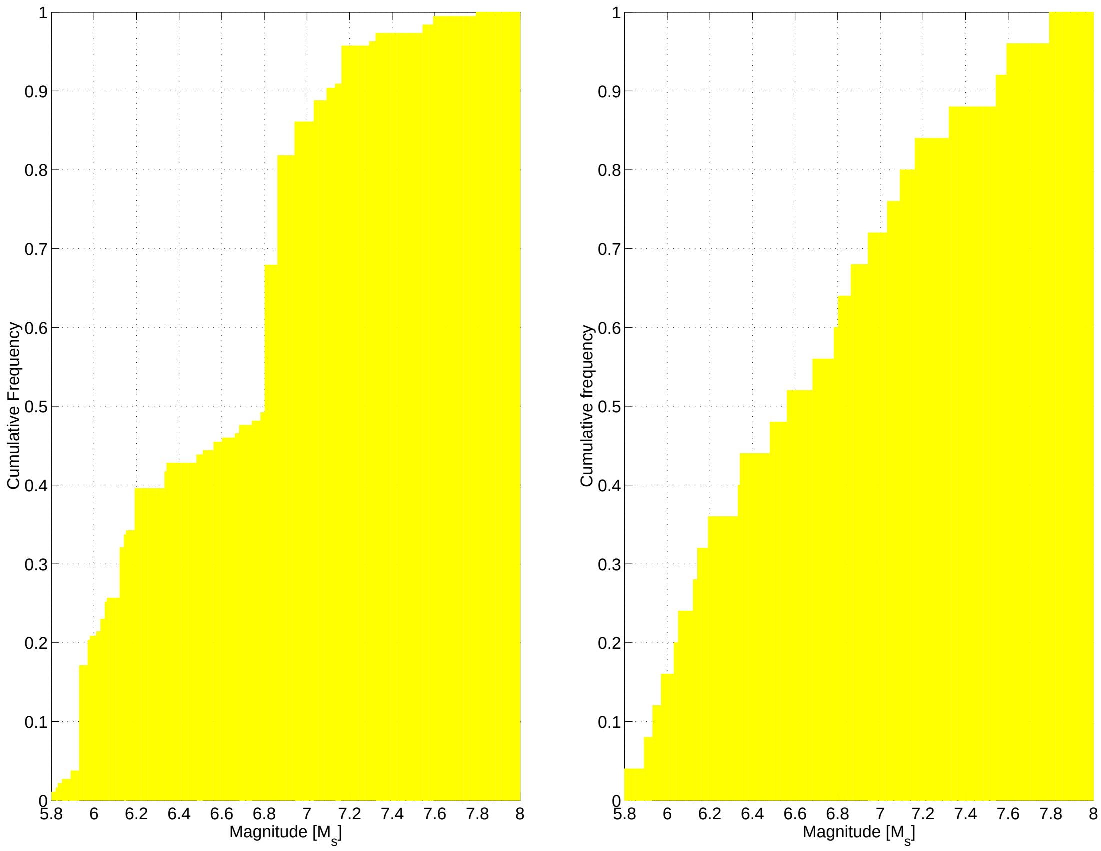

(a) One-stage method

(b) Two-stage method

Fig. 7.3: Cumulative frequency distribution of records used for magnitude scaling.

trend line and seems to be having a large influence on the least squares fit from the second step.

To check this difference, the analysis was repeated without the two records from this earthquake. It was found that the distance dependence remains almost exactly the same but the magnitude dependence is quite different. From the one-stage method the magnitude coefficient b_2 becomes 0.222 and from the two-stage method 0.195, with corresponding changes in b_1. This shows that the Kocaeli records have a significant effect on the magnitude dependence, especially in the two-stage method.

In what follows the one-stage method is adopted for the analysis.

One question here is whether $M_{s,z} = 7.8$, as determined by USGS, is the representative surface-wave magnitude of this shock, for which there is insufficient data as yet to assess its magnitude from the Prague formula. The moment magnitude estimates for this earthquake vary from 7.2 (from ERI AutoCMT) to 7.6 (Harvard CMT); slightly lower than the surface-wave magnitude. Since no other M_s value is available and to assess the effect of M_s being overestimated for this earthquake, which has a large effect on the magnitude dependent coefficient of the attenuation relations, the horizontal PGA equation was recalculated using $M_s = 7.4$ (using equation (1) of Ekström & Dziewonski

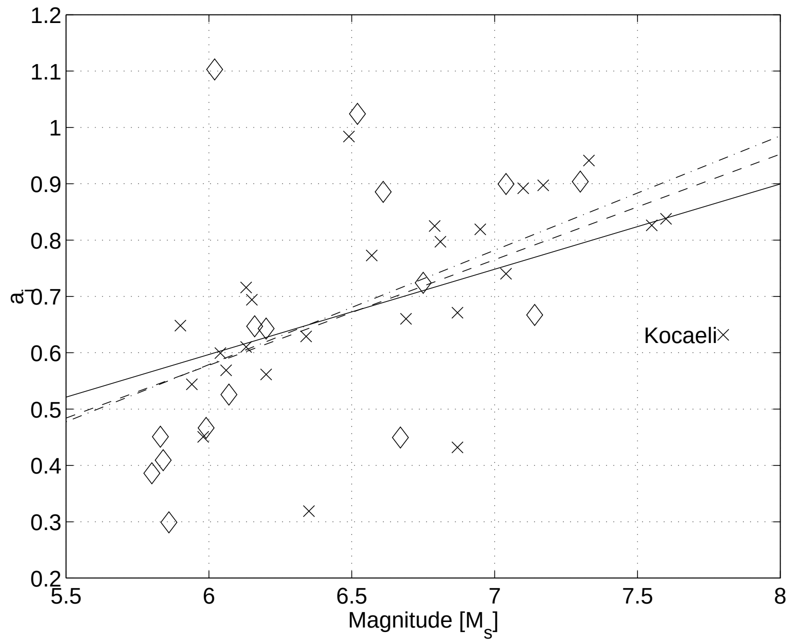

Fig. 7.4: Variation of amplitude factors, a_i, with magnitude, crosses are those earthquakes which have more than one record associated with them and diamonds are for one-record earthquakes. Solid line is the magnitude dependence obtained from the two-stage method ignoring the earthquakes with only one record, dashed line is from the two-stage method including all earthquakes and dash-dotted line is from the one-stage method.

(1988) with $M_w = 7.4$). This change has a negligible effect on the one-stage equation except for large magnitudes ($M_s > 7.5$) for which the equation using $M_s = 7.4$ for Kocaeli predicts slightly higher accelerations. The two-stage equation is affected more by this change, the magnitude dependence increases slightly making the one-stage and two-stage equations more alike. Without additional information the surface-wave magnitude for this earthquake should not be changed from $M_s = 7.8$ and this check on the effect of an incorrect magnitude shows that even if in the future this magnitude was found to be an overestimate changing it does not have a large effect.

7.2.1 Inclusion of site geology in the ground motion model

The method used by Ambraseys *et al.* (1996) to include site geology in the attenuation was also used in this study because there are 8 records without a site classification. The residuals, ϵ_i ($\log y_i - b_1' - b_2 M_i - b_3 d_i$), from the first stage of the regression are found. Then a regression is performed on $\epsilon = b_4 S_R + b_5 S_A + b_6 S_S$, where: $S_R = 1$ if the site is classified as rock and 0 otherwise, and S_A and S_S are similarly defined for stiff (A) and soft (S) soil sites. Then new coefficients are defined as follows: $b_1 = b_1' + b_4$, $b_A = b_5 - b_4$ and $b_S = b_6 - b_4$ and the error σ is recalculated with respect to the site-dependent prediction, using only those records with known site conditions.

7.3 Horizontal PGA ($y = \log a_h$)

The equation for the prediction of horizontal PGA (a_h) in the near-field is estimated to be:

$$\log a_h = -0.659 + 0.202 M_s - 0.0238 d + 0.020 S_A + 0.029 S_S \quad \text{with} \quad \sigma = 0.214. \tag{7.2}$$

The magnitude and distance coefficients are significant at the 5% level but the soil terms are not significant at this level, but were retained for comparison with other studies.

Figure 7.5 shows comparison between the peak ground acceleration predicted by Equation 7.2 and that predicted by four other widely used equations. Figure 7.5 shows the following important features.

- Equation 7.2 predicts much lower accelerations than the equation of Ambraseys *et al.* (1996) especially for large magnitudes, for example for $M_s = 7.5$ and $d = 0\,\mathrm{km}$ the equation of Ambraseys *et al.* (1996) predicts horizontal PGA for soft soil of about $1.4\,\mathrm{g}$ [$14\,\mathrm{ms}^{-2}$] compared with Equation 7.2 which predicts horizontal PGA for soft soil of about $0.8\,\mathrm{g}$ [$8\,\mathrm{ms}^{-2}$]. This over-estimation of PGA by the equation of Ambraseys *et al.* (1996) is probably due to the large number of weak ground motions in the records used. Equation 7.2 predicts similar horizontal PGA to those predicted by the equations of Boore *et al.* (1993) and Campbell (1997) reflecting the large number of records from large magnitudes and short distances in their sets. Equation 7.2 predicts slightly larger horizontal PGA than the equation of Spudich *et al.* (1999) for extensional regimes, again confirming the finding of Spudich *et al.* (1999) that the strong ground motion in extensional regimes is smaller than that in other tectonic regimes. Spudich *et al.* (1999) use the geometric mean of the two horizontal components rather than the larger horizontal component which could be one factor reducing the predicted accelerations.

- Equation 7.2 exhibits a lower dependence on magnitude than the equation of Ambraseys *et al.* (1996). The equation of Ambraseys *et al.* (1996) was derived using mainly data from small magnitude ($M_s < 6$) earthquakes and so the point source assumption is roughly valid and consequently the equation reflects global fault conditions. For the data used to derive Equation 7.2 the point source assumption is not adequate and so the equation reflects the local fault conditions leading to lower magnitude dependence. The magnitude dependence however, is almost identical to that in the equations of Boore *et al.* (1993) and Spudich *et al.* (1999) showing that these equations can be used for ground motion estimation in the near-field. The magnitude dependence of Equation 7.2 is larger than that of the equation of Campbell (1997) possibly due to the form of the equation adopted by Campbell (1997) which allows for distance saturation or because of the distance measure used by Campbell (1997) (seismogenic distance) differs from that used here (distance to the surface projection of the rupture plane).

- The distance dependence of Equation 7.2 is almost identical to that of Boore *et al.* (1993) and Spudich *et al.* (1999) and is similar to that of Ambraseys *et al.* (1996) and Campbell (1997) showing that the attenuation mechanism that is dominant in the near-field cannot be determined.

- Equation 7.2 predicts near-field horizontal PGA which is almost independent of site conditions, unlike the equations of Boore *et al.* (1993), Ambraseys *et al.* (1996) and Spudich *et al.* (1999) which show significant dependence of horizontal PGA with site conditions. The site dependence is also lower than that predicted by the equation of Campbell (1997) which allows for site amplifications which are dependent on magnitude and distance. The negligible dependence of near-field horizontal PGA on site conditions shows, as pointed out by Faccioli & Reseńdiz (1976), that close to the source, site conditions are less important in determining ground motions than source and path. Also it may indicate non-linear soil behaviour at large strains which occur in the near field of large earthquakes leading to lower soil amplification than for weak ground motions.

- The associated standard deviation of Equation 7.2 ($\sigma = 0.214$) is slightly smaller than that of the equation of Ambraseys *et al.* (1996) ($\sigma = 0.25$) but similar to that of Boore *et al.* (1993) ($\sigma = 0.205$), Spudich *et al.* (1999) ($\sigma = 0.204$) and Campbell (1997) (0.169–0.239 dependent on horizontal PGA). This shows that near-field horizontal PGA is not less variable than intermediate-field and far-field horizontal PGA.

7.4 Vertical PGA ($y = \log a_v$)

The equation estimated for the prediction of vertical PGA (a_v) in the near-field is:

$$\log a_v = -0.959 + 0.226M_s - 0.0312d + 0.024S_A + 0.075S_S \quad \text{with} \quad \sigma = 0.270. \tag{7.3}$$

As for the horizontal components whereas the magnitude and distance dependences are significant at the 5% level, the soil terms are not.

A comparison of Equations 7.2 and 7.3 shows that the decay with distance of vertical PGA is faster than that of horizontal PGA probably because vertical ground motions are generally of higher frequency than horizontal ground motions and high frequency waves attenuate more rapidly than low frequency waves. Further, the standard deviation of an observation for Equation 7.3 is much larger than that of Equation 7.2.

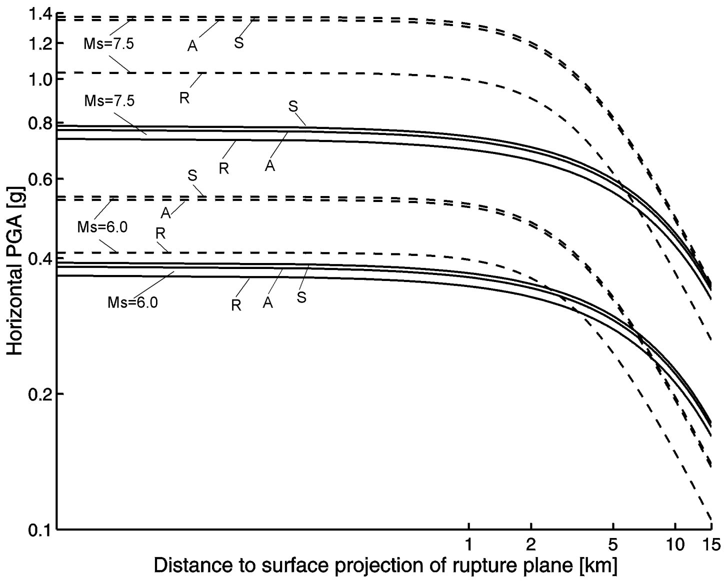

(a) Comparison with Ambraseys et al. (1996) (dashed lines).

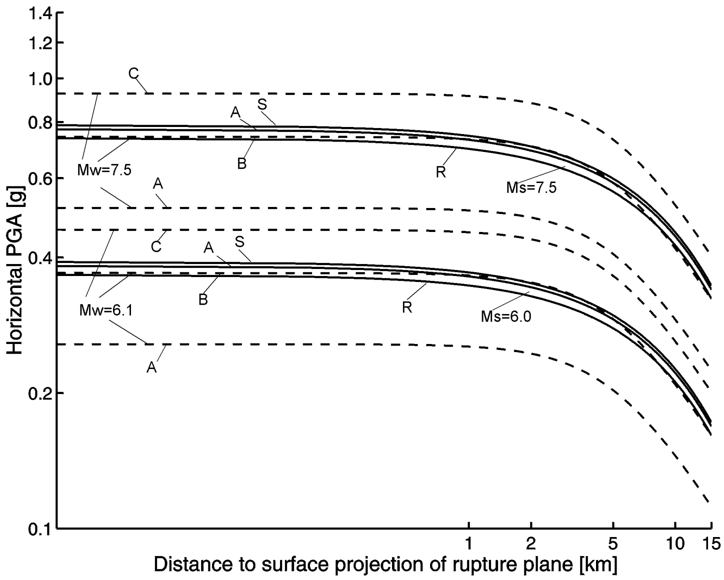

(b) Comparison with Boore et al. (1993) (larger component) (dashed lines).

Fig. 7.5: Comparison of predicted horizontal PGA (Equation 7.2 solid lines) and that predicted using the equations of Ambraseys *et al.* (1996), Boore *et al.* (1993), Campbell (1997) and Spudich *et al.* (1999) (dashed lines) for $M_s = 6$, 7.5 (corresponding to $M_w = 6.1$, 7.5 using equation (2) of Ekström & Dziewonski (1988)) for different site categories. The equation of Campbell (1997) is plotted for strike-slip faulting assuming a vertical rupture plane and depth to top of seismogenic zone of $3\,\mathrm{km}$. Note Equation 7.2 is converted to g when plotted.

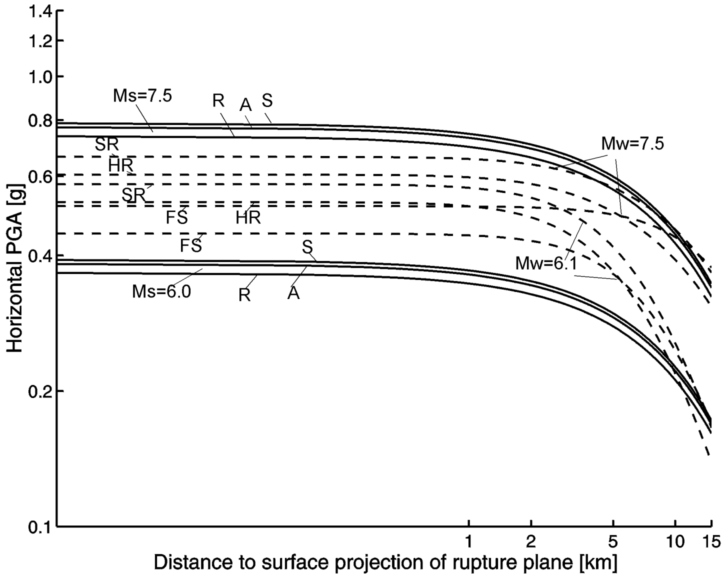

(c) Comparison with Campbell (1997) (dashed lines). FS is for alluvial or firm soil sites, SR is for soft rock sites and HR is for hard rock sites.

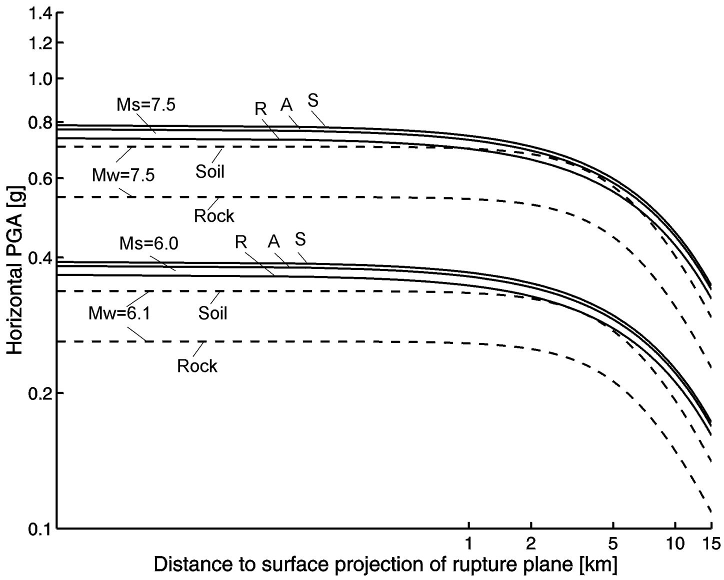

(d) Comparison with Spudich et al. (1999) (dashed lines).

Fig. 7.5: *Continued.*

Figure 7.6 shows comparisons between the peak ground acceleration predicted by Equation 7.3 and that predicted by two other widely-used equations. Figure 7.6 shows the following important features.

- Equation 7.3 predicts slightly larger vertical PGA than the equation of Ambraseys & Simpson (1996) and lower vertical PGA, especially for earthquakes with magnitudes about $M_s = 6$, than the equation of Campbell (1997).
- The dependence of vertical PGA on site conditions is similar to that predicted by the equations of Ambraseys & Simpson (1996) and Campbell (1997) showing that nonlinear soil behaviour at large strains is apparently not as common for vertical ground motions as is for horizontal motions.
- As for horizontal PGA the associated standard deviation ($\sigma = 0.270$) is similar to that from the equation of Ambraseys & Simpson (1996) ($\sigma = 0.25$) and Campbell (1997) ($\sigma = 0.231$–0.285 dependent on PGA).

7.5 Vertical to horizontal absolute PGA ratio ($y = \log q = \log a_v/a_h$)

The ratio, q, of the vertical, a_v, to the maximum horizontal, a_h, ground acceleration can be derived either by combining the two equations which individually predict peak vertical and horizontal accelerations (e.g. Abrahamson & Litehiser, 1989; Campbell & Bozorgnia, 2000), or by performing a regression directly on the ratios of maximum acceleration (e.g. Ambraseys & Bommer, 1991; Ambraseys & Simpson, 1996).

Note that whereas Ambraseys & Simpson (1996) regressed directly on the ratio, a_v/a_h, in this study the regression was done on the logarithm of the ratio. This is because the equation then has a physical meaning and also because the error is multiplicative not additive so negative ratios cannot be predicted. No site coefficients were derived because they do not have a physical meaning, unlike those for horizontal and vertical components separately, and also as demonstrated above local site conditions in the near field are not as important as at greater distances.

Table 7.1 gives the equations obtained for the subsets: all earthquakes, normal faulting earthquakes, thrust faulting earthquakes, strike-slip faulting earthquakes and European earthquakes. Only those coefficients which are significant at the 5% level are retained. If a coefficient was not significant then the regression was repeated with that coefficient constrained to zero.

Figure 7.7 shows comparison between the ratio of vertical PGA to horizontal PGA predicted by the equations given in Table 7.1 and that predicted by equations from two other widely used studies. Figure 7.7 shows the following important features.

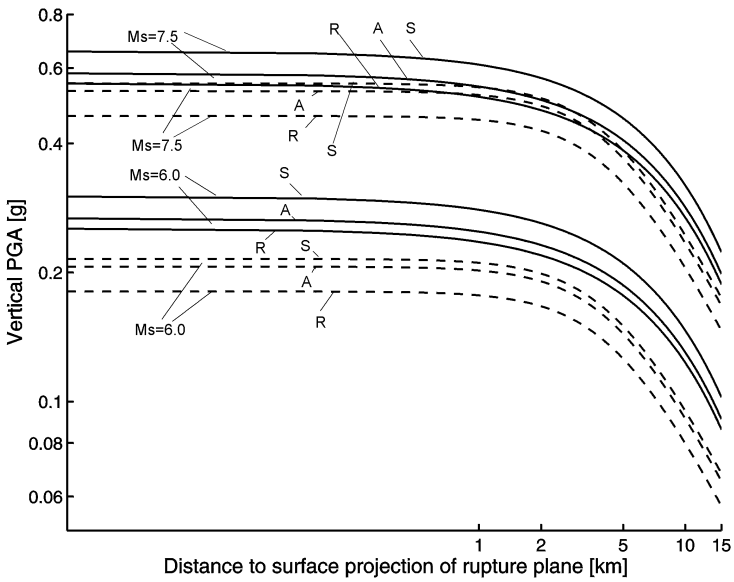

(a) Comparison with Ambraseys & Simpson (1996) (dashed lines).

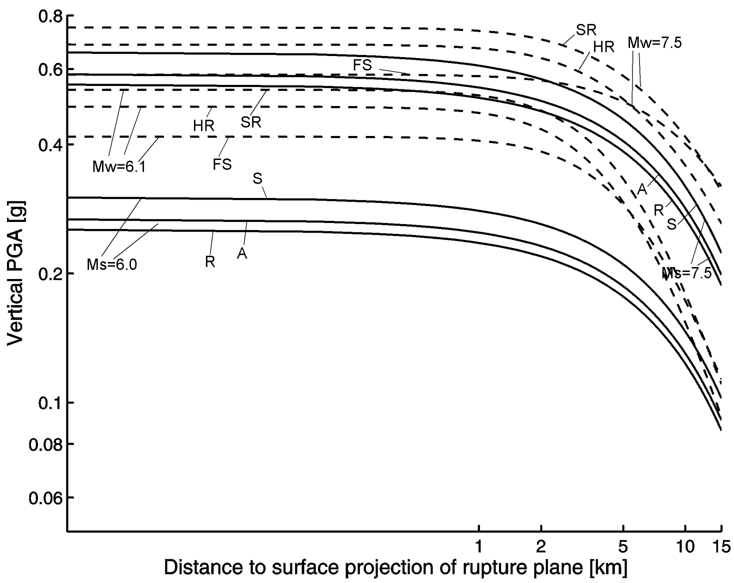

(b) Comparison with Campbell (1997) (dashed lines). FS is for alluvial or firm soil sites, SR is for soft rock sites and HR is for hard rock sites.

Fig. 7.6: Comparison of predicted vertical PGA (Equation 7.3 solid lines) and that predicted using the equations of Ambraseys & Simpson (1996) and Campbell (1997) (dashed lines) for $M_s = 6, 7.5$ (corresponding to $M_w = 6.1, 7.5$ using equation (2) of Ekström & Dziewonski (1988)) for different site categories. The equation of Campbell (1997) is plotted for strike-slip faulting assuming a vertical rupture plane and depth to top of seismogenic zone of $3\,\mathrm{km}$. Note Equation 7.3 is converted to g when plotted.

Tab. 7.1: Equations for the prediction of vertical to horizontal PGA ratio (q) in the near field of large earthquakes for the subsets: all earthquakes, normal faulting earthquakes, thrust faulting earthquakes, strike-slip faulting earthquakes and European earthquakes, and their standard deviations (σ).

Subset	Equation	σ
All	$\log q = \log a_v/a_h = -0.119 - 0.00799d$	$0{\cdot}21$
Normal	$\log q = \log a_v/a_h = -0.216$	$0{\cdot}13$
Thrust	$\log q = \log a_v/a_h = -0.103 - 0.0133d$	$0{\cdot}17$
Strike-slip	$\log q = \log a_v/a_h = -0.138$	$0{\cdot}25$
European	$\log q = \log a_v/a_h = -1.11 + 0.132M_s$	$0{\cdot}16$

- The equations given in Table 7.1 predict much smaller ratios of vertical to horizontal PGA than do the equations of Ambraseys & Simpson (1996) and Campbell & Bozorgnia (2000). The equations of Ambraseys & Simpson (1996) predict larger ratios because they use: a) a non-physical model which assumes error is additive rather than multiplicative; b) only records with vertical PGA larger than $0.1\,\mathrm{g}$ thereby biasing the ratios upwards; c) the largest vertical to horizontal PGA ratio (i.e. smallest horizontal component) rather than smallest vertical to horizontal PGA ratio (i.e. largest horizontal component); and d) a small set of records. One reason Campbell & Bozorgnia (2000) predict larger ratios is that they use the geometric mean of the two horizontal PGAs rather than the larger horizontal PGA.
- The equations given in Table 7.1, the equations of Ambraseys & Simpson (1996), and the equations of Campbell & Bozorgnia (2000), all predict slightly higher vertical to horizontal PGA ratios for strike-slip faulting than thrust faulting.

The equations given in Table 7.1 show that the commonly used ratios between vertical and horizontal PGA, q, of $\frac{1}{2}$ to $\frac{2}{3}$ are reasonable. However, since q represents the ratio of two functions whose maxima occur at different times, its value is a conservative estimate of the combined loading that could occur during an earthquake.

7.5.1 Theoretical ratio using seismic wave equations

An alternative way of computing the ratio of vertical to horizontal PGA is through theoretical equations governing each type of incident waves as they strike the free surface. The waves are considered to be plane waves because of the simplifications this brings, although close to the source they will be spherical. The waves responsible for the PGA though are usually of high frequency and so this assumption is valid.

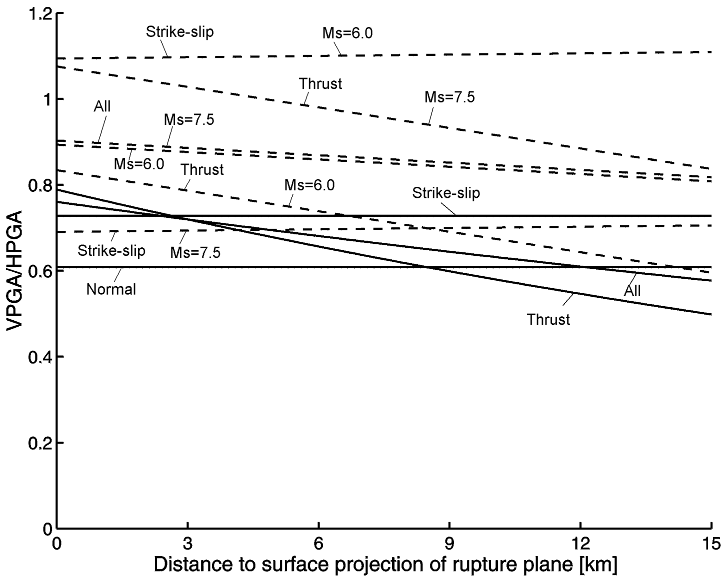

(a) Comparison with Ambraseys & Simpson (1996) (dashed lines).

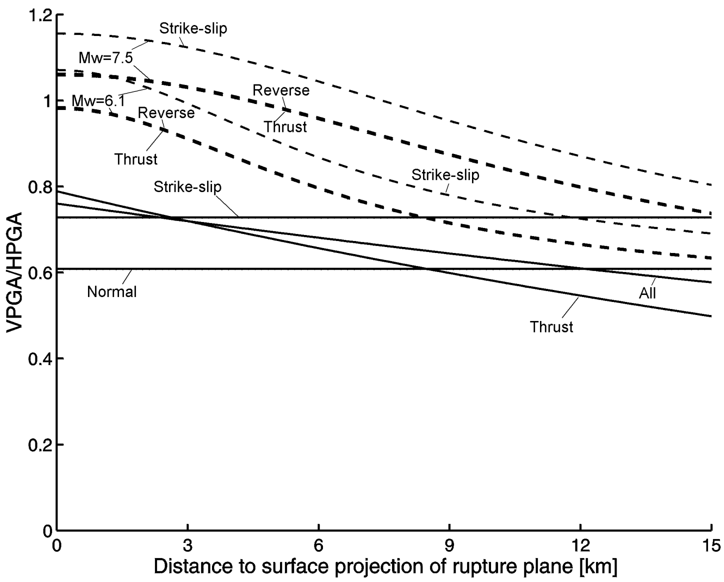

(b) Comparison with Campbell & Bozorgnia (2000) (dashed lines).

Fig. 7.7: Comparison of predicted ratios of vertical PGA to horizontal PGA (Table 7.1 solid lines) and those predicted using the equations of Ambraseys & Simpson (1996) and Campbell & Bozorgnia (2000) (dashed lines) for $M_s = 6$, 7.5 (corresponding to $M_w = 6.1$, 7.5 using equation (2) of Ekström & Dziewonski (1988)) for different source mechanisms. The equation of Campbell & Bozorgnia (2000), for the ratio of uncorrected vertical PGA to horizontal PGA, is plotted for Holocene soil assuming a vertical rupture plane and depth to top of seismogenic zone of $3\,\mathrm{km}$.

Three types of seismic waves are considered: P, SV (S waves polarised vertically) and SH (S waves polarised horizontally). Surface waves are not considered because close to the source their generation depends upon the geologic structure and distance between source and station (Gregor, 1995). Also surface waves are of long period and usually PGA is not associated with such waves.

First consider SH waves. When such a wave is reflected off a free surface no vertical component of motion is generated (Bullen, 1963). Therefore the expected vertical to horizontal ratio is zero.

The displacements corresponding to P or SV waves are given by Ewing *et al.* (1957):

$$
\begin{aligned}
u &= \frac{\partial \phi}{\partial x} - \frac{\partial \psi}{\partial z}; \\
\text{and } w &= \frac{\partial \phi}{\partial z} + \frac{\partial \psi}{\partial x}; \\
\text{where} & \\
\phi &= A_1 \exp\left[ik\left(ct + z\sqrt{\frac{c^2}{\alpha^2} - 1} - x\right)\right] + A_2 \exp\left[ik\left(ct - z\sqrt{\frac{c^2}{\alpha^2} - 1} - x\right)\right], \\
\text{and } \psi &= B_1 \exp\left[ik\left(ct + z\sqrt{\frac{c^2}{\beta^2} - 1} - x\right)\right] + B_2 \exp\left[ik\left(ct - z\sqrt{\frac{c^2}{\beta^2} - 1} - x\right)\right].
\end{aligned}
$$

x is measured horizontally, z is measured vertically downwards from the surface, u is horizontal displacement, w is vertical displacement, t is time, α is P-wave velocity and β is S-wave velocity.

Now $\tan(e) = \sqrt{c^2/\alpha^2 - 1}$, $\tan(f) = \sqrt{c^2/\beta^2 - 1}$ and $c = \alpha \sec(e) = \beta \sec(f)$. At the free surface the stresses must disappear and so the boundary conditions are:

$$
\begin{aligned}
[p_{zx}]_{z=0} = \mu \left(\frac{\partial w}{\partial x} + \frac{\partial u}{\partial z}\right) &= 0; \\
\text{and } [p_{zz}]_{z=0} = \lambda \left(\frac{\partial u}{\partial x} + \frac{\partial w}{\partial z}\right) + 2\mu \frac{\partial w}{\partial z} &= 0;
\end{aligned}
$$

where μ and λ are the Lamé constants.

When only P waves are incident, at angle e from the horizontal, $B_1 = 0$ so using the above equations gives:

$$\left|\frac{w}{u}\right| = |-\cot 2f| \tag{7.4}$$

where $\tan(f) = \alpha/\beta\sqrt{\tan^2(e) + 1 - \beta^2/\alpha^2}$

As the distance from the source becomes large, e becomes small, and the ratio of vertical to horizontal amplitudes tends to $\frac{\alpha^2/\beta^2 - 2}{2\sqrt{\alpha^2/\beta^2 - 1}}$. For a solid for which the Poisson relationship holds, i.e. $\alpha/\beta = \sqrt{3}$, this means the ratio tends to $1/2\sqrt{2} \approx 0.35$.

For SV waves, incident at angle f from the horizontal $A_1 = 0$ and so:

$$\left|\frac{w}{u}\right| = \left|\frac{-2\tan(e)}{1-\tan^2(f)}\right| \tag{7.5}$$

where $\tan e = \beta/\alpha\sqrt{\tan^2 f + 1 - \alpha^2/\beta^2}$.

Since $\alpha/\beta > 1$ it can be seen that for values of $f < \tan^{-1}(\sqrt{\alpha^2/\beta^2 - 1})$ angle e is complex. This corresponds to no reflected P waves being generated and a phase change in the reflected SV wave. In the far-field the ratio tends to $2\sqrt{1-\beta^2/\alpha^2}$. For a solid for which the Poisson relationship holds the ratio tends to $2\sqrt{2/3} \approx 1.63$.

Figure 7.8 shows comparison between the ratio of vertical PGA to horizontal PGA predicted by the equations given in Table 7.1 and that predicted by Equations 7.4 and 7.5.

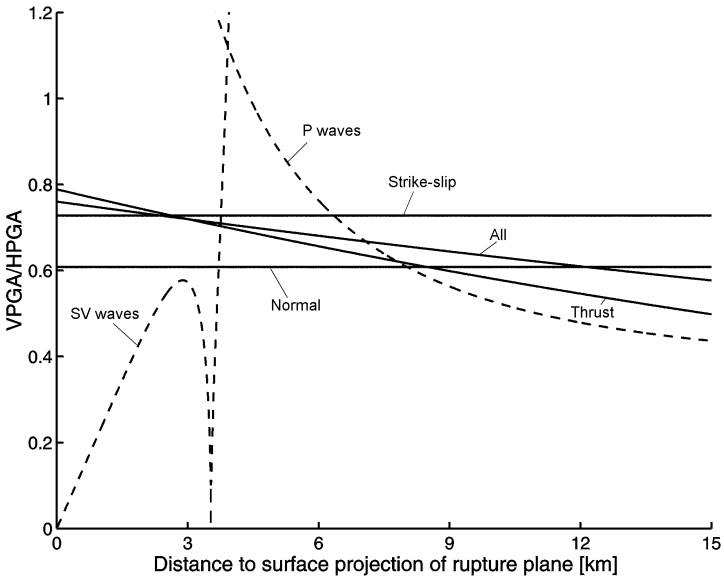

Fig. 7.8: Comparison of predicted ratios of vertical PGA to horizontal PGA using the equations given in Table 7.1 (solid lines) and those predicted using Equations 7.4 and 7.5 (dashed lines) assuming a focal depth of $5\,\mathrm{km}$ and the Poisson relationship, $\alpha/\beta = \sqrt{3}$.

Figure 7.8 shows that Equation 7.4 predicts similar vertical to horizontal PGA ratios to the equations given in Table 7.1 but the predictions made by Equation 7.5 do not match with those from the equations given in Table 7.1.

7.6 Vertical to horizontal simultaneous PGA ratio ($y = \log q_{\mathrm{sim}} = \log a_v(t_{\mathrm{max}})/a_h$)

The vertical to horizontal simultaneous PGA ratio is defined as, $q_{\mathrm{sim}} = a_v(t_{\mathrm{max}})/a_h$, where $a_v(t)$ is the vertical ground acceleration, a_h is horizontal PGA and t_{max} is the time at which this peak occurs. It gives the vertical acceleration to be resisted at the time of the design horizontal acceleration. For all subsets neither the magnitude and/or the distance dependence are significant, therefore the mean of the logarithm and the standard deviation were found (see Table 7.2).

Tab. 7.2: Equations for the prediction of vertical to horizontal simultaneous PGA ratio (q_{sim}) in the near field of large earthquakes for the subsets: all earthquakes, normal faulting earthquakes, thrust faulting earthquakes, strike-slip faulting earthquakes and European earthquakes, and their standard deviations (σ).

Subset	Equation	σ
All	$\log q_{\mathrm{sim}} = \log a_v(t_{\mathrm{max}})/a_h = -0.996$	0·56
Normal	$\log q_{\mathrm{sim}} = \log a_v(t_{\mathrm{max}})/a_h = -0.830$	0·44
Thrust	$\log q_{\mathrm{sim}} = \log a_v(t_{\mathrm{max}})/a_h = -1.04$	0·58
Strike-slip	$\log q_{\mathrm{sim}} = \log a_v(t_{\mathrm{max}})/a_h = -0.978$	0·56
European	$\log q_{\mathrm{sim}} = \log a_v(t_{\mathrm{max}})/a_h = -0.939$	0·58

No estimates of the vertical to horizontal simultaneous PGA ratio appear to have been published. A comparison of predicted simultaneous ratios (see Table 7.2) to predicted absolute ratios (see Table 7.1) shows that the simultaneous PGA ratios, q_{sim}, are much smaller than the absolute ratios, q, but the standard deviations are much higher (Figure 7.9). Hence large vertical accelerations can occur at the same time as the horizontal PGA but often the vertical ground acceleration at the time of the horizontal PGA is small and so using the absolute ratio of vertical to horizontal PGA, q, for design may be overconservative.

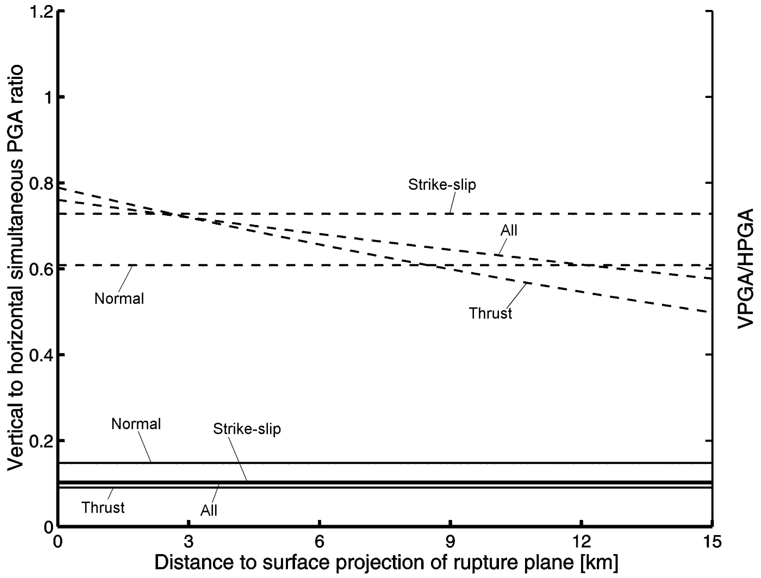

Fig. 7.9: Comparison of predicted vertical to horizontal simultaneous PGA ratio using Table 7.2 (solid lines) and predicted ratios of vertical PGA to horizontal PGA using Table 7.1 (dashed lines).

7.7 Horizontal energy density ($y = \log E_h$)

The energy density, E, of a strong-motion record is defined as $E = \int_0^T v(t)^2 \, \mathrm{d}t$, where T is the length of the record and $v(t)$ is the ground velocity at time t (Sarma, 1971). Since energy density, E, uses the velocity time-history, which is more sensitive to the correction procedure used, energy densities are less well defined than PGAs or spectral accelerations. This equation for the prediction of horizontal energy density (E_h), in units of $\mathrm{cm}^2\mathrm{s}^{-1}$, in the near-field obtained here is:

$$\log E_h = -3.11 + 0.937 M_s - 0.0567 d + 0.180 S_A + 0.417 S_S \quad \text{with} \quad \sigma = 0.419 \tag{7.6}$$

The soil term for stiff soil (A) is not significant at the 5% level, whereas for soft soil (S) the term is significant at that level.

No attenuation relations for energy density appear to have been published. The predicted horizontal energy density using Equation 7.6 shows strong dependence of energy density on magnitude (Figure 7.10) which is expected because magnitude is a measure of the energy released during an earthquake. Horizontal energy density is seen to be strongly dependent on local site conditions.

7.8 Vertical energy density ($y = \log E_v$)

The equation for the prediction of vertical energy density (E_v) in the near-field obtained here is:

$$\log E_v = -3.88 + 0.969 M_s - 0.0527 d + 0.000 S_A + 0.111 S_S \quad \text{with} \quad \sigma = 0.422 \tag{7.7}$$

The soil terms are not significant at the 5% level.

Like the equation for horizontal energy density, Equation 7.6, Equation 7.7 shows the expected strong dependence on magnitude (Figure 7.10). However, unlike horizontal energy density the effect of local soil conditions on vertical energy density is negligible.

7.9 Vertical to horizontal energy density ratio $y = \log q_E = \log E_v/E_h$

Equations for the vertical to horizontal energy density ratio, $q_E = E_v/E_h$, have been derived. For all subsets neither the magnitude and/or the distance dependence are significant, so the mean of the logarithm and the standard deviation are given (see Table 7.3).

It is clear that vertical ground motion contains much less energy than horizontal ground motion even though the peak ground accelerations are similar (Figure 7.11). This is because usually vertical ground motions are of higher frequency than horizontal ground motions.

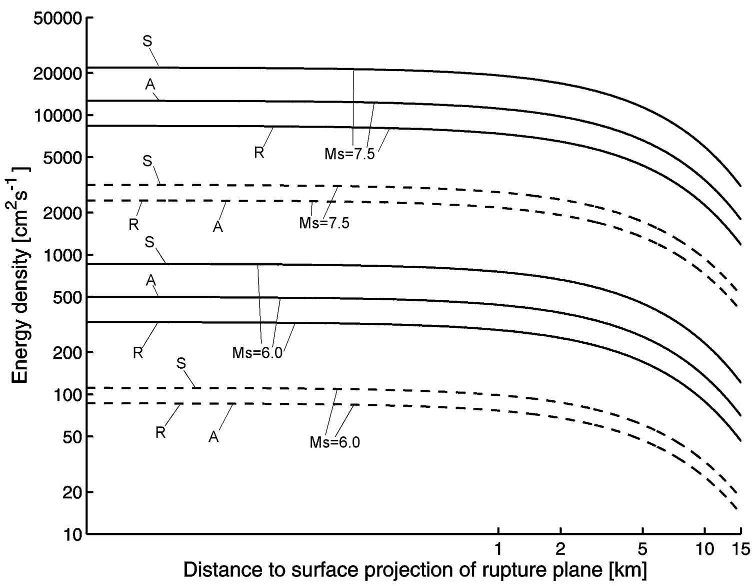

Fig. 7.10: Comparison of predicted horizontal energy density by Equation 7.6 (solid lines) and the predicted vertical energy density by Equation 7.7 (dashed lines) for $M_s = 6$, 7.5.

7.10 Horizontal spectral acceleration ($y = \log \mathrm{SA_h}$)

Table E.1 lists the coefficients of the horizontal spectral acceleration attenuation relations for 5% damping and 46 periods between 0.1 and $2\,\mathrm{s}$.

Comparing the predicted horizontal spectral accelerations using the coefficients in Table E.1 with those predicted by four other widely used sets of equations shows a number of important features (Figures 7.12 to 7.15).

- Predicted horizontal spectral accelerations using the coefficients in Table E.1 are much lower than those predicted by the equations of Ambraseys *et al.* (1996) for large magnitudes ($M_s > 6.5$) especially for very short distances, for example at horizontal natural period $T = 0.5\,\mathrm{s}$ the equations of Ambraseys *et al.* (1996) predict a spectral acceleration on soft soil of about $2.3\,\mathrm{g}[23\,\mathrm{ms}^{-2}]$ whereas using the coefficients in Table E.1 gives an estimate of about $1.4\,\mathrm{g}[14\,\mathrm{ms}^{-2}]$. The reason for such large differences for large magnitudes is that the set of records used by Ambraseys *et al.* (1996) is dominated by records from small magnitude earthquakes which control the equation. The magnitude dependence for the short period range ($T < 1\,\mathrm{s}$) of the near-field equations derived in this study is much less than that in the equations of Ambraseys *et al.* (1996) so the predicted accelerations for large magnitude earthquakes are less. The equations of Boore *et al.* (1993), Campbell (1997) and Spudich *et al.* (1999) however, predict horizontal response spectra similar to those given by the coefficients in Table E.1 because their sets have a large proportion of near-field large-magnitude data and they include terms to account for magnitude saturation which means the predicted spectral accelerations

Tab. 7.3: Equations for the prediction of vertical to horizontal energy density ratio (q_E) in the near field of large earthquakes for the subsets: all earthquakes, normal faulting earthquakes, thrust faulting earthquakes, strike-slip faulting earthquakes and European earthquakes, and their standard deviations (σ).

Subset	Equation	σ
All	$\log q_E = \log E_v/E_h = -0.756$	0·34
Normal	$\log q_E = \log E_v/E_h = -0.540$	0·25
Thrust	$\log q_E = \log E_v/E_h = -0.762$	0·34
Strike-slip	$\log q_E = \log E_v/E_h = -0.795$	0·35
European	$\log q_E = \log E_v/E_h = -0.632$	0·32

for large magnitudes do not become unrealistically large.

- As for horizontal PGA the dependence of spectral acceleration on site conditions is much less in the near-field equations derived in this study than that found in the equations of Ambraseys *et al.* (1996), Boore *et al.* (1993) and Spudich *et al.* (1999) especially in the very short period range ($T < 0.2$ s). This is probably due to nonlinear soil behaviour due to large strains which would reduce the short period ground motion more than the longer period ground motion, such behaviour is modelled in the equations of Campbell (1997).

- As for the equation for horizontal PGA the near-field equations derived in this study are associated with similar standard deviations as the equations of Ambraseys *et al.* (1996), Boore *et al.* (1993), Campbell (1997) and Spudich *et al.* (1999).

7.11 Vertical spectral acceleration ($y = \log \mathrm{SA_v}$)

Table E.2 lists the coefficients of the vertical spectral acceleration attenuation relation for 5% damping and 46 periods between 0.1 and 2 s.

Vertical spectral acceleration for periods less than about 1 s show faster decay with distance than horizontal spectral accelerations. Unlike the PGA this faster decay cannot be explained by vertical ground motions having the usual higher frequency than the horizonal motions (and high frequencies attenuate faster than low frequencies) because spectral acceleration is a narrow-band measure and so both horizontal and vertical spectral acceleration decay should be similar. As for PGA the standard deviations associated with the near-field equations for vertical spectral acceleration derived here are much higher than those for horizontal spectral acceleration, especially for short periods. For example for $T = 0.1$ s the standard deviation for horizontal spectral acceleration is 0.240 whereas for vertical spectral acceleration it is 0.308.

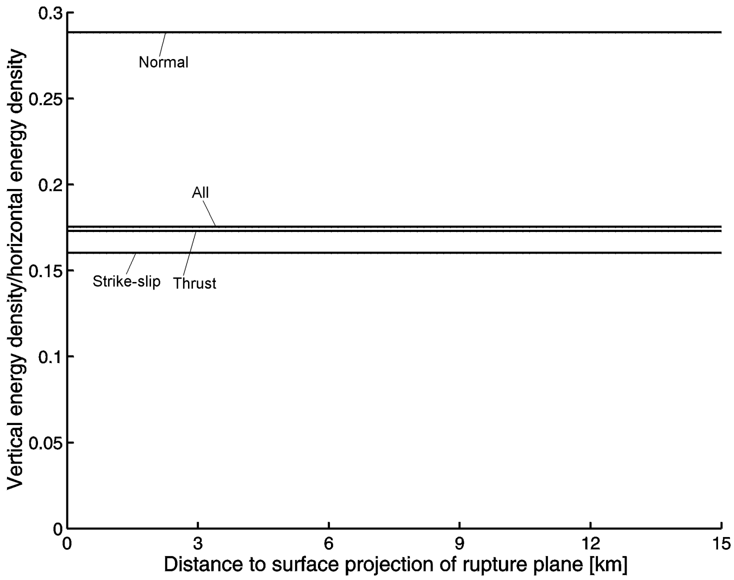

Fig. 7.11: Predicted ratio of vertical energy density to horizontal energy density using the equations given in Table 7.3.

Soil coefficients for both soft and stiff soils show amplitude reduction, with respect to rock, at long periods ($T > 1\,\mathrm{s}$). To check this is not simply due to the distribution of soil classes within the dataspace all the Northridge records were removed, because many of the soft soil records are from the Northridge earthquake, and the analysis repeated. All the coefficients, including the soil coefficients, were almost unchanged by the removal of these 34 records, hence the reduction in amplitude seems genuine.

Comparing the predicted vertical spectral accelerations using the coefficients in Table E.2 with those predicted by two other widely used sets of equations shows a number of important features (Figures 7.16 and 7.17).

- Predicted vertical spectral accelerations using the coefficients in Table E.2 are similar to those predicted by the equations of Ambraseys & Simpson (1996) and Campbell (1997) except in the short period where the equations of Campbell (1997) predict higher values, for example for $M_s = 7.5$ and $d = 0\,\mathrm{km}$ the predicted spectral acceleration on rock using the coefficients in Table E.2 is about $0.8\,\mathrm{g}[8\,\mathrm{ms}^{-2}]$ whereas on soft rock using the equations of Campbell (1997) it is about $1.4\,\mathrm{g}[14\,\mathrm{ms}^{-2}]$. This difference could be due to the different definition of distance used by Campbell (1997) compared to that used here.

- The dependence of site conditions on vertical spectral accelerations in the near-field equations is similar to that found by Ambraseys & Simpson (1996) and is much less than that found for horizontal spectral accelerations. The dependence on site conditions is less than that found by Campbell (1997) which could be due to the different site categories used or because the vertical spectral acceleration equation of Campbell (1997) was derived using equations for

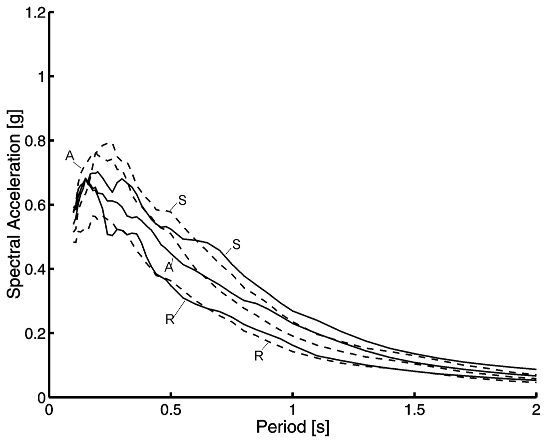

(a) $M_s = 6$, $d = 5\text{km}$

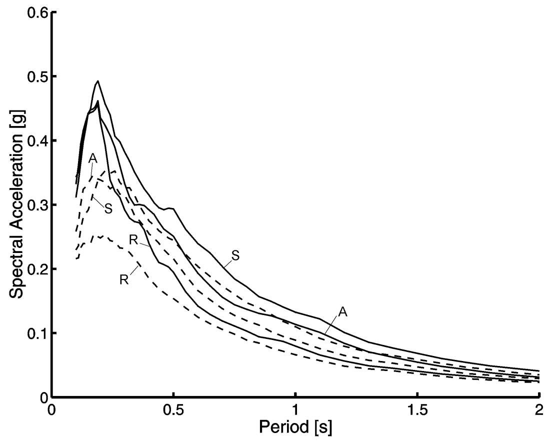

(b) $M_s = 6$, $d = 15\text{km}$

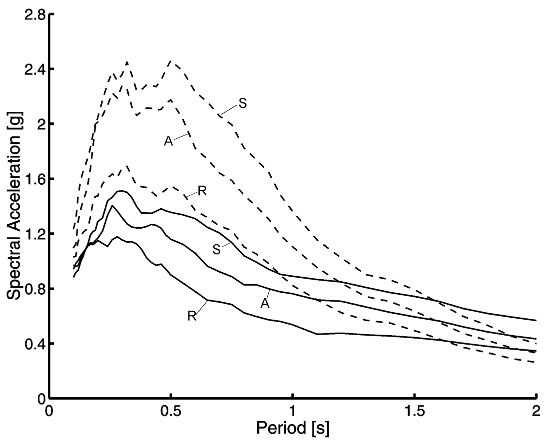

(c) $M_s = 7.5$, $d = 5\text{km}$

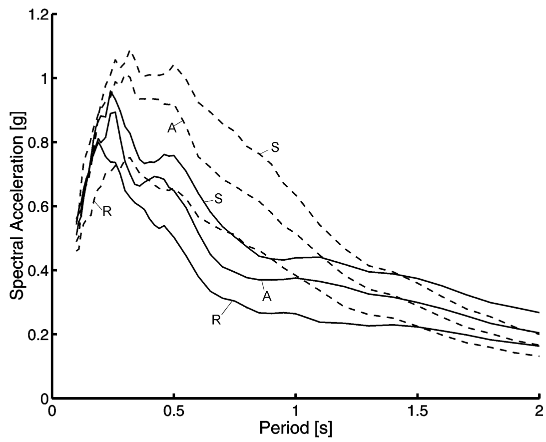

(d) $M_s = 7.5$, $d = 15\text{km}$

Fig. 7.12: Comparison of predicted horizontal response spectra using coefficients given in Table E.1 (solid lines) and those predicted using the equations of Ambraseys *et al.* (1996) (dashed lines) for $M_s = 6$, 7.5 and $d = 5$, $15\,\text{km}$ for different site categories. Note the spectra predicted using coefficients given in Table E.1 are converted to g when plotted.

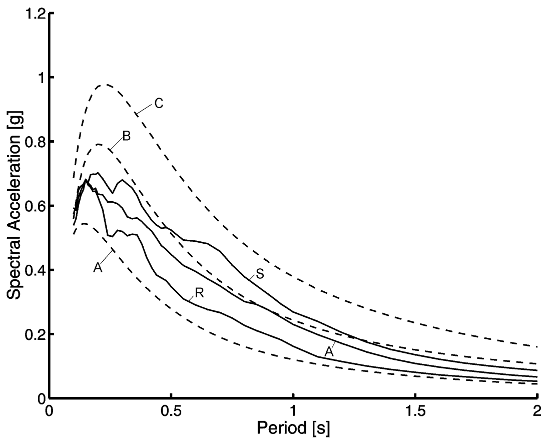

(a) $M_s = 6$ ($M_w = 6.1$), $d = 5$km

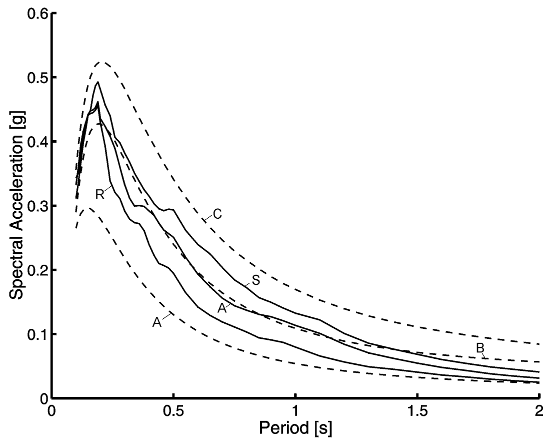

(b) $M_s = 6$ ($M_w = 6.1$), $d = 15$km

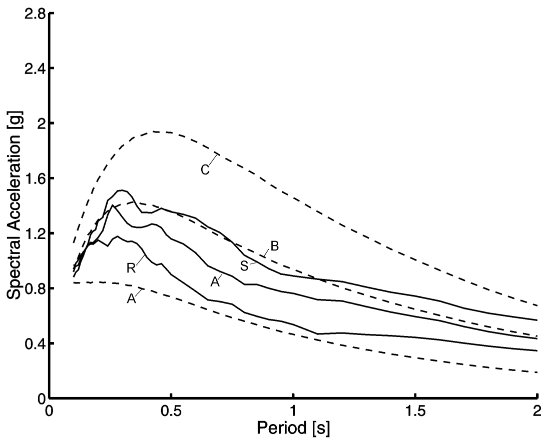

(c) $M_s = 7.5$ ($M_w = 7.5$), $d = 5$km

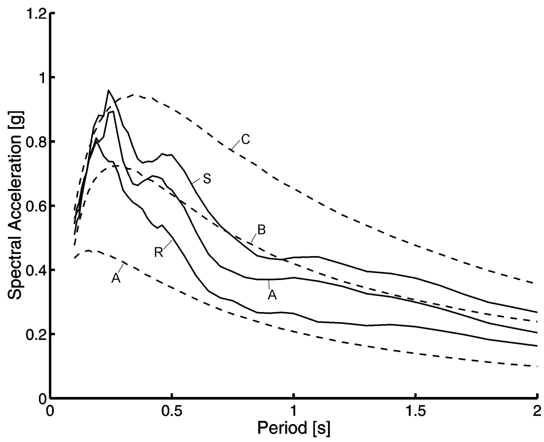

(d) $M_s = 7.5$ ($M_w = 7.5$), $d = 15$km

Fig. 7.13: Comparison of predicted horizontal response spectra using coefficients given in Table E.1 (solid lines) and those predicted using the equations of Boore *et al.* (1993) (dashed lines) for $M_s = 6,\ 7.5$ (corresponding to $M_w = 6.1,\ 7.5$ using equation (2) of Ekström & Dziewonski (1988)) and $d = 5,\ 15\,\mathrm{km}$ for different site categories. Note the spectra predicted using coefficients given in Table E.1 are converted to g when plotted. Boore *et al.* (1993) equations give pseudo-acceleration response spectra.

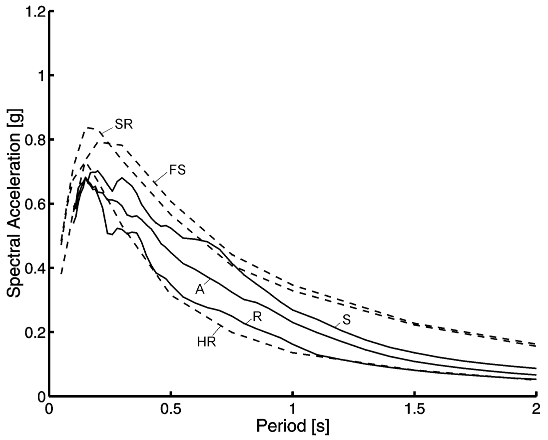

(a) $M_s = 6$ ($M_w = 6.1$), $d = 5$km

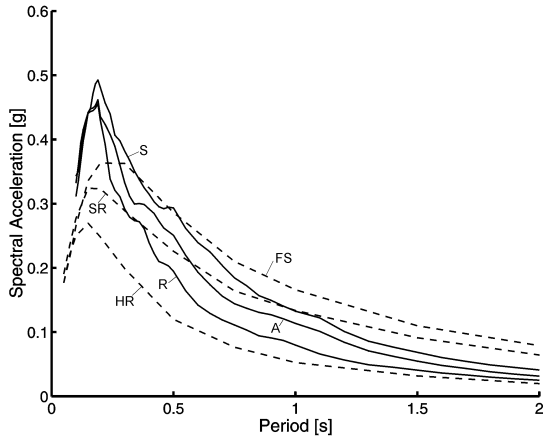

(b) $M_s = 6$ ($M_w = 6.1$), $d = 15$km

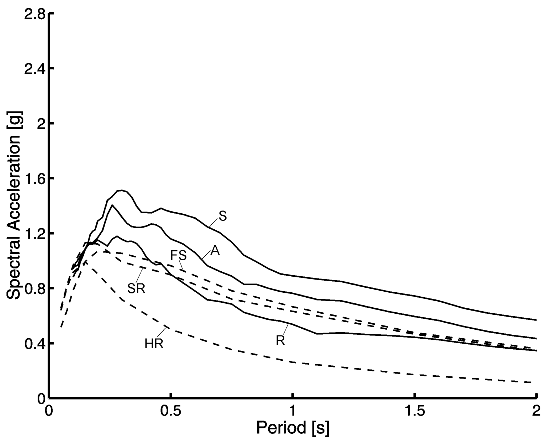

(c) $M_s = 7.5$ ($M_w = 7.5$), $d = 5$km

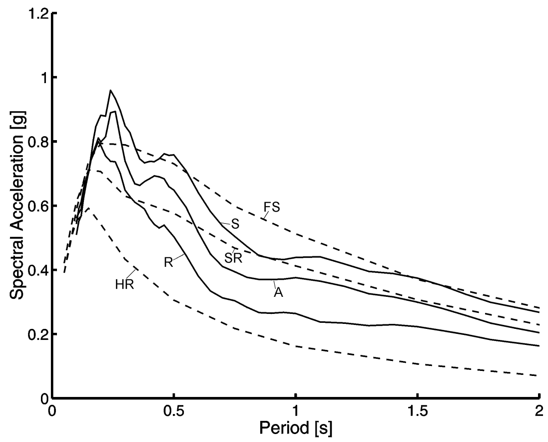

(d) $M_s = 7.5$ ($M_w = 7.5$), $d = 15$km

Fig. 7.14: Comparison of predicted horizontal response spectra using coefficients given in Table E.1 (solid lines) and those predicted using the equations of Campbell (1997) (dashed lines) for $M_s = 6, 7.5$ (corresponding to $M_w = 6.1, 7.5$ using equation (2) of Ekström & Dziewonski (1988)) and $d = 5, 15\,\mathrm{km}$ for different site categories. The equation of Campbell (1997) is plotted for strike-slip faulting assuming a vertical rupture plane and depth to top of seismogenic zone of $3\,\mathrm{km}$. FS is firm soil, SR is soft rock and HR is hard rock. For firm soil and soft rock a depth to basement rock of $2\,\mathrm{km}$ is assumed. Note the spectra predicted using coefficients given in Table E.1 are converted to g when plotted. Campbell (1997) equations give pseudo-acceleration response spectra.

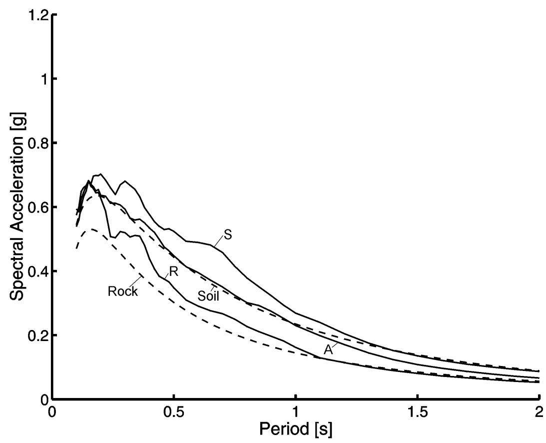

(a) $M_s = 6$ ($M_w = 6.1$), $d = 5$km

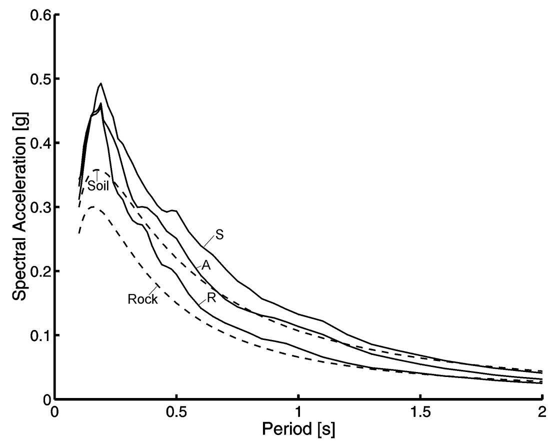

(b) $M_s = 6$ ($M_w = 6.1$), $d = 15$km

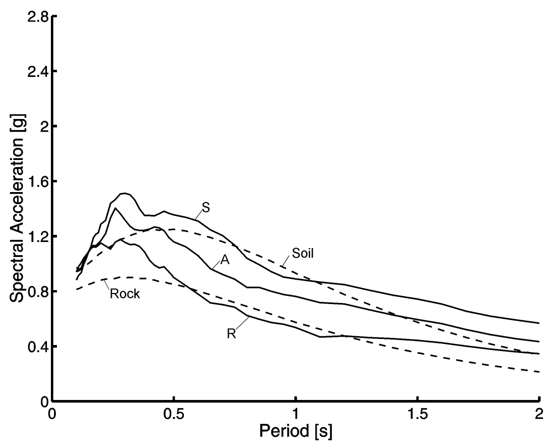

(c) $M_s = 7.5$ ($M_w = 7.5$), $d = 5$km

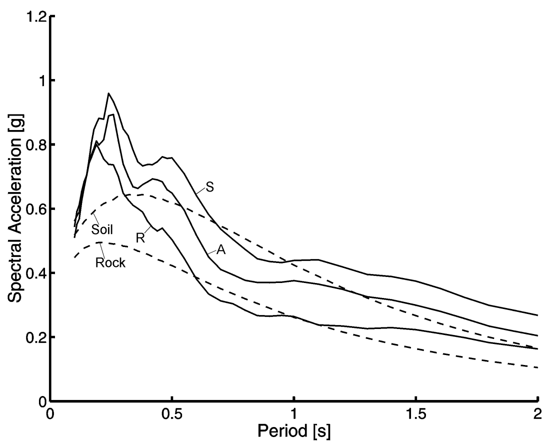

(d) $M_s = 7.5$ ($M_w = 7.5$), $d = 15$km

Fig. 7.15: Comparison of predicted horizontal response spectra using coefficients given in Table E.1 (solid lines) and those predicted using the equations of Spudich *et al.* (1999) (dashed lines) for $M_s = 6$, 7.5 (corresponding to $M_w = 6.1$, 7.5 using equation (2) of Ekström & Dziewonski (1988)) and $d = 5$, $15\,\mathrm{km}$ for different site categories. Note the spectra predicted using coefficients given in Table E.1 are converted to g when plotted. Spudich *et al.* (1999) equations give pseudo-acceleration response spectra.

horizontal spectral acceleration as a base.

Comparing predicted horizontal response spectra (Figures 7.12 to 7.15) with predicted vertical response spectra (Figures 7.16 and 7.17) shows the expected higher frequency of vertical ground motions.

7.12 Horizontal spectral acceleration (bending model) ($y = \log \mathrm{SA}_{\mathrm{h,b}}$)

Attenuation relations for the prediction of spectral acceleration using the bending model described in Section 4.4 were also derived.

7.12.1 Infinite vertical stiffness

Table E.3 contains the coefficients of the horizontal spectral acceleration (buckling model) attenuation relation for 5% damping, $\gamma = 0.3$ and 46 periods between 0.1 and $2\,\mathrm{s}$ and infinite vertical stiffness.

The inclusion of the vertical ground motion has little effect. Figure 7.18 shows the ratio between the spectral acceleration including the effect of the vertical accelerations and not including the vertical accelerations (note that this ratio is between models not including soil terms). For a site on the surface projection of the rupture plane (i.e. $d = 0\,\mathrm{km}$) of an earthquake with $M_s = 7.8$ the increase due to the vertical accelerations is about 8% and for smaller magnitudes and larger distances it is less. Therefore the effect of vertical excitation on this type of SDOF system can be neglected when it stays stable (see Chapter 6).

7.12.2 Finite vertical stiffness

As noted in Chapter 6 instability occurs for some of the near-field records for $\gamma > 0.1$. This is much lower than load ratios in most structures. Therefore no attenuation relations are derived for the bending model for finite vertical stiffness.

7.13 Horizontal spectral acceleration (hinging model) ($y = \log \mathrm{SA}_{\mathrm{h,h}}$)

Attenuation relations for the prediction of spectral acceleration using the hinging model described in Section 4.5 were also derived.

7.13.1 Infinite vertical stiffness

Table E.4 lists the coefficients of the horizontal spectral acceleration (hinging model) attenuation relation for 5% damping, $l = 2\,\mathrm{m}$ and 46 periods between 0.1 and $2\,\mathrm{s}$ and infinite vertical stiffness.

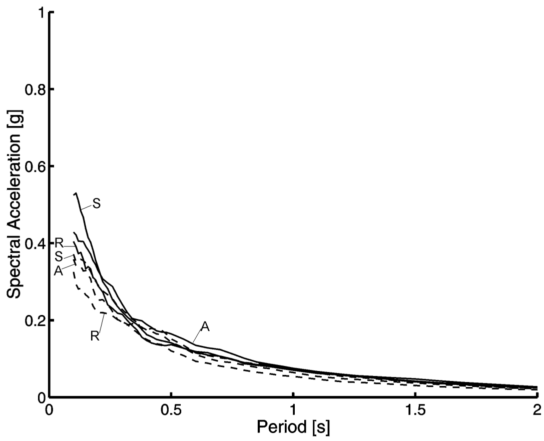

(a) $M_s = 6$, $d = 5\text{km}$

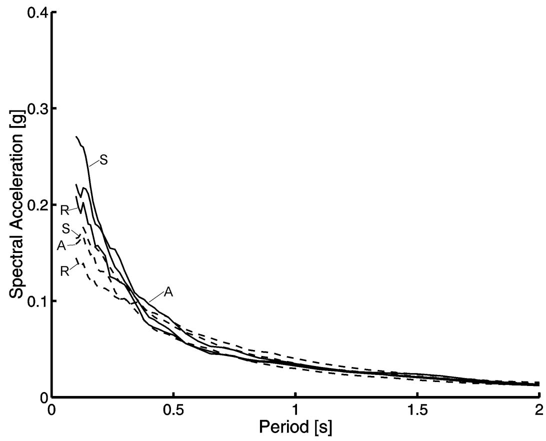

(b) $M_s = 6$, $d = 15\text{km}$

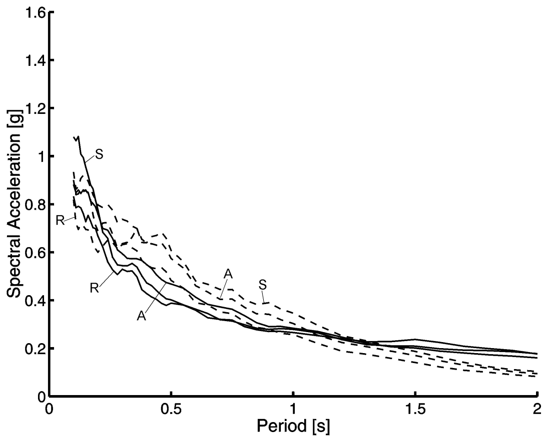

(c) $M_s = 7.5$, $d = 5\text{km}$

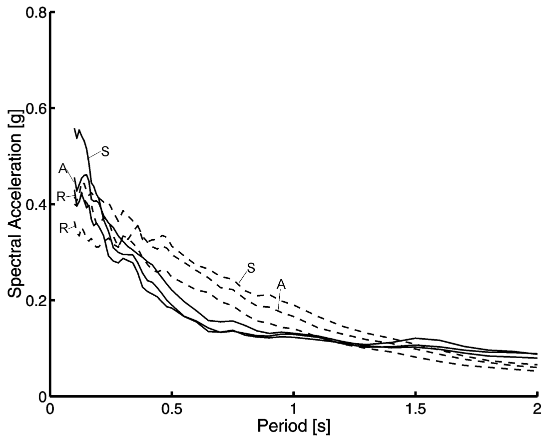

(d) $M_s = 7.5$, $d = 15\text{km}$

Fig. 7.16: Comparison of predicted vertical response spectra using coefficients given in Table E.1 (solid lines) and those predicted using the equations of Ambraseys & Simpson (1996) (dashed lines) for $M_s = 6$, 7.5 and $d = 5$, $15\,\text{km}$ for different site categories. Note the spectra predicted using coefficients given in Table E.1 are converted to g when plotted.

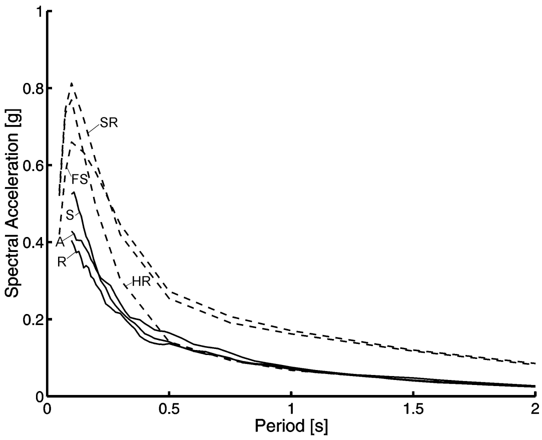

(a) $M_s = 6$ ($M_w = 6.1$), $d = 5$km

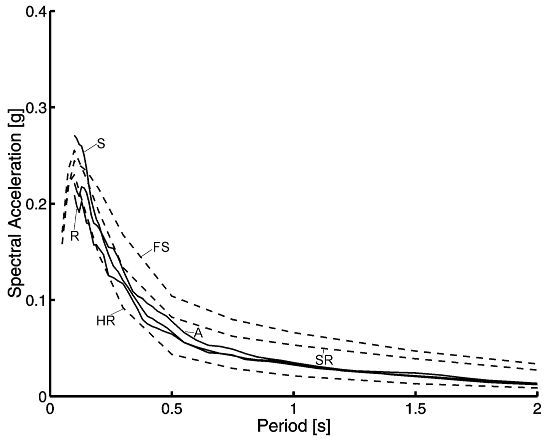

(b) $M_s = 6$ ($M_w = 6.1$), $d = 15$km

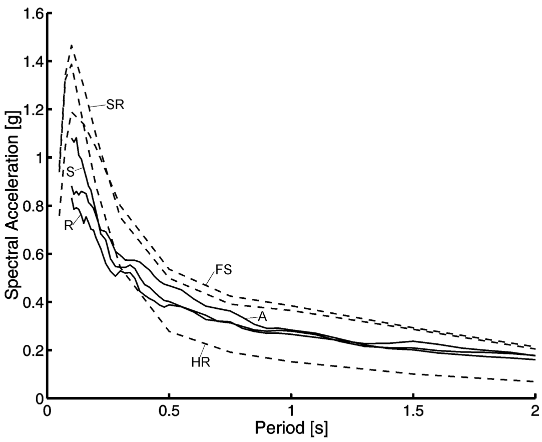

(c) $M_s = 7.5$ ($M_w = 7.5$), $d = 5$km

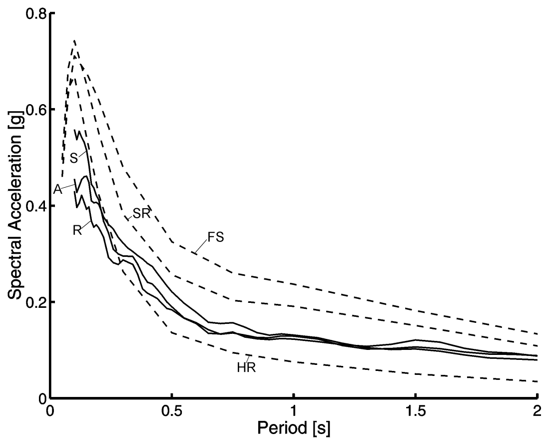

(d) $M_s = 7.5$ ($M_w = 7.5$), $d = 15$km

Fig. 7.17: Comparison of predicted vertical response spectra using coefficients given in Table E.1 (solid lines) and those predicted using the equations of Campbell (1997) (dashed lines) for $M_s = 6, 7.5$ (corresponding to $M_w = 6.1, 7.5$ using equation (2) of Ekström & Dziewonski (1988)) and $d = 5, 15\,\text{km}$ for different site categories. The equation of Campbell (1997) is plotted for strike-slip faulting assuming a vertical rupture plane and depth to top of seismogenic zone of $3\,\text{km}$. FS is firm soil, SR is soft rock and HR is hard rock. For firm soil and soft rock a depth to basement rock of $2\,\text{km}$ is assumed. Note the spectra predicted using coefficients given in Table E.1 are converted to g when plotted. Campbell (1997) equations give pseudo-acceleration response spectra.

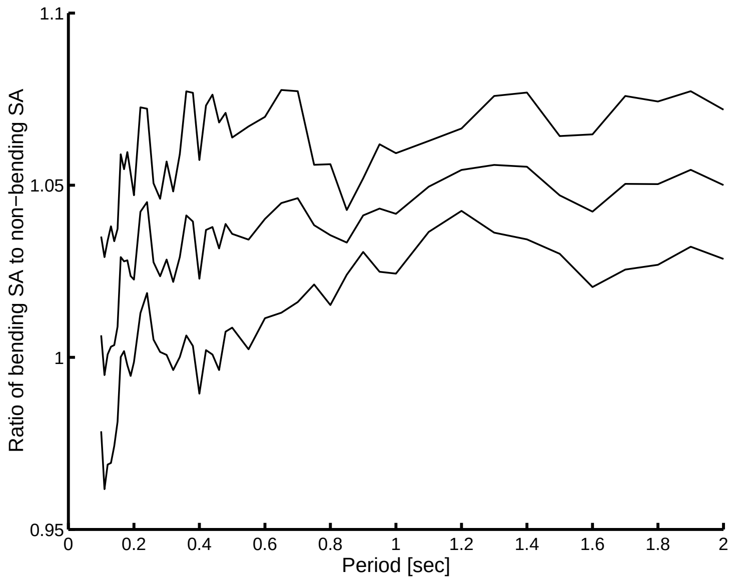

Fig. 7.18: Ratio between the predicted spectral acceleration when the vertical ground motion is included (bending model for $\gamma = 0.3$) and the predicted spectral acceleration when it is ignored for $M_s = 5.8$, 6.8 and 7.8 at distance $0\,\mathrm{km}$.

The inclusion of the vertical ground motion has little effect. Figure 7.19 shows the ratio between the spectral acceleration with and without the effect of the vertical accelerations (note that this ratio is between models not including soil terms). For a site $0\,\mathrm{km}$ from an earthquake with $M_s = 7.8$ the increase due to the vertical accelerations is about 9% and for smaller magnitudes and larger distances it is less. Therefore the effect of vertical excitation on this type of SDOF system can be neglected when it stays stable (see Chapter 6).

7.13.2 Finite vertical stiffness

Attenuation relations have been derived for the hinging model with finite vertical stiffness, for 5% horizontal and vertical damping, $l = 2\,\mathrm{m}$ and 46 horizontal and vertical periods between 0.1 and $2\,\mathrm{s}$. There were $46 \times 46 = 2116$ sets of coefficients derived and so because of lack of space they are not presented here. Figure 7.20 shows a contour plot of the ratio between the predicted spectral acceleration when vertical ground motion is included (finite vertical stiffness hinging model for $l = 2\,\mathrm{m}$) and the predicted spectral acceleration when it is ignored for 7.8 at distance $0\,\mathrm{km}$. The maximum increase due to the vertical excitation is about 25% which occurs for a horizontal natural period of about $2\,\mathrm{s}$ and a vertical natural period of about $1\,\mathrm{s}$ (Figure 7.20) and so is probably due to parametric resonance which occurs for vertical periods which are half the horizontal period (see Section 6.6). The effect of vertical excitation on this type of SDOF system can be neglected even when the vertical stiffness is finite.

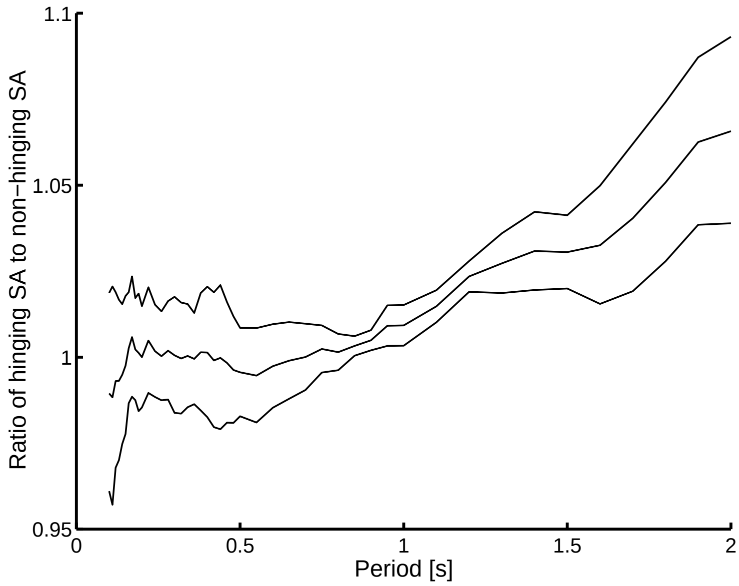

Fig. 7.19: Ratio between the predicted spectral acceleration when the vertical ground motion is included (hinging model for $l = 2\,\mathrm{m}$) and the predicted spectral acceleration when it is ignored for $M_s = 5.8$, 6.8 and 7.8 at distance $0\,\mathrm{km}$.

7.14 Horizontal maximum absolute input energy ($y = \log \mathrm{I_h}$)

The maximum absolute input energy, I, is defined as $I = \max_t \int_0^t [u_{tt}(t) + a(t)] v(t)\,\mathrm{d}t$, where u_{tt} is the response acceleration of the SDOF system, $a(t)$ is the ground acceleration and $v(t)$ is the ground velocity (Chapman, 1999). In the following two sections maximum absolute input energy will simply be referred to as energy.

Table E.5 lists the coefficients of the horizontal energy attenuation relations for 5% damping and 46 periods between 0.1 and $2\,\mathrm{s}$.

The coefficients of Table E.5 show that there is a strong dependence of horizontal maximum absolute input energy on magnitude as is expected because magnitude is roughly related to energy. The coefficients also display a faster decay with distance than spectral acceleration and also a stronger dependence on site conditions. The standard deviations of the equations for horizontal energy are also much higher than those for horizontal spectral acceleration, for example for $T = 0.1\,\mathrm{s}$ the associated standard deviation for horizontal spectral acceleration is 0.240 whereas for horizontal maximum absolute input energy it is 0.397.

Comparing the predicted energy using the coefficients in Table E.5 with those predicted by the only other set of attenuation relations for horizontal energy available in the literature (Figure 7.21) shows the following important features.

- Predicted horizontal energies using the coefficients in Table E.5 are similar to those predicted by the equations of Chapman (1999) because many of the records used by Chapman (1999)

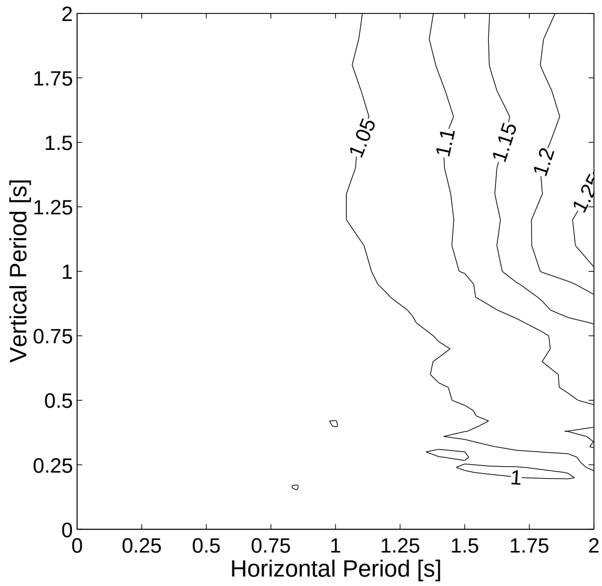

Fig. 7.20: Contour plot of ratio between the predicted spectral acceleration when the vertical ground motion is included (finite vertical stiffness hinging model for $l = 2\,\mathrm{m}$) and the predicted spectral acceleration when it is ignored for 7.8 at distance $0\,\mathrm{km}$.

are from large earthquakes and also because the equations allow magnitude saturation. The predicted energies are thus not unrealistically high.

- As for horizontal PGA and spectral acceleration there is evidence for nonlinear soil behaviour in the near-field because the dependence of horizontal energy on local site conditions is less than the dependence found by Chapman (1999) who uses intermediate-field and far-field records as well as near-field records.

- The standard deviations of the near-field equations derived in this study and those of the equations of Chapman (1999) are similar.

7.15 Vertical maximum absolute input energy ($y = \log \mathrm{I_v}$)

Table E.6 lists the coefficients of the vertical maximum absolute input energy attenuation relations for 5% damping and 46 periods between 0.1 and $2\,\mathrm{s}$.

As for horizontal energy there is a strong dependence of vertical energy on magnitude, a faster decay with distance than for vertical spectral acceleration, greater dependence on local site conditions and also much larger associated standard deviations than the equations for vertical spectral acceleration.

As for vertical spectral acceleration and horizontal spectral acceleration there is much lower dependence of vertical energy on local site conditions than for horizontal energy.

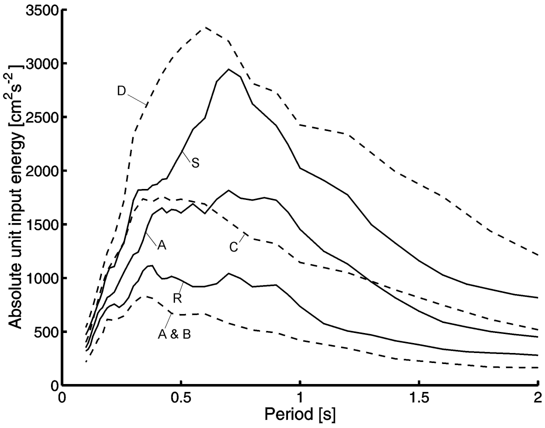

(a) $M_s = 6$ ($M_w = 6.1$), $d = 5$km

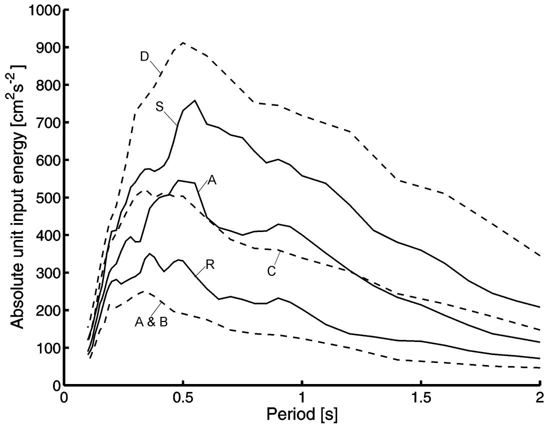

(b) $M_s = 6$ ($M_w = 6.1$), $d = 15$km

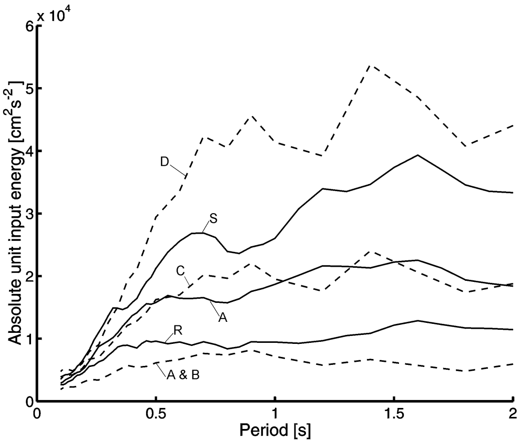

(c) $M_s = 7.5$ ($M_w = 7.5$), $d = 5$km

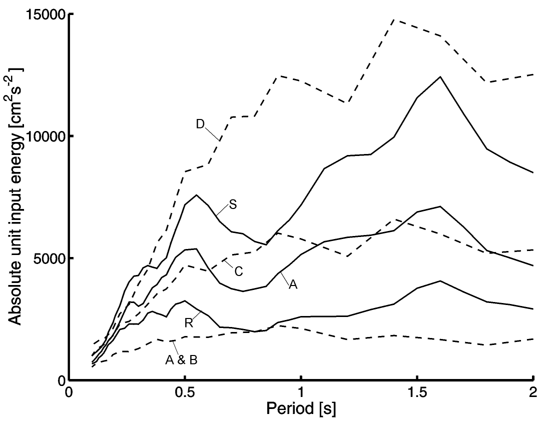

(d) $M_s = 7.5$ ($M_w = 7.5$), $d = 15$km

Fig. 7.21: Comparison of predicted absolute unit input energy spectra using coefficients given in Table E.5 (solid lines) and those predicted using the equations of Chapman (1999) (dashed lines) for $M_s = 6$, 7.5 (corresponding to $M_w = 6.1$, 7.5 using equation (2) of Ekström & Dziewonski (1988)) and $d = 5$, $15\,\mathrm{km}$ for different site categories. Chapman (1999) equations are converted from absolute input energy equivalent velocity, V_{ea}.

No attenuation relations for the prediction of vertical elastic maximum absolute input energy such have been derived here (Figure 7.22) appear to have been published.

7.16 *Vertical to horizontal spectral ratio (Absolute) ($y = \log q_s = \log \mathrm{SA_v}/\mathrm{SA_h}$)*

There are two methods for finding the predicted vertical to horizontal spectral ratios a) divide the predicted vertical spectral accelerations (given by equations like Table E.2) by the predicted horizontal accelerations (given by equations like Table E.1) or b) regress directly on the spectral ratio to find new attenuation equations for the ratio. The first technique was used by Niazi & Bozorgnia (1992a), Bozorgnia *et al.* (2000) and Campbell & Bozorgnia (2000). Its main advantage is simplicity. The second technique was used by Feng *et al.* (1988) and Ambraseys & Simpson (1996).

Equations to predict the vertical to horizontal spectral ratio, q_s, were derived assuming magnitude and distance dependence. For some periods, the magnitude coefficient is significant, for some the distance coefficient is significant but for most neither are significant. Therefore it was decided to simply provide the mean of the logarithms and the standard error. Note that even though the magnitude and distance coefficients of the horizontal and vertical spectral acceleration equations (Tables E.1 and E.2) are significant at the 5% level the coefficients for prediction of the ratio are not. Therefore workers who find distance and magnitude dependence of the spectral ratios (e.g. Niazi & Bozorgnia, 1992a; Bozorgnia *et al.*, 2000; Campbell & Bozorgnia, 2000) from regressing on the horizontal and vertical spectral ordinates separately may find that this dependence is not significant if the regression is done directly on the ratio.

Table E.7 contains the coefficients and means for all earthquakes, normal, thrust and strike-slip and European earthquakes separately. No site coefficients were derived for the same reasons as given in Section 7.5.

Comparing the predicted vertical to horizontal spectral ratios using the coefficients in Table E.7 with those predicted by two other widely used sets of equations (Figures 7.23 and 7.24) show the following important features.

- Predicted vertical to horizontal spectral ratios using the coefficients in Table E.7 are much lower than those predicted using the equations of Ambraseys & Simpson (1996) for the same reasons that the predicted vertical to horizontal PGA ratios were lower (see Section 7.5). However, predicted vertical to horizontal spectral ratios using the coefficients in Table E.7 and those predicted using the equations of Campbell & Bozorgnia (2000) are almost identical except for short periods ($T < 0.4\,\mathrm{s}$) where the equations of Campbell & Bozorgnia (2000) predict higher ratios; this is similar to the vertical to horizontal PGA ratios (see Section 7.5).
- Predicted vertical to horizontal spectral ratios using the coefficients in Table E.7 for all source mechanisms, except for normal faulting, are almost identical, as was found by Campbell &

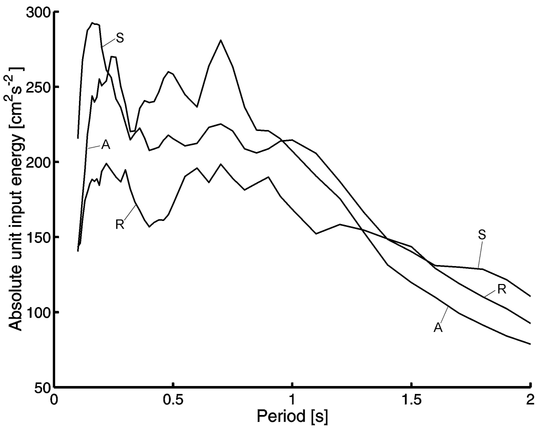

(a) $M_s = 6$, $d = 5$km

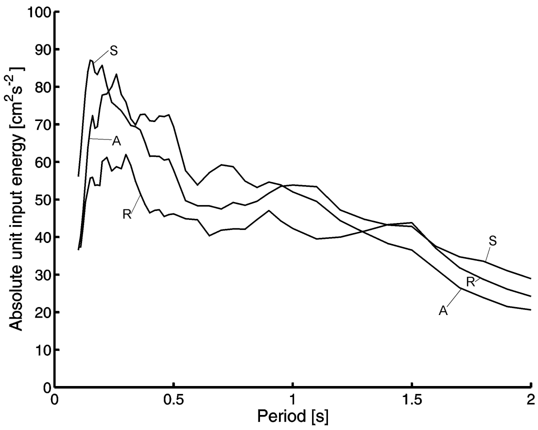

(b) $M_s = 6$, $d = 15$km

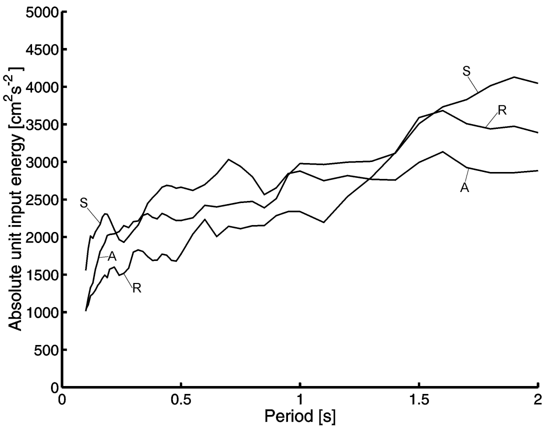

(c) $M_s = 7.5$, $d = 5$km

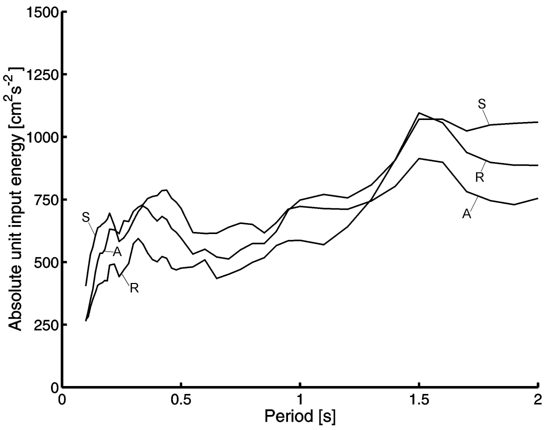

(d) $M_s = 7.5$, $d = 15$km

Fig. 7.22: Predicted vertical maximum absolute unit input energy spectra using coefficients given in Table E.6 for $M_s = 6$, 7.5 and $d = 5$, $15\,\mathrm{km}$ for different site categories.

Bozorgnia (2000). The apparent differences for different source mechanisms found by Ambraseys & Simpson (1996) are probably due to: a) the non-physical model used by Ambraseys & Simpson (1996) which assumes error is additive rather than multiplicative and b) the small set of records. The differences in the vertical to horizontal spectral ratios found for normal faulting earthquakes may not be genuine because only a small number of records (15) from normal faulting earthquakes were used.

The absolute spectral ratios for the bending model (see Section 4.4) and the hinging model (see Section 4.5) are almost identical to those for the ordinary SDOF system, due to the similarity in the horizontal response spectra from the three models (see Sections 7.12 and 7.13) and so are not given here.

7.17 Vertical to horizontal spectral ratio (Simultaneous) ($y = \log q_i = \log u_{tt,v}(t_{\max})/\mathrm{SA_h}$)

A major draw-back of the absolute acceleration ratio q or q_s for practical purposes is that in an earthquake the maximum ground or response accelerations in the vertical and horizontal direction occur at different times.

Equations to predict the attenuation of vertical to horizontal simultaneous spectral ratio were found. This ratio is defined as: $q_i = u_{tt,v}(t_{\max})/\mathrm{SA_h}$; where $u_{tt,v}(t)$ is the vertical response acceleration and $t_{\max}$ is the time as which the maximum horizontal response acceleration occurs. This ratio gives the size of the vertical accelerations which need to be withstood at the time of the design maximum horizontal acceleration.

The natural period of a structure in the vertical direction is usually different than that in the horizontal direction therefore these ratios, Q_i, were found for all combinations of vertical and horizontal natural period, i.e. $46 \times 46 = 2116$. Due to lack of space the actual coefficients are only be given for equal vertical and horizontal period (see Table E.8).

As for the absolute ratio, for some periods the magnitude coefficient is significant, for some the distance coefficient is significant but for most neither are significant. Therefore it was decided to simply provide the mean of the logarithms and the standard error.

Table E.8 lists the means and standard deviations for all earthquakes, normal, thrust and strike-slip and European earthquakes separately. No site coefficients were derived for the reasons given in Section 7.5.

The predicted q_i for the all earthquakes and for each of the separate mechanism (normal, thrust and strike-slip) shows that the ratios are almost the same for each type of faulting except for normal faulting (Figure 7.25). The results for normal mechanism earthquakes are based on only 15 records; it is difficult to base conclusions on such a small number of records so more records are required

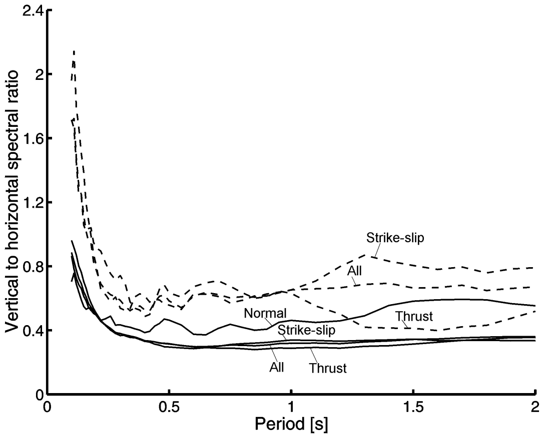

(a) $M_s = 6$, $d = 5$km

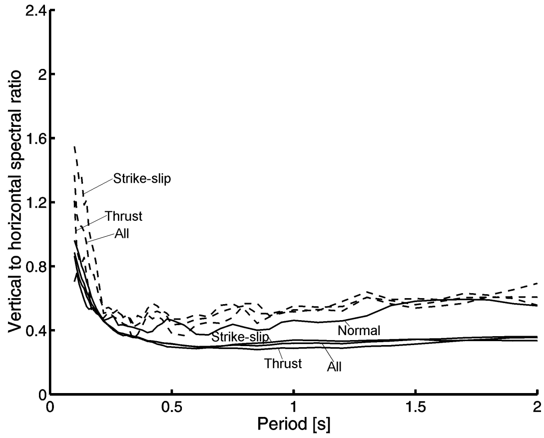

(b) $M_s = 6$, $d = 15$km

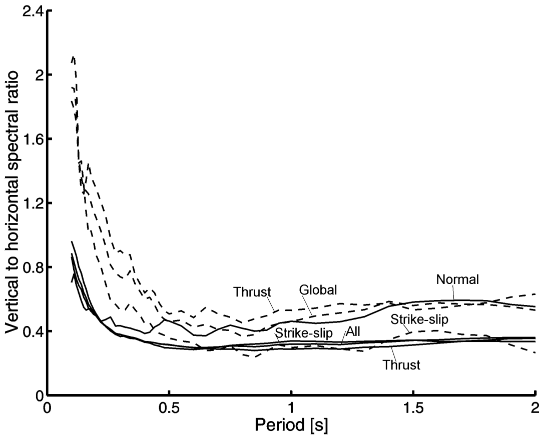

(c) $M_s = 7.5$, $d = 5$km

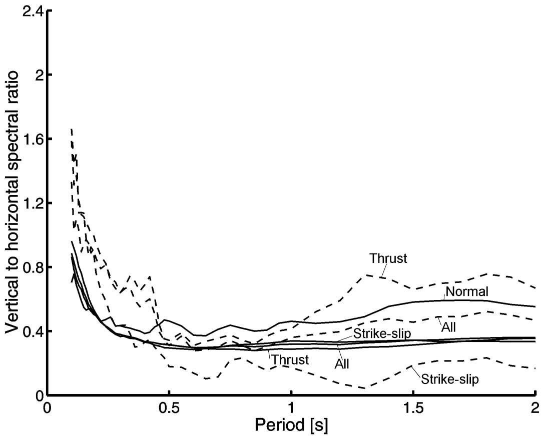

(d) $M_s = 7.5$, $d = 15$km

Fig. 7.23: Comparison of predicted vertical to horizontal spectral ratios using coefficients given in Table E.7 (solid lines) and those predicted using the equations of Ambraseys & Simpson (1996) (dashed lines) for $M_s = 6, 7.5$ and $d = 5, 15$ km for different source mechanisms.

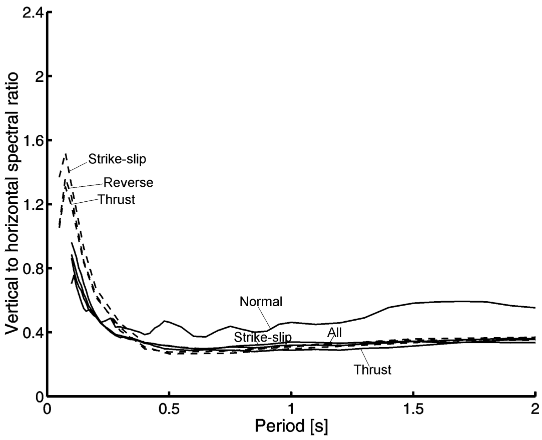

(a) $M_s = 6$ ($M_w = 6.1$), $d = 5$km

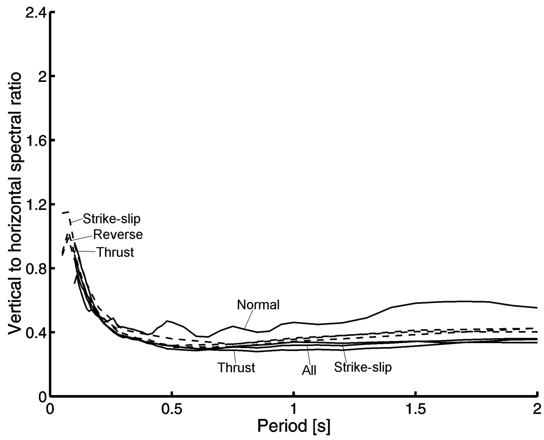

(b) $M_s = 6$ ($M_w = 6.1$), $d = 15$km

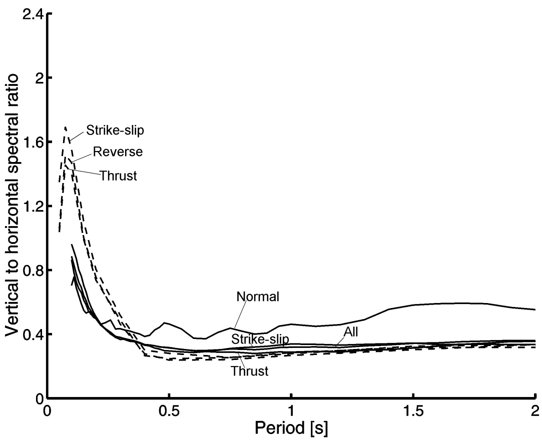

(c) $M_s = 7.5$ ($M_w = 7.5$), $d = 5$km

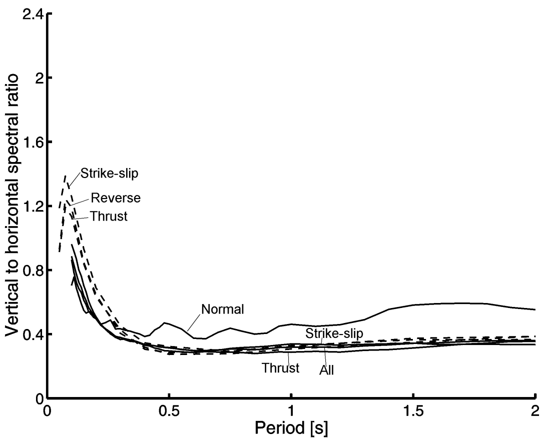

(d) $M_s = 7.5$ ($M_w = 7.5$), $d = 15$km

Fig. 7.24: Comparison of predicted vertical to horizontal spectral ratios using coefficients given in Table E.7 (solid lines) and those predicted using the equations of Campbell & Bozorgnia (2000) (dashed lines) for $M_s = 6, 7.5$ and $d = 5, 15\,\mathrm{km}$ (corresponding to $M_w = 6.1, 7.5$ using equation (2) of Ekström & Dziewonski (1988)) for different source mechanisms. The equation of Campbell & Bozorgnia (2000), for the ratio of uncorrected vertical PGA to horizontal PGA, is plotted for Holocene soil assuming a vertical rupture plane and depth to top of seismogenic zone of $3\,\mathrm{km}$.

from normal earthquakes to check this finding. As Figure 7.25 shows the simultaneous ratios, q_i, are much less than the absolute ratios, q_s, especially for short periods. Also it can be seen that the ratios are roughly independent of period.

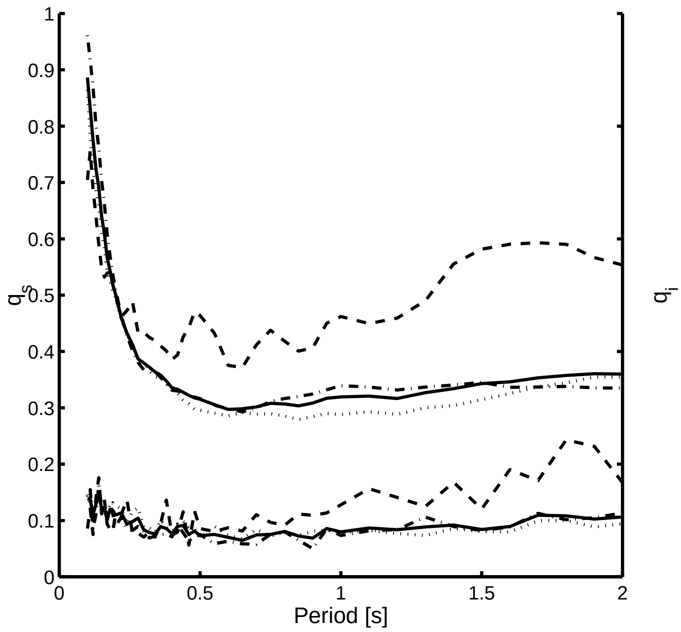

Fig. 7.25: Predicted vertical to horizontal spectral ratio, $q_s = \mathrm{SA_v}/\mathrm{SA_h}$ (top set of curves) and simultaneous ratio, $q_i = R_v(t_{\max})/\mathrm{SA_h}$ for different types of faulting. All earthquakes (solid line), normal (dashed line), thrust (dotted line) and strike-slip (dash-dotted line).

Figure 7.26 shows the predicted vertical to horizontal simultaneous spectral ratio, Q_i, for all combinations of T_h and T_v. Figure 7.27 shows the standard deviations[2] of the regression.

For short vertical and long horizontal periods the simultaneous ratio, Q_i, can reach about 0.5 but for most periods the ratio is less than about 0.2 (Figure 7.26). The standard error is much higher than for the absolute ratio and it is roughly independent of period and equal to about 0.6 (Figure 7.27). Why there are much higher standard errors at certain, seemingly random, combinations of periods is not known.

7.18 Vertical to horizontal maximum absolute input energy ratio ($y = \log q_e = \log \mathrm{I_v}/\mathrm{I_h}$)

Table E.9 lists the means and standard deviations for all earthquakes, normal, thrust and strike-slip and European earthquakes separately. No site coefficients were derived for the reasons given in Section 7.5.

Figure 7.28 shows the predicted ratio, q_e, for all earthquakes and considering the three source mechanisms separately. As for the response spectral equations only predicted ratios for normal mechanism earthquakes are different than those for other types of faulting, although this may be

[2] This the the standard deviations of the logarithms.

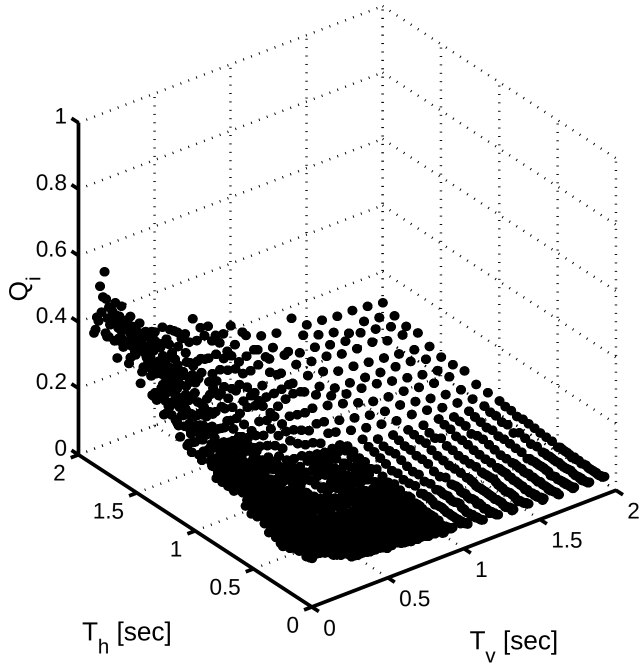

Fig. 7.26: Predicted vertical to horizontal simultaneous spectral ratio, $Q_i = R_v(t_{\max})/\mathrm{SA_h}$.

due to a small number of records from normal earthquakes. Figure 7.28 shows that even for short periods vertical ground motions contain much less energy than horizontal ground motions.

7.19 Validation of models

Once a regression model is derived it is important to validate it, i.e. to check that the predictions it gives are not biased and are adequate over the entire dataspace (Snee, 1977; Weisburg, 1985).

7.19.1 Examination of residuals

It is important in regression analysis to examine graphs of the residuals against the independent variables and also against the predictions made using the equation. Such graphs should show no obvious trends due to non-constant variance, errors in calculation or because higher order terms in the independent variables were not included (Draper & Smith, 1981, Chapter 3). Residuals are defined as:

$$\epsilon_i = y_i^{\mathrm{observed}} - y_i^{\mathrm{predicted}} \tag{7.8}$$

where y is the dependent variable.

Figures 7.29 and 7.30 show the residuals against the independent variables, magnitude and distance, and the dependent variable, logarithm of acceleration, for horizontal and vertical PGA and spectral acceleration at $0.2\,\mathrm{s}$, $0.5\,\mathrm{s}$ and $1\,\mathrm{s}$. The residuals for records with associated site categories are taken with respect to the final equation and those with unknown site categories are taken with

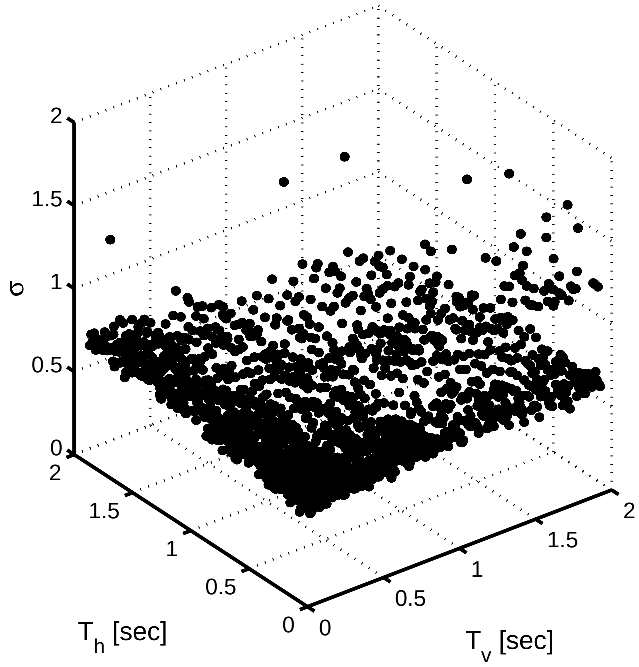

Fig. 7.27: Standard error of prediction, σ, of vertical to horizontal simultaneous spectral ratio, $Q_i = R_v(t_{\max})/\mathrm{SA}_{\mathrm{h}}$.

respect to the equation derived in the first step where site conditions are not considered. They do not show any obvious trends although there is evidence that ground motions for large magnitude earthquakes could be overestimated by the equations derived here. This however is based on only four records (two records from the Kocaeli earthquake and two records from the Chi-Chi earthquake) and so may not be a general feature of large earthquakes.

The residuals for the other equations derived in this chapter were examined and similar features were observed. Because of lack of space they are not presented here.

Overall the equations derived in this chapter seem to be unbiased for the entire dataspace.

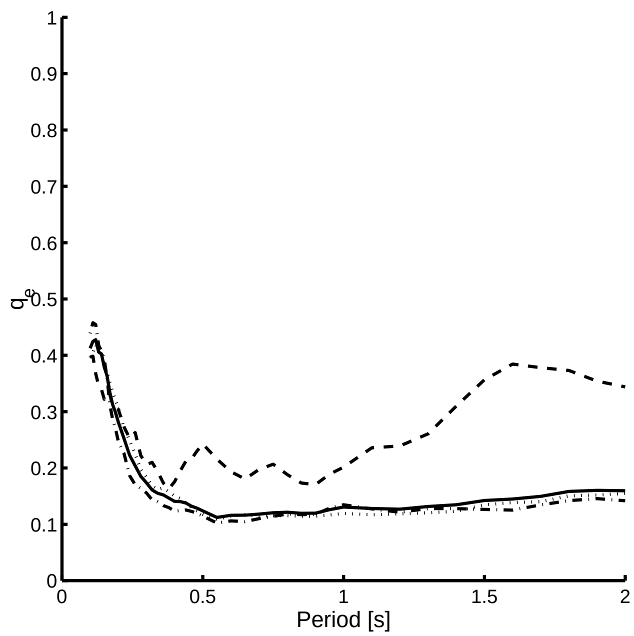

Fig. 7.28: Predicted vertical to horizontal maximum absolute input energy ratio, $q_e = I_v/I_h$ for different types of faulting. All earthquakes (solid line), normal (dashed line), thrust (dotted line) and strike-slip (dash-dotted line).

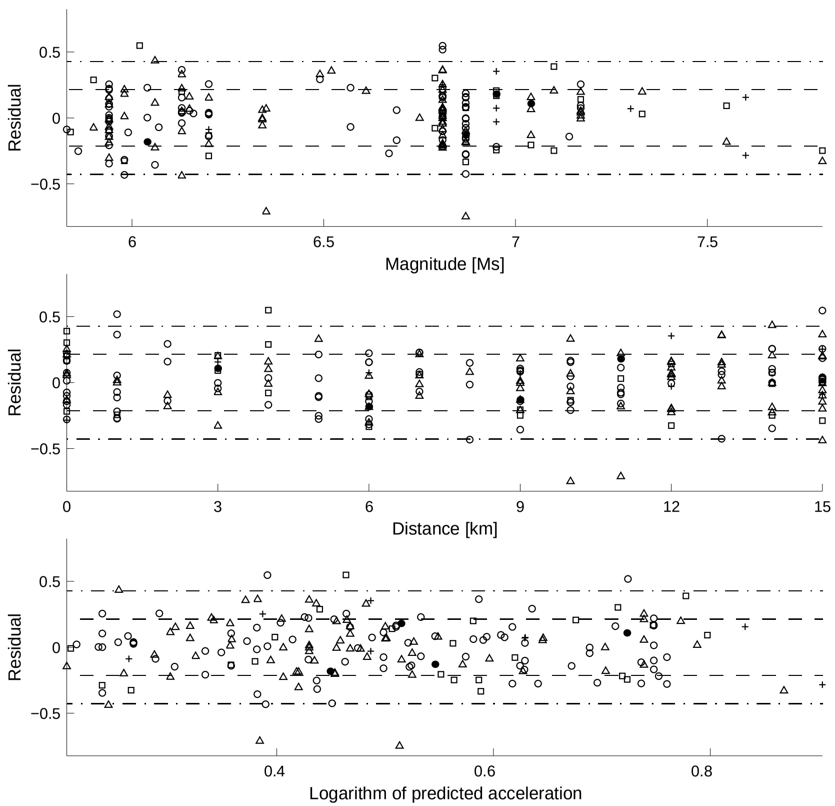

(a) Graphs of residuals for horizontal PGA.

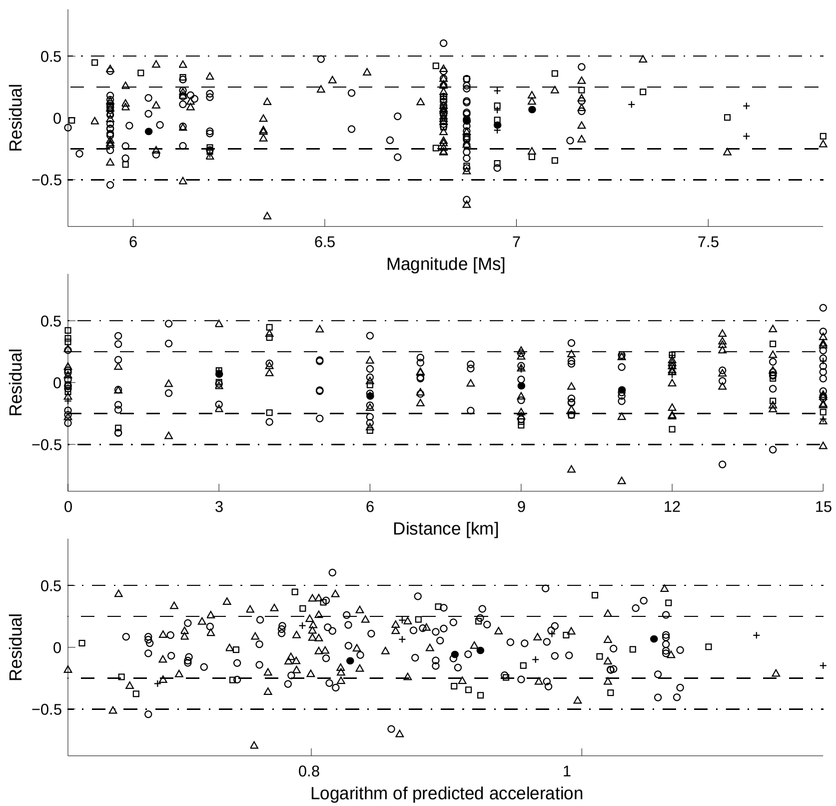

(b) Graphs of residuals for horizontal SA at 0.2s.

Fig. 7.29: Residuals of the logarithm of observed amplitude with respect to predicted acceleration for horizontal PGA and spectral acceleration at $0.2\,\mathrm{s}$, $0.5\,\mathrm{s}$ and $1.0\,\mathrm{s}$ against magnitude, distance and logarithm of predicted acceleration. + denotes unknown site category, ● denotes very soft soil (L), ○ denotes soft soil (S), △ denotes stiff soil (A) and □ denotes rock (R). Dashed lines are at ± 1 standard deviation and dash-dotted lines are at ± 2 standard deviations.

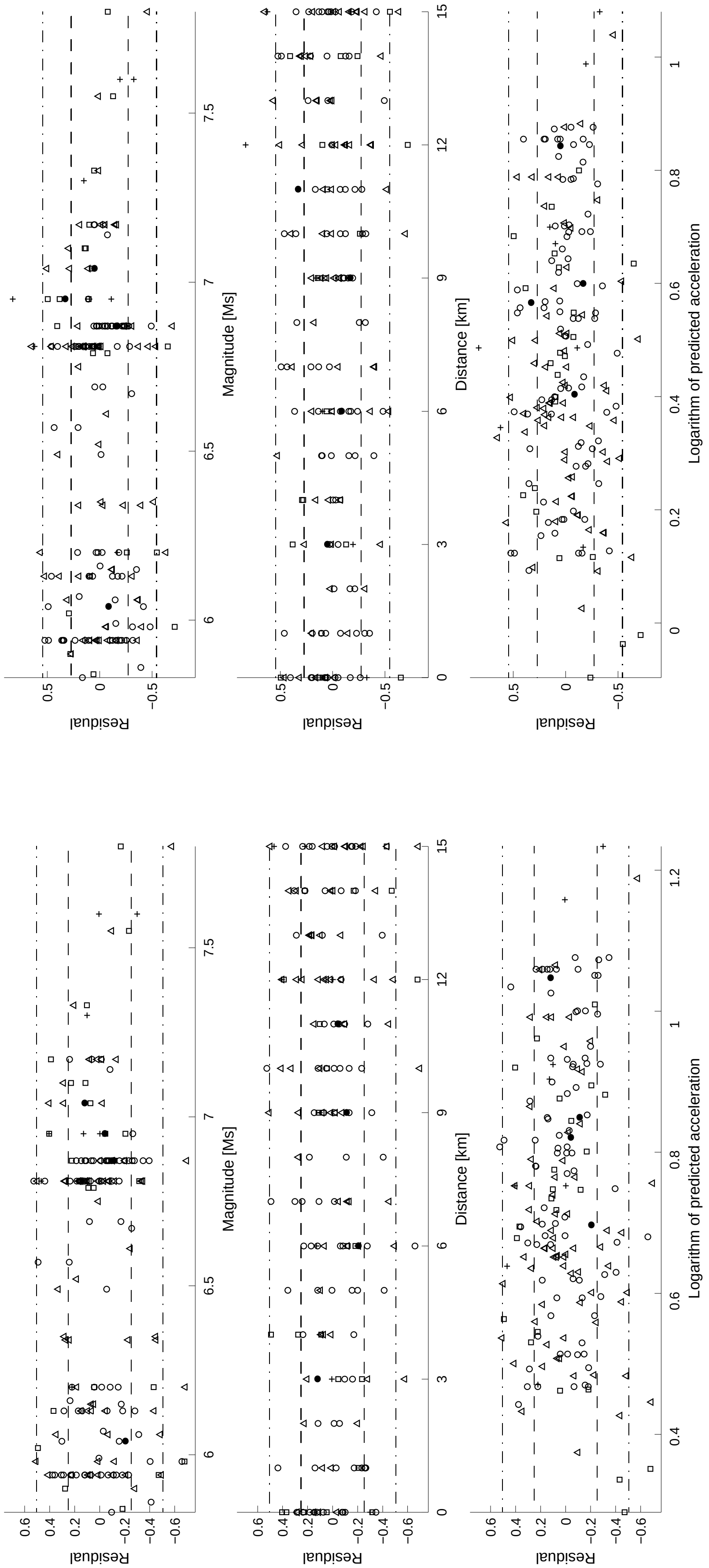

(c) Graphs of residuals for horizontal SA at 0.5s.

(d) Graphs of residuals for horizontal SA at 1.0s.

Fig. 7.29: *Continued.*

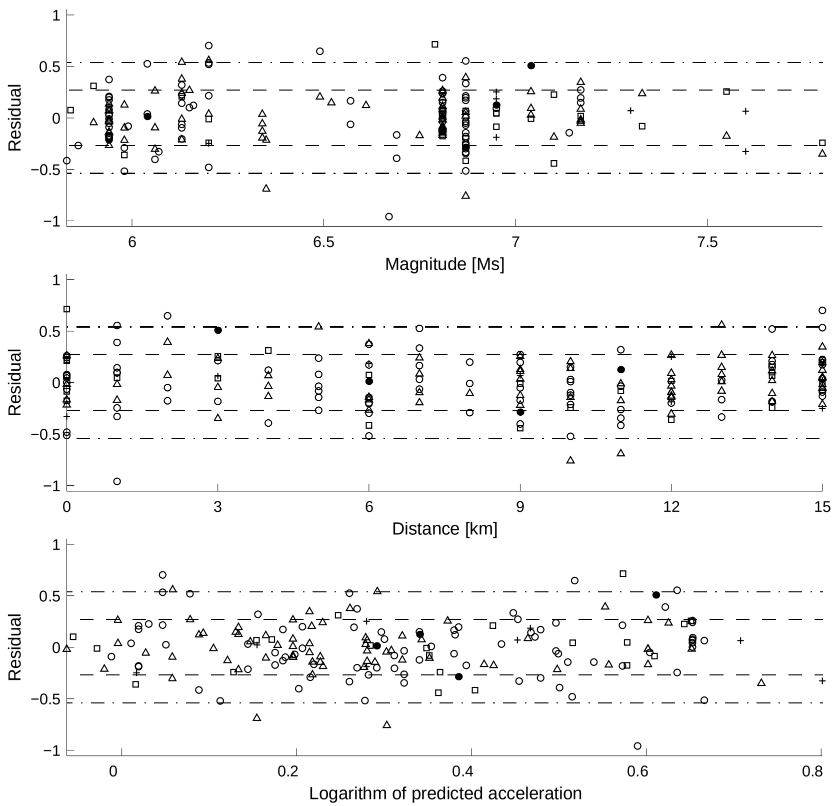

(a) Graphs of residuals for vertical PGA.

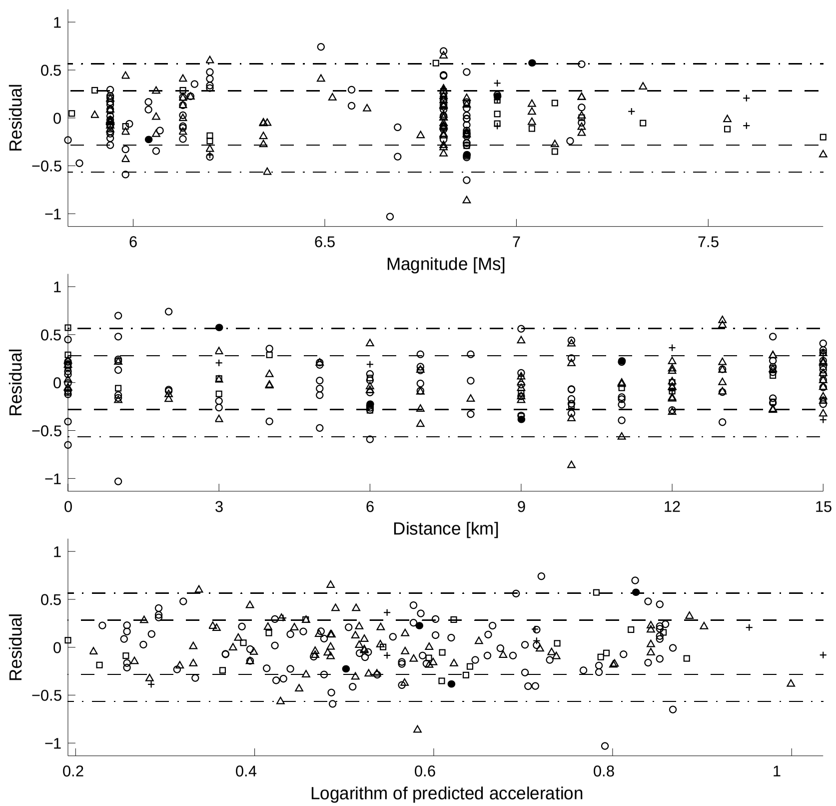

(b) Graphs of residuals for vertical SA at 0.2s.

Fig. 7.30: Residuals of the logarithm of observed amplitude with respect to predicted acceleration for vertical PGA and spectral acceleration at $0.2\,\mathrm{s}$, $0.5\,\mathrm{s}$ and $1.0\,\mathrm{s}$ against magnitude, distance and logarithm of predicted acceleration. + denotes unknown site category, $\bullet$ denotes very soft soil (L), $\circ$ denotes soft soil (S), $\triangle$ denotes stiff soil (A) and $\square$ denotes rock (R). Dashed lines are at ± 1 standard deviation and dash-dotted lines are at ± 2 standard deviations.

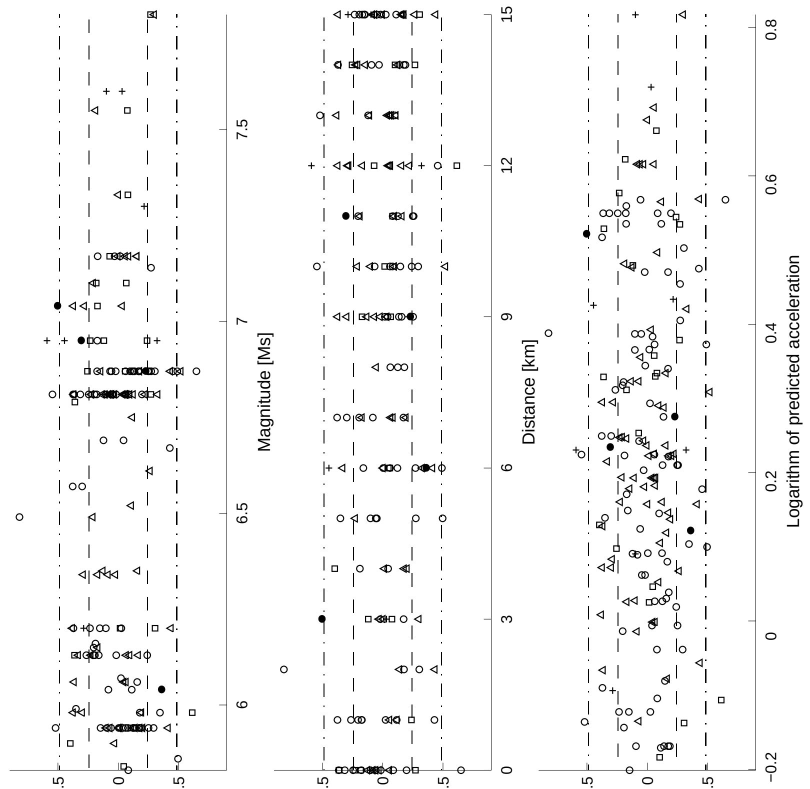

(c) Graphs of residuals for vertical SA at 0.5s.

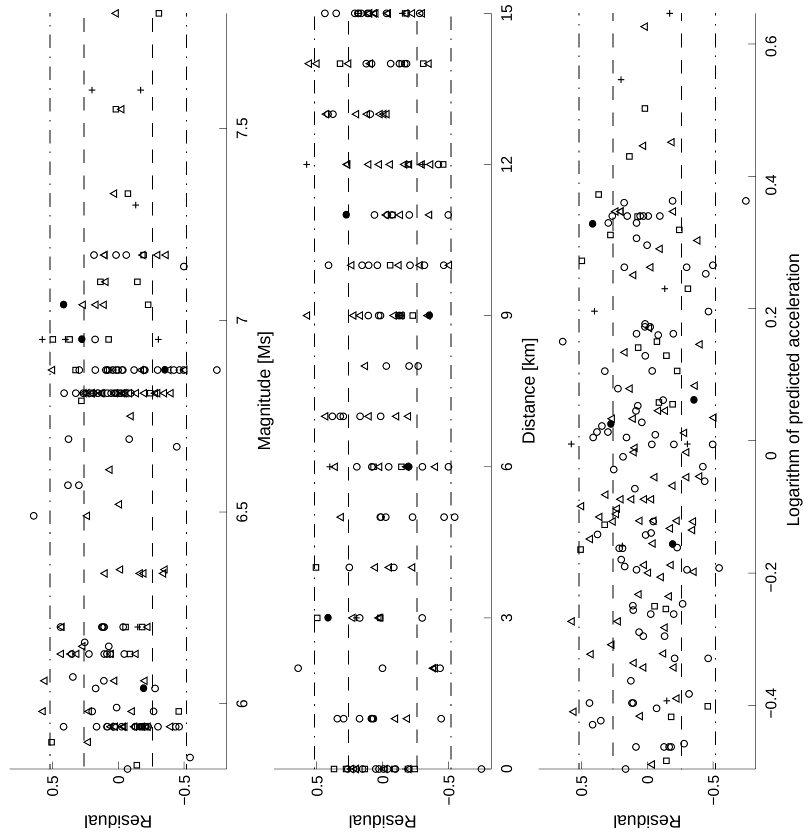

(d) Graphs of residuals for vertical SA at 1.0s.

Fig. 7.30: *Continued.*

7.19.2 Use of a validation set

One attractive method for the validation of a regression model, whenever large amounts of data are available, is to check that the equation derived using a construction set gives predictions close to the observations in a validation set, which were not used to derive the equation (Snee, 1977; Weisburg, 1985).

Here this is difficult because all the near-field data, available at the time, fulfilling the criteria in Chapter 5 are used as the construction set to derive the equations. However, since the equations were derived 45 records, that fulfil the criteria have become available; 43 from the Chi-Chi earthquake (20/9/1999) and two from other earthquakes. To supplement this small, poorly distributed validation set, the free-field criteria were relaxed and records from dam-related free-field sites (7 records) and structure-related free-field sites (32 records) added to the validation set. This gives a further 39 mainly triaxial[3] records from 11 earthquakes. In total there are 84 records from 14 earthquakes in the validation set (Table D.2). The distribution of this set with site category is: very soft soil (L), 0 records; soft soil (S), 19 records; stiff soil (A), 3 records; rock (R), 7 records and unknown, 55 records. The distribution of this set in terms of source mechanism is: normal (N), 2 earthquakes, 2 records; thrust (T), 6 earthquakes, 64 records and strike-slip (S), 6 earthquakes, 18 records. As can be seen this validation set is not well distributed, the vast majority of the records come from thrust earthquakes and also for most there is no local site information.

For each record in the validation set the residual was calculated (using Equation 7.8) with respect to the derived attenuation relations. The residuals for records with known site categories are taken with respect to the final equation and those with unknown site categories with respect to the equation derived in the first step where site conditions are not considered. The mean and standard deviations of these residuals are computed for horizontal and vertical PGA and spectral acceleration. The mean of these residuals gives the bias of the equation, negative values mean the equation over predicts ground motion on average and positive values mean the equation under predicts ground motion on average. Figure 7.31 show these means and standard derivations against period. Figure 7.31 shows that the equations significantly over predict the near-field ground motion in the validation set especially for short periods ($T < 1\,\mathrm{s}$). Examining the plots of the individual residuals (not shown) revealed that two groups of records were significantly over estimated by the near-field equations. The first group consisted of the 11 records from the Morgan Hill earthquake (24/4/1984) recorded on the ground floor of large buildings in San Jose (Town Park Towers, 10 storeys, Great Western Savings, 10 storeys, and Commercial Building Gardens, 13 storeys). The short-period ground motions of records from large buildings are likely to have been reduced by soil-structure interaction and therefore they were removed from the validation set. The second group were the

[3] 13 of these records have only one or two components.

43 records from the Chi-Chi earthquake (20/9/1999) which was the largest earthquake, $M_s = 7.6$, in the validation set. As was suggested by the residual plots (Section 7.19.1) the derived near-field equations seem to over predict ground motions from large magnitude earthquakes probably due to the lack of a magnitude saturation term, such as $-b_4M^2$, used by for example Boore *et al.* (1993). Therefore the records from the Chi-Chi earthquake are also removed from the validation set and the means and standard deviations re-computed using the small validation set of 29 records (see Figure 7.31). Figure 7.31 shows that once these records are removed the derived near-field equations predict the ground motions in the validation set reasonably well, i.e. the bias is almost zero. The standard deviations of the residuals is similar to that derived using the construction set.

In conclusion, the validation set technique is a powerful method for checking derived attenuation relations. This technique has shown that the equations derived in this chapter for the prediction of strong ground motion in the near-field of moderate to large earthquakes show no obvious bias except for very large magnitudes ($M_s \gtrsim 7.6$) where the equations tend to over predict ground motion especially for short periods. This problem possibly can be addressed by using a term to account for nonlinear scaling of accelerations with magnitude such as employed by, for example, Boore *et al.* (1993). Use of a validation set also shows the importance of soil-structure interaction for significantly reducing short-period ground motion.

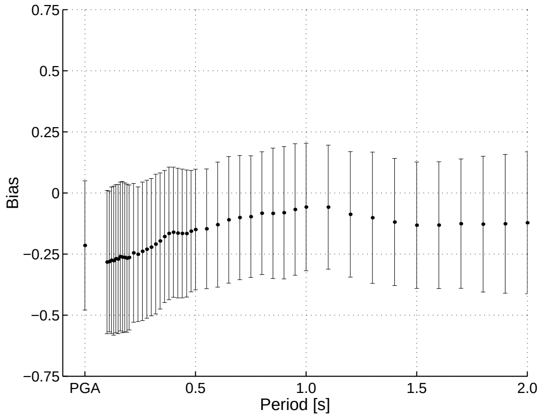

(a) Bias in horizontal PGA and spectral acceleration equations (complete validation set).

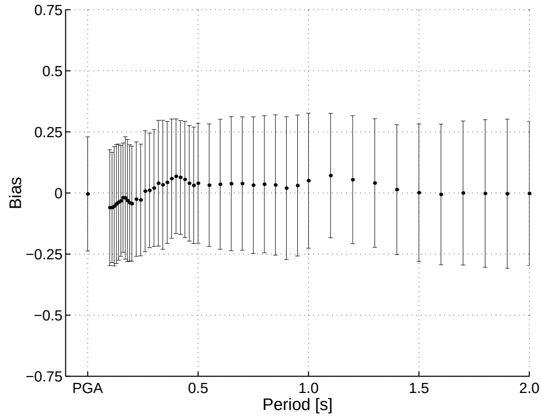

(b) Bias in horizontal PGA and spectral acceleration equations (limited validation set).

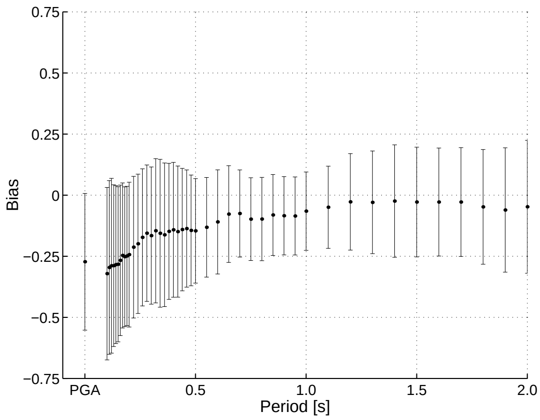

(c) Bias in vertical PGA and spectral acceleration equations (complete validation set).

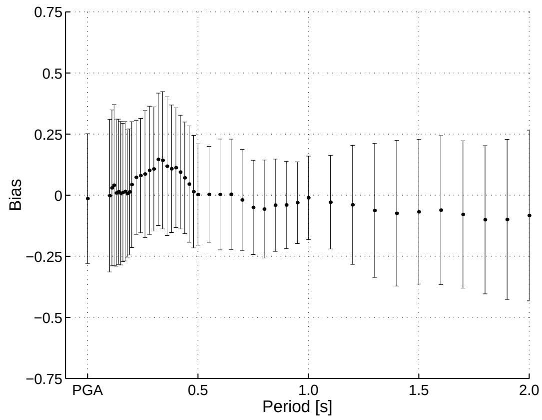

(d) Bias in vertical PGA and spectral acceleration equations (limited validation set).

Fig. 7.31: Bias in horizontal and vertical PGA and spectral acceleration equations found by using validation set (both complete validation set and limited validation set). Dots are means of residuals and bars are the standard deviations of residuals with respect to the derived near-field attenuation relations.

8. THE SIZE AND CAUSES OF INACCURACIES IN GROUND MOTION PREDICTION

8.1 Uncertainties in attenuation relations

The uncertainty in strong-motion estimates, expressed as a factor of ± 1 standard deviation[1], has not decreased over the past thirty years and is usually between 1.5 and 2 (Figure 8.1).

During this time the quantity and quality of data used has increased (see Sections 3.3 & 3.4). Further, the number of records used has no effect on the uncertainty associated with the attenuation equation (Figure 8.2). Although the uncertainty in attenuation relations has not significantly decreased with increasing observations the median ground motion becomes more precisely defined because the standard deviation of the mean is inversely proportional to $\sqrt{n}$, where n is the number of records (e.g. Moroney, 1990). This improvement in the precision of the median ground motion is demonstrated by the close agreement between predicted ground motions using recent attenuation relations (e.g. Ambraseys *et al.*, 1996; Abrahamson & Shedlock, 1997).

The functional form of the attenuation equation has also become much more complicated (see Sections 3.6, 3.7 & 3.8) and regression techniques have become more complex (see Section 3.9). The number of coefficients derived during the analysis, which is directly related to the complexity of the equation, does not reduce the associated uncertainty, as shown by Figure 8.3.

This lower limit on the uncertainty associated with attenuation relations is assessed in this chapter using a technique which does not involve regression or an assumed functional form. The possible reasons why there is a limit on the attainable accuracy of strong-motion attenuation relations exists and some improvements which may increase the predictive power of such equations are then discussed.

[1] Sometimes this is known as geometric spread.

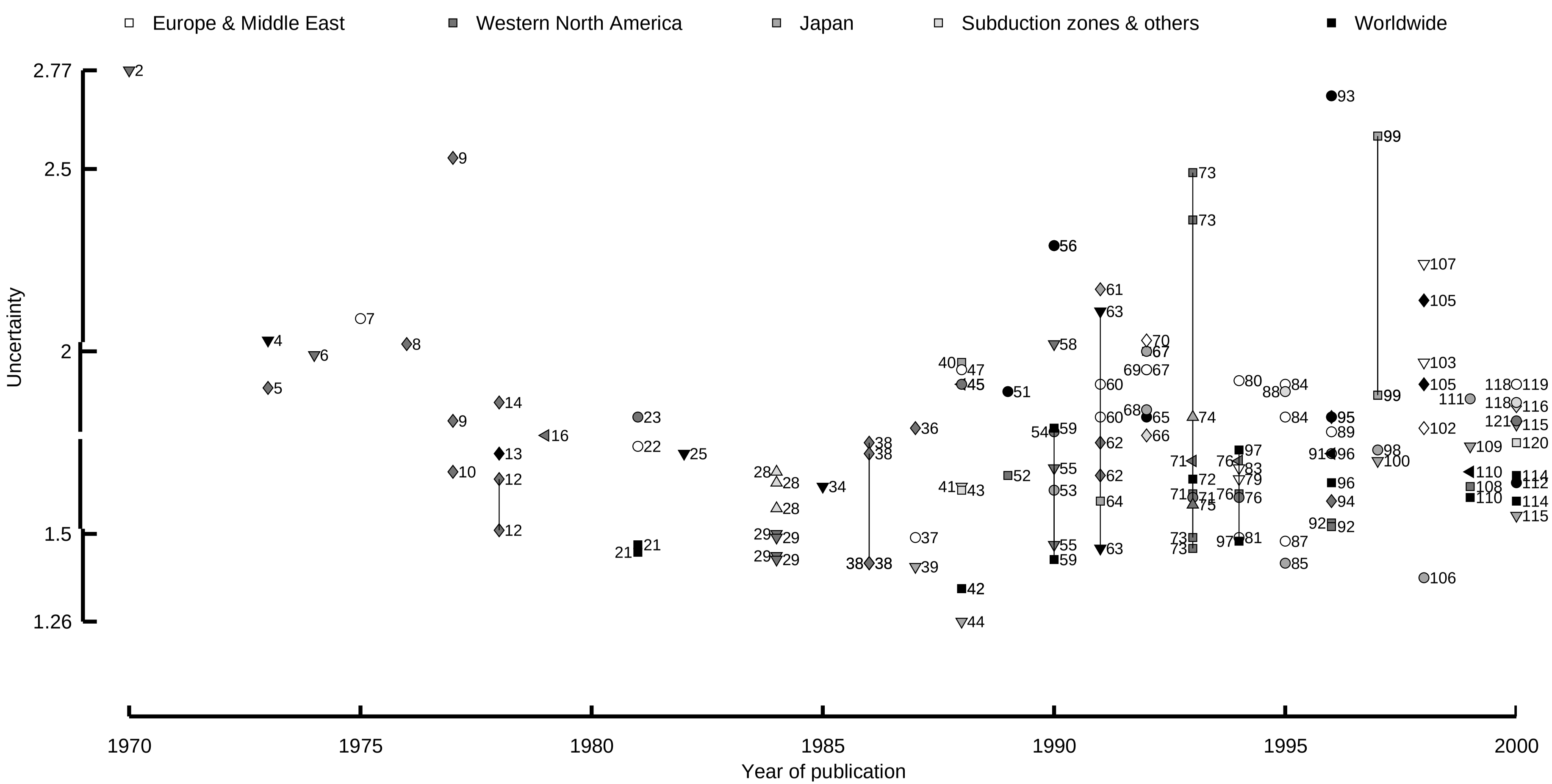

Fig. 8.1: Uncertainty, in terms of ± 1 standard deviation, against year of publication of the attenuation relation. The greyscale corresponds to the region where the equation applies and the shape of the dot corresponds to how the horizontal components are used: circle (larger), square (geometric or arithmetic mean), diamond (both), up triangle (resolved), left triangle (randomly chosen) and down triangle (unknown). The numbers refer to the subsectional numbers of each equation in Douglas (2001).

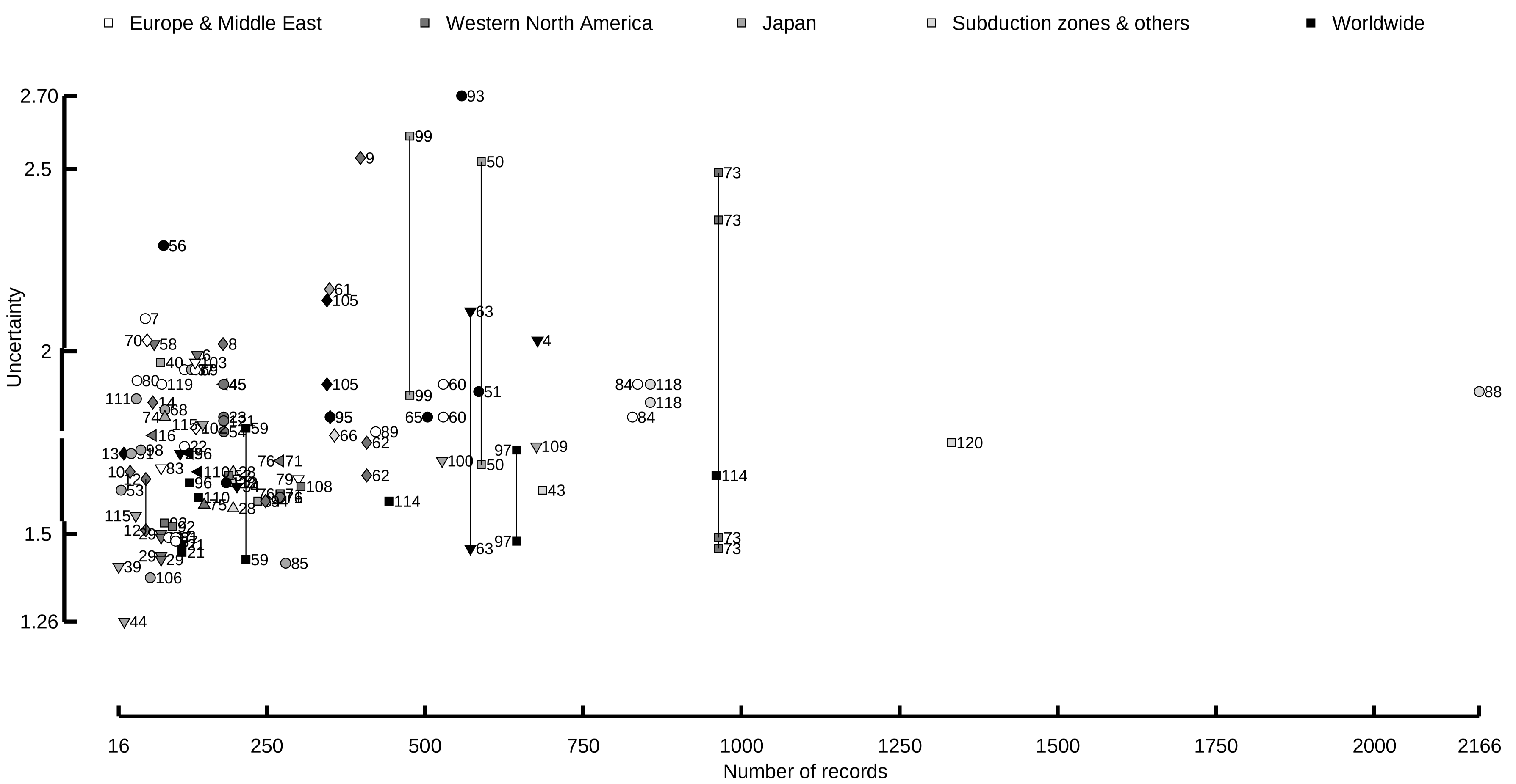

Fig. 8.2: Uncertainty, in terms of ± 1 standard deviation, against number of records used to derive the attenuation relation. The greyscale corresponds to the region where the equation applies and the shape of the dot corresponds to how the horizontal components are used: circle (larger), square (geometric or arithmetic mean), diamond (both), up triangle (resolved), left triangle (randomly chosen) and down triangle (unknown). The numbers refer to the subsectional numbers of each equation in Douglas (2001).

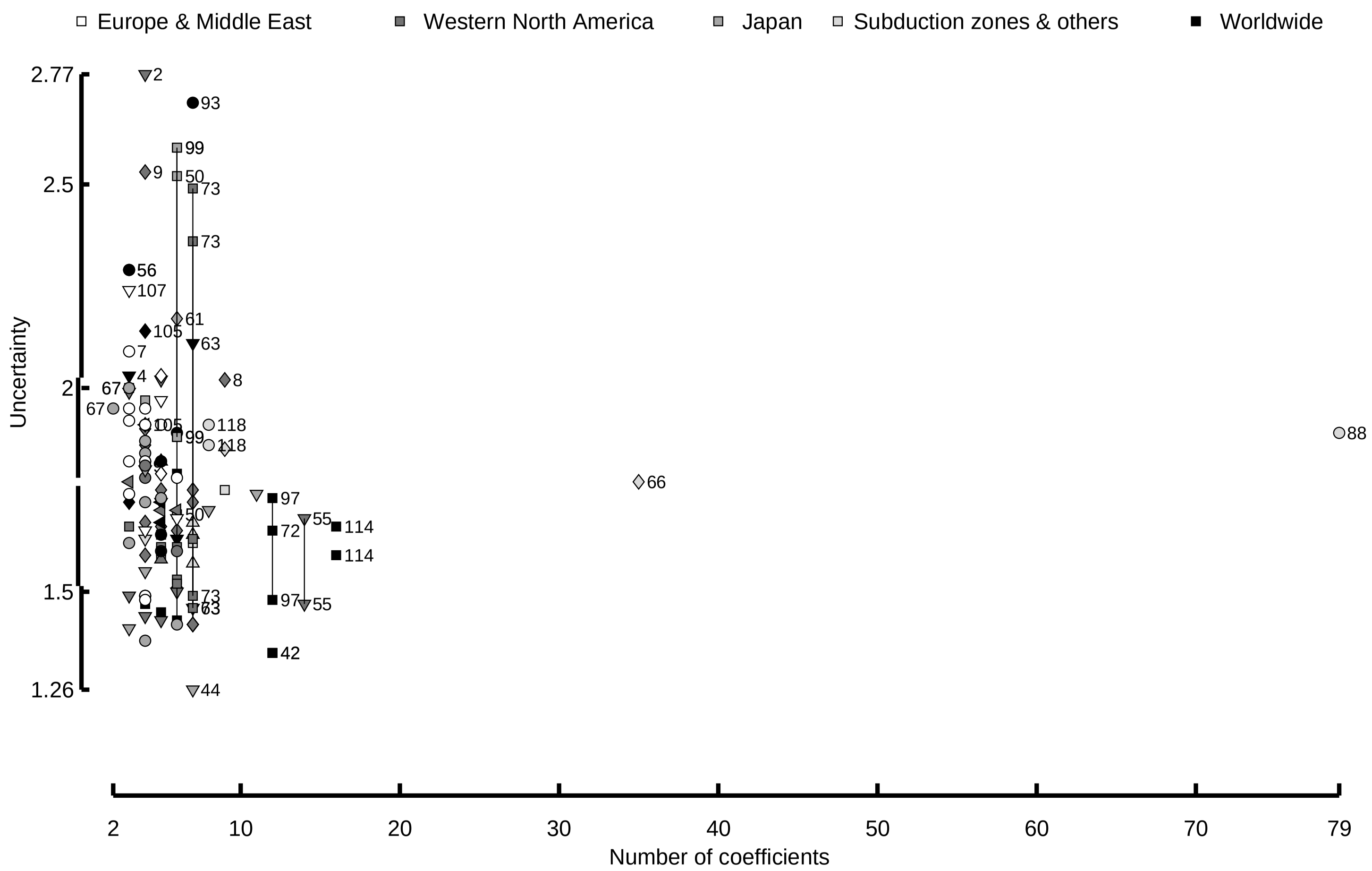

Fig. 8.3: Uncertainty, in terms of ± 1 standard deviation, against number of coefficients in the attenuation relation. The greyscale corresponds to the region where the equation applies and the shape of the dot corresponds to how the horizontal components are used: circle (larger), square (geometric or arithmetic mean), diamond (both), up triangle (resolved), left triangle (randomly chosen) and down triangle (unknown). The numbers refer to the subsectional numbers of each equation in Douglas (2001).

8.2 Causes of scatter

The derivation of attenuation relations is an observational study rather than an experimental study and hence the independent variables used cannot be controlled, only measured. Such measurement is often imprecise which introduces some of the uncertainty into the final equation (see Section 8.4). Another source of scatter is the use of inappropriate independent variables, such as distance measures or site categories, which cannot adequately model differences in recorded ground motion (see Section 8.4). However the major reason for the scatter in attenuation relations is that many factors which are thought to affect strong ground motions are not included in the equation, often because they cannot be precisely measured or because adequate data does not exist for the records used. The factors affecting strong ground motion are shown to be numerous and complex in Chapter 2 whereas Chapter 3 shows that current attenuation relations do not model many of these factors or if factors are modelled then simple functional forms are used. The absence of important factors and the inadequacy of the functional forms used is the main cause of scatter; this is known as modelling uncertainty (Toro *et al.*, 1997).

8.3 Pure error

Draper & Smith (1981, pp. 33–42) discuss the idea of 'pure error' which gives the upper bound on the accuracy which equations obtained by regression can achieve; its estimation requires 'repeat runs', where the independent parameters are the same. Then the pure error is simply the best estimate of the unbiased population standard deviation (i.e. standard deviation with the $n/(n-1)$ correction factor), σ, of the dependent parameter for each repeat run. Simple attenuation relations would predict the same ground motions for the same magnitude earthquake recorded at the same distance, therefore comparing two or more such ground motions would yield the pure error.

Obviously in earthquake seismology[2] there are no repeat runs, therefore 'approximate repeats' need to be used to compute the pure error in a set of records. For this study the data space is divided into $2\,\mathrm{km}$ by 0.2 M_s unit intervals and the records within each bin are assumed to be approximate repeats. This interval size was used because it is thought to be a good balance between a smaller interval where ground motions should be more similar but there are too few records to give a reliable mean and standard deviation, and a larger interval where there are enough records to give a reliable mean and standard deviation but the ground motion variation could be due to differences in distance and magnitude. Pure error analysis assumes that the explanatory variables (here M_s, d and site category) are accurately measured as does regression analysis, used for the derivation of strong-motion attenuation relations, and so no further assumption is made in this study, over that which is assumed by previous studies on attenuation relations.

[2] Explosions fired at test sites approximate to repeat runs for travel time studies.

This concept can be taken further by removing the scatter which can be explained by more independent parameters, such as soil type (see Section 8.3.4), focal mechanism and focal depth, by dividing the observations into more categories. As more parameters are included the number of records which are rough repeats decreases significantly and hence the reliability of such estimates of pure error decreases.

Pure error analysis provides the lower bound on the standard deviation possible by fitting any functional form, no matter how complex, to the data and so shows how much improvement in the accuracy of ground motion estimation is possible using the current data.

In this study discussion is limited to the scatter associated with peak ground acceleration (PGA) and spectral acceleration (SA) for natural periods, 0.2, 0.5 and $1\,\mathrm{s}$ at 5% damping using the largest horizontal component and vertical component of each record. The characteristics of the data used are given in Section 5.2.

8.3.1 Acceleration dependent uncertainty (Distribution of errors)

All previously published attenuation relations, except those by Bolt & Abrahamson (1982) and Brillinger & Preisler (1984), have assumed the errors are proportional to the size of the ground motion (even if this is not explicitly stated) and hence have taken the logarithm of the recorded ground motion, see for example Draper & Smith (1981, pp. 237–238). Donovan & Bornstein (1978), Campbell (1997) and others show evidence, that once the regression analysis has been preformed, the uncertainty depends on the size of the ground motion (larger ground motions are associated with smaller uncertainty than smaller ground motions) even after taking the logarithm. If this dependence of uncertainty on the amplitude of the ground motion is significant then it means that logarithmic transformation is not correct (Draper & Smith, 1981, pp. 237–238). Donovan & Bornstein (1978), Campbell (1997) and others have first assumed that strong-motion amplitudes are lognormally distributed and following regression analysis this basic assumption is tested by inspection of the residuals. However, such a technique may be biased into yielding residuals which appear lognormally distributed when in fact they are not; a point noted by Campbell (1985).

Non-linearity of site response is suggested as a possible reason for acceleration dependent uncertainty because local site conditions will amplify strong ground motions less than weak ground motions and so differences in ground motions on different sites will be less for stronger ground motions (Donovan & Bornstein, 1978).

The hypothesis that errors are proportional to ground motions, and so the logarithmic transformation is justified, can be tested with pure error analysis. Within each magnitude-distance interval the mean, η, and unbiased standard deviation, σ, of the untransformed ground motion (PGA and SA) was calculated using the maximum-likelihood method (Spudich *et al.*, 1999, p. 1170). Figures 8.4(a) to 8.4(d) show the coefficient of variation, $V = 100\sigma/\eta$, against η for horizontal PGA and SA for the three periods. If σ is proportional to η then these graphs should show no trend with increasing ground motion. A linear equation $V = \alpha + \beta\eta$ was fitted to each of these graphs and is also shown on these graphs. In the captions α, β, their 95% confidence intervals, standard deviation, the computed and critical Student's t value for $\beta = 0$ for 5% significance level and the degrees of freedom are given. β is not significantly different than zero for PGA or any of the three periods because computed t is not bigger than critical t.

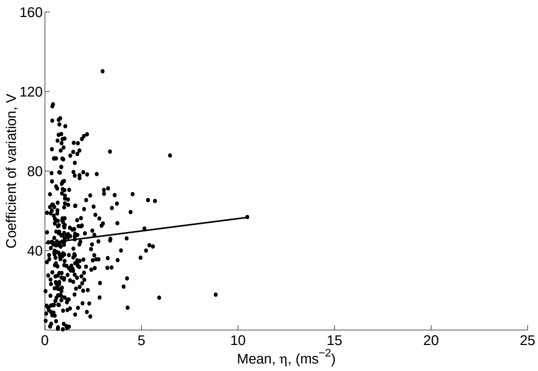

(a) PGA. $\alpha = 43.62 \pm 4.38$, $\beta = 1.24 \pm 2.20$, $\sigma = 26.43$ and $t(\beta) = 1.11$.

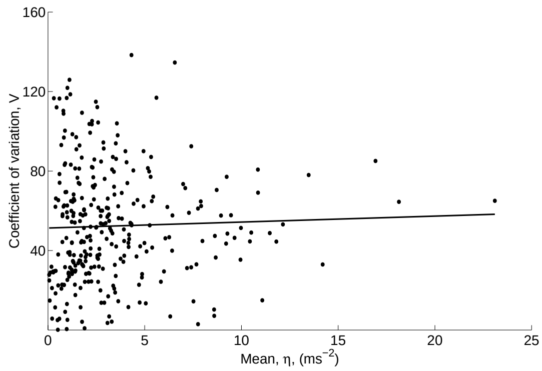

(b) SA at $T = 0.2$s. $\alpha = 51.31 \pm 4.65$, $\beta = 0.30 \pm 1.01$, $\sigma = 28.31$ and $t(\beta) = 0.59$.

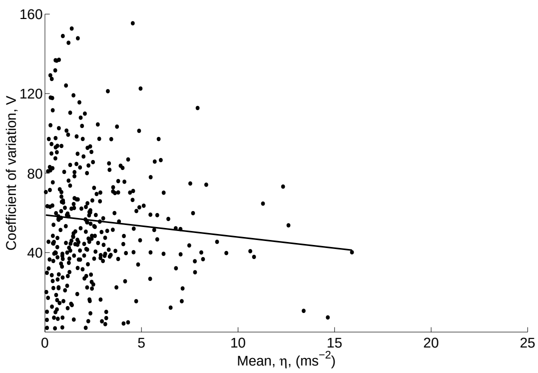

(c) SA at $T = 0.5$s. $\alpha = 58.93 \pm 5.15$, $\beta = -1.11 \pm 1.40$, $\sigma = 32.09$ and $t(\beta) = 1.57$.

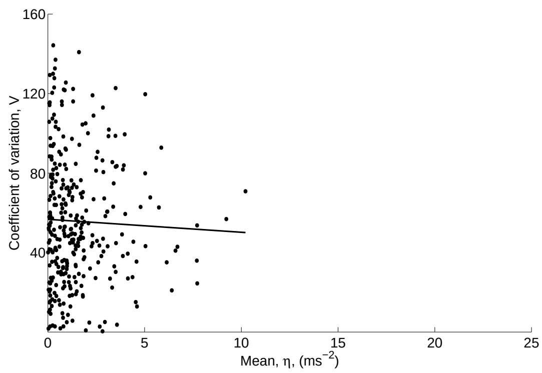

(d) SA at $T = 1.0$s. $\alpha = 56.74 \pm 4.95$, $\beta = -0.65 \pm 2.20$, $\sigma = 32.24$ and $t(\beta) = 0.58$.

Fig. 8.4: Coefficient of variation, V, against mean ground motion, η, for horizontal peak ground acceleration and horizontal spectral acceleration at $T = 0.2$, 0.5 and $1.0\,\text{s}$ and the computed statistics of the least squares lines. Critical $t = 1.97$ and degrees of freedom $= 306$.

Figures 8.5(a) to 8.5(d) show the coefficient of variation, V, against η for vertical PGA and SA for the three periods. There seems to be a significant *increase* in the scatter for increasing ground motion for vertical PGA but this is mainly due to the large coefficient of variation, $V = 135$, of the bin with the largest mean, $\eta = 9.8\,\text{ms}^{-2}$, in the data, therefore it is probably not significant. For

SA none of the periods show significant trends.

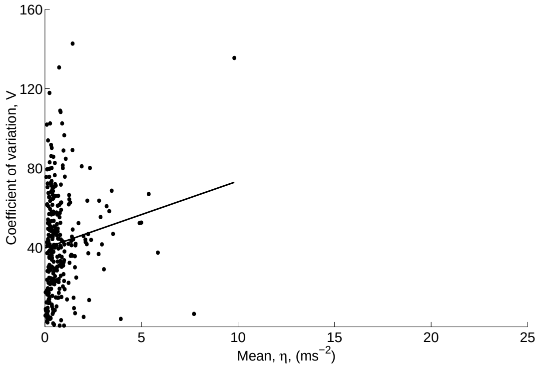

(a) PGA. $\alpha = 39.64 \pm 3.55$, $\beta = 3.38 \pm 2.66$, $\sigma = 25.36$ and $t(\beta) = 2.50$.

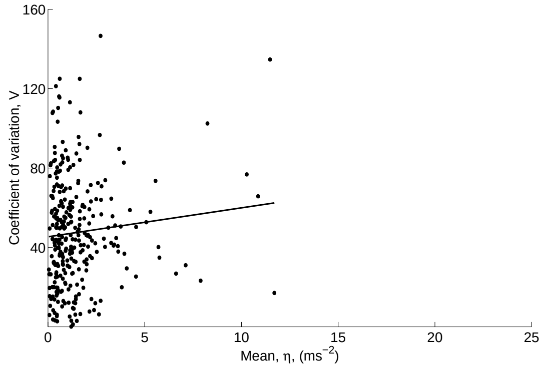

(b) SA at $T = 0.2$s. $\alpha = 45.36 \pm 4.02$, $\beta = 1.46 \pm 1.79$, $\sigma = 27.00$ and $t(\beta) = 1.60$.

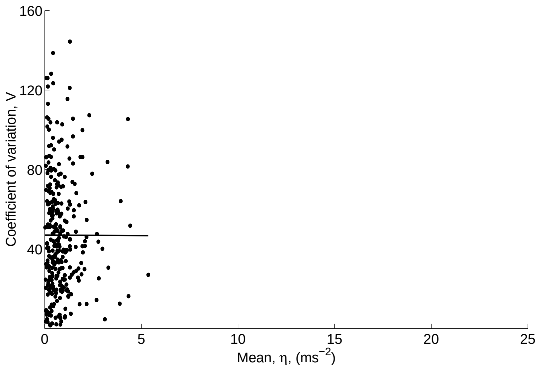

(c) SA at $T = 0.5$s. $\alpha = 47.00 \pm 4.75$, $\beta = -0.04 \pm 4.00$, $\sigma = 29.47$ and $t(\beta) = 0.02$.

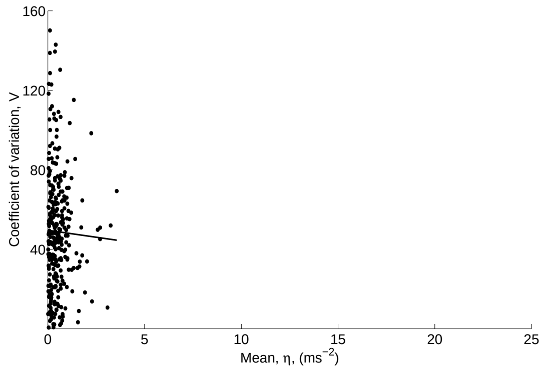

(d) SA at $T = 1.0$s. $\alpha = 49.57 \pm 4.60$, $\beta = -1.40 \pm 6.09$, $\sigma = 29.44$ and $t(\beta) = 0.45$.

Fig. 8.5: Coefficient of variation, V, against mean ground motion, η, for vertical peak ground acceleration and vertical spectral acceleration at $T = 0.2$, 0.5 and $1.0\,$s and the computed statistics of the least squares lines. Critical $t = 1.97$ and degrees of freedom $= 306$.

Thus the hypothesis that the scatter associated with measured ground motion is proportional to the amplitude of the ground motion cannot be rejected, so the logarithmic transformation is justified.

8.3.2 Magnitude-dependent uncertainty

Youngs *et al.* (1995), Campbell (1997) and others have found that the computed standard deviations associated with their attenuation relations are magnitude dependent. However such a pattern in the residuals of regression analysis means that the analysis needs to be repeated using weighted least squares or preliminary transformation on the dependent variable and the regression analysis reperformed (e.g. Draper & Smith, 1981, pp. 112–115, p. 148). The other problem with applying regression analysis to examine this question is that a functional form must be assumed. The hypothesis that uncertainty depends on magnitude was tested using pure error analysis by plotting V against mean M_s of the interval, see Figures 8.6(a) to 8.6(d) for horizontal ground motion and Figures 8.7(a) to 8.7(d) for vertical ground motion. The fitted line coefficients show that there is a decrease in error with increasing M_s and the t test shows that the hypothesis that the error is independent of M_s can be rejected at the 5% significance level.

To check that the statistically significant dependence of V on M_s was not simply due to the distribution of records in the dataset a series of Monte Carlo simulations were conducted. Using the most appropriate attenuation relationship for this data, that of Ambraseys *et al.* (1996), and its associated magnitude-independent standard deviation, 0.25 in logarithmic terms, 100 simulated datasets of 1484 horizontal PGA values, with the same magnitude, distance and site category distribution as the true dataset, were generated. This attenuation relation is believe to be the most appropriate for the data used here because Ambraseys *et al.* (1996) use M_s, their records cover a similar magnitude and distance range as used here and their records come from a similar geographical region to those used here. Where site conditions are unknown they are assumed to have stiff soil. The pure error analysis was applied to each of the simulated datasets. None of these datasets showed a significant decrease of V with M_s and eight showed a significant increase. For horizontal SA at $0.2\,\mathrm{s}$, no simulated dataset showed a significant decrease of V with M_s and 14 showed a significant increase and for horizontal SA at $0.5\,\mathrm{s}$ and $1.0\,\mathrm{s}$ no simulated dataset showed a significant decrease of V with M_s and 16 showed a significant increase. Therefore the statistically significant dependence of observed V on M_s is probably real and is not due to the distribution of the data with M_s.

Nonlinear site response for large amplitude ground motions (which are more likely to come from large magnitude earthquakes than small magnitude earthquakes) would mean a reduction in amplifications due to local site conditions and hence less differences between sites. To test this hypothesis, the only bins used in the analysis are those with mean ground motions, η, below a threshold ground-motion level at which nonlinear response may become significant. Tables 8.1(a) to 8.1(d) give β, $t(\beta)$, critical t and the number of bins used for horizontal PGA and SA for this experiment. These results show that nonlinear soil behaviour may account for some of the observed decrease in scatter with increasing magnitude because if only weak motion, e.g. $\leq 0.5\,\mathrm{ms}^{-2}$ [$\leq 0.05\,\mathrm{g}$], is included then the observed decrease is not significant at the 5% level for PGA and SA at $0.2\,\mathrm{s}$. However, it is probably not the only reason for the observed decrease in scatter with increasing magnitude. A similar conclusion was reached by Youngs *et al.* (1995). Also since scatter is not found to be significantly dependent on amplitude, nonlinear soil behaviour is unlikely to be a major cause of the decrease in scatter with increasing magnitude because it would be apparent in plots such as Figures 8.4(a) to 8.4(d).

Seekins & Hanks (1978) find an increase with decreasing magnitude in the standard deviations of PGAs from a number of different sites at similar distances from aftershocks of the Oroville

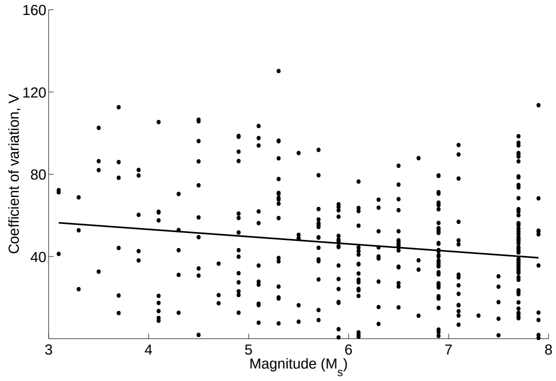

(a) PGA. $\alpha = 67.34 \pm 14.35$, $\beta = -3.54 \pm 2.27$, $\sigma = 26.08$ and $t(\beta) = 3.07$.

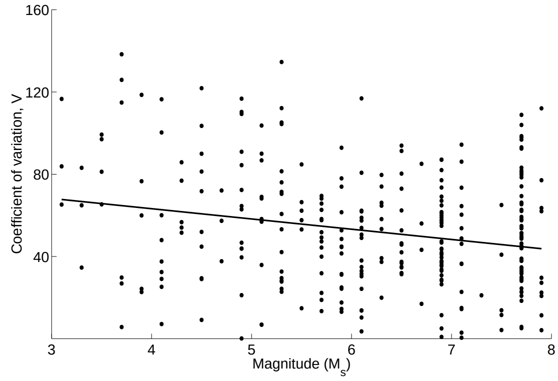

(b) SA at $T = 0.2$s. $\alpha = 83.19 \pm 15.17$, $\beta = -4.99 \pm 2.40$, $\sigma = 27.58$ and $t(\beta) = 4.09$.

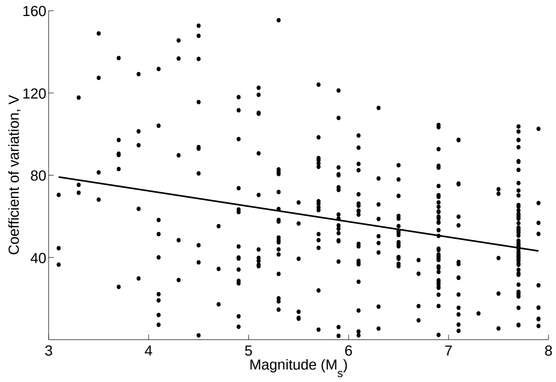

(c) SA at $T = 0.5$s. $\alpha = 102.39 \pm 16.90$, $\beta = -7.50 \pm 2.67$, $\sigma = 30.73$ and $t(\beta) = 5.52$.

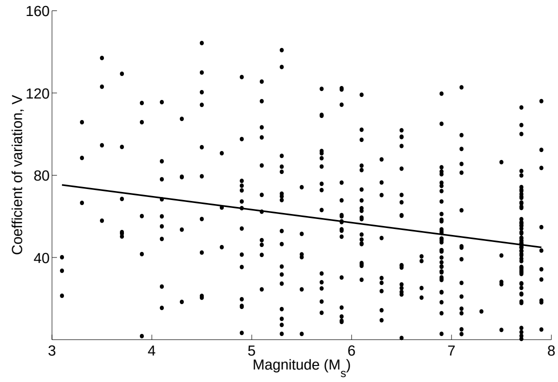

(d) SA at $T = 1.0$s. $\alpha = 94.87 \pm 17.17$, $\beta = -6.32 \pm 2.72$, $\sigma = 31.21$ and $t(\beta) = 4.58$.

Fig. 8.6: Coefficient of variation, V, against M_s for horizontal peak ground acceleration and horizontal spectral acceleration at $T = 0.2$, 0.5 and $1.0\,$s and the computed statistics of the least squares lines. Critical $t = 1.97$ and degrees of freedom $= 306$.

earthquake with magnitudes $3 \leq M_L \leq 5$. They suggested that this is because increased elastic scattering of amplitudes, attendant to a shift to higher predominant frequencies with decreasing magnitude. This results in increased numerical scatter about the mean value as magnitude decreases. This possible explanation for magnitude dependence of PGA scatter cannot explain the observed magnitude-dependent uncertainty of spectral acceleration because SA is a narrow-band measure which is not affected by a shift in predominant frequency of the ground motion.

The duration of strong ground motion at a site roughly increases with magnitude. Using random vibration theory the variability of the peak values of a stationary signal decreases with increasing duration; Youngs *et al.* (1995) suggest this may explain some of the observed magnitude dependence.

Youngs *et al.* (1995) find evidence that the range of stress drops decreases as magnitude in-

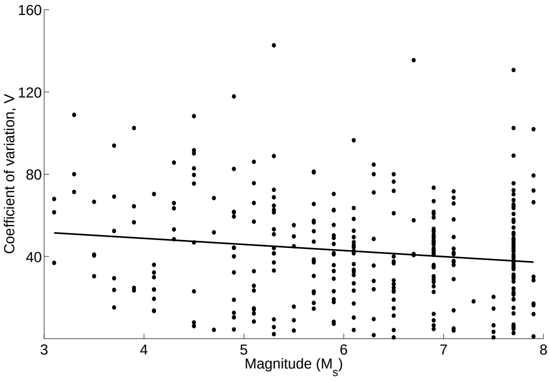

(a) PGA. $\alpha = 60.66 \pm 13.94$, $\beta = -2.96 \pm 2.20$, $\sigma = 25.33$ and $t(\beta) = 2.64$.

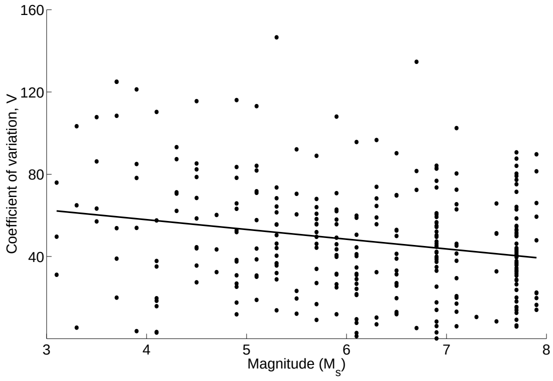

(b) SA at $T = 0.2$s. $\alpha = 76.82 \pm 14.53$, $\beta = -4.74 \pm 2.30$, $\sigma = 26.41$ and $t(\beta) = 4.05$.

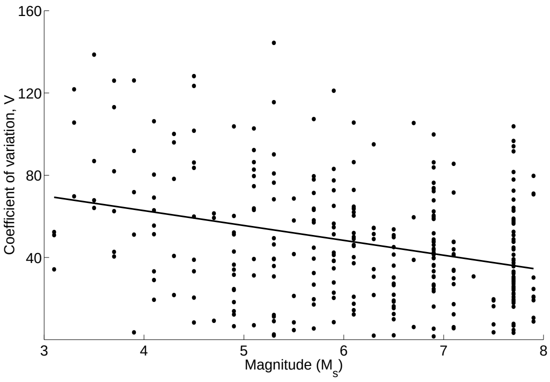

(c) SA at $T = 0.5$s. $\alpha = 91.69 \pm 15.37$, $\beta = -7.23 \pm 2.43$, $\sigma = 27.95$ and $t(\beta) = 5.85$.

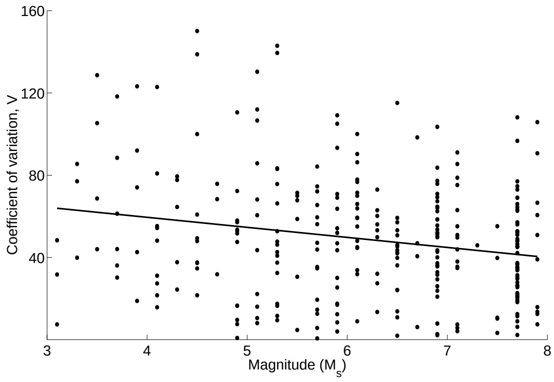

(d) SA at $T = 1.0$s. $\alpha = 79.05 \pm 15.83$, $\beta = -4.88 \pm 2.50$, $\sigma = 28.77$ and $t(\beta) = 3.84$.

Fig. 8.7: Coefficient of variation, V, against M_s for vertical peak ground acceleration and vertical spectral acceleration at $T = 0.2$, 0.5 and 1.0 s and the computed statistics of the least squares lines. Critical $t = 1.97$ and degrees of freedom $= 306$.

creases and as stress drop scales high-frequency ground-motion amplitudes Youngs *et al.* (1995) believe this could explain some of the observed reduction in scatter with increasing magnitude.

One likely reason for some of the apparent decrease in scatter for larger magnitudes is that the independent variables of large magnitude earthquakes are better determined than those of small magnitude earthquakes. This is partly because small earthquakes are not usually studied in detail because of their low significance for hazard analysis and partly because of the lack of high-quality data to accurately determine the necessary independent parameters. However, Abrahamson (1988) finds magnitude dependence for PGAs recorded at the dense SMART 1 array in Taiwan without using the magnitude or distance of the earthquakes. Therefore the observed decrease in scatter cannot be completely attributed to larger errors in the measurement of magnitude and distance for smaller earthquakes.

Max. (ms^{-2})	Bins	β	t	Critical t
0.5	50	-0.33	0.12	2.01
1	151	-4.28	2.88	1.98
2	240	-3.59	2.84	1.97
5	296	-3.65	3.12	1.97

(a) PGA.

Max. (ms^{-2})	Bins	β	t	Critical t
0.5	76	-2.35	1.17	1.99
1	152	-4.92	3.56	1.98
2	242	-5.12	4.22	1.97
5	293	-5.09	4.41	1.97

(b) SA at $T = 0.2$s

Max. (ms^{-2})	Bins	β	t	Critical t
0.5	125	-9.81	5.18	1.98
1	219	-7.88	5.92	1.97
2	282	-7.58	6.03	1.97
5	305	-7.21	5.82	1.97

(c) SA at $T = 0.5$s

Max. (ms^{-2})	Bins	β	t	Critical t
0.5	188	-5.23	3.12	1.97
1	268	-4.90	3.62	1.97
2	297	-4.90	3.80	1.97
5	306	-4.88	3.84	1.97

(d) SA at $T = 1.0$s

Tab. 8.1: Computed statistics of least squares lines of $V = \alpha + \beta M_s$ fitted to data using only bins with mean ground motion, η, less than or equal to given threshold (Max.) for horizontal PGA and SA for 0.2, 0.5 and $1\,\mathrm{s}$ at 5% damping.

8.3.3 Uncertainty using magnitude and distance

Figures 8.8(a) to 8.8(d) show the pure error, σ, of the logarithm of horizontal PGA and SA at the three choices of natural period,against magnitude and distance. These graphs show that the pure error associated with PGA is about 0.2 for stronger ground motion (i.e. large magnitude and short distance) which is equivalent to a factor of 1.6 in terms of ± 1 standard deviation. This uncertainty is about the same as that obtained in attenuation relations, showing that current models are about as accurate as possible, without the introduction of more independent parameters. Also note that weaker motion (i.e. low magnitude or long distance) is associated with greater uncertainty, about 0.4. Greater uncertainties are often found for attenuation studies using only weaker motion for their derivation (e.g. Smit, 1998), which is supported by the results obtained here. Attenuation relations derived using weaker motion to supplement the few data from earthquakes with engineering significance may thus overestimate the true uncertainty.

Spectral acceleration shows increasing uncertainty with period, as is expected, and the difference between the pure error associated with weaker motion compared with stronger motion increases with increasing period.

Figures 8.9(a) to 8.9(d) show similar results for vertical PGA and SA as for horizontal PGA and SA.

The results are almost identical if the correlation of motions within each bin from the same earthquake is neglected, i.e. the normal mean and standard deviation are computed rather than

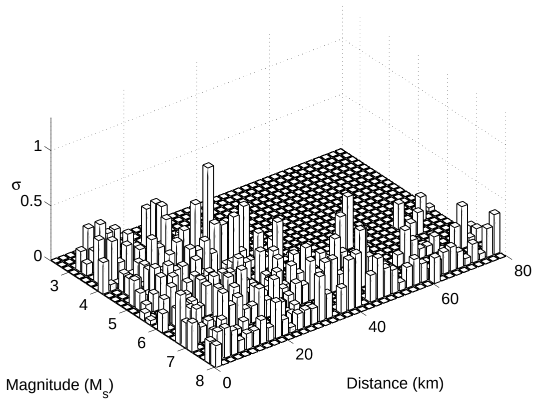

(a) PGA.

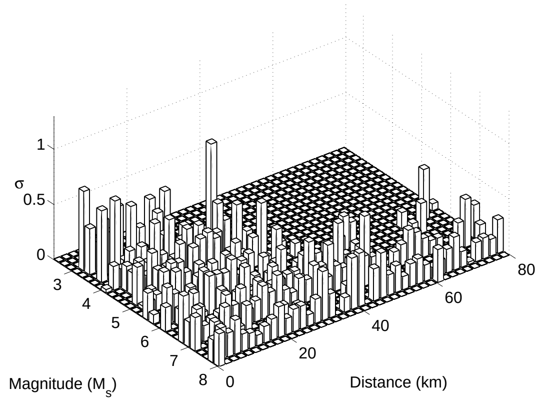

(b) SA at $T = 0.2$s.

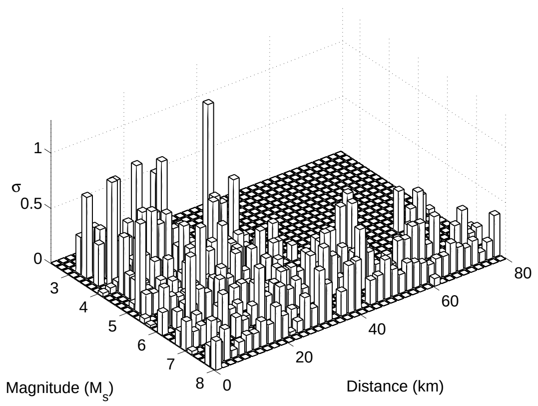

(c) SA at $T = 0.5$s.

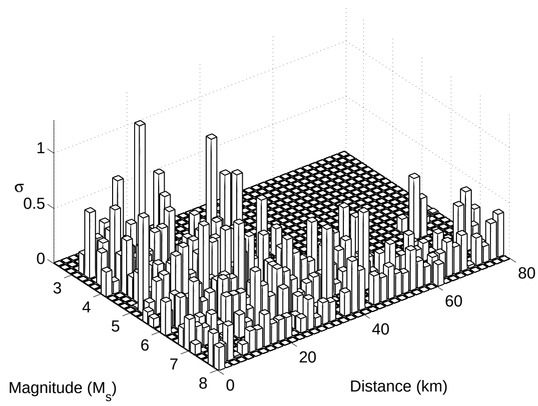

(d) SA at $T = 1.0$s.

Fig. 8.8: Pure error of logarithm of recorded ground motion, σ, for horizontal peak ground acceleration and horizontal spectral acceleration at $T = 0.2$, 0.5 and $1.0\,$s.

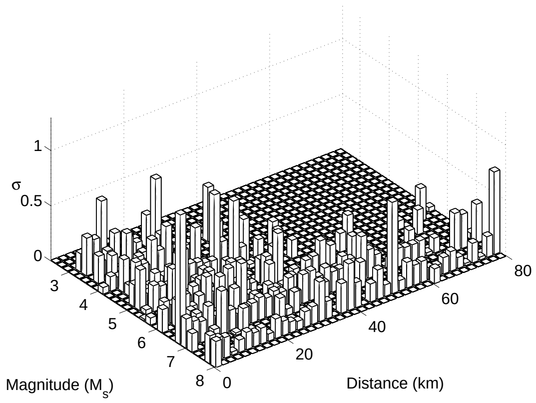

(a) PGA.

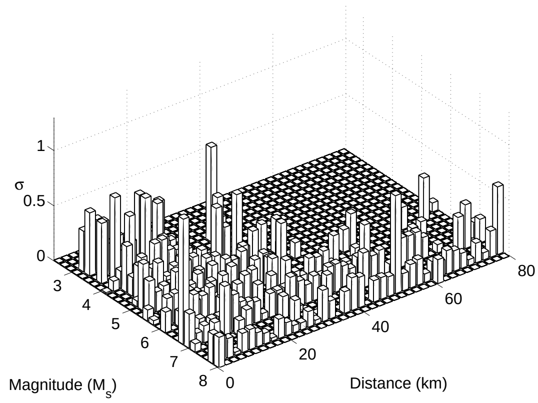

(b) SA at $T = 0.2$s.

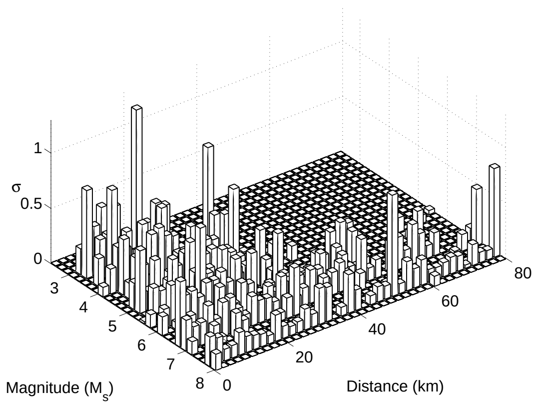

(c) SA at $T = 0.5$s.

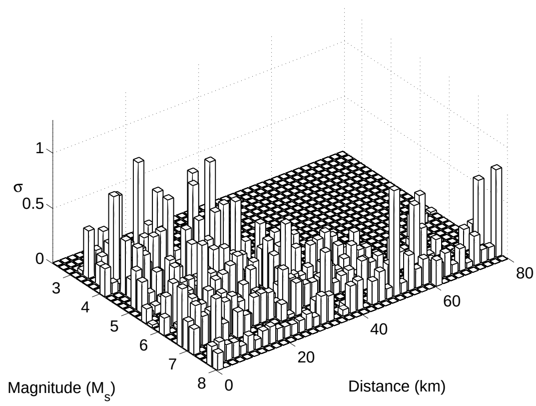

(d) SA at $T = 1.0$s.

Fig. 8.9: Pure error of logarithm of recorded ground motion, σ, for vertical peak ground acceleration and vertical spectral acceleration at $T = 0.2$, 0.5 and $1.0\,$s.

the maximum-likelihood values. This is because most bins either contain records from only a single earthquake or only single records from many earthquakes; the maximum-likelihood mean and standard deviation are then equal to the normal mean and standard deviation. For large magnitudes the pure error shown in the figures is based on only a few earthquakes therefore the error may be only the intra-earthquake component rather than the combined intra- and inter-earthquake scatter. The analysis was repeated but using only one randomly chosen record from each earthquake in each interval thus the inter-earthquake uncertainty is found. It is found that the estimate of pure error using this method is only slightly greater than that using all records.

One possible cause for the increase in scatter at large distances are differences in scattering properties of the crust in different regions of the Earth. Suhadolc & Chiaruttini (1987) believe differences in crustal structure are a major cause of the observed scatter in attenuation relations.

Some of the apparent scatter in this study is due to the use of 'approximate repeats' rather than true 'repeat runs'. To get an estimate of the apparent pure error simply due to the small differences in distance (up to $2\,\mathrm{km}$) and magnitude (up to 0.2 units) of records in each bin the PGA attenuation relation of Ambraseys *et al.* (1996) is used. Using this attenuation relation median PGA values are found for the same magnitude, distance and site category points as the original data. Then the apparent pure error due simply to the coarseness of the bins used is found by repeating the pure error analysis using the simulated data. The largest standard deviation of the logarithm of the ground motion within a magnitude-distance interval due to the binning procedure was 0.12 but the mean standard deviation was only 0.03. Therefore almost all of the pure error found is due to the real variability of ground motions and not due to the 'approximate repeats' assumption.

8.3.4 Uncertainty using magnitude, distance and site category

Local site response has an important effect on the ground motion recorded at a site and is usually incorporated into attenuation relations (see Section 3.8). The analysis is repeated separately for each site category so that the scatter caused by local site conditions, as modelled by attenuation relations, is removed.

Figures 8.10(a) to 8.10(d) show graphs of the pure error for the stiff soil category, σ_A, against the pure error estimate for the same interval neglecting the site category, σ_T, for horizontal PGA and SA. As can be seen there is a slight reduction in the pure error but it is still large. Figure 8.11(a) to 8.11(d) show similar graphs for vertical PGA and SA and also demonstrate only a limited reduction in the pure error when crude site classification is used. Similar small reductions occur for soft soil and rock categories although both these categories have less available data and are not shown here.

The apparent unimportance of local site conditions for reducing the uncertainty associated with

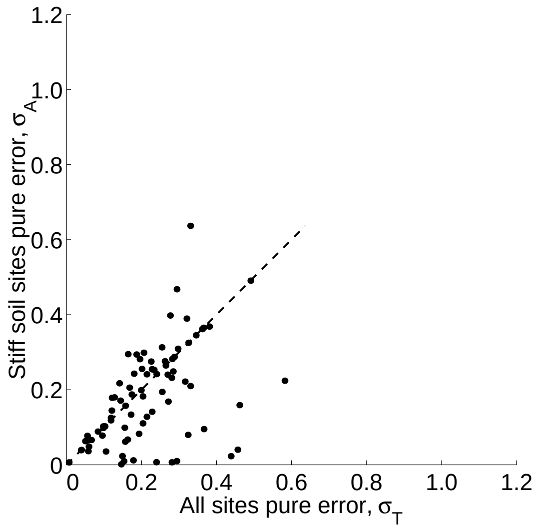

(a) PGA.

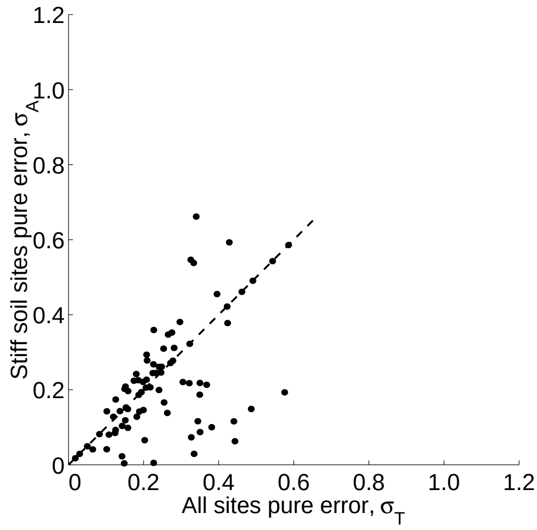

(b) SA at $T = 0.2$s.

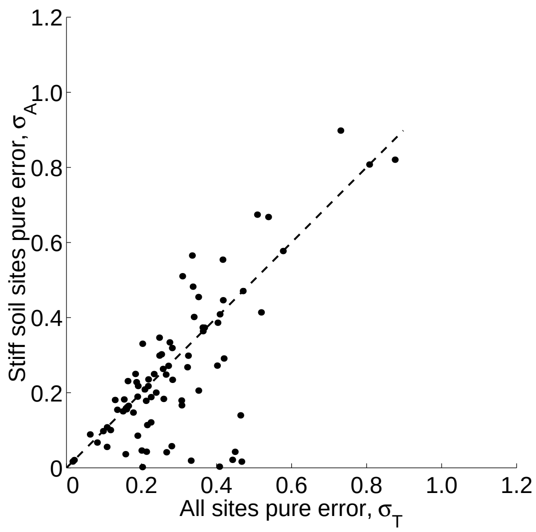

(c) SA at $T = 0.5$s.

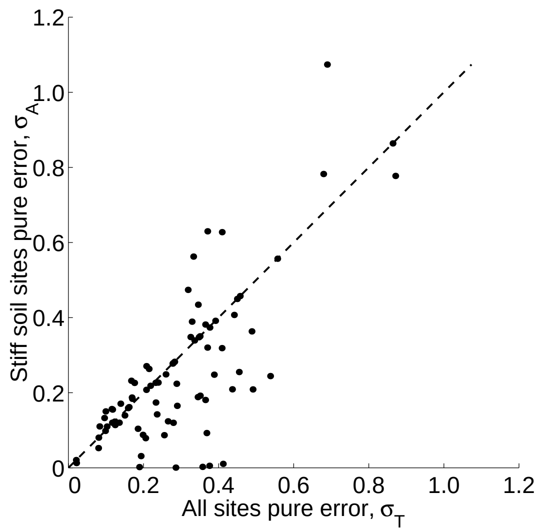

(d) SA at $T = 1.0$s.

Fig. 8.10: Pure error of logarithm of recorded ground motion for stiff soil sites, σ_A, against pure error for all sites, σ_T, for horizontal peak ground acceleration and horizontal spectral acceleration at $T = 0.2$, 0.5 and 1.0 s. Dashed line is $\sigma_A = \sigma_T$ and so if points plot below this line there is a reduction in pure error due to the inclusion of crude site classifications.

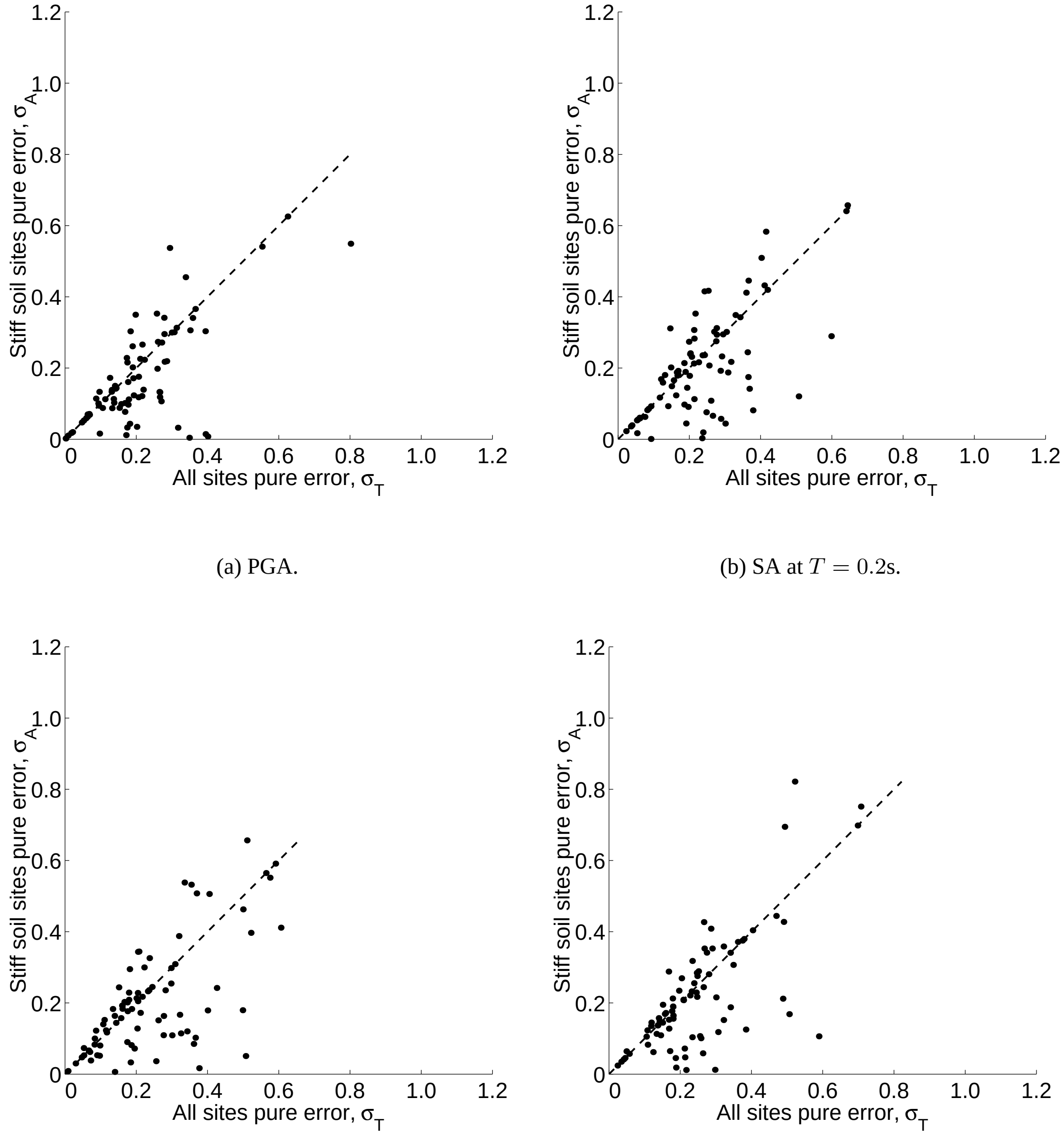

(a) PGA.

(b) SA at $T = 0.2$s.

(c) SA at $T = 0.5$s.

(d) SA at $T = 1.0$s.

Fig. 8.11: Pure error of logarithm of recorded ground motion for stiff soil sites, σ_A, against pure error for all sites, σ_T, for vertical peak ground acceleration and vertical spectral acceleration at $T = 0.2$, 0.5 and $1.0\,$s. Dashed line is $\sigma_A = \sigma_T$ and so if points plot below this line there is a reduction in pure error due to the inclusion of crude site classifications.

attenuation relations is not because the soil does not affect the ground motion but because of the crude site categories currently used. Better characterisation of the local site conditions needs to be used if the uncertainty in attenuation relations is to be significantly reduced. As a consequence reliable geotechnical parameters of the local site conditions are required which are not available for many accelerograph stations.

8.3.5 Previous studies

Abrahamson (1988) assumes that the variations in PGAs observed across the SMART 1 array are due to near-receiver scattering. This assumption is made because the source, travel-path and local site conditions for records in the dense array are almost equal and therefore the variation cannot be attributed to these effects. Abrahamson (1988) refers to this source as 'inherent' uncertainty which cannot be reduced through better modelling. This 'inherent' uncertainty ranges from a factor of 1.43 for $M = 4$ to 1.19 for $M = 7.8$ and so is much less than the observed uncertainty found here. Therefore the uncertainty in attenuation relations can be significantly reduced through better modelling of the source, travel-path and local site conditions. Abrahamson (1988) deals only with PGA which is a short period measure and hence is more likely to be affected by near-receiver scattering than longer period measures, therefore 'inherent' uncertainty of longer period ground motions is likely to be lower than for PGA.

McCann Jr. & Boore (1983) study ground motions from the San Fernando earthquake within three circles of $0.5\,\mathrm{km}$ radius, to assess uncertainty due entirely to local site effects, including those of the buildings, and find a standard deviation equivalent to a factor of up to 1.3 for PGA. Therefore the uncertainties in predictions made using PGA attenuation relations could be reduced by a factor of about 1.3 by accurately modelling local site effects. However, Lee *et al.* (1998) examine the residuals from attenuation relationships to find the relative contribution to the scatter of source/path and site effects. They find that for PGA (a high frequency measure) the possible reduction from using a more sophisticated method to characterise the site rather than simple soil/rock categories is small (about a 4% reduction in standard deviation). They find that for spectral acceleration at $3\,\mathrm{s}$ period and 5% damping the reduction is greater (about 11% in standard deviation). This shows that site effects are not that important in reducing the standard deviation although they note that this is for a small sample in southern California.

8.3.6 Weighted least-squares method

Pure error analysis gives estimates of the uncertainty in the ground motion which can be used in the weighting matrix for regression analysis rather than using, as Campbell (1997) does, a weighting matrix based on how many records occurred in a particular distance range. Weighting the regression analysis in this way should remove unwanted trends in the residuals (the recorded minus the predicted ground motion) (e.g. Draper & Smith, 1981, pp. 112–115).

8.3.7 Conclusions

The main conclusions from this work are given below.

- The hypothesis in almost all attenuation relations that the error is proportional to the size of the ground motion cannot be rejected at the 5% significance level for both horizontal and vertical PGA and SA for 5% damping.
- There is a dependence, significant at the 5% level, of error on M_s for both horizontal and vertical PGA and SA for 5% damping; larger magnitude earthquakes are associated with smaller errors than smaller earthquakes.
- Current uncertainties in attenuation relations are about the best achievable without including more independent parameters.

Therefore to significantly reduce the standard deviation associated with attenuation relations more independent variables must be incorporated into the equation. There are three types of independent parameter: firstly those which can be known exactly before an earthquake occurs; secondly those which can be estimated before an earthquake occurs; and thirdly those which cannot be known before an earthquake occurs. If an important independent parameter cannot be measured after an earthquake or assessed before an earthquake then a proxy variable could be used instead.

The first type of variable, mainly local site conditions, can be measured at the site of interest and will not change significantly over time; these can and should be incorporated into attenuation relationships if they can be assessed reliably.

The second type of variable includes such parameters as focal mechanism and focal depth which possibly can be estimated using data from previous earthquakes in the region and seismological and geological information; these should be included in the equation if the design engineer considers a range of values for each parameter.

The third type of variable includes such factors as direction of rupture and distribution of slip along the fault which at present are impossible to predict before an earthquake occurs. If such parameters are introduced into the equation then there will be additional parametric uncertainty which represents the uncertainty in values of the model's source, path and site parameters for future earthquakes (Toro *et al.*, 1997). Therefore some modelling uncertainty will be transferred to parametric uncertainty but the total uncertainty will not change (Toro *et al.*, 1997). Including these factors into the model requires a large amount of data so that the coefficients associated with the parameters are precisely defined. The inclusion of many factors would also make the equation complex to use.

However, not including factors which are thought to have a large effect on ground motion but cannot be predicted before an earthquake will obviously lead to a large standard deviation and could also lead to biased predictions of the median ground motion. If many of the records are from a particular combination of these unmodelled *and unknown* factors then the equation should only be used for the prediction of ground motion from sources, travel-paths and sites with that combination of unmodelled *and unknown* factors. If the number of observations used to determine the equation is large enough the spread of different combinations could mean this possible bias will not occur.

All independent parameters to be included in equations for estimating future ground motions should be judged using the four criteria listed below.

Measurability How easy is the independent parameter to measure for each record in the set used for the derivation of the attenuation relation? If an independent parameter cannot be calculated for all records then its use is obviously precluded.

Reliability How reliable and accurate are the estimates of the independent parameter? This is linked to measurability. If estimates of the independent parameter are unreliable then conclusions drawn from the derived equation and estimates of future ground motion made using the equation will be associated with high uncertainty.

Usefulness How useful is the independent parameter in modelling variations in ground motions? An equation should only include those parameters which are useful in modelling the observed variations in ground motion otherwise the derived coefficients will not be stable.

Predictability How easy is the independent parameter to predict or estimate for future earthquakes? If the independent parameters included in an equation cannot be to estimated, within a narrow range, by the design engineer then modelling uncertainty is just transferred to parametric uncertainty and the total uncertainty is unchanged.

8.4 Distance measures used in attenuation relations

This section discusses the previously proposed distance metrics with respect to the four criteria given in Section 8.3.7.

Joyner & Boore (1981) state that the correct distance to use in attenuation relations is the distance from the origin of the actual wave, which produced the measurement of ground motion (for example PGA or SA), to the station but this is difficult to determine for past earthquakes and impossible to predict for future earthquakes. To overcome this difficulty ten different measures have been proposed to characterise the distance to the earthquake source:

Epicentral distance d_e: Distance to the epicentre of the earthquake, i.e. the distance to the horizontal projection of the rupture's starting point.

Hypocentral distance d_h*:* Distance to the hypocentre of the earthquake, i.e. the distance to the rupture's starting point.

Rupture centroid distance d_c*:* Distance to the centroid of the rupture.

Centre-of-energy-release distance d_E*:* Distance to a point on the fault rupture where energy considered to be concentrated (Crouse *et al.*, 1988; Crouse, 1991).

Surface projection distance (also called Joyner-Boore or fault distance) d_f*:* Distance to the surface projection of the rupture plane of the fault (Joyner & Boore, 1981); for a point within the projection $d_f = 0$.

Surface projection distance with focal depth $d_{f,h}$*:* Distance to the projection of the rupture on a plane at the focal depth.

Rupture distance (also called source or fault distance) d_r*:* Distance to rupture surface.

Seismogenic distance d_s*:* Distance to seismogenic rupture surface, assumes that the near-surface rupture in sediments is non-seismogenic (Campbell, 1997).

Elliptical distance D *or average site to rupture end distance* ASRED*:* Half sum of the distances to the extremities of the fault surface rupture (Bureau, 1978; Zhou *et al.*, 1989), if no surface rupture occurred then the projection of the top of the rupture should be used.

Equivalent hypocentral distance EHD*:* Distance from a virtual point source that provides the same energy to the site as does a finite-size fault (Ohno *et al.*, 1993). Defined by: $1/\mathrm{EHD}^2 = \sum_{i=1}^{n} M_{0,i}^2 X_i^{-2} / \sum_{i=1}^{n} M_{0,i}^2$, where n is the number of segments on the rupture plane, $M_{0,i}$ is the seismic moment density on the ith segment and X_i is the distance between ith segment and site.

Idriss (1978) splits distance measurements into two groups: those measured to a point (d_e, d_h, d_c and d_E) and those measured to a line or surface (d_f, $d_{f,h}$, d_r, d_s, D and EHD). Some of these distance measures obey inequalities: $d_f \leq d_r \leq d_s$ ($d_f = d_r$ for vertical ruptures which reach the surface and for points on the foot wall of ruptures which reach the surface) and $d_f \leq d_e \leq D$. At large distances from the source all measures become almost equal, thus at great distances which is used is unimportant.

Figure 8.12 shows the contours of equal distance using the epicentral, surface projection, rupture and elliptical distances from a fault of length $50\,\mathrm{km}$, width $20\,\mathrm{km}$, dip 30° which reached the surface, with the hypocentre at the bottom of the north eastern corner of the rupture. Only these four different distances are plotted because hypocentral, surface projection with focal depth and seismogenic distances all have similar characteristics to those contours for epicentral, surface projection and rupture distance respectively. Figure 8.12 shows the different assumptions, of how ground motion attenuates with distance, made when different distance metrics are used.

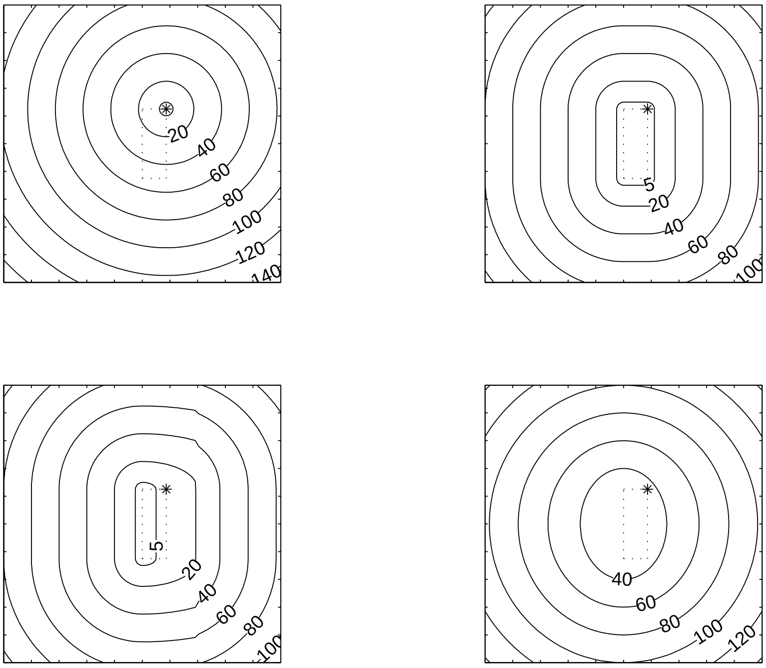

Fig. 8.12: Comparison of the contours of equal distance using four different distance measures for a fault of length $50\,\mathrm{km}$, width $20\,\mathrm{km}$, dip 30° (corresponding to an earthquake of $M_w \approx 7.0$ (Wells & Coppersmith, 1994)) which reached the surface, with the hypocentre at the bottom of the north eastern corner of the rupture. Dotted box is the surface projection of the rupture plane. Top left is for epicentral distance, top right is for surface projection distance, bottom left is for rupture distance and bottom right is for elliptical distance.

8.4.1 Epicentral distance

This is the easiest distance measure to use because the epicentre is the location information given for all earthquakes. There are two types of error in epicentre locations: absolute errors (bias) which are systematic offsets caused by large scale earth structure and pseudorandom scatter which is the scatter of locations of different earthquakes relative to each other (Pavlis, 1992). Pseudorandom scatter has a number of causes: systematic errors due to inaccurate station coordinates, network timing errors, or picking errors and inaccuracy in reading arrival times (Di Giovambattista & Barba, 1997), limited amounts of data and inadequate station distributions (Di Giovambattista & Barba, 1997), nonlinear effects because conventional earthquake location algorithms are based on a linear approximation to a set of nonlinear equations, the interaction of errors in modelling travel times with variations in the number and quality of arrivals recorded from different earthquakes and variations in how errors in modelling travel times vary with position inside the Earth (Pavlis, 1992). In a wellmaintained network accuracies due to systematic errors are negligible (Di Giovambattista & Barba, 1997).

Macroseismic determined epicentres can provide a check on instrumental determined epicentres (Ambraseys, 2001). Ambraseys (2001) calculates the average distance shift in teleseismically-determined epicentres to macroseismically-determined epicentres for 384 earthquakes with $4.0 \leq M_s \leq 6.5$ between 1918 and 1997 in the Eastern Mediterranean and the Middle East. It is found that the average shift is $61\,\mathrm{km}$ before 1940, $23\,\mathrm{km}$ between 1940 and 1965 and $13\,\mathrm{km}$ from 1965. The location errors are smaller if data from local networks and region specific velocity models are used.

Estimates of the effect of errors in epicentral locations on attenuation relations and their standard deviations are found using a Monte Carlo simulation scheme. Firstly the effect of the difference between the true and assumed epicentres on the distance associated with each record needs to be found.

Let the true and assumed epicentres be a distance ϵ apart and assume a station is a distance r from the true epicentre. Then the absolute error in the epicentral distance is given by $\mid \sqrt{r^2 - 2\epsilon r \cos\theta + \epsilon^2} - r \mid$ where θ is the angle subtended between the line from the true epicentre to the assumed epicentre and the line from the true epicentre and the station. This equation describes the distribution of errors in epicentral distance with angle and hence is used to simulated realistic errors in epicentral distances in the Monte Carlo simulation. As $r \to \infty$ the average error, if the stations are distributed evenly with θ, tends to $2\epsilon/\pi$. In fact this limiting value is reached rapidly; for example for $r = 2\epsilon$ the average error taken over $0 \leq \theta < 2\pi$ is within 1% of $2\epsilon/\pi$. Therefore if the difference between the true and assumed epicentre is $5\,\mathrm{km}$ the average error in epicentral distance is about $3.2\,\mathrm{km}$ although it will range from $0\,\mathrm{km}$ to $5\,\mathrm{km}$ for particular pairs of stations.

If it is assumed that accelerographs are distributed uniformly in the region surrounding an earthquake then the distribution of epicentral distances for the set of strong-motion records of the earthquake will follow a linear probability distribution function (p.d.f.) . As accelerographs are usually concentrated in areas of highest seismicity and are often in closely-spaced arrays the distribution is not strictly linear. However for this Monte Carlo experiment the distances are assumed to follow a linear p.d.f.

100 sets of data with $n = 20$, 50 and 100 points were randomly simulated for $\epsilon = 0\,\mathrm{km}$ (no error in epicentre), $\epsilon = 5\,\mathrm{km}$ and $\epsilon = 10\,\mathrm{km}$ using the horizontal PGA attenuation relation of Ambraseys *et al.* (1996) (standard deviation 0.25) for rock sites using $M_s = 5$ and with true epicentral distances between 0 and $50\,\mathrm{km}$. This magnitude was chosen because earthquakes of the size are effectively point sources (about $1\,\mathrm{km}$ in length (Ambraseys & Jackson, 1998)), however, the magnitude used is irrelevant to the analysis. The true epicentral distances were altered using the incorrect epicentre and θ chosen from a uniform p.d.f. between 0 and 2π. New attenuation relations

are derived using these sets of data with simulated errors in the epicentral distances assuming a ground motion model: $\log y = a_1 + a_3 \log \sqrt{d^2 + a_5^2}$, i.e. the same form as used to simulate the data without the magnitude dependence. Figure 8.13 shows the results of these experiments.

Figure 8.13 shows the dramatic effect errors in epicentral distances can have on the derived attenuation relation especially for small numbers of observations. For example, with error in the epicentre of $10\,\mathrm{km}$ and 20 records from the earthquake the predicted accelerations from the derived attenuation relations do not match the predicted accelerations from the equation used to simulate the data for distances less than about $50\,\mathrm{km}$. As the number of records used increases to 50 the derived curves match for distances greater than about $30\,\mathrm{km}$ and for 100 records the curves match for distances greater than about $15\,\mathrm{km}$. If there are few records from short distances and these distances are associated with a significant error then derived equation will not match the true variation of the ground motion with distance in the near-source distance range. The lack of near-source data even if the distances are known exactly can have a significant effect on the predicted ground motions for short distances, see Figure 8.13(a). The standard deviations of each derived attenuation relation show only a small increase compared with the standard deviation of the original equation, for example for $\epsilon = 10\,\mathrm{km}$ and $n = 20$ the average increase in the associated uncertainty due to the errors in the epicentral distances, in terms of ± 1 standard deviation, is only 4%. This Monte Carlo experiment only simulates records from one earthquake and assumes that the distribution of stations is uniform throughout the region where the earthquake occurred so the true effect of epicentral distance error is likely to be less than shown in Figure 8.13.

The use of epicentral distance in hazard analysis is for small earthquakes reasonably straightforward because easily available catalogues of previous epicentres can be used as the future sources or if line or surface source zones are used then epicentres can be distributed on these source zones.

8.4.2 Hypocentral distance

Like epicentres, hypocentres are reported for most earthquakes but accurate measures of focal depth are often difficult to obtain unless there is a good distribution of stations with distance from the source (Gubbins, 1990). Most damaging earthquakes occur within a shallow region of the crust (about the top $30\,\mathrm{km}$) and hence d_e and d_h become equal at intermediate and large distances.

Accuracy of focal depths from waveform modelling of P and SH waveforms is about $\pm 4\,\mathrm{km}$ for earthquakes with $M_s > 5.5$ but focal depths determined by routine methods could be associated with larger errors (Ambraseys, 2001). These errors in depth translate into errors in hypocentral distances for records from short distances and hence increase the standard deviation of the derived equation. Westaway & Smith (1989) assume error in hypocentral distances is $3\,\mathrm{km}$.

Since focal depth becomes less important as the size of the earthquake increases (because the

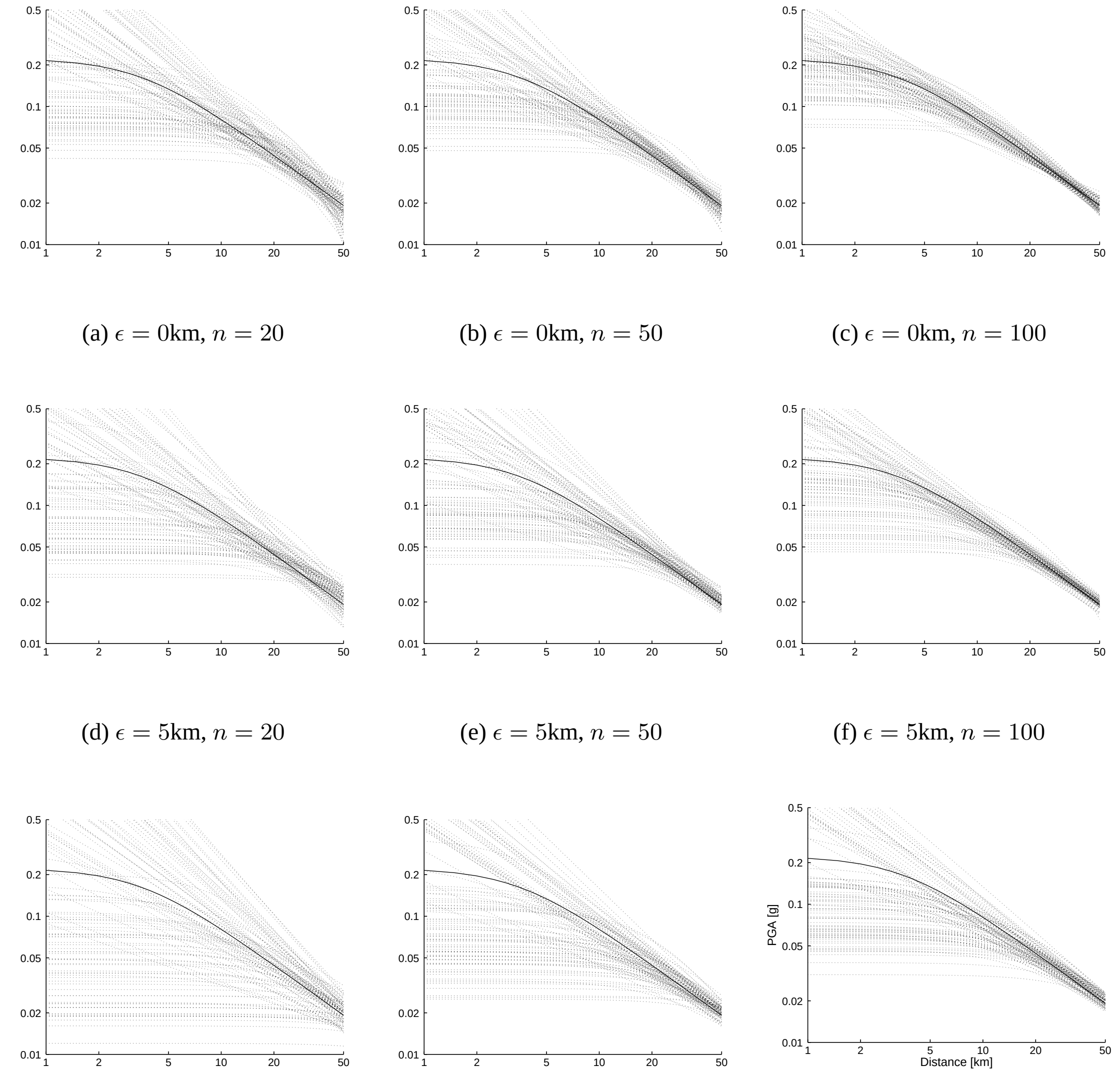

(a) $\epsilon = 0$km, $n = 20$ (b) $\epsilon = 0$km, $n = 50$ (c) $\epsilon = 0$km, $n = 100$

(d) $\epsilon = 5$km, $n = 20$ (e) $\epsilon = 5$km, $n = 50$ (f) $\epsilon = 5$km, $n = 100$

(g) $\epsilon = 10$km, $n = 20$ (h) $\epsilon = 10$km, $n = 50$ (i) $\epsilon = 10$km, $n = 100$

Fig. 8.13: Predicted horizontal accelerations using simulated sets of data, with n points, with errors in the epicentral distances of $\epsilon\,\mathrm{km}$ (dotted curves) and predicted horizontal accelerations given by equation of Ambraseys *et al.* (1996) for M_s at rock sites (solid curves).

earthquake ruptures the entire seismogenic layer) and because focal depths of small earthquakes, for which depth is important, are likely to be associated with large errors, the use of hypocentral distance in attenuation relations is unlikely to decrease the standard deviation of the final equation. This conclusion is only valid for shallow crustal earthquakes.

The use of hypocentral distance in attenuation relations also means that further information needs to be gathered, compared with distance measures that do not include depth, during hazard assessment. However, available catalogues of previous earthquakes usually contain depth information.

8.4.3 Rupture centroid distance

This distance measure requires an estimate of the dimensions of the rupture plane so that the centroid can be defined and therefore the comments made in Section 8.4.5 on the difficult of defining this plane are relevant. However, because it is measured to a point source uncertainties in defining the exact location of the rupture plane will have less of an effect on rupture centroid distances than for line or surface measures. Murray *et al.* (1996) find that the centre of the rupture plane of the Cape Mendocino earthquake (25/4/1992) is resolved to within about $4\,\mathrm{km}$.

For small magnitude earthquakes the rupture centroid distance will become equivalent to the hypocentre and hence the comments in Section 8.4.2 are relevant.

8.4.4 Centre-of-energy-release distance

This distance is similar to rupture centroid distance and so the comments in Section 8.4.3 also apply here.

Crouse *et al.* (1988) and Crouse (1991) use hypocentral distance for all earthquakes with $M < 7.5$ and the centroid of the fault plane defined by aftershocks for most larger earthquakes. If studies of source characteristics and aftershock distribution are known for an earthquake then the centre-of-energy-release is assumed to be the location of the greatest energy release.

8.4.5 Surface projection distance

For line or surface distances (EHD, D, d_f, $d_{f,h}$, d_r and d_s) and also the point distances d_c and d_E the location of the rupture plane must be known. The uncertainties and problems involved in finding rupture planes are discussed by workers developing relationships between magnitude and gross characteristics of faulting such as rupture length (e.g. Bonilla *et al.*, 1984; Wells & Coppersmith, 1994).

There are a number of ways of estimating the rupture plane of an earthquake: surface faulting, aftershock distribution, geodetic modelling, corner frequencies of seismograms, slip-history modelling using strong-motion or teleseismic data, macroseismic intensity distribution, tsunami records or information on general tectonics of area with information on fault mechanism and approximate size of rupture. Boore (1983) notes that much non-uniqueness may exist in the source properties derived from limited data, so it is important to use all available data in the inversion process. Teleseismic records complement near-source accelerograms because they contain information radiated at different take-off angles from the source region and at different frequencies.

Primary surface faulting related to tectonic rupture is the most direct way of identifying the rupture plane. However, this will only give the top edge of the plane and so if the rupture plane is not vertical other methods are required to define the bottom edge. Secondary movements, such as fractures formed by ground shaking or landslides, which look similar to primary faulting can make defining the rupture plane more difficult (Wells & Coppersmith, 1994). The location of primary surface faulting is also in doubt if the fault terminates in water or in an unmapped area (Wells & Coppersmith, 1994).

Primary surface faulting from earthquakes with $M < 6$ may not have occurred or maybe expressed as a discontinuous trace so it may be only an incomplete part of the true rupture zone. Bonilla (1988) finds that the smallest magnitude for which sudden surface faulting has been reported is about $M_L = 5$ but that for ideal conditions (fault plane at shallow depth with steep dip and a timely and detailed field examination) coseismic surface faulting of a few millimetres associated with earthquakes with $M_w \approx 3$ could be recognised by simple field methods.

If many similar sized earthquakes occur during a sequence it can be difficult to correlate surface faulting with individual earthquakes.

Aftershock distributions are often used to estimate rupture planes because aftershocks occur at the perimeter of the coseismic rupture zone. However Kanamori & Anderson (1975) state that the aftershock zone is not an unambiguous concept. The aftershock activity immediately after the main shock (hours or days) is consistent with dimensions of fault length but for small earthquakes ($M < 6$) the aftershock area tends to overestimate fault area because of uncertainty in aftershock locations and temporal expansion of aftershock area (Kanamori & Anderson, 1975). Aftershock zones many months after the earthquake give on average 75% larger areas than given by moment (Kanamori, 1977). An example of an earthquake where the aftershock locations do not correlate well with the proposed rupture plane is the Erzincan earthquake (13/3/1992, $M_w = 6.6$). Bernard *et al.* (1997a) propose a rupture plane for this earthquake based on waveform modelling which is many kilometres away from the main concentration of the aftershocks and hence distances based on the aftershock locations may be in error.

Aftershocks are not always clearly distinguishable from normal background seismicity especially if the earthquake of interest occurs during a sequence of closely located earthquakes of similar size. For example in the Mammoth Lake sequence there are four earthquakes with magnitudes about 6 that took place between 25/5 and 27/5/1980 within a small area. Hence for these main shocks relating the aftershocks to any particular one is almost impossible, see Figure 8.14.

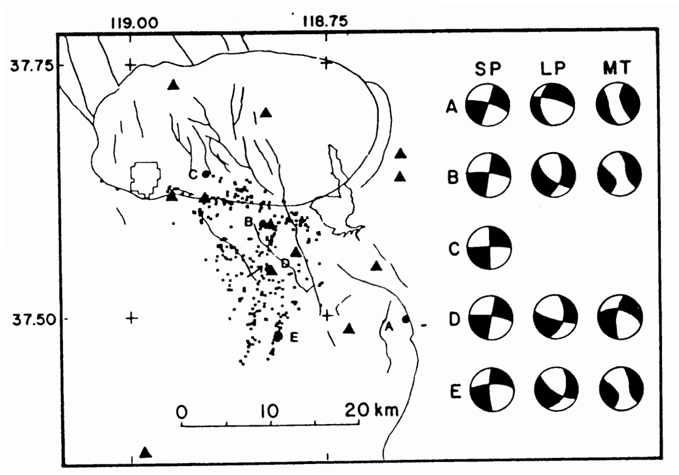

Fig. 8.14: Spatial distribution of the 352 aftershocks in the Mammoth Lakes area where four earthquakes (epicentres labelled B, C, D, E) occurred between 25/5/1980 and 27/5. Aftershocks were located to an accuracy of better than $300\,\mathrm{m}$. From Lide & Ryall (1985). Note how there is no clear pattern in the aftershocks and consequently defining rupture planes for these four earthquakes of similar magnitude is almost impossible.

Aftershocks of earthquakes with $M_w < 4.7$ are rarely the subject of detailed investigation (Wells & Coppersmith, 1994) although this is not a problem as such earthquakes have small rupture planes.

Das & Scholz (1981) find that isolated clusters of aftershocks occur off the fault plane in the normal direction due to an increase in shear stress caused by the earthquake. These aftershocks may have a cross shaped distribution and hence increase the difficulty in defining the rupture plane especially as there is always indeterminacy in defining the main and auxiliary fault planes using focal mechanisms.

The depth of aftershocks often have larger uncertainties than epicentres so it is difficult to obtain dip estimates from the aftershock distribution (Wells & Coppersmith, 1994). This is not a problem for obtaining the surface projection of the rupture plane because the projection only uses the horizontal distribution.

Aftershock distributions are sometimes difficult to correlate with the observed surface faulting (Darragh & Bolt, 1987).

Rupture planes calculated using geodetic modelling or the corner frequencies of seismograms may not represent the full extent of true rupture plane (Wells & Coppersmith, 1994).

One study which mentions the effect of uncertain faults distances on the derivation of attenuation relations is by Niazi & Bozorgnia (1992b) who investigate the attenuation of horizontal and vertical PGA during the Manjil, Iran, earthquake (20/6/1990, $M_w = 7.3$). Two possible fault traces, both about $80\,\mathrm{km}$ long, are suggested for this earthquake separated by several kilometres. Also one of the suggested fault traces includes a fault splay which affects only the distance to the closest station (at a distance of either 5, 8 or $12\,\mathrm{km}$ depending on the accepted interpretation). Using these three different sets of distances simple attenuation relations are estimated using the functional form: $\ln Y = a + d \ln(R + c)$. It is found that the coefficients, hence the predicted PGAs, are sensitive to the distances used especially in the near-field. Also the standard deviations differ; for horizontal PGA it is between $\sigma = 0.33$ (equivalent to a factor of 1.39 in terms of ± 1 standard deviation) and $\sigma = 0.44$ (factor of 1.55) and for vertical PGA it is between $\sigma = 0.27$ (factor of 1.31) and $\sigma = 0.39$ (factor of 1.48). One fault interpretation, and hence one set of distances, is associated with the smallest standard errors suggesting that it may be the correct interpretation although this is not clearly shown.

In general far-field inversions of teleseismic data for the rupture of larger earthquakes are poorly constrained even though they use recordings from stations at many different azimuths. Near-field inversions are often limited by two factors: azimuthal coverage is poor because few records are available and the dynamic range of most accelerometers is limited restricting the size of smaller shocks to be used as Green's functions (Hellweg & Boatwright, 1999). Hellweg & Boatwright (1999) are able to calculate the rupture process of two small earthquakes in the Parkfield area (14/1/1993, 20/12/1994) with moment magnitudes of only 4.6 and 4.7 using a simultaneous inversion procedure. One of the rupture planes is only about $1\,\mathrm{km} \times 1\,\mathrm{km}$. This is possible because of the large number of accelerograms (16 to 18) within $30\,\mathrm{km}$ with excellent azimuthal distribution.

The most unreliable method of finding the location of a rupture plane is to use the focal mechanism, the epicentre, an assumed length of rupture (from empirical equations relating fault length to magnitude (e.g Wells & Coppersmith, 1994)) and general tectonics of the area. This is possibly the only way to find projections for earthquakes with a number of similar sized aftershocks occurring close together in time and space with no surface faulting, for example the Mammoth Lakes sequence. However, such a technique is associated with large uncertainty, for example because the epicentre may be anywhere along the fault plane and so the error in distances for some stations could be equal to length of the rupture plane. Therefore it is probably better to use well-defined epicentral (or hypocentral) distances rather than introduce possible errors by using uncertain surface projection (or rupture) distances. The use of point source distances instead of line or surface distances is only likely to cause large differences in the derived attenuation relation in the near-field therefore unless there were near-field accelerograms recorded during the earthquake the use of point source measures will cause little error. If there are near-field accelerograms recorded then waveform modelling is possible and likely to have been done and so the rupture plane may be better known. The maximum size of earthquakes for which no adequate information is available but there are enough near-source records so that using a point source distance metric will cause significant error, is about $M_w = 6$ (corresponding to a rupture length of about $10\,\mathrm{km}$).

If Wells & Coppersmith (1994) find a number of studies with different fault characteristics (length, width etc.) and they all are equally reliable then averages and error bounds of the obtain fault characteristics are computed. This can be done for studies such as Wells & Coppersmith (1994) because it deals with scalar quantities but an 'average' rupture plane, which is a surface, cannot be defined. Therefore a single rupture plane, from one study, needs to be assumed for an earthquake leading to one set of surface projection distances. These distances will be associated with an unknown uncertainty.

Below the Aigion earthquake (15/6/1995) is used as a case study to investigate the problem of defining the rupture plane of earthquakes on attenuation relations. There are a large number of published studies on surface faulting, aftershocks, GPS measurements and waveform-modelling and hence the uncertainty in distances can be estimated. Most earthquakes have not been studied to the same extent and so the uncertainty in distances is unknown.

Aigion (also called Aigio, Egion, Aegion and Egio) earthquake (15/6/1995, $M_w = 6.5$)

The normal faulting Aigion earthquake occurred in the Gulf of Corinth, Greece, on 15th June 1995 and the location of the rupture plane has been the subject of much debate. The interpretations of the available data have lead to wide variations in the location of the source.

Koukouvelas & Doutsos (1996) measured coseismic displacements (up to $3\,\mathrm{cm}$) along $7.2\,\mathrm{km}$ of the Aigion fault along three segments (Agios Konstantinos, Aigion and Stafidalona) and assumed this was mainly the result of the mainshock although there were many large aftershocks which occurred before and during the survey. They measured the average slope of the fault escarpment as $37°$. Three networks were installed across the fault after the earthquake to measure the afterslip which showed continuous uplift of the foot wall block and subsidence of the hanging wall block as is expected for normal faulting earthquakes. Using Figure 3 of Koukouvelas & Doutsos (1996) the locations of the three fault segments were digitised, a dip of $37°$ was assumed from the geology and a width of $17\,\mathrm{km}$ was used so that the horizontal projection of the fault reached northwards to the same latitude as the epicentre of the earthquake. The strike of the mapped surface rupture means that it is impossible for the derived surface projection to include the epicentre; this obviously casts doubt as to the validity of this rupture plane location. Table 8.2 gives the fault characteristics of the proposed rupture plane, Figure 8.17 shows this fault projection and Table 8.3 gives the calculated surface projection distances for the accelerograph stations which recorded this earthquake using this projection.

Using the calculated focal mechanism of the earthquake which gives a dip of 20–$25°$, GPS and

SAR data Lekkas *et al.* (1998) conclude that the earthquake occurred on a low-angle detachment fault beneath the Gulf of Corinth. However, they believe that the fault slip propagated towards the surface via two steeper (dips about $60°$), parallel to each other, E-W trending faults, that merged with the detachment zone at depth. The first one may have released the higher amount of energy and develops offshore just north of Cape Gyftissa and the second is the Aigion fault. Using their Figures 3 and 1 the location of these suggested rupture planes are estimated [3] (see Table 8.2 and Figure 8.17) and the surface projection distances calculated (see Table 8.3).

Tselentis *et al.* (1997) located 293 aftershocks of the Aigion earthquake using high-quality data from nine vertical short-period seismometers and one three-component seismometer of the Seismological Network of the University of Patras (PATNET). Average errors in the horizontal locations and depths are $\pm 2.1\,\mathrm{km}$ and $\pm 2.6\,\mathrm{km}$ respectively. They conclude that the distribution of the aftershocks does not immediately suggest a rupture plane but rather defines a volume of size $15 \times 35 \times 20\,\mathrm{km}$ (see Figure 8.15). However, they believe that the Eliki fault ruptured during the main earthquake (see Figure 8.15) although the aftershocks do not match its location well. The location of this suggested rupture plane is estimated using Figure 4 and 5 of Tselentis *et al.* (1997) although this is difficult to do given the lack of a clear pattern in the aftershock locations. The area of highest concentration of aftershocks was used to define the eastern and western edges of the suggested rupture plane and the dip and width of the two parts of the suggested rupture plane were measured from Figure 5(a) of Tselentis *et al.* (1997). Table 8.2 gives the required fault characteristics of the proposed rupture plane, Figure 8.17 shows the surface projection of the rupture plane suggested by Tselentis *et al.* (1997) and Table 8.3 gives the calculated surface projection distances using this rupture plane.

A detail study using aftershock locations, an investigation of the surface breaks, inversion of teleseismic P and SH waveforms, mainshock relocation, GPS surveying and SAR interferogram modelling was undertaken by Bernard *et al.* (1997b) to find this earthquake's rupture plane. They conclude that because they did not find surface breaks along the entire Aigion fault and that the clearest ground displacements occur in relatively flat areas filled with sediment that the observed surface breaks may be of non-tectonic origin caused by the strong ground motions. The seismic network of 10 vertical and 10 three-component digital seismometers which they installed three days after the mainshock recorded thousands of aftershocks. The 800 best located aftershocks from 22 to 28 June with standard horizontal and vertical errors less than $1\,\mathrm{km}$ are shown in Figure 8.16. When they compare their locations with Tselentis *et al.* (1997) they find a systemic shift to the NE because Tselentis *et al.* (1997) used records from stations outside the aftershock zone which lead to a systematic bias. They used 35 geodetic points from the Corinth GPS network to measure

[3] Since their Figure 3 is an approximate block diagram there was some difficulty in defining the location of the different faults exactly.

Tab. 8.2: Fault plane characteristics from four different studies on the Aigion earthquake (15/6/1995). Characteristics given are latitude and longitude of the two ends of the top of each fault segment (fault dips to right as go from first to second point), the dip angle (δ), the width of the fault segment (in plane of fault), W, and the depth to the top of fault segment, h, (not used for computing surface projection distance).

Reference	Lat. 1	Long. 1	Lat. 2	Long. 2	δ	W (km)	h (km)
Koukouvelas & Doutsos (1996)	38.254	22.119	38.256	22.091	37	17	0
	38.255	22.092	38.258	22.061	37	17	0
	38.258	22.060	38.264	22.026	37	17	0
Lekkas *et al.* (1998)	38.225	22.223	38.275	22.028	60	6	0
	38.273	22.225	38.305	22.044	60	7	0
	38.251	22.232	38.301	22.037	25	14	5
Tselentis *et al.* (1997)	38.207	22.079	38.286	21.905	55	17	0
	38.287	22.125	38.366	21.951	15	17	14
Bernard *et al.* (1997b)	38.272	22.314	38.292	22.135	33	9	4.5

the horizontal and vertical movement caused by the earthquake. Also a SAR interferogram was constructed to measure the mainly vertical movement. Both show little permanent displacement on the southern side of the Gulf of Corinth therefore excluding the Aigion fault as the major causative fault of the earthquake. All of these data and the waveform modelling lead Bernard *et al.* (1997b) to propose the fault model shown in Figure 8.16 as the most probable cause of the Aigion earthquake. They interpreted the distribution of the aftershocks, mainly to the west of the rupture plane, as the result of an increase in the Coulomb stress on both sides of the fault, which reaches a critical level to the west, but not to the east where the 1992 Galaxidi earthquake released the local stress. Table 8.2 gives the required fault characteristics of the proposed rupture plane, Figure 8.17 shows the surface projection of the rupture plane suggested by Bernard *et al.* (1997b) and Table 8.3 gives the calculated surface projection distances using this rupture plane.

Figure 8.17 shows the large differences which can occur between different studies in locating the causative rupture plane of an earthquake; Table 8.3 shows the large effect these differences have on the surface projection distance especially for stations close to the source. For example, the surface projection distance of Nafpaktos varies between 11 and $28\,\mathrm{km}$ depending on which proposed rupture plane is adopted and the distance associated with Patra is between 16 and $36\,\mathrm{km}$. For certain stations however, e.g. Amfissa, different proposed rupture planes do not have a large effect on the associated distance because of the location of the station. Large differences in the distances of stations close to the source because of a different choice of rupture plane has a large effect on the derived attenuation relation for a particular earthquake. However, when the set of records used comes from many earthquakes the errors in distances, even though individually large, are likely to

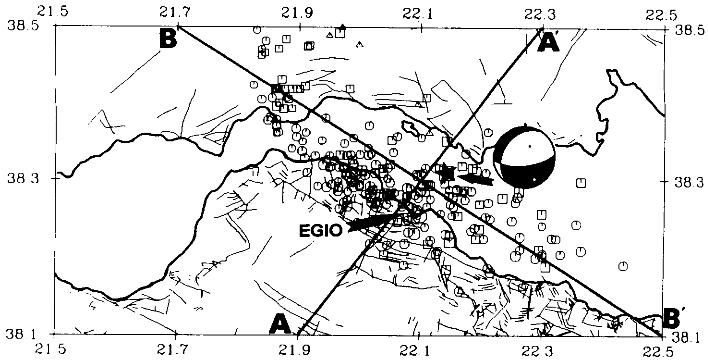

(a) Map showing located aftershocks

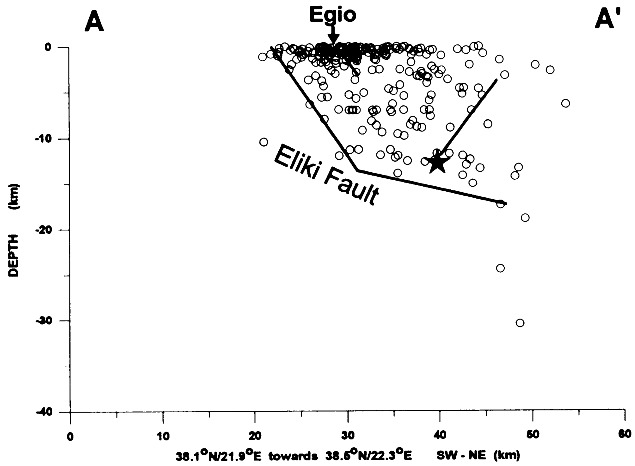

(b) SW-NE cross-section

Fig. 8.15: Spatial distribution of the 293 well-located aftershocks during the first 17 days after the Aigion earthquake (15/6/1995). On b) the rupture plane (Eliki fault) which Tselentis *et al.* (1997) believed caused the earthquake is shown. From Tselentis *et al.* (1997).

have a small effect on the equation derived but will increase the standard deviation associated with the final equation. For distant stations, e.g. Korinthos and Levadia, although absolute difference in surface projection distance are still large (up to 15 and 16 km respectively) the relative difference is less and consequently, because the logarithm of distance is usually used in attenuation relations, the effect on the derived equation and the standard deviation is less.

For this particular earthquake it is clear that the study of Bernard *et al.* (1997b) uses the most amount of data and the analysis is the most careful of all the studies conducted on this earthquake. Therefore the rupture plane derived by Bernard *et al.* (1997b) is the one which should be adopted for future studies and the required distances derived using it. However, it is not always clear which study of an earthquake is the most reliable of those published.

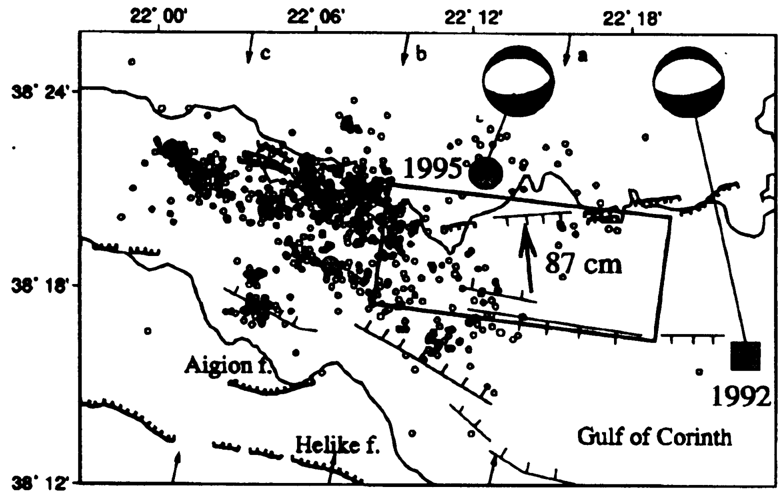

Fig. 8.16: Spatial distribution of the 800 best recorded aftershocks of the Aigion earthquake (15/6/1995) between 22/6 and 28/6/1995 and the location of the rupture plane of the final model. From Bernard *et al.* (1997b).

An example of an earthquake for which many studies have been published on the location of the rupture plane but it is less clear which of the possible rupture planes should be used is the Cape Mendocino earthquake (25/4/1992).

Cape Mendocino (also called Petrolia) earthquake (25/4/1992, $M_w = 7.2$)

The Cape Mendocino earthquake occurred on the northern coastline of California, USA, on 25th April 1992. The earthquake was on a thrust fault and many accelerograms were recorded in the near field. Several studies have been conducted to estimate the fault plane. No surface ruptures were observed (Murray *et al.*, 1996) which makes the determination of the rupture plane more difficult and the pattern of the aftershocks is complex.

Oppenheimer *et al.* (1993) use measurements of the coastal uplift resulting from the earthquake, to estimate a uniform-slip fault model; uplift being estimated from the distribution of intertidal organisms, and coseismic horizontal and vertical site displacements determined from GPS surveys. A suite of acceptable models were investigated and the one which best matched the measured displacements was chosen. They find that the model is consistent with the main shock focal mechanism, the hypocentral location, and the aftershock distribution. The modelled coastal uplift and geodetic moment are lower than those measured, which they believe could show the need for a more complex model with nonuniform slip along the rupture plane. Table 8.4 gives the required fault characteristics of the proposed rupture plane, Figure 8.18 shows this fault projection and Table 8.5

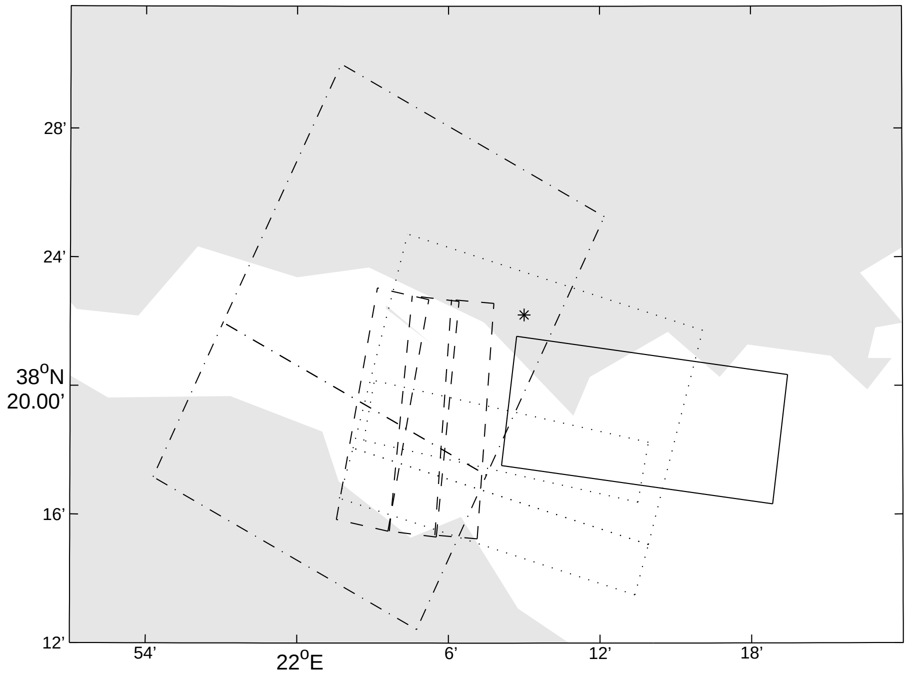

Fig. 8.17: Surface projections of the rupture plane of the Aigion earthquake (15/6/1995) from four different studies showing the large differences which can occur in locating the fault plane. Dashed is using Koukouvelas & Doutsos (1996), dotted is using Lekkas *et al.* (1998), dashed-dotted is using Tselentis *et al.* (1997) and solid is using Bernard *et al.* (1997b). Asterisk is location of the epicentre as located by Bernard *et al.* (1997b).

gives the calculated surface projection distances for the accelerograph stations which recorded this earthquake using this projection.

Murray *et al.* (1996) present a revised fault model for this earthquake using 13 horizontal and vertical displacements from GPS, 88 section-elevation differences between levelling monuments and 12 coastal uplift measurements. They correct the GPS measurements using observations of horizontal interseismic deformation derived from nine years of Geodolite trilateration measurements, a correction not made by Oppenheimer *et al.* (1993). A Monte Carlo technique was used to estimate the optimal fault geometry which had uniform slip and was rectangular and its uncertainties using the geodetic measurements. The strike and slip of the fault are only resolved to an accuracy of $\pm 20^\circ$ and there is an inverse correlation between slip and width. The moment from the geodetic inversion is about 70% of the observed seismic moment. Using all the data the optimal fault plane is Model A, see Table 8.4, Table 8.5 and Figure 8.18. However, Murray *et al.* (1996) find that the levelling data along three routes are inconsistent with the other data possibly due to unmodelled interseismic deformation or to non-tectonic disturbance of benchmarks. If this data is not used in the inversion then Model B is the optimal fault plane, see Table 8.4, Table 8.5 and Figure 8.18, which is more consistent with the seismological estimates of the fault geometry. Murray *et al.* (1996) find that

Tab. 8.3: Calculated surface projection distances for strong-motion stations which recorded the Aigion earthquake (15/6/1995) using the different proposed locations of the rupture plane.

Station	Using Koukouvelas & Doutsos (1996) d_f (km)	Using Lekkas *et al.* (1998) d_f (km)	Using Tselentis *et al.* (1997) d_f (km)	Using Bernard *et al.* (1997b) d_f (km)
Aigion	1	1	0	7
Amfissa	28	21	20	22
Korinthos	80	70	81	66
Levadia	66	54	59	50
Mornos Dam	17	14	7	19
Nafpaktos	19	20	11	28
Patra	26	26	16	36

Tab. 8.4: Fault plane characteristics from four different studies on the Cape Mendocino earthquake (25/4/1992). Characteristics given are latitude and longitude of the two ends of the top of each fault segment (fault dips to right as go from first to second point), the dip angle (δ), the width of the fault segment (in plane of fault), W, and the depth to the top of fault segment, h, (not used for computing surface projection distance).

Reference	Lat. 1	Long. 1	Lat. 2	Long. 2	δ	W (km)	h (km)
Oppenheimer *et al.* (1993)	40.271	-124.380	40.462	-124.427	12	16	6.3
Murray *et al.* (1996) (Model A)	40.328	-124.469	40.444	-124.408	28	15.2	1.5
Murray *et al.* (1996) (Model B)	40.302	-124.436	40.434	-124.461	27	18.8	1.5
Oglesby & Archuleta (1997)	40.216	-124.510	40.512	-124.578	14	32	4.2

the levelling data with uncertain accuracy, if valid, could provide critical information for resolving greater details of the fault geometry and slip. They also note that allowing nonuniform slip on the rupture plane may improve the fit.

An nonlinear frequency domain inversion for slip, rupture time, and rise time, using five near-source strong-motion records was conducted by Oglesby & Archuleta (1997) using the fault model given in Table 8.4. From the inversion a concentration of high slip (up to $3\,\mathrm{m}$) is found in a $12 \times 12\,\mathrm{km}$ lobe but slip of more than about $1\,\mathrm{m}$ is found over the entire fault plane. Table 8.5 gives the calculated surface projection distances using this fault plane model and Figure 8.18 shows the surface projection of this fault plane.

As Figure 8.18 and Table 8.5 show the proposed rupture planes for this earthquake differ greatly and consequently so do the surface projection distances for each station. For example the surface projection distance for Butler Valley station ranges from 37 to $53\,\mathrm{km}$ depending on the surface projection adopted and the distance of Loleta Fire Station is between 8 and $27\,\mathrm{km}$. Unlike the studies of the Aigion earthquake those of the studies of the Cape Mendocino earthquake reported

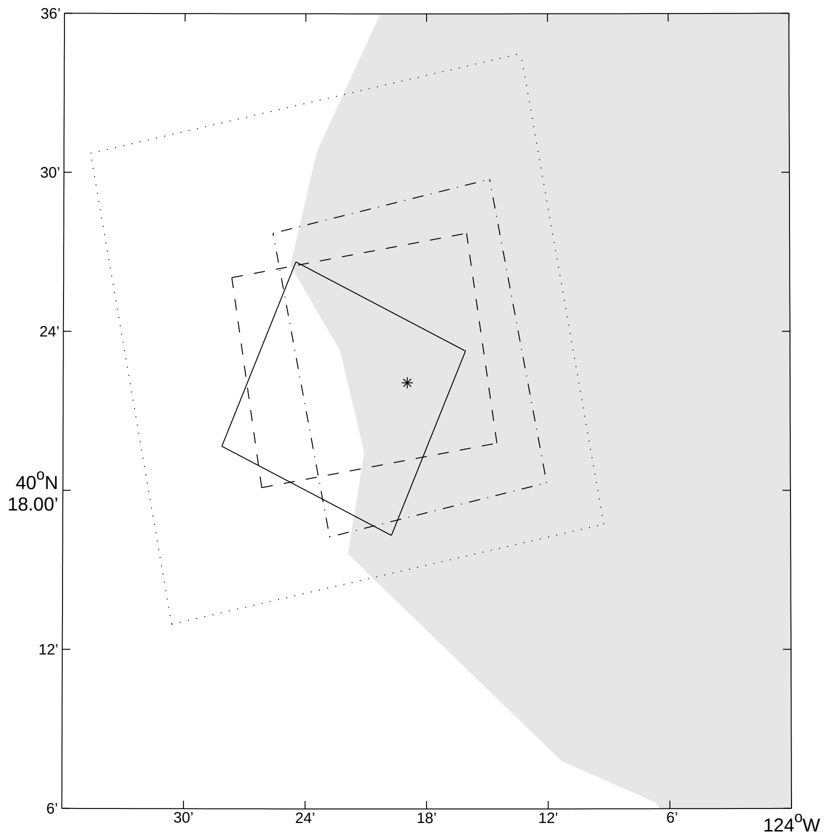

Fig. 8.18: Surface projections of the rupture plane of the Cape Mendocino earthquake (25/4/1992) from four different studies showing the large differences which can occur in locating the fault plane. Dashed is using Murray *et al.* (1996) (Model B), dotted is using Oglesby & Archuleta (1997), dashed-dotted is using Oppenheimer *et al.* (1993) and solid is using Murray *et al.* (1996) (Model A). Asterisk is location of the epicentre.

here use high-quality modelling and data to estimate the rupture plane so it is difficult to choose which proposed rupture plane, and associated distances, to use. Because the Murray *et al.* (1996) study is a revision of Oppenheimer *et al.* (1993) their estimate of the rupture plane are likely to be more accurate than those in Oppenheimer *et al.* (1993). However as Murray *et al.* (1996) state the optimal rupture plane (Model A) they find does not match the seismological data as well as the model of Oppenheimer *et al.* (1993) or their Model B. Also Oppenheimer *et al.* (1993) and Murray *et al.* (1996) state that the constraint of uniform slip across the rupture plane means that their rupture planes are possible not optimal. Oglesby & Archuleta (1997) allow for nonuniform slip, and find that the slip does vary considerably across the plane, but they state that there is possibly not enough strong-motion data for an accurate inversion. Probably none of the proposed fault planes for this earthquake are the true fault plane and to try to estimate this true rupture plane would require an inversion using all the available data (geodetic and seismological) such as has been done, for example, for the Northridge earthquake (17/1/1994) by Wald *et al.* (1996).

Tab. 8.5: Calculated surface projection distances for strong-motion stations which recorded the Cape Mendocino earthquake (25/4/1992) using the different proposed locations of the rupture plane.

Station	Using Oppenheimer *et al.* (1993) d_f (km)	Using Murray *et al.* (1996) (A) d_f (km)	Using Murray *et al.* (1996) (B) d_f (km)	Using Oglesby & Archuleta (1997) d_f (km)
Cape Mendocino	0	0	0	0
Bunker Hill	1	9	4	0
Butler Valley	44	53	48	37
Centerville Beach	7	11	10	0
College of the Redwoods	23	33	27	14
Ferndale Fire Station	9	18	13	1
Fortuna Fire Station	14	24	18	6
Loleta Fire Station	17	27	21	8
South Bay Union School	27	37	31	18
Shelter Cove — Airport	33	36	37	29

In conclusion, surface projection distances can have large uncertainties (up to $20\,\mathrm{km}$ for certain earthquakes and stations) because there are no published studies on the rupture plane or because there are several and no obvious way of deciding which is best. The errors in surface projection distances could be larger for earthquakes occurring during a sequence of similar sized shocks when aftershocks and geodetic data are likely to be difficult to use. Such earthquakes will probably have $M < 6$ and hence rupture lengths of around $10\,\mathrm{km}$, so epicentral distance will be more reliable than surface projection distance. The current practice of quoting surface projection distances to one decimal place should not be taken as meaning that the distances are accurately known to $0.1\,\mathrm{km}$.

8.4.6 Surface projection distance with focal depth

The horizontal distance part of surface projection distance with focal depth are obviously associated with the same uncertainty as surface projection distance (see Section 8.4.5) and errors in focal depths have already been discussed in Section 8.4.2.

8.4.7 Rupture distance

Estimates of this distance requires the same information as for d_f together with the depth of rupture which like focal depth is difficult to obtain for many earthquakes. The vertical resolution of aftershock locations can be poor and so it is difficult to define the dip of the fault.

Hanks & Johnson (1976) consider their rupture distances accurate to 50% but often they may not be as accurate as this.

Tab. 8.6: Calculated rupture distances for strong-motion stations which recorded the Aigion earthquake (15/6/1995) using the different proposed locations of the rupture plane.

Station	Using Koukouvelas & Doutsos (1996) d_r (km)	Using Lekkas *et al.* (1998) d_r (km)	Using Tselentis *et al.* (1997) d_r (km)	Using Bernard *et al.* (1997b) d_r (km)
Aigion	1	1	6	8
Amfissa	28	24	20	24
Korinthos	80	71	81	66
Levadia	66	55	59	51
Mornos Dam	20	18	8	21
Nafpaktos	20	21	11	29
Patra	26	27	16	36

Table 8.6 gives the rupture distances calculated using the fault characteristics given in Table 8.2 using four different proposals for the location of the rupture plane of the Aigion earthquake (15/6/1995). As with surface projection distance there is a large difference in the rupture distances of some stations calculated using the different proposed rupture planes; for example, the distance of Nafpaktos varies from 11 to $29\,\mathrm{km}$ depending on the choice of rupture plane. Table 8.7 gives the rupture distances calculated using the fault characteristics given in Table 8.4 using four different estimates of the rupture plane of the Cape Mendocino earthquake (25/4/1992). Again there are large differences in the rupture distance calculated using the different proposed planes. Such large uncertainties will have a similar effect on the standard deviation associated with attenuation relations as do uncertainties in surface projection distance (see Section 8.4.5).

For future earthquakes, rupture distance can be estimated using mapped faults although it requires that the dip and depth of the faults are known.

8.4.8 Seismogenic distance

Marone & Scholz (1998) find that well-developed faults, i.e. faults that have undergone significant net displacement and as a result contain thick zones of wear material (gouge), display an absence of seismicity in about the top $3\,\mathrm{km}$. Therefore such faults may exhibit stable slip within this zone and unstable slip below this depth where the gouge becomes consolidated. On the other hand poorly-developed faults, i.e. faults with little or no net displacement and hence no appreciable gouge zone, display seismic failure throughout the upper zone. Seismogenic distance is measured to the part of fault where unstable slip occurs.

Campbell (1997) believes that seismogenic distance can be 'reliably and easily determined for most significant earthquakes' but, in fact, it has the same difficulties in its determination as rupture distance, which has been shown can be large, plus the requirement of defining depth to the

Tab. 8.7: Calculated rupture distances for strong-motion stations which recorded the Cape Mendocino earthquake (25/4/1992) using the different proposed locations of the rupture plane.

Station	Using Oppenheimer *et al.* (1993) d_r (km)	Using Murray *et al.* (1996) (A) d_r (km)	Using Murray *et al.* (1996) (B) d_r (km)	Using Oglesby & Archuleta (1997) d_r (km)
Cape Mendocino	7	6	5	8
Bunker Hill	9	11	9	9
Butler Valley	45	55	49	39
Centerville Beach	10	12	12	8
College of the Redwoods	25	34	29	18
Ferndale Fire Station	13	20	16	11
Fortuna Fire Station	17	27	21	14
Loleta Fire Station	19	28	23	14
South Bay Union School	28	37	32	21
Shelter Cove — Airport	34	36	38	31

seismogenic layer.

There will be little difference between rupture and seismogenic distance if rupture distances are defined to a rupture plane which is defined by: aftershock distribution, because aftershocks do not occur in stable slip zones; or fault slip inversion, which will define the part of the rupture plane where most slip occurred which correlates with the unstable zone (e.g. Archuleta, 1984; Marone & Scholz, 1998). Seismogenic distances are only likely to be significantly different to rupture distances for earthquakes with surface rupture which if it occurred for a well-developed fault, such as the Imperial Valley fault, would be considered to be the result of unstable slip at depth and not the stable slip in the gouge near the surface.

Campbell (1997) provides an equation for estimating the minimum seismogenic distance possible given M_w, rupture width, dip of rupture, depth to top of seismogenic zone and depth to bottom of seismogenic zone for a future earthquake, if no other information is available. However, the use of this equation in hazard assessment means that any reduction in uncertainty brought about by the use of seismogenic distance, compared with other distance measures, will be reintroduced.

8.4.9 Elliptical distance

No measurements of the width or depth of rupture are needed so elliptical distance has less uncertainty than either surface projection, rupture or seismogenic distances.

One consequence of using elliptical distance is that it automatically models near-field flattening of the attenuation curves without needing an equivalent depth term. For large magnitudes this flat area increases in size and elliptical distance use forces a nonlinear increase in acceleration with increase in magnitude. The consequence of using this distance is that the magnitude dependent terms including in the decay part of attenuation equations by some authors (e.g. Campbell, 1981) do not need to be included separately. Consider a vertical fault of length L and a site a perpendicular distance d from the middle of the fault. Then the surface projection distance would be d and would be independent of L (and hence magnitude) but the elliptical distance would be, $D = \sqrt{d^2 + (L/2)^2}$. Since L is related to the magnitude, M, for example through an equation: $\ln L = a + bM$, then have $D = \sqrt{d^2 + k \exp cM}$. This form of distance dependence is similar to that proposed by Campbell (1997).

As elliptical distance requires only the ends of a fault to be located it is easier to estimate for future earthquakes occurring along defined surface faults.

*8.4.10 Equivalent Hypocentral Distance (*EHD*)*

A recent distance metric which includes the effects of fault size, fault geometry and inhomogeneous slip distribution is Equivalent Hypocentral Distance (EHD) (Ohno *et al.*, 1993). Ohno *et al.* (1996), Kawano *et al.* (2000) and Si & Midorikawa (2000) use EHD to derive their attenuation equations.

To calculate EHD reliably requires much more information about an earthquake than other distance metrics used in attenuation equations, namely it needs the distribution of displacement on the fault plane (assuming that the source time function is the same for all small segments on the fault plane) (Ohno *et al.*, 1993). For large ($M \gtrsim 6.5$), well recorded earthquakes maps of such distributions are being increasingly produced and published although for the same earthquake there are occasionally many different interpretations of the rupture for the same earthquake.

For certain simple distributions of displacement along vertical faults there exist analytical solutions for EHD; these solutions are presented here to display the effect of different distributions of slip along a fault.

Equivalent Hypocentral Distance, d_q, is defined by:

$$\frac{1}{d_q^2} = \frac{\sum_{i=1}^{n} \frac{M_{0i}^2}{d_i^2}}{\sum_{i=1}^{n} M_{0i}^2};$$

where n is the number of segments that the fault is broken up into. In the limit as $n \to \infty$ these summations become integrals, over the rupture plane S, therefore have:

$$\frac{1}{d_q^2} = \frac{\int^S \frac{M^2}{d^2}\,\mathrm{d}S}{\int^S M^2\,\mathrm{d}S}.$$

Assume a line fault at depth, z', from $y = 0$ to $y = L$ with a seismic moment function, $M(y)$, and assume a station at $(x', y', 0)$ hence $d = \sqrt{(y - y')^2 + x'^2 + z'^2}$, then this integral becomes:

$$\frac{1}{d_q^2} = \frac{\int_0^L \frac{M(y)^2}{(y'-y)^2+x'^2+z'^2}\,\mathrm{d}y}{\int_0^L M(y)^2\,\mathrm{d}y}. \tag{8.1}$$

Assume also that the earthquake has a total seismic moment M_0, therefore:

$$\int_0^L M(y)\,\mathrm{d}y = M_0.$$

For a linear seismic moment function, i.e. $M(x) = a + by$, analytical solution of Equation 8.1 exists and hence have:

$$\begin{aligned} d_q &= \{L[(bL)^2/3 + abL + a^2]/ \\ &\quad [b^2\sqrt{x'^2+z'^2}(L - \tan^{-1}(L - y'/\sqrt{x'^2+z'^2}) + \tan^{-1}(-y'/\sqrt{x'^2+z'^2})) \\ &\quad + b(by'+a)(\ln((L-y')^2 + x'^2 + z'^2) - \ln(y'^2 + x'^2 + z'^2)) \\ &\quad + (by'+a)^2(x'^2+z'^2)^{-\frac{1}{2}}(\tan^{-1}(L - y'/\sqrt{x'^2+z'^2}) - \tan^{-1}(-y'/\sqrt{x'^2+z'^2}))]\}^{\frac{1}{2}}. \end{aligned} \tag{8.2}$$

Also have: $M_0 = L(a + bL/2)$.

For the special case $b = 0$ have $a = M_0/L$ which leads to (from Equation 8.2):

$$d_q = \left[\frac{L\sqrt{x'^2+z'^2}}{\tan^{-1}(L - y'/\sqrt{x'^2+z'^2}) - \tan^{-1}(-y'/\sqrt{x'^2+z'^2})}\right]^{\frac{1}{2}}. \tag{8.3}$$

Equation 8.3 is the same as that defined by Todorovska & Lee (1995) and by Harmsen (1997) who calls it average distance. The special case of uniform slip across line and plane sources has been investigated by Ambraseys & Srbulov (1998).

Figure 8.19 compares contours of equal EHD for uniform moment release along a horizontal line source to linearly increasing moment release along a horizontal line source.

EHD for faults with linearly increasing moment release predicts slower decay of ground motion at the end where most moment is released compared with the end where the moment release is least (Figure 8.19). As distance from the fault increases the contours of equal EHD for both uniform and linearly increasing ground motion become most circular and hence the decay of ground motion is modelled as if the energy was released from a point source. For uniform moment release the point source is at the centre of the fault and for linearly increasing moment it is near the end of the fault where most of the moment was released. This compares with surface projection distance and rupture distance where the contours of equal distance never become circular (see Figure 8.12) and so there is not one point source from which all the energy is assumed to be radiated.

Reliable determination of the fault slip that occurred during an earthquake, which is required for calculation of EHD, needs a large number of near-field accelerograms. Therefore it can only

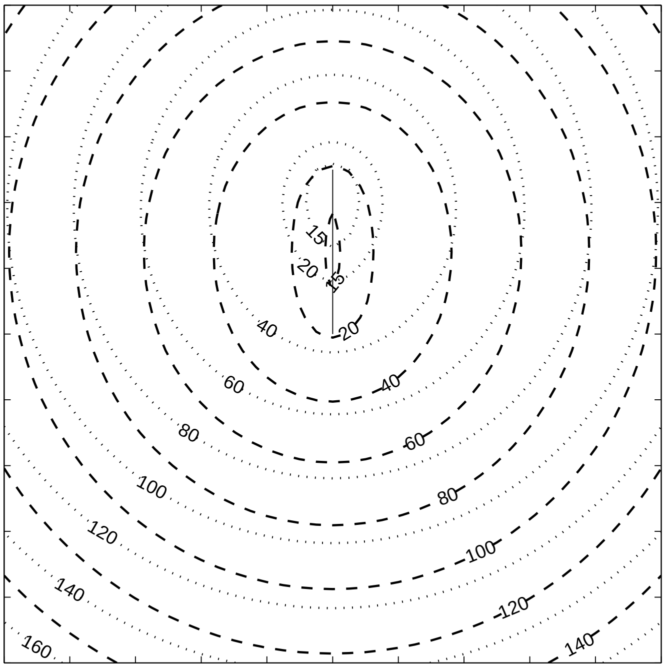

Fig. 8.19: Comparison of the contours of Equivalent Hypocentral Distance for uniform moment release (dashed curves) and linearly increasing moment release (dotted curves) for horizontal line source (solid line). Length of fault $50\,\mathrm{km}$ and $M_0 = 1.6 \times 10^{19}\,\mathrm{Nm}$.

be estimated where there is a high density of accelerographs, such as California, Japan and Taiwan. Even when such data does exists the determined fault slip is still not precisely defined as can be demonstrated by comparing some of the different inversions of fault slip for the Imperial Valley earthquake (15/10/1979). The earthquake has been, and continues to be, intensely studied because of the wealth of high-quality near-field strong-motion data and there have been many different fault slip determinations made. Figure 8.20 shows a comparison of six of these inversions. From Figure 8.20 it can be seen that although there are similarities between the inversions, such as the area of large slip (about $2\,\mathrm{m}$) in the centre of the fault, there are also significant differences. These differences in slip translate into differences in the EHDs for the stations which recorded the earthquake.

When no inversions of the fault slip have been made, either uniform slip along the entire fault is assumed or hypocentral distance is used such as was done by Ohno *et al.* (1996) for some small magnitude earthquakes and for earthquakes with limited near-source recordings.

As short period ground motions (including PGA) is caused by local variations in the fault slip (Hanks & Johnson, 1976; McGarr, 1981; Boatwright & Boore, 1982; McGarr, 1982) EHD is unlikely to improve the modelling of such motions as it is an average of the moment release over the entire fault which does not have a large effect on short period motions. Therefore any possible improvement in modelling the variation due to distance by using EHD is probably likely to be for long

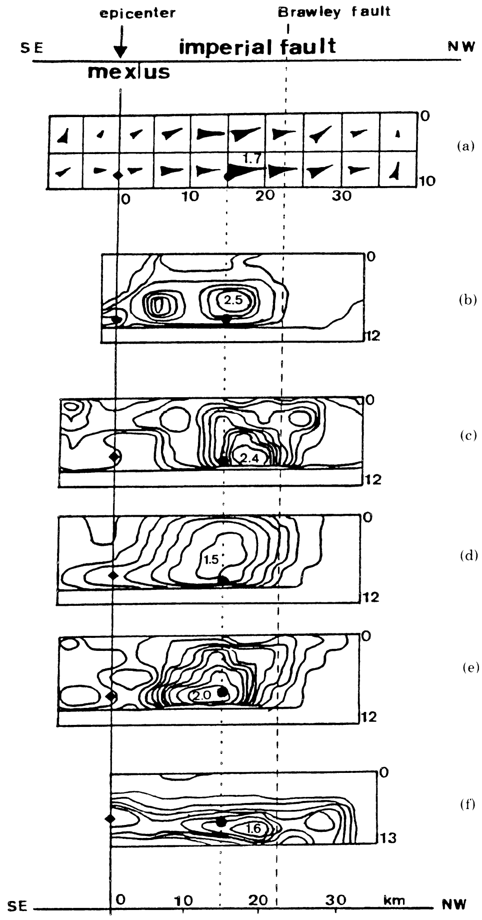

Fig. 8.20: Results of different inversions of fault slip performed for the Imperial Valley earthquake (15/10/1979), a) Olson & Apsel (1982), b) Hartzell & Helmberger (1982), c), d), e) Hartzell & Heaton (1983) and f) Archuleta (1984). From Gariel *et al.* (1990).

period ground motions which are more dependent on the moment release over the entire fault. Ohno *et al.* (1996) and Si & Midorikawa (2000) have not found significantly lower standard deviations by using EHD rather than simpler distance metrics.

EHD is obviously much more difficult to calculate than the more common distance measures such as epicentral, hypocentral, surface projection or rupture distance.

At present the estimation of the pattern of fault slip in future earthquakes is impossible therefore the use of EHD in hazard analysis is also impossible except if uniform or simple slip patterns (as illustrated above) are assumed.

For all these reasons, although EHD, compared with simpler distance metrics, is a more physically-based distance metric and possibly has the ability to more adequately model the variations in long period ground motions, its use in attenuation relations will not significantly reduce the associated uncertainty.

8.4.11 Attenuation relations derived using different distance measures

To investigate which is the most appropriate distance measure for use in attenuation studies, attenuation relations for horizontal peak ground acceleration and spectral acceleration at 0.2, 0.5 and $1.0\,\mathrm{s}$ for 5% damping were found for five well recorded and studied earthquakes using four different distance measures: surface projection distance, rupture distance, epicentral and elliptical. For all the earthquakes chosen published information about the rupture was available so reliable surface projection and rupture distances could be found. This section therefore addresses the question of usefulness (see Section 8.3.7) of the different distance measures.

When different distance measures are employed in published works the form of the attenuation equation, records used and predictor parameters are often different. Therefore it is impossible to decide which part of the results is due to using a different distance variable and which is due to other factors. Thus here everything is kept constant except the distance measure; the form of the attenuation relation used being: $\log y = b_1 + b_3 \log \sqrt{d^2 + b_5^2}$. Hence all differences are due to the distance variable.

In order to make comparison each relations was plotted separately with the actual measured values so that the accuracy of the relation can be seen. Due to the definition of elliptical distance there is a minimum distance which is possible for each earthquake, $L/2$, where L is the length of the fault, which occurs for stations halfway along the fault. This minimum distance is given for each earthquake in brackets after the minimum distance for which a PGA value is known, for example for Loma Prieta the minimum elliptical distance is $23\,\mathrm{km}$. For ruptures which do not reach the surface the minimum possible rupture distance is equal to the depth to the top of the rupture, thus the attenuation relationships using rupture distance for these equations should not be used for shorter distance. This distance is given for each earthquake in brackets after the minimum distance for which a PGA value is known, for example for Northridge this distance is $5\,\mathrm{km}$.

Tables 8.8 to 8.12 and Figures 8.21 to 8.25 show the results. $d_{\min}$ and $d_{\max}$ are the distance to the closest and furthermost station for which a PGA value was used in the derivation of the equation.

Tab. 8.8: North Palm Springs earthquake (8/7/1986, $M_w = 6.0$, $M_s = 6.13$) attenuation relations using 33 stations.

	PGA				SA(0.2 s)				SA(0.5 s)				SA(1.0 s)					
Measure	b_1	b_3	b_5	σ	b_1	b_3	b_5	σ	b_1	b_3	b_5	σ	b_1	b_3	b_5	σ	$d_{\min}$	$d_{\max}$
d_f	1.24	-0.78	3.0	0.166	1.66	-0.82	3.2	0.221	1.92	-1.20	6.7	0.267	2.00	-1.44	6.7	0.301	0	84
d_r	1.62	-1.01	0	0.163	2.03	-1.04	0	0.221	2.11	-1.31	3.9	0.269	2.13	-1.51	0	0.300	7 (7)	84
d_e	1.85	-1.11	9.7	0.187	2.14	-1.07	7.7	0.241	2.82	-1.67	14.3	0.265	2.61	-1.74	10.0	0.303	5	91
D	1.57	-0.99	0	0.156	2.01	-1.01	0	0.216	2.25	-1.37	6.5	0.264	2.39	-1.64	6.6	0.303	6 (5)	88

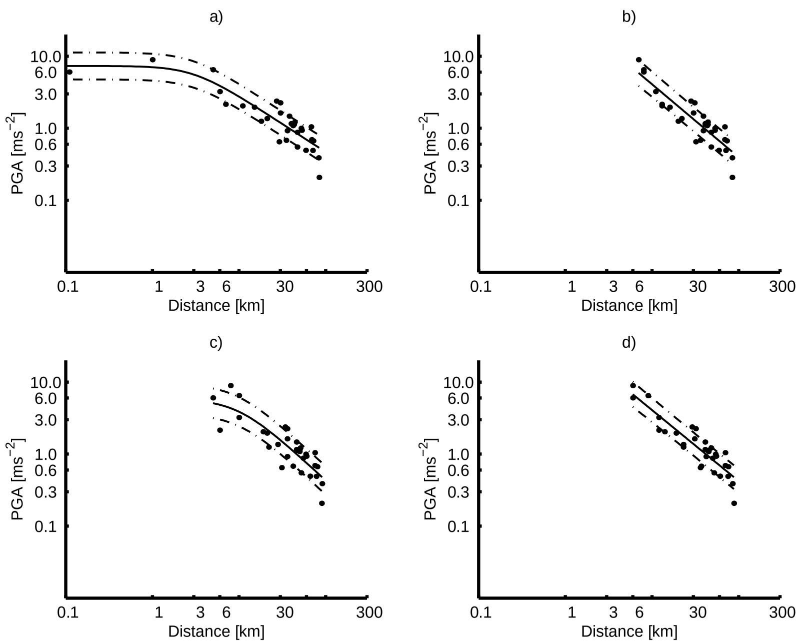

Fig. 8.21: Comparison of different North Palm Springs attenuation relations for horizontal PGA using different distance measures. Solid line is median acceleration and dash-dotted are the 16th and 84th percentiles and dots are the measured PGA values. a) surface projection distance, b) rupture distance, c) epicentral distance and d) elliptical distance.

Tab. 8.9: Imperial Valley earthquake (15/10/1979, $M_w = 6.5$, $M_s = 6.87$) attenuation relations using 35 stations.

	PGA				SA(0.2 s)				SA(0.5 s)				SA(1.0 s)					
Measure	b_1	b_3	b_5	σ	b_1	b_3	b_5	σ	b_1	b_3	b_5	σ	b_1	b_3	b_5	σ	$d_{\min}$	$d_{\max}$
d_f	1.15	-0.67	6.0	0.175	1.53	-0.64	9.2	0.226	1.66	-0.86	7.6	0.224	1.24	-0.78	4.9	0.215	0	46
d_r	1.21	-0.71	6.4	0.176	1.60	-0.68	10.2	0.227	1.72	-0.90	8.0	0.224	1.32	-0.84	5.3	0.214	1 (0)	46
d_e	3.07	-1.61	33.4	0.190	4.11	-1.94	43.0	0.211	3.11	-1.53	26.5	0.234	4.46	-2.39	40.0	0.241	2	84
D	1.97	-1.08	0	0.189	2.03	-0.87	0	0.225	2.46	-1.24	0	0.235	2.37	-1.36	0	0.237	20 (20)	66

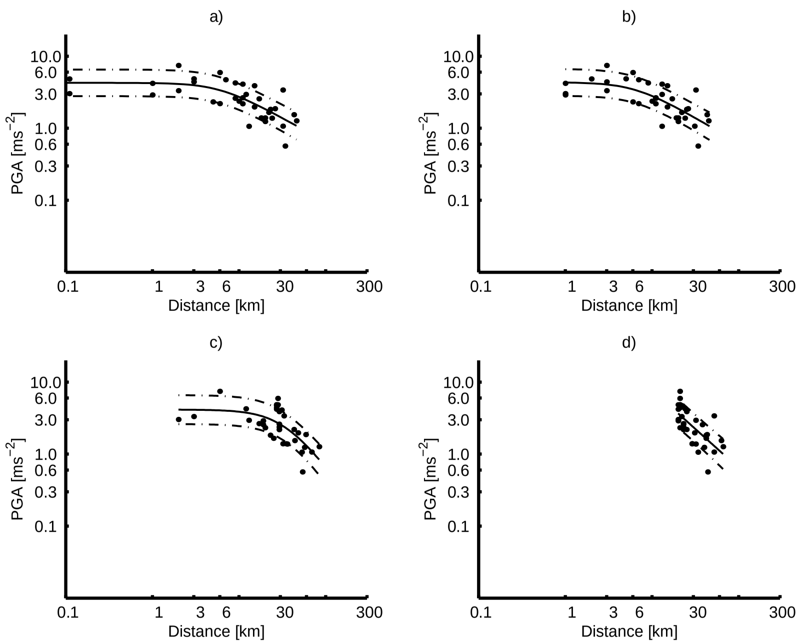

Fig. 8.22: Comparison of different Imperial Valley attenuation relations for horizontal PGA using different distance measures. Solid line is median acceleration and dash-dotted are the 16th and 84th percentiles and dots are the measured PGA values. a) surface projection distance, b) rupture distance, c) epicentral distance and d) elliptical distance.

Tab. 8.10: San Fernando earthquake (9/2/1971, $M_w = 6.6$, $M_s = 6.61$) attenuation relations using 21 stations.

	PGA				SA(0.2 s)				SA(0.5 s)				SA(1.0 s)					
Measure	b_1	b_3	b_5	σ	b_1	b_3	b_5	σ	b_1	b_3	b_5	σ	b_1	b_3	b_5	σ	$d_{\min}$	$d_{\max}$
d_f	2.24	-1.46	12.1	0.220	2.91	-1.61	19.3	0.302	2.44	-1.38	21.0	0.237	1.78	-1.19	5.0	0.164	15	215
d_r	2.28	-1.48	12.6	0.222	3.08	-1.68	22.5	0.305	2.40	-1.37	19.5	0.236	1.78	-1.19	0	0.160	17 (0)	215
d_e	3.02	-1.79	21.0	0.234	3.56	-1.87	24.5	0.308	2.99	-1.60	27.0	0.248	2.25	-1.37	0	0.180	23	228
D	3.61	-2.04	38.7	0.244	4.71	-2.36	51.0	0.318	2.94	-1.58	29.2	0.231	2.16	-1.34	10.1	0.153	17 (12)	232

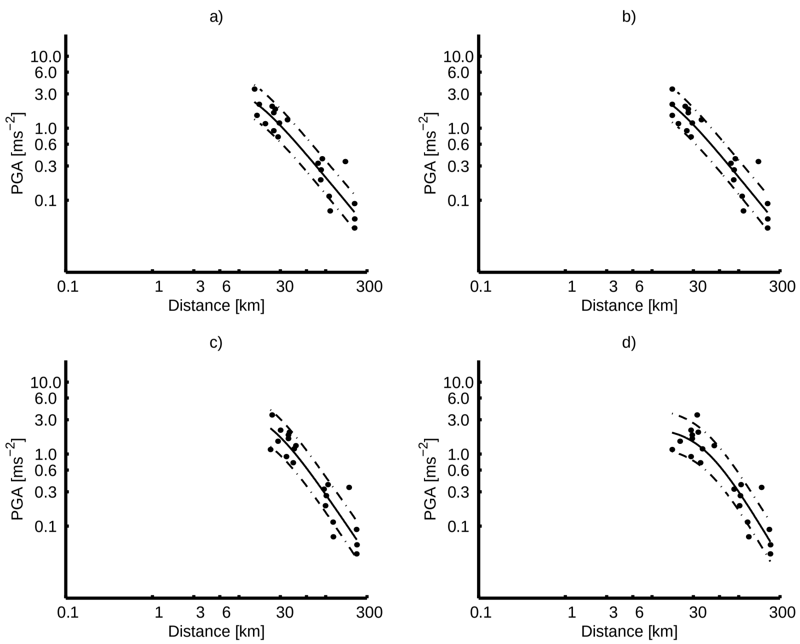

Fig. 8.23: Comparison of different San Fernando attenuation relations for horizontal PGA using different distance measures. Solid line is median acceleration and dash-dotted are the 16th and 84th percentiles and dots are the measured PGA values. a) surface projection distance, b) rupture distance, c) epicentral distance and d) elliptical distance.

Tab. 8.11: Northridge earthquake (17/1/1994, $M_w = 6.7$, $M_s = 6.81$) attenuation relations using 135 stations.

	PGA				SA(0.2 s)				SA(0.5 s)				SA(1.0 s)					
Measure	b_1	b_3	b_5	σ	b_1	b_3	b_5	σ	b_1	b_3	b_5	σ	b_1	b_3	b_5	σ	$d_{\min}$	$d_{\max}$
d_f	1.39	-0.82	5.7	0.188	1.96	-0.89	10.0	0.212	1.56	-0.70	4.0	0.217	1.29	-0.76	2.3	0.208	0	145
d_r	1.91	-1.08	8.2	0.203	2.41	-1.13	13.4	0.221	1.98	-0.93	4.5	0.231	1.89	-1.10	0	0.220	5 (5)	145
d_e	1.20	-1.11	9.5	0.193	2.39	-1.10	12.7	0.209	2.11	-0.99	6.8	0.220	2.00	-1.13	6.3	0.237	3	150
D	2.14	-1.15	9.2	0.216	2.75	-1.26	18.2	0.231	2.15	-0.98	1.8	0.242	2.24	-1.24	0	0.229	9 (9)	154

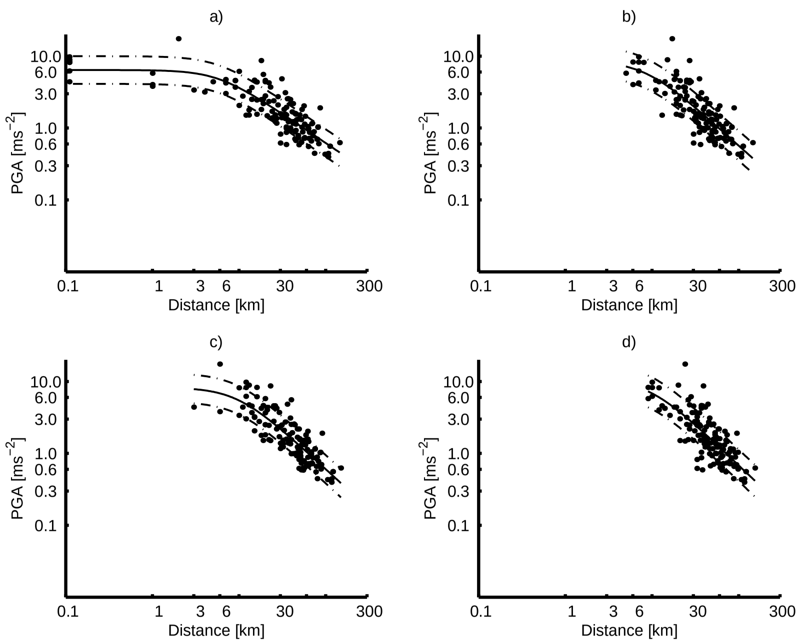

Fig. 8.24: Comparison of different Northridge attenuation relations for horizontal PGA using different distance measures. Solid line is median acceleration and dash-dotted are the 16th and 84th percentiles and dots are the measured PGA values. a) surface projection distance, b) rupture distance, c) epicentral distance and d) elliptical distance.

Tab. 8.12: Michoacán earthquake (19/9/1985, $M_w = 8.0$, $M_s = 7.9$) attenuation relations using 38 stations.

	PGA				$\mathrm{SA}(0.2\,\mathrm{s})$				$\mathrm{SA}(0.5\,\mathrm{s})$				$\mathrm{SA}(1.0\,\mathrm{s})$					
Measure	b_1	b_3	b_5	σ	b_1	b_3	b_5	σ	b_1	b_3	b_5	σ	b_1	b_3	b_5	σ	$d_{\min}$	$d_{\max}$
d_f	0.63	-0.41	9.5	0.289	10.97	-4.43	157.4	0.314	1.43	-0.48	7.1	0.250	0.77	-0.21	5.9	0.315	0	326
d_r	1.10	-0.61	18.6	0.289	10.55	-4.26	151.0	0.314	2.06	-0.76	16.3	0.254	0.99	-0.31	0	0.317	14 (6)	329
d_e	2.84	-1.24	115.5	0.293	50.49	-17.84	570.4	0.324	4.04	-1.48	99.1	0.250	1.38	-0.44	17.4	0.317	53	436
D	1.98	-0.90	0.0	0.306	7.21	-2.75	103.3	0.340	3.22	-1.15	0.0	0.284	1.21	-0.36	0.0	0.334	87 (74)	474

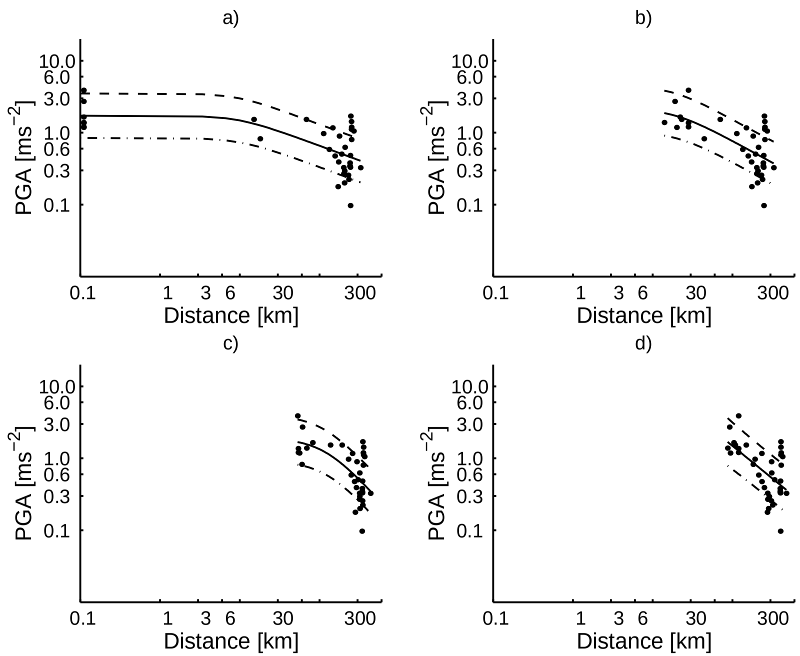

Fig. 8.25: Comparison of different Michoacán attenuation relations for horizontal PGA using different distance measures. Solid line is median acceleration and dash-dotted are the 16th and 84th percentiles and dots are the measured PGA values. a) surface projection distance, b) rupture distance, c) epicentral distance and d) elliptical distance.

Conclusions

Where the epicentre of a large earthquake is at one end of the fault, for example Imperial Valley, the attenuation equations based on epicentral distance show different characteristics to those based on surface projection and rupture distance. The b_5 term is much larger because some stations are close to the fault but are far from the epicentre so the flattened area of the curve is larger. To compensate, the decay coefficient b_3 is smaller for epicentral distance. For large earthquakes, such as Michoacán, with large rupture areas (Michoacán earthquake's rupture area is $150 \times 140\,\mathrm{km}$) this distance range of low attenuation is also large (up to distances to the surface projection of about $100\,\mathrm{km}$) and this can result in the geometric attenuation coefficient, b_3, having an unphysical value (such as -17.84 for $\mathrm{SA}(0.2\,\mathrm{s})$ and epicentral distance).

The uncertainty of the equations varies between different earthquakes with σ values between 0.17 for PGA (North Palm Springs and Imperial Valley earthquakes) and 0.29 for PGA (Michoacán earthquake). The spectral attenuation relations for different earthquakes also show a large variation in σ. For example, for $\mathrm{SA}(0.2\,\mathrm{s})$, σ varies between 0.22 (North Palm Springs and Imperial Valley earthquakes) and 0.31 (San Fernando and Michoacán earthquakes).

The study does not show clearly which distance variable is best although the equations derived using epicentral and elliptical distance have slightly higher σ values than those which used rupture or surface projection distances. Campbell (1985) claims that using epicentral or hypocentral distances leads to considerably greater scatter, but this is not shown by this experiment. It is surprising that for an earthquake with a large rupture area such as Michoacán using surface projection distance or rupture distance does not lead to a considerable lower σ than using epicentral distance. This is probably because the stations which recorded this earthquake were in two main areas, in the Guerrero accelerograph array in the epicentral region and in Mexico City in the far-field. Therefore a simple decay of ground motion with distance is observed whatever distance measure is used. The attenuation relationships based on rupture and surface projection distances have similar uncertainties and so it is impossible to conclude which is better.

The findings for epicentral distance given here are probably applicable to all point source distance measures (hypocentral distance, rupture centroid distance and centre-of-energy-release distance) although to a less extent for rupture centroid and centre-of-energy-release distance because they are measured to a point which is more representative of the rupture plane.

8.5 Effect of technique for combining horizontal components

As Appendix B.4 shows there are a large number of ways of using data from the two horizontal components of an accelerogram. The effect of each of the techniques on the amplitude of the dependent variable (PGA and SA at 5% damping) and on the associated uncertainty of the ground

Tab. 8.13: Minimum and maximum ratios of PGA values predicted using seven different methods for considering the two horizontal components and the standard deviations of the attenuation equations. The ratios are the predicted PGA using the method of combination of the row divided by the predicted PGA using the method of combination of the column.

	Vectorial	Resolved	Larger	Random	Arithmetic	Geometric	Both	σ
Vectorial	1	1.18–1.18	1.25–1.28	1.38–1.57	1.43–1.44	1.44–1.47	1.44–1.47	0.210
Resolved	0.84–0.85	1	1.06–1.08	1.18–1.32	1.21–1.23	1.22–1.25	1.22–1.25	0.213
Larger	0.78–0.80	0.93–0.94	1	1.10–1.24	1.12–1.15	1.13–1.18	1.13–1.18	0.210
Random	0.64–0.72	0.76–0.85	0.81–0.91	1	0.92–1.04	0.93–1.05	0.93–1.05	0.224
Arithmetic	0.69–0.70	0.82–0.83	0.87–0.89	0.97–1.09	1	1.01–1.02	1.01–1.02	0.210
Geometric	0.68–0.69	0.80–0.82	0.85–0.88	0.95–1.07	0.98–0.99	1	1	0.211
Both	0.68–0.69	0.80–0.82	0.85–0.88	0.95–1.07	0.98–0.99	1	1	0.224

motion prediction is investigated here.

The 180 records in the near-field set of records with both horizontal components (see Section 5.1) are used to derive a set of attenuation relations for horizontal PGA and SA at 5% damping using the seven different techniques for combining the two horizontal components. The same functional form is adopted as in Chapter 7 but no site coefficients (b_A, b_S) are derived.

For each derived equation predicted PGAs at all points within $5.8 \leq M_s \leq 7.8$ and $0 \leq d \leq 15\,\mathrm{km}$ are computed and then the ratios of these predicted values using the different methods for considering the two horizontal components are calculated. The maximum and minimum ratios and the standard deviations of the seven attenuation relations are given in Table 8.13.

Table 8.13 shows that distance and magnitude does not have a large effect on the ratio of horizontal PGA however the two horizontal components are used, at least for the limited magnitude and distance range of the near-field data considered in this study. This was also found by Westaway & Smith (1989). Therefore the current use of global ratios relating PGA combining the two horizontal components one way or combining them in another way is justified. Table 8.13 also shows that using a randomly chosen horizontal component, the arithmetic mean of the two horizontal components, the geometric mean of the two horizontal components or both horizontal components[4] gives similar predicted PGA values. The standard deviations of these horizontal PGA attenuation relations are all similar as is also shown by Sadigh *et al.* (1978) in a less comprehensive study.

Figure 8.26 shows a comparison of the standard deviations of the attenuation relations for SA for 5% damping using different methods for combining the two horizontal components. It shows that the standard deviations of the equations found using arithmetic, geometric and vectorial addition are similar and are smaller than those found using the larger or the resolved component which in turn

[4] The exact equivalence of the use of the geometric mean and the use of both horizontal components is demonstrated in Appendix B.4.

are smaller than those found using a randomly chosen component or both horizontal components. These differences are reasonably constant for the entire period range ($0.1 \leq T \leq 2$ s).

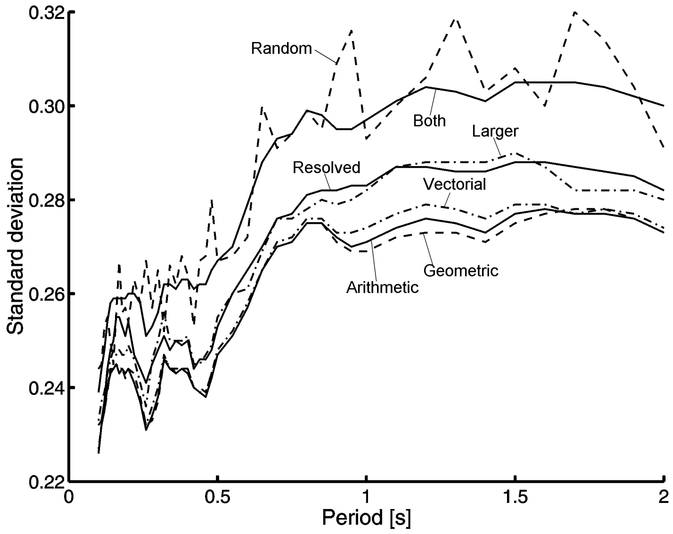

Fig. 8.26: Comparison of the standard deviations of the attenuation relations for SA for 5% damping using different methods for combining the two horizontal components.

For each derived equation predicted SAs for 5% damping at all points within $5.8 \leq M_s \leq 7.8$ and $0 \leq d \leq 15$ km are computed. The ratios of these predicted values are then calculated for each of the different methods of using the two horizontal components. The maximum and minimum ratios and the standard deviations of the seven attenuation relations are given in Table 8.14 for three periods, 0.2, 1.0 and 2.0 s.

Table 8.14 shows that period has only a small effect on the ratio of SA whatever method of combining the two horizontal components is used. Distance and magnitude also do not have a large effect on this ratio. Therefore the current use of global ratios relating SAs using different combination methods is justified. Table 8.13 also shows that using a randomly chosen horizontal component, the arithmetic mean of the two horizontal components, the geometric mean of the two horizontal components or both horizontal components gives similar predicted SA values.

8.6 Regression methods for the inclusion of site category information

8.6.1 Introduction

Two main regression methods have been proposed for using site category information within attenuation equations, these are: a) joint estimation of the site category coefficients and the distance coefficients (e.g. Boore *et al.*, 1993); or b) estimation of site category coefficients by using the residuals from the derived equation without considering soil conditions (e.g. Ambraseys *et al.*, 1996).

Method (a) requires each record to be assigned a site category whereas for method (b), because it relies on residuals, site information can be missing for some records.

Ambraseys *et al.* (1996) find that the two methods give greatly different coefficients for their PGA data; with method (a) giving much smaller coefficients than method (b). This difference requires investigation. This is the subject of this section.

8.6.2 The importance of the mean of the independent variable

Let $\boldsymbol{y} = (y_1, \ldots, y_N)^{\mathrm{T}}$ be logarithms of measured ground motions from a single earthquake at distances $\boldsymbol{d} = (d_1, \ldots, d_N)^{\mathrm{T}}$. Let y_1 to y_{n_1} be from site category 1 (the base category which is expected to be associated with the weakest ground motion; this is usually rock), y_{n_1+1} to $y_{n_1+n_2}$ from site category 2 and so on. y_{N-n_C+1} to y_N are from the final site category, so that there are C site categories with n_i records within each. Define[5] $\boldsymbol{x} = (\log\sqrt{d_1^2 + h^2}, \ldots, \log\sqrt{d_N^2 + h^2})^{\mathrm{T}}$.

Consider the attenuation relation for this single earthquake (i.e. neglecting magnitude and other source terms) which just involves distance and site category: $y = a_1 + a_2 x + a_3 S_2 + a_4 S_3 + \ldots + a_{C+1} S_C$, where $S_i = 1$ for sites within category i and 0 otherwise.

Define the set of $\boldsymbol{u}_i$ ($1 \leq i \leq C+1$) as:

$$\{\boldsymbol{u}_1, \boldsymbol{u}_2, \boldsymbol{u}_3, \boldsymbol{u}_4, \ldots \boldsymbol{u}_{C+1}\} = \left\{ \begin{pmatrix} 1 \\ \vdots \\ \vdots \\ \vdots \\ \vdots \\ \vdots \\ \vdots \\ \vdots \\ \vdots \\ \vdots \\ \vdots \\ \vdots \\ 1 \end{pmatrix}, \begin{pmatrix} x_1 \\ \vdots \\ x_{n_1} \\ x_{n_1+1} \\ \vdots \\ x_{n_1+n_2} \\ x_{n_1+n_2+1} \\ \vdots \\ x_{n_1+n_2+n_3} \\ \vdots \\ x_{N-n_C+1} \\ \vdots \\ x_N \end{pmatrix}, \begin{pmatrix} 0 \\ \vdots \\ 0 \\ 1 \\ \vdots \\ 1 \\ 0 \\ \vdots \\ \vdots \\ \vdots \\ \vdots \\ \vdots \\ 0 \end{pmatrix}, \begin{pmatrix} 0 \\ \vdots \\ \vdots \\ \vdots \\ \vdots \\ 0 \\ 1 \\ \vdots \\ 1 \\ \vdots \\ 0 \\ \vdots \\ 0 \end{pmatrix}, \ldots, \begin{pmatrix} 0 \\ \vdots \\ \vdots \\ \vdots \\ \vdots \\ \vdots \\ \vdots \\ \vdots \\ 0 \\ \vdots \\ 1 \\ \vdots \\ 1 \end{pmatrix} \right\}$$

Then the least squares solution, $\boldsymbol{a}$, of the attenuation equation is found by solving (e.g. Draper & Smith, 1981, p. 74):

[5] The transformation used at this stage does not effect the results it is done here only to relate these general results directly to attenuation relations

$$X^{\mathrm{T}} X \boldsymbol{a} = X^{\mathrm{T}} \boldsymbol{y} \tag{8.4}$$

where X is the matrix formed by the vectors, $\boldsymbol{u}_i$, defined above. Equation 8.4 then takes the general form:

$$\begin{pmatrix} N & \sum_{i=1}^{N} x_i & n_2 & \dots & n_C \\ \sum_{i=1}^{N} x_i & \sum_{i=1}^{N} x_i^2 & \sum_{i=n_1+1}^{n_1+n_2} x_i & \dots & \sum_{i=N-n_C+1}^{N} x_i \\ n_2 & \sum_{i=n_1+1}^{n_1+n_2} x_i & n_2 & \dots & 0 \\ \vdots & \vdots & \vdots & \ddots & \vdots \\ n_C & \sum_{i=N-n_C+1}^{N} x_i & 0 & \dots & n_C \end{pmatrix} \begin{pmatrix} a_1 \\ a_2 \\ a_3 \\ \vdots \\ a_{C+1} \end{pmatrix} = \begin{pmatrix} \sum_{i=1}^{N} y_i \\ \sum_{i=1}^{N} x_i y_i \\ \sum_{i=n_1+1}^{n_1+n_2} y_i \\ \vdots \\ \sum_{i=N-n_C+1}^{N} y_i \end{pmatrix} \tag{8.5}$$

Consider the special case where the mean transformed distances of the records within each site category are equal (and hence, of course, also equal to the mean transformed distance of all the records regardless of site category), i.e.:

$$\bar{x} = \frac{1}{N} \sum_{i=1}^{N} x_i = \frac{1}{n_1} \sum_{i=1}^{n_1} x_i = \ldots = \frac{1}{n_C} \sum_{N-n_C+1}^{N} x_i$$

Then Equation 8.5 simplifies to:

$$\begin{pmatrix} N & N\bar{x} & n_2 & \dots & n_C \\ N\bar{x} & \sum_{i=1}^{N} x_i^2 & n_2\bar{x} & \dots & n_C\bar{x} \\ n_2 & n_2\bar{x} & n_2 & \dots & 0 \\ \vdots & \vdots & \vdots & \ddots & \vdots \\ n_C & n_C\bar{x} & 0 & \dots & n_C \end{pmatrix} \begin{pmatrix} a_1 \\ a_2 \\ a_3 \\ \vdots \\ a_{C+1} \end{pmatrix} = \begin{pmatrix} \sum_{i=1}^{N} y_i \\ \sum_{i=1}^{N} x_i y_i \\ \sum_{i=n_1+1}^{n_1+n_2} y_i \\ \vdots \\ \sum_{i=N-n_C+1}^{N} y_i \end{pmatrix} \tag{8.6}$$

Applying Gaussian elimination to the first two lines of Equation 8.6, a_2 is found to be:

$$a_2 = \frac{N \sum_{i=1}^{N} x_i y_i - \sum_{i=1}^{N} x_i \sum_{i=1}^{N} y_i}{N \sum_{i=1}^{N} x_i^2 - (\sum_{i=1}^{N} x_i)^2} \tag{8.7}$$

This is equal to that value of a_2 found if the soil category is neglected in the first stage (i.e. the first step of method (b)). It can be shown (solving Equation 8.6 completely) that, for this special case, the two methods, (a) and (b), give exactly the same values for the other coefficients, a_1 and a_3 to a_{C+1}.

Therefore if the mean transformed distances of the records within each soil category are equal to each other then methods (a) and (b) yield exactly the same coefficients. This equality is true whatever the distribution of records with distance within the different soil categories or however many records there are in each category.

8.6.3 Numerical examples

To illustrate the above result two small artificial sets of PGA values were generated using the coefficients of Ambraseys *et al.* (1996) with $M_s = 6^6$, including random scatter introduced by the addition of a normally distributed term with mean of 0 and standard deviation of 0.25 (the error associated with Equation (5) of Ambraseys *et al.* (1996)). Two soil categories are considered: rock (R) with 14 PGA values, four from $1\,\mathrm{km}$ and 10 from $100\,\mathrm{km}$ giving a mean transformed distance of 1.59; and stiff soil (A) (using the amplification factor over rock derived by Ambraseys *et al.* (1996)) which contained 5 PGA values, three from $30\,\mathrm{km}$ and two from $60\,\mathrm{km}$ which gives a mean transformed distance of 1.60. Note that these two sets are much different in distribution and size but their mean transformed distances are almost identical. Also note that such poor distributions with distance and the small size of the sets, means that the derived coefficients will be highly uncertain and will usually differ greatly from the coefficients used to generate the data, but this is not the object of this example. One thousand sets (14 rock and 5 stiff soil values) of artificial PGA values were generated and the coefficients of the least squares equation found using method (a) and method (b). The maximum absolute difference between the coefficients derived using the two methods are extremely small, for a_1 it is 5.7×10^{-3}, for a_2 it is 3.4×10^{-3} and for a_3 3.8×10^{-5}. Therefore confirming the result obtained above.

If however the mean transformed distance of the soil categories are not equal, as in Ambraseys *et al.* (1996)[7], then differences between the coefficients derived using the two methods (a) and (b) should be expected. Note, however, that the result given above does not mean than if the average of the transformed distances for the different site categories are not the same, then the coefficients are always different.

Another pair of artificial sets of PGA values, again generated using the coefficients of Ambraseys *et al.* (1996), were created to confirm this. The rock PGA set consists of 50 values at random distances from a uniform distribution between 0 and $50\,\mathrm{km}$, hence the mean transformed distance is about 1.3, and the stiff soil PGA set consists of 50 values at random distance from a uniform distribution between 50 and $100\,\mathrm{km}$, hence the transformed distance is about 1.9. Note that these distributions are highly artificial and are not likely to occur in practice but they provide an illustration of why the mean transformed distance controls the difference between the solution using method (a) or (b). Again one thousand random sets of values were generated and the least squares curves are found using methods (a) and (b). The maximum absolute differences in coefficients found was: 0.57; 0.42; 0.22 for a_1, a_2 and a_3 respectively. Figure 8.27 shows the equations along with the artificial PGA values used.

[6] This means the coefficients used were $a_1 = -1.48 + 0.266 \times 6 = 0.116$, $a_2 = -0.922$, $a_3 = 0.117$ and $h = 3.5$

[7] In this case the mean transformed distances (using h from the paper) are rock (R): 1.56, stiff soil (A): 1.47 and soft soil (S): 1.32

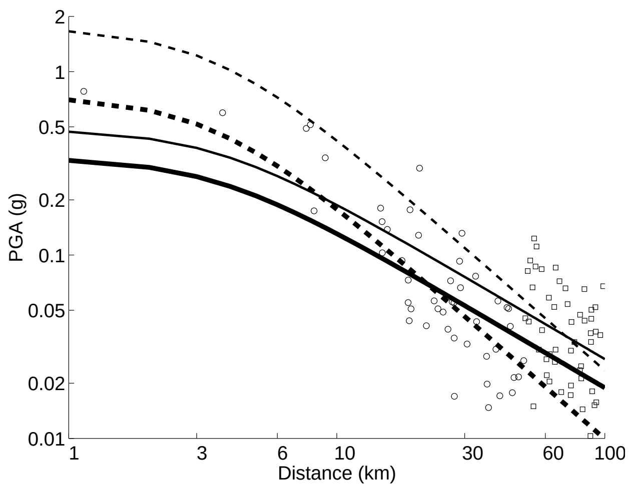

Fig. 8.27: PGA attenuation relations derived using method (a) dashed line and method (b) solid line where the thicker line is for rock and the thinner line is for stiff soil. Circles are artificial rock PGA values and squares are artificial stiff soil PGA values.

Figure 8.27 shows the great difference in predicted PGA for the two different methods; although such great difference should not occur for real data because the distribution with distance for the different soil categories should be much more equal. The decay rate derived using method (b) is lower than it should be because it is biased by the distant stiff soil values which are higher than the close rock values. Although the overall fit of the two sets of curves is similar, if the fit for the two site categories is examined individually then it is seen that the rock curve from method (b) does not pass through the actual rock data whereas the rock curve from method (a) does. This example shows the importance of the means of the transformed distance in deriving valid coefficients from regression analysis.

8.6.4 Extension for more independent parameters

An extension of this result holds for attenuation relations which include other independent parameters, such as magnitude. Then if all of the site categories have the same means of the independent variables (or transformed independent variables) methods (a) and (b) give exactly the same coefficients. This was confirmed analytically (by solving similar equations to Equation 8.5 and 8.6) and numerically using artificial sets of data.

8.6.5 Conclusions

The main conclusion of this section is that the mean of the transformed distances within each site category, governs whether the two major methods for the inclusion of site geology in attenuation relationships yield the same coefficients.

If all records used for the derivation of a attenuation relation are put into site categories then the site coefficients should be derived in the same step as the other coefficients rather than being found from the residuals of the regression; there being no advantages in using residuals (except perhaps it is easier to implement) and it could lead to incorrect distance and site coefficients. Ambraseys *et al.* (1996) use method (b) for same reasons that the two-stage method of Joyner & Boore (1981) is applied, to decouple the determination of the dependence of ground motion on different independent parameters. For soil categories this decoupling is not desirable as is shown above.

If however there is no site information for some of the records then either the records should not be used or, if they provide useful data points, then the site coefficients can be derived using the residuals of the first stage of the regression (which did not include site information) provided that the means of the independent variables for each site category are approximately equal.

The attenuation relations which do not contain coefficients to model the differences between ground motions on different sites conditions, must be checked to ensure that the data in each site category does not come from distances or magnitudes which give different means of the independent variables. Thus even if a study does not explicitly consider site conditions the results obtained may be influenced by the distribution of data with respect to site conditions.

If a nonlinear form of equation is employed then the result here are unlikely to hold exactly but probably they are roughly true and provide guidance to when method (b) can be used with confidence.

	Vectorial	Resolved	Larger	Random	Arithmetic	Geometric	Both
Vectorial	1	1.15–1.17	1.23–1.26	1.45–1.50	1.44–1.45	1.46–1.50	1.46–1.50
Resolved	0.86–0.87	1	1.06–1.08	1.25–1.30	1.23–1.26	1.25–1.30	1.25–1.30
Larger	0.80–0.81	0.92–0.94	1	1.17–1.20	1.14–1.18	1.16–1.22	1.16–1.22
Random	0.67–0.69	0.77–0.80	0.83–0.85	1	0.96–1.00	0.97–1.03	0.97–1.03
Arithmetic	0.69–0.70	0.79–0.81	0.85–0.87	1.00–1.04	1	1.02–1.03	1.02–1.03
Geometric	0.66–0.69	0.77–0.80	0.82–0.86	0.97–1.03	0.97–0.98	1	1
Both	0.66–0.69	0.77–0.80	0.82–0.86	0.97–1.03	0.97–0.98	1	1

(a) $T = 0.2$s

	Vectorial	Resolved	Larger	Random	Arithmetic	Geometric	Both
Vectorial	1	1.10–1.13	1.19–1.23	1.48–1.53	1.43–1.49	1.44–1.58	1.44–1.58
Resolved	0.88–0.91	1	1.08–1.09	1.32–1.37	1.26–1.35	1.27–1.44	1.27–1.44
Larger	0.81–0.84	0.92–0.93	1	1.22–1.27	1.16–1.25	1.17–1.33	1.17–1.33
Random	0.66–0.67	0.73–0.76	0.79–0.82	1	0.96–0.98	0.96–1.05	0.96–1.05
Arithmetic	0.67–0.70	0.74–0.79	0.80–0.86	1.02–1.05	1	1.01–1.07	1.01–1.07
Geometric	0.63–0.69	0.70–0.79	0.75–0.85	0.95–1.04	0.94–0.99	1	1
Both	0.63–0.69	0.70–0.79	0.75–0.85	0.95–1.04	0.94–0.99	1	1

(b) $T = 1.0$s

	Vectorial	Resolved	Larger	Random	Arithmetic	Geometric	Both
Vectorial	1	1.12–1.14	1.18–1.22	1.44–1.65	1.45–1.48	1.48–1.56	1.48–1.56
Resolved	0.88–0.90	1	1.05–1.08	1.29–1.45	1.27–1.32	1.30–1.39	1.30–1.39
Larger	0.82–0.85	0.92–0.95	1	1.19–1.38	1.20–1.23	1.24–1.29	1.24–1.29
Random	0.61–0.69	0.69–0.78	0.72–0.84	1	0.88–1.02	0.90–1.08	0.90–1.08
Arithmetic	0.68–0.69	0.76–0.79	0.81–0.84	0.98–1.14	1	1.02–1.06	1.02–1.06
Geometric	0.64–0.67	0.72–0.77	0.78–0.81	0.92–1.11	0.95–0.98	1	1
Both	0.64–0.67	0.72–0.77	0.78–0.81	0.92–1.11	0.95–0.98	1	1

(c) $T = 2.0$s

Tab. 8.14: Minimum and maximum ratios of SA for 5% damping values for 0.2, 1 and $2\,\mathrm{s}$ predicted using the seven different methods for considering the two horizontal components. The ratios are the predicted SA using the method of combination of the row divided by the predicted SA using the method of combination of the column.

9. ACCELEROGRAM PROCESSING TECHNIQUES

9.1 Introduction

Many authors have noted the importance of the accelerogram correction technique used in deriving attenuation relations, see Section 3.4, although the difference associated with different procedures has not been fully investigated in the past. This is the subject of this chapter, concentrating on long-period errors.

This is an important topic because different correction techniques introduce further uncertainties into ground motion prediction, using attenuation relations, since the recorded ground motion on which the equations are based may contain errors or may be biased simply because of the correction technique employed.

9.2 Errors in recorded ground motion

An important publication on the sources and sizes of errors in strong-motion records is Trifunac *et al.* (1973).

9.2.1 Digitisation errors

Many estimates of the maximum size of digitisation errors have been made, for example Schiff & Bogdanoff (1967), Trifunac *et al.* (1973), Hudson (1979), Shoja-Taheri (1980) and Levine & Beck (1990). Converting the estimates of digitisation errors from these studies into ms^{-2}, assuming the peak acceleration that can be recorded on a instrument is $10\,\mathrm{ms}^{-2}$, gives a range of errors from $0.01\,\mathrm{ms}^{-2}$ (Hudson, 1979) to $0.05\,\mathrm{ms}^{-2}$ (Schiff & Bogdanoff, 1967; Levine & Beck, 1990). Hudson (1979) demonstrates that digitisation errors closely fit a normal distribution.

Anderson & Hough (1984) find for a digital recorder (Kinemetrics DSA-1) that the Fourier amplitude spectrum of acceleration above $40\,\mathrm{Hz}$ is flat and equal to a spectral amplitude of about $0.1\,\mathrm{cms}^{-1}$ which is appropriate for digitisation process with random round-off errors at an amplitude of $\pm 0.005\,\mathrm{ms}^{-2}$ least count.

Westaway & Smith (1989) argue that there is a 20% variability in calculation of PGA due to instrumental calibration, digitisation, and in fitting of baseline through the records.

9.2.2 Long-period errors

Figure 9.1 shows the results of a test of the accuracy of hand digitisation performed by Trifunac *et al.* (1973) where each operator used the equipment for digitising strong-motion records to digitise a diagonal straight line. Figure 9.1 shows the random digitisation errors generated by the operators, discussed in Section 9.2.1, but also long-period errors, some of which are systematic and due to the digitising machine.

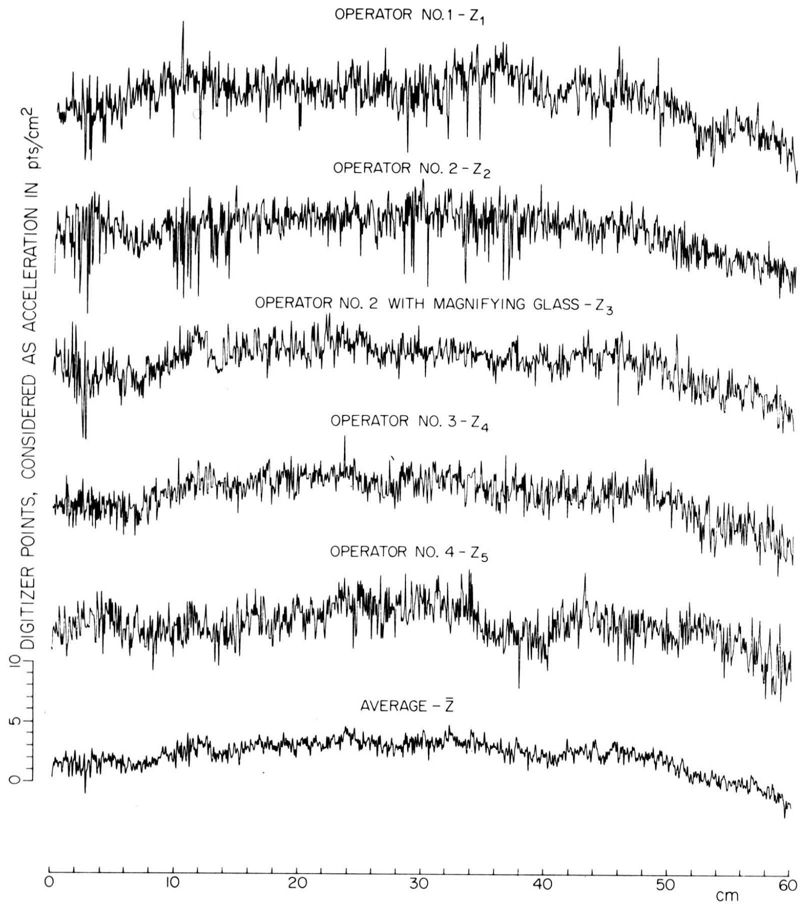

Fig. 9.1: Five independent digitisations of a straight line and their average. From Trifunac *et al.* (1973).

It is common practice to digitise the fixed traces on most analogue accelerograms and subtract them from the digitised acceleration time-histories. This removes systematic long-period errors due to the digitisation machine as well as warping and transverse play of the recording paper or film. However such a procedure does not remove the long-period errors introduced by the operator of the digitisation table and usually a low-frequency filter is applied to the time-history to remove such errors. Trifunac *et al.* (1973) conclude that accurate computed displacement curves may be obtained for periods up to about $16\,\mathrm{s}$.

Hudson (1979) says that 'permanent displacements (zero frequency components) would be practically impossible to separate from noise, so that even as estimates they would be valueless.' Schiff & Bogdanoff (1967) come to a similar conclusion but they also state that 'for a 30 second record and a sample rate of 100 samples per second (6 times the current rate), the standard deviation of the reading errors would have to be 0.02 per cent of the full scale reading to determine the net displacement to within $0.5\,\mathrm{in}$ $[1.3\,\mathrm{cm}]$, 68 per cent of the time.' Modern digitisation is often performed with a sample rate of 200 samples per second and digitisation errors are of the order 0.01 to $0.05\,\mathrm{ms}^{-2}$ (see Section 9.2.1), hence calculation of the true ground displacement may be possible.

The accuracy of long-period motions from accelerograms depends on the signal-to-noise ratio so accelerograms recorded close to the source or from large earthquakes will, relatively speaking, provide more accurate long-period data than those records from greater distances or small earthquakes (Trifunac & Lee, 1974).

The major problem with the recovery of true ground velocity and displacement is that the zero acceleration level (baseline or centreline) is not indicated on the accelerogram (Schiff & Bogdanoff, 1967; Trifunac, 1971b). The main difficulties in determining the baseline position are: a) initial part of shock is not recorded, b) final acceleration or velocity cannot be assumed to be zero, due to the presence of background noise and c) the final displacement is not known.

9.2.3 Errors in records from digital instruments

Errors in records from digital instruments come from (Chiu, 1997): non-zero background noise; instrument noise (sensitive to temperature fluctuations); slow-drifting of the baseline due to material fatigue of sensor; initial value of velocity; imperfect knowledge of the instrument response; insufficient resolution; and too low a sampling rate. The effect of imperfect instrument response and low sampling rate are usually negligible for low-frequencies.

9.3 Correction of long period errors: The recovery of true ground displacements

When an earthquake occurs the region surrounding the causative fault undergoes permanent deformation. If an accelerograph station is located in this region then it will also suffer a permanent shift in position.

Being able to recover residual displacements from strong-motion records is important for lifeline earthquake engineering because damage to pipelines can often be related to large strains which occurred during and after earthquakes. Accurate estimates of the displacement field around a fault could also enable the earthquake source to be better known. Perhaps most importantly if a near-field record is corrected assuming no permanent displacement then it no longer represents the true ground motion during the earthquake, thus affecting long period ground motion measurements such as peak ground velocity (PGV) and peak ground displacement (PGD).

9.3.1 Tilts

Many strong motion transducers are (or are equivalent to) pendulums that rotate due to acceleration of their supports (Trifunac & Todorovska, 2001). Figure 9.2 is a diagram of one of these pendulums which measures horizontal translation acceleration $\ddot{x}$.

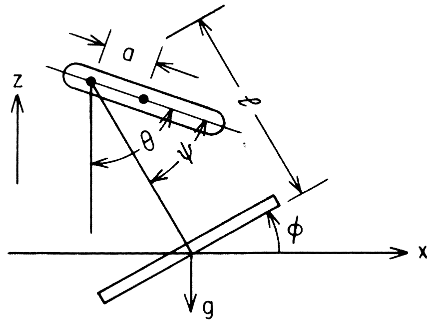

Fig. 9.2: Schematic of strong-motion transducer pendulum making angle ψ, relative to its support frame, which in turn is tilted by angle ϕ, with respect to the fixed gravity vector g. From Bradner & Reichle (1973).

The equation of motion of the system in Figure 9.2 using the small angle approximation is (Bradner & Reichle, 1973):

$$I\ddot{\theta} = -\mu a\dot{\psi} - ma\,\mathrm{g}\theta + ma\ddot{x} + mal\ddot{\phi}$$

Now the horizontal deflection of the mass $y = a\psi$ is measured by the instrument, $\theta = \phi + \psi$ and letting $2\xi\omega = \mu a/I$ and $\omega^2 = ma\,\mathrm{g}/I$ gives:

$$\ddot{y} + 2\xi\omega\dot{y} + \omega^2 y = \frac{a\omega^2}{\mathrm{g}}\ddot{x} - a\omega^2\phi + a\left(\frac{l\omega^2}{\mathrm{g}} - 1\right)\ddot{\phi}$$

The coefficients of horizontal translational acceleration, $\ddot{x}$, and the horizontal components of gravity caused by the tilt, approximately $\mathrm{g}\phi$, are identical. Therefore the displacement, x, cannot be found by double integration of the output of the accelerometer (Bradner & Reichle, 1973); Trifunac & Todorovska (2001) have recently restated this although they use a slightly different equation of motion which includes cross-axis sensitivity. The equation of motion for instruments that measure vertical accelerations is not affected by tilts of the instrument (Bradner & Reichle, 1973). If the effects of tilts on the recorded ground motion can be ignored then the recovery of the true ground displacement may be possible using an appropriate processing technique (Graizer, 1979).

Tilts of the ground occur because of: wind, pressure changes, trees, permanent deformation of the ground due to faulting, the passage of seismic waves and nonlinear soil behaviour such as lateral spreading. Wind, pressure changes and trees are all likely to have a negligible, and almost unrecordable (Mat-Isa & Usher, 1992), effect on the recorded translational ground motions. Tilts due to the accelerometer not being exactly level will not change with time and so can be removed easily from accelerograms.

Tilts caused by the permanent ground deformation due to faulting can be estimated using equations predicting the static deformation of the ground from faulting, such as was done by Hasegawa (1975). Mansinha & Smylie (1971) give equations for the deformations caused by slip along inclined, finite dip-slip and strike-slip faults and are used here. Tilts are given by: $\partial u_z/\partial x$ and $\partial u_z/\partial y$ where x and y are distances in the two horizontal directions and u_z is displacement in the vertical direction. Figure 9.3 shows moment magnitude, $M_w = 2/3 \log M_0 - 6$, versus the maximum tilt which may be expected for dip-slip faulting. The tilts, due to the permanent ground deformation, are clearly small (Figure 9.3). The accelerations due to these tilts are given by $\mathrm{g}\phi$, where ϕ is the tilt and g is acceleration due to gravity, and so are much smaller than translational accelerations in the near field and consequently can possibly be neglected when correcting near-field accelerograms. However, in the near field the ground may exhibit non-linear behaviour resulting in large tilts; such tilts perhaps cannot be ignored.

Although it is not possible to measure horizontal accelerations without also recording tilts, recording tilts without recording horizontal accelerations is reasonably easy (Mat-Isa & Usher, 1992). Mat-Isa & Usher (1992) provide details of an accelerometer which records tilts, especially wind-induced tilts. The accelerograms from this instrument can then be subtracted from the motions recorded on normal accelerometers to yield the exact translational accelerations.

9.3.2 Expected permanent displacements

Mansinha & Smylie (1971) give equations for calculating the theoretical permanent displacement at a location due to strike-slip and dip-slip faulting. These equations are for rectangular ruptures with average slip, u, along the entire fault. As both these assumptions may not be met and because a number of other factors (for example slumping, liquefaction and the top soil layer becoming detached from the bedrock) are ignored the actual displacements which occur during an earthquake can be different than those given by these equations. There exist freely-available computer programs for the calculation of coseismic displacements from much more complex faults (e.g. Gomberg & Ellis, 2001), however, because all that is required for rough verification of the recovered displacements from strong-motion records are estimated coseismic displacements given by simple models, such programs were not used in this study. For more rigorous verification of the recovered displacements more complex computer modelling should be used.

Figure 9.4 shows moment magnitude versus the maximum distance at which certain permanent displacements may be expected for vertical strike-slip faulting. From Figure 9.4 it may be seen

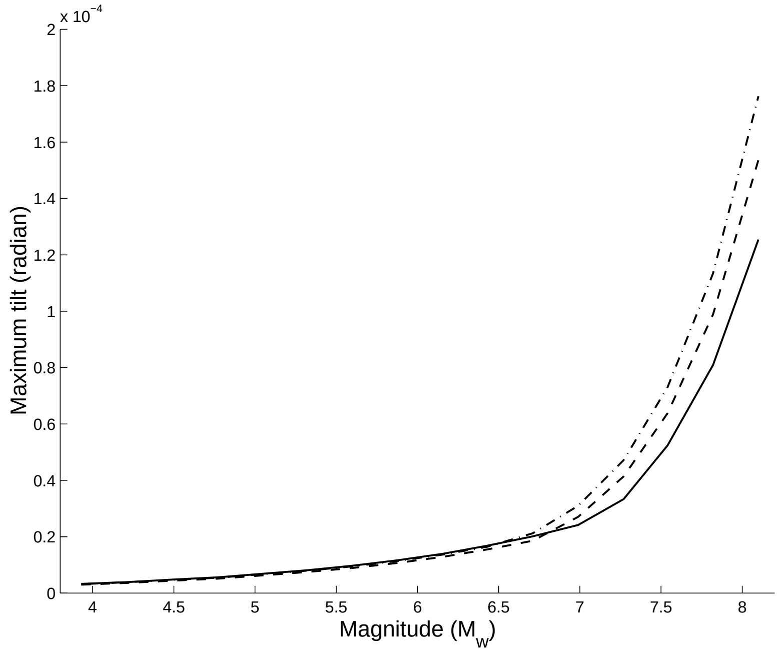

Fig. 9.3: Maximum tilts due to the permanent ground deformation caused by dip-slip faulting. Solid line is for a fault dipping at $30°$, dashed line is for a fault dipping at $45°$ and dash-dotted line is for a fault dipping at $60°$. These curves were calculated using Mansinha & Smylie (1971) dip-slip equations along a perpendicular line to the fault, on the surface, from the centre of the rupture. Parameters used were distance to top of fault, $d = 0\,\mathrm{km}$, Wells & Coppersmith (1994) equation for all faults: $\log u = -4.80 + 0.69M_w$ where u is the average displacement along the fault, area of rupture, $A = LW$ from: $M_0 = \mu Au$ (where the rigidity of the crust $\mu = 3 \times 10^{10}\,\mathrm{Nm}$) and $W = L$ for $L \leq 20/\sin(\theta)\,\mathrm{km}$ and $W = 20/\sin(\theta)\,\mathrm{km}$ for $L > 20/\sin(\theta)\,\mathrm{km}$ (assuming a depth of the seismogenic layer equal to $20\,\mathrm{km}$), where θ is the dip of the fault.

that for large earthquakes the permanent displacements are still large enough to be important for correct processing of strong-motion records even at considerable distances. For example for a $M_w = 7.5$ earthquake deformations of about $1\,\mathrm{m}$ are to be expected at distances of up to $10\,\mathrm{km}$. Therefore a technique which can recover these movements would lead to corrected records which more adequately represent the actual ground motion that occurred at the station.

Figure 9.5 and 9.6 show examples of the large permanent displacements from the near field of large earthquakes.

Anderson & Luco (1983a) find from their simulations of near-field strong ground motions that peak ground displacements in the direction parallel to the fault are due to the permanent ground deformation. Therefore failure to recover such displacements could seriously underestimate the actual displacements.

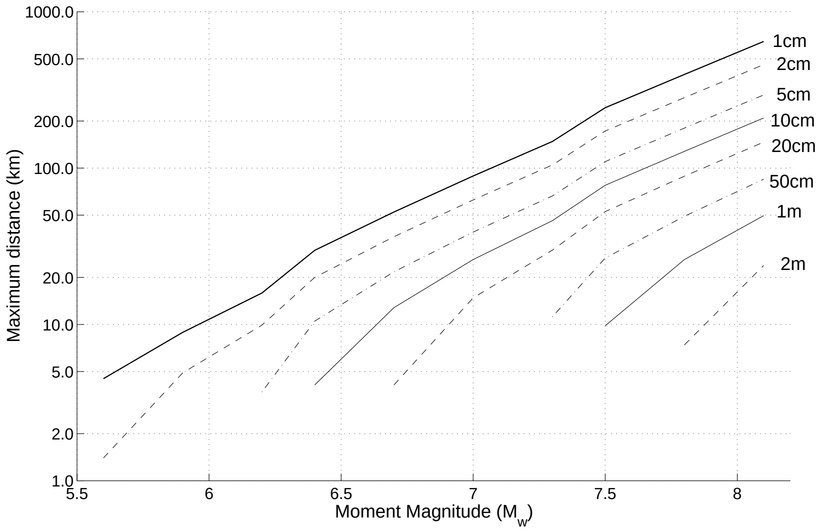

Fig. 9.4: Moment magnitude, M_w, versus maximum distance from fault which undergoes a permanent deformation of $1\,\mathrm{cm}$, $2\,\mathrm{cm}$, $5\,\mathrm{cm}$, $10\,\mathrm{cm}$, $20\,\mathrm{cm}$, $50\,\mathrm{cm}$, $1\,\mathrm{m}$ or $2\,\mathrm{m}$. These curves were calculated using Mansinha & Smylie (1971) strike-slip equations along a perpendicular line to the fault, on the surface, from the centre of the rupture. Parameters used were dip of fault, $\theta = 89.9^{\circ}$ (this was used because of a singularity in the equations if $\theta = 90^{\circ}$), distance to top of fault, $d = 0\,\mathrm{km}$, Wells & Coppersmith (1994) equation for strike-slip faults: $\log u = -6.32 + 0.90 M_w$ where u is the average displacement along the fault, area of rupture, $A = LW$ from: $M_0 = \mu A u$ (where the rigidity of the crust $\mu = 3 \times 10^{10}\,\mathrm{Nm}$) and $W = L$ for $L \leq 20\,\mathrm{km}$ and $W = 20\,\mathrm{km}$ for $L > 20\,\mathrm{km}$ (assuming a depth of the seismogenic layer equal to $20\,\mathrm{km}$).

9.3.3 Previous studies

The problem of determining the true ground displacement from accelerograms has been investigated since the 1940s, see for example Neumann (1943) and Housner (1947). These early studies were based on fitting low-degree polynomials to the acceleration or velocity traces. In Housner (1947) a long-period ($15.2\,\mathrm{s}$) sine wave needed to be subtracted from the displacement trace in order to give a realistic result.

There are some techniques which can be used if the displacement at the end of record is known (e.g. Poppitz, 1968; Trujillo & Carter, 1982; Mumme & McLaughlin, 1985; Borsoi & Ricard, 1985). For most strong-motion records the final displacement values are not known. Even if the expected displacement could be found, using equations such as those in Mansinha & Smylie (1971), because of other non-tectonic causes of permanent displacements these expected displacements are only estimates and they could be greatly in error.

Iwan *et al.* (1985) introduce a simple baseline correction method, specifically for the Kinemetrics PDR-1 digital accelerograph, which allows three parts of the acceleration baseline (that before the strong motion, that during the strong motion and that after the strong motion) to have different zero levels. This procedure was used because tests revealed an instrument anomaly, thought to be due to mechanical or electrical hysteresis within the transducer, which prevented the true ground displacement being recovered simply through integrating twice the acceleration time-history. Results obtain by Iwan *et al.* (1985) for test recordings and for one record from an aftershock of the Coalinga earthquake (8/5/1983, $M_L = 5.5$), by Anderson *et al.* (1986) and Mendez & Anderson (1991) for records of the Michoacán earthquake (19/9/1985, $M_w = 8.0$), by Boore (1999, 2001c) for records from the Chi-Chi earthquake (20/9/1999, $M_w = 7.6$) and by Boore *et al.* (2002) for records from the Hector Mine earthquake (16/10/1999, $M_w = 7.1$) show that realistic ground displacements can be obtained by this method.

One of the main polynomial correction methods was developed at the Earthquake Engineering Research Laboratory (California Institute of Technology). A parabolic acceleration baseline (cubic baseline on the velocity) is assumed which is fixed by minimizing the mean square ground velocity (Hudson *et al.*, 1969). Graizer (1979, 1980) develops a technique based on this idea. Graizer (1979, 1980) uses this method to correct the 65° component of the Parkfield-Cholame Shandon Array 2W record from the Parkfield earthquake (28/6/1966) and achieves a good match with theoretical results.

In Graizer (1982, 1983) the method is used on the accelerogram recorded at Karakyr during the Gazli earthquake (17/5/1976). Graizer can only reliably recover residual displacements for the vertical component (for the horizontal components a filtering technique is used). The movement found is $65\,\mathrm{cm}$ which compares well with geodetic measurements.

In Graizer (1985, 1988) a number of different acceleration time-histories are processed using Graizer's original method and also the more normal filtering method. Graizer (1988) states that 'another possible method for processing such records is the increase of the base-line correction polynomial degree.' Also he concludes that one correction algorithm is not applicable to all records and that the recovery of residual displacements can only be accomplished for accelerograms with a high dynamic range.

Iwan & Chen (1994), it is believed, used a similar method to this to correct the Lucerne Valley record from Landers earthquake (28/6/1992). Iwan (1994) used the same method as Iwan & Chen (1994) to correct four Northridge earthquake (17/1/1994) records. This technique was used by Akkar & Gülkan (1999) to correct the Erzincan record from the Erzincan earthquake (13/3/1992). The same technique was used by Akkar & Gülkan (2000) to correct two records of the Kocaeli earthquake (17/8/1999) (Düzce and Sakarya) and one record of the Düzce earthquake (12/11/1999)

(Düzce); realistic permanent displacements mainly in the direction of fault slip were found.

Two records (Yarimca and Sakarya) from the Kocaeli earthquake were processed using a scheme to retain the expected permanent displacement at the station by Rathje *et al.* (2000). Little information is given about the procedure used except that '[a] baseline correction was applied, but only at times beyond the static displacement.' Rathje *et al.* (2000) also note that the results from this study are preliminary but that evidence for static ground displacements in the other near-fault recordings should also be sought and addressed appropriately. Three records (Izmit, Yarimca and Sakarya) from the Kocaeli earthquake are also corrected by Safak *et al.* (2000) to retain the permanent displacements and the displacements compare well with the measured fault offsets; however no details of the procedure are given. Anderson *et al.* (2000) present the results of integrating the digital Sakarya record to yield a permanent displacement which matches well with predicted displacements found by a steady state dislocation model.

Rather than fit the baseline to the 'quiet' section of the velocity curve Vostrikov (1998) fits it to the displacement trace between 0 and T_1 and T_2 and T (the end of the record), probably because the records considered are from the far-field where no permanent displacements are expected. This adaption was also suggested in Graizer (1979). It is thought that the general ideas of Vostrikov (1998) should be applicable however the baseline was found. Vostrikov (1998) assumes the error in a seismic record is composed of two parts, a high frequency part due to digitisation and long-period 'background' oscillations which are inherent in the ground motion itself and not simply due to noise. Vostrikov (1998) finds that the long-period reconstruction error can be estimated from:

$$\delta x^* = \frac{\Delta x^*}{A_x} 10^{0.5w/T_n}; \tag{9.1}$$

where

$$\begin{aligned}
\Delta x^* &= \frac{\Delta x_0^{*2} + \Delta x_B^{*\,2}}{\Delta x_0^* + \Delta x_B^*}, \\
\Delta x_B^* &= \gamma_B A_B \left(\frac{T_B}{T_n}\right), \\
\Delta x_0^* &= \gamma_0 c_0 \left(\frac{T}{n\Delta t}\right)^{2+\nu} \Delta y \Delta t^3, \\
\text{and } T_n &= \frac{2T}{n}.
\end{aligned}$$

T is the duration of record, n the degree of the correction polynomial, Δt the digitisation time step, Δy the maximum high-frequency error due to digitisation, T_B the characteristic period of the 'background' error, A_B the amplitude of this error, A_x the maximum ground motion, and $w = T_2 - T_1$. The constants are defined using numerical experiments as $\gamma_B = 1.4$, $\nu = 0.54$, $\gamma_0 = 0.050$[1] for

[1] There is a typography error on page 158 of Vostrikov (1998).

uniformly distributed digitisation errors and $\gamma_0 = 0.024$ for normally distributed digitisation errors.

9.3.4 Extended Graizer Method

An alternative implementation of the Graizer (1979, 1980) method is described below and used to produce the results in Section 9.3.10. Graizer (1979, 1980) uses the corrected displacement time-history to find the corrected acceleration and velocity through numeric differentiation after smoothing the calculated displacement by five points. The following procedure should give similar results and has the advantage of altering the acceleration time-history by less.

Let the digitised accelerogram be T seconds long. Firstly the uncorrected acceleration time-history is integrated once to get the uncorrected velocity, $\dot{x}(t)$. Next a polynomial, $y(t)$, which fits the beginning and the end of $\dot{x}(t)$ is found by minimizing:

$$W = \int_0^{T_1} (\dot{x} - y)^2 \, \mathrm{d}t + \int_{T_2}^{T} (\dot{x} - y)^2 \, \mathrm{d}t;$$

where $t = 0$ to $t = T_1$ is the 'quiet' part of the record before the strong motion begins and $t = T_2$ to $t = T$ is the 'quiet' part after the strong motion has died out.

For a digitised record this is equivalent to the well-known least-squares method. Once $y(t)$ is found it is differentiated and this differentiated polynomial is subtracted from the *entire* acceleration time-history to find the corrected acceleration record. This is then integrated once to find the corrected velocity record and again to find the corrected displacement record. Normal methods for removing the effect of the instrument, for example finite difference or filtering algorithms, can be applied although they were not used in this study because for calculation of ground velocity and displacement, which are smoothing processes, accelerogram records do not have to be corrected for instrument response (Trifunac, 1971b).

The idea behind this technique is that the long period noise in the record can be approximated by a polynomial and also that it can be found using only the 'quiet' part of the record. This assumption means that the baseline found is not affected by the strong part of the record which may contain large velocity pulses which are likely to be present in near-field records (Somerville & Graves, 1993).

The extended Graizer method can remove a periodic error of period $T_M = D/\mathrm{int}(n/2)$, where D is record length, n is degree of polynomial used and int means the integer part. Therefore if there is a periodic error of period T_E and $T_E < T_M$ it cannot be removed fully.

The use of polynomials to approximate the long-period error in accelerograms seems to be justified because Figure 9.1 shows that the errors in human digitisation approximately follow a polynomial shape.

9.3.5 Computer implementation of Graizer correction technique

A FORTRAN computer program, Gra_Cor, was written to achieve the extended Graizer correction efficiently and to provide an option to: remove the instrument response; and to apply a high-cut filter to remove high frequency noise. This program is the subject of this section.

The program was originally based on the $KK = 2$ option in the POLYCOR program (Menu, 1987), adapted to ignore the part of velocity trace between T_1 and T_2, but this program is limited to only fitting cubics to the velocity trace and not lower or higher degree polynomials. Another problem with POLYCOR is that the high frequency part of the time-history is not corrected (e.g. through high-cut filtering), although there is an option to apply an instrument correction using finite differences, which Menu (1986) shows does not adequately recover all high-frequency information.

Both these limitations lead to the development of a new algorithm to fit any degree of polynomial through the velocity time-history and to incorporate an algorithm to correct the high frequencies. It is also possible to implement most of the extended Graizer technique using standard subroutines for least-squares fitting, such as 'lfit' given in Press *et al.* (1992) (Boore, 2001a).

Firstly the uncorrected acceleration time-history is linearly interpolated to a user specified time interval, usually $0.005\,\mathrm{s}$ (200 samples per second), for consistency with the other correction techniques commonly used. However, this interpolation does not affect the results.

Next, if the user wishes, the acceleration time-history is instrument corrected and a high cut filter applied to remove high frequencies which are thought to be mainly noise. The instrument correction and the high cut filtering subroutines from the Butterworth filtering program, BUTTER, (Vorgia, 1992) were incorporated in Gra_Cor after thorough verification of their results and conversion to the new Imperial College strong-motion format. The subroutines in BUTTER were taken from the BAP program (Converse, 1992) which is the standard processing software of the U.S. Geological Survey.

The acceleration time-history is then integrated once to yield velocity and twice to yield displacement (these are uncorrected time-histories), using these formulae (from the trapezium rule):

$$\begin{aligned} v_i &= v_{i-1} + \frac{\Delta t}{2}(a_i + a_{i-1}); \\ \text{and } d_i &= d_{i-1} + \Delta t v_{i-1} + \frac{\Delta t^2}{6}(2a_{i-1} + a_i); \end{aligned}$$

where a_i, v_i and d_i are acceleration, velocity and displacement respectively at time step i and Δt is the time step.

The integrals of displacement at time step i, $I_{i,j}$, are then calculated; where j is the number of integrations of displacement performed. Remember that $I_{i,1} = 0$ for all i. The displacement at time t where $0 \leq t \leq \Delta t$ is given by:

$$d(t) = d_{i-1} + v_{i-1}t + \frac{t^2}{2}a_{i-1} + \frac{t^3}{6\Delta t}(a_i - a_{i-1}). \tag{9.2}$$

Equation 9.2 is integrated and initial conditions at $t = 0$ applied giving:

$$I_{i,1} = I_{i-1,1} + d_{i-1}\Delta t + \frac{\Delta t}{2}v_{i-1} + \frac{\Delta t^3}{24}(3a_{i-1} + a_i). \tag{9.3}$$

This integration is continued until j equals the degree of the polynomial to fit to velocity time-history. The iterative formula used is:

$$I_{i,j} = I_{i-1,j} + \frac{\Delta t^{j-1}}{(j-1)!}I_{i-1,1} + \ldots + \Delta t I_{i-1,j-1} + \frac{\Delta t^j}{j!}d_{i-1} + \frac{\Delta t^{j+1}}{(j+1)!}v_{i-1} + \frac{\Delta t^{j+2}}{(j+3)!}[(j+2)a_{i-1} + a_i].$$

To find the least-squares polynomial (of degree j) fitting the velocity v in the time windows 0 to T_1 and T_2 to T requires:

$$S = \int_0^{T_1} (v - \sum_{i=0}^{j} b_i t^i)^2 \,\mathrm{d}t + \int_{T_2}^{T} (v - \sum_{i=0}^{j} b_i t^i)^2 \,\mathrm{d}t$$

to be minimized. The $b_0, \ldots, b_j$ which minimize S have $\partial S/\partial b_0 = \ldots = \partial S/\partial b_j = 0$. Consider $\partial S/\partial b_k = 0$:

$$\int_0^{T_1} vt^k \,\mathrm{d}t - \sum_{i=0}^{j} b_i \int_0^{T_1} t^{i+k} \,\mathrm{d}t + \int_{T_2}^{T} vt^k \,\mathrm{d}t - \sum_{i=0}^{j} b_i \int_{T_2}^{T} t^{i+k} \,\mathrm{d}t = 0.$$

Calculating these integrals, by repeated integration by parts, yields a set of simultaneous equations which in matrix form are:

$$D\boldsymbol{b} = \boldsymbol{m}; \tag{9.4}$$

where $\boldsymbol{b}$ is a vector of the coefficients $b_0, \ldots, b_j$, D is a matrix whose elements are $d_{q+1,r+1} = T_1^{q+r+1} + T^{q+r+1} - T_2^{q+r+1}$, for $0 \leq q \leq j$ and $0 \leq r \leq j$, and $\boldsymbol{m}$ is a vector whose elements are given below.

Let $\boldsymbol{m}$ have elements m_i, then the values of these elements can be calculated using an iterative technique (a sort of reduction formula). Let the times T_1, T_2 and T correspond to time steps N_1, N_2 and N respectively. Let Z be an array of elements, $z_{k,l}$, then:

$$\begin{aligned}
z_{0,l} &= I_{l,N_1} + I_{l,N} - I_{l,N_2} \quad \text{for:} \quad 1 \leq l \leq j \\
z_{k,0} &= d_{N_1}T_1^k + d_N T^k - d_{N_2}T_2^k - kz_{k-1,1} \quad \text{for:} \quad 1 \leq k \leq j \\
z_{k,p} &= I_{p,N_1}T_1^k + I_{p,N}T^k - I_{p,N_2}T_2^k - kz_{k-1,p+1} \quad \text{for:} \quad 1 \leq p \leq j - k
\end{aligned}$$

Then $m_1 = d(T_1) + d(T) - d(T_2)$ and $m_{i+1} = z_{i,0}$ for $1 \leq i \leq j$.

The linear system given in Equation 9.4 is then solved to find $b_0 \ldots b_j$ using Gaussian elimination with partial pivoting, to increase accuracy of results, through the subroutines GEFAPP and GESLPP (Moore, 1997a).

To constrain the initial velocity to be equal to 0 at $t = 0$, b_0 is set to 0 and the solution found for the smaller linear system, $D\boldsymbol{b} = \boldsymbol{m}$; where $\boldsymbol{b}$ is a vector of the coefficients $b_1, \ldots, b_j$, D has the elements $d_{q,r} = T_1^{q+r+1} + T^{q+r+1} - T_2^{q+r+1}$, for $1 \leq q \leq j$ and $1 \leq r \leq j$ and $\boldsymbol{m}$ has the elements $m_2, \ldots, m_{j+1}$ given above.

The polynomial found is differentiated once and subtracted from the acceleration time-history to yield the corrected acceleration time-history. Finally the corrected acceleration record is integrated once to find velocity and again to find displacement including the non-zero initial velocity if a polynomial which is not constrained to 0 at $t = 0$ is fitted.

All steps in this algorithm were implemented using double precision arithmetic so that accurate results were obtained. Gra_Cor was rigorously tested by using time-histories of polynomials as the input acceleration record; the correction algorithm removed the polynomial exactly. Although Gra_Cor can compute the coefficients of any degree of least-squares polynomial only polynomials with degrees less than 10 were used to correct the time-histories. This was done partly because accuracy problems are likely to occur when fitting high degree polynomials but mainly because it was found that if a realistic correction could not be achieved with a polynomial of degree less than 10 then increasing the degree of polynomial is unlikely to lead to an improved corrected record.

9.3.6 Verification of extended Graizer correction method

The corrected time-histories obtained using the extended Graizer method can be verified to check that they are physically realistic in three main ways.

Examination of the velocity and displacement traces

The simplest verification method is to examine the corrected velocity and displacement traces. If the velocity at the end of the record differs appreciably from zero then the correction achieved must be wrong because no energy should still be arriving at the station after the end of the earthquake. However, because the algorithm is based on a minimization of the velocity in the time before T_1 and the time after T_2 the final velocity is almost guaranteed to be zero whether the correction is adequate or not. Therefore this criterion is of little help.

A stricter criterion, but one that is not always possible, is to compare the velocity and displacement curves obtained with simulated time-histories. Many papers (e.g. Haskell, 1969; Luco & Anderson, 1983) have calculated theoretical displacement traces for locations in the near field of large earthquakes against which the corrected displacement time-histories can be judged. For example Figure 9.7 shows the comparison of the corrected time-histories from Gilroy #6 during Coyote Lake earthquake and those simulated by Luco & Anderson (1983) for a similar earthquake at a similar distance.

Accelerograms recorded very close to the fault are influenced mainly by source mechanism rather than by inhomogeneities along travel path and consequently can be relatively simple (Hasegawa, 1975). Therefore one criterion useful in the verification of the extended Graizer method is that the velocity and displacement time-histories are relatively simple, for example the velocity time-history could be composed mainly of a single large pulse which has been observed in both simulated and observed ground motions.

The corrected displacement time-histories should not show long-period waves present throughout the entire record which cannot be true ground motion because they do not begin at the beginning of the strong-motion portion of the record. The displacement should be roughly equal to zero for the part of the record before the strong-motion portion and then again constant in the part of the record after the strong-motion portion.

There are few studies which try to reproduce the recorded ground motions on near-field accelerograms to *include* the permanent displacement. Usually the computed ground motions are filtered to match the filtered accelerograms. For the Parkfield earthquake (28/6/1966) there are two studies (Haskell, 1969; Hartzell *et al.*, 1978) which do model the ground motions recorded at Cholame-2, without applying any filtering. Figure 9.8 show the comparison between the ground motions computed by Haskell (1969) and Hartzell *et al.* (1978) and those recovered from the accelerogram using the extended Graizer method. A similar comparison is shown by Graizer (1979). It shows that the velocity and displacement time-histories found using the extended Graizer method for this strong-motion record are sensible and that the recovered permanent displacement, $-8.3\,\mathrm{cm}$, is in rough agreement with the modelled permanent displacements, $-6.2\,\mathrm{cm}$ (Haskell, 1969) and $-3.7\,\mathrm{cm}$ (Hartzell *et al.*, 1978). Figure 9.19 shows a similar comparison for the Pacoima Dam record from the San Fernando earthquake (9/2/1971), again showing the similarity between the recovered displacement from the accelerogram and the modelled displacement. However, such a direct method of verification is often impossible because modelling of many near-field accelerograms has not been done.

Filtering techniques have been shown (Trifunac & Lee, 1974) to give accurate velocity and displacement time-histories, at least for a limited period range. Therefore if the velocity and displacement time-histories found using the extended Graizer method closely match those given by filtering then it is likely that the extended Graizer method yields reasonable corrected records for that accelerogram.

Comparison of recovered permanent displacement with measured displacements

After a large earthquake measurements of the coseismic displacements (permanent displacements due to the earthquake) are now often made. The most accurate and quickest methods currently used are measurements from the Global Positioning System (GPS) or Interferometric Synthetic Aperture Radar (InSAR) (e.g. Zebker *et al.*, 1994) although these methods have only been possible in the past decade before which more time consuming methods such as triangulation or levelling were used. These measurements, if they exist, are extremely valuable in verifying the correction achieved by the extended Graizer method. If there are large differences between the measured coseismic displacement at a station and the recovered displacement from records at that station then the correction must be in error. Unfortunately measurements exist for only a few earthquakes and then the measurements are often not made exactly at the strong-motion stations thus differences between measured coseismic displacements and recovered displacements may be due to local effects at the station such as foundation failure.

When measured coseismic displacements could be found for a studied earthquake these were compared with recovered displacements (see below).

Calculation of response spectra for long periods

The Runge-Kutta algorithm described in Appendix B.1 was used for the calculation of all response spectra in this chapter. It is important to use double rather than single precision arithmetic in the computer implementation of any algorithm, including that by Nigam & Jennings (1969) (Boore, 2001b), for calculating spectral displacements at long periods ($T \gtrsim 50\,\mathrm{s}$). Also if the initial velocity is not constrained to zero then the negative of this needs to be used as the initial condition for the response velocity in response spectra calculations (Boore, 2001a). This was done when an unconstrained correction was achieved.

Figure 9.9 shows the velocity response spectra of three records, corrected using the extended Graizer method, from three earthquakes with increasing M_w; Figure 9.10 shows the displacement response spectra of the same records. These figures show that spectral velocity becomes equal to PGV at a period, $T_{E,V}$, which is dependent on the magnitude of the earthquake, i.e. for small earthquakes spectral velocity becomes equal to PGV at periods much shorter than for large earthquakes. For periods greater than $T_{E,V}$ spectral velocity is roughly constant and equal to PGV which shows that there is no significant energy in the corrected time-history at these longer periods. A similar period exists for displacement spectra, $T_{E,D}$, where spectral displacement becomes equal to PGD and for longer periods spectral displacement is approximately constant and equal to PGD. Note that $T_{E,V}$ is less than $T_{E,D}$ for these three records.

Liu & Helmberger (1983) find that the Coyote Lake earthquake (6/8/1979) has a rupture length of $6\,\mathrm{km}$ and a rupture velocity of $2.8\,\mathrm{kms}^{-1}$, which gives a rupture duration of about $2\,\mathrm{s}$. Bouchon (1982) calculates a rupture length of $14\,\mathrm{km}$ and a rupture velocity of $2.6\,\mathrm{kms}^{-1}$ and which gives a rupture duration of about $5\,\mathrm{s}$ for this earthquake. These rupture durations assume unilateral rupture. Figures 9.9 a and 9.10 a show that these calculated durations are roughly equal to the period at which spectral velocity becomes equal to PGV and the spectral displacement becomes equal to PGD.

For the Imperial Valley earthquake (15/10/1979) Hartzell & Helmberger (1982) find a rupture length of about $36\,\mathrm{km}$ and a rupture velocity between 2.5 and $2.7\,\mathrm{kms}^{-1}$ and hence a rupture duration of about $14\,\mathrm{s}$ and Archuleta (1982) gives $37.5\,\mathrm{km}$ for the rupture length and between 2.5 and $2.6\,\mathrm{kms}^{-1}$ for the rupture velocity giving a rupture duration of about $15\,\mathrm{s}$. These rupture durations assume unilateral rupture. As for the Coyote Lake earthquake the period at which spectral velocity and displacement become equal to PGV and PGD respectively, is close to the computed rupture duration of the Imperial Valley earthquake.

Yagi & Kikuchi (1999) find the Chi-Chi earthquake (20/9/1999) has a rupture duration of about $32\,\mathrm{s}$, which is again similar to the period at which spectral velocity and displacement become equal to PGV and PGD respectively.

This finding is not completely new, for example Basili & Brady (1978) note that it is important to use a low cut-off frequency less than the reciprocal of the length of strong-motion portion of the record which they note is roughly equivalent to the faulting duration and Trifunac (1994) states that the corner frequency of source spectra is inversely proportional to rupture duration. However it is believed to be the first time that it has been clearly demonstrated using actual strong-motion records.

From this study of three near-field records it can be seen that an examination of the velocity and displacement response spectra of a record corrected using the extended Graizer algorithm is useful in deciding whether the correction achieved is reasonable. The correction procedure can be assumed to be adequate if the periods at which spectral velocity is roughly equal to PGV and spectral displacement roughly equals PGD is less than or equal to the rupture duration of the earthquake and that for longer periods the spectral ordinates are constant. If however, there is significant energy within the time-history for periods greater than the rupture duration, i.e. the spectral velocity and/or spectral displacement are not constant for periods greater than rupture duration, then this would mean that the correction made using the extended Graizer technique is probably incorrect.

The impact this result has on the recovery of PGV and PGD from strong-motion records using a filtering correction technique is discussed in Section 9.3.12.

9.3.7 Choice of T_1 and T_2

A physically based way of choosing T_1 and T_2 is required. Simply choosing T_1 and T_2 as the first and last times a given acceleration level is exceeded is not a good choice because high accelerations are not necessarily associated with the portion of the record when the permanent displacements occurred. The way T_1 and T_2 are chosen in this study is firstly by filtering the uncorrected time-history using an elliptical filter (Sunder & Connor, 1982; Sunder & Schumacker, 1982; Menu, 1986) and plotting the energy density. For near-field strong-motion records energy density plots usually show a characteristic shape, see Figure 9.11.

T_1 is chosen as the time just before the steepest part of the curve and T_2 as the time just after the steepest part of the curve. The extended Graizer method is then applied with these choices and the displacement curves plotted.

If the displacement curve is not reasonable then T_1 and T_2 are varied slightly until a better looking curve is found. However, a number of tests were made which showed that the permanent displacements and time-histories obtained are fairly insensitive to the choice of T_1 and T_2, a similar finding to that of Graizer (1979). Some of these tests are shown in Section 9.3.9.

9.3.8 Choice of degree of polynomial

For each accelerogram, as well as T_1 and T_2, the degree of polynomial needs to be chosen. The accelerogram is first corrected with a linear polynomial (degree equals 1) and the acceleration, velocity and displacement judged against the criteria outlined in Section 9.3.6. If the correction is deemed not acceptable then the degree is increased by one, the correction applied again to the uncorrected accelerogram and the time-history examined. The smallest polynomial that yields an adequately corrected time-history, according to the criteria in Section 9.3.6, is selected. This procedure partly runs in parallel to the procedure to select T_1 and T_2.

9.3.9 Sensitivity of extended Graizer correction method to choices of T_1, T_2 and degree of polynomial

In this section some examples of the sensitivity of the corrected velocity and displacement time-histories to different choices of T_1, T_2 and the degree of polynomial used to make the correction are presented for some analogue records.

Figure 9.12 and Table 9.1 display the corrected acceleration, velocity and displacement time-histories and the peak ground velocity, PGV, peak ground displacement, PGD, and the residual (permanent) displacement, RD, found for the El Centro #5 (140° component) record of the Imperial Valley earthquake (15/10/1979) for different choices of T_1 and T_2.

Figure 9.12 and Table 9.1 show that for this strong-motion record the corrected accelerations and velocities are almost identical for different choices of T_1 and T_2 but that the permanent displacements recovered vary greatly, from $-12.3\,\mathrm{cm}$ (for $T_1 = 4\,\mathrm{s}$ and $T_2 = 10\,\mathrm{s}$) to $26.7\,\mathrm{cm}$ (for $T_1 = 0\,\mathrm{s}$ and $T_2 = 15\,\mathrm{s}$). However, the effect of different T_1 and T_2 on the peak ground displacement is much smaller; PGD only varies from $66.5\,\mathrm{cm}$ (for $T_1 = 4\,\mathrm{s}$ and $T_2 = 10\,\mathrm{s}$) to $70.3\,\mathrm{cm}$ (for $T_1 = 0\,\mathrm{s}$ and $T_2 = 15\,\mathrm{s}$ and for $T_1 = 2\,\mathrm{s}$ and $T_2 = 15\,\mathrm{s}$). Since the effect of different T_1 and T_2 on PGV and PGD is small the velocity and displacement response spectra for the different choices of T_1 and T_2 are almost identical and are not given here. All of the velocity and displacement spectra show the same behaviour mentioned in Section 9.3.6, i.e. the period at which spectral velocity and spectral displacement become equal to PGV and PGD is roughly equal to the rupture duration, which for this earthquake is about 15–20 s.

This example demonstrates the difficulty in recovering permanent displacements from strong-motion records using the extended Graizer method; different reasonable choices of T_1 and T_2 can lead to significantly different recovered permanent displacements. The velocity and displacement time-histories using these different choices of T_1 and T_2 can all look realistic and the velocity and displacement response spectra can also conform to the observation mentioned in Section 9.3.6. Therefore unless there are estimates of the true permanent displacement with which to compare the recovered permanent displacement it is difficult to choose one correction over another. However, different choices of T_1 and T_2 do not significantly affect PGV and PGD so the extended Graizer method could be more useful in recovering PGV and PGD than permanent ground displacement.

Figure 9.13 and Table 9.2 display the corrected acceleration, velocity and displacement time-histories and PGV, PGD and RD found for the Lexington Dam Left Abutment (0° component) record of the Loma Prieta earthquake (18/10/1989) for different choices of degree of polynomial.

Figure 9.13 and Table 9.2 show that for this strong-motion record the corrected accelerations and velocities are almost identical for different choices of degree of polynomial but that the peak ground displacements and permanent displacements recovered vary considerably. PGD varies from $-25.5\,\mathrm{cm}$ (for 4th degree polynomial) to $-42.0\,\mathrm{cm}$ (for 2nd degree polynomial) and RD varies from $-16.0\,\mathrm{cm}$ (for 5th degree polynomial) to $-33.3\,\mathrm{cm}$ (for 2nd degree polynomial). The displacement response spectra for different degrees of polynomial vary considerably and this can be used to reject some choices of degree of polynomial. For example for 1st, 2nd and 3rd degree polynomials the spectral displacement does not reach PGD until periods greater than about 50 s, much longer than the rupture duration of this earthquake, and hence using the observation made in Section 9.3.6 such corrected records are rejected. For polynomials of degree 4 and greater PGD and RD are much less variable and hence for this record it is possible to recover stable PGD and RD estimates. In Table 9.15 it is shown that the recovered permanent displacement from this earthquake matches well with the measured permanent displacement.

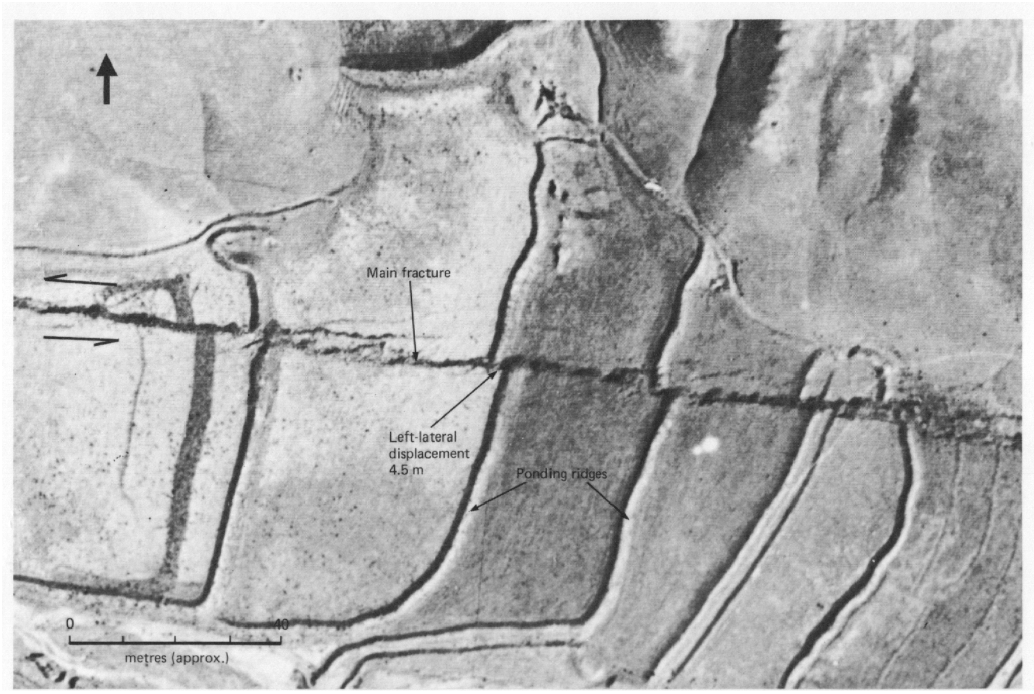

Fig. 9.5: Permanent displacement caused by the Dasht-I Biyaz, Iran, earthquake (31/8/1968, $M_s = 7.2$). Picture courtesy of N. N. Ambraseys.

Fig. 9.6: Permanent displacement caused by the Gediz, Turkey, earthquake (28/3/1970, $M_s = 7.1$). Picture courtesy of N. N. Ambraseys.

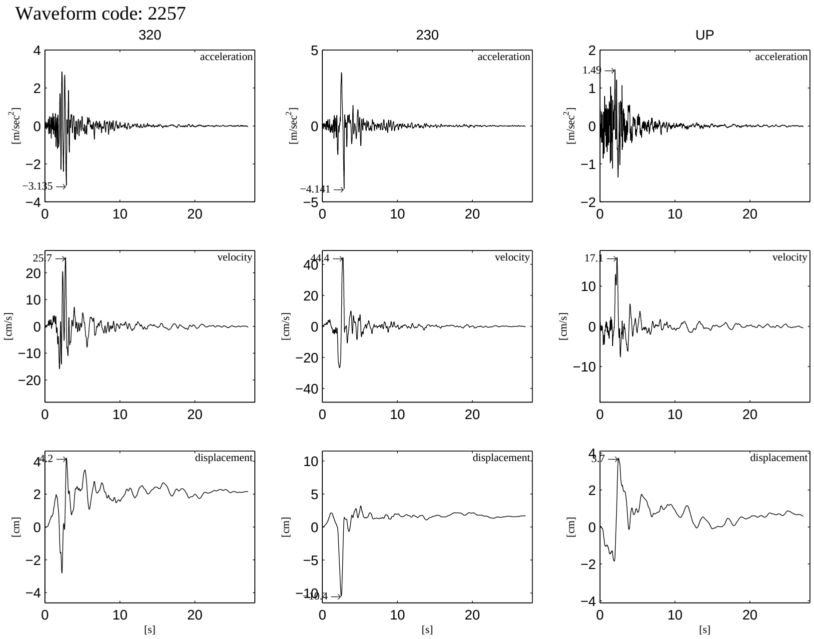

(a) Recorded time-histories corrected using extended Graizer method.

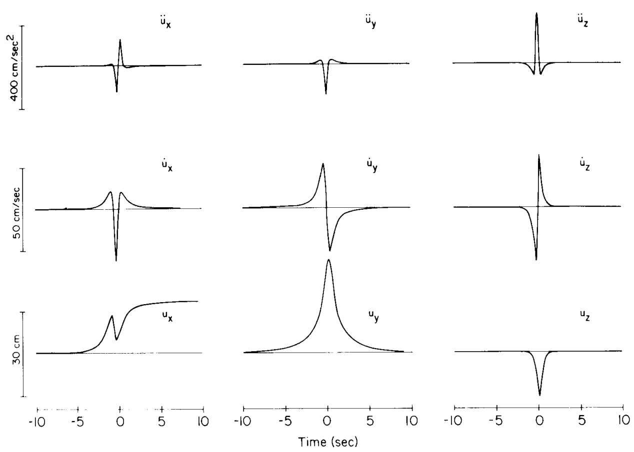

(b) Simulated time-histories from Luco & Anderson (1983).

Fig. 9.7: Comparison of recording from Gilroy #6 during Coyote Lake earthquake and those simulated in Luco & Anderson (1983) for similar earthquake recorded at a similar distance. Note similarities between recorded and simulated displacements especially for horizontal components.

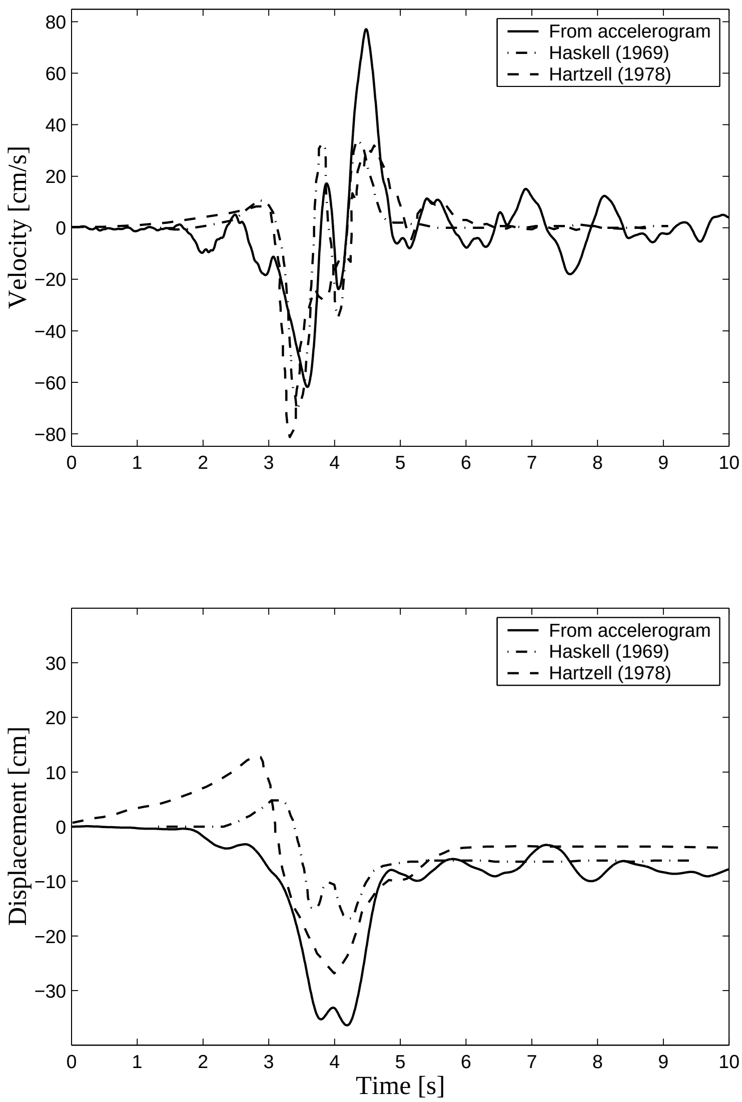

Fig. 9.8: Comparison between velocity and displacement recovered from the accelerogram recorded at Cholame-2 during the Parkfield earthquake (28/6/1966) corrected using the extended Graizer method (constrained to zero initial velocity) and the velocity and displacement at this station modelled by Haskell (1969) and Hartzell *et al.* (1978). The velocity and displacement of Haskell (1969) have been unnormalised using $T = 0.3\,\mathrm{s}$ and an average fault displacement $D_0 = 200\,\mathrm{cm}$ which means that the modelled peak ground acceleration matches that recorded at Cholame-2. They have also been shifted by $1\,\mathrm{s}$ so that the time of the peak ground displacements coincide.

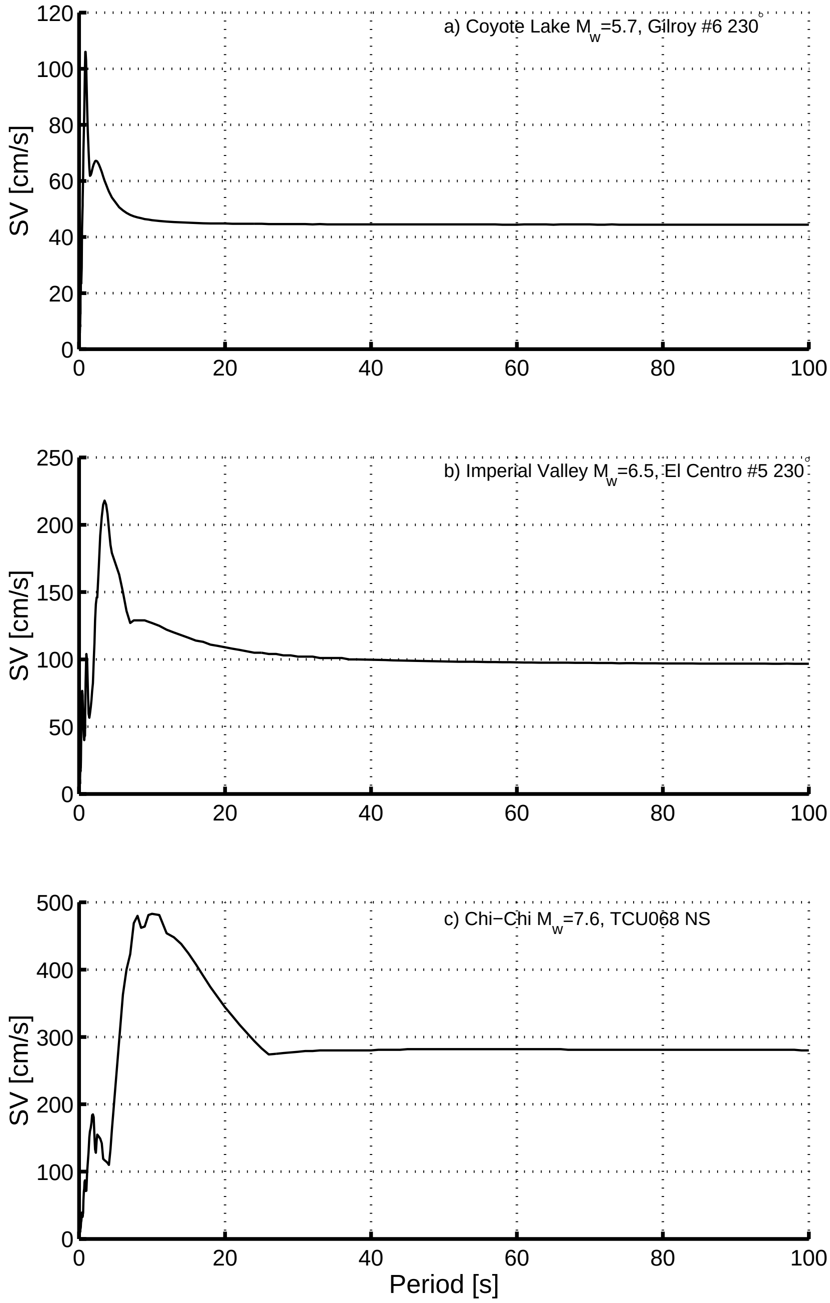

Fig. 9.9: Comparison of velocity response spectrum, 5% damping, of a) Gilroy #6 230° record (Coyote Lake, $M_w = 5.7$), b) El Centro #5 230° record (Imperial Valley, $M_w = 6.5$) and c) TCU068 NS (Chi-Chi, $M_w = 7.6$) from records corrected using extended Graizer method.

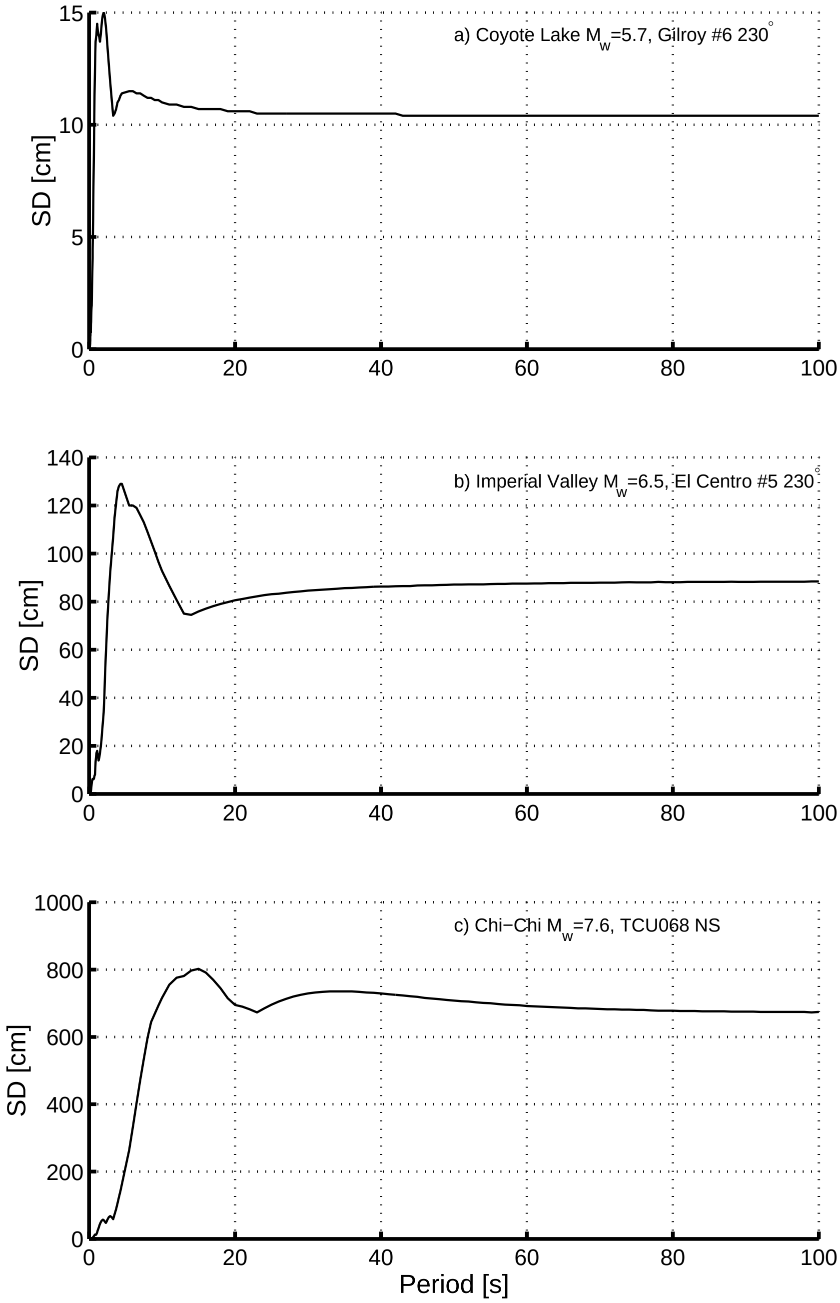

Fig. 9.10: Comparison of displacement response spectrum, 5% damping, of a) Gilroy #6 230° record (Coyote Lake, $M_w = 5.7$), b) El Centro #5 230° record (Imperial Valley, $M_w = 6.5$) and c) TCU068 NS (Chi-Chi, $M_w = 7.6$) from records corrected using extended Graizer method.

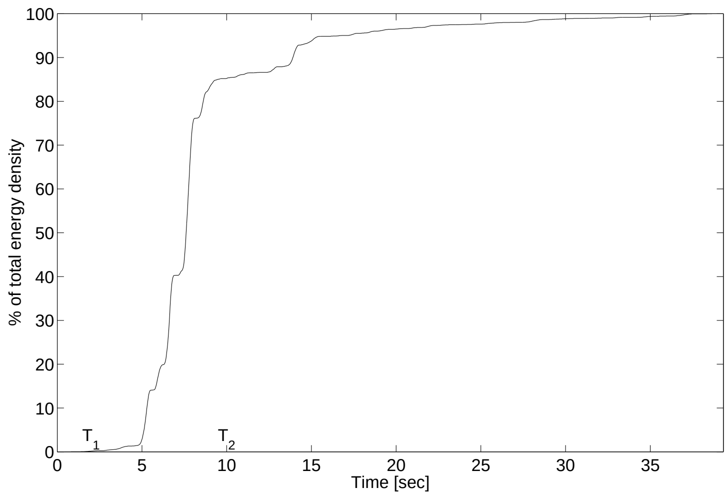

Fig. 9.11: Normalised energy density against time for the El Centro #6 $140°$ component from the Imperial Valley earthquake (15/10/1979) showing the choice of T_1 and T_2 made.

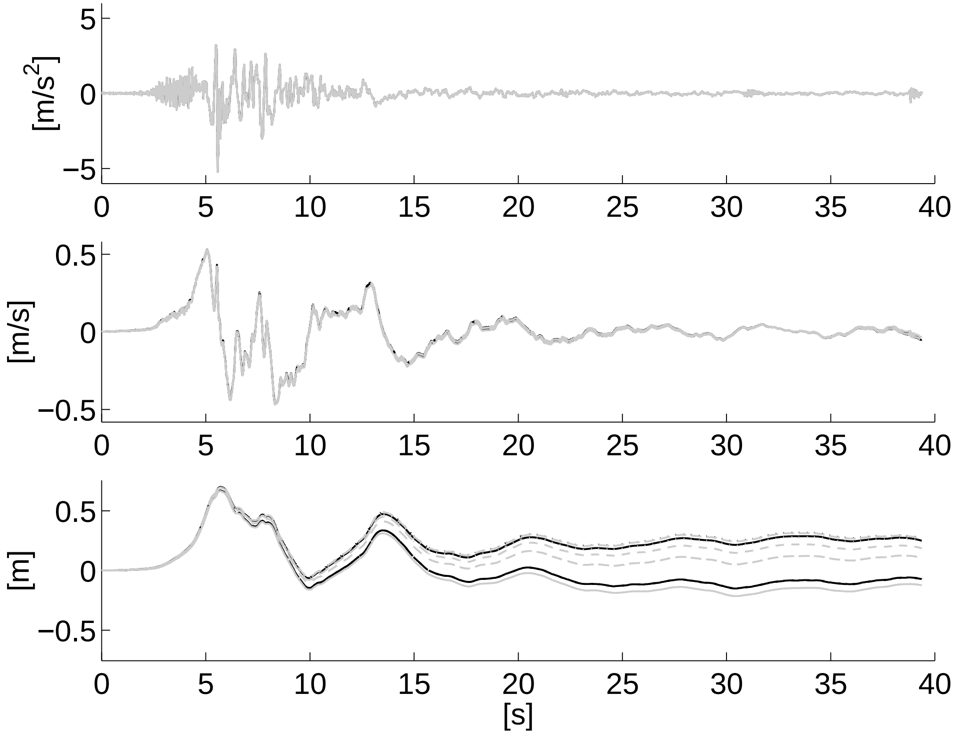

Fig. 9.12: Corrected acceleration, velocity and displacement time-histories of the El Centro #5 ($140°$ component) of the Imperial Valley earthquake (15/10/1979) corrected using the extended Graizer method with the initial velocity constrained to zero using a 2nd degree polynomial and different choices of T_1 and T_2.

T_1 (s)	T_2 (s)	PGV (cms^{-1})	PGD (cm)	RD (cm)
0	10	52·4	67·1	−7·0
0	15	53·4	70·3	26·7
0	20	53·3	70·0	24·9
2	10	52·4	67·0	−7·2
2	15	53·4	70·3	26·4
2	20	53·3	70·0	24·4
4	10	52·2	66·5	−12·3
4	15	53·1	69·5	18·6
4	20	52·9	68·7	10·6

Tab. 9.1: Different choices of T_1 and T_2 to correct the El Centro #5 ($140°$ component) of the Imperial Valley earthquake (15/10/1979) using the extended Graizer method with the initial velocity constrained to zero using a 2nd degree and the peak ground velocity, PGV, peak ground displacement, PGD, the residual displacement, RD, found.

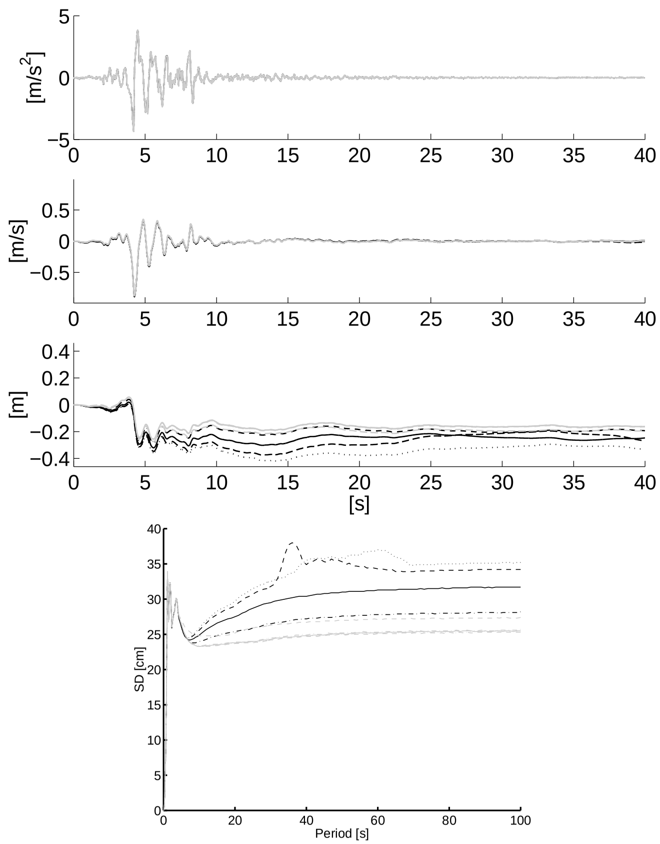

Fig. 9.13: Corrected acceleration, velocity and displacement time-histories and displacement response spectrum of the Lexington Dam Left Abutment (0° component) record of the Loma Prieta earthquake (18/10/1989) corrected using the extended Graizer method with the initial velocity constrained to zero using $T_1 = 3\,\mathrm{s}$ and $T_2 = 7\,\mathrm{s}$ and different choices of degree of polynomial.

Degree	PGV (cms^{-1})	PGD (cm)	RD (cm)
1	−89·8	−37·5	−27·0
2	−90·0	−42·0	−33·3
3	−89·1	−32·1	−24·7
4	−88·2	−28·4	−19·3
5	−87·6	−25·5	−16·0
6	−87·6	−25·6	−16·1
7	−87·6	−25·7	−16·1
8	−87·7	−25·8	−16·4
9	−88·5	−27·5	−19·2

Tab. 9.2: Different choices of degree of polynomial to correct the Lexington Dam Left Abutment (0° component) record of the Loma Prieta earthquake (18/10/1989) corrected using the extended Graizer method with the initial velocity constrained to zero using $T_1 = 3\,\mathrm{s}$ and $T_2 = 7\,\mathrm{s}$ and the peak ground velocity, PGV, peak ground displacement, PGD, the residual displacement, RD, found.

9.3.10 Results

In the following tables: ‘Station’ is the recording station, d_f is the distance to the surface projection of the fault, ‘Inst.’ is the type of strong-motion instrument used, ‘Comp.’ is the component direction of the record, T_1 and T_2 are the times used for the extended Graizer correction, ‘d’ is the degree of the polynomial used for the extended Graizer correction, PGV and PGD are the peak ground velocity and displacement of the record corrected using the extended Graizer method, RD is the permanent displacement at the end of the record, ‘V’ and ‘D’ are the periods at which the spectral velocity and displacement, for 5% damping, become approximately equal to PGV and PGD. The results when the initial velocity is constrained to zero are given in the columns headed ‘Constrained’ and those for when the initial velocity is not constrained are given in the columns headed ’Unconstrained’.

Some records included in this study are not considered to be truly free-field (see Section 3.8).

Coyote Lake (6/8/1979, $M_w = 5.7$)

Only those time-histories for which a realistic correction was achieved are given in Table 9.3. Many of the accelerograms from this earthquake are affected by long period noise.

The coseismic displacements resulting from this right-lateral strike-slip earthquake were measured by King *et al.* (1981) using line length changes in a trilateration network. At trilateration station Gil (which is $4.3\,\mathrm{km}$ from Gilroy #1) the measured coseismic displacement is about $1\,\mathrm{cm}$ and at Sheep (which is about $3.9\,\mathrm{km}$ from Coyote Lake Dam) the measured coseismic displacement is about $1.5\,\mathrm{cm}$. The source model of Liu & Helmberger (1983) and the equations of Mansinha & Smylie (1971) is used to estimate coseismic displacements at the strong-motion stations. Since the equations of Mansinha & Smylie (1971) are for uniform slip across the fault, the average slip ($29\,\mathrm{cm}$) across the fault plane found by Liu & Helmberger (1983) is used. This was calculated using their estimated seismic moment ($3.5 \times 10^{17}\,\mathrm{Nm}$) and fault area ($40\,\mathrm{km}^2$).

The comparison between the recovered and estimated permanent displacements is given in Table 9.4 and shows that the recovered permanent displacements are of a similar absolute size to the theoretical permanent displacements, although the recovered displacements are usually slightly larger. For some components parallel to the fault, i.e. 320° from Gilroy #6, 140° from Gilroy #3 and 320° from Gilroy #1, the polarities of the displacements match with that expected. However, the extended Graizer method cannot be relied upon to yield the correct residual displacements because the coseismic displacements were small for this earthquake ($< 2\,\mathrm{cm}$).

Tab. 9.3: Results from Graizer correction of Coyote Lake records

Station	Inst.	d_f (km)	Comp.	T_1 (s)	T_2 (s)	Constrained d	PGV (cms^{-1})	PGD (cm)	RD (cm)	V (s)	D (s)	Unconstrained d	PGV (cms^{-1})	PGD (cm)	RD (cm)	V (s)	D (s)
			320°	0	4	5	25·7	4·2	2·1	3	4	3	25·5	−4·4	0·1	3	5
Gilroy # 6	SMA-1	2	230°	0	4	2	44·4	−10·4	1·7	4	4	2	44·3	−10·7	1·3	4	4
			Up	1	4	3	17·1	3·8	0·7	4	6	3	17·5	4·8	2·2	4	6
Coyote Lake Dam	SMA-1	3	250°	1	5	3	21·3	3·8	2·2	3	3	3	21·5	4·6	3·1	3	4
Gilroy # 4	SMA-1	6	360°	2	4	3	32·0	7·0	0·3	5	6	4	31·9	5·5	−0·6	5	6
Gilroy # 3	SMA-1	8	140°	2	4	3	−30·1	−8·5	−2·6	4	5	3	−30·1	−8·3	−2·3	4	5
			50°	2	5	3	−17·9	−3·8	0·6	4	6	3	−18·4	−7·0	−2·4	4	6
			140°	2	4	5	32·5	−5·8	2·0	6	6	4	33·1	−5·4	2·9	5	6
Gilroy # 2	SMA-1	10	50°	2	4	8	−10·1	−4·2	−1·9	5	5	4	−9·8	−4·0	−1·8	6	6
			Up	4	6	6	7·0	1·5	0·8	5	5	6	7·0	1·5	0·9	4	6
Gilroy # 1	SMA-1	11	320°	2	5	8	11·0	3·4	1·5	4	6	6	11·1	3·2	2·0	4	6

Tab. 9.4: Recovered from accelerograms and theoretical permanent displacements of the Coyote Lake earthquake (6/8/1979). 'Cons RD' is permanent displacement recovered with initial velocity constrained to zero, 'Uncons RD' is permanent displacement recovered with initial velocity unconstrained and 'TD' is theoretical permanent displacement predicted using equations of Mansinha & Smylie (1971).

Station	d_f (km)	Comp.	Cons RD (cm)	Uncons RD (cm)	TD (cm)
Gilroy # 6	2	320°	2·1	0·1	0·9
		230°	1·7	1·3	−0·8
		Up	0·7	2·2	−0·6
Coyote Lake Dam	3	250°	2·2	3·1	−0·6
Gilroy # 4	6	360°	0·3	−0·6	1·2
Gilroy # 3	8	140°	−2·6	−2·3	−0·7
		50°	0·6	−2·4	0·8
Gilroy # 2	10	140°	2·0	2·9	−0·5
		50°	−1·9	−1·8	0·6
		Up	0·8	0·9	−0·1
Gilroy # 1	11	320°	1·5	2·0	0·5

Whittier Narrows (1/10/1987, $M_w = 5.9$)

There are a large number of accelerograms recorded at short distances from this earthquake. Unfortunately they all seem to be affected by long period noise with period of about $10\,\mathrm{s}$ which means that realistic displacement time-histories could not be recovered from any of the accelerograms.

Lin & Stein (1987) give the vertical coseismic displacements which occurred during this earthquake; the largest vertical uplift measured was $3.24\,\mathrm{cm}$ (with a standard deviation of $0.66\,\mathrm{cm}$). They also predict the vertical and horizontal coseismic displacements using a model of the source; the largest predicted horizontal coseismic displacement is about $1\,\mathrm{cm}$ (from their Figure 8b).

The permanent displacements that occurred at strong-motion stations that recorded this earthquake are less than about $2\,\mathrm{cm}$ vertical and $1\,\mathrm{cm}$ horizontal (from Figure 8 of Lin & Stein (1987)). The extended Graizer method does not seem to be able to recover such small displacements, especially in analogue records which exhibit long period noise. Not recovering small displacements of the order of $1\,\mathrm{cm}$ is unlikely to strongly bias a correction method based on filtering so the extended Graizer method does not need to be used.

North Palm Springs (8/7/1986, $M_w = 6.0$)

Only those time-histories for which a realistic correction is achieved are given in Table 9.6. Component directions of the records from Devers Substation are from Hartzell (1989).

Hartzell (1989) estimates the slip distribution over the fault for this earthquake using strong-motion and teleseismic records and a range of methods (linear and nonlinear inversion and empirical Green's functions). It is found that the fault length is between about 12 and $20\,\mathrm{km}$ although all of the obtained fault boundaries are irregular and are not rectangular. Savage *et al.* (1993) finds a rupture length of $11\,\mathrm{km}$. Using these rupture lengths and rupture velocities of between 2 and $3\,\mathrm{kms}^{-1}$ gives rupture durations of between 2 and $5\,\mathrm{s}$ because the rupture is bilateral. Thus the periods at which the spectral velocities and displacement attain PGV and PGD for the records corrected using the extended Graizer method are slightly too high.

No measurements of horizontal coseismic displacements associated with this earthquake seem to be available with which to compare the permanent displacements recovered from the strong-motion records. Savage *et al.* (1993) does give the measured uplift in the epicentral region due to this earthquake. The largest measured uplift was about $5\,\mathrm{cm}$ directly over the rupture plane. The model of Savage *et al.* (1993) was used to compute predicted permanent displacements at each of the strong-motion stations using the equations of Mansinha & Smylie (1971). The model of Savage *et al.* (1993) consists of $18\,\mathrm{cm}$ of right-lateral slip and $24\,\mathrm{cm}$ of reverse slip so the predicted displacements are computed using the dip-slip with $24\,\mathrm{cm}$ of slip and the strike-slip equations with $18\,\mathrm{cm}$ of slip and the displacements added together. The displacements recovered from the accelerograms and the predicted displacements are given in Table 9.5.

Table 9.5 shows that almost all the recovered displacements are much larger than the predicted displacements suggesting that the extended Graizer correction technique does not work well for these records. The model of the rupture found by Savage *et al.* (1993) was found using line length changes and elevation changes. The elevation changes were measured in the epicentral area and so the vertical deformation predicted by the faulting model is well constrained and so the reverse-slip part of the model is likely to be accurate. However, the line length changes used data from two trilateration network (Joshua and Monitor) which do not provide good coverage in the epicentral area of this earthquake; only three lines are within about $10\,\mathrm{km}$ of the epicentral and none of these directly passed over the rupture plane. Therefore the horizontal deformation of the model is poorly constrained and could be inaccurate. A rupture model of this earthquake is presented in Hartzell (1989) and it shows up to $40\,\mathrm{cm}$ of right-lateral slip on the fault plane, compared with $18\,\mathrm{cm}$ in the model of Savage *et al.* (1993). Therefore the permanent displacements that occurred at the four strong-motion stations are possibly higher than the estimates given in Table 9.5.

As a further check of the results obtained using the extended Graizer method the corrected hor-

Tab. 9.5: Recovered from accelerograms and theoretical permanent displacements of the North Palm Springs earthquake (8/7/1986). 'Cons RD' is permanent displacement recovered with initial velocity constrained to zero, 'Uncons RD' is permanent displacement recovered with initial velocity unconstrained and 'TD' is theoretical permanent displacement predicted using equations of Mansinha & Smylie (1971).

Station	d_f (km)	Comp.	Cons RD (cm)	Uncons RD (cm)	TD (cm)
White Water Canyon	0	180°	1·4	5·5	0·2
		270°	−4·3	−4·3	−1·7
Devers Substation	1	0°	−14·9	−10·6	−0·6
		90°	2·6	2·9	1·9
N. Palm Springs P.O.	5	210°	−11·0	−16·3	−0·5
		300°	6·6	11·3	1·5
Morongo Valley	7	45°	0·9	−0·1	0·4
		135°	8·4	19·2	0·2

izontal displacements from the two horizontal components of the four accelerograms were rotated into directions: $0°$ and $90°$ east of north. Figure 9.14 shows these rotated displacements and the locations of the strong-motion stations where they were recorded.

Figure 9.14 shows that there are similarities between the time-histories recorded at White Water Canyon and Devers Substation, although the displacements at Devers Substation in the $0°$ east of north direction are much larger than those at White Water Canyon. Also the $90°$ east of north components at all four stations have some similar features, for example the increase in the displacement in the positive direction at about 2 s, although the $90°$ component record at Morongo Valley has three large oscillations between about 2 and 7 s which are not on the records from the other stations. The $0°$ east of north component at North Palm Springs Post Office is similar to the component in the opposite direction at Devers Substation which suggests that possibly the polarity of this component is incorrect. All corrected displacement traces at the four strong-motion stations (Table 9.6), corrected using the extended Graizer method, display a number of similarities between them which suggests that, although the permanent displacements recovered from the strong-motion records do not closely match the predicted displacements, the extended Graizer method may be an appropriate correction procedure for these records.

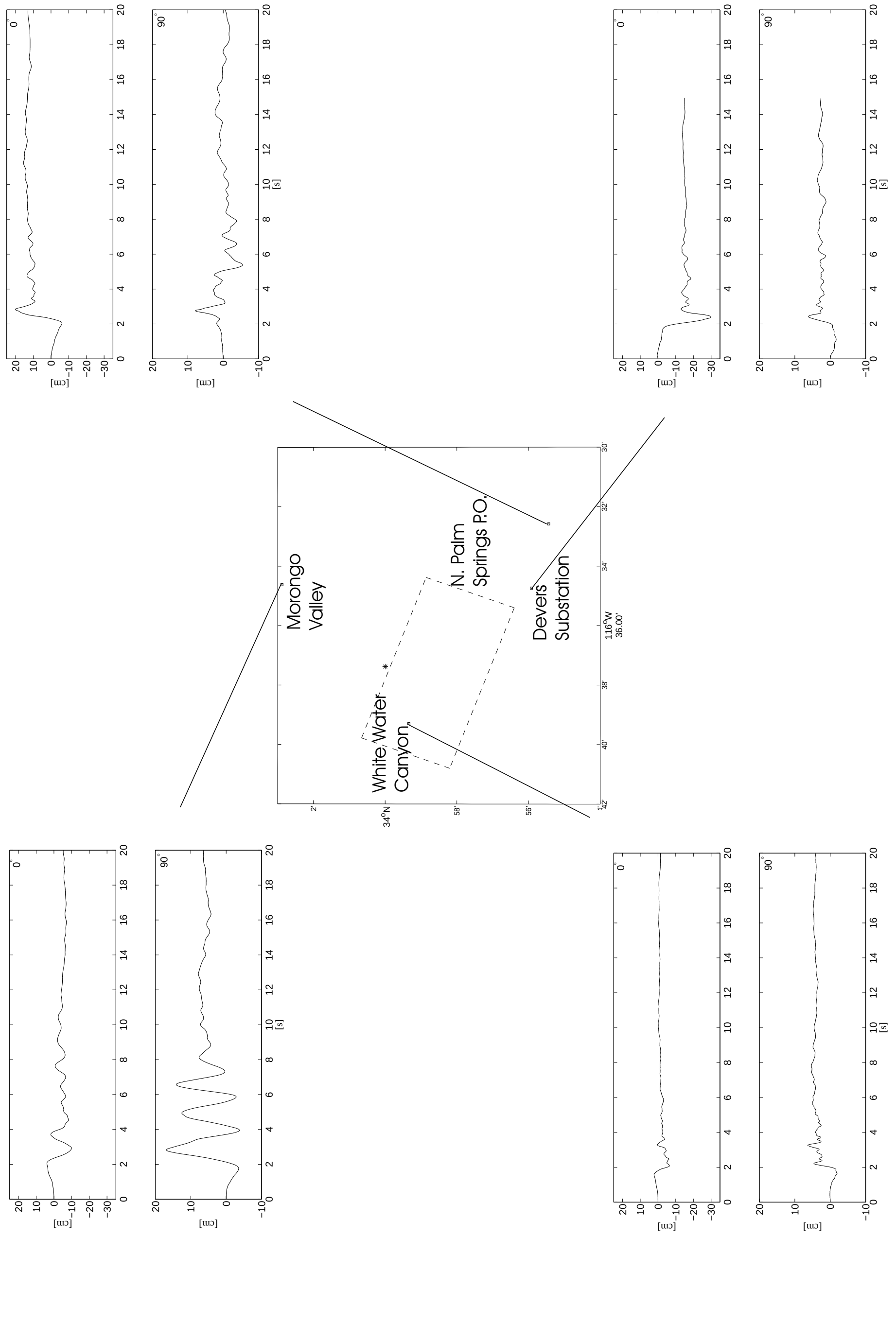

Fig. 9.14: Corrected displacements (using the extended Graizer method with the initial velocity constrained to zero) in the directions 0° and 90° east of north at four strong-motion stations which recorded the North Palm Springs earthquake (8/7/1986). The dashed rectangle is the surface projection of the rupture plane from Savage *et al.* (1993) and the star is the epicentre.

Parkfield (28/6/1966, $M_w = 6.2$)

Sensible velocity and displacement time-histories could only be achieved for the record given in Table 9.7. The other records are all affected by long period noise.

For this record Table 9.7 shows the PGVs, PGDs and RDs obtained by constraining the initial velocity to $0\,\mathrm{cms}^{-1}$ and not applying the constraint are very similar.

The rupture length of this earthquake is about $32\,\mathrm{km}$ and is mainly unilateral (Mendoza & Hartzell, 1988) which using a rupture velocity of 2 to $3\,\mathrm{kms}^{-1}$ gives a rupture duration of between 11 and $16\,\mathrm{s}$. This agrees well with the period at which spectral velocity and displacement become equal to PGV and PGD (10 and $15\,\mathrm{s}$ respectively).

Smith & Wyss (1968) report geodimeter and triangulation measurements before and after the earthquake (October 1965 and July 1966) which shows that points 6–$8\,\mathrm{km}$ distant from the fault plane moved about $20\,\mathrm{cm}$ in a right lateral sense with respect to points $12\,\mathrm{km}$ on the other side of the fault. A surface displacement of $4.5\,\mathrm{cm}$ on Highway 46 (close to Parkfield 2W) was found 9 hours and 34 minutes after the earthquake (Smith & Wyss, 1968).

Figure 9.8 shows that the constrained recovered velocity and displacement time-histories match the modelled velocity and displacement of Haskell (1969) and Hartzell *et al.* (1978) reasonably well. There is a similar close match when the initial velocity is constrained to $0\,\mathrm{cms}^{-1}$. Therefore the extended Graizer method works well for this record.

Aigion (15/6/1995, $M_w = 6.5$)

Sensible velocity and displacement time-histories could only be achieved for one record (Table 9.9).

Table 9.9 shows that both constraining the initial velocity to $0\,\mathrm{cms}^{-1}$ and not constraining it gives almost identical PGVs and similar PGDs and residual displacements for this record.

Bernard *et al.* (1997b) present GPS measurements of a point near to the Aigion OTE station (their point D). The measured horizontal displacement is about $4\,\mathrm{cm}$ in a direction about 30° west of due south. Thus the recovered displacements of $-4.2\,\mathrm{cm}$ or $-3.4\,\mathrm{cm}$ from the N component of the Aigion OTE record are realistic.

The main rupture of this earthquake lasted 4 to $5\,\mathrm{s}$ (Bernard *et al.*, 1997b) which is also roughly the period at which the spectral velocity and spectral displacement tend to PGV and PGD respectively for the record given above.

The agreement of the permanent displacements measured by GPS and recovered from the strong motion record and the velocity and displacement spectra suggest that the extended Graizer correction method works well for the N component of the Aigion OTE record from the Aigion earthquake.

Tab. 9.6: Results from Graizer correction of North Palm Springs records

Station	Inst.	d_f	Comp.	T_1	T_2	Constrained						Unconstrained					
						d	PGV	PGD	RD	V	D	d	PGV	PGD	RD	V	D
		(km)		(s)	(s)		(cms^{-1})	(cm)	(cm)	(s)	(s)		(cms^{-1})	(cm)	(cm)	(s)	(s)
White Water Canyon	SMA-1	0	180°	1	4	1	−37·9	6·5	1·4	4	5	1	−37·3	8·0	5·5	4	5
			270°	1	4	5	−30·0	−6·4	−4·3	5	5	5	−29·9	6·6	−4·3	5	5
Devers Substation		1	0°	1	4	2	84·9	−30·0	−14·9	8	8	2	85·7	−26·8	−10·6	8	8
			90°	2	3	6	−29·6	6·2	2·6	8	8	5	−30·0	6·2	2·9	5	4
N. Palm Springs P.O.	SMA-1	5	210°	2	4	3	−69·5	−20·9	−11·0	5	5	3	−70·6	−26·4	−16·3	5	5
			300°	2	3	4	29·8	9·9	6·6	5	5	7	31·9	14·7	11·3	5	10
Morongo Valley	SMA-1	7	45°	2	8	1	31·3	7·2	0·9	4	6	1	31·2	−7·4	−0·1	4	8
			135°	2	8	1	42·1	18·8	8·4	5	5	1	43·6	23·1	19·2	5	5

Tab. 9.7: Results from Graizer correction of Parkfield records

Station	Inst.	d_f	Comp.	T_1	T_2	Constrained						Unconstrained					
						d	PGV	PGD	RD	V	D	d	PGV	PGD	RD	V	D
		(km)		(s)	(s)		(cms^{-1})	(cm)	(cm)	(s)	(s)		(cms^{-1})	(cm)	(cm)	(s)	(s)
Parkfield 2W	AR-240	0	N065	2	5	3	76·9	−37·6	−8·3	10	15	3	77·1	−36·3	−6·8	10	15

Imperial Valley (15/10/1979, $M_w = 6.5$)

Only those time-histories for which a sensible correction is obtained are given in Table 9.8. Many of the time-histories include prominent surface waves which limits the applicability of the extended Graizer correction.

The theoretical displacements at each station were found using Mansinha & Smylie (1971) strike-slip equations. The fault rupture is assumed to run from the epicentre to the end of the surface rupture from the surface to $10\,\mathrm{km}$ depth (the hypocentral depth) at a dip of 75° (Archuleta, 1982). This gives a rupture plane $37.5\,\mathrm{km}$ long by $10/\cos(75^\circ)$ wide. Uniform slip is set equal to $62\,\mathrm{cm}$, which was the maximum horizontal slip measured at the surface (Archuleta, 1982). Slade *et al.* (1984) present the predicted static displacements calculated using a finite element technique and non-uniform slip along the fault plane; the displacements found are similar to those found using this simple model.

Mansinha & Smylie (1971) equations do not allow the slip to vary with depth or along the length thus the more complex slip behaviour found by Archuleta (1982), Sharp *et al.* (1982) and Reilinger & Larsen (1986) could not be modelled. The predicted vertical displacements found from this model are much smaller than those measured, so for example $4\,\mathrm{km}$ north of El Centro #6 and #7 the measured vertical displacement was $36\,\mathrm{cm}$ (Archuleta, 1982), whereas the predicted vertical displacement is about $5\,\mathrm{cm}$. This needs to be considered when comparing the displacements recovered from the accelerograms and those predicted by Mansinha & Smylie (1971) equations.

Tab. 9.8: Results from Graizer correction of Imperial Valley records

Station	Inst.	d_f	Comp.	T_1	T_2	Constrained d	PGV	PGD	RD	V	D	Unconstrained d	PGV	PGD	RD	V	D
		(km)		(s)	(s)		(cms^{-1})	(cm)	(cm)	(s)	(s)		(cms^{-1})	(cm)	(cm)	(s)	(s)
Aeropuerto	SMA-1	0	45°	2	10	2	−44·7	−19·9	−12·2	10	15	2	−44·9	−17·7	−11·6	10	15
El Centro #5	SMA-1	0	140°	2	15	2	53·4	70·3	26·4	15	20	2	53·6	72·0	29·4	15	20
			230°	2	10	2	−96·8	86·3	−2·5	10	15	2	−96·5	89·1	1·3	10	15
			Up	2	10	4	−43·1	−32·2	−1·8	10	15	4	−41·6	−24·5	5·4	10	15
El Centro #6	SMA-1	1	140°	2	10	2	−69·4	−36·4	−22·9	10	15	2	−69·5	−37·5	−24·2	10	15
			230°	2	10	2	116·6	93·2	15·8	10	10	1	114·2	71·6	−9·3	15	15
Meloland (F.F.)	CRA-1	1	0°	2	10	3	−70·4	45·0	11·1	15	15	3	−70·5	44·3	10·0	15	15
			270°	2	10	3	91·3	−38·9	−3·6	5	15	2	90·8	−43·0	−8·4	5	15
			Up	0	10	4	−28·3	11·2	−1·8	5	10	5	−27·7	14·0	3·6	5	15
Meloland (N. Emb.)	CRA-1	1	0°	2	10	1	−77·0	48·6	24·7	10	15	1	−77·2	47·8	21·6	15	15
			270°	2	10	3	96·9	−39·6	−5·4	5	15	3	96·6	−41·5	−8·6	5	15
			Vert	0	10	6	−28·8	−7·5	−2·1	5	10	3	−29·5	−8·9	−6·7	5	10
Agrarias	DCA-310	2	3°	4	10	4	−35·0	8·8	3·1	10	10	4	−35·1	8·8	2·8	10	10
			273°	4	10	4	43·5	12·7	2·7	5	10	4	42·8	11·9	0·8	5	15
Bonds Corner	SMA-1	2	140°	2	10	1	−45·9	35·5	14·0	10	15	1	−46·5	30·5	4·0	10	15

continued on next page

Tab. 9.8: *continued*

Station	Inst.	d_f	Comp.	T_1	T_2	Constrained						Unconstrained					
						d	PGV	PGD	RD	V	D	d	PGV	PGD	RD	V	D
		(km)		(s)	(s)		(cms^{-1})	(cm)	(cm)	(s)	(s)		(cms^{-1})	(cm)	(cm)	(s)	(s)
El Centro #4	SMA-1	3	140°	4	10	1	−41·1	−41·6	−30·2	5	20	1	−42·8	−72·8	−55·5	5	15
			230°	4	10	1	82·9	98·5	11·5	10	15	1	82·3	95·2	4·3	15	15
El Centro #7	SMA-1	3	140°	3	10	2	51·7	−37·9	0·7	10	25	2	51·9	−35·6	3·5	10	25
			230°	3	10	1	115·9	60·9	27·8	8	10	1	114·2	47·1	3·4	8	15
			Up	2	10	3	28·3	16·8	2·6	8	10	2	27·9	15·0	4·7	8	15
Holtville	SMA-1	5	225°	4	13	1	−51·4	51·0	19·3	10	20	1	−53·2	37·9	−9·5	10	20
			315°	5	20	2	−54·1	−58·5	−5·9	10	15	2	−53·2	−46·3	7·7	10	15
Brawley Airport	SMA-1	6	315°	4	12	2	43·0	26·5	19·8	10	20	2	42·8	22·6	16·2	10	20
			225°	4	12	2	37·6	34·0	10·7	10	15	2	37·7	35·3	12·1	15	15
El Centro #8	SMA-1	6	140°	2	10	1	−56·7	−54·2	−1·0	15	20	1	−56·0	−49·6	8·6	15	20
			230°	4	10	2	−51·5	45·3	−1·8	12	12	1	−50·7	57·4	7·2	12	15
			Up	2	12	3	25·8	24·4	4·6	10	15	3	24·6	18·4	−4·7	10	15
El Centro D.A.	SMA-1	7	360°	3	12	2	40·9	21·8	−5·7	5	15	2	−41·1	−25·9	−19·1	10	15
			270°	3	12	1	−71·5	83·6	35·6	15	15	1	−72·1	79·4	26·7	15	15
			Up	2	12	3	−22·6	21·9	−13·9	10	15	4	−21·8	−14·1	−11·8	10	15

continued on next page

Tab. 9.8: *continued*

Station	Inst.	d_f	Comp.	T_1	T_2	Constrained d	PGV	PGD	RD	V	D	Unconstrained d	PGV	PGD	RD	V	D
		(km)		(s)	(s)		(cms^{-1})	(cm)	(cm)	(s)	(s)		(cms^{-1})	(cm)	(cm)	(s)	(s)
Casa Flores	SMA-1	9	270°	2	12	4	−32·7	−10·7	1·5	5	10	1	−32·1	−9·5	−3·3	5	10
El Centro #3	SMA-1	9	140°	5	12	3	47·5	−20·9	−9·0	5	15	3	47·5	−20·5	−8·6	5	20
			230°	5	12	2	−41·7	32·7	11·8	10	20	2	−42·7	−28·8	−4·0	10	20
Imperial Co. Cen.	SMA-1	10	2°	4	10	3	39·4	22·5	10·5	10	15	3	39·2	20·0	8·1	10	15
			92°	4	10	5	72·8	−55·8	1·9	15	15	4	73·7	−52·5	7·8	15	15
			Up	4	10	5	−20·0	−13·6	−6·8	10	10	4	−19·5	−17·6	−7·4	10	15
Calexico	SMA-1	11	315°	3	15	5	19·5	19·6	10·6	20	20	5	19·4	17·5	8·5	20	20
			225°	3	12	4	−23·2	−12·9	−4·1	10	15	2	−22·7	−14·0	−2·5	10	15
El Centro #2	SMA-1	11	230°	7	12	3	−36·8	−59·1	−47·8	15	15	2	−37·0	−51·8	−41·2	15	15
El Centro #10	RFT-250	11	320°	5	15	5	−49·9	−48·8	−31·1	10	20	5	−51·2	−53·0	−36·1	10	20
			50°	5	10	2	52·9	43·5	28·1	10	15	2	53·2	48·1	31·9	10	15
Cucapah	DSA-1	12	N085	4	20	8	36·0	−13·5	−0·3	5	15	8	36·0	−12·9	0·3	5	15
Westmorland		14	N180	4	10	2	22·9	13·3	2·3	10	15	2	23·0	13·9	3·2	10	15
			N090	4	10	2	−23·0	−22·5	−5·5	15	15	2	−23·7	−27·5	−13·1	15	15

continued on next page

Tab. 9.8: *continued*

Station	Inst.	d_f	Comp.	T_1	T_2	Constrained d	Constrained PGV	Constrained PGD	Constrained RD	Constrained V	Constrained D	Unconstrained d	Unconstrained PGV	Unconstrained PGD	Unconstrained RD	Unconstrained V	Unconstrained D
		(km)		(s)	(s)		(cms^{-1})	(cm)	(cm)	(s)	(s)		(cms^{-1})	(cm)	(cm)	(s)	(s)
El Centro #11	SMA-1	15	140°	5	15	1	−35·3	30·9	14·6	10	15	1	−34·6	41·3	26·6	10	15
			230°	5	12	2	−44·3	31·4	7·3	10	20	2	−45·0	20·7	−5·2	10	20

Tab. 9.9: Results from Graizer correction of Aigion records

Station	Inst.	d_f	Comp.	T_1	T_2	Constrained d	Constrained PGV	Constrained PGD	Constrained RD	Constrained V	Constrained D	Unconstrained d	Unconstrained PGV	Unconstrained PGD	Unconstrained RD	Unconstrained V	Unconstrained D
		(km)		(s)	(s)		(cms^{-1})	(cm)	(cm)	(s)	(s)		(cms^{-1})	(cm)	(cm)	(s)	(s)
Aigion OTE	SMA-1	7	N	2	5	4	−52·8	−12·3	−4·2	3	5	4	−52·7	−11·4	−3·4	3	5

Tab. 9.10: Recovered from accelerograms and theoretical permanent displacements of the Imperial Valley earthquake (15/10/1979). ‘Cons RD’ is permanent displacement recovered with initial velocity constrained to zero, ‘Uncons RD’ is permanent displacement recovered with initial velocity unconstrained and ‘TD’ is theoretical permanent displacement predicted using equations of Mansinha & Smylie (1971).

Station	d_f (km)	Comp.	Cons RD (cm)	Uncons RD (cm)	TD (cm)
Aeropuerto	0	45°	−12·2	−11·6	−0·1
El Centro #5	0	140°	26·4	29·4	25·0
		230°	−2·5	1·3	4·7
		Up	−1·8	5·4	0·3
El Centro #6	1	140°	−22·9	−24·2	32·9
		230°	15·8	−9·3	5·3
Meloland (F.F.)	1	0°	11·1	10·0	21·1
		270°	−3·6	−8·4	14·5
		Up	−3·9	3·6	0·0
Meloland (N. Emb.)	1	0°	24·7	21·6	21·1
		270°	−5·4	−8·6	14·5
		Vert	−2·1	−6·7	0·0
Agrarias	2	3°	3·1	2·8	−4·2
		273°	2·7	0·8	−15·7
Bonds Corner	2	140°	14·0	4·0	23·5
El Centro #4	3	140°	−30·2	−55·5	17·7
		230°	11·5	4·3	3·9
El Centro #7	3	140°	0·7	3·5	−22·9
		230°	27·8	3·4	0·4
		Up	2·6	4·7	0·2
Holtville	5	225°	19·3	−9·5	3·1
		315°	−5·9	7·7	−16·7
Brawley Airport	6	315°	19·8	16·2	−6·3
		225°	10·7	12·1	8·4

continued on next page

Tab. 9.10: *continued*

Station	d_f (km)	Comp.	Cons RD (cm)	Uncons RD (cm)	TD (cm)
El Centro #8	6	140°	$-1{\cdot}0$	$8{\cdot}6$	$-14{\cdot}8$
		230°	$-1{\cdot}8$	$7{\cdot}2$	$1{\cdot}3$
		Up	$4{\cdot}6$	$-4{\cdot}7$	$0{\cdot}2$
El Centro D.A.	7	360°	$-5{\cdot}7$	$-19{\cdot}1$	$9{\cdot}2$
		270°	$35{\cdot}6$	$26{\cdot}7$	$9{\cdot}4$
		Up	$-13{\cdot}9$	$-11{\cdot}8$	$0{\cdot}2$
Casa Flores	9	270°	$1{\cdot}5$	$-3{\cdot}3$	$8{\cdot}7$
El Centro #3	9	140°	$-9{\cdot}0$	$-8{\cdot}6$	$9{\cdot}0$
		230°	$11{\cdot}8$	$-4{\cdot}0$	$2{\cdot}7$
Imperial Co. Cen.	10	2°	$10{\cdot}5$	$8{\cdot}1$	$5{\cdot}1$
		92°	$1{\cdot}9$	$7{\cdot}8$	$-8{\cdot}2$
		Up	$-6{\cdot}8$	$-7{\cdot}4$	$-0{\cdot}3$
Calexico	11	315°	$10{\cdot}6$	$8{\cdot}5$	$8{\cdot}4$
		225°	$-4{\cdot}1$	$-2{\cdot}5$	$-2{\cdot}4$
El Centro #2	11	230°	$-47{\cdot}8$	$-41{\cdot}2$	$2{\cdot}6$
El Centro #10	11	320°	$-31{\cdot}1$	$-36{\cdot}1$	$8{\cdot}5$
		50°	$28{\cdot}1$	$31{\cdot}9$	$-2{\cdot}4$
Cucapah	12	N085	$-0{\cdot}3$	$0{\cdot}3$	$2{\cdot}6$
Westmorland	14	N180	$2{\cdot}3$	$3{\cdot}2$	$0{\cdot}7$
		N090	$-5{\cdot}5$	$-13{\cdot}1$	$1{\cdot}8$
El Centro #11	15	140°	$14{\cdot}6$	$26{\cdot}$	$-5{\cdot}9$
		230°	$7{\cdot}3$	$-5{\cdot}2$	$2{\cdot}3$

The results (Table 9.10) show that for most of the strong-motion records the recovered permanent displacements do not match the theoretical displacements, so the extended Graizer technique does not work well on these records.

As shown in Section 9.3.6, the rupture duration for this earthquake is probably about $15\,\mathrm{s}$, which matches well with the period at which spectral velocity and displacement become equal to PGV and PGD, respectively, for most of the records given in Table 9.8. This suggests that although the permanent displacements obtained from the strong-motion records may be greatly in error the corrected velocity and parts of the corrected displacements may be more reliable. Many of the time-histories of this earthquake are affected by directivity effects because the epicentre was at the southern end of the fault and most of the instruments were towards the northern end of the fault; however this does not seem to have affected the period at which spectral velocity and displacement become equal to PGV and PGD, respectively.

The theoretical and recovered displacement at Bonds Corner may differ due to lateral spreading. The accelerogram recorded at Bonds Corner has spikes in the coda which are similar to those recorded at the Wildlife Liquefaction Array during the Superstition Hills earthquake (24/11/1987). The spikes on the record from the Wildlife Liquefaction Array are interpreted by Zorapapel & Vucetic (1994) as being due to lateral spreading from the build-up of excess pore water pressures.

Figures 9.15 and 9.16 display the corrected displacement time-histories for 18 stations given in Table 9.8 and the locations of the strong-motion stations that recorded them. The horizontal components were rotated into directions: roughly parallel (azimuth $140°$) and perpendicular (azimuth $230°$) to the strike.

Figure 9.15 shows that after correction some of the displacements parallel to the strike show similarities, for example El Centro #7, El Centro #8, El Centro Differential Array and Imperial County Centre. These similarities suggest that the extended Graizer method may work for these records. However, there are a number of corrected displacements in the strike direction which do not match with the displacements at nearby stations, for example El Centro #6 and El Centro #4. The large differences in the corrected displacements at these stations and those at stations within $1\,\mathrm{km}$ strongly suggest that the extended Graizer method has failed.

In comparison Figure 9.16 shows that most of the corrected displacements perpendicular to the strike display similarities, so the extended Graizer method appears to work well for this direction. For example, a positive pulse after about $5\,\mathrm{s}$ is seen on most of the records. However, the corrected displacement trace from El Centro #2 has a different shape than the displacement traces at the nearby stations, suggesting the extended Graizer method is not applicable to this record.

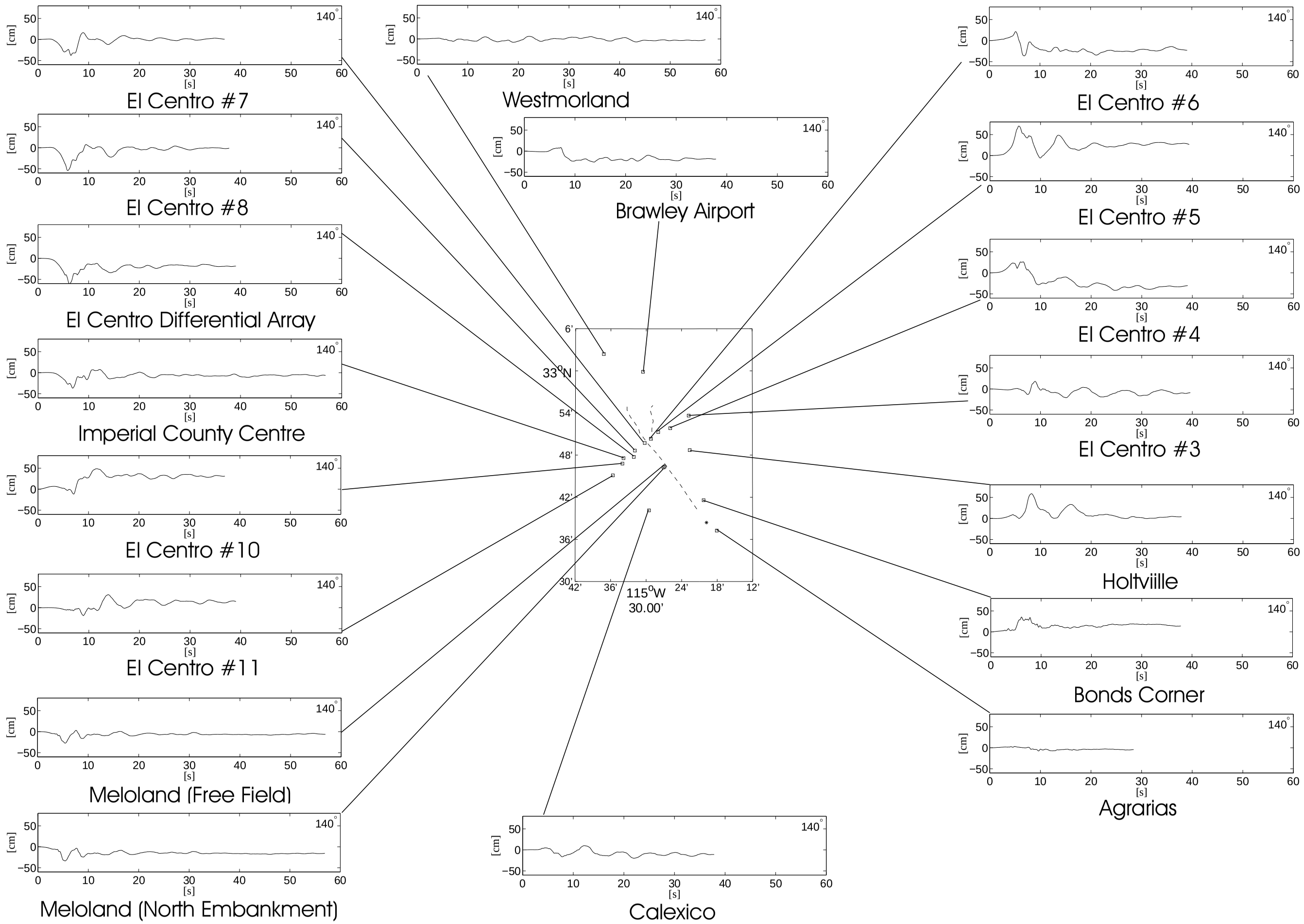

Fig. 9.15: Corrected displacements (using the extended Graizer method with the initial velocity constrained to zero) in the direction 140° east of north at 18 strong-motion stations which recorded the Imperial Valley earthquake (15/10/1979). The dashed line is the surface break and the star is the epicentre.

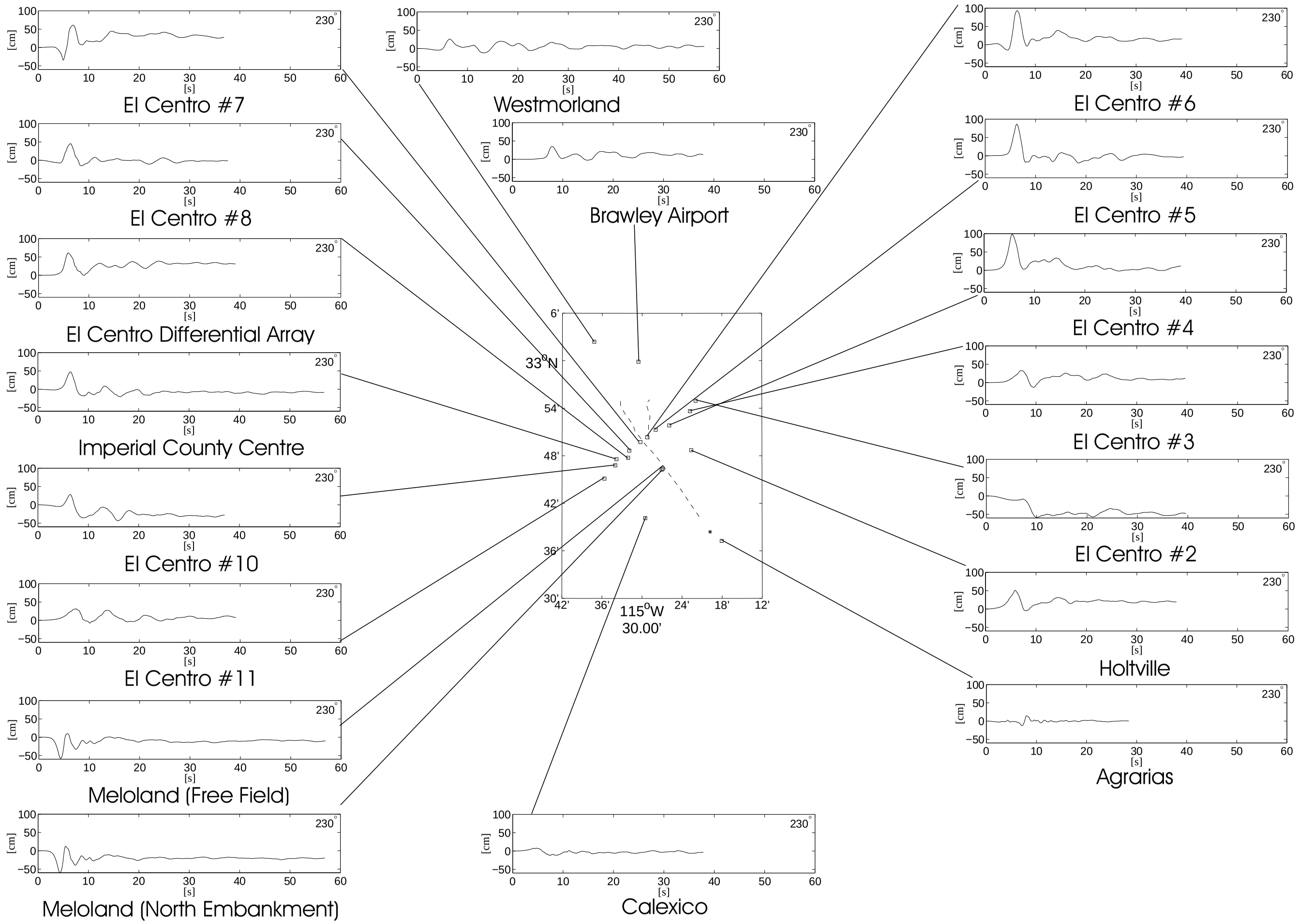

Fig. 9.16: Corrected displacements (using the extended Graizer method with the initial velocity constrained to zero) in the direction $230°$ east of north at 18 strong-motion stations which recorded the Imperial Valley earthquake (15/10/1979). The dashed line is the surface break and the star is the epicentre.

The records from this earthquake are used as a test of the equations given by Vostrikov (1998) (see Section 9.3.3) for predicting the required degree of polynomial needed to give the most accurate correction.

Figure 9.17 shows the strike-parallel component from the El Centro #5 instrument corrected and filtered using a Butterworth filter with cut-off frequencies $0.1\,\mathrm{Hz}$ and 23–$25\,\mathrm{Hz}$. The final $20\,\mathrm{s}$ of this record (ignoring the zero padding introduced during the filtering) shows three waves with average amplitude about $5\,\mathrm{cm}$ and period about $7\,\mathrm{s}$. Using the equations of Vostrikov (1998) with $T_1 = 2\,\mathrm{s}$, $T_2 = 15\,\mathrm{s}$ (see Table 9.8), $A_B = 0.05\,\mathrm{m}$, $T_B = 7\,\mathrm{s}$, $T = 39.380\,\mathrm{s}$ (the length of the record), $\Delta y = 0.01\,\mathrm{ms}^{-2}$ (digitisation error), $\Delta t = 0.005\,\mathrm{s}$ (digitisation interval) and assuming normally distributed errors, gives the long-period reconstruction error δx^* (ignoring the scaling factor A_x) against degree of polynomial, n (Figure 9.18).

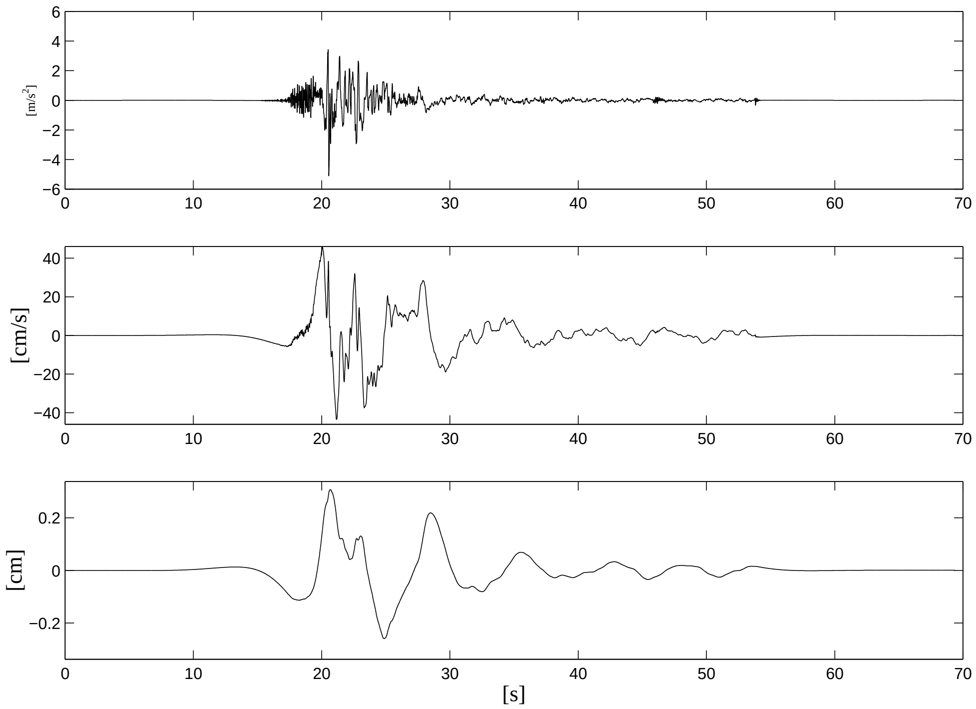

Fig. 9.17: Acceleration, velocity and displacement recorded at El Centro #5 during the Imperial Valley earthquake (15/10/1979), instrument corrected and filtered using a Butterworth filter with cut-offs at $0.1\,\mathrm{Hz}$ and 23–$25\,\mathrm{Hz}$ ($140°$ component). Note the three waves present in the last $20\,\mathrm{s}$ of the record (ignoring the zero padding introduced by the correction procedure) with amplitudes about $5\,\mathrm{cm}$ and periods of about $7\,\mathrm{s}$.

Figure 9.18 shows that for this component the smallest reconstruction error is likely to occur when a cubic (degree 3) polynomial is used and that the reconstruction error when a quadratic (degree 2) or quartic (degree 4) is not much greater. For this component a quadratic (degree 2) polynomial was used for the correction (Table 9.8).

For each of the records for which a sensible correction was achieved (i.e. those given in Ta-

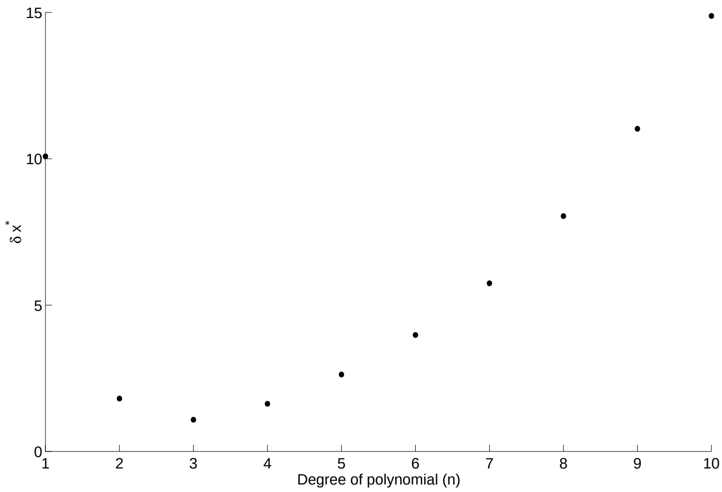

Fig. 9.18: Long-period reconstruction error, δx^*, of El Centro #5 $140°$ component predicted using equations of Vostrikov (1998) against degree of polynomial used, n. Used $T_1 = 2\,\mathrm{s}$, $T_2 = 15\,\mathrm{s}$, $A_B = 0.05\,\mathrm{m}$, $T_B = 7\,\mathrm{s}$, $T = 39.380\,\mathrm{s}$, $\Delta y = 0.01\,\mathrm{ms}^{-2}$, $\Delta t = 0.005\,\mathrm{s}$ and assuming normally distributed errors hence $\gamma = 0.024$, $\gamma_b = 1.4$, $\nu = 0.54$ and $c_0 = 1$.

ble 9.8) the predicted degree of polynomial using the equations of Vostrikov (1998) is calculated by the procedure given above for the strike-parallel component of the El Centro #5 record. The results are given in Table 9.11.

Tab. 9.11: Degree of polynomial with the smallest predicted long-period reconstruction error, ‘Pred. deg.’, using equations of Vostrikov (1998) for the strong-motion records of the Imperial Valley earthquake (15/10/1979) for which realistic correction was achieving using the extended Graizer technique. Always used $\Delta y = 0.01\,\mathrm{ms}^{-2}$, $\Delta t = 0.005\,\mathrm{s}$ and assumed normally distributed errors hence $\gamma = 0.024$, $\gamma_b = 1.4$, $\nu = 0.54$ and $c_0 = 1$. ‘Used deg.’ is the degree of polynomial used when initial velocity constrained to zero. ‘*’ means prediction curve is has a flat minimum.

Station	d_f (km)	Comp.	T (s)	T_1 (s)	T_2 (s)	T_B (s)	A_B (m)	Pred. deg.	Used deg.
Aeropuerto	0	45°	14·765	2	10	0	0	8*	2
El Centro #5	0	140°	39·380	2	15	7	0·05	3	2
		230°	39·385	2	10	7	0·10	2	2
		Up	39·330	2	10	4	0·03	4	4
El Centro #6	1	140°	39·085	2	10	6	0·05	3	2
		230°	39·095	2	10	8	0·08	3	2

continued on next page

Tab. 9.11: *continued*

Station	d_f (km)	Comp.	T (s)	T_1 (s)	T_2 (s)	T_B (s)	A_B (m)	Pred. deg.	Used deg.
Meloland (F.F.)	1	0°	56·895	2	10	8	0·02	5*	3
		270°	56·935	2	10	4	0·02	6*	3
		Up	56·955	0	10	4	0·01	7*	4
Meloland (N. Emb.)	1	0°	56·940	2	10	8	0·02	5*	1
		270°	56·935	2	10	4	0·02	6*	3
		Vert	56·920	0	10	4	0·01	7*	6
Agrarias	2	3°	28·435	4	10	10	0·02	3	4
		273°	28·435	4	10	8	0·01	3	4
Bonds Corner	2	140°	37·790	2	10	6	0·02	4	1
El Centro #4	3	140°	39·090	4	10	8	0·07	3	1
		230°	39·100	4	10	9	0·10	2	1
El Centro #7	3	140°	36·870	3	10	9	0·05	3	2
		230°	36·875	3	10	9	0·06	3	1
		Up	36·865	2	10	5	0·03	3	3
Holtville	5	225°	37·870	4	13	9	0·04	3	1
		315°	37·885	5	20	10	0·05	3	2
Brawley Airport	6	315°	37·880	4	12	8	0·04	3	2
		225°	37·885	4	12	7	0·04	3	2
El Centro #8	6	140°	37·770	2	10	8	0·08	2	1
		230°	37·600	4	10	6	0·05	3	2
		Up	37·820	2	12	3	0·01	5*	3
El Centro D.A.	7	360°	39·100	3	12	8	0·03	3	2
		270°	39·105	3	12	6	0·05	3	1
		Up	39·075	2	12	9	0·01	4	3
Casa Flores	9	270°	18·995	2	12	6	0·01	2	4
El Centro #3	9	140°	39·615	5	12	8	0·08	3	3
		230°	39·630	5	12	9	0·05	3	2
Imperial Co. Cen.	10	2°	56·875	4	10	7	0·02	6*	3
		92°	56·810	4	10	8	0·04	4*	5
		Up	56·865	4	10	3	0·01	8*	5

continued on next page

Tab. 9.11: *continued*

Station	d_f (km)	Comp.	T (s)	T_1 (s)	T_2 (s)	T_B (s)	A_B (m)	Pred. deg.	Used deg.
Calexico	11	315°	37·845	3	15	5	0·05	3	5
		225°	37·845	3	12	7	0·02	4	4
El Centro #2	11	230°	39·630	5	12	9	0·05	3	2
El Centro #10	11	320°	37·020	5	15	5	0·05	3	5
		50°	37·060	5	10	5	0·02	4	2
Cucapah	12	N085	92·529	4	20	7	0·02	8*	8
Westmorland	14	N180	56·995	4	10	5	0·02	6*	2
		N090	56·995	4	10	5	0·03	5*	2
El Centro #11	15	140°	39·080	5	15	7	0·05	3	1
		230°	39·145	5	12	9	0·07	3	2

The equations of Vostrikov (1998) do a reasonable job of predicting the required degree of polynomial needed to yield a realistic correction (Table 9.11). This agreement between the predicted degree of polynomial required for the best correction and the degree of polynomial which actually gives sensible velocity and displacement time-histories suggests a way of removing some of the subjectivity required when using the extended Graizer method for the correction of near-field strong-motion records.

Kaoiki, Hawaii (16/11/1983, $M_w = 6.6$*)*

Only those time-histories for which a sensible correction is obtained are given in Table 9.12. Certain choices of T_1, T_2 and the degree of polynomial to use for the correction yielded sensible velocity and displacement time-histories for other components and for the record from Pahala Kau-Hospital, however the velocity and displacement spectra did not conform to the finding in Section 9.3.6 so these results are not given in Table 9.12.

Jackson *et al.* (1992) measured displacements in the epicentral region of this earthquake using a trilateration network. The closest station to Hawaii National Park — Volcanic Observatory was $13\,\mathrm{km}$ away where the measured displacement was about $70\,\mathrm{cm}$ on an azimuth of $195°$. Therefore the recovered displacement found by constraining the initial velocity to zero (of $8.2\,\mathrm{cm}$ on an azimuth of $158°$) seems reasonable. The displacements (of $41.6\,\mathrm{cm}$ on an azimuth of $246°$) found when the initial velocity is constrained seem too large. The closest station to Mauna Loa-Weather Observatory was $15\,\mathrm{km}$ away where the measured displacement was about $25\,\mathrm{cm}$ in a direction $50°$ clockwise from north. Therefore the recovered displacements for both the constrained and unconstrained cases seem reasonable.

The rupture is bilateral and from the aftershock locations has a length of approximately $12\,\mathrm{km}$ (Jackson *et al.*, 1992). Using rupture velocities between 2 and $3\,\mathrm{kms}^{-1}$ gives a rupture duration between 2 to $3\,\mathrm{s}$. Therefore the period at which spectral velocity and displacement become equal to PGV and PGD for the corrected records from this earthquake are too high. This means the extended Graizer correction method may not work well on these records; however the velocity and displacement time-histories are sensible and the permanent displacements also seem to match those measured.

San Fernando (9/2/1971, $M_w = 6.6$)

The only time-histories for which a sensible correction is obtained are given in Table 9.13.

The component directions are those of Trifunac (1974) who finds that the original component directions (S16E and S74W or N74E and N16W) are wrong. However, the component directions of the Pacoima Dam record are still given in many databanks as N74E and N16W. The three components of this accelerogram currently stored in the Imperial College databank have the reverse polarity (the instrument response rather than the ground response) to those of Trifunac (1974) (see his Figure 6) therefore the polarities of the permanent displacement (Table 9.13) must be reversed when compared with measured displacements.

Burford *et al.* (1971) find that the elevation of the Pacoima Dam station increased by $38.3\,\mathrm{cm}$ because of the San Fernando earthquake, which is a similar value to that obtained by Castle *et al.* (1975) using much more levelling data. The results of Castle *et al.* (1975) show that permanent displacement of less than $2\,\mathrm{cm}$ are expected at other strong-motion stations which recorded this earthquake hence the extended Graizer technique does not need to be used for these records nor does it produce sensible results.

There is a large difference between the permanent displacement recovered from the Pacoima Dam strong-motion record in the vertical direction with initial velocity constrained to zero, $6.8\,\mathrm{cm}$, and the actual measured coseismic displacement, $38.3\,\mathrm{cm}$. The PGD of the vertical component, $32.6\,\mathrm{cm}$, which is the sum of the transient and permanent displacements is also less than the coseismic displacement. The velocity and displacement response spectra of the vertical component are constant for periods greater than $10\,\mathrm{s}$ for velocity and $15\,\mathrm{s}$ for displacement. These periods are slightly greater than the rupture duration which Liu & Heaton (1984) estimate to be about $7\,\mathrm{s}$. This lack of agreement between recovered and measured displacements and because the periods at which the velocity and displacement spectra become constant do not match the rupture duration suggests that the extended Graizer method correction of the vertical component is wrong although the the velocity and displacement time-histories for this component look sensible. Larger permanent displacements can be recovered from the vertical component of the Pacoima Dam record by using higher degree polynomials, for example using fourth and fifth degree polynomials (and leaving T_1 and T_2 unchanged; Table 9.13) gives $29.2\,\mathrm{cm}$ and $61.8\,\mathrm{cm}$ of permanent displacement respectively. These corrections give velocity and displacement spectra with similar periods where the spectral velocity becomes equal to PGV and the spectral displacement becomes equal to PGD to the correction used above. These correction also yield sensible time-histories. However, they were not used here because of the criteria adopted, that the lowest degree polynomial which gives a realistic velocity and displacement time-histories and response spectra is chosen. However, if the initial velocity is not constrained to zero the recovered permanent displacement, $22.9\,\mathrm{cm}$, matches the measured better than for the constrained correction although the recovered displacement is still less than the measured. The velocity and displacement response spectra for the unconstrained and the constrained case are similar.

The total recovered horizontal displacement[2], $24.4\,\mathrm{cm}$, (vector sum of the two horizontal components) although there are no measured values to compare them with, seems roughly correct; the earthquake had a shallow dipping thrust mechanism so the horizontal permanent displacement is probably similar to the vertical movement.

Trifunac (1974) and Heaton (1982) calculated the expected displacements, including the permanent ground displacement, at Pacoima Dam for this earthquake. These calculated displacements provide an excellent test of the ability of the extended Graizer technique to correct the Pacoima Dam record. The corrected displacements of the Pacoima Dam record, using the extended Graizer correction technique (initial velocity not constrained to zero) and the displacements modelled by Trifunac (1974) match well for all components (Figure 9.19). Further, the corrected displacements match the displacements at Pacoima Dam modelled by Heaton (1982) well for the N75W and down components but poorly for the S15W component (Figure 9.19). Therefore the extended Graizer method seems to work for this record.

[2] Both the constrained and unconstrained correction technique give similar results for the horizontal components.

Tab. 9.12: Results from Graizer correction of Kaoiki, Hawaii, records

						Constrained						Unconstrained					
Station	Inst.	d_f	Comp.	T_1	T_2	d	PGV	PGD	RD	V	D	d	PGV	PGD	RD	V	D
		(km)		(s)	(s)		(cms^{-1})	(cm)	(cm)	(s)	(s)		(cms^{-1})	(cm)	(cm)	(s)	(s)
Volcano Obs.	SMA-1	13	360	2	10	3	−80·6	−35·3	−7·6	8	10	2	−82·1	−46·8	−17·1	8	5
			270	2	10	2	73·7	−35·1	−3·1	10	15	2	77·8	52·3	37·9	8	8
Weather Obs.	SMA-1	18	030	5	10	2	34·5	16·6	12·9	10	15	2	35·0	23·9	19·3	10	15

Tab. 9.13: Results from Graizer correction of San Fernando records

						Constrained						Unconstrained					
Station	Inst.	d_f	Comp.	T_1	T_2	d	PGV	PGD	RD	V	D	d	PGV	PGD	RD	V	D
		(km)		(s)	(s)		(cms^{-1})	(cm)	(cm)	(s)	(s)		(cms^{-1})	(cm)	(cm)	(s)	(s)
Pacoima Dam	AR-240	0	S15W	2	12	3	109·3	−71·6	−24·4	8	10	4	111·3	−59·8	−24·4	8	10
			N75W	2	12	5	57·4	12·0	0·9	5	15	4	57·9	−12·6	1·8	5	15
			Down	2	12	2	−57·8	32·6	6·8	10	15	2	59·7	41·8	22·9	10	15

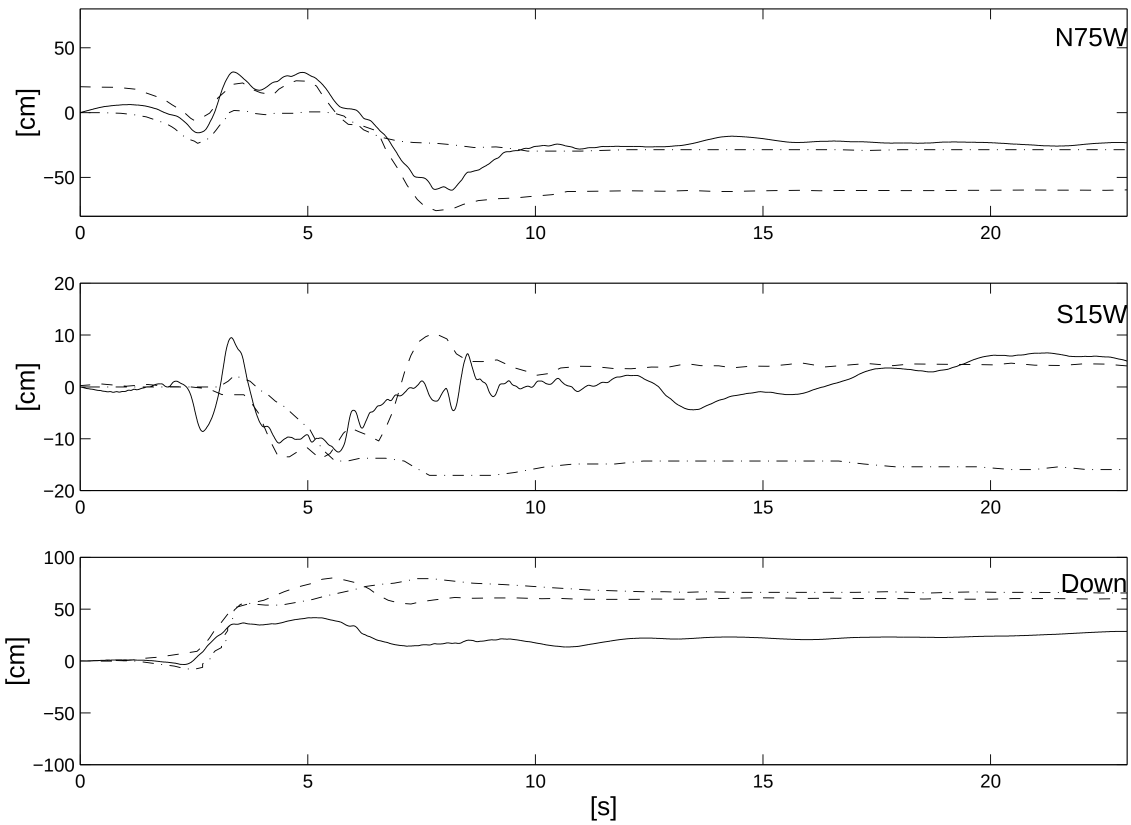

Fig. 9.19: Comparison between corrected displacements of the Pacoima Dam record of the San Fernando earthquake (9/2/1971), using the extended Graizer method with the initial velocity not constrained to zero, and those modelled by Trifunac (1974) and Heaton (1982) for this station. The solid lines are the corrected displacements from the accelerogram and the dashed lines are the modelled displacements of Trifunac (1974) (his Figure 6) and the dash-dotted lines are the modelled displacements of Heaton (1982) (his Figure 10). The displacements of Trifunac (1974) were shifted by $1.5\,\mathrm{s}$ so that they coincided with the displacements from the accelerogram.

Campano Lucano (23/11/1980, $M_w = 6.9$)

All of the near-field accelerograms (there are four from within $15\,\mathrm{km}$ of the surface projection of the rupture plane) of this earthquake show two shocks separated by only about 20–$30\,\mathrm{s}$. As there is not a long enough 'quiet' period before and after each shock the extended Graizer method does not yield sensible results; this demonstrates a problem with the extended Graizer technique for multiple-shock earthquakes.

Loma Prieta (18/10/1989, $M_w = 7.0$)

Only those time-histories for which a sensible correction is obtained are given in Table 9.14. For three near-field records from this earthquake: Corralitos ($d_f = 1\,\mathrm{km}$), Capitola ($d_f = 9\,\mathrm{km}$) and Santa Cruz ($d_f = 15\,\mathrm{km}$), containing more complex waveforms than the records presented in Table 9.14, sensible correction using the extended Graizer technique is not possible. This seems to be a general result, the extended Graizer correction method seems to work well with simple near-field time-histories compared with more complex time-histories such as those recorded in the intermediate and far-field.

Rupture duration estimates for this earthquake range from 6 to $20\,\mathrm{s}$ (Spudich, 1996) therefore the periods at which spectral velocity and displacement attain and remain equal to PGV and PGD for the records corrected using the extend Graizer method are sensible.

Measurements of the horizontal deformations caused by this earthquake have been made using triangulation/trilateration data and GPS data (Williams & Segall, 1996; Snay *et al.*, 1991) and of the vertical deformations using levelling data (Marshall *et al.*, 1991) and GPS data (Williams & Segall, 1996). Unfortunately none of the deformation measurements were taken directly at the strong-motion stations listed in Table 9.14 so an exact comparison cannot be made.

Table 9.15 lists the recovered permanent displacements (RD) from the strong-motion records and those measured, at the closest location to the strong-motion station, by Snay *et al.* (1991) for horizontal deformations and by Marshall *et al.* (1991) for vertical deformations (MD). The distance from the strong-motion station to the point where the measurement of coseismic deformation was taken is also given (D).

The recovered permanent displacements from a number of the strong-motion records match reasonably well with the measured permanent displacements especially in the direction of largest coseismic movement (e.g. Lexington $0°$; Watsonville #3, #4 and #13; Gilroy #1 and #2 $90°$; Gavilan College $67°$; Gilroy #2 $90°$) (Table 9.15). However, for many component of the strong-motion records, especially the vertical components, the recovered permanent displacements are much larger than the measured coseismic displacements (Table 9.15), suggesting that the extended Graizer technique does not work for these components.

Figure 9.20 displays the corrected displacement time-histories for the ten stations given in Table 9.14 and the locations of the strong-motion stations that recorded them. The horizontal components were rotated into NS and EW directions and all the vertical components have positive upward.

Tab. 9.14: Results from Graizer correction of Loma Prieta records

Station	Inst.	d_f	Comp.	T_1	T_2	Constrained						Unconstrained					
						d	PGV	PGD	RD	V	D	d	PGV	PGD	RD	V	D
		(km)		(s)	(s)		(cms^{-1})	(cm)	(cm)	(s)	(s)		(cms^{-1})	(cm)	(cm)	(s)	(s)
Lexington (L. Ab.)	SMA-1	5	0	3	7	4	−88·2	−28·2	−19·3	5	8	4	−88·0	−25·7	−17·0	5	8
			90	3	5	6	−100·0	−36·1	−24·3	5	10	6	−99·4	−37·1	−26·0	5	12
Saratoga	SMA-1	7	0	4	8	3	−42·5	15·5	−8·9	8	12	3	−42·5	−16·1	−9·6	8	12
			90	4	11	3	−47·6	−32·1	−8·4	10	15	3	−47·7	−35·7	−11·5	10	15
			Up	4	11	3	29·7	19·9	7·3	10	12	3	29·9	23·7	10·6	10	12
Watsonville #3	CRA-1	7	0	2	10	5	34·6	16·0	11·6	8	12	5	34·4	16·5	9·9	8	14
Watsonville #4	CRA-1	7	0	2	10	2	36·4	19·5	13·1	8	12	2	36·9	22·2	17·6	8	12
Watsonville #13	CRA-1	7	90	2	7	4	56·0	−30·9	−2·3	5	10	4	56·1	−26·5	1·8	5	10
Gilroy #1	SMA-1	12	0	2	5	5	35·6	18·8	13·7	5	10	6	37·4	24·7	21·0	5	10
			90	2	6	6	31·3	19·5	12·5	10	10	6	31·8	17·7	12·6	10	10
			Up	1	5	6	−17·6	−15·1	−10·9	10	10	6	−17·6	−16·4	−12·3	10	12
Gavilan Coll.	SMA-1	12	337	2	5	4	24·8	9·6	7·2	5	10	4	25·3	14·1	11·4	5	10
			67	2	5	4	33·3	19·0	15·4	5	15	4	33·3	19·1	15·5	5	15
			Up	2	5	3	−15·4	−13·8	−11·1	8	12	3	−16·4	−22·3	−18·5	8	12

continued on next page

Tab. 9.14: *continued*

						Constrained						Unconstrained					
Station	Inst.	d_f (km)	Comp.	T_1 (s)	T_2 (s)	d	PGV (cms^{-1})	PGD (cm)	RD (cm)	V (s)	D (s)	d	PGV (cms^{-1})	PGD (cm)	RD (cm)	V (s)	D (s)
			0	3	7	2	35·2	10·6	3·1	10	10	2	36·2	16·9	11·2	10	10
Gilroy #2	SMA-1	14	90	3	7	7	41·2	19·9	11·8	5	10	7	41·8	19·6	12·7	5	10
			Up	1	5	3	−17·7	−12·5	−10·2	10	12	3	−18·5	−17·8	−15·6	10	15
			180	3	5	7	−22·7	8·7	5·9	5	10	7	−22·6	8·5	5·9	5	10
Gilroy Hist.	SMA-1	15	90	3	5	7	−41·2	15·6	6·5	10	10	7	−41·3	15·8	6·5	10	10
			Up	1	5	6	−15·0	−19·6	−14·7	15	15	6	−15·0	−19·9	−15·0	15	15
			0	3	8	6	38·8	23·4	16·5	5	10	6	38·8	23·3	16·5	5	10
Gilroy #3	SMA-1	15	90	4	7	6	46·0	25·2	5·8	5	8	6	46·5	23·8	5·6	5	8
			Up	2	6	6	−19·3	−23·7	−19·5	10	10	6	−19·0	−23·5	−19·4	10	10

Tab. 9.15: Recovered and measured permanent displacements for Loma Prieta earthquake

Station	d_f (km)	Comp.	Cons RD (cm)	Uncons RD (cm)	MD (cm)	Station	D (km)
Lexington	5	0	−19·3	−17·0	−23·5	St Josephs	2·4
		90	−24·3	−26·0	6·6	St Josephs	2·4
Saratoga	7	0	−8·9	−9·6	−0·5	El Sereno	3·9
		90	−8·4	−11·5	5·9	El Sereno	3·9
		Up	7·3	10·6	−8·09	HS3188	4·9
Watsonville #3	7	0	11·6	9·9	27·0	Pajaro	3·3
Watsonville #4	7	0	13·1	17·6	27·0	Pajaro	3·3
Watsonville #13	7	90	−2·3	1·8	−1·1	Pajaro	3·3
Gilroy #1	12	0	13·7	21·0	6·7	Gilroy	3·9
		90	12·5	12·6	12·8	Gilroy	3·9
		Up	−10·9	−12·3	−4·28	GU2189	2·4
Gavilan Coll.	12	337	7·2	11·4	1·2	Gilroy	4·4
		67	15·4	15·5	14·4	Gilroy	4·4
		Up	−11·1	−18·5	−4·28	GU2189	2·2
Gilroy #2	14	0	3·1	11·2	6·7	Gilroy	5·4
		90	11·8	12·7	12·8	Gilroy	5·4
		Up	−10·2	−15·6	−3·85	GU2190	0·5
Gilroy Hist.	15	180	5·9	5·9	−6·7	Gilroy	5·4
		90	6·5	6·5	12·8	Gilroy	5·4
		Up	−14·7	−15·0	−3·44	HS2720	0·2
Gilroy #3	15	0	16·5	16·5	6·7	Gilroy	7·3
		90	5·8	5·6	12·8	Gilroy	7·3
		Up	−19·5	−19·4	−3·85	GU2190	0·9

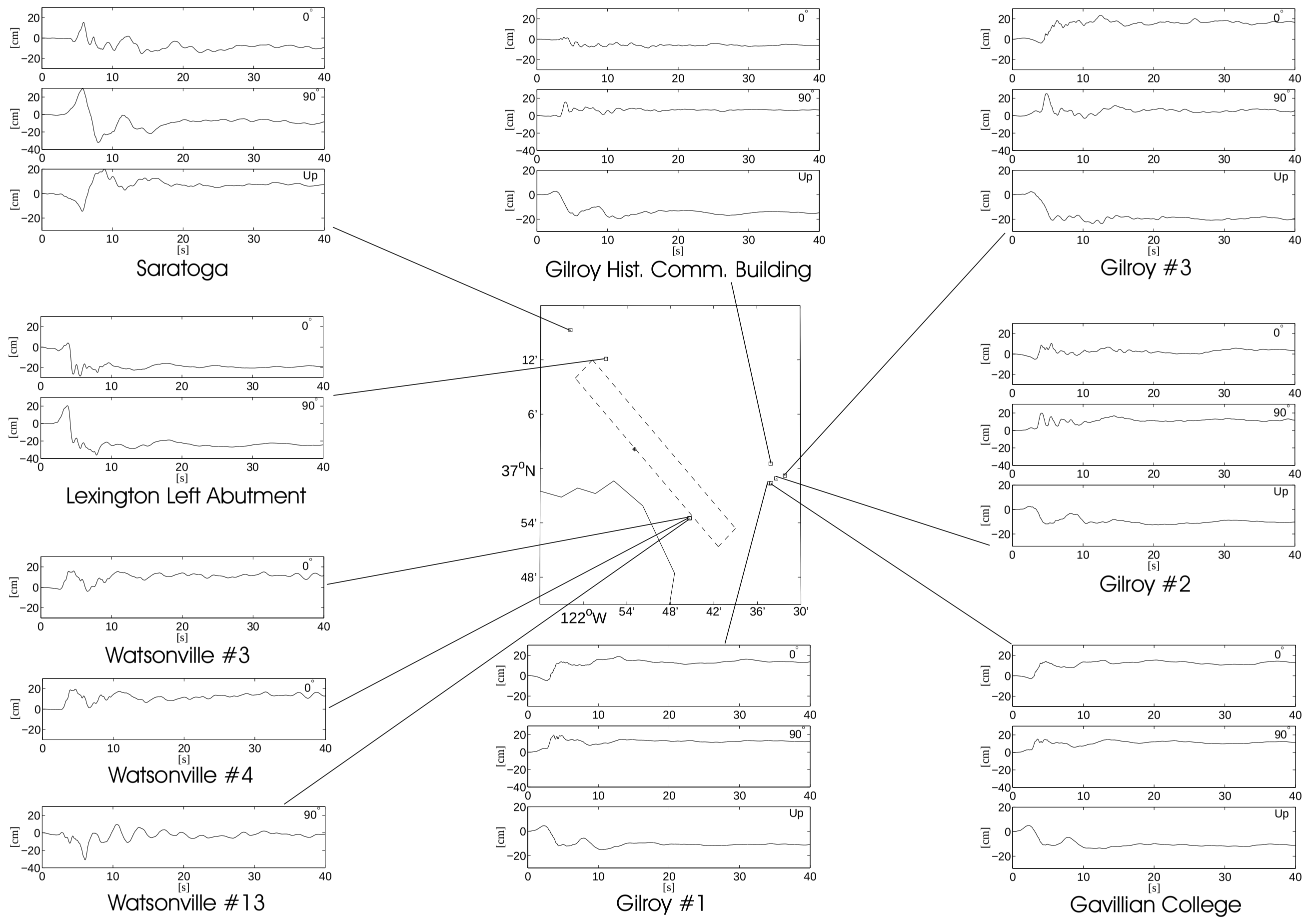

Fig. 9.20: Corrected displacements (using the extended Graizer method with the initial velocity constrained to zero) in the directions $0°$ and $90°$ east of north and upwards at ten strong-motion stations which recorded the Loma Prieta earthquake (18/10/1989). The dashed rectangle is the surface projection of the rupture plane from Stevens & Day (1994) and the star is the epicentre.

Figure 9.20 shows that many of the corrected displacement traces exhibit similar features, suggesting that the extended Graizer method yields a sensible correction for these records. In particular note the agreement in the displacement time-histories for all three components from Gilroy #1, Gavillian College, Gilroy #2 and Gilroy #3 and also the similarity between the NS components at Watsonville #3 and Watsonville #4. The horizontal components at Saratoga and Lexington Left Abutment also show similar features. The displacement in the NS direction at Gilroy Historical Commercial Building has a similar shape to the displacement trace in the same direction at the nearby stations: Gilroy #1, #2 and #3 and Gavillian College, but in the opposite direction suggesting that possibly the polarity of this component is wrong.

Cape Mendocino (25/4/1992, $M_w = 7.2$)

The only time-histories for which a sensible correction is obtained are given in Table 9.16. Unfortunately some of the near-field accelerograms are currently only available in already corrected form. Some of the near-field accelerograms include prominent surface-waves at the end of the record which prevents the extend Graizer method yielding realistic results.

The rupture duration of this earthquake has been estimated by Oglesby & Archuleta (1997) using strong-motion modelling as about $10\,\mathrm{s}$. The periods at which the velocity and displacement spectra reach PGV and PGD match this well.

There was a GPS station (Bear Ridge 2) only $0.5\,\mathrm{km}$ from the Bunker Hill (Transmitter) strong-motion station, at which coseismic displacements of $19.73{\pm}0.52\,\mathrm{cm}$ west and $11.39{\pm}0.76\,\mathrm{cm}$ south were measured (Murray *et al.*, 1996). Comparing these measured coseismic displacements with those recovered from the Bunker Hill (Transmitter) accelerograms, $21.1\,\mathrm{cm}$ south for constrained fit ($21.9\,\mathrm{cm}$ for unconstrained fit) and $59.5\,\mathrm{cm}$ west for constrained fit ($71.2\,\mathrm{cm}$ for unconstrained fit), shows that although the direction of the permanent displacement is about right the size of the recovered displacements is too large. This difference between the recovered and measured coseismic displacements shows that the extended Graizer method does not work well on this strong-motion record although the corrected velocity and displacement time-histories look sensible.

Düzce (12/11/1999, $M_w = 7.2$)

The only time-history for which a sensible correction is obtained is given in Table 9.17.

Tab. 9.16: Results from Graizer correction of Cape Mendocino records

						Constrained						Unconstrained					
Station	Inst.	d_f	Comp.	T_1	T_2	d	PGV	PGD	RD	V	D	d	PGV	PGD	RD	V	D
		(km)		(s)	(s)		(cms^{-1})	(cm)	(cm)	(s)	(s)		(cms^{-1})	(cm)	(cm)	(s)	(s)
Bunker Hill	SMA-1	9	360	2	6	1	−51·4	−31·0	−21·1	5	10	1	−51·5	−31·5	−21·9	5	10
			270	2	6	1	76·0	71·1	59·5	8	10	1	77·2	85·7	71·2	8	10

Tab. 9.17: Results from Graizer correction of Duzce records

						Constrained						Unconstrained					
Station	Inst.	d_f	Comp.	T_1	T_2	d	PGV	PGD	RD	V	D	d	PGV	PGD	RD	V	D
		(km)		(s)	(s)		(cms^{-1})	(cm)	(cm)	(s)	(s)		(cms^{-1})	(cm)	(cm)	(s)	(s)
			NS	5	20	2	−56·5	−35·6	−2·3	5	20	2	−56·5	−35·8	−2·5	5	20
Bolu	GSR-16	18	EW	5	20	2	65·4	−22·4	−8·7	5	10	2	65·4	−22·6	−8·9	5	10
			Up	5	20	2	25·3	26·4	22·5	10	15	2	25·3	25·3	20·8	10	15

Coseismic displacements for this earthquake were measured using GPS data (Ayhan *et al.*, 2001). Unfortunately the closest GPS station to the Bolu strong-motion station is $21\,\mathrm{km}$ away where the measured permanent displacements are about $15\,\mathrm{cm}$ (azimuth $310°$) horizontally and about $8\,\mathrm{cm}$ vertically (both measured from Figure 1 of Ayhan *et al.* (2001)). Comparing these with the permanent displacement recovered from the Bolu accelerogram (see Table 9.17) shows that the permanent displacement from the EW component (8.7 or $8.9\,\mathrm{cm}$ west) matches well with the measured displacement ($15 \times \sin 50° = 11.5\,\mathrm{cm}$ west), the permanent displacement from the NS component (2.3 or $2.5\,\mathrm{cm}$ south) does not match well with the measured displacement ($15 \times \cos 50° = 9.6\,\mathrm{cm}$ north) and neither does the permanent displacement from the Up component (22.5 or $20.8\,\mathrm{cm}$) match the measured displacement ($8\,\mathrm{cm}$) well. However, due to the large distance between the GPS station and the strong-motion station the predicted permanent displacement at Bolu, using the model presented by Ayhan *et al.* (2001) assuming only strike-slip faulting (see Table 1 of Ayhan *et al.* (2001)) and the equations of Mansinha & Smylie (1971), was calculated. Note that the Düzce earthquake had a significant normal faulting component (Ayhan *et al.*, 2001) so the predicted permanent displacements are likely to be only roughly correct when only strike-slip faulting is modelled. This modelling gives a predicted horizontal displacement of $22\,\mathrm{cm}$ in a direction about $45°$ west of north and a predicted vertical uplift of $3\,\mathrm{cm}$ for the Bolu strong-motion station.

Therefore the permanent displacement recovered from the Bolu strong-motion record does not seem to match the actual coseismic displacement well except for the EW component where the match is good. However, because the true displacement which occurred at the Bolu station is unknown (the nearest measured displacement was about $21\,\mathrm{km}$ away) and the modelling which was done here is simple the match between the recovered and true displacement may be better than this analysis suggests.

The rupture duration of this earthquake is estimated to be about $14\,\mathrm{s}$ (Tibi *et al.*, 2001), this is a good match to the period at which spectral displacement becomes roughly equal to PGD (10–20 s) for the Bolu record. The period at which spectral velocity becomes roughly equal to PGV for the Bolu record (5–10 s) is much less than the rupture duration.

Tabas (16/9/1978, $M_w = 7.4$)

The only time-history for which a reasonable correction is obtained is given in Table 9.19. The other near-source accelerograms from this earthquake had the appearance similar to what would occur if the original film had occasionally slipped on the digitisation table during the digitisation process (Shoja-Taheri & Anderson, 1988). These long-period errors prevent the extended Graizer method from yielding a realistic correction.

Table 9.19 shows that there is a large difference in the PGD and RD recovered from the Tabas accelerogram when the initial velocity is constrained to $0\,\mathrm{cms}^{-1}$ and when it is not. The corrected velocity and displacement traces when the initial velocity is unconstrained, look less reliable than the corrected velocity and displacement when the initial velocity is constrained to $0\,\mathrm{cms}^{-1}$ as do the velocity and displacement response spectra.

Rupture velocities for this earthquake range from $2.5\,\mathrm{kms}^{-1}$ (Hartzell & Mendoza, 1991) to $2.7\,\mathrm{kms}^{-1}$ (Shoja-Taheri & Anderson, 1988). From inversion of strong-motion and teleseismic data, Hartzell & Mendoza (1991) calculate that the rupture propagated about $70\,\mathrm{km}$ to the NW of the epicentre and about $20\,\mathrm{km}$ to the SE of the epicentre, therefore using a rupture velocity of 2.5–$2.7\,\mathrm{kms}^{-1}$ gives a rupture duration of between 26 and $28\,\mathrm{s}$. This matches the period at which spectral displacement is about equal to PGD (20–$30\,\mathrm{s}$) but is much larger than the period at which spectral velocity becomes about equal to PGV (10–$15\,\mathrm{s}$).

Unfortunately measurements of the horizontal permanent displacements for this earthquake do not seem to have been made except directly on the surface break (Berberian, 1979). Therefore estimates of the permanent ground displacements were estimated using the dip slip equations of Mansinha & Smylie (1971) using the surface projection of the L1 fault plane calculated by Hartzell & Mendoza (1991) (length $90\,\mathrm{km}$ and width about $25\,\mathrm{km}$) for their inversion and a uniform slip of $225\,\mathrm{cm}$ from the surface faulting (Berberian, 1979). The estimated distribution of slip on the rupture plane found by Hartzell & Mendoza (1991) is complex so the calculated permanent displacement using this simple model can only be a rough estimate. Also Hartzell & Mendoza (1991) note that the fault plane they use for the inversion does not exactly correlate with the observed surface faulting which is a further source of error in the calculated permanent displacements using this simple model. The permanent displacement using the extended Graizer method (initial velocity constrained to zero) is $32.2\,\mathrm{cm}$, azimuth $12°$. The calculated horizontal permanent displacement at Tabas using the simple model is $81.5\,\mathrm{cm}$, azimuth $59°$. Therefore the permanent displacement recovered from the accelerogram does not match closely the estimated permanent displacement although the corrected velocity and displacement look sensible.

Kocaeli (17/8/1999, $M_w = 7.4$)

Only those time-histories for which a sensible correction to obtained are given in Table 9.18. The records from Izmit are cut at $33\,\mathrm{s}$ because of a second shock. Records from Sakarya are cut at $100\,\mathrm{s}$ because of multiple shocks.

The component directions for Yarimca are from Anderson *et al.* (2000) and are slightly different than those originally reported ($330°$ was reported as North-South and $60°$ as East-West).

Tab. 9.18: Results from Graizer correction of Kocaeli records

Station	Inst.	d_f	Comp.	T_1	T_2	Constrained						Unconstrained					
						d	PGV	PGD	RD	V	D	d	PGV	PGD	RD	V	D
		(km)		(s)	(s)		(cms^{-1})	(cm)	(cm)	(s)	(s)		(cms^{-1})	(cm)	(cm)	(s)	(s)
Sakarya	GSR-16	3	EW	None		0	80·7	209·1	201·6	20	25	0	80·7	209·1	201·6	20	25
			Up	30	40	6	−43·3	−26·4	−22·0	15	25	6	−43·3	−26·6	−22·2	15	25
Yarimca-Petkim	GSR-16	5	330°	5	30	2	87·3	155·5	140·7	15	25	1	85·7	130·4	108·0	15	20
			60°	5	30	4	87·2	180·2	158·2	15	20	4	87·3	181·3	159·5	15	20
			Up	5	30	2	31·4	−43·1	−22·3	15	25	2	31·6	−40·7	−16·6	15	25
Izmit	SMA-1	8	SN	2	10	6	26·2	34·5	22·6	8	25	6	24·8	28·1	14·7	8	25
			EW	2	10	7	40·8	29·5	9·3	8	15	7	42·6	33·3	15·6	8	15
Duzce	SMA-1	14	SN	None		0	58·4	−62·1	−31·4	20	25	0	58·4	−62·1	−31·4	20	25
			West	5	10	3	61·8	52·5	38·3	10	20	2	60·0	45·9	35·1	10	20
Iznik	SMA-1	29	SN	10	15	6	−19·0	−12·6	−3·0	15	20	6	−19·0	−12·3	−2·6	10	20
			WE	10	20	3	−27·3	−42·5	−4·1	15	20	2	−29·8	−41·3	−24·3	20	20
			Up	10	20	7	10·4	10·6	2·8	15	25	6	10·8	15·3	8·8	15	25
Goynuk	SMA-1	31	NS	6	11	8	−11·6	−4·9	−3·2	10	20	8	−11·5	−4·4	−2·7	10	20
			EW	7	13	8	14·0	13·1	10·4	10	20	8	13·6	11·5	8·7	10	10
			Up	7	15	4	−17·2	14·0	−9·2	20	25	4	−16·9	15·6	−6·1	10	30

continued on next page

Tab. 9.18: *continued*

Station	Inst.	d_f	Comp.	T_1	T_2	Constrained d	PGV	PGD	RD	V	D	Unconstrained d	PGV	PGD	RD	V	D
		(km)		(s)	(s)		(cms^{-1})	(cm)	(cm)	(s)	(s)		(cms^{-1})	(cm)	(cm)	(s)	(s)
Gebze — Tubitak	SMA-1	32	NS	4	14	4	−47·1	−86·3	0·3	20	25	3	−45·5	−81·4	14·8	20	25
Gebze — Arcelik	GSR-16	60	NS	5	50	1	16·7	66·4	33·0	40	20	1	16·8	68·0	37·7	40	20
			EW	5	50	1	−44·4	−65·9	−28·0	20	15	1	−44·3	−64·8	−25·1	20	15
			Down	5	50	3	8·3	7·2	0·5	20	30	3	8·3	7·3	0·6	20	30

Tab. 9.19: Results from Graizer correction of Tabas records

Station	Inst.	d_f	Comp.	T_1	T_2	Constrained d	PGV	PGD	RD	V	D	Unconstrained d	PGV	PGD	RD	V	D
		(km)		(s)	(s)		(cms^{-1})	(cm)	(cm)	(s)	(s)		(cms^{-1})	(cm)	(cm)	(s)	(s)
Tabas	SMA-1	3	N74E	5	20	8	−99·6	92·8	15·3	10	25	8	−96·3	123·1	51·2	10	25
			N16W	5	20	9	−107·2	−107·3	28·3	15	20	9	−114·0	−162·2	−45·4	15	30

A detailed GPS survey was conducted after the earthquake and the measured coseismic displacements are given in Reilinger *et al.* (2000). A comparison of the permanent displacements measured using GPS and those from the accelerograms using the extended Graizer method (with initial velocity constrained to zero) (see Table 9.20) shows that the recovered displacements from Sakarya and Duzce match the measured coseismic displacements well, both in size and direction (Figure 9.21). The recovered displacements at Yarimca and Izmit are much different than the measured displacements and so the extended Graizer method fails for these two records. The recovered permanent displacements at Goynuk and Iznik are both small, as measured in the area around the stations and hence the extended Graizer method may work for these records. The recovered permanent displacements at Gebze — Arcelik are in exactly the opposite direction to those measured at nearby GPS stations however the corrected velocity and displacement traces are sensible and show a simple near-field shape (see Figure 9.22) suggesting that the polarities of this record are incorrect and that the extended Graizer method does work on this record. Also this simple near-field shape suggests that the rupture of this earthquake did reach farther west than the end of the observed surface fault break and hence the surface projection distances given in Table 9.18 need to be changed because they are based on the observed surface fault break.

The rupture duration of the main shock of this earthquake is estimated to be between $20\,\mathrm{s}$ (Yagi & Kikuchi, 2000) and $25\,\mathrm{s}$ (Tibi *et al.*, 2001). The estimates are a good match to the period at which spectral velocity and spectral displacement become roughly equal to PGV and PGD, respectively, for the records reported in Table 9.18.

Chi-Chi (20/9/1999, $M_w = 7.6$)

Only strong-motion records within $10\,\mathrm{km}$ of the surface projection of the rupture plane of this earthquake were corrected using the Graizer correction technique because of the large number of high-quality strong-motion records. The results are given in Table 9.20.

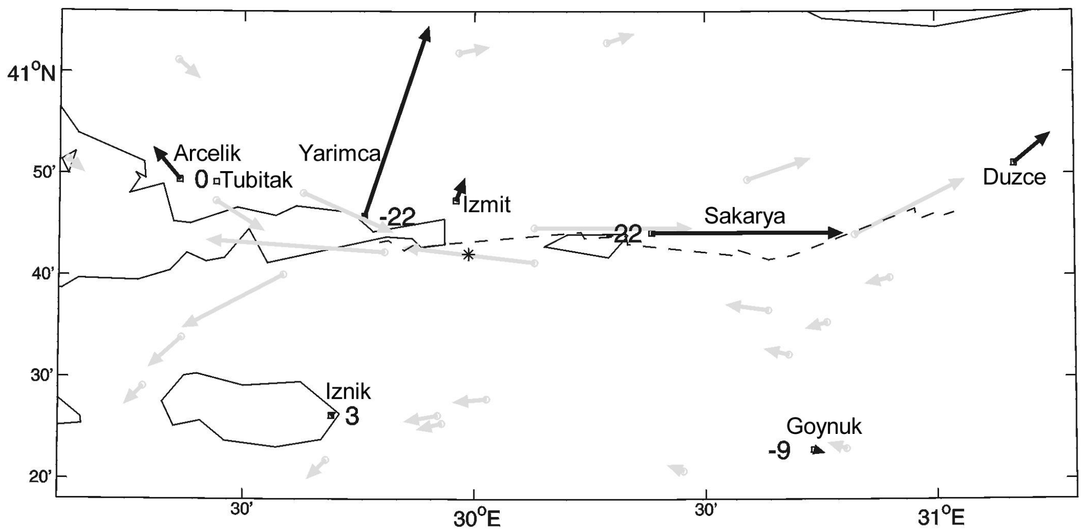

Fig. 9.21: Comparison of the permanent displacements recovered from the accelerograms corrected using the extend Graizer method constraining the initial velocity to zero with those measured using GPS for the Kocaeli earthquake (17/8/1999). Black arrows are the recovered permanent displacements from the accelerograms and grey arrows are the measured displacements from GPS measurements. The dashed line is the observed surface fault break. The numbers are the vertical uplifts recovered. Only the EW component of the Sakarya instrument worked so assumed that the coseismic displacement was entirely in a EW direction. The extended Graizer correction technique only yield reasonable velocity and displacement time-histories for the NS component of the Gebze – Tubitak record so assumed the coseismic displacement was entirely in the NS direction.

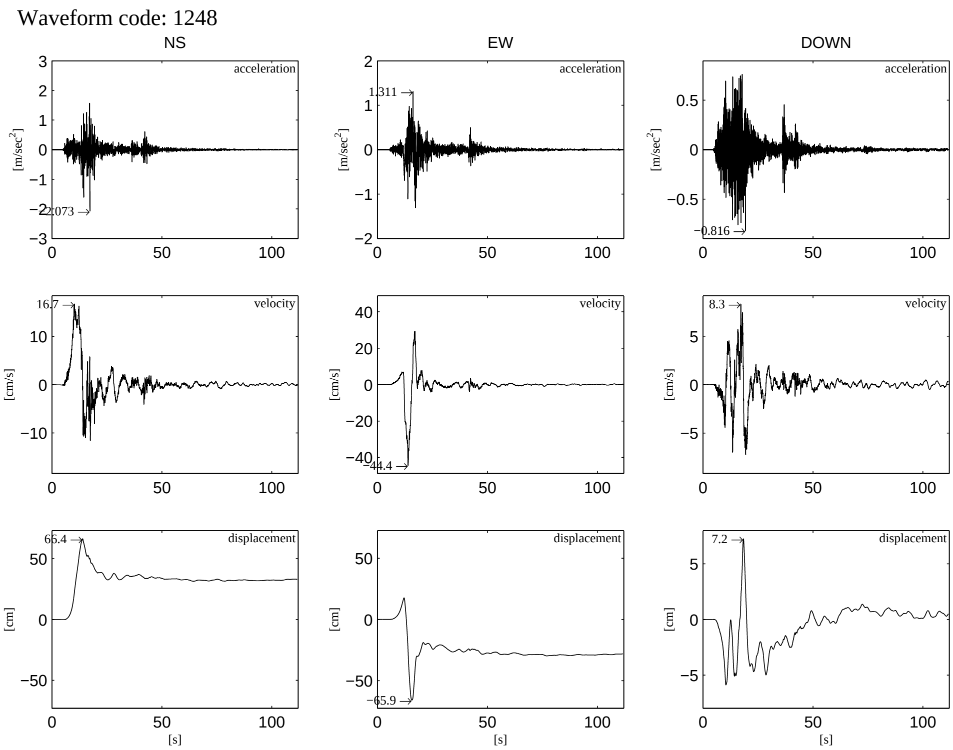

Fig. 9.22: Corrected acceleration, velocity and displacement, using the extended Graizer method (with the initial velocity constrained to zero) recorded at Gebze – Arcelik. Note the simple near-field shape especially of the two horizontal components.

Tab. 9.20: Results from Graizer correction of Chi-Chi records

Station	Inst.	d_f	Comp.	T_1	T_2	Constrained						Unconstrained					
		(km)		(s)	(s)	d	PGV (cms^{-1})	PGD (cm)	RD (cm)	V (s)	D (s)	d	PGV (cms^{-1})	PGD (cm)	RD (cm)	V (s)	D (s)
CHY080	A900	0	NS	20	60	6	−91·2	−44·4	−13·3	15	30	6	−91·1	−44·3	−13·3	15	30
			V	20	60	3	−40·8	27·3	7·0	15	30	3	−40·8	27·0	5·8	15	30
CHY074	A900	0	NS	20	60	2	−20·8	−32·2	−27·8	20	20	2	−20·9	−33·6	−28·6	20	20
			EW	20	60	4	−32·3	−30·0	−23·9	15	20	4	−32·3	−30·2	−24·1	15	20
TCU052	A900	1	NS	20	50	2	213·4	598·0	455·7	25	30	2	213·3	614·1	465·4	25	30
			EW	20	50	3	−170·5	−380·6	−208·6	25	30	3	−171·5	−387·3	−224·0	25	30
			V	20	50	1	168·5	381·8	315·3	20	30	1	168·8	398·3	334·1	20	30
TCU068	A900	1	NS	20	60	3	281·4	677·2	340·9	25	30	3	282·6	689·9	369·8	25	30
			EW	20	60	6	−285·6	−758·8	−651·2	20	30	6	−285·7	−759·7	−651·9	20	30
			V	20	60	1	229·0	455·5	348·5	15	25	1	229·0	453·4	346·0	15	25
TCU065	A900	1	EW	20	60	2	131·4	199·4	102·5	20	20	2	131·6	185·2	107·9	20	20
			V	20	60	1	69·2	−56·4	−2·4	15	15	1	69·1	−60·2	−7·4	15	15
TCU129	A900	2	NS	20	60	5	−54·0	−46·9	−1·0	15	15	5	−54·2	−48·9	−10·1	15	15
			EW	20	60	6	68·4	129·5	14·1	20	20	6	68·5	130·0	14·7	20	20
			V	20	60	3	38·6	21·2	2·3	10	20	3	38·6	21·3	3·7	10	20

continued on next page

Tab. 9.20: *continued*

Station	Inst.	d_f	Comp.	T_1	T_2	Constrained						Unconstrained					
		(km)		(s)	(s)	d	PGV (cms^{-1})	PGD (cm)	RD (cm)	V (s)	D (s)	d	PGV (cms^{-1})	PGD (cm)	RD (cm)	V (s)	D (s)
			NS	20	60	2	−54·3	−75·3	−33·5	20	40	2	−54·3	78·4	−31·6	20	40
TCU067	A900	2	EW	20	60	2	98·9	201·7	140·7	20	30	2	99·0	199·7	141·5	20	30
			V	20	60	3	−51·2	−72·9	−60·2	10	25	3	−51·5	−78·6	−66·5	10	25
			NS	20	60	1	−71·1	−93·0	−60·8	15	30	1	−71·3	100·8	−70·1	15	30
TCU102	A900	3	EW	20	60	1	−86·1	196·1	131·6	20	30	1	−86·4	180·1	112·2	20	30
			V	20	60	1	68·0	50·1	−4·3	15	20	1	68·0	50·3	−3·9	15	20
			NS	20	60	5	−65·2	−97·8	−84·2	20	30	5	−65·1	−94·9	−80·8	20	30
TCU076	A900	3	EW	20	60	3	66·7	93·6	−2·8	15	30	3	66·8	93·5	0·8	15	30
			V	20	60	2	−32·6	−26·9	−7·6	20	20	2	−32·5	−28·2	−7·0	20	20
			NS	20	60	2	−37·1	−60·0	−44·2	15	30	2	−37·1	−59·7	−44·7	15	30
TCU075	A900	3	EW	20	60	1	116·0	166·9	95·9	20	20	1	116·0	168·0	97·4	20	20
			V	20	60	1	49·7	−45·5	−33·7	10	15	1	49·8	−44·2	−32·2	10	15
			NS	5	30	1	−55·6	−112·2	−89·4	20	20	1	−55·8	−117·8	−95·2	20	20
TCU101	A900	4	EW	5	30	1	−72·5	137·5	87·5	30	30	1	−72·3	143·1	95·7	30	30
			V	5	30	1	46·1	47·0	−11·5	20	20	1	46·3	51·3	−5·4	20	20

continued on next page

Tab. 9.20: *continued*

						Constrained						Unconstrained					
Station	Inst.	d_f	Comp.	T_1	T_2	d	PGV	PGD	RD	V	D	d	PGV	PGD	RD	V	D
		(km)		(s)	(s)		(cms^{-1})	(cm)	(cm)	(s)	(s)		(cms^{-1})	(cm)	(cm)	(s)	(s)
CHY028	A900	4	V	20	50	2	−30·6	26·1	7·5	20	20	2	−30·6	25·6	7·2	20	20
			NS	20	60	1	59·7	−104·2	−52·4	20	30	1	59·7	−107·2	−55·4	20	30
TCU049	A900	6	EW	20	60	1	55·9	105·3	26·3	30	30	1	56·1	117·8	41·6	30	30
			V	20	60	1	27·0	−24·1	−15·7	15	20	1	27·0	−20·6	−12·0	15	20
			NS	20	60	5	−21·7	−63·2	−32·8	15	25	5	−21·6	−58·5	−25·4	15	25
TCU103	A900	7	EW	20	60	1	−68·3	108·2	57·5	20	30	1	−68·4	105·5	54·3	20	30
			V	20	60	1	−61·2	50·8	−10·0	20	20	1	−61·1	51·8	−8·8	20	20
			NS	20	60	1	43·5	−124·9	−74·3	15	30	1	43·7	−112·4	−61·9	15	30
TCU053	A900	8	EW	20	60	1	42·8	112·4	59·1	30	30	1	42·9	115·8	63·3	30	30
			V	20	60	2	32·2	−31·0	−10·2	15	20	2	32·1	−30·5	−10·8	15	20
			NS	20	60	2	−45·7	−147·0	−101·8	25	30	2	−45·8	−146·4	−103·9	25	30
TCU054	A900	8	EW	20	60	1	46·3	128·5	68·6	30	30	1	46·2	124·3	63·5	30	30
			V	20	60	1	29·5	−37·1	−23·5	10	15	1	29·5	−33·4	−19·7	10	15

continued on next page

Tab. 9.20: *continued*

Station	Inst.	d_f	Comp.	T_1	T_2	Constrained						Unconstrained					
						d	PGV	PGD	RD	V	D	d	PGV	PGD	RD	V	D
		(km)		(s)	(s)		(cms^{-1})	(cm)	(cm)	(s)	(s)		(cms^{-1})	(cm)	(cm)	(s)	(s)
			NS	20	60	1	−43·9	−127·2	−90·9	25	30	1	−43·8	−118·2	−82·0	25	30
TCU082	A900	8	EW	20	60	1	−52·4	139·0	45·5	30	30	1	−52·2	148·4	57·2	30	30
			V	20	60	2	−35·3	26·9	−18·1	15	15	2	−35·4	27·4	−18·4	15	15
			NS	20	60	1	34·8	−45·1	−27·5	15	20	1	34·8	−41·5	−24·0	15	20
TCU120	A900	9	EW	20	60	1	62·4	104·2	41·2	20	30	1	62·4	102·5	38·9	20	30
			V	20	60	1	−35·9	−31·7	−26·3	20	20	1	−35·9	−30·7	−25·3	20	20
			NS	7	40	1	−51·3	−92·4	−18·3	20	20	1	−50·4	−58·9	15·8	20	30
TCU055	A900	9	EW	10	40	1	53·8	142·2	62·5	30	30	1	53·6	138·6	57·0	30	30
			V	10	40	1	−58·6	33·9	0·4	20	20	1	−58·3	41·0	10·4	20	20
			NS	20	60	2	−44·3	−79·6	−53·4	15	30	2	−44·3	−80·4	−53·0	15	30
TCU087	A900	9	EW	20	60	2	−45·5	59·5	−22·0	20	30	2	−45·5	61·0	−22·7	20	30
			V	20	60	1	−58·8	52·5	−16·0	20	15	1	−58·8	56·1	−11·7	20	15
			NS	20	60	1	43·2	−35·4	−2·6	15	20	1	43·2	−33·0	0·1	15	20
TCU122	A900	10	EW	20	60	1	45·3	107·5	83·1	20	30	1	45·1	97·9	71·7	20	30
			V	20	60	2	41·4	35·3	7·4	20	20	2	41·5	33·5	8·1	20	20

continued on next page

Tab. 9.20: *continued*

						Constrained						Unconstrained					
Station	Inst.	d_f (km)	Comp.	T_1 (s)	T_2 (s)	d	PGV (cms^{-1})	PGD (cm)	RD (cm)	V (s)	D (s)	d	PGV (cms^{-1})	PGD (cm)	RD (cm)	V (s)	D (s)
CHY024	A900	10	NS	20	60	1	43·6	34·6	16·2	15	15	1	43·5	29·6	9·8	15	15
			V	20	60	1	46·7	−36·1	−17·4	20	20	1	46·8	−30·8	−10·5	20	20
TCU051	A900	10	NS	20	60	1	41·6	−98·8	−58·3	30	30	1	41·6	−103·3	−62·7	30	30
			EW	20	60	2	−51·8	118·1	49·1	30	30	2	−51·8	118·1	49·1	30	30
			V	20	60	1	−30·7	−34·3	−25·8	15	15	1	−30·7	−33·4	−24·9	15	15
TCU060	A900	10	NS	20	60	2	−43·9	−94·5	−46·9	20	30	2	−44·0	−93·8	−48·0	20	30
			EW	20	60	1	37·3	112·9	84·6	30	30	1	37·2	105·2	75·0	30	30
			V	20	60	1	−28·4	−33·7	−6·2	15	20	1	−28·4	−29·5	−1·7	15	20
TCU136	IDS	10	NS	20	60	2	−52·8	−83·7	−35·5	20	20	2	−52·8	−83·6	−35·3	20	20
			EW	20	60	1	−44·0	92·8	32·1	20	30	1	−43·8	103·0	46·7	20	30
			V	20	60	2	−33·4	36·5	10·7	10	20	2	−33·4	36·1	10·3	10	20

A detailed GPS survey was conducted after the earthquake and the measured coseismic displacements are given in Central Geological Survey (1999). Comparing the recovered permanent displacements from the accelerograms using the extended Graizer method (with initial velocity to zero) (see Table 9.20) with those measured using GPS shows that the recovered displacements from the accelerograms are a good match to those measured and hence the extended Graizer method seems to work for these records (Figure 9.23).

The rupture duration of this earthquake is estimated as about $32\,\mathrm{s}$ (Yagi & Kikuchi, 1999) which is similar to the period at which spectral velocity and displacement become approximately equal to PGV and PGD respectively.

Although sensible corrected velocity and displacement time-histories could be found using the extended Graizer method on the strong-motion records from TCU071, TCU072, TCU078, TCU079, TCU084 and TCU089 the spectral velocity and spectral displacement calculated using these corrected records did not become equal to PGV and PGD until periods much greater than the rupture duration. Therefore these results are not reported in Table 9.20. One possible reason for this behaviour of these records is that they are from the region in which the largest tilts probably occurred during this earthquake. Figure 9.24 shows the calculated tilt and horizontal displacement perpendicular to the fault strike, the uplift that occurred during this earthquake and the approximate location of these six stations. The tilts and displacements were calculated using the dip-slip equations of Mansinha & Smylie (1971) and hence are only estimates; the model was not optimised to match with the GPS data.

Figure 9.24 shows that the six strong-motion stations stations: TCU071, TCU072, TCU078, TCU079, TCU084 and TCU089 are all located in the area where large tilts, up to $3 \times 10^{-4}\,\mathrm{rads}$, occurred. Such large tilts are likely to have had a large effect on the recorded ground motions which are assumed to be a record of only the translational ground displacement. The other stations which recorded this earthquake, including those for which large permanent displacements occurred and were recovered from the accelerograms (e.g. TCU052 and TCU068) probably experienced smaller tilts than occurred at TCU071, TCU072, TCU078, TCU079, TCU084 and TCU089, hence the true translational ground displacement was recorded. Note that the largest tilts, due to the static faulting, do not occur where the largest vertical displacements occurred for this earthquake.

Michoacán (19/9/1985, $M_w = 8.0$)

Only those time-histories for which a sensible correction is obtained are given in Table 9.21.

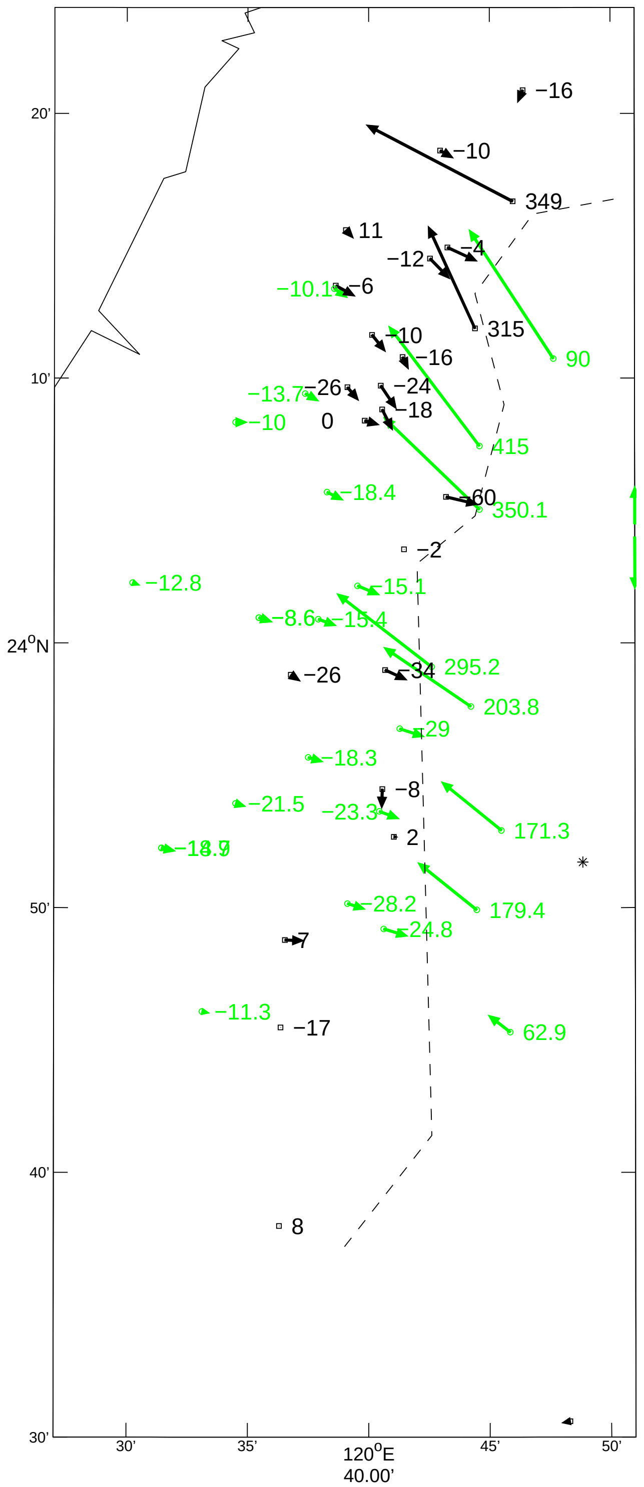

Fig. 9.23: Comparison of the permanent displacements recovered from the accelerograms corrected using the extend Graizer method constraining the initial velocity to zero with those measured using GPS for the Chi-Chi earthquake (20/9/1999). Black arrows are the recovered permanent displacements from the accelerograms and grey arrows are the measured displacements from GPS measurements. The dashed line is the observed surface fault break. The numbers are the vertical uplifts recovered or measured.

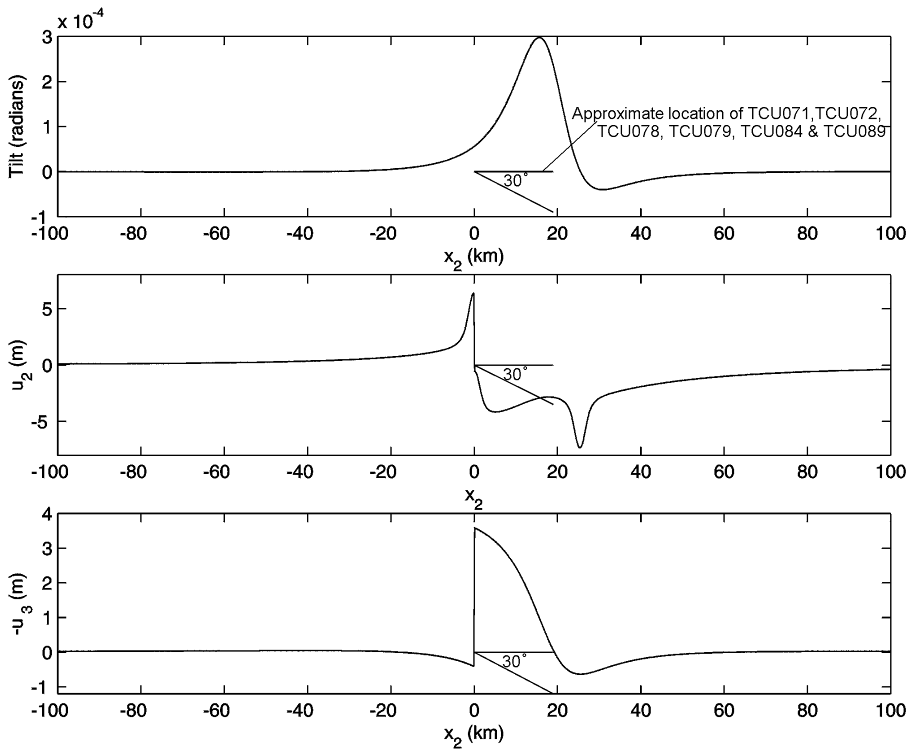

Fig. 9.24: Calculated tilt and horizontal displacement perpendicular to the fault strike and the uplift that occurred during the Chi-Chi earthquake (20/9/1999) using the dip-slip equations of Mansinha & Smylie (1971) and the approximate location of the strong-motion stations: TCU071, TCU072, TCU078, TCU079, TCU084 and TCU089. Parameters used were: length of fault $76\,\mathrm{km}$ (from surface fault break), dip 30° (from focal mechanism), width $22\,\mathrm{km}$ (from focal depth of $11\,\mathrm{km}$ and dip) and uniform slip $-8\,\mathrm{m}$ (from surface fault break). Tilts and displacements are given along a line in the middle of the fault and perpendicular to the fault strike.

Tab. 9.21: Results from Graizer correction of Michoacán records

Station	Inst.	d_f	Comp.	T_1	T_2	Constrained d	Constrained PGV	Constrained PGD	Constrained RD	Constrained V	Constrained D	Unconstrained d	Unconstrained PGV	Unconstrained PGD	Unconstrained RD	Unconstrained V	Unconstrained D
		(km)		(s)	(s)		(cms^{-1})	(cm)	(cm)	(s)	(s)		(cms^{-1})	(cm)	(cm)	(s)	(s)
Caleta de Campos	DSA-1	0	N180	5	30	3	24·5	67·2	46·6	40	40	3	24·8	70·5	51·7	40	40
			N090	5	30	1	−19·5	−49·3	−30·3	20	25	1	−19·5	−49·4	−30·4	20	25
			Up	5	30	1	16·4	79·2	66·0	40	40	1	16·5	81·1	68·3	40	40
Infiernillo Margen Der INMSS	SMA-1	0	N065	6	20	2	−8·6	−17·5	−11·5	40	50	2	−9·3	−36·2	−28·4	40	50
			N335	6	40	6	11·3	29·1	−9·4	20	40	6	11·5	32·2	−7·0	20	40
			Vert	5	30	2	11·0	−21·8	−8·3	30	30	2	11·6	28·4	20·5	30	30
Infiernillo N-120	SMA-1	0	N335	15	60	5	18·0	42·2	−11·9	20	40	5	18·2	43·5	−10·4	20	40
			N065	15	40	6	−15·4	−36·7	−23·0	25	40	6	−15·7	−36·6	−22·5	25	40
			Vert	10	40	4	13·9	25·6	19·8	20	30	4	13·8	25·2	19·0	20	30
La Union	DSA-1	0	N180	7	30	3	26·1	105·9	89·5	30	40	3	25·5	102·9	84·1	30	40
			N090	7	40	4	−13·6	10·1	3·8	30	40	4	−13·2	12·8	10·2	30	40
			Up	7	40	6	17·7	48·2	36·8	20	40	6	17·9	51·0	39·9	20	40
La Villita	DSA-1	0	N180	6	15	2	25·9	62·3	46·0	15	30	2	25·5	55·5	40·0	15	30
			Up	6	15	4	11·6	−17·8	6·0	30	30	4	11·5	−16·0	6·9	30	30

continued on next page

Tab. 9.21: *continued*

Station	Inst.	d_f	Comp.	T_1	T_2	Constrained						Unconstrained					
						d	PGV	PGD	RD	V	D	d	PGV	PGD	RD	V	D
		(km)		(s)	(s)		(cms^{-1})	(cm)	(cm)	(s)	(s)		(cms^{-1})	(cm)	(cm)	(s)	(s)
			N180	10	40	1	20·1	40·0	5·6	10	35	1	20·5	47·3	17·9	10	35
Zihuatanejo	DCA-333	16	N270	10	40	2	17·2	−21·2	1·2	20	30	1	17·1	16·1	−0·5	20	30
			Up	15	40	3	14·4	28·1	9·8	25	35	3	14·6	27·9	12·8	25	35
			N180	15	40	2	13·8	29·8	5·0	20	40	2	13·6	24·5	0·0	20	40
Papanoa	DCA-333	68	N270	15	40	3	7·8	23·2	12·0	30	40	2	8·1	23·6	16·3	30	40
			Up	15	40	5	10·3	13·9	3·8	20	40	5	10·3	13·9	3·7	20	40
			N180	15	40	1	15·3	18·1	−3·4	20	50	1	15·3	18·8	−2·6	20	50
Suchil	DCA-333	111	N270	15	45	1	6·8	8·1	0·9	15	50	1	6·8	10·0	2·9	15	50
			Up	15	45	1	6·4	−9·1	−0·1	30	40	1	6·4	−9·2	−0·1	30	40

Estimates of the coastal uplift resulting from this earthquake were made by Bodin & Klinger (1986) by using a survey of the vertical distribution of intertidal organisms. At Caleta de Campos estimates of the uplift range from 57–$61\,\mathrm{cm}$ to 100–$113\,\mathrm{cm}$, hence the recovered vertical permanent displacement from the accelerogram ($66.0\,\mathrm{cm}$ for initial velocity constrained to zero and $68.3\,\mathrm{cm}$ for initial velocity unconstrained) matches well. At Zihuatanejo the measured uplifts were 25–$40\,\mathrm{cm}$ and 30–$40\,\mathrm{cm}$ and at Papanoa measured uplifts were 15–$22\,\mathrm{cm}$, 17–$24\,\mathrm{cm}$ and 19–$23\,\mathrm{cm}$. The recovered vertical permanent displacements approximately match these displacements although they are slightly smaller. About $10\,\mathrm{km}$ from La Villita and about $20\,\mathrm{km}$ from La Union measured uplift was 11–$15\,\mathrm{cm}$. The recovered vertical permanent displacement at La Villita ($6.0\,\mathrm{cm}$ for initial velocity constrained to zero and $6.9\,\mathrm{cm}$ for initial velocity unconstrained) roughly matches these uplifts although they are slightly smaller while those at La Union ($36.8\,\mathrm{cm}$ for initial velocity constrained to zero and $39.9\,\mathrm{cm}$ for initial velocity unconstrained) are too large. No measurements of the horizontal permanent displacement that occurred during this earthquake could be found. However, because the earthquake occurred on a shallow north-east dipping thrust fault the horizontal displacements obtained (mainly to the south-west and of similar size to the vertical permanent displacements) are reasonable.

Somerville *et al.* (1991a) model the rupture plane of this earthquake as $150\,\mathrm{km}$ long by $140\,\mathrm{km}$ wide. The hypocentre is about $60\,\mathrm{km}$ from the end of the fault and so the length of unilateral rupture is about $90\,\mathrm{km}$. Using rupture velocities of between 2 and $3\,\mathrm{kms}^{-1}$ gives a rupture duration of between 30 and $45\,\mathrm{s}$; therefore the periods at which spectral velocity and displacement become equal to PGV and PGD in the extended Graizer corrected records are roughly equal to the rupture duration.

Figure 9.25 displays the corrected displacement time-histories for the eight stations given in Table 9.21 and the locations of the strong-motion stations that recorded them. The horizontal components were rotated into NS and EW directions and all the vertical components are in the upward direction.

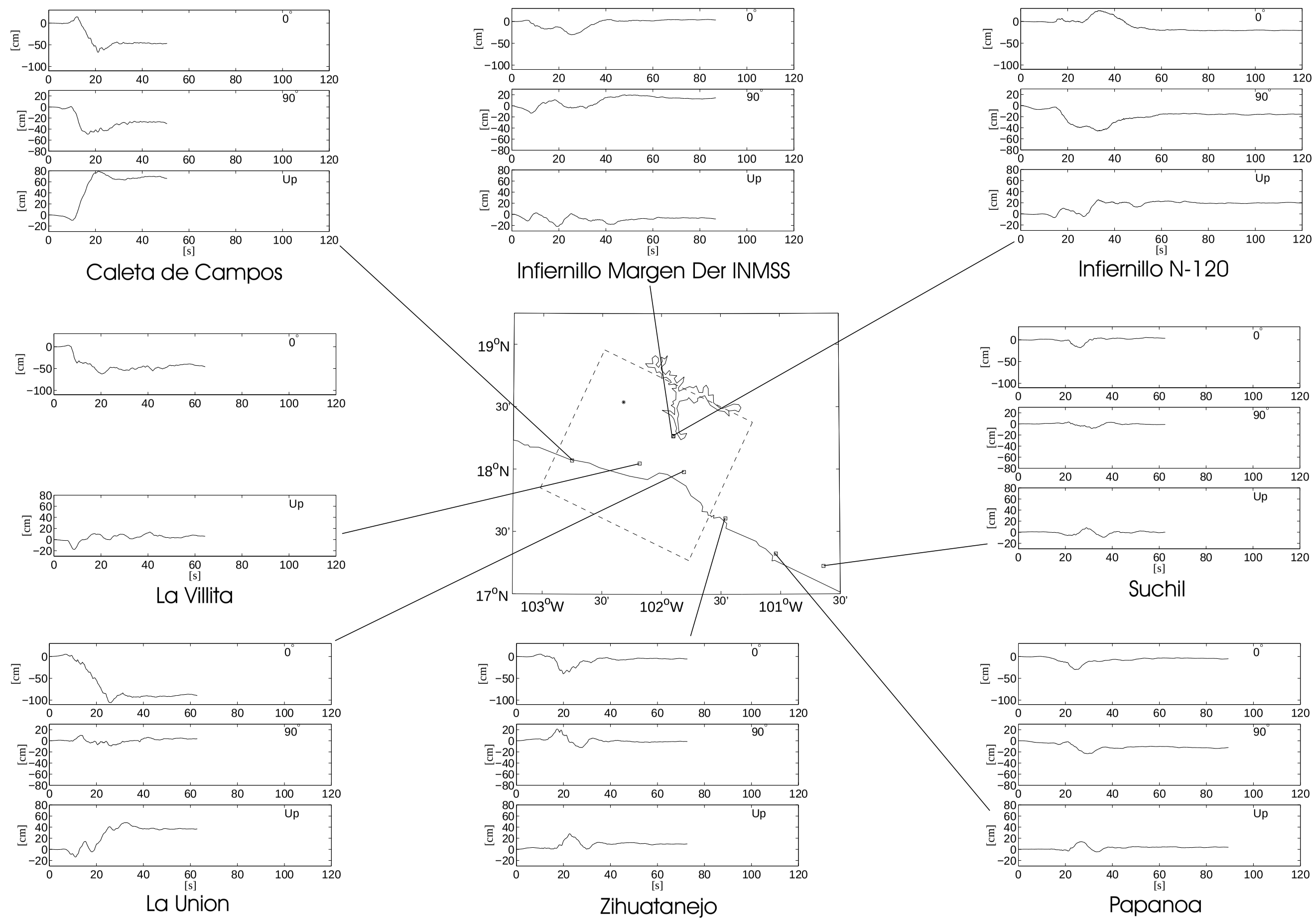

Fig. 9.25: Corrected displacements (using the extended Graizer method with the initial velocity constrained to zero) in the directions 0° and 90° east of north and upwards at eight strong-motion stations which recorded the Michoacán earthquake (19/9/1985). The dashed rectangle is the surface projection of the rupture plane from Somerville *et al.* (1991a) and the star is the epicentre.

Figure 9.25 shows that most of the corrected displacement traces exhibit similar features even though they are separated by $40–50\,\mathrm{km}$, suggesting that the extended Graizer method yields a realistic correction for these records. In particular note the agreement in the displacement time-histories for all three components from Zihuatanejo, Papanoa and Suchil and also the similarity between the records recorded at Caleta de Campos and La Union both of which show large permanent ground displacements. The lack of agreement between the displacement traces recorded at Infiernillo Margen Der INMSS and Infiernillo N-120, stations which are less than $1\,\mathrm{km}$ apart strongly suggests that the correction of either or both these records is not appropriate. It is most likely that the corrected record from Infiernillo Margen Der INMSS is incorrect because the displacement traces from Infiernillo N-120 display some of the features of the other records from this earthquake, for example compare with the record from Caleta de Campos.

9.3.11 Importance of instrument type

Most of the strong-motion records corrected using the extended Graizer technique in this study were recorded on analogue media (film or paper), for example records from AR-240, CRA-1 and SMA-1 instruments. The accelerograms from such instruments need to be digitised before they can be processed, and so are likely to have larger long-period errors than those recorded digitally, for example records from A900, DSA-1, DCA-333 and GSR-16 instruments. This greater long-period noise is demonstrated by the fact that the permanent displacements recovered from records from digital instruments more often match those measured or predicted, for example records from the Chi-Chi earthquake, compared with those recovered from analogue instruments which often do not match those measured or predicted, for example records from North Palm Springs. However,this comparison is difficult because records from the large earthquakes (for which large permanent displacements are expected) in this study were often from digital instruments whereas those from the small earthquakes (for which small permanent displacements are expected) in this study were often from analogue instruments.

9.3.12 Recovery of PGV *and* PGD *through filtering*

Almost all strong-motion records are corrected using filtering techniques, the details of which vary but the results are similar namely that the low-frequency (long period) motion is removed. The low-frequency cut-offs which are usually employed are usually less than $0.1\,\mathrm{Hz}$–$0.2\,\mathrm{Hz}$ especially for acceleration time-histories from digital instruments. Filters are designed so that they have little effect on frequencies inside their pass-band and because the natural period of almost all engineering structures is less than about $4\,\mathrm{s}$ there should be little difference between frequency-domain parameters (such as response spectral values) calculated using different types of filter or different low-cut frequencies (as long as the low-cut frequency is below about $0.2\,\mathrm{Hz}$). Time-domain parameters such as peak ground velocity, PGV, and peak ground displacement, PGD, though can be greatly affected by differing correction procedures because such parameters are governed by a wide range of frequencies some of which may be altered by the correction procedure used. Commonly used low-frequency cut-offs can lead to recovering significantly smaller PGV and PGD values in the near field of large earthquakes than actually occurred.

It was found above that the period at which spectral velocity and spectral displacement becomes equal to PGV and PGD respectively is approximately equal to the rupture duration. This period is unaffected by directivity. Therefore using a low cut-off frequency which is greater than the reciprocal of the rupture duration will lead to the recovery of smaller velocities and displacements. The low cut-off frequencies for which this is a problem are shown in Figure 9.26 using equations connecting fault-length to magnitude and different rupture velocities and assuming unilateral rupture.

From Figure 9.26 it can be seen that the commonly used low cut-off frequency of $0.1\,\mathrm{Hz}$ will yield the correct PGV and PGD for earthquakes with moment magnitudes $M_w \lesssim 6.5$ but will mean the recovered near-field PGV and PGD from larger earthquakes could be less than the actual PGV and PGD that occurred. For large earthquakes $M_w > 7$ the low cut-off frequency that should be used to recover the ground velocity and displacement would have to be less than $0.05\,\mathrm{Hz}$ which is less than that currently used for routine processing. Note however, that such a small low cut-off frequency cannot be used for many records because there is too much noise. For such records recovery of the true PGV and PGD is impossible.

All of the records in this chapter were also filtered using an elliptical filter (Sunder & Connor, 1982; Sunder & Schumacker, 1982; Menu, 1986) with low cut-off frequencies of 0.1 and $0.2\,\mathrm{Hz}$. Figure 9.27 shows the ratio of PGV and PGD using the Graizer corrected records to PGV and PGD using the filtered records for two cut-off frequencies. It was assumed that all of the Graizer corrected records are realistic although as was shown above some of the corrected displacements were probably incorrect. The main conclusion, however, is not likely to be strongly affected.

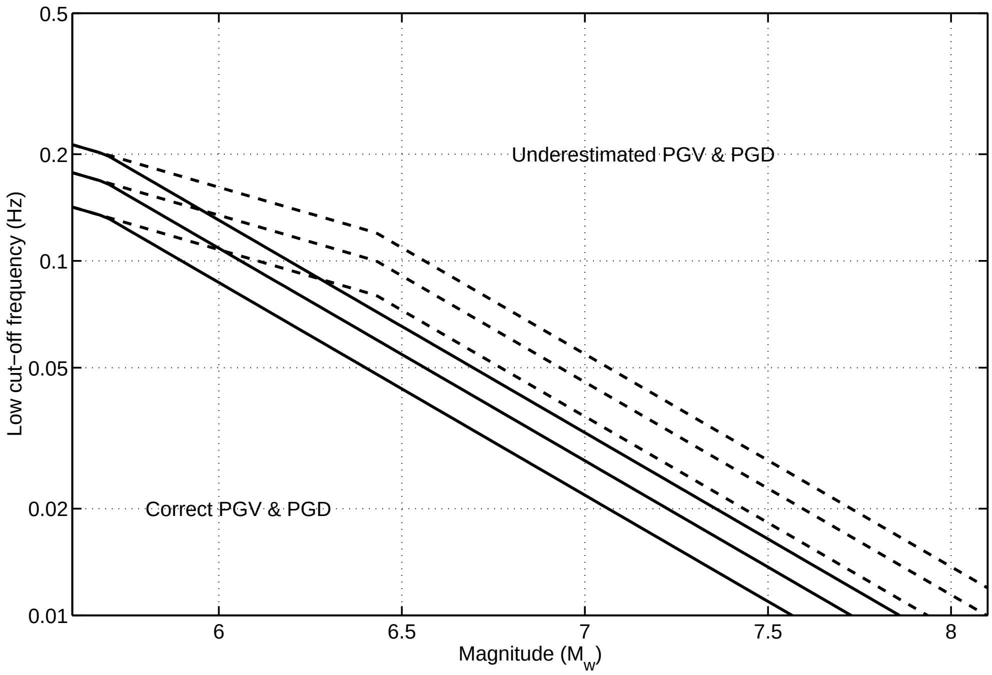

Fig. 9.26: Graph showing the choices of low cut-off frequency used to filter a strong-motion record from an earthquake of moment magnitude, M_w, which will yield correct PGV and PGD values and those choices which will recover underestimated PGV and PGD. The strike-slip equation ($\log(u) = -6.32 + 0.90M_w$) connecting slip, u, and moment magnitude, M_w from Wells & Coppersmith (1994) was used with the definition of seismic moment, $M_0 = \mu LWu$ with $\mu = 3 \times 10^{10}\,\mathrm{Nm}^{-2}$ and different seismogenic widths and rupture velocities. Solid lines are for seismogenic width of $15\,\mathrm{km}$ and dashed lines are for seismogenic width of $25\,\mathrm{km}$ and the three lines for each seismogenic width are for rupture velocities 2, 2.5 and $3\,\mathrm{kms}^{-1}$.

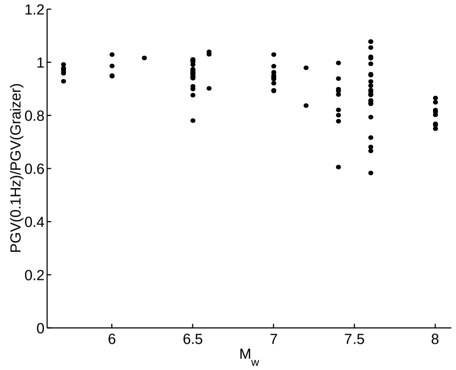

(a) PGV with low cut-off frequency of 0.1Hz

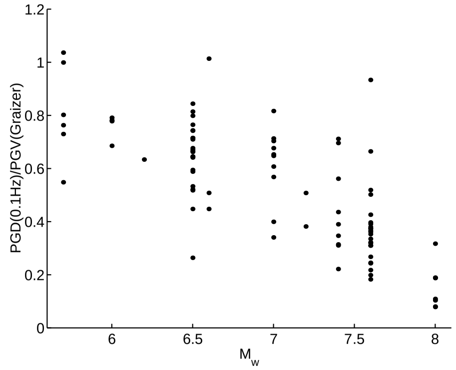

(b) PGD with low cut-off frequency of 0.1Hz

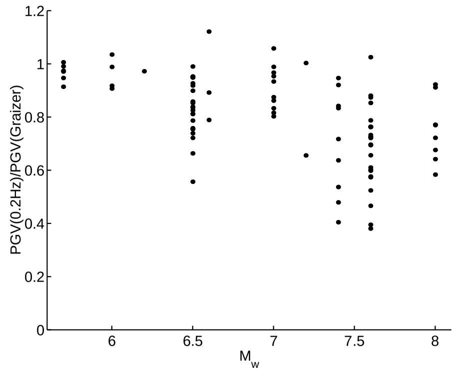

(c) PGV with low cut-off frequency of 0.2Hz

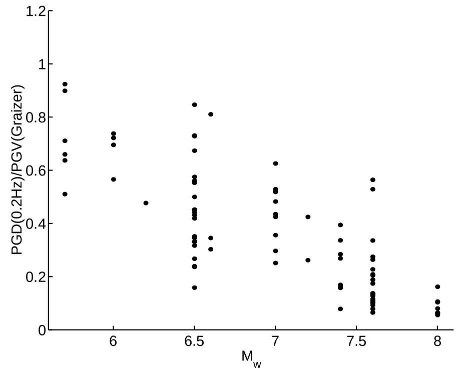

(d) PGD with low cut-off frequency of 0.2Hz

Fig. 9.27: Ratio of PGV and PGD using a elliptical filter with low cut-off frequencies of 0.1 Hz and 0.2 Hz to PGV and PGD using the extended Graizer method with the initial velocity constrained to zero. The largest horizontal component was used.

Figure 9.27 shows that PGV is underestimated for records from earthquakes with $M_w > 7$ using a low cut-off frequency of $0.1\,\mathrm{Hz}$ and it is underestimated for records from earthquakes with $M_w > 6.5$ using a low cut-off frequency of $0.2\,\mathrm{Hz}$. These are larger magnitudes for underestimated PGV than suggested by Figure 9.26 because for most records spectral velocity reached PGV at a period significantly less than the rupture duration. Therefore use of filtering techniques, with low cut-off frequencies 0.1–$0.2\,\mathrm{Hz}$, for the correction of accelerograms from earthquakes with $M_w < 6.5$ will not significantly underestimate PGV. However, for near-field accelerograms from earthquakes with $M_w > 6.5$ filtering with standard low cut-off frequencies of 0.1–$0.2\,\mathrm{Hz}$ will lead to significant underestimation of PGV; for such records either the low cut-off frequencies needs to be reduced or baseline correction procedures, like that investigated here, adopted.

Figure 9.27 shows that PGD is greatly underestimated for records from earthquakes with $M_w > 6$ using a low cut-off frequency of $0.1\,\mathrm{Hz}$ or $0.2\,\mathrm{Hz}$ and that the size of the underestimation increases with magnitude. For records from earthquakes with $M_w = 8$ the PGD recovered from the strong-motion records using a filter with a low cut-off frequency of $0.2\,\mathrm{Hz}$ is about ten times smaller than that recovered using the extended Graizer method. Part of the reason why filtering near-field records yields much smaller PGD than the extended Graizer method is that filtering does not recover the permanent ground displacement, which as has been shown is large and increases with magnitude. Therefore if permanent displacement is significant at a strong-motion station, filtering will lead to much lower estimates of PGD than would a baseline correction procedure, like that used in this chapter. However, even if significant permanent displacement did not occur at a strong-motion station filtering will lead to underestimation of PGD unless the low cut-off frequency is less than that suggested by Figure 9.26.

9.3.13 Conclusions

The extended Graizer correction technique presented here has a number of limitations:

- The minimum displacement which can be recovered from a strong-motion record from an analogue instrument, such as an SMA-1, is about $5\,\mathrm{cm}$. Therefore the minimum magnitude of earthquake which this procedure can be used on is about $M_w = 6.2$ (Figure 9.4) and only on records within a few kilometres of the rupture. Although records some smaller earthquakes, such as Coyote Lake ($M_w = 5.7$), may possibly be corrected using this procedure if the quality of the records is high and/or the coseismic displacements at the station are larger than the magnitude would suggest. Graizer (1979) finds that the correction technique is only reliable if residual displacement exceeds 15% of maximum displacement.
- Records which contain only simple waveforms which last for a short time (e.g. near-field records) are more likely to yield realistic corrected velocity and displacement time-histories

when corrected using the extended Graizer method than those with complex waveforms, such as surface waves.

- The method does not seem to be as useful for correcting time-histories from vertical components compared with correcting those from horizontal components. This may be because they feature more P-waves than horizontal components and such waves arrive before the S-waves which are more prominent in horizontal components, hence the initial ground motions may be missed or because there is too small a ‘quiet’ interval before the strongest shaking to which the fitted polynomial can be constrained. For most of the earthquakes included in this study the expected vertical permanent ground displacements are smaller than the expected horizontal permanent ground displacements. Since it is more difficult to accurately recover small displacements compared with large displacements this may explain why it seems that the extended Graizer method does not work as well for vertical records as it does for horizontal records.

When there is a long pre-event time, for example for records from digital instruments, the constrained and unconstrained results are similar because the initial velocity is small. Digital instruments are designed to record the entire ground motion including the pre-event portion so the initial velocity should be zero. It is better to constrain the initial velocity to zero, for such records, so that there is one less coefficient to find.

Permanent ground displacements happen over a few seconds and therefore it is doubtful that they are important for buildings. Thus the transient part of the ground motion that occurred during the earthquake may be a more useful measure of the displacement for engineering design. However, a consistent and useful definition of transient peak ground displacement is difficult to find because PGD is strongly affected by the low-frequency cut-off and also because it is difficult to separate the transient and permanent ground displacement.

Conclusions on the recovery of PGV and PGD from near-field strong-motion records (see Section 9.3.12) are:

- Commonly used low-frequency cut-offs of 0.1–$0.2\,\mathrm{Hz}$ lead to the recovery of PGVs and PGDs in the near field of large earthquakes that are much smaller than the true velocity and displacement. This under-recovery is much worse for displacement because permanent ground displacements cannot be recovered by filtering techniques and they could significantly increase PGD whereas velocity must be zero at the end of the strong ground motion and so PGV is less affected.

- Filtering correction techniques, employing commonly used low cut-off frequencies, for small earthquakes ($M_w \lesssim 6$) can adequately recover PGV and PGD because permanent ground displacements will be small and because there is little energy in the long period range which is affected by filtering.

These conclusions only apply in the near field where it is possible to use the extended Graizer method. Whether such conclusions apply in the intermediate- and far-fields is not possible to ascertain. However, it is likely that similar conclusions can be drawn by making use of source spectra models such as those by Brune (1970, 1971), Ishida (1979) and Joyner (1984). In fact, Joyner & Boore (1988) note that it is important to use a low cut-off frequency less than the corner frequency of the Brune (1970, 1971) source model otherwise the time-history will be significantly altered by filtering.

10. CONCLUSIONS AND SUGGESTIONS FOR FURTHER WORK

10.1 Conclusions

This thesis gives the results of investigations of a number of problems in engineering seismology which have mainly been neglected in the past. There were three main themes addressed in this study.

The first theme is the accuracy of currently used equations for the estimation of strong ground motion derived using strong-motion records of past earthquakes. It is shown (Chapter 8) that over the past thirty years there has been little improvement in the accuracy of estimates of the ground motion that would occur at some chosen site given the occurrence of an earthquake.

Pure error analysis shows that the reason for this lack of improvement is not an inadequate functional form (Chapter 8) but rather that current equations for ground motion estimation (Chapter 3) do not adequately account for the factors known to influence ground motion (Chapter 2). Therefore more independent parameters need to be included in the equation if the associated standard deviation of the final equation is to be reduced.

However, there is a large ambiguity in calculating some independent parameters which possibly can increase the precision of ground motion estimates, such as stress drop (Chapter 2). Also other possibly important factors, such as topography or basin effects, whose inclusion also could improve the precision of ground motion estimates, have been shown to be highly complex and difficult to incorporate into simple equations (Chapter 2).

Even independent parameters that are always included in attenuation relations, such as source-to-site distance, have been shown to be only known imprecisely (Chapter 8). This imprecision accounts for some of the associated uncertainty in the final equation. It is found that because of the difficulty in calculating precise distances even for such simple distance measures, as that to the surface projection of the rupture plane, using complex distance metrics, such as seismogenic distance or equivalent hypocentral distance, is not justified and will not lead to an improvement in the accuracy of ground motion estimates (Chapter 8).

A set of equations for the estimation of peak ground acceleration (PGA), energy density, spectral acceleration (SA) and maximum absolute input energy in the near-field of large earthquakes is derived (Chapter 7). It was found that even by only using records from within a narrow range of distances (between 0 and $15\,\mathrm{km}$) and from earthquakes within a narrow range of surface-wave magnitudes (between 5.8 and 7.8) does not reduce the standard deviation of the equations compared with equations which used data from a much wider range of distances and magnitudes. Also, it is found that the predicted ground motions are similar to those estimated from previous equations except the importance of local site conditions is less in the new equations, particularly for short periods. This effect can be attributed to non-linear soil behaviour at large strains.

It is found that the currently used assumption that the error in recorded ground motions is proportional to the amplitude of the ground motions cannot be rejected and hence should continue to be used (Chapter 8). However, the recent suggestion by a number of workers that the scatter in recorded ground motions in proportion to the amplitude of the ground motions is dependent on the magnitude of the associated earthquake, is supported by a large set of data (Chapter 8).

Any further improvement of the scaling of ground motions with seismological parameters and local site conditions depends primarily on the acquisition of more high-quality observational data.

The second theme of the thesis is the importance of vertical ground motions. A comprehensive review of the available literature concerning the effect of vertical motions on horizontal response was conducted and shows that there is a requirement for more detailed study (Chapter 4). The results of a detailed study, using over 180 near-field strong-motion records, is given in Chapters 6 and 7. It is concluded that the effect of vertical ground motion on horizontal response for linear elastic SDOF systems can almost always be neglected. For extremely intense vertical motions the bending model (see Chapter 4) can breakdown or experience large amplifications for realistic structural parameters, but for most recorded vertical motions the effect of vertical motion is negligible (Chapters 6 and 7). The hinging model (see Chapter 4) does not breakdown nor does it experience large amplifications, due to vertical motions, for even the most intense recorded vertical motions except for unrealistic structural parameters (Chapters 6 and 7).

From the derived equations for the estimation of vertical to horizontal ratios for peak ground acceleration (both absolute and simultaneous), spectral acceleration (both absolute and simultaneous), energy density and maximum absolute input energy it is concluded that vertical ground motion is less important than horizontal ground motion for seismic design (Chapter 7). This conclusion is reached because it is found that even in the near field of large earthquakes vertical PGA is less than horizontal PGA, vertical SA is less than horizontal SA even at short periods and vertical ground motion contains much less energy than horizontal ground motion both in absolute terms (energy density) and as an input to SDOF systems (maximum absolute input energy). It is found that, in contrast to what is expected, that the ratio of vertical to horizontal PGA, SA, energy density and maximum absolute input energy is independent of fault mechanism. Further, the associated standard deviations of the derived equations for vertical strong-motion characteristics are higher than the associated standard deviations of corresponding equations for horizontal strong motion.

The third theme is an investigation into the correction of accelerograms for long-period errors.

A polynomial correction technique based on the work of Graizer is used for the correction of many near-field accelerograms from 16 earthquakes. A number of methods were suggested, and studied, to select the required correction parameters. If such selection techniques can be applied then a reasonably objective process is possible; however some subjective judgement is still required which can lead to uncertainty in estimates of peak ground velocity (PGV), peak ground displacement (PGD) and permanent displacement. For records from analogue instruments, it was found that when the size of the permanent displacement is large, about $5\,\mathrm{cm}$, and the digitisation is of sufficiently high-quality it is sometimes possible to get an estimate of the displacement that occurred at the instrument site. For records from digital instruments, it is found that the permanent displacement that occurred could almost always be recovered except for records which may have undergone large tilts due to faulting.

As a consequence of the investigation into the correction of long-period errors in accelerograms it was found that the low cut-off period used for routine filtering of near-field accelerograms from large earthquakes should be less than the duration of the fault rupture if PGV and PGD are to be fully recovered. For large earthquakes, whose durations of rupture are greater than $10\,\mathrm{s}$, this finding means that commonly used low cut-off frequencies of about $0.1\,\mathrm{Hz}$ will underestimate PGV and PGD.

10.2 Suggestions for further work

For each large earthquake for which the location of the rupture plane has been studied the precision of the distance estimates should be quantified. These estimates of the precision should be useful in deciding which earthquakes are included in the construction sets for the derivation of attenuation relations. Also such estimates could be useful in deciding on a rigorous weighting scheme for the derivation of attenuation relations, i.e. those records with well-defined independent parameters should be given a larger weighting than those with poorly-defined parameters.

More pure error analyses should be conducted for other strong-motion parameters and, when there is sufficient data, such analysis should be conducted investigating the improvement in ground motion estimation using more independent parameters, such as fault mechanism and focal depth. This may suggest the independent parameters which are likely to be useful in reducing the associated standard deviations of derived equations. The results of pure error analysis should be used in weighted least-squares analysis for the derivation of attenuation relations; this would remove the dependence of standard deviation on magnitude and would also give more weight to the motions with engineering significance which are associated with lower scatter.

The finding that vertical ground motions seem to be more unpredictable than horizontal ground motions, should be investigated further.

Future studies deriving attenuation relations should use validation sets to check the derived equations.

Computer programs, such as 3d$\sim$def (Gomberg & Ellis, 2001), for calculation of expected coseismic displacements should be used instead of the equations of Mansinha & Smylie (1971) to get estimates of the permanent displacements that occurred at strong-motion stations.

The equations of Vostrikov (1998) for estimating the degree of polynomial required for the correction of accelerograms using the extended Graizer should be tried for records from different earthquakes.

BIBLIOGRAPHY

Abdelkareem, K. H., & Machida, A. 2000. Effect of vertical motion of earthquake on failure mode and ductility of RC bridge piers. *In: Proceedings of Twelfth World Conference on Earthquake Engineering*. Paper No. 0463.

Abrahamson, N. A. 1988. Statistical properties of peak ground accelerations recorded by the SMART 1 array. *Bulletin of the Seismological Society of America*, **78**(1), 26–41.

Abrahamson, N. A., & Litehiser, J. J. 1989. Attenuation of vertical peak acceleration. *Bulletin of the Seismological Society of America*, **79**(3), 549–580.

Abrahamson, N. A., & Shedlock, K. M. 1997. Overview. *Seismological Research Letters*, **68**(1), 9–23.

Abrahamson, N. A., & Silva, W. J. 1997. Empirical response spectral attenuation relations for shallow crustal earthquakes. *Seismological Research Letters*, **68**(1), 94–127.

Abrahamson, N. A., & Somerville, P. G. 1996. Effects of the hanging wall and footwall on ground motions recorded during the Northridge earthquake. *Bulletin of the Seismological Society of America*, **86**(1B), S93–S99.

Acharya, H. K. 1979. Regional variations in the rupture-length magnitude relationships and their dynamical significance. *Bulletin of the Seismological Society of America*, **69**(6), 2063–2084.

Adams, R. D. 1982. Local earthquake quantification. *Tectonophysics*, **84**(1), 35–39.

Aki, K. 1967. Scaling law of seismic spectrums. *Journal of Geophysical Research*, **72**, 1217–1231.

Aki, K. 1968. Seismic displacements near a fault. *Journal of Geophysical Research*, **73**(16), 5359–5376.

Aki, K. 1980. Scattering and attenuation of shear waves in the lithosphere. *Journal of Geophysical Research*, **85**(B11), 6496–6504.

Aki, K., & Larner, K. L. 1970. Surface motion of a layered medium having an irregular interface due to incident plane SH waves. *Journal of Geophysical Research*, **75**(5), 933–954.

Aki, K., & Richards, P. G. 1980. *Quantitative Seismology: Theory and methods*. Vol. I. W. H. Freeman and Company.

Akkar, S., & Gülkan, P. 1999. Effect of record processing schemes on damage potential of near field earthquakes. *Pages 1101–1106 of: Structural dynamics — EURODYN '99*, vol. 2.

Akkar, S., & Gülkan, P. 2000 (Nov). Examination of selected recent ground motion records from Turkey in terms of displacement design procedures. *In: Proceedings of the Sixth International Conference on Seismic Zonation*.

Alford, J. L., Housner, G. W., & Martel, R. R. 1951 (Aug). *Spectrum analysis of strong-motion earthquakes*. Office of Naval Research report. Contract N6onr-244. Task order 25. California Institute of Technology, Pasadena. Not seen.

Allen, C. R., Brune, J. N., Cluff, L. S., & Barrows, Jr., A. G. 1998. Evidence for unusually strong near-field ground motion on the hanging wall of the San Fernando fault during the 1971 earthquake. *Seismological Research Letters*, **69**(6), 524–531.

Alsaker, A., Kvamme, L. B., Hansen, R. A., Dahle, A., & Bungum, H. 1991. The M_L scale in Norway. *Bulletin of the Seismological Society of America*, **81**(2), 379–398.

Ambraseys, N., & Douglas, J. 2000. Reappraisal of surface wave magnitudes in the Eastern Mediterranean region and the Middle East. *Geophysical Journal International*, **141**(2), 357–373.

Ambraseys, N., Smit, P., Beradi, R., Rinaldis, D., Cotton, F., & Berge, C. 2000 (Sep). *Dissemination of European Strong-Motion Data*. CD-ROM collection. European Commission, Directorate-General XII, Environmental and Climate Programme, ENV4-CT97-0397, Brussels, Belgium.

Ambraseys, N. N. 1975. Trends in engineering seismology in Europe. *Pages 39–52 of: Proceedings of Fifth European Conference on Earthquake Engineering*, vol. 3.

Ambraseys, N. N. 1995. The prediction of earthquake peak ground acceleration in Europe. *Earthquake Engineering and Structural Dynamics*, **24**(4), 467–490.

Ambraseys, N. N. 2001. Reassessment of earthquakes, 1900–1999, in the eastern Mediterranean and the Middle East. *Geophysical Journal International*, **145**(2), 471–485.

Ambraseys, N. N., & Bommer, J. J. 1991. The attenuation of ground accelerations in Europe. *Earthquake Engineering and Structural Dynamics*, **20**(12), 1179–1202.

Ambraseys, N. N., & Bommer, J. J. 1995. Attenuation relations for use in Europe: An overview. *Pages 67–74 of:* Elnashai, A. S. (ed), *Proceedings of Fifth SECED Conference on European Seismic Design Practice*.

Ambraseys, N. N., & Jackson, J. A. 1998. Faulting associated with historical and recent earthquakes in the Eastern Mediterranean region. *Geophysical Journal International*, **133**(2), 390–406.

Ambraseys, N. N., & Menu, J. 1988. Earthquake-induced ground displacements. *Earthquake Engineering and Structural Dynamics*, **16**, 985–1006.

Ambraseys, N. N., & Simpson, K. A. 1996. Prediction of vertical response spectra in Europe. *Earthquake Engineering and Structural Dynamics*, **25**(4), 401–412.

Ambraseys, N. N., & Srbulov, M. 1998. A note on the point source approximation in ground motion attenuation relations. *Journal of Earthquake Engineering*, **2**(1), 1–24.

Ambraseys, N. N., Simpson, K. A., & Bommer, J. J. 1996. Prediction of horizontal response spectra in Europe. *Earthquake Engineering and Structural Dynamics*, **25**(4), 371–400.

Anderson, E. M. 1951. *The Dynamics of Faulting and Dyke Formation with Applications to Britain*. 2nd revised edn. Edinburgh and London: Oliver & Boyd.

Anderson, J. C., & Bertero, V. V. 1973. Effect of gravity loads and vertical ground acceleration on the seismic response of multistory frames. *Pages 2914–2923 of: Proceedings of Fifth World Conference on Earthquake Engineering*, vol. 2.

Anderson, J. G. 1991. Strong motion seismology. *Reviews of Geophysics*, **29**(Apr), 700–720. Part 2.

Anderson, J. G., & Brune, J. N. 1991. The Victoria accelerogram for the 1980 Mexicali Valley earthquake. *Earthquake Spectra*, **7**(1), 29–43.

Anderson, J. G., & Hough, S. E. 1984. A model for the shape of the Fourier amplitude spectrum of acceleration at high frequencies. *Bulletin of the Seismological Society of America*, **74**(5), 1969–1993.

Anderson, J. G., & Luco, J. E. 1983a. Parametric study of near-field ground motion for a strike-slip dislocation model. *Bulletin of the Seismological Society of America*, **73**(1), 23–43.

Anderson, J. G., & Luco, J. E. 1983b. Parametric study of near-field ground motions for oblique-slip and dip-slip dislocation models. *Bulletin of the Seismological Society of America*, **73**(1), 45–57.

Anderson, J. G., Bodin, P., Brune, J. N., Prince, J., Singh, S. K., Quaas, R., & Onate, M. 1986. Strong ground motion from the Michoacan, Mexico, earthquake. *Science*, **233**(Sep), 1043–1049.

Anderson, J. G., Sucuoglu, H., Erberik, A., Yilmaz, T., Inan, E., Durukal, E., Erdik, M., Anooshehpoor, R., Brune, J. N., & Ni, S.-D. 2000. Implications for seismic hazard analysis. *Chap. 6, pages 113–137 of:* Youd, T. L., Bardet, J.-P., & Bray, J. D. (eds), *Kocaeli, Turkey, Earthquake of August 17, 1999 Reconnaissance Report (supplement A to Volume 16 of Earthquake Spectra)*. Oakland, California: Earthquake Engineering Research Institute.

Annaka, T., & Nozawa, Y. 1988. A probabilistic model for seismic hazard estimation in the Kanto district. *Pages 107–112 of: Proceedings of Ninth World Conference on Earthquake Engineering*, vol. II.

Anooshehpoor, A., & Brune, J. N. 1989. Foam rubber modeling of topographic and dam interaction effects at Pacoima Dam. *Bulletin of the Seismological Society of America*, **79**(5), 1347–1360.

Archuleta, R. J. 1982. Analysis of near-source static and dynamic measurements from the 1979 Imperial Valley earthquake. *Bulletin of the Seismological Society of America*, **72**(6), 1927–1956. Part A.

Archuleta, R. J. 1984. A faulting model for the 1979 Imperial Valley earthquake. *Journal of Geophysical Research*, **89**(B6), 4559–4585.

Archuleta, R. J., & Brune, J. N. 1975. Surface strong motion associated with a stick-slip event in a foam rubber model of earthquakes. *Bulletin of the Seismological Society of America*, **65**(5), 1059–1071.

Atkinson, G. M. 1997. Empirical ground motion relations for earthquakes in the Cascadia region. *Canadian Journal of Civil Engineering*, **24**, 64–77.

Atkinson, G. M., & Beresnev, I. 1997. Don't call it stress drop. *Seismological Research Letters*, **68**(1), 3–4.

Atkinson, G. M., & Boore, D. M. 1990. Recent trends in ground motion and spectral response relations for North America. *Earthquake Spectra*, **6**(1), 15–35.

Ayhan, M. E., Bürgmann, R., McClusky, S., Lenk, O., Aktug, B., Herece, E., & Reilinger, R. E. 2001. Kinematics of the $Mw = 7.2$, 12 November 1999, Düzce, Turkey earthquake. *Geophysical Research Letters*, **28**(2), 367–370.

Bard, P.-Y., & Bouchon, M. 1980a. The seismic response of sediment-filled valleys. Part 1. The case of incident SH waves. *Bulletin of the Seismological Society of America*, **70**(4), 1263–1286.

Bard, P.-Y., & Bouchon, M. 1980b. The seismic response of sediment-filled valleys. Part 2. The case of incident P and SV waves. *Bulletin of the Seismological Society of America*, **70**(5), 1921–1941.

Bard, P.-Y., & Bouchon, M. 1985. The two-dimensional resonance of sediment-filled valleys. *Bulletin of the Seismological Society of America*, **75**(2), 519–541.

Bard, P.-Y., & Gariel, J.-C. 1986a. A numerical study of the variations of ground motion parameters across two-dimensional sediment-filled valleys. *Pages 1–8 of: Proceedings of Eighth European Conference on Earthquake Engineering*, vol. 2. 5.4.

Bard, P.-Y., & Gariel, J.-C. 1986b. The seismic response of two-dimensional sedimentary deposits with large vertical velocity gradients. *Bulletin of the Seismological Society of America*, **76**(2), 343–366.

Basili, M., & Brady, G. 1978. Low frequency filtering and the selection of limits for accelerogram corrections. *Pages 251–258 of: Proceedings of Sixth European Conference on Earthquake Engineering*, vol. 1.

Båth, M. 1981. Earthquake magnitude — recent research and current trends. *Earth-Science Reviews*, **17**(4), 315–398.

Beaudet, P. R., & Wolfson, S. J. 1970. Digital filters for response spectra. *Bulletin of the Seismological Society of America*, **60**(3), 1001–1013.

Ben-Menahem, A. 1961. Radiation of seismic surface-waves from finite moving sources. *Bulletin of the Seismological Society of America*, **51**(3), 401–435.

Ben-Menahem, A. 1962. Radiation of seismic body waves from a finite moving source in the earth. *Journal of Geophysical Research*, **67**(1), 345–350.

Benioff, H. 1934. The physical evaluation of seismic destructiveness. *Bulletin of the Seismological Society of America*, **24**, 398–403.

Benito, B., Rinaldis, D., Gorelli, V., & Paciello, A. 1992. Influence of the magnitude, distance and natural period of soil in the strong ground motion. *Pages 773–779 of: Proceedings of Tenth World Conference on Earthquake Engineering*, vol. 2.

Bent, A. L., & Helmberger, D. V. 1989. Source complexity of the October 1, 1987, Whittier Narrows earthquake. *Journal of Geophysical Research*, **94**, 9548–9556.

Benz, H. M., & Smith, R. B. 1987. Kinematic source modelling of normal-faulting earthquakes using the finite element method. *Geophysical Journal of the Royal Astronomical Society*, **90**(2), 305–325.

Berardi, R., Longhi, G., & Rinaldis, D. 1991. Qualification of the European strong-motion databank: Influence of the accelerometric station response and pre-processing techniques. *European Earthquake Engineering*, **V**(2), 38–53.

Berberian, M. 1979. Earthquake faulting and bedding thrust associated with the Tabas-E-Golshan (Iran) earthquake of September 16,1978. *Bulletin of the Seismological Society of America*, **69**(6), 1861–1887.

Bernal, D. 1987. Amplification factors for inelastic dynamic P-Δ effects in earthquake analysis. *Earthquake Engineering and Structural Dynamics*, **15**(5), 635–651.

Bernard, P., Gariel, J.-C., & Dorbath, L. 1997a. Fault location and rupture kinematics of the magnitude 6.8 1992 Erzincan earthquake, Turkey, from strong ground motion and regional records. *Bulletin of the Seismological Society of America*, **87**(5), 1230–1243.

Bernard, P., Briole, P., Meyer, B., Lyon-Caen, H., Gomez, J.-M., Tiberi, C., Berge, C., Cattin, R., Hatzfeld, D., Lachet, C., Lebrun, B., Deschamps, A., Courboulex, F., Larroque, C., Rigo, A., Massonnet, D., Papadimitriou, P., Kassaras, J., Diagourtas, D., Makropoulos, K., Veis, G., Papazisi, E., Mitsakaki, C., Karakostas, V., Papadimitriou, E., Papanastassiou, D., Chouliaras, M., & Stavrakakis, G. 1997b. The $M_s = 6.2$, June 15, 1995 Aigion earthquake (Greece): Evidence for low angle normal faulting in the Corinth rift. *Journal of Seismology*, **1**, 131–150.

Berrill, J. B. 1975. *A study of high-frequency strong ground motion from the San Fernando earthquake*. Ph.D. thesis, California Institute of Technology, Pasadena, California.

Betbeder-Matibet, J. 1995. Attenuation laws in the nearfield. *Pages 949–956 of: Proceedings of the Fifth International Conference on Seismic Zonation*, vol. II.

Biot, M. A. 1941. A mechanical analyzer for the prediction of earthquake stresses. *Bulletin of the Seismological Society of America*, **31**(2), 151–171.

Blume, J. A. 1977. The SAM procedure for site-acceleration-magnitude relationships. *Pages 416–422 of: Proceedings of Sixth World Conference on Earthquake Engineering*, vol. I.

Blume, J. A. 1980. Distance partitioning in attenuation studies. *Pages 403–410 of: Proceedings of Seventh World Conference on Earthquake Engineering*, vol. 2.

Boatwright, J. 1984. Seismic estimates of stress release. *Journal of Geophysical Research*, **89**(B8), 6961–6968.

Boatwright, J., & Boore, D. M. 1982. Analysis of the ground accelerations radiated by the 1980 Livermore Valley earthquakes for directivity and dynamic source characteristics. *Bulletin of the Seismological Society of America*, **72**(6), 1843–1865.

Bodin, P., & Klinger, T. 1986. Coastal uplift and mortality of intertidal organisms caused by the September 1985 Mexico earthquakes. *Science*, **233**(Sep), 1071–1073.

Bolotin, V. V. 1964. *The Dynamic Stability of Elastic Systems*. Holden-Day, Inc. Translated by V.I. Weingarten, L.B. Greszczuk, K.N. Trirogoff and K.D. Gallegos.

Bolt, B. A. 1970. Elastic waves in the vicinity of the earthquake source. *Chap. 1, pages 1–20 of:* Wiegel, R. L. (ed), *Earthquake Engineering*. Englewood Cliffs, New Jersey, USA: Prentice-Hall, Inc.

Bolt, B. A., & Abrahamson, N. A. 1982. New attenuation relations for peak and expected accelerations of strong ground motion. *Bulletin of the Seismological Society of America*, **72**(6), 2307–2321.

Bolt, B. A., & Abrahamson, N. A. 1983. Reply to W. B. Joyner and D. M. Boore's "Comments on 'New attenuation relations for peak and expected accelerations of strong ground motion' ". *Bulletin of the Seismological Society of America*, **73**(5), 1481–1483.

Bommer, J. J., Elnashai, A. S., Chlimintzas, G. O., & Lee, D. 1998 (Mar). *Review and development of response spectra for displacement-based seismic design*. ESEE Report 98-3. Department of Civil Engineering, Imperial College, London.

Bonamassa, O., Vidale, J. E., Houston, H., & Schwartz, S. Y. 1991. Directional site resonance and the influence of near-surface geology on ground motion. *Geophysical Research Letters*, **18**(5), 901–904.

Bonilla, M. G. 1988. Minimum earthquake magnitude associated with coseismic surface faulting. *Bulletin of the Association of Engineering Geologists*, **XXV**(1), 17–29.

Bonilla, M. G., Mark, R. K., & Lienkaemper, J. J. 1984. Statistical relations among earthquake magnitude, surface rupture length, and surface fault displacement. *Bulletin of the Seismological Society of America*, **74**(6), 2379–2411.

Boore, D. M. 1972. A note on the effect of simple topography on seismic SH waves. *Bulletin of the Seismological Society of America*, **62**(1), 275–284.

Boore, D. M. 1973. The effect of simple topography on seismic waves: Implications for the accelerations recorded at Pacoima Dam, San Fernando valley, California. *Bulletin of the Seismological Society of America*, **63**(5), 1603–1609.

Boore, D. M. 1983. Strong-motion seismology. *Reviews of Geophysics and Space Physics*, **21**(6), 1308–1318.

Boore, D. M. 1989. The Richter scale: Its development and use for determining earthquake source parameters. *Tectonophysics*, **166**(1–3), 1–14.

Boore, D. M. 1999. *Effect of baseline corrections on response spectra for two recordings of the 1999 Chi-Chi, Taiwan, earthquake*. Open-File Report 99-545, Version 1.0. US Geological Survey.

Boore, D. M. 2001a (Mar). Email message received 15/3/2001.

Boore, D. M. 2001b (Mar). Email message received 13/3/2001.

Boore, D. M. 2001c. Effect of baseline corrections on displacements and response spectra for several recordings of the 1999 Chi-Chi, Taiwan, earthquake. *Bulletin of the Seismological Society of America*, **91**(5), 1199–1211.

Boore, D. M., & Joyner, W. B. 1978. The influence of rupture incoherence on seismic directivity. *Bulletin of the Seismological Society of America*, **68**(2), 283–300.

Boore, D. M., & Joyner, W. B. 1982. The empirical prediction of ground motion. *Bulletin of the Seismological Society of America*, **72**(6), S43–S60. Part B.

Boore, D. M., & Zoback, M. D. 1974. Near-field motions from kinematic models of propagating faults. *Bulletin of the Seismological Society of America*, **64**(2), 321–342.

Boore, D. M., Joyner, W. B., & Fumal, T. E. 1993. *Estimation of response spectra and peak accelerations from western North American earthquakes: An interim report*. Open-File Report 93-509. U.S. Geological Survey.

Boore, D. M., Joyner, W. B., & Fumal, T. E. 1994a. *Estimation of response spectra and peak accelerations from western North American earthquakes: An interim report. Part 2*. Open-File Report 94-127. U.S. Geological Survey.

Boore, D. M., Joyner, W. B., & Fumal, T. E. 1994b. *Ground motion estimates for strike- and reverse-slip faults*. Provided to the Southern California Earthquake Center and widely distributed as an insert in Boore *et al.* (1994a). Not seen. Reported in Boore *et al.* (1997).

Boore, D. M., Joyner, W. B., & Fumal, T. E. 1997. Equations for estimating horizontal response spectra and peak acceleration from western North American earthquakes: A summary of recent work. *Seismological Research Letters*, **68**(1), 128–153.

Boore, D. M., Stephens, C. D., & Joyner, W. B. 2002. Comments on baseline correction of digital strong-motion data: Examples from the 1999 Hector Mine, California, earthquake. *Bulletin of the Seismological Society of America*, **92**(4), 1543–1560.

Borsoi, L., & Ricard, A. 1985 (Aug). A simple accelerogram correction method to prevent unrealistic displacement shift. *Pages 101–107 of: Transactions of the 8th International Conference on Structural Mechanics in Reactor Technology*, vol. K(a). K 2/7.

Bouchon, M. 1973. Effect of topography on surface motion. *Bulletin of the Seismological Society of America*, **63**(5), 615–632.

Bouchon, M. 1982. The rupture mechanism of the Coyote Lake earthquake of 6 August 1979 inferred from near-field data. *Bulletin of the Seismological Society of America*, **72**(3), 745–757.

Bouchon, M., & Barker, J. S. 1996. Seismic response of a hill: The example of Tarzana, California. *Bulletin of the Seismological Society of America*, **86**(1A), 66–72.

Bozorgnia, Y., Campbell, K. W., & Niazi, M. 2000. Observed spectral characteristics of vertical ground motion recorded during worldwide earthquakes from 1957 to 1995. *In: Proceedings of Twelfth World Conference on Earthquake Engineering*. Paper No. 2671.

Bradner, H., & Reichle, M. 1973. Some methods for determining acceleration and tilt by use of pendulums and accelerometers. *Bulletin of the Seismological Society of America*, **63**(1), 1–7.

Brady, A. G., Trifunac, M. D., & Hudson, D. E. 1973 (Feb). *Analyses of strong motion earthquake accelerograms — response spectra*. Tech. rept. Earthquake Engineering Research Laboratory — California Institute of Technology.

Brillinger, D. R., & Preisler, H. K. 1984. An exploratory analysis of the Joyner-Boore attenuation data. *Bulletin of the Seismological Society of America*, **74**(4), 1441–1450.

Brillinger, D. R., & Preisler, H. K. 1985. Further analysis of the Joyner-Boore attenuation data. *Bulletin of the Seismological Society of America*, **75**(2), 611–614.

Brune, J. N. 1970. Tectonic stress and the spectra of seismic shear waves from earthquakes. *Journal of Geophysical Research*, **75**(26), 4997–5009.

Brune, J. N. 1971. Correction. *Journal of Geophysical Research*, **76**(20), 5002.

Brune, J. N. 1976. The physics of earthquake strong motion. *Chap. 4, pages 71–139 of:* Lomnitz, C., & Rosenblueth, E. (eds), *Seismic Risk and Engineering Decisions*. Elsevier Scientific Publishing Company.

Brune, J. N. 1996. Particle motions in a physical model of shallow angle thrust faulting. *Proceedings of the Indian Academy of Science (Earth and Planetary Sciences)*, **105**(2), L197–L206.

Brune, J. N., & Allen, C. R. 1967. A low-stress-drop, low-magnitude earthquake with surface faulting: The Imperial, California, earthquake of March 4, 1966. *Bulletin of the Seismological Society of America*, **57**(3), 501–514.

Brune, J. N., & Anooshehpoor, A. 1991. Foam rubber modeling of the El Centro Terminal Substation building. *Earthquake Spectra*, **7**(1), 45–79.

Brune, J. N., & Anooshehpoor, A. 1999. Dynamic geometrical effects on strong ground motion in a normal fault model. *Journal of Geophysical Research*, **104**(B1), 809–815.

Brune, J. N., Vernon III, F. L., & Simons, R. S. 1982. Strong-motion data recorded in Mexico during the main shock. *Pages 319–349 of: The Imperial Valley, California, Earthquake of October 15, 1979*. U.S. Geological Survey Professional Paper, no. 1254. Washington: United States Government Printing Office.

Bullen, K. E. 1963. *An Introduction to the Theory of Seismology*. Cambridge University Press.

Bureau, G. J. 1978 (Jun). Influence of faulting on earthquake attenuation. *Pages 290–307 of: Proceedings of the ASCE Geotechnical Engineering Division Speciality Conference: Earthquake Engineering and Soil Dynamics*, vol. I.

Burford, R. O., Castle, R. O., Church, J. P., Kinishita, W. T., Kirby, S. H., Ruthven, R. T., & Savage, J. C. 1971. Preliminary measurements of tectonic movement. *In: The San Fernando, California, earthquake of February 9, 1971*. U.S. Geological Survey Professional Paper, no. 733. Washington: United States Government Printing Office.

Burger, R. W., Somerville, P. G., Barker, J. S., Herrmann, R. B., & Helmberger, D. V. 1987. The effect of crustal structure on strong ground motion attenuation relations in eastern North America. *Bulletin of the Seismological Society of America*, **77**(2), 420–439.

Bycroft, G. N. 1960. White noise representation of earthquake. *Journal of the Engineering Mechanics Division, ASCE*, **86**(EM2), 1–16.

Bycroft, G. N. 1978. The effect of soil-structure interaction on seismometer readings. *Bulletin of the Seismological Society of America*, **68**(2), 823–843.

Caillot, V., & Bard, P. Y. 1993. Magnitude, distance and site dependent spectra from Italian accelerometric data. *European Earthquake Engineering*, **VII**(1), 37–48.

Campbell, K. W. 1981. Near-source attenuation of peak horizontal acceleration. *Bulletin of the Seismological Society of America*, **71**(6), 2039–2070.

Campbell, K. W. 1985. Strong motion attenuation relations: A ten-year perspective. *Earthquake Spectra*, **1**(4), 759–804.

Campbell, K. W. 1989. The dependence of peak horizontal acceleration on magnitude, distance, and site effects for small-magnitude earthquakes in California and eastern North America. *Bulletin of the Seismological Society of America*, **79**(5), 1311–1346.

Campbell, K. W. 1991. An empirical analysis of peak horizontal acceleration for the Loma Prieta, California, earthquake of 18 October 1989. *Bulletin of the Seismological Society of America*, **81**(5), 1838–1858.

Campbell, K. W. 1997. Empirical near-source attenuation relationships for horizontal and vertical components of peak ground acceleration, peak ground velocity, and pseudo-absolute acceleration response spectra. *Seismological Research Letters*, **68**(1), 154–179.

Campbell, K. W., & Bozorgnia, Y. 1994a. Empirical analysis of strong motion from the 1992 Landers, California, earthquake. *Bulletin of the Seismological Society of America*, **84**(3), 573–588.

Campbell, K. W., & Bozorgnia, Y. 1994b (Jul). Near-source attenuation of peak horizontal acceleration from worldwide accelerograms recorded from 1957 to 1993. *Pages 283–292 of: Proceedings of the Fifth U.S. National Conference on Earthquake Engineering*, vol. III.

Campbell, K. W., & Bozorgnia, Y. 2000 (Nov). New empirical models for predicting near-source horizontal, vertical, and V/H response spectra: Implications for design. *In: Proceedings of the Sixth International Conference on Seismic Zonation*.

Cash, J. R. 1996. *Mathematical Methods lecture notes*. Department of Mathematics — Imperial College, London.

Castle, R. O., Church, J. P., Elliott, M. R., & Morrison, N. L. 1975. Vertical crustal movements preceding and accompanying the San Fernando earthquake of February 9, 1971: A summary. *Tectonophysics*, **29**, 127–140.

Çelebi, M. 1987. Topographical and geological amplifications determined from strong-motion and aftershock records of the 3 March 1985 Chile earthquake. *Bulletin of the Seismological Society of America*, **77**(4), 1147–1167.

Çelebi, M. 1991. Topographical and geological amplification: Case studies and engineering implications. *Structural Safety*, **10**(1–3), 199–217.

Central Geological Survey. 1999. *Investigative Report on the Earthquake Geology of the September 21 Earthquake*. Tech. rept. Central Geological Survey, The Ministry of Economic Affairs, Taiwan, Republic of China. In Chinese.

Chapman, M. C. 1999. On the use of elastic input energy for seismic hazard analysis. *Earthquake Spectra*, **15**(4), 607–635.

Cheng, F. Y., & Oster, K. B. 1976. Ultimate instability of earthquake structures. *Journal of Structural Division, ASCE*, **102**(ST5), 961–972.

Cheng, F. Y., & Oster, K. B. 1977. Ductility studies of parametrically excited systems. *Pages 1118–1123 of: Proceedings of Sixth World Conference on Earthquake Engineering*, vol. II.

Chiaruttini, C., & Siro, L. 1981. The correlation of peak ground horizontal acceleration with magnitude, distance, and seismic intensity for Friuli and Ancona, Italy, and the Alpide belt. *Bulletin of the Seismological Society of America*, **71**(6), 1993–2009.

Chin, B.-H., & Aki, K. 1991. Simultaneous study of the source, path, and site effects on strong ground motion during the 1989 Loma Prieta earthquake: A preliminary result on pervasive nonlinear site effects. *Bulletin of the Seismological Society of America*, **81**(5), 1859–1884.

Chiu, H.-C. 1997. Stable baseline correction of digital strong-motion data. *Bulletin of the Seismological Society of America*, **87**(4), 932–944.

Chopra, A. K. 1995. *Dynamics of Structures — Theory and Application to Earthquake Engineering*. Prentice Hall International, Inc.

Chouw, N., & Hirose, S. 1999. Behaviour of a frame structure during near-source earthquakes. *Pages 1191–1196 of: Structural Dynamics — EuroDyn '99*, vol. 2.

Choy, G. L., & Boatwright, J. L. 1995. Global patterns of radiated seismic energy and apparent stress. *Journal of Geophysical Research*, **100**(B9), 18205–18225.

Clough, R. W., & Penzien, J. 1993. *Dynamics of Structures*. 2nd edn. New York, USA, and London, UK: McGraw-Hill, Inc.

Cocco, M., & Rovelli, A. 1989. Evidence for the variation of stress drop between normal and thrust faulting earthquakes in Italy. *Journal of Geophysical Research*, **94**(B7), 9399–9416.

Comision Federal de Electricidad. 1993. *Manual de diseño de obras civiles, diseño por sismo, Comision Federal de Electricidad*.

Converse, A. M. 1992 (Mar). *BAP basic strong-motion accelerogram processing software, version 1.0*. Open-File Report 92-296A. US Geological Survey.

Cormier, V. F., & Beroza, G. C. 1987. Calculation of strong ground motion due to an extended earthquake source in a laterally varying structure. *Bulletin of the Seismological Society of America*, **77**(1), 1–13.

Cornell, C. A. 1968. Engineering seismic risk analysis. *Bulletin of the Seismological Society of America*, **58**(5), 1583–1606.

Cousins, W. J., Zhao, J. X., & Perrin, N. D. 1999. A model for the attenuation of peak ground acceleration in New Zealand earthquakes based on seismograph and accelerograph data. *Bulletin of the New Zealand Society for Earthquake Engineering*, **32**(4), 193–220.

Crouse, C. B. 1991. Ground-motion attenuation equations for earthquakes on the Cascadia subduction zones. *Earthquake Spectra*, **7**(2), 201–236.

Crouse, C. B., & Hushmand, B. 1989. Soil-structure interaction at CDMG and USGS accelerograph stations. *Bulletin of the Seismological Society of America*, **79**(1), 1–14.

Crouse, C. B., & McGuire, J. W. 1996. Site response studies for purpose of revising NEHRP seismic provisions. *Earthquake Spectra*, **12**(3), 407–439.

Crouse, C. B., Liang, G. C., & Martin, G. R. 1984. Experimental study of soil-structure interaction at an accelerograph station. *Bulletin of the Seismological Society of America*, **74**(5), 1995–2013.

Crouse, C. B., Vyas, Y. K., & Schell, B. A. 1988. Ground motion from subduction-zone earthquakes. *Bulletin of the Seismological Society of America*, **78**(1), 1–25.

Dahle, A., Bugum, H., & Kvamme, L. B. 1990a. Attenuation modelling based on intraplate earthquake recordings. *Pages 121–129 of: Proceedings of Ninth European Conference on Earthquake Engineering*, vol. 4-A.

Dahle, A., Bungum, H., & Kvamme, L. B. 1990b. Attenuation models inferred from intraplate earthquake recordings. *Earthquake Engineering and Structural Dynamics*, **19**(8), 1125–1141.

Dahle, A., Climent, A., Taylor, W., Bungum, H., Santos, P., Ciudad Real, M., Linholm, C., Strauch, W., & Segura, F. 1995. New spectral strong motion attenuation models for Central America. *Pages 1005–1012 of: Proceedings of the Fifth International Conference on Seismic Zonation*, vol. II.

Darragh, R. B., & Bolt, B. A. 1987. A comment on the statistical regression relation between earthquake magnitude and fault rupture length. *Bulletin of the Seismological Society of America*, **77**(4), 1479–1484.

Darragh, R. B., & Shakal, A. F. 1991. The site response of two rock and soil station pairs to strong and weak ground motion. *Bulletin of the Seismological Society of America*, **81**(5), 1885–1899.

Das, S., & Scholz, C. H. 1981. Off-fault aftershock clusters caused by shear stress increase? *Bulletin of the Seismological Society of America*, **71**(5), 1669–1675.

Das, S., & Scholz, C. H. 1983. Why large earthquakes do not nucleate at shallow depths. *Nature*, **305**(Oct), 621–623.

Davis, L. L., & West, L. R. 1973. Observed effects of topography on ground motion. *Bulletin of the Seismological Society of America*, **63**(1), 283–298.

Day, S. M. 1982. Three-dimensional finite difference simulation of fault dynamics: Rectangular faults with fixed rupture velocity. *Bulletin of the Seismological Society of America*, **72**(3), 705–727.

Denham, D., & Small, G. R. 1971. Strong motion data centre: Bureau of mineral resources, Canada. *Bulletin of the New Zealand Society for Earthquake Engineering*, **4**(1), 15–30.

Devillers, C., & Mohammadioun, B. 1981. French methodology for determining site-adapted SMS (Séisme Majoré de Sécurité) spectra. *In: Transactions of the 6th International Conference on Structural Mechanics in Reactor Technology*, vol. K(a). K 1/9.

Di Giovambattista, R., & Barba, S. 1997. An estimate of hypocentre location accuracy in a large network: Possible implications for tectonic studies in Italy. *Geophysical Journal International*, **129**, 124–132.

Diotallevi, P. P., & Landi, L. 2000. Effect of the axial force and of the vertical ground motion component on the seismic response of R/C frames. *In: Proceedings of Twelfth World Conference on Earthquake Engineering*. Paper No. 1026.

Donovan, N. C. 1973. A statistical evaluation of strong motion data including the February 9, 1971 San Fernando earthquake. *Pages 1252–1261 of: Proceedings of Fifth World Conference on Earthquake Engineering*, vol. 1.

Donovan, N. C., & Bornstein, A. E. 1978. Uncertainties in seismic risk analysis. *Journal of the Geotechnical Engineering Division, ASCE*, **104**(GT7), 869–887.

Douglas, A. 1997. Comment on ‘Source complexity of the October 1, 1987, Whittier Narrows earthquake’ by Allison L. Bent and Donald V. Helmberger. *Journal of Geophysical Research*, **102**(B8), 17899–17904.

Douglas, A., Hudson, J. A., & Pearce, R. G. 1988. Directivity and the Doppler effect. *Bulletin of the Seismological Society of America*, **78**(3), 1367–1372.

Douglas, J. 2001 (Jan). *A comprehensive worldwide summary of strong-motion attenuation relationships for peak ground acceleration and spectral ordinates (1969 to 2000)*. ESEE Report 01-1. Department of Civil and Environmental Engineering, Imperial College, London.

Draper, N. R., & Smith, H. 1981. *Applied Regression Analysis*. 2nd edn. John Wiley & Sons.

Dravinski, M. 1982. Influence of interface depth upon strong ground motion. *Bulletin of the Seismological Society of America*, **72**(2), 597–614.

Ekström, G., & Dziewonski, A. M. 1988. Evidence of bias in estimations of earthquake size. *Nature*, **332**(Mar), 319–323.

Elnashai, A. S., & Papazoglou, A. J. 1997. Procedure and spectra for analysis of RC structures subjected to strong vertical earthquake loads. *Journal of Earthquake Engineering*, **1**(1), 121–155.

Esteva, L. 1970. Seismic risk and seismic design. *Pages 142–182 of:* Hansen, R.J. (ed), *Seismic Design for Nuclear Power Plants*. The M.I.T. Press.

Ewing, W. M., Jardetzky, W. S., & Press, F. 1957. *Elastic Waves in Layered Media*. McGraw-Hill Book Company.

Faccioli, E. 1978 (Jun). Response spectra for soft soil sites. *Pages 441–456 of: Proceedings of the ASCE Geotechnical Engineering Division Speciality Conference: Earthquake Engineering and Soil Dynamics*, vol. I.

Faccioli, E., & Reseńdiz, D. 1976. Soil dynamics: Behavior including liquefaction. *Chap. 4, pages 71–139 of:* Lomnitz, C., & Rosenblueth, E. (eds), *Seismic Risk and Engineering Decisions*. Elsevier Scientific Publishing Company.

Feng, D., Theofanopoulos, N., & Watabe, M. 1988. Consideration on the design velocity response spectra along the principal axes. *Pages 855–860 of: Proceedings of Ninth World Conference on Earthquake Engineering*, vol. II.

Fenwick, R. C., Davidson, B. J., & Chung, B. T. 1992. P-Delta actions in seismic resistant structures. *Bulletin of the New Zealand National Society for Earthquake Engineering*, **25**(1), 56–69.

Field, E. H., Johnson, P. A., Beresnev, I. A., & Zeng, Y. 1997. Nonlinear ground-motion amplification by sediments during the 1994 Northridge earthquake. *Nature*, **390**(Dec), 599–602.

Fukushima, Y., & Tanaka, T. 1990. A new attenuation relation for peak horizontal acceleration of strong earthquake ground motion in Japan. *Bulletin of the Seismological Society of America*, **80**(4), 757–783.

Fukushima, Y., Tanaka, T., & Kataoka, S. 1988. A new attenuation relationship for peak ground acceleration derived from strong-motion accelerograms. *Pages 343–348 of: Proceedings of Ninth World Conference on Earthquake Engineering*, vol. II.

Fukushima, Y., Gariel, J.-C., & Tanaka, R. 1995. Site-dependent attenuation relations of seismic motion parameters at depth using borehole data. *Bulletin of the Seismological Society of America*, **85**(6), 1790–1804.

Fuller, W. A. 1987. *Measurement Error Models*. John Wiley & Sons.

Gallant, A. R. 1975. Nonlinear regression. *The American Statistician*, **29**(2), 73–81.

Garcia-Fernandez, M., & Canas, J.A. 1995. Regional peak ground acceleration estimates in the Iberian peninsula. *Pages 1029–1034 of: Proceedings of the Fifth International Conference on Seismic Zonation*, vol. II.

Gariel, J.-C., Archuleta, R. J., & Bouchon, M. 1990. Rupture process of an earthquake with kilometric size fault inferred from the modeling of near-source records. *Bulletin of the Seismological Society of America*, **80**(4), 870–888.

Gaull, B. A. 1988. Attenuation of strong ground motion in space and time in southwest Western Australia. *Pages 361–366 of: Proceedings of Ninth World Conference on Earthquake Engineering*, vol. II.

Geli, L., Bard, P.-Y., & Jullien, B. 1988. The effect of topography on earthquake ground motion: A review and new results. *Bulletin of the Seismological Society of America*, **78**(1), 42–63.

Gomberg, J., & Ellis, M. 2001 (Jul). *3d∼def*. On Internet: http://www.ceri.memphis.edu/3ddef/3d˜def_guide.html.

Graizer, V. M. 1979. Determination of the true ground displacement by using strong motion records. *Izvestiya Academy of Sciences, USSR, Physics of the Solid Earth*, **15**(12), 875–885.

Graizer, V. M. 1980. On the determination of displacement from strong-motion accelerograms. *Pages 391–394 of: Proceedings of Seventh World Conference on Earthquake Engineering*, vol. 2.

Graizer, V. M. 1982. Complete analysis of the May 17 1976 Gazli earthquake. *Pages 197–202 of: Proceedings of Seventh European Conference on Earthquake Engineering*, vol. 2.

Graizer, V. M. 1983. The movement near the focus of the Gazli earthquake. *Izvestiya Academy of Sciences, USSR, Physics of the Solid Earth*, **19**(3), 172–178.

Graizer, V. M. 1985 (Jun). Analysis of results of signals processing. *Pages 211–221 of: Preliminary proceedings of workshop on investigation of strong motion processing procedures — Rome, Italy*, vol. II.

Graizer, V. M. 1988 (Aug). Processing of strong-motion test records. *Pages 37–50 of: Proceedings of the second workshop on processing of seismic strong motion records — Tokyo, Japan*.

Gregor, N. J. 1995 (Jun). *The attenuation of strong ground motion displacements*. Tech. rept. Earthquake Engineering Research Centre, University of California at Berkeley. UCB/EERC-95/02.

Griffiths, D. W., & Bollinger, G. A. 1979. The effect of Appalachian mountain topography on seismic waves. *Bulletin of the Seismological Society of America*, **69**(4), 1081–1105.

Gubbins, D. 1990. *Seismology and Plate Tectonics*. Cambridge University Press.

Gürpinar, A., & Yao, J. T. P. 1973. Design of columns for seismic loads. *Journal of Structural Division, ASCE*, **99**(ST9), 1875–1889.

Gutenberg, B. 1945. Amplitudes of surface waves and magnitudes of shallow earthquakes. *Bulletin of the Seismological Society of America*, **35**(1), 3–12.

Gutenberg, B., & Richter, C. F. 1956. Magnitude and energy of earthquakes. *Annali di geofisica*, **9**, 1–15. Not seen. Cited in Brune (1970).

Hadley, D. M., & Helmberger, D. V. 1980. Simulation of strong ground motions. *Bulletin of the Seismological Society of America*, **70**(2), 617–630.

Haines, A. J. 1981. A local magnitude scale for New Zealand earthquakes. *Bulletin of the Seismological Society of America*, **71**(1), 275–294.

Hanks, T. C. 1979. b values and $\omega^{-\gamma}$ seismic source models: Implications for tectonic stress variations along active crustal fault zones and the estimation of high-frequency strong ground motion. *Journal of Geophysical Research*, **84**(B5), 2235–2242.

Hanks, T. C. 1982. $f_{\max}$. *Bulletin of the Seismological Society of America*, **72**(6), 1867–1879.

Hanks, T. C., & Johnson, D. A. 1976. Geophysical assessment of peak accelerations. *Bulletin of the Seismological Society of America*, **66**(3), 959–968.

Hanks, T. C., & Kanamori, H. 1979. A moment magnitude scale. *Journal of Geophysical Research*, **84**(B5), 2348–2350.

Hanks, T. C., & McGuire, R. K. 1981. The character of high-frequency strong ground motion. *Bulletin of the Seismological Society of America*, **71**(6), 2071–2095.

Hara, F. 1984. Seismic vibration analysis of a vertical mechanical structure subjected to horizontal and vertical 2D excitation. *Transactions of the Japan Society of Mechanical Engineers*, **50**(458-C), 2029–2036. In Japanese.

Hara, F. 1985. Seismic vibration analysis of a vertical mechanical structure subjected to horizontal and vertical 2D random excitation. *Pages 135–140 of: Transactions of the 8th International Conference on Structural Mechanics in Reactor Technology*, vol. M.

Hardin, B. O., & Drnevich, V. P. 1972. Shear modulus and damping in soils: Design equations and curves. *Journal of the Soil Mechanics and Foundations Division, ASCE*, **98**(SM7), 667–692.

Harmsen, S. C. 1997. Determination of site amplification in the Los Angeles urban area from inversion of strong-motion records. *Bulletin of the Seismological Society of America*, **87**(4), 866–887.

Hartzell, S. 1989. Comparison of seismic waveform inversion results for the rupture history of a finite fault: Application to the 1986 North Palm Springs, California, earthquake. *Journal of Geophysical Research*, **94**(B6), 7515–7534.

Hartzell, S., & Helmberger, D. V. 1982. Strong-motion modeling of the Imperial Valley earthquake of 1979. *Bulletin of the Seismological Society of America*, **72**(2), 571–596.

Hartzell, S., & Mendoza, C. 1991. Application of an iterative least-squares waveform inversion of strong-motion and teleseismic records to the 1978 Tabas, Iran, earthquake. *Bulletin of the Seismological Society of America*, **81**(2), 305–331.

Hartzell, S. H., & Heaton, T. H. 1983. Inversion of strong ground motion and teleseismic waveform data for the fault rupture history of the 1979 Imperial Valley, California, earthquake. *Bulletin of the Seismological Society of America*, **73**(6), 1553–1583.

Hartzell, S. H., Frazier, G. A., & Brune, J. N. 1978. Earthquake modeling in a homogeneous half-space. *Bulletin of the Seismological Society of America*, **68**(2), 301–316.

Hasegawa, H. S. 1975. Seismic ground motion and residual deformation near a vertical fault. *Canadian Journal of Earth Sciences*, **12**(4), 523–538.

Haskell, N. A. 1969. Elastic displacements in the near-field of a propagating fault. *Bulletin of the Seismological Society of America*, **59**(2), 865–908.

Heaton, T. H. 1982. The 1971 San Fernando earthquake: A double event? *Bulletin of the Seismological Society of America*, **72**(6), 2037–2062.

Heaton, T. H., & Hartzell, S. H. 1988. Earthquake ground motions. *Annual Review of Earth and Planetary Science*, **16**, 121–145.

Hellweg, M., & Boatwright, J. 1999. Mapping the rupture process of moderate earthquakes by inverting accelerograms. *Journal of Geophysical Research*, **104**(B2), 7319–7328.

Hinzen, K.-G. 1986. Comparison of fault-plane solutions and moment tensors. *Journal of Geophysics*, **59**(2), 112–118.

Hjelmstad, K. D., & Williamson, E. B. 1998. Dynamic stability of structural systems subjected to base excitation. *Engineering Structures*, **20**(4–6), 425–432.

Holzer, S. M. 1970. Stability of columns with transient loads. *Journal of the Engineering Mechanics Division, ASCE*, **96**(EM6), 913–930.

Housner, G. W. 1941. Calculating the response of an oscillator to arbitrary ground motion. *Bulletin of the Seismological Society of America*, **31**(2), 143–149.

Housner, G. W. 1947. Ground displacement computed from strong-motion accelerograms. *Bulletin of the Seismological Society of America*, **37**(4), 299–305.

Housner, G. W., Martel, R. R., & Alford, J. L. 1953. Spectrum analysis of strong-motion earthquakes. *Bulletin of the Seismological Society of America*, **43**(2), 97–119.

Hu, Y., Hu, Y., & Chen, X.-W. 1984. Analyses of earthquake damage of brick smokestacks. *Pages 15–21 of: Proceedings of Eighth World Conference on Earthquake Engineering*, vol. VII.

Hu, Y.-X., Liu, S.-C., & Dong, W. 1996. *Earthquake Engineering*. 1st edn. E & FN Spon, Imprint of Chapman & Hall, London.

Hudson, D. E. 1979. *Reading and Interpreting Strong Motion Accelerograms*. Berkeley, USA: Earthquake Engineering Research Institute.

Hudson, D. E. 1988. Some recent near-source strong motion accelerograms. *Pages 271–276 of: Proceedings of Ninth World Conference on Earthquake Engineering*, vol. II.

Hudson, D. E., Nigam, N. C., & Trifunac, M. D. 1969. Analysis of strong-motion accelerograph records. *Pages A2(1)–A2(17) of: Proceedings of Fourth World Conference of Earthquake Engineering*, vol. I.

Huo, J., & Hu, Y. 1991. Attenuation laws considering the randomness of magnitude and distance. *Earthquake Research in China*, **5**(1), 17–36.

Husid, R. 1969. The effect of gravity on the collapse of yielding structures with earthquake excitation. *Pages A–4 31–43 of: Proceedings of Fourth World Conference of Earthquake Engineering*, vol. II.

Hutton, L. K., & Boore, D. M. 1987. The M_L scale in southern California. *Bulletin of the Seismological Society of America*, **77**(6), 2074–2094.

IASPEI. 1967. Recommendations of the committee on magnitudes. *Comptes rendus*, **15**, 65. Not seen. Cited in Ambraseys & Douglas (2000).

Ida, Y. 1973. The maximum acceleration of seismic ground motion. *Bulletin of the Seismological Society of America*, **63**(3), 959–968.

Idriss, I. M. 1978 (Jun). Characteristics of earthquake ground motions. *Pages 1151–1265 of: Proceedings of the ASCE Geotechnical Engineering Division Speciality Conference: Earthquake Engineering and Soil Dynamics*, vol. III.

Irikura, K., Matsuo, K., & Yoshikawa, S. 1971. An analysis of strong motion accelerograms near the epicenter. *Bulletin of the Disaster Prevention Research Institute, Kyoto University*, **20**(182). Part 4.

Ishida, K. 1979. Study of the characteristics of strong-motion Fourier spectra on bedrock. *Bulletin of the Seismological Society of America*, **69**(6), 2101–2115.

Iwan, W. D. 1994. Near-field considerations in specification of seismic design motions for structures. *Pages 257–267 of: Proceedings of Tenth European Conference on Earthquake Engineering*, vol. 1.

Iwan, W. D., & Chen, X. 1994. Important near-field ground motion data from the Landers earthquake. *Pages 229–234 of: Proceedings of Tenth European Conference on Earthquake Engineering*, vol. 1.

Iwan, W. D., Moser, M. A., & Peng, C.-Y. 1985. Some observations on strong-motion earthquake measurements using a digital accelerograph. *Bulletin of the Seismological Society of America*, **75**(5), 1225–1246.

Iwasaki, T., Kawashima, K., & Saeki, M. 1980. Effects of seismic and geotechnical conditions on maximum ground accelerations and response spectra. *Pages 183–190 of: Proceedings of Seventh World Conference on Earthquake Engineering*, vol. 2.

Iyengar, R. N., & Saha, T. K. 1977. Effect of vertical ground motion on the response of cantilever structures. *Pages 1166–1171 of: Proceedings of Sixth World Conference on Earthquake Engineering*, vol. II.

Iyengar, R. N., & Shinozuka, M. 1972. Effect of self-weight and vertical acceleration on the behaviour of tall structures during earthquakes. *Earthquake Engineering and Structural Dynamics*, **1**, 69–78.

Jackson, M. D., Endo, E. T., Delaney, P. T., Arnadottir, T., & Rubin, A. M. 1992. Ground ruptures of the 1974 and 1983 Kaoiki earthquakes, Mauna Loa volcano, Hawaii. *Journal of Geophysical Research*, **97**(B6), 8775–8796.

Jackson, P. S. 1971. The focusing of earthquakes. *Bulletin of the Seismological Society of America*, **61**(3), 685–695.

Jennings, P. C., & Husid, R. 1968. Collapse of yielding structures during earthquakes. *Journal of the Engineering Mechanics Division, ASCE*, **94**(EM5), 1045–1065.

Jennings, P. C., & Kanamori, H. 1979. Determination of local magnitude, M_L, from seismoscope records. *Bulletin of the Seismological Society of America*, **69**(4), 1267–1288.

Joyner, W. B. 1984. A scaling law for the spectra of large earthquakes. *Bulletin of the Seismological Society of America*, **74**(4), 1167–1188.

Joyner, W. B. 1987. Strong-motion seismology. *Reviews of Geophysics*, **25**(6), 1149–1160.

Joyner, W. B. 2000. Strong motion from surface waves in deep sedimentary basins. *Bulletin of the Seismological Society of America*, **90**(6B), S95–S112.

Joyner, W. B., & Boore, D. M. 1981. Peak horizontal acceleration and velocity from strong-motion records including records from the 1979 Imperial Valley, California, earthquake. *Bulletin of the Seismological Society of America*, **71**(6), 2011–2038.

Joyner, W. B., & Boore, D. M. 1983. Comments on "New attenuation relations for peak and expected accelerations of strong ground motion," by B.A. Bolt and N.A. Abrahamson. *Bulletin of the Seismological Society of America*, **73**(5), 1479–1480.

Joyner, W. B., & Boore, D. M. 1988. Measurement, characterization, and prediction of strong ground motion. *Pages 43–102 of: Proceedings of Earthquake Engineering & Soil Dynamics II*. Geotechnical Division, ASCE.

Joyner, W. B., & Boore, D. M. 1993. Methods for regression analysis of strong-motion data. *Bulletin of the Seismological Society of America*, **83**(2), 469–487.

Joyner, W. B., & Boore, D. M. 1996 (Aug). Recent developments in strong motion attenuation relationships. *Pages 101–116 of: Proceedings of the 28th Joint Meeting of the U.S.-Japan Cooperative Program in Natural Resource Panel on Wind and Seismic Effects*.

Joyner, W. B., & Fumal, T. E. 1984. Use of measured shear-wave velocity for predicting geologic site effects on strong ground motion. *Pages 777–783 of: Proceedings of Eighth World Conference on Earthquake Engineering*, vol. II.

Joyner, W. B., Warrick, R. E., & Fumal, T. E. 1981. The effect of quaternary alluvium on strong ground motion in the Coyote Lake, California, earthquake of 1979. *Bulletin of the Seismological Society of America*, **71**(4), 1333–1349.

Kamiyama, M. 1995. An attenuation model for the peak values of strong ground motions with emphasis on local soil effects. *Pages 579–585 of: Proceedings of the First International Conference on Earthquake Geotechnical Engineering*, vol. 1.

Kamiyama, M., & Yanagisawa, E. 1986. A statisical model for estimating response spectra of strong earthquake ground motions with emphasis on local soil conditions. *Soils and Foundations*, **26**(2), 16–32.

Kamiyama, M., O'Rourke, M.J., & Flores-Berrones, R. 1992 (Sep). *A semi-empirical analysis of strong-motion peaks in terms of seismic source, propagation path and local site conditions*. Tech. rept. NCEER-92-0023. National Center for Earthquake Engineering Research.

Kanamori, H. 1974. Long-period ground motion in the epicentral area of major earthquakes. *Tectonophysics*, **21**(4), 341–356.

Kanamori, H. 1977. The energy release in great earthquakes. *Journal of Geophysical Research*, **82**(20), 2981–2987.

Kanamori, H., & Anderson, D. L. 1975. Theoretical basis of some empirical relations in seismology. *Bulletin of the Seismological Society of America*, **65**(5), 1073–1095.

Kanamori, H., & Jennings, P. C. 1978. Determination of local magnitude, M_L, from strong-motion accelerograms. *Bulletin of the Seismological Society of America*, **68**(2), 471–485.

Kappos, A. J. 1999. Evaluation of behaviour factors on the basis of ductility and overstrength studies. *Engineering Structures*, **21**, 823–835.

Kawano, H., Takahashi, K., Takemura, M., Tohdo, M., Watanabe, T., & Noda, S. 2000. Empirical response spectral attenuations on the rocks with $\mathrm{VS} = 0.5$ to $3.0\,\mathrm{km/s}$ in Japan. *In: Proceedings of Twelfth World Conference on Earthquake Engineering*. Paper No. 0953.

Kawase, H. 1988. Time-domain response of a semi-circular canyon for incident SV, P, and rayleigh waves calculated by the discrete wavenumber boundary element method. *Bulletin of the Seismological Society of America*, **78**(4), 1415–1437.

Kawase, H., & Aki, K. 1990. Topography effect at the critical SV-wave incidence: Possible explanation of damage pattern by the Whittier narrows, California, earthquake of 1 October 1987. *Bulletin of the Seismological Society of America*, **80**(1), 1–22.

Kawashima, K., Aizawa, K., & Takahashi, K. 1984. Attenuation of peak ground motion and absolute acceleration response spectra. *Pages 257–264 of: Proceedings of Eighth World Conference on Earthquake Engineering*, vol. II.

Kawashima, K., Aizawa, K., & Takahashi, K. 1986. Attenuation of peak ground acceleration, velocity and displacement based on multiple regression analysis of Japanese strong motion records. *Earthquake Engineering and Structural Dynamics*, **14**(2), 199–215.

Kehoe, B. E., & Attalla, M. R. 2000. Considerations of vertical acceleration on structural response. *In: Proceedings of Twelfth World Conference on Earthquake Engineering*. Paper No. 1065.

Kikuchi, M., Dan, K., & Yashiro, K. 2000. Seismic behaviour of a reinforced concrete building due to large vertical ground motions in near-source regions. *In: Proceedings of Twelfth World Conference on Earthquake Engineering*. Paper No. 1876.

Kim, W.-Y. 1998. The M_L scale in eastern North America. *Bulletin of the Seismological Society of America*, **88**(4), 935–951.

King, J. L., & Tucker, B. E. 1984. Observed variations of earthquake motion across a sediment-filled valley. *Bulletin of the Seismological Society of America*, **74**(1), 137–151.

King, N. E., Savage, J. C., Lisowski, M., & Prescott, W. H. 1981. Preseismic and coseismic deformation associated with the Coyote Lake, California, earthquake. *Journal of Geophysical Research*, **86**(B2), 892–898.

Kobayashi, H., & Midorikawa, S. 1982. A semi-empirical method for estimating response spectra of near-field ground motions with regard to fault rupture. *Pages 161–168 of: Proceedings of Seventh European Conference on Earthquake Engineering*, vol. 2.

Kobayashi, S., Takahashi, T., Matsuzaki, S., Mori, M., Fukushima, Y., Zhao, J. X., & Somerville, P. G. 2000. A spectral attenuation model for Japan using digital strong motion records of JMA87 type. *In: Proceedings of Twelfth World Conference on Earthquake Engineering*. Paper No. 2786.

Koukouvelas, I. K., & Doutsos, T. T. 1996. Implications of structural segmentation during earthquakes: The 1995 Egion earthquake, Gulf of Corinth, Greece. *Journal of Structural Geology*, **18**(12), 1381–1388.

Kramer, S. L. 1996. *Geotechnical Earthquake Engineering*. Prentice-Hall, Inc.

Krinitzky, E. L., & Chang, F. K. 1987. *State-of-the-art for assessing earthquake hazards in the United States: Parameters for specifying intensity-related earthquake ground motions*. Tech. rept. 25. U.S. Army Corps of Engineers Waterways Experiment Station. Not seen.

Krinitzsky, E. L., Gould, J. P., & Edinger, P. H. 1993. *Fundamentals of Earthquake Resistant Construction*. John Wiley & Sons.

Langston, C. A., & Lee, J.-J. 1983. Effect of structure geometry on strong ground motions: The Duwamish river valley, Seattle, Washington. *Bulletin of the Seismological Society of America*, **73**(6), 1851–1863.

Langston, C. A., Brazier, R., Nyblade, A. A., & Owens, T. J. 1998. Local magnitude scale and seismicity rate for Tanzania, east Africa. *Bulletin of the Seismological Society of America*, **88**(3), 712–721.

Lawson, R. S., & Krawinkler, H. 1994. Cumulative damage potential of seismic ground motion. *Pages 1079–1086 of: Proceedings of Tenth European Conference on Earthquake Engineering*, vol. 2.

Lee, V. W. 1993. Scaling PSV from earthquake magnitude, local soil, and geologic depth of sediments. *Journal of the Geotechnical Engineering Division, ASCE*, **119**(1), 108–126.

Lee, V. W. 1995. Pseudo relative velocity spectra in former Yugoslavia. *European Earthquake Engineering*, **IX**(1), 12–22.

Lee, Y., Zeng, Y., & Anderson, J. G. 1998. A simple strategy to examine the sources of errors in attenuation relations. *Bulletin of the Seismological Society of America*, **88**(1), 291–296.

Lekkas, E. L., Lozios, S. G., Skourtsos, E. N., & Kranis, H. D. 1998. Egio earthquake (15 June 1995): An episode in the neotectonic evolution of Corinthiakos Gulf. *Journal of Geodynamics*, **26**(2–4), 487–499.

Levine, M. B., & Beck, J. L. 1990. A new approach to processing accelerograms based on probability. *Pages 457–466 of: Proceedings of the Fourth U.S. National Conference on Earthquake Engineering*, vol. 1.

Lide, C. S., & Ryall, A. S. 1985. Aftershock distribution related to the controversy regarding mechanisms of the May 1980, Mammoth Lakes, California, earthquakes. *Journal of Geophysical Research*, **90**(B13), 11151–11154.

Lin, J., & Stein, R. S. 1987. Coseismic folding, earthquake recurrence, and the 1987 source mechanism at Whittier Narrows, Los Angeles basin, California. *Journal of Geophysical Research*, **94**(B7), 9614–9632.

Lin, Y. K. 2000 (May). Email message received 23/5/2000.

Lin, Y. K., & Shih, T.-Y. 1980. Column response to horizontal-vertical earthquakes. *Journal of the Engineering Mechanics Division, ASCE*, **106**(EM6), 1099–1109.

Liu, H.-L., & Heaton, T. 1984. Array analysis of the ground velocities and accelerations from the 1971 San Fernando, California, earthquake. *Bulletin of the Seismological Society of America*, **74**(5), 1951–1968.

Liu, H.-L., & Helmberger, D. V. 1983. The near-source ground motion of the 6 August 1979 Coyote Lake, California, earthquake. *Bulletin of the Seismological Society of America*, **73**(1), 201–218.

Liu, H.-L., & Helmberger, D. V. 1985. The 23:19 aftershock of the 15 October 1979 Imperial Valley earthquake: More evidence for an asperity. *Bulletin of the Seismological Society of America*, **75**(3), 689–708.

Liu, S. C., & Jhaveri, D. P. 1969. Spectral and correlation analysis of ground-motion accelerograms. *Bulletin of the Seismological Society of America*, **59**(4), 1517–1534.

Loh, C. H., & Ma, M. J. 1997. Reliability assessment of structures subjected to horizontal-vertical random earthquake excitations. *Structural Safety*, **19**(1), 153–168.

Lubkin, S., & Stoker, J. J. 1943. Stability of columns and strings under periodically varying forces. *Quarterly of Applied Mathematics*, **1**, 215–236.

Luco, J. E., & Anderson, J. G. 1983. Steady-state response of an elastic half-space to a moving dislocation of finite width. *Bulletin of the Seismological Society of America*, **73**(1), 1–22.

Luco, J. E., Anderson, J. G., & Georgevich, M. 1990. Soil-structure interaction effects on strong motion accelerograms recorded on instrument shelters. *Earthquake Engineering and Structural Dynamics*, **19**(1), 119–131.

Lungu, D., Demetriu, S., Radu, C., & Coman, O. 1994. Uniform hazard response spectra for Vrancea earthquakes in Romania. *Pages 365–370 of: Proceedings of Tenth European Conference on Earthquake Engineering*, vol. 1.

Lungu, D., Cornea, T., Craifaleanu, I., & Aldea, A. 1995. Seismic zonation of Romania based on uniform hazard response ordinates. *Pages 445–452 of: Proceedings of the Fifth International Conference on Seismic Zonation*, vol. I.

Madariaga, R. 1977. High-frequency radiation from crack (stress drop) models of earthquake faulting. *Geophysical Journal of the Royal Astronomical Society*, **51**(3), 625–651.

Mansinha, L., & Smylie, D. E. 1971. The displacement fields of inclined faults. *Bulletin of the Seismological Society of America*, **61**(5), 1433–1440.

Marone, C., & Scholz, C. H. 1998. The depth of seismic faulting and the upper transition from stable to unstable slip regimes. *Geophysical Research Letters*, **15**(6), 621–624.

Marshall, G. A., Stein, R. S., & Thatcher, W. 1991. Faulting geometry and slip from co-seismic elevation changes: The 18 October 1989, Loma Prieta, California, earthquake. *Bulletin of the Seismological Society of America*, **81**(5), 1660–1693.

Martínez-Pereira, A. 1999 (Mar). *The characterisation of near-field earthquake ground-motions for engineering design*. Ph.D. thesis, University of London.

Martínez-Pereira, A., & Bommer, J. J. 1998 (Mar). What is the near-field? *Pages 245–252 of:* Booth, E. (ed), *Proceedings of the Sixth SECED Conference on Seismic Design Practice into the Next Century*.

Mat-Isa, A. R., & Usher, M. J. 1992. An angular accelerometer for reducing the effects of tilt in seismic records. *Geophysical Journal International*, **109**(1), 197–208.

McCann Jr., M. W., & Boore, D. M. 1983. Variability in ground motions: Root mean square acceleration and peak acceleration for the 1971 San Fernando, California, earthquake. *Bulletin of the Seismological Society of America*, **73**(2), 615–632.

McCann Jr., M. W., & Echezwia, H. 1984. Investigating the uncertainty in ground motion prediction. *Pages 297–304 of: Proceedings of Eighth World Conference on Earthquake Engineering*, vol. II.

McCue, K., Gibson, G., & Wesson, V. 1988. Intraplate recording of strong motion in southeastern Australia. *Pages 355–360 of: Proceedings of Ninth World Conference on Earthquake Engineering*, vol. II.

McGarr, A. 1981. Analysis of peak ground motion in terms of a model of inhomogenous faulting. *Journal of Geophysical Research*, **86**(B5), 3901–3912.

McGarr, A. 1982. Upper bounds on near-source peak ground motion based on a model of inhomogeneous faulting. *Bulletin of the Seismological Society of America*, **72**(6), 1825–1841.

McGarr, A. 1984. Scaling of ground motion parameters, state of stress, and focal depth. *Journal of Geophysical Research*, **89**(B8), 6969–6979.

McGuire, R. K. 1977. Seismic design spectra and mapping procedures using hazard analysis based directly on oscillator response. *Earthquake Engineering and Structural Dynamics*, **5**, 211–234.

McGuire, R. K. 1978. Seismic ground motion parameter relations. *Journal of the Geotechnical Engineering Division, ASCE*, **104**(GT4), 481–490.

McLachlan, N. W. 1951. *Theory of Vibrations*. Dover Publications, Inc.

McVerry, G. H., Zhao, J. X., Abrahamson, N. A., & Somerville, P. G. 2000. Crustal and subduction zone attenuation relations for New Zealand earthquakes. *In: Proceedings of Twelfth World Conference on Earthquake Engineering*. Paper No. 1834.

Mendez, A. J., & Anderson, J. G. 1991. The temporal and spatial evolution of the 19 September 1985 Michoacán earthquake as inferred from near-source ground-motion records. *Bulletin of the Seismological Society of America*, **81**(3), 844–861.

Mendoza, C., & Hartzell, S. H. 1988. Aftershock patterns and main shock faulting. *Bulletin of the Seismological Society of America*, **78**(4), 1438–1449.

Menu, J. M. 1987 (Dec). *Interpolation, correction and integration of earthquake strong ground motions with low degree polynomials*. Tech. rept. Department of Civil Engineering — Imperial College of Science and Technology, London.

Menu, J. M. H. 1986. *Engineering study of near-field earthquake strong-motions*. Ph.D. thesis, University of London.

Midorikawa, S. 1993. Semi-empirical estimation of peak ground acceleration from large earthquakes. *Tectonophysics*, **218**, 287–295.

Milne, W. G., & Davenport, A. G. 1969. Distribution of earthquake risk in Canada. *Bulletin of the Seismological Society of America*, **59**(2), 729–754.

Minster, J. B., & Day, S. M. 1986. Decay of wave fields near an explosive source due to high-strain nonlinear attenuation. *Journal of Geophysical Research*, **91**(B2), 2113–2122.

Miranda, E., & Bertero, V. V. 1994. Evaluation of strength reduction factors for earthquake-resistant design. *Earthquake Spectra*, **10**(2), 357–379.

Mohammadioun, B. 1991. The prediction of response spectra for the anti-seismic design of structures specificity of data from intracontinential environments. *European Earthquake Engineering*, **V**(2), 8–17.

Mohammadioun, B. 1994a. Prediction of seismic motion at the bedrock from the strong-motion data currently available. *Pages 241–245 of: Proceedings of Tenth European Conference on Earthquake Engineering*, vol. 1.

Mohammadioun, G. 1994b. Calculation of site-adapted reference spectra from the statistical analysis of an extensive strong-motion data bank. *Pages 177–181 of: Proceedings of Tenth European Conference on Earthquake Engineering*, vol. 1.

Molas, G. L., & Yamazaki, F. 1995. Attenuation of earthquake ground motion in Japan including deep focus events. *Bulletin of the Seismological Society of America*, **85**(5), 1343–1358.

Moore, G. 1997a. *Computational Linear Algebra lecture notes*. Department of Mathematics — Imperial College, London.

Moore, G. 1997b. *Non-linear Equations and Unconstrained Optimisation lecture notes*. Department of Mathematics — Imperial College, London.

Moroney, M. J. 1990. *Facts from Figures*. 2nd edn. Penguin Books.

Mostaghel, N. 1975. Stability of columns subjected to earthquake support motion. *Earthquake Engineering and Structural Dynamics*, **3**(4), 347–352.

Mumme, I. A., & McLaughlin, R. 1985 (Aug). Adjustment of accelerograms using dynamic programming to give realistic velocity and displacement information. *Pages 109–113 of: Transactions of the 8th International Conference on Structural Mechanics in Reactor Technology*, vol. K(a). K 2/8.

Munson, C. G., & Thurber, C. H. 1997. Analysis of the attenuation of strong ground motion on the island of Hawaii. *Bulletin of the Seismological Society of America*, **87**(4), 945–960.

Murray, M. H., Marshall, G. A., Lisowski, M., & Stein, R. S. 1996. The 1992 $M = 7$ Cape Mendocino, California, earthquake: Coseismic deformation at the south end of the Cascadia megathrust. *Journal of Geophysical Research*, **101**(B8), 17707–17725.

National Earthquake Hazard Reduction Program. 1994. *Recommended provisions for seismic regulations for new buildings*. FEMA 222A.

Neumann, F. 1943. An apprasial of numerical integration methods as applied to strong motion data. *Bulletin of the Seismological Society of America*, **33**(1), 21–60.

Newmark, N. M. 1959. A method of computation for structural dynamics. *Journal of the Engineering Mechanics Division, ASCE*, **85**, 67–94.

Newmark, N. M., & Hall, W. J. 1987. *Earthquake Spectra and Design*. Earthquake Engineering Research Institute.

Newmark, N. M., & Rosenblueth, E. 1971. *Fundamentals of Earthquake Engineering*. Englewood Cliffs, New Jersey, USA: Prentice-Hall, Inc.

Niazi, M. 1982. Source dynamics of the 1979 Imperial Valley earthquake from near-source observations (of ground acceleration and velocity). *Bulletin of the Seismological Society of America*, **72**(6), 1957–1968.

Niazi, M., & Bozorgnia, Y. 1991. Behaviour of near-source peak horizontal and vertical ground motions over SMART-1 array, Taiwan. *Bulletin of the Seismological Society of America*, **81**(3), 715–732.

Niazi, M., & Bozorgnia, Y. 1992a. Behaviour of near-source vertical and horizontal response spectra at SMART-1 array, Taiwan. *Earthquake Engineering and Structural Dynamics*, **21**, 37–50.

Niazi, M., & Bozorgnia, Y. 1992b. The 1990 Manjil, Iran, earthquake: Geology and seismology overview, PGA attenuation, and observed damage. *Bulletin of the Seismological Society of America*, **82**(2), 774–799.

Nigam, N. C., & Jennings, P. C. 1969. Calculation of response spectra from strong-motion earthquake records. *Bulletin of the Seismological Society of America*, **59**(2), 909–922.

Nisar, A., & Golesorkhi, C. 1995. Development of vertical design response spectrum for use in near-field. *Pages 1075–1082 of: Proceedings of the Fifth International Conference on Seismic Zonation*, vol. II.

Nuttli, O. W. 1973. Seismic wave attenuation and magnitude relation for eastern North America. *Journal of Geophysical Research*, **78**(5), 876–885.

Nuttli, O. W., & Herrmann, R. B. 1982. Earthquake magnitude scales. *Journal of the Geotechnical Engineering Division, ASCE*, **108**(GT5), 783–786.

Oglesby, D. D., & Archuleta, R. J. 1997. A faulting model for the 1992 Petrolia earthquake: Can extreme ground acceleration be a source effect? *Journal of Geophysical Research*, **102**(B6), 11877–11897.

Oglesby, D. D., Archuleta, R. J., & Nielsen, S. B. 1996. Earthquakes on dipping faults: The effects of broken symmetry. *Science*, **280**(May), 1055–1059.

Oglesby, D. D., Archuleta, R. J., & Nielsen, S. B. 2000a. Dynamics of dip-slip faulting: Explorations in two dimensions. *Journal of Geophysical Research*, **105**(B6), 13643–13653.

Oglesby, D. D., Archuleta, R. J., & Nielsen, S. B. 2000b. The three-dimensional dynamics of dipping faults. *Bulletin of the Seismological Society of America*, **90**(3), 616–628.

Ohno, S., Ohta, T., Ikeura, T., & Takemura, M. 1993. Revision of attenuation formula considering the effect of fault size to evaluate strong motion spectra in near field. *Tectonophysics*, **218**, 69–81.

Ohno, S., Takemura, M., Niwa, M., & Takahashi, K. 1996. Intensity of strong ground motion on pre-quaternary stratum and surface soil amplifications during the 1995 Hyogo-ken Nanbu earthquake, Japan. *Journal of Physics of the Earth*, **44**(5), 623–648.

Ohsaki, Y., Watabe, M., & Tohdo, M. 1980a. Analyses on seismic ground motion parameters including vertical components. *Pages 97–104 of: Proceedings of Seventh World Conference on Earthquake Engineering*, vol. 2.

Ohsaki, Y., Sawada, Y., Hayashi, K., Ohmura, B., & Kumagai, C. 1980b. Spectral characteristics of hard rock motions. *Pages 231–238 of: Proceedings of Seventh World Conference on Earthquake Engineering*, vol. 2.

Olson, A. H., & Apsel, R. J. 1982. Finite faults and inverse theory with applications to the 1979 Imperial Valley earthquake. *Bulletin of the Seismological Society of America*, **72**(6), 1969–2001.

Oppenheimer, D., Beroza, G., Carver, G., Dengler, L., Eaton, J., Gee, L., Gonzalez, F., Jayko, A., Li, W. H., Lisowski, M., Magee, M., Marshall, G., Murray, M., McPherson, R., Romanowicz, B., Satake, K., Simpson, R., Somerville, P., Stein, R., & Valentine, D. 1993. The Cape Mendocino, California, earthquakes of April 1992: Subduction at the Triple Junction. *Science*, **261**(Jul), 433–438.

Orabi, I. I., & Ahmadi, G. 1988. Response of structures subjected to horizontal-vertical random earthquake excitations. *Soil Dynamics and Earthquake Engineering*, **7**(1), 9–14.

Orphal, D. L., & Lahoud, J. A. 1974. Prediction of peak ground motion from earthquakes. *Bulletin of the Seismological Society of America*, **64**(5), 1563–1574.

Osborne, M. R. 1972. Some aspects of non-linear least squares calculations. *Pages 171–189 of:* Lootsma, F.A. (ed), *Numerical methods for non-linear optimization*. London: Academic Press Inc.

Papadopoulou, O. 1989 (Aug). *The effect of vertical excitation on reinforced concrete multi-storey structures*. MSc. dissertation, University of London. Not seen. Reported in Papazoglou & Elnashai (1996).

Papageorgiou, A. S., & Kim, J. 1991. Study of the propagation and amplification of seismic waves in Caracas valley with reference to the 29 July 1967 earthquake: SH waves. *Bulletin of the Seismological Society of America*, **81**(6), 2214–2233.

Papaleontiou, C., & Roesset, J. M. 1993. Effect of vertical acceleration on the seismic response of frames. *Pages 19–27 of: Structural Dynamics — EuroDyn '93*, vol. 1.

Papaleontiou, C. G. 1992. *Dynamic analysis of building structures under combined horizontal and vertical vibrations*. Ph.D. thesis, The University of Texas at Austin.

Papazoglou, A. J., & Elnashai, A. S. 1996. Analytical and field evidence of the damaging effect of vertical earthquake ground motion. *Earthquake Engineering and Structural Dynamics*, **25**(10), 1109–1137.

Pavlis, G. L. 1992. Appraising relative earthquake location errors. *Bulletin of the Seismological Society of America*, **82**(2), 836–859.

Pedersen, H., Le Brun, B., Hatzfeld, D., Campillo, M., & Bard, P.-Y. 1994. Ground-motion amplitude across ridges. *Bulletin of the Seismological Society of America*, **84**(6), 1786–1800.

Peng, K.-Z., Wu, F. T., & Song, L. 1985. Attenuation characteristics of peak horizontal acceleration in northeast and southwest China. *Earthquake Engineering and Structural Dynamics*, **13**(3), 337–350.

Poppitz, J. V. 1968. Velocity and displacement of explosion-induced earth tremors derived from acceleration. *Bulletin of the Seismological Society of America*, **58**(2), 1573–1582.

Press, W. H., & Teukolsky, S. A. 1992. Adaptive stepsize Runge-Kutta. *Computers in Physics*, **6**(2), 188–191.

Press, W. H., Teukolsky, S. A., Vetterling, W. T., & Flannery, B. P. 1992. *Numerical Recipes in FORTRAN: The Art of Scientific Computing*. 2nd edn. Cambridge University Press.

Rathje, E., Idriss, I. M., Somerville, P., Ansal, A., Bachhuber, J., Baturay, M., Erdik, M., Frost, D., Lettis, W., Sozer, B., Stewart, J., & Ugras, T. 2000. Strong ground motions and site effects. *Chap. 4, pages 65–96 of:* Youd, T. L., Bardet, J.-P., & Bray, J. D. (eds), *Kocaeli, Turkey, Earthquake of August 17, 1999 Reconnaissance Report (supplement A to Volume 16 of Earthquake Spectra)*. Oakland, California: Earthquake Engineering Research Institute.

Reilinger, R., & Larsen, S. 1986. Vertical crustal deformation associated with the 1979 $M = 6.6$ Imperial Valley, California earthquake: Implications for fault behaviour. *Journal of Geophysical Research*, **91**(B14), 14044–14056.

Reilinger, R. E., Ergintav, S., Bürgmann, R., McClusky, S., Lenk, O., Barka, A., Gurkan, O., Hearn, L., Feigl, K. L., Cakmak, R., Aktug, B., Ozenen, H., & Töksoz, M. N. 2000. Coseismic and postseismic fault slip for the 17 August 1999, $M = 7.5$, Izmit, Turkey earthquake. *Science*, **289**(Sep), 1519–1524.

Reimer, R. B., Clough, R. W., & Raphael, J. M. 1973. Evaluation of the Pacoima Dam accelerogram. *Pages 2328–2337 of: Proceedings of Fifth World Conference on Earthquake Engineering*, vol. 2.

Reyes-Salazar, A., & Halder, A. 2000. Consideration of vertical acceleration and flexibility of connections on seismic response of steel frames. *In: Proceedings of Twelfth World Conference on Earthquake Engineering*. Paper No. 1171.

Rezapour, M., & Pearce, R. G. 1998. Bias in surface-wave magnitude M_s due to inadequate distance corrections. *Bulletin of the Seismological Society of America*, **88**(1), 43–61.

Rial, J. A. 1984. Caustics and focusing produced by sedimentary basins: Applications of catastrophe theory to earthquake seismology. *Geophysical Journal of the Royal Astronomical Society*, **79**(3), 923–938.

Rial, J. A., Pereyra, V., & Wojcik, G. L. 1986. An explanation for USGS station 6 record, 1979 Imperial Valley earthquake: A caustic induced by a sedimentary wedge. *Geophysical Journal of the Royal Astronomical Society*, **84**(2), 257–278.

Richter, C. F. 1935. An instrumental earthquake magnitude scale. *Bulletin of the Seismological Society of America*, **25**, 1–32.

Richter, C. F. 1958. *Elementary Seismology*. San Francisco, USA: Freeman and Co.

Rogers, A. M., Katz, L. J., & Bennett, T. J. 1974. Topographic effects on ground motion for incident P waves: A model study. *Bulletin of the Seismological Society of America*, **64**(2), 437–456.

Rogers, A. M., Borcherdt, R. D., Covington, P. A., & Perkins, D. M. 1984. Comparative ground response study near Los Angeles using recordings of Nevada nuclear tests and the 1971 San Fernando earthquake. *Bulletin of the Seismological Society of America*, **74**(5), 1925–1949.

Ruge, A. C. 1934. The determination of earthquake stresses in elastic structures by means of models. *Bulletin of the Seismological Society of America*, **24**(3), 169–230.

Sabetta, F., & Pugliese, A. 1987. Attenuation of peak horizontal acceleration and velocity from Italian strong-motion records. *Bulletin of the Seismological Society of America*, **77**(5), 1491–1513.

Sabetta, F., & Pugliese, A. 1996. Estimation of response spectra and simulation of nonstationary earthquake ground motions. *Bulletin of the Seismological Society of America*, **86**(2), 337–352.

Sadigh, K., Youngs, R. R., & Power, M. S. 1978. A study of attenuation of peak horizontal accelerations for moderately strong earthquakes. *Pages 243–250 of: Proceedings of Sixth European Conference on Earthquake Engineering*, vol. 1.

Sadigh, K., Chang, C.-Y., Egan, J. A., Makdisi, F., & Youngs, R. R. 1997. Attenuation relationships for shallow crustal earthquakes based on California strong motion data. *Seismological Research Letters*, **68**(1), 180–189.

Sadigh, R. K., & Egan, J. A. 1998. Updated relationships for horizontal peak ground velocity and peak ground displacement for shallow crustal earthquakes. *In: Proceedings of the Sixth U.S. National Conference on Earthquake Engineering*.

Şafak, E. 2000 (Nov). A simple method to account for the effects of vertical loads on the horizontal seismic response of buildings. *In: Proceedings of the Sixth International Conference on Seismic Zonation*.

Safak, E., Erdik, M., Beyen, K., Carver, D., Cranswick, E., Celebi, M., Durukal, E., Ellsworth, W., Holzer, T., Meremonte, M., Mueller, C., Ozel, O., & Toprak, S. 2000. Recorded main shock and aftershock motions. *Chap. 5, pages 97–112 of:* Youd, T. L., Bardet, J.-P., & Bray, J. D. (eds), *Kocaeli, Turkey, Earthquake of August 17, 1999 Reconnaissance Report (supplement A to Volume 16 of Earthquake Spectra)*. Oakland, California: Earthquake Engineering Research Institute.

Sánchez-Sesma, F. J. 1987. Site effects on strong ground motion. *Soil Dynamics and Earthquake Engineering*, **6**(2), 124–136.

Sánchez-Sesma, F. J., & Esquivel, J. A. 1979. Ground motion on alluvial valleys under incident plane SH waves. *Bulletin of the Seismological Society of America*, **69**(4), 1107–1120.

Sarma, S. K. 1971. Energy flux of strong earthquakes. *Tectonophysics*, **11**, 159–173.

Sarma, S. K., & Srbulov, M. 1996. A simplified method for prediction of kinematic soil-foundation interaction effects on peak horizontal acceleration of a rigid foundation. *Earthquake Engineering and Structural Dynamics*, **25**(8), 815–836.

Savage, J. C., & Wood, M. D. 1971. The relation between apparent stress and stress drop. *Bulletin of the Seismological Society of America*, **61**(5), 1381–1388.

Savage, J. C., Lisowski, M., & Murray, M. 1993. Deformation from 1973 through 1991 in the epicentral area of the 1992 Landers, California, earthquake ($M_s = 7.5$). *Journal of Geophysical Research*, **98**(B11), 19951–19958.

Schenk, V. 1982. Peak particle ground motions in earthquake near-field. *Pages 211–217 of: Proceedings of Seventh European Conference on Earthquake Engineering*, vol. 2.

Schenk, V. 1984. Relations between ground motions and earthquake magnitude, focal distance and epicentral intensity. *Engineering Geology*, **20**(1/2), 143–151.

Schiff, A., & Bogdanoff, J. L. 1967. Analysis of current methods of interpreting strong-motion accelerograms. *Bulletin of the Seismological Society of America*, **57**(5), 857–874.

Scholz, C. H. 1982. Scaling relations for strong ground motion in large earthquakes. *Bulletin of the Seismological Society of America*, **72**(6), 1903–1909.

Scholz, C. H., Aviles, C. A., & Wesnousky, S. G. 1986. Scaling differences between large interplate and intraplate earthquakes. *Bulletin of the Seismological Society of America*, **76**(1), 65–70.

Seed, H. B., & Idriss, I. M. 1969. Influence of soil conditions on ground motions during earthquakes. *Journal of the Soil Mechanics and Foundations Division, ASCE*, **95**(SM1), 99–137.

Seekins, L. C., & Hanks, T. C. 1978. Strong-motion accelerograms of the Oroville aftershocks and peak acceleration data. *Bulletin of the Seismological Society of America*, **68**(3), 677–689.

Shabestari, K. T., & Yamazaki, F. 2000. Attenuation relation of response spectra in Japan considering site-specific term. *In: Proceedings of Twelfth World Conference on Earthquake Engineering*. Paper No. 1432.

Shabestari, T. K., & Yamazaki, F. 1998. Attenuation of JMA seismic intensity using recent JMA records. *Pages 529–534 of: Proceedings of the 10th Japan Earthquake Engineering Symposium*, vol. 1. Not seen. Reported in Shabestari & Yamazaki (2000).

Sharma, M. L. 1998. Attenuation relationship for estimation of peak ground horizontal acceleration using data from strong-motion arrays in India. *Bulletin of the Seismological Society of America*, **88**(4), 1063–1069.

Sharma, M. L. 2000. Attenuation relationship for estimation of peak ground vertical acceleration using data from strong motion arrays in India. *In: Proceedings of Twelfth World Conference on Earthquake Engineering*. Paper No. 1964.

Sharp, R. V., Lienkaemper, J. J., Bonilla, M. G., Burke, D. B., Fox, B. F., Herd, D. G., Miller, D. M., Morton, D. M., Ponti, D. J., Rymer, M. J., Tinsley, J. C., Yount, J. C., Kahle, J. E., Hart, E. W., &

Sieh, K. E. 1982. Surface faulting in the central Imperial Valley. *Pages 119–143 of: The Imperial Valley, California, Earthquake of October 15, 1979*. U.S. Geological Survey Professional Paper, no. 1254. Washington: United States Government Printing Office.

Shearer, P. M., & Orcutt, J. A. 1987. Surface and near-surface effects on seismic waves — theory and borehole seismometer results. *Bulletin of the Seismological Society of America*, **77**(4), 1168–1196.

Shi, B., Anooshehpoor, A., Brune, J. N., & Zeng, Y. 1998. Dynamics of thrust faulting: 2D lattice model. *Bulletin of the Seismological Society of America*, **88**(6), 1484–1494.

Shih, T.-Y., & Lin, Y. K. 1982a. Vertical seismic load effect on building response. *Journal of the Engineering Mechanics Division, ASCE*, **108**(EM2), 331–343.

Shih, T.-Y., & Lin, Y. K. 1982b. Vertical seismic load effect on hysteric columns. *Journal of the Engineering Mechanics Division, ASCE*, **108**(EM2), 242–254.

Shin, T. C., Kuo, K. W., Lee, W. H. K., Teng, T. L., & Tsai, Y. B. 2000. A preliminary report on the 1999 Chi-Chi (Taiwan) earthquake. *Seismological Research Letters*, **71**(1), 24–30.

Shoja-Taheri, J. 1980. A new assessment of errors from digitization and base line corrections of strong-motion accelerograms. *Bulletin of the Seismological Society of America*, **70**(1), 293–303.

Shoja-Taheri, J., & Anderson, J. G. 1988. The 1978 Tabas, Iran, earthquake: An interpretation of the strong motion records. *Bulletin of the Seismological Society of America*, **78**(1), 142–171.

Shoja-Taheri, J., & Bolt, B. A. 1977. A generalized strong-motion accelerogram based on spectral maximization from two horizontal components. *Bulletin of the Seismological Society of America*, **67**(3), 863–876.

Shteinburg, V. V., Chernov, Y. K., & Ivanova, T. G. 1980. Near field ground motion. *Pages 373–378 of: Proceedings of Seventh World Conference on Earthquake Engineering*, vol. 2.

Si, H., & Midorikawa, S. 2000. New attenuation relations for peak ground acceleration and velocity considering effects of fault type and site condition. *In: Proceedings of Twelfth World Conference on Earthquake Engineering*. Paper No. 0532.

Sigbjörnsson, R., & Baldvinsson, G. I. 1992. Seismic hazard and recordings of strong ground motion in Iceland. *Pages 419–424 of: Proceedings of Tenth World Conference on Earthquake Engineering*, vol. 1.

Singh, S. K., Mena, E., Castro, R., & Carmona, C. 1987. Empirical prediction of ground motion in Mexico City from coastal earthquakes. *Bulletin of the Seismological Society of America*, **77**(5), 1862–1867.

Sirovich, L. 1994. A case of the influence of radiation pattern on peak accelerations. *Bulletin of the Seismological Society of America*, **84**(5), 1658–1664.

Slade, M. A., Lyzenga, G. A., & Raefsky, A. 1984. Modeling of the surface static displacements and fault plane slip for the 1979 Imperial Valley earthquake. *Bulletin of the Seismological Society of America*, **74**(6), 2413–2433.

Smit, P. 1998 (Sep). Strong motion attenuation model for central Europe. *In: Proceedings of Eleventh European Conference on Earthquake Engineering*. smisma.

Smith, S. W., & Wyss, M. 1968. Displacement of the San Andreas fault subsequent to the 1966 Parkfield earthquake. *Bulletin of the Seismological Society of America*, **58**(6), 1955–1973.

Snay, R. A., Neugebauer, H. C., & Prescott, W. H. 1991. Horizontal deformation associated with the Loma Prieta earthquake. *Bulletin of the Seismological Society of America*, **81**(5), 1647–1659.

Snee, R. D. 1977. Validation of regression models: Methods and examples. *Technometrics*, **19**(4), 415–428.

Somerville, P., & Graves, R. 1993. Conditions that give rise to usually large long period ground motions. *The Structural Design of Tall Buildings*, **2**(3), 211–232.

Somerville, P., & Yoshimura, J. 1990. The influence of critical Moho reflections on strong ground motions recorded in San Francisco and Oakland during the 1989 Loma Prieta earthquake. *Geophysical Research Letters*, **17**(8), 1203–1206.

Somerville, P., Sen, M., & Cohee, B. 1991a. Simulation of strong ground motions recorded during the 1985 Michoacán, Mexico and Valparaíso, Chile earthquakes. *Bulletin of the Seismological Society of America*, **81**(1), 1–27.

Somerville, P. G., McLaren, J. P., Sen, M. K., & Helmberger, D. V. 1991b. The influence of site conditions on the spatial incoherence of ground motions. *Structural Safety*, **10**, 1–13.

Spudich, P. 1996. Synopsis. *Pages A1–A7 of:* Spudich, P. (ed), *The Loma Prieta, California, earthquake of October 17, 1989 — Main-shock characteristics*. U.S. Geological Survey Professional Paper, nos. 1550–A. Washington: United States Government Printing Office.

Spudich, P., Hellweg, M., & Lee, W. H. K. 1996a. Directional topographic site response at Tarzana observed in aftershocks of the 1994 Northridge, California, earthquake: Implications for main-shock motions. *Bulletin of the Seismological Society of America*, **86**(1B), S193–S208.

Spudich, P., Fletcher, J., Hellweg, M., Boatwright, J., Sullivan, C., Joyner, W., Hanks, T., Boore, D., McGarr, A., Baker, L., & Lindh, A. 1996b. *Earthquake ground motions in extensional tectonic regimes*. Open-File Report 96-292. U.S. Geological Survey. Not seen. Reported in Spudich *et al.* (1997).

Spudich, P., Fletcher, J. B., Hellweg, M., Boatwright, J., Sullivan, C., Joyner, W. B., Hanks, T. C., Boore, D. M., McGarr, A., Baker, L. M., & Lindh, A. G. 1997. SEA96 — A new predictive relation for earthquake ground motions in extensional tectonic regimes. *Seismological Research Letters*, **68**(1), 190–198.

Spudich, P., Joyner, W. B., Lindh, A. G., Boore, D. M., Margaris, B. M., & Fletcher, J. B. 1999. SEA99: A revised ground motion prediction relation for use in extensional tectonic regimes. *Bulletin of the Seismological Society of America*, **89**(5), 1156–1170.

Stevens, J. L., & Day, S. M. 1994. Simulation of strong ground motion. *Pages A53–A60 of: The Loma Prieta, California, Earthquake of October 17, 1989 – Strong Ground Motion*. U.S. Geological Survey Professional Paper, nos. 1551–A. Washington: United States Government Printing Office.

Stewart, J. P. 2000. Variations between foundation-level and free-field earthquake ground motions. *Earthquake Spectra*, **16**(2), 511–532.

Stewart, R. R., Toksöz, M. N., & Timur, A. 1983. Strain dependent attenuation: Observations and a proposed mechanism. *Journal of Geophysical Research*, **88**(B1), 546–554.

Suhadolc, P., & Chiaruttini, C. 1987. A theoretical study of the dependence of the peak ground acceleration on source and structure parameters. *Pages 143–183 of:* Erdik, M.O., & Toksöz, M.N. (eds), *Strong ground motion seismology*. D. Reidel Publishing Company.

Sun, C. K., Berg, G. V., & Hanson, R. D. 1973. Gravity effect on single-degree inelastic system. *Journal of the Engineering Mechanics Division, ASCE*, **99**(EM1), 183–200.

Sun, F., & Peng, K. 1993. Attenuation of strong ground motion in western U.S.A. *Earthquake Research in China*, **7**(1), 119–131.

Sunder, S. S., & Connor, J. J. 1982. A new procedure for processing strong-motion earthquake signals. *Bulletin of the Seismological Society of America*, **72**(2), 643–661.

Sunder, S. S., & Schumacker, B. 1982. Earthquake motions using a new data processing scheme. *Journal of the Engineering Mechanics Division, ASCE*, **108**(EM6), 1313–1329.

Tani, S., & Soda, S. 1977. Vertical load effect on structural dynamics. *Pages 1028–1033 of: Proceedings of Sixth World Conference on Earthquake Engineering*, vol. II.

Tento, A., Franceschina, L., & Marcellini, A. 1992. Expected ground motion evaluation for Italian sites. *Pages 489–494 of: Proceedings of Tenth World Conference on Earthquake Engineering*, vol. 1.

Theodulidis, N. P., & Papazachos, B. C. 1992. Dependence of strong ground motion on magnitude-distance, site geology and macroseismic intensity for shallow earthquakes in Greece: I, peak horizontal acceleration, velocity and displacement. *Soil Dynamics and Earthquake Engineering*, **11**, 387–402.

Theodulidis, N. P., & Papazachos, B. C. 1994. Dependence of strong ground motion on magnitude-distance, site geology and macroseismic intensity for shallow earthquakes in Greece: II horizontal pseudovelocity. *Soil Dynamics and Earthquake Engineering*, **13**(5), 317–343.

Tibi, R., Bock, G., Xia, Y., Baumbach, M., Grosser, H., Milkereit, C., Karakisa, S., Zünbül, S., Kind, R., & Zschau, J. 2001. Rupture processes of the 1999 August 17 Izmit and November 12 Düzce (Turkey) earthquakes. *Geophysical Journal International*, **144**, F1–F7.

Tocher, D., Patwardhan, A. S., & Cluff, L. S. 1977. Estimation of near field characteristics of earthquake motion. *Pages 470–476 of: Proceedings of Sixth World Conference on Earthquake Engineering*, vol. I.

Todorovska, M. I., & Lee, V. W. 1995. A note on sensitivity of uniform probability spectra on modeling the fault geometry in areas with a shallow seismogenic zone. *European Earthquake Engineering*, **IX**(5), 14–22.

Tong, H., & Katayama, T. 1988. Peak acceleration attenuation by eliminating the ill-effect of the correlation between magnitude and epicentral distance. *Pages 349–354 of: Proceedings of Ninth World Conference on Earthquake Engineering*, vol. II.

Toro, G. R., Abrahamson, N. A., & Schneider, J. F. 1997. Model of strong ground motions from earthquake in central and eastern North America: Best estimates and uncertainties. *Seismological Research Letters*, **68**(1), 41–57.

Trifunac, M. D. 1971a. Surface motion of a semi-cylindrical alluvial valley for incident plane SH waves. *Bulletin of the Seismological Society of America*, **61**(6), 1755–1770.

Trifunac, M. D. 1971b. Zero baseline correction of strong-motion accelerograms. *Bulletin of the Seismological Society of America*, **61**(5), 1201–1211.

Trifunac, M. D. 1973. Scattering of plane SH waves by a semi-cylindrical canyon. *Earthquake Engineering and Structural Dynamics*, **1**(3), 267–281.

Trifunac, M. D. 1974. A three-dimensional dislocation model for the San Fernando, California, earthquake of February 9, 1971. *Bulletin of the Seismological Society of America*, **64**(1), 149–172.

Trifunac, M. D. 1976. Preliminary analysis of the peaks of strong earthquake ground motion – dependence of peaks on earthquake magnitude, epicentral distance, and recording site conditions. *Bulletin of the Seismological Society of America*, **66**(1), 189–219.

Trifunac, M. D. 1980. Effects of site geology on amplitudes of strong motion. *Pages 145–152 of: Proceedings of Seventh World Conference on Earthquake Engineering*, vol. 2.

Trifunac, M. D. 1994. Earthquake source variables for scaling spectral and temporal characteristics of strong ground motion. *Pages 2585–2590 of: Proceedings of Tenth European Conference on Earthquake Engineering*, vol. 4.

Trifunac, M. D., & Brady, A. G. 1975. On the correlation of peak acceleration of strong motion with earthquake magnitude, epicentral distance and site conditions. *Pages 43–52 of: Proceedings of the U.S. National Conference on Earthquake Engineering*.

Trifunac, M. D., & Brady, A. G. 1976. Correlations of peak acceleration, velocity and displacement with earthquake magnitude, distance and site conditions. *Earthquake Engineering and Structural Dynamics*, **4**(5), 455–471.

Trifunac, M. D., & Lee, V. W. 1974. A note on the accuracy of computed ground displacements from strong-motion accelerograms. *Bulletin of the Seismological Society of America*, **64**(4), 1209–1219.

Trifunac, M. D., & Lee, V. W. 1989. Empirical models for scaling pseudo relative velocity spectra of strong earthquake accelerations in terms of magnitude, distance, site intensity and recording site conditions. *Soil Dynamics and Earthquake Engineering*, **8**(3), 126–144.

Trifunac, M. D., & Todorovska, M. I. 2001. A note on the useable dynamic range of accelerographs recording translation. *Soil Dynamics and Earthquake Engineering*, **21**(4), 275–286.

Trifunac, M. D., Udwadia, F. E., & Brady, A. G. 1973. Analysis of errors in digitized strong-motion accelerograms. *Bulletin of the Seismological Society of America*, **63**(1), 157–187.

Trujillo, D. M., & Carter, A. L. 1982. A new approach to the integration of accelerometer data. *Earthquake Engineering and Structural Dynamics*, **10**(4), 529–535.

Tselentis, G.-A., Melis, N. S., Sokos, E., & Papatsimpa, K. 1997. The Egion June 15, 1995 ($6.2M_L$) earthquake, western Greece. *Pure and Applied Geophysics*, **147**(1), 83–98.

Tucker, B. E., & King, J. L. 1984. Dependence of sediment-filled valley response on input amplitude and valley properties. *Bulletin of the Seismological Society of America*, **74**(1), 153–165.

Vassiliou, M. S., & Kanamori, H. 1982. The energy release in earthquakes. *Bulletin of the Seismological Society of America*, **72**(2), 371–387.

Vidale, J. E. 1989. Influence of focal mechanism on peak accelerations of strong motions of the Whittier Narrows, California, earthquake and an aftershock. *Journal of Geophysical Research*, **94**(B7), 9607–9613.

Vorgia, E. E. 1992 (Aug). *Influence of strong motion processing on regressions to derive attenuation relations*. MSc. dissertation, University of London.

Vostrikov, Y. N. 1998. Extension of the correction polynomial method for ground motion reconstruction from long seismic records. *Izvestiya, Physics of the Solid Earth*, **34**(2), 151–159. Translated from *Fizika Zemli*, pp. 72–80.

Wald, D. J., Heaton, T. H., & Hudnut, K. W. 1996. The slip history of the 1994 Northridge, California, earthquake determined from strong-motion, teleseismic, GPS, and leveling data. *Bulletin of the Seismological Society of America*, **86**(1B), S49–S70.

Wang, B.-Q., Wu, F. T., & Bian, Y.-J. 1999. Attenuation characteristics of peak accele-ration in north China and comparison with those in the eastern part of North America. *Acta Seismologica Sinica*, **12**(1). On internet at: http://www.chinainfo.gov.cn/periodical/dizhen-E/dzxb99/dzxb9901/990104.htm.

Weisburg, S. 1985. *Applied Linear Regression*. 2nd edn. John Wiley & Sons.

Wells, D. L., & Coppersmith, K. J. 1994. New empirical relationships among magnitude, rupture length, rupture width, rupture area, and surface displacement. *Bulletin of the Seismological Society of America*, **84**(4), 974–1002.

Wen, K.-L., Yeh, Y. T., & Huang, W.-G. 1992. Effects of an alluvial basin on strong ground motions. *Bulletin of the Seismological Society of America*, **82**(2), 1192–1133.

Westaway, R., & Smith, R. B. 1989. Strong ground motion in normal-faulting earthquakes. *Geophysical Journal*, **96**(3), 529–559.

Williams, C. R., & Segall, P. 1996. Coseismic displacements measured with the Global Positioning System. *Pages A263–A277 of:* Spudich, P. (ed), *The Loma Prieta, California, earthquake of October 17, 1989 — Main-shock characteristics*. U.S. Geological Survey Professional Paper, nos. 1550–A. Washington: United States Government Printing Office.

Wirsching, P. H., & Yao, J. T. P. 1971. Random behaviour of columns. *Journal of the Engineering Mechanics Division, ASCE*, **97**(EM3), 605–618.

Wong, H. L., & Trifunac, M. D. 1974. Surface motion of a semi-elliptical alluvial valley for incident plane SH waves. *Bulletin of the Seismological Society of America*, **64**(5), 1389–1408.

Xiang, J., & Gao, D. 1994. The attenuation law of horizontal peak acceleration on the rock site in Yunnan area. *Earthquake Research in China*, **8**(4), 509–516.

Xu, Z., Shen, X., & Hong, J. 1984. Attenuation relation of ground motion in northern China. *Pages 335–342 of: Proceedings of Eighth World Conference on Earthquake Engineering*, vol. II.

Yagi, Y., & Kikuchi, M. 1999. *Spatiotempoal distribution of source rupture process for Taiwan earthquake (*$\mathrm{Ms} = 7.7$*)*. On Internet, http://wwweic.eri.u-tokyo.ac.jp/yuji/taiwan/taiwan.html.

Yagi, Y., & Kikuchi, M. 2000. Source rupture process of the Kocaeli, Turkey, earthquake of August 17, 1999, obtained by joint inversion of near-field data and teleseismic data. *Geophysical Research Letters*, **27**(13), 1969–1972.

Yamabe, K., & Kanai, K. 1988. An empirical formula on the attenuation of the maximum acceleration of earthquake motions. *Pages 337–342 of: Proceedings of Ninth World Conference on Earthquake Engineering*, vol. II.

Yamazaki, S., Minami, S., Mimura, H., & Udagawa, K. 2000. Effects of vertical ground motions on earthquake response of steel frames. *In: Proceedings of Twelfth World Conference on Earthquake Engineering*. Paper No. 0663.

Youngs, R. R., Abrahamson, N., Makdisi, F. I., & Sadigh, K. 1995. Magnitude-dependent variance of peak ground acceleration. *Bulletin of the Seismological Society of America*, **85**(4), 1161–1176.

Youngs, R. R., Chiou, S.-J., Silva, W. J., & Humphrey, J. R. 1997. Strong ground motion attenuation relationships for subduction zone earthquakes. *Seismological Research Letters*, **68**(1), 58–73.

Zahradník, J., & Hron, F. 1987. Seismic ground motion of sedimentary valleys — example La Molina, Lima, Peru. *Journal of Geophysics*, **62**(1), 31–37.

Zebker, H. A., Rosen, P. A., Goldstein, R. M., Gabriel, A., & Werner, C. L. 1994. On the derivation of coseismic displacement fields using differential radar interferometry: The Landers earthquake. *Journal of Geophysical Research*, **99**(B10), 19617–19634.

Zhao, J. X., Dowrick, D. J., & McVerry, G. H. 1997. Attenuation of peak ground acceleration in New Zealand earthquakes. *Bulletin of the New Zealand National Society for Earthquake Engineering*, **30**(2), 133–158.

Zhou, X., Su, J., & Wang, G. 1989. A modification of the fault-rupture model and its application in seismic hazard analysis. *Earthquake Research in China*, **3**(4), 351–365.

Zorapapel, G. T., & Vucetic, M. 1994. The effects of seismic pore water pressure on ground motion. *Earthquake Spectra*, **10**(2), 403–438.

APPENDIX

A. GLOSSARY OF TERMS

A.1 Source

Apparent stress, σ_a The apparent stress is the average stress associated with radiation resistance and is given by Savage & Wood (1971):

$$\sigma_a = \eta\bar{\sigma} = \frac{1}{2}\Delta\sigma - (\sigma_f - \sigma_1)$$

Must have σ_a between 0 and $\Delta\sigma/2$ (Savage & Wood, 1971).

An alternative definition is:

$$\sigma_a = \mu E_s / M_0$$

Body-wave magnitude, m_b There are two main methods of calculation:

1. Uses the amplitude of one-second compressional, P, waves recorded at distances exceeding $2000\,\mathrm{km}$. These can be affected by abnormal attenuation in depth interval 75–$200\,\mathrm{km}$ and this can lead to different values for different areas of the Earth even if the earthquake has the same one-second near-field spectral amplitude (Nuttli & Herrmann, 1982). This scale is sometimes referred to as $m_{b,P}$.

2. Uses the amplitude of one-second period higher-mode Rayleigh, Lg, waves from vertical component seismograms. Lg waves do not penetrate into the strongly attenuating zone so that earthquakes with same one-second near-field spectral amplitude anywhere in the world give the same magnitude (Nuttli & Herrmann, 1982). This scale is often referred to as $m_{b,Lg}$. It was defined by Nuttli (1973) for eastern North America by making the values from these equations equal the value found from teleseismic P or Pn waves:

$$\begin{aligned} m_{b,Lg} &= 3.75 + 0.90\log\Delta + \log A/T \quad \text{for:} \quad 0.5^\circ \leq \Delta \leq 4^\circ, \\ m_{b,Lg} &= 3.30 + 1.66\log\Delta + \log A/T \quad \text{for:} \quad 4^\circ \leq \Delta \leq 30^\circ, \end{aligned}$$

where Δ is epicentral distance in degrees and A/T is maximum ground velocity in microns per second.

Dynamic frictional stress, σ_f While slip is occurring on the fault, the motion is opposed by the stress, σ_f, associated with dynamic friction. In a gravitational field σ_f represents the sum of the shear stresses associated with the gravitational work and frictional stress. As long as the elastic stress exceeds σ_f sliding will continue, hence: $\sigma_f > \sigma_0$.

Energy magnitude, M_E Choy & Boatwright (1995) define energy magnitude, M_E, by: $M_E = \frac{2}{3}\log E_s - 3.2$ where E_s is in Nm.

Energy released by faulting (strain energy change), E Using a suitable definition of average stress it can be shown that the energy released by faulting is given by (Savage & Wood, 1971):

$$E = S\bar{\sigma}\bar{D}.$$

Therefore:

$$E = \frac{M_0\bar{\sigma}}{\mu}.$$

If the stress drop is complete then $\Delta\sigma = 2\bar{\sigma}$ so:

$$E = \frac{\Delta\sigma M_0}{2\mu}.$$

If the stress drop is partial then this equation gives the minimum strain energy change (Kanamori, 1977).

Focal mechanism There are two main types of focal mechanism (Kramer, 1996, pp. 34–37):

Dip-Slip Fault movement occurs primarily in direction of slip (or perpendicular to strike). Two types of movement are possible:

Normal Horizontal component of dip slip movement is extensional and material above the inclined fault (the hanging wall) moves *downwards* relative to material below the fault (the foot wall). Associated with tensile stresses in crust and results in horizontal lengthening of the crust.

Reverse Horizontal component of dip slip movement is compressional and material above the inclined fault (the hanging wall) moves *upwards* relative to material below the fault (the foot wall). Oglesby *et al.* (1996) define all compressional earthquakes with dip angle more than $45°$ as reverse. Results in horizontal shortening of the crust. A special type of reverse fault is:

Thrust Occurs when the fault plane has a small dip angle. Oglesby *et al.* (1996) define all compressional earthquakes with dip angle less than $45°$ as thrust.

Strike-slip Fault movement occurs parallel to strike. Usually such faults are nearly vertical and can produce large movements. These faults are occasionally referred to as wrench faults (Anderson, 1951). Two types of movement are possible:

Right lateral strike-slip Observer standing near such a fault would observe the ground on the opposite side of the fault moving to the *right*.

Left lateral strike-slip Observer standing near such a fault would observe the ground on the opposite side of fault moving to the *left*.

The angle between the rupture plane and the surface on the hanging wall side is always acute and it is always obtuse on the foot wall side.

Many earthquakes contain a mixture of dip-slip and strike-slip movements, such focal mechanisms are called *oblique*.

Fault-plane solutions use the direction of the first P wave motion from the vertical component thus it contains only information about the situation at rupture initiation whereas the inversion of entire waveform for the optimum point source, like CMT, is an average over the whole spatio-temporal dimension of source (Hinzen, 1986). Hinzen (1986) examines 120 NEIS and CMT solutions and finds that most first motion and CMT solutions differ by only a small amount but that for 19% the rake angles differ by $45°$ or more and there is no dependence of this difference on M_0.

Local magnitude, M_L Introduced by Richter (1935). It was originally defined as $M_L = \log_{10} A - \log_{10} A_0(\Delta)$, where A is the maximum recorded amplitude in $\mu\,\mathrm{m}$ at a distance of $100\,\mathrm{km}$ from the earthquake on a Wood-Anderson seismograph (period $0.8\,\mathrm{s}$, magnification 2800, damping 0.8 of critical) and $A_0(\Delta)$ is an empirically derived distance calibration function where Δ is epicentral distance. Richter (1935) used a group of southern Californian earthquakes to derive an empirical formula relating amplitude and distance, from which was deduced the maximum amplitude as a function of distance, $A_0(\Delta)$, that would be generated by an earthquake registering $1\mu\,\mathrm{m}$ on a Wood-Anderson seismograph at an epicentral distance of $100\,\mathrm{km}$.

Hutton & Boore (1987) have re-examined M_L for southern California using a large body of data and determined a new distance calibration function, $A_0(r)$ where r is hypocentral distance.

Measurements from Wood-Anderson seismographs, of the type used by Richter (1935) to define M_L, are not now usually used for magnitude determination because they have been replaced by more modern instruments. Therefore records from other types of instruments are deconvolved and then reconvolved to produce synthetic Wood-Anderson records. Examples of this is the use of strong-motion records (Kanamori & Jennings, 1978) or seismoscope records (Jennings & Kanamori, 1979) to give M_L.

Mean stress, $\bar{\sigma}$ $\bar{\sigma} = (\sigma_0 + \sigma_1)/2$.

Moment magnitude, M_w By considering the radiated seismic energy released during earthquakes Kanamori (1977) and Hanks & Kanamori (1979) define a moment-magnitude scale, M_w, by the equation:

$$\begin{aligned} \log M_0 &= 1.5M_w + 16.1, \\ \text{or: } M_w &= \frac{2}{3}\log M_0 - 10.73. \end{aligned}$$

Hanks & Kanamori (1979) note that this equation is almost identical to empirical equations relating $\log M_0$ to M_s and M_L therefore they define a single moment magnitude, $\boldsymbol{M}$, by:

$$\boldsymbol{M} = \frac{2}{3}\log M_0 - 10.7.$$

Although this definition of $\boldsymbol{M}$ is identical to that for M_w Hanks & Kanamori (1979) note that it is only valid for $3 \lesssim M_L \lesssim 7$, $5 \lesssim M_s \lesssim 7\frac{1}{2}$ and $M_w \gtrsim 7\frac{1}{2}$. There has been much confusion in the literature over whether to use M_w or $\boldsymbol{M}$ with some authors using M_w and some using $\boldsymbol{M}$.

Q For a volume cycled in stress at a frequency ω a dimensionless measure of material friction (or anelasticity) is (Aki & Richards, 1980):

$$\frac{1}{Q(\omega)} = -\frac{\Delta E}{2\pi E}$$

where ΔE is the energy lost in each cycle due to imperfections in elasticity of material and E is the peak strain energy in volume. Now since the amplitude of a wave, A, is proportional to $E^{1/2}$ then have for $Q \gg 1$:

$$\frac{1}{Q(\omega)} = -\frac{\Delta A}{\pi A}$$

where ΔA is the decrease in amplitude of the wave per cycle. For spatial decay of A have:

$$\Delta A = \frac{\mathrm{d}A}{\mathrm{d}x}\lambda$$

where λ is wavelength in terms of phase velocity, c, and equals $2\pi c/\omega$. Thus the amplitude of the waves at x is:

$$A(x) = A_0 \exp\left(\frac{-\omega x}{2cQ}\right)$$

Radiated seismic energy, E_s Choy & Boatwright (1995) calculate E_s from P wave group using:

$$E_s = 4\pi \langle F^P \rangle^2 (R^P / F^{gP})^2 \epsilon^*_{gP},$$

where $\langle F^P \rangle$ is mean-square radiation-pattern coefficient for P waves, R^P is P wave geometrical spreading factor, F^{gP} is generalised radiation pattern coefficient for P wave group and ϵ^*_{gP} is integral of velocity squared over duration of body wave arrival.

Brune (1976) shows that the amount of energy released by the earthquake is given by: $E_s = \frac{1}{\mu}\mathrm{d}V\Delta\sigma\sigma_0$, where $\mathrm{d}V$ is a small volume and μ is the Lamé parameter.

Rise time, τ Rise time is a measure of the time that the dislocation takes to reach its final state after the arrival of the rupture at a point on the fault. Day (1982) analyses 3D finite difference solutions for a simple shear-crack model of faulting and finds that rise time $\tau \approx W/2v_R$.

Rupture duration, t_c Rupture duration is equal to the sum of the length of time taken for the rupture to propagate from the epicentre to both ends of the fault and the rise time, τ. For unilateral rupture the length of time taken for the rupture to propagate from the epicentre, at one end of the fault, to the other end is L/v_R, for bilateral rupture this propagation time is $L/2v_R$ and for other types of ruptures the propagation time is between these values. Since τ is often found to be much smaller that the propagation time it is often ignored.

Seismic efficiency, η Seismic efficiency measures how efficiently the energy released by faulting (strain energy change) was converted into radiated seismic energy during the earthquake. η must always be between 0 and 1. Thus:

$$\eta = \frac{E_s}{E}.$$

Using a suitable definition of average stress, $\bar{\sigma}$, this is equivalent to (Westaway & Smith, 1989):

$$\eta = \frac{\bar{\sigma} - \sigma_f}{\bar{\sigma}}.$$

Seismic moment, M_0 An earthquake fault is mathematically modelled by a shear displacement discontinuity (dislocation) across a surface, Σ, in an elastic medium. The dislocation is equivalent to a distribution of double couples on this surface whose total moment is (Kanamori & Anderson, 1975):

$$M_0 = \mu S \bar{D},$$

where μ is rigidity of the crust, S is fault area and $\bar{D}$ is the average slip along the fault.

The dislocation is, in general, a function of time so M_0 is a function of time, t. In a restricted usage, the value of M_0 at $t \rightarrow \infty$ is called seismic moment. In practice, however the period at which determination of M_0 is made depends on the kind of available data. Geodetic data (e.g. surface faulting, pre-seismic and post-seismic geodetic and geological data and spatial distribution of aftershocks) gives M_0 at $t \rightarrow \infty$, long period surface-wave or free oscillation data give M_0 at t equal to minutes or hours and body-wave data gives M_0 at relatively short periods (Kanamori & Anderson, 1975). It is usually assumed that M_0 is determined at sufficiently long periods so that it represents the value at $t \rightarrow \infty$, a reasonable assumption but not necessarily self-evident (Kanamori & Anderson, 1975).

Strain change (strain drop), $\Delta\tilde{e}$ $\Delta\tilde{e} = \bar{D}/\tilde{L}$.

Surface-wave magnitude, M_s Originally introduced by Gutenberg (1945) who used the maximum horizontal ground displacement, $A_{\max}$, from waves with periods around $20\,\mathrm{s}$. Today the commonly used formula for the calculation of surface-wave magnitude is referred to as the 'Prague formula' and is given by (IASPEI, 1967):

$$M_s = \log(A/T)_{\max} + 1.66 \log D + 3.3,$$

where $(A/T)_{\max}$ is the maximum ground particle velocity in microns per second and D is the epicentral distance in degrees. A depth adjustment is to be used for earthquakes with focal depths greater than $40\,\mathrm{km}$. Recommended period ranges corresponding to maximum amplitudes of surface waves at different epicentral distances are given in IASPEI (1967) and by others.

Different agencies and authors employ slightly different selection criteria of the recordings used to calculate M_s and also different distance calibration functions (the part of the formula of the form $a \log D + b$) have been proposed (e.g. Rezapour & Pearce, 1998), hence the surface-wave magnitudes given by different workers may be different. See Ambraseys & Douglas (2000) for a discussion of these differences.

Work done against friction, E_f The work done against friction during faulting is (Savage & Wood, 1971):

$$E_f = \int \int u\sigma_f \, \mathrm{d}x \, \mathrm{d}y,$$

where the integral is taken over the complete fault surface. Using a suitable definition of average stress this gives (Savage & Wood, 1971):

$$E_f = S\sigma_f \bar{D}.$$

A.2 Symbols used here and in Chapter 2

$\bar{D}$	Average slip
L	Fault length
$\tilde{L}$	Characteristic dimension
S	Fault area
v_R	Rupture velocity
W	Fault width
β	Shear-wave velocity
μ	Rigidity of crust
σ_1	Final stress on a fault

B. METHODS USED IN THIS STUDY

Numerous programs were written in FORTRAN and MATLAB for this study. The most important and complex programs and the methods used to check them are discussed in this chapter.

B.1 Methods for calculation of response spectra

Numerous methods for the calculation of response spectra have been proposed, for example methods based on linear interpolation of excitation (Nigam & Jennings, 1969), central difference methods, Newmark's method (Newmark, 1959) and using digital filters (Beaudet & Wolfson, 1970). Chopra (1995, chap. 6) gives a description of some of these methods, along with examples.

The method of Nigam & Jennings (1969) is probably the most widely used for the calculation of normal response spectra (i.e. solutions of Equation 4.1) because it is accurate and efficient when the time interval between acceleration points is constant. The exact solution to linearly-interpolated acceleration time-histories are found. Much of the calculation is made only once for each period and damping, because Equation 4.1 is linear, rather than at each time step thus reducing computation time. Equations 4.14, 4.15, 4.19 & 4.20 are non-linear hence it is no longer computationally advantageous to use this method because the exact solution on which it relies does not hold and so an iterative technique needs to be combined with it to yield the correct solution.

One method of implementing this iterative technique is to rearrange the equation of motion into:

$$u_{tt} + 2\xi_1\omega_1 u_t + \omega_1^2 u = -U_{tt} + \omega_1^2 \beta V_{tt} u.$$

Then assume U_{tt}, V_{tt} *and* u can be linearly interpolated so that:

$$u_{tt} + 2\xi_1\omega_1 u_t + \omega_1^2 u = -U_{tt}^i - \frac{U_{tt}^{i+1} - U_{tt}^i}{t^{i+1} - t^i}\tau + \omega_1^2 \beta (V_{tt}^i + \frac{V_{tt}^{i+1} - V_{tt}^i}{t^{i+1} - t^i}\tau)(u^i + \frac{u^{i+1} - u^i}{t^{i+1} - t^i}\tau) \quad \text{(B.1)}$$

where $0 \leq \tau \leq t^{i+1} - t^i$ and the superscripts denote the value of the variable at time $t = t^i$. Since u^{i+1} is unknown an iterative solution of Equation B.1 is required. Firstly u^{i+1} is assumed, the exact solution of Equation B.1 is found[1], the displacement for time t^{i+1}, u^{i+1} compared with the assumed value and if the difference is too large then the step is repeated using the new value of u^{i+1}. This process is repeated at each time step.

[1] This can be computed, since the RHS is a quadratic in τ, using Duhamel's integral (Chopra, 1995, p. 122) or otherwise.

This algorithm was not implemented because the limits on the stability and the computational error associated with it are unknown, unlike techniques for solving Equation 4.1 (Chopra, 1995, pp.170–172).

The algorithm chosen for this study was an adaptive step length Runge-Kutta-Fehlberg technique (Press & Teukolsky, 1992; Cash, 1996). The solution at each time is computed using fourth order and fifth order Runge-Kutta formulae and their solutions compared. The difference between these two estimates of the solution is a measure of the truncation error, which is used to adjust the stepsize. This leads to a solution which has a chosen accuracy and is efficient, because small time steps are only used when required.

A FORTRAN computer program, HVSPECTRA, was written to implement this algorithm. For this study the accuracy level set was $10^{-6}\,\mathrm{m}$ and $10^{-6}\,\mathrm{ms^{-1}}$. It takes about $5\,\mathrm{s}$ on a P.C. with a $350\,\mathrm{MHz}$ processor and $64\,\mathrm{MB}$ to compute 46 spectral accelerations, velocities and displacements, using Equation 4.1, for time histories with about 4000 samples. This is about 5 times slower than using the method of Nigam & Jennings (1969) for calculating normal response spectra.

B.1.1 Time lag between different components of same accelerogram

When calculating response spectra due to combined horizontal and vertical ground accelerations the two components must have the same start time. This would be so for instruments with a vertical acceleration trigger, which starts all three components recording. Some analog accelerograms may have different time lags for each component between the trigger being activated and the start of the recording. Also some components may not be synchronous because of differences in digitization and correction procedures. It cannot be known whether these problems actually occur for the set of records used in this analysis. Any time lag between the components should be small enough to be neglected.

B.1.2 Definition of natural period and damping

When considering the effect of vertical acceleration on response spectra it is important to have a clear definition of natural period and damping. Zero gravity spectral values (see Section 4.3) are plotted against *unloaded, undamped* period, T_0, and *unloaded* damping level, ξ_0. Damped frequency, T_d, is not used because for low levels of damping $T_d \approx T_0$ and to simplify comparisons between different damping levels. When the models include gravity there are two periods which can be used, T_0 or T_1 and two different damping levels, ξ_0 and ξ_1. Either both the unloaded or both the loaded parameters must be used throughout, they cannot be mixed. If T_0 and ξ_0 are used then the spectra of loaded and unloaded structures cannot easily be compared because of shifts, in period and damping, that the loading causes. If T_1 and ξ_1 are used then the spectra can be compared, therefore it was decided to use the loaded parameters in this study.

B.1.3 Checking solution from HVSPECTRA computer program

Solution of Equation 4.1

The zero-gravity response spectra computed using Nigam & Jennings (1969) and the Runge-Kutta-Fehlberg method have been compared. It is found that the spectral values differ by 3% or less (Figure B.1).

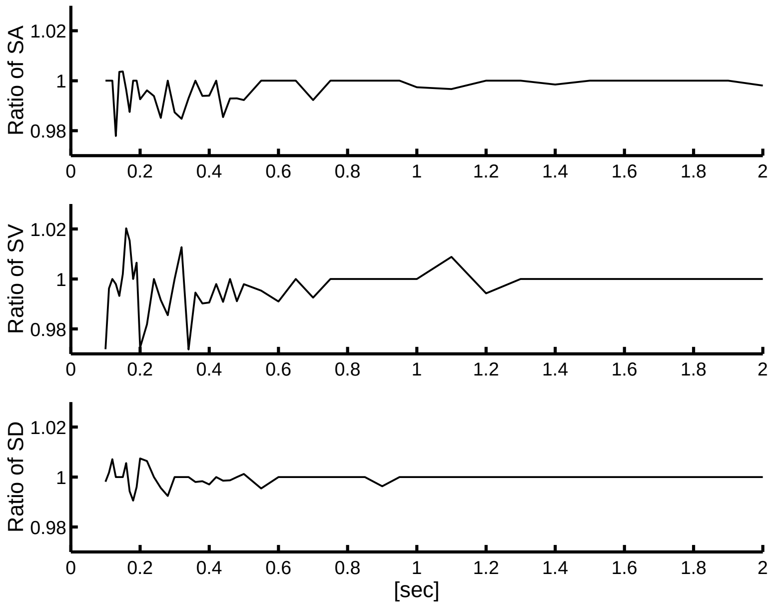

Fig. B.1: Ratio of response spectrum, for 5% damping, of Tabas N74E component, (from Tabas earthquake (16/9/1978), computed using Nigam & Jennings (1969) to that computed using Runge-Kutta-Fehlberg method.

The results obtained for Equation 4.1 and the equations including vertical excitation are thus consistent with each other, and so the Runge-Kutta-Fehlberg method is used to compute the response spectrum of all time-histories in this study.

Comparison with results from Orabi & Ahmadi (1988)

Orabi & Ahmadi (1988) present results on the bending model (solution of Equation 4.14) using the El Centro NS component record, from the El Centro earthquake(19/5/1940). They give relative velocity response spectra for different combinations of damping and load ratios. These graphs can be used as another check on HVSPECTRA. Figure 14 of Orabi & Ahmadi (1988) was digitized to reproduce their spectrum for this thesis. Figure B.2 shows the buckling model relative velocity response spectrum computed using HVSPECTRA and that given by Orabi & Ahmadi (1988) for the El Centro NS component record. Figure B.2 shows that HVSPECTRA gives the same results as Orabi & Ahmadi (1988) to accuracy with which their graph can be digitised. For long periods ($T > 3\,\mathrm{s}$) differences in the correction procedure could be why the solution from HVSPECTRA differs from Figure 14 of Orabi & Ahmadi (1988). Figure 15 of Orabi & Ahmadi (1988) is also reproduced using HVSPECTRA although the spectrum is not shown here. Therefore HVSPECTRA computes the correct response.

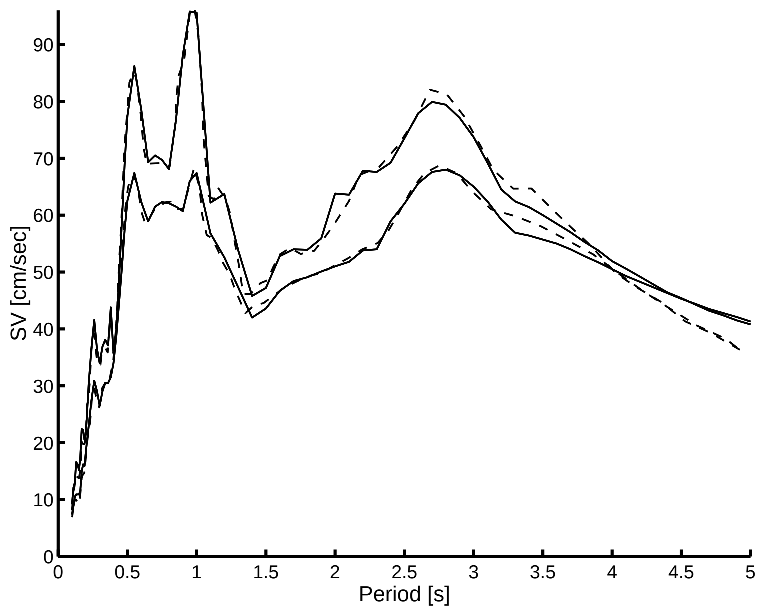

Fig. B.2: Relative velocity response spectrum for buckling model ($\gamma = 0.8$), for 5% and 10% damping, of El Centro NS component (from El Centro (19/5/1940) earthquake) computed using HVSPECTRA (solid line) and that in Orabi & Ahmadi (1988) (dashed line).

B.2 Method for calculation of energy spectra

For calculation of energy spectra HVSPECTRA was adapted to create ESPECTRA which calculates maximum absolute input energy, $I_A(T)$, and maximum relative input energy, $I_R(T)$, at the end of the record (T is the length of the record) and maximum absolute input energy, $\max_t[I_A(t)]$, and maximum relative input energy, $\max_t[I_R(t)]$, at any time during the record. The formulae used are

(Chapman, 1999):

$$I_A(t) = \int_0^t [u_{tt}(t) + a(t)]v(t)\,\mathrm{d}t;$$

$$I_R(t) = -\int_0^t u_{tt}(t)v(t)\,\mathrm{d}t;$$

where u_{tt} is the response acceleration of the SDOF system, $a(t)$ is the ground acceleration and $v(t)$ is the ground velocity.

To achieve accurate input energies for short and long periods the accuracy level to be achieved had to be increased (to $10^{-8}\,\mathrm{m}$ and $10^{-8}\,\mathrm{ms}^{-1}$) from that used to compute response spectra. This leads to an increase in the program running time but it is still only a few seconds for most records.

The calculated energy spectrum of the E-W component of the Alhambra-Fremont School record (from the Northridge earthquake (17/1/1994)) was compared with the energy spectrum present in Chapman (1999) for the same record and they are found to agree within digitisation accuracy (see Figure B.3). Therefore ESPECTRA computes correct energy spectra.

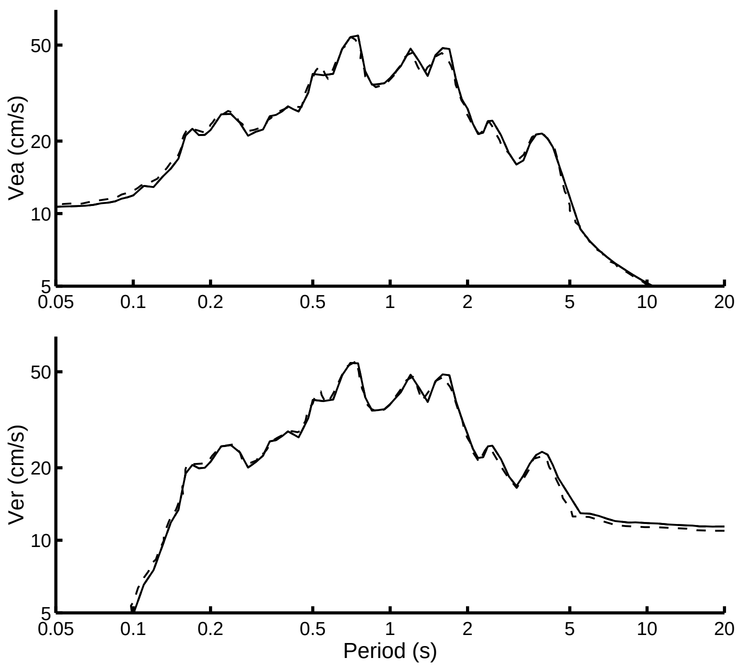

Fig. B.3: Energy-based velocity spectra ($\mathrm{Vea} = \sqrt{2\max_t[I_A(t)]}$ and $\mathrm{Ver} = \sqrt{2\max_t[I_R(t)]}$) for the E-W component of the Alhambra-Fremont School record (from the Northridge earthquake (17/1/1994)) at 5% damping computed using ESPECTRA (solid lines) and that given in Chapman (1999) (dashed lines).

B.3 Methods for regression analysis

For this study an ordinary least squares regression technique was adopted due to its simplicity and because different regression procedures do not seriously affect the results. Forms of the attenuation equation used in this study are nonlinear meaning that the method which relies on solving the set of normal equation used for linear equations, e.g. Draper & Smith (1981, chap. 2), cannot be used. An iterative procedure is required to minimize the sum of squares.

Originally a back-tracking Newton's method for minimization, with a procedure to ensure that the Hessian matrix stayed positive definite, (Moore, 1997b) was used. This was found to be quick and yield accurate answers. Its drawback though was that it was not easy to try different forms of the attenuation equation because second order derivatives need to be found for the Hessian matrix.

Therefore a computer program, called SPATTEN, using Marquardt's algorithm, as implement by Osborne (1972), was written in MATLAB. MATLAB was used because of its excellent matrix handling abilities. Equations from Gallant (1975) were used for calculating standard error estimates of the coefficients, also see Draper & Smith (1981); Weisburg (1985). Although this program is slightly slower than the one mentioned above it still only takes a few seconds to compute the least squares coefficients.

B.3.1 Checking the SPATTEN computer program

A number of checks of SPATTEN were made to confirm that it calculates the correct coefficients. Ambraseys *et al.* (1996) give a table listing the magnitudes, distances and peak ground accelerations they used for their analysis. The same data was used to derive this equation, using SPATTEN, for horizontal PGA using the one step method:

$$\log(a) = -1.51 + 0.261M_s - 0.00043r - 0.817\log r \quad \text{with:} \quad \sigma = 0.25$$

where $r = \sqrt{d^2 + 1.9^2}$. This compares with Ambraseys *et al.* (1996) who find (their Equation (6)):

$$\log(a) = -1.52 + 0.261M_s - 0.00045r - 0.815\log r \quad \text{with:} \quad \sigma = 0.25$$

where $r = \sqrt{d^2 + 1.9^2}$. The small differences in the coefficients come from the different method used for calculating the h_0 (the term inside the square root) and differences in rounding. Ambraseys *et al.* (1996) use a simple search technique where trial values at intervals of 0.1 are tried and the best solution selected whereas SPATTEN finds all the coefficients to the same accuracy (chosen as 1×10^{-5}).

Ambraseys *et al.* (1996) also derive an equation using the two-stage regression technique of Joyner & Boore (1988)[2]. They give the standard error, σ, calculated using the final coefficients as

[2] They state that they use the two-stage technique of Joyner & Boore (1981), where earthquakes with only one record

if they where calculated in a one-stage algorithm. Joyner & Boore (1981) state that the formula $\sigma = \sqrt{\sigma_1^2 + \sigma_2^2}$, where σ_1 and σ_2 are the standard errors associated with the first and second stage regressions respectively, should be used. Applying this method of Ambraseys *et al.* (1996) to their data using SPATTEN leads to[3]:

$$\log a = -1.38 + 0.264 M_s - 0.919 \log r \quad \text{with:} \quad \sigma = 0.25$$

where $r = \sqrt{d^2 + 3.2^2}$. Ambraseys *et al.* (1996) give this equation (their Equation (5)):

$$\log a = -1.39 + 0.266 M_s - 0.922 \log r \quad \text{with:} \quad \sigma = 0.25$$

where $r = \sqrt{d^2 + 3.5^2}$. Again the small differences are due to rounding and the method for finding h_0.

Finally the horizontal PGA data of Joyner & Boore (1981) is used to derive this equation, using the two-stage procedure where the earthquakes for which there is only one record are ignored in the second stage and the standard error is given by $\sigma = \sqrt{\sigma_1^2 + \sigma_2^2}$:

$$\log a = -1.01 + 0.248 \boldsymbol{M} - \log r - 0.00255 r \quad \text{with:} \quad \sigma = 0.26$$

where $r = \sqrt{d^2 + 7.3^2}$. Joyner & Boore (1981) find (their Equation (4)):

$$\log a = -1.02 + 0.249 \boldsymbol{M} - \log r - 0.00255 r \quad \text{with:} \quad \sigma = 0.26$$

where $r = \sqrt{d^2 + 7.3^2}$. Small differences are again due to rounding and the method for finding h, the coefficient inside the square root.

As can be seen SPATTEN calculates the correct regression coefficients for the attenuation relations.

B.4 Combination of horizontal measurements

Most accelerograms consist of three mutually orthogonal components: two horizontal and one vertical. Seven different ways of combining the horizontal components have been investigated, these are given below.

1. Arithmetic mean: $a_M = [\max |a_1(t)|_{\text{for } t} + \max |a_2(t)|_{\text{for } t}]/2$.

2. Both: $a_{B,1} = \max |a_1(t)|_{\text{for } t}$ and $a_{B,2} = \max |a_2(t)|_{\text{for } t}$

associated with them are ignored in the second stage but in fact they use the weighting scheme proposed in Joyner & Boore (1988). Using the method of Joyner & Boore (1981) yields: $\log a = -1.48 + 0.279 M_s - 0.919 \log r$ with $r = \sqrt{d^2 + 3.2^2}$.

[3] If Joyner & Boore (1981) method for calculating the standard error is followed then $\sigma = 0.29$

3. Geometric mean: $a_G = \sqrt{\max |a_1(t)|_{\text{for }t} \max |a_2(t)|_{\text{for }t}}$.

   Note that: $\log a_G = \{\log[\max |a_1(t)|_{\text{for }t}] + \log[\max |a_2(t)|_{\text{for }t}]\}/2$.

4. Largest component: $a_L = \max[\max |a_1(t)|_{\text{for }t}, \max |a_2(t)|_{\text{for }t}]$

5. Random: $a_r = \max |a_1(t)|_{\text{for }t}$ or $a_r = \max |a_2(t)|_{\text{for }t}$, chosen randomly.

6. Resultant: $a_R = \max[\max |a_1(t) \cos \theta + a_2(t) \sin \theta|_{\text{for }t}]_{\text{for }\theta}$. Note that this is similar to the spectrally maximized record technique introduced by Shoja-Taheri & Bolt (1977), except their method maximises the Fourier amplitude spectrum in the frequency domain and then transformed back into the time domain.

7. Vectorial addition: $a_V = \sqrt{\max |a_1(t)|^2_{\text{for }t} + \max |a_2(t)|^2_{\text{for }t}}$.

Using both horizontal components or the geometric mean of the two components leads to exactly the same regression coefficients when logarithms of the ground motion measurements are used. This can be demonstrated as follows by considering the normal equations which are solved to give the least squares estimate of the coefficients.

Assume the ground motion measurements, a_i, of the two horizontal components are numbered in ascending order and the two components corresponding to the same record are adjacent. Therefore have a set of $2N$ measurements like this $\{(a_1, a_2), \dots (a_{2i-1}, a_{2i}), \dots, (a_{2N-1}, a_{2N})\}$, where the components in brackets correspond to the same record. Let $f(c_1, \dots c_n)$ be the attenuation relation, where $c_1, \dots c_n$ are the n coefficients in the equation to be found.

Then when using the geometric mean this sum of squares, S_G, needs to be minimized:

$$S_G = \sum_{i=1}^{N} [\log \sqrt{a_{2i-1} a_{2i}} - f(c_1 \dots c_n)]^2.$$

The normal equations which need to be solved to find $c_1 \dots c_n$ are $\frac{\partial S_G}{\partial c_j} = 0$ for $j = 1, \dots n$. Thus have generally, since $\log \sqrt{a_{2i-1} a_{2i}} = \frac{1}{2} \log a_{2i-1} + \frac{1}{2} \log a_{2i}$:

$$\frac{\partial S_G}{\partial c_j} = -2 \sum_{i=1}^{N} (\frac{1}{2} \log a_{2i-1} + \frac{1}{2} \log a_{2i} - f) \frac{\partial f}{\partial c_j} = 0,$$

and splitting the summation into two parts gives:

$$-\left[\sum_{i=1}^{N} (\log_{2i-1} - f) \frac{\partial f}{\partial c_j} + \sum_{i=1}^{N} (\log_{2i} - f) \frac{\partial f}{\partial c_j}\right] = 0.$$

Recombining the summations and multiplying both sides by 2 gives:

$$-2 \sum_{i=1}^{2N} (\log a_i - f) \frac{\partial f}{\partial c_j} = 0. \tag{B.2}$$

Now when using both horizontal components this sum of squares, S_B, needs to be minimized in order to find the least squares equation $g(d_1 \ldots d_n)$:

$$S_B = \sum_{i=1}^{2N} [\log a_i - g(d_1 \ldots d_n)]^2.$$

The general normal equation to be solved to minimize this equation is:

$$\frac{\partial S_G}{\partial c_j} = -2 \sum_{i=1}^{2N} (\log a_i - g) \frac{\partial g}{\partial c_j} = 0. \quad \text{(B.3)}$$

Note that if $f(c_1 \ldots c_n)$ solves Equation B.2 then it also solves Equation B.3, hence the attenuation equation found using the geometric mean and both components are the same. The estimate of the standard error though is different for the two methods.

B.4.1 Calculation of resultant spectral ordinates

To calculate the resultant spectral values an efficient method is required. One method is simply to form the resultant ground acceleration in a direction θ from the two horizontal components then calculate and store the resultant response spectrum. Then repeat this for all angles θ and find the maximum spectral value at each period from the set of calculated spectra. This algorithm though is highly inefficient because a response spectrum needs to be calculated for each angle θ.

The most efficient procedure relies on the linearity of the equations of motion derived in Chapter 4. Let $a^1_{tt}(t)$ and $a^2_{tt}(t)$ be the two components of horizontal ground acceleration and $a^v_{tt}(t)$ be the vertical excitation (either zero, the ground acceleration or the vertical response acceleration). Let $u^1(t)$ and $u^2(t)$ be the response displacement caused by $a^1_{tt}(t)$ and $a^2_{tt}(t)$ respectively, i.e.:

$$u^1_{tt} + 2\xi\omega u^1_t + \omega^2(1 - \beta a^v_{tt})u^1 = -a^1_{tt}, \quad \text{(B.4)}$$

$$u^2_{tt} + 2\xi\omega u^2_t + \omega^2(1 - \beta a^v_{tt})u^2 = -a^2_{tt}. \quad \text{(B.5)}$$

Multiply equations B.4 & B.5 by $\cos\theta$ and $\sin\theta$ respectively and add to give:

$$\begin{aligned}(u^1_{tt}\cos\theta + u^2_{tt}\sin\theta) + 2\xi\omega(u^1_t\cos\theta + u^2_t\sin\theta)& \\ + \omega^2(1 - \beta a^v_{tt})(u^1\cos\theta + u^2\sin\theta) &= -(a^1_{tt}\cos\theta + a^2_{tt}\sin\theta)\end{aligned}$$

Therefore $u = u^1\cos\theta + u^2\sin\theta$ is the response displacement of the SDOF system subjected to the resultant ground acceleration $a^1_{tt}\cos\theta + a^2_{tt}\sin\theta$.

Now compute and store the response displacements, velocities and accelerations u^1, u^1_t, u^1_{tt}, u^2, u^2_t and u^2_{tt}. Then compute u, u_t and u_{tt} for a given θ and find and store the maximum acceleration, velocity and displacement for each period and that choice of θ. Repeat for different θ and hence find the resultant response spectrum. This algorithm was implemented using HVSPECTRA.

B.5 Calculation of distance to surface projection of rupture plane

After a literature survey and a search on the Internet no computer programs for the calculation of the distance from a point to a line or surface could be found; therefore a FORTRAN program, Flt_Dis was written to calculate the distance between a station and the surface projection of the rupture plane.

Originally this program, then called Faultdis, only calculated the distance between the station and *one* surface projection. This program was modified by Patrick Smit to enable the distance to *any number* of surface projections; he also made a few other minor modifications to make the program easier to use. He did not change, however, the algorithm.

Calculations of distances on the surface of the globe should ideally be made in spherical geometry for accuracy. Unfortunately because calculating the location of the surface projection in spherical geometry is difficult this part of the program used plane geometry but the actual distances were calculated using the Dis_Az, subroutine written by Patrick Smit, which uses spherical geometry and an ellipticity correction. The lost of accuracy due to this approximation is thought to be less than $1\,\mathrm{km}$ which is adequate given the uncertainty in the location of the rupture planes of earthquakes.

The parameters needed to specify the rupture are: latitude and longitude of its two top ends, its width in plane of rupture, W, and the dip of the plane, δ. The program assumes that each rupture segment is a rectangle therefore complex ruptures are difficult, but not impossible, to use in the program. Again the uncertainty in the actual rupture plane means that modelling it as a series of rectangular segments is unlikely to increase the uncertainty significantly.

Firstly the gradient of the line connecting the two top ends of the rupture is calculated. This gradient is used to define the two components of the normalised direction vector, $\boldsymbol{b} = (x_m, y_m)$, which defines the top line of the rupture through the equation $\boldsymbol{r} = \boldsymbol{a} + \lambda\boldsymbol{b}$. Note that for N-S or E-W trending faults $\boldsymbol{b} = (0,1)^{\mathrm{T}}$ and $\boldsymbol{b} = (1,0)^{\mathrm{T}}$ respectively.

Next the other two corners of the projection (x_3, y_3) and (x_4, y_4) are calculated using the equations:

$$
\begin{aligned}
x_3 &= x_1 \pm W_r|y_m/\cos(y_1)|;\\
y_3 &= y_1 \mp W_r x_m;\\
x_4 &= x_2 \pm W_r|y_m/\cos(y_1)|;\\
y_4 &= y_2 \mp W_r x_m;
\end{aligned}
$$

where (x_1, y_1) and (x_2, y_2) are the coordinates of the two top ends of the rupture, $W_r = (W/111.195)\cos(\delta)$ (the width of the fault in degrees resolved onto the surface) and the signs depend on the direction

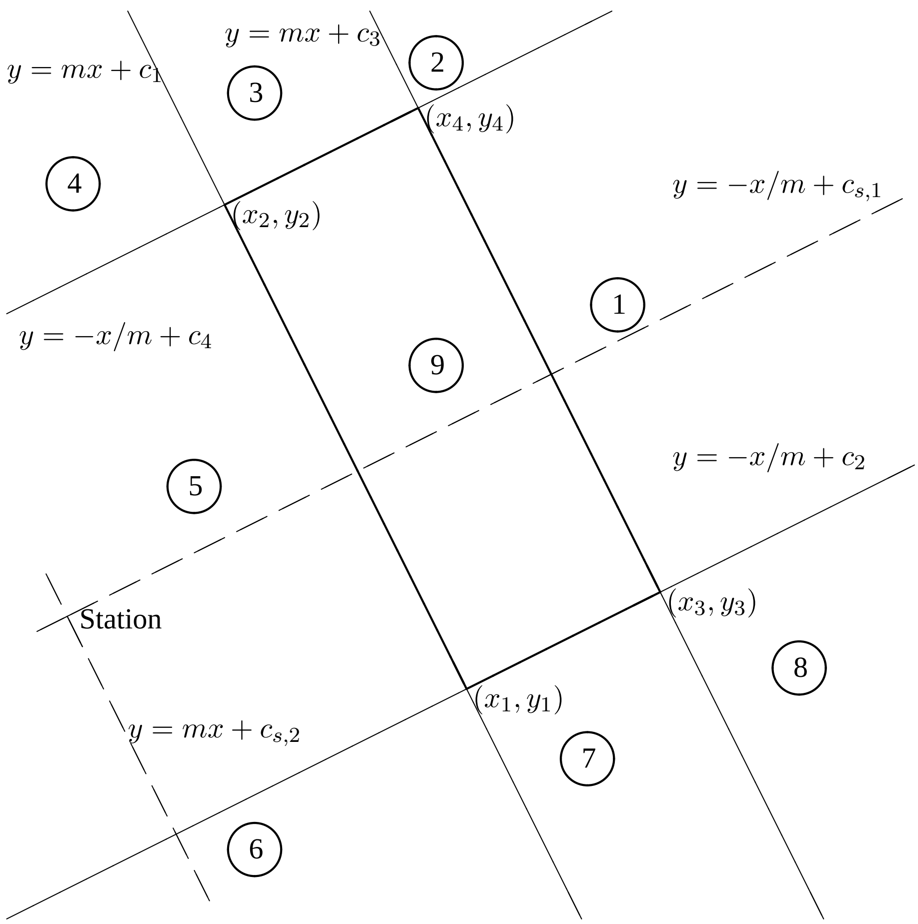

Fig. B.4: Diagram showing locations of the nine zones for calculation of distance to surface projection of rupture plane, the numbering of the four corners of the surface projection, the equations of the lines defining the edges of the projection and the equations of the lines parallel and perpendicular to the projection through the station.

that the fault dips.

The four corners of the surface projection are then renumbered so that they are arranged as shown in Figure B.4.

The gradient of the line connecting (x_1, y_1) and (x_2, y_2), m, is then calculated. If the length in the x-direction of the line connecting (x_1, y_1) and (x_2, y_2) is shorter than that connecting (x_1, y_1) and (x_3, y_3) then it is more accurate (due to limited machine precision) to calculate the gradient of (x_1, y_1) to (x_2, y_2) as the negative reciprocal of the gradient of (x_1, y_1) to (x_3, y_3). This gradient is then used to calculate the intercepts in the equation of the lines defining the edge of the projection, $y = mx+c$. This gradient is also used to calculate the intercepts in the equations of the lines parallel and perpendicular to the edge of the projection through the strong-motion station (Figure B.4).

The set of constants defining the edges of the surface projection, $c_1, \dots c_4$, and the constants for the parallel and perpendicular lines through the station, $c_{s,1}$ and $c_{s,2}$, are used to find which zone the station is in (see Figure B.4).

If the station is in zone 2, 4, 6 or 8 then the corners of the projection are the closest points to the station and the distance is calculated using the subroutine Dis_Az. If the station is in zone 9 then the distance to the surface projection is zero. If the station is in zone 1, 3, 5 or 7 the point on the projection closest to the station is the intersection of the line defining the edge and the line perpendicular to this through the station. The equations of this point, (x_f, y_f), are for zone 1:

$$\begin{aligned} x_f &= (c_{s,1} - c_3)/(m + 1/m); \\ y_f &= mx_f + c_3; \end{aligned}$$

for zone 5:

$$\begin{aligned} x_f &= (c_{s,1} - c_1)/(m + 1/m); \\ y_f &= mx_f + c_1; \end{aligned}$$

for zone 3:

$$\begin{aligned} x_f &= (c_4 - c_{s,2})/(m + 1/m); \\ y_f &= -x_f/m + c_4; \end{aligned}$$

and for zone 7:

$$\begin{aligned} x_f &= (c_2 - c_{s,2})/(m + 1/m); \\ y_f &= -x_f/m + c_2. \end{aligned}$$

Note for N-S or E-W trending projections simpler expressions apply for the closest points on the projection. Given (x_f, y_f) the distance is found using the subroutine Dis_Az.

Flt_Dis was rigourously tested by examining each element of the program and by plotting the location of the projection, the station and the point on the projection which is closest to the station.

This program was used to calculate distances for many earthquakes and these were compared with published distances for the same earthquakes and stations, for example those contained in Joyner & Boore (1981) and Boore *et al.* (1993). The distances calculated using Flt_Dis were slightly different to the published values by 1 or $2\,\mathrm{km}$ which could be because plane geometry rather than spherical geometry was used although it is more likely to be due to the use of slightly different fault parameters. Although Flt_Dis may be less accurate than the published distances to the surface projection of the rupture plane it is better to use a consistent surface projection for all stations which recorded an earthquake rather than use distances from a number of different studies.

B.6 Calculation of distance to rupture plane

A FORTRAN computer program, Rup_Dis, was also written for the calculation of the distances to the fault rupture. This was based on Flt_Dis but obviously because rupture distances are calculated in three dimensions it is more complicated.

As with Flt_Dis plane geometry was used to define the rupture plane but spherical geometry was used to calculate the distances.

The parameters needed to specify the rupture are: latitude and longitude of its two top ends, its width in plane of rupture, W, the depth of the top of the plane vertically, D, and the dip of the plane, δ. The rupture planes are all assumed to be rectangles, like in Flt_Dis.

Two projections of the rupture plane are required for the calculation of rupture distance, one vertically upwards onto the surface (which is calculated as in Flt_Dis) and one perpendicular to the rupture plane onto the surface. This perpendicular projection is calculated in the second stage of Rup_Dis.

As with the vertical projection the gradient of the line connecting the two top ends of the rupture is calculated. This gradient is used to define the two components of the normalised direction vector, $\boldsymbol{b} = (x_m, y_m)$, which defines the top line of the rupture through the equation $\boldsymbol{r} = \boldsymbol{a} + \lambda\boldsymbol{b}$. Note that for N-S or E-W trending faults $\boldsymbol{b} = (0,1)^{\mathrm{T}}$ and $\boldsymbol{b} = (1,0)^{\mathrm{T}}$ respectively.

Next the other two corners of the perpendicular projection ((x_3, y_3) and (x_4, y_4)) are found using the equations:

$$
\begin{aligned}
x_3 &= x_1 \pm D_r |y_m / \cos(y_1)|; \\
y_3 &= y_1 \mp W_r x_m; \\
x_4 &= x_2 \pm D_r |y_m / \cos(y_1)|; \\
y_4 &= y_2 \mp W_r x_m;
\end{aligned}
$$

where (x_1, y_1) and (x_2, y_2) are the coordinates of the two top ends of the rupture, $W_r = (W/111.195)/\cos(\delta)$ (the width of the fault in degrees resolved perpendicularly to the rupture plane onto the surface), $D_r = (D/111.195)\tan(\delta)$ (the depth of the top of the rupture in degrees resolved perpendicularly to the rupture plane onto the surface). The signs depend on the direction that the fault dips.

The four corners of both surface projections are renumbered as shown in Figure B.5.

Next the gradient of the line connecting (x_1, y_1) and (x_2, y_2), m, is calculated. If the length in the x-direction of the line connecting (x_1, y_1) and (x_2, y_2) is shorter than that connecting (x_1, y_1) and (x_3, y_3) then it is more accurate (due to limited machine precision) to calculate the gradient of (x_1, y_1) to (x_2, y_2) as the negative reciprocal of the gradient of (x_1, y_1) to (x_3, y_3). This gradient is then used to calculate the intercepts in the equations of the lines defining the edge of the projection, $y = mx + c$. The gradient is also used to calculate the intercepts in the equations of the lines parallel and perpendicular to the edge of the projection through the strong-motion station (Figure B.5). Also

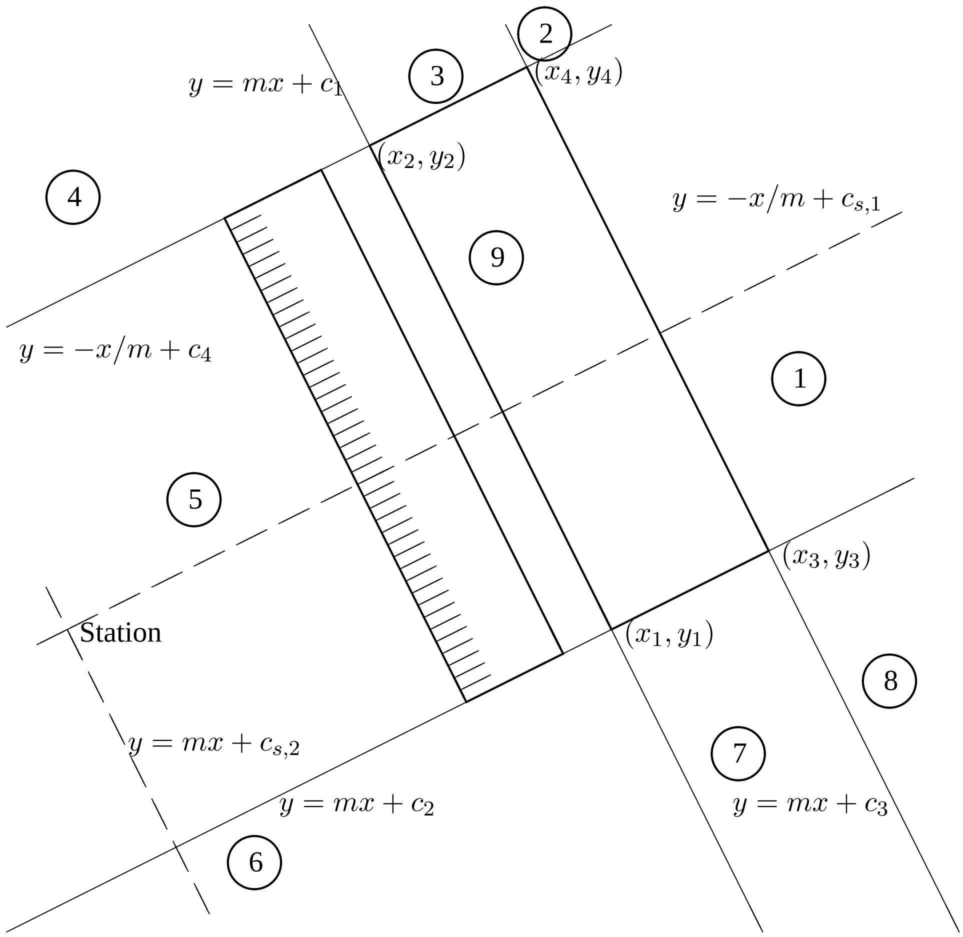

Fig. B.5: Diagram showing locations of the nine zones for calculation of distance to the rupture plane, the numbering of the four corners of the perpendicular projection, the equations of lines defining the edges of the projection and the equations of the lines parallel and perpendicular to the projection through the station.

calculated is the gradient of the line connecting the two top ends of the vertical projection, m^v. The gradient should equal m but due to limited machine precision it is calculated separately. The gradient is used to calculate the intercepts in the equations of the lines defining the edges of the vertical projection, $y = m^v x + c^v$, and the intercepts in the lines parallel and perpendicular to the edges of the vertical projection through the strong-motion station.

The set of constants defining the edges of the perpendicular projection, $c_1, \ldots c_4$ and the constants for the parallel and perpendicular lines through the station, $c_{s,1}$ and $c_{s,2}$, are used to find which zone the station is in (see Figure B.5).

If the station is in zone 2, 4, 6 or 8 then the corners of the *vertical* projection are the closest point to the station and the horizontal distance is calculated using the subroutine Dis_Az. The vertical distance is either the depth to the top of the rupture (for zones 4 and 6) or the depth to the bottom of the rupture (for zones 2 and 8). The final rupture distance is the square root of the sum of squares of these horizontal and vertical distances.

If the station is in zone 1 or 5 the closest point is the intersection of the line through the station and the line defining the edge of the *vertical* projection. The equations of this point, (x_f, y_f), are for zone 1:

$$\begin{aligned} x_f &= (c^v_{s,1} - c^v_3)/(m^v + 1/m^v); \\ y_f &= m^v x_f + c^v_3; \end{aligned}$$

and for zone 5:

$$\begin{aligned} x_f &= (c^v_{s,1} - c^v_1)/(m^v + 1/m^v); \\ y_f &= m^v x_f + c^v_1. \end{aligned}$$

The horizontal distance from the station to (x_f, y_f) is calculated using the subroutine Dis_Az. The vertical distance is either the depth to the top of the rupture (for zone 5) or the depth to the bottom of the rupture (for zone 1). The final rupture distance is the square root of the sum of squares of these horizontal and vertical distances.

If the station is in zone 3 or 7 the required point is the intersection of the line through the station and the line defining the edge of the *perpendicular* projection. The equations of this point, (x_f, y_f), are for zone 3:

$$\begin{aligned} x_f &= (c_4 - c_{s,2})/(m + 1/m); \\ y_f &= m x_f + c_4; \end{aligned}$$

and for zone 7:
$$\begin{aligned} x_f &= (c_2 - c_{s,2})/(m + 1/m); \\ y_f &= m x_f + c_2. \end{aligned}$$

The vertical distance, z_f, is calculated using, for zone 3 and zone 7:

$$z_f = \cos(\delta)[D + d\tan(\delta)];$$

where d is the distance between (x_f, y_f) and (x_2, y_2) for stations in zone 3 and between (x_f, y_f) and (x_1, y_1) for stations in zone 7. The horizontal distance from the station to (x_f, y_f) is calculated using the subroutine Dis_Az. The final rupture distance is the square root of the sum of squares of the horizontal and vertical distance.

The above explanation assumes that the fault orientation is as shown in Figure B.5, i.e the rupture dips NW. If however the rupture dips in one of the other three possible directions (SE, NE or SW) then although the zones are numbered as shown in Figure B.5 the equations for calculating the rupture distance are slightly altered but they follow the same pattern as those above. Note for N-S or E-W trending projections simpler expressions apply for the closest points on the projection.

For stations in zone 9 the required point on the surface, (x_f, y_f), is given by the intersection of the line through the station and the line defining the top edge of the fault. The distance from the station to this point, d, is then used to calculate the rupture distance, d_r, by:

$$d_r = \cos(\delta)[D + d\tan(\delta)].$$

Rup_Dis was rigourously tested by examining each element of the program and by plotting the location of the projection, the station and the point on the projection which is closest to the station.

The program was used to calculate distances for many earthquakes and these were compared with published distances for the same earthquakes and stations, for example those contained in Campbell (1981). The distances calculated using Rup_Dis are slightly different to those published values by 1 or $2\,\mathrm{km}$ which could be due to the use of plane geometry rather than spherical geometry for the calculation although it is more likely to be due to the use of slightly different fault parameters. Although the accuracy of Rup_Dis may be less than the published distances to the rupture plane it is better to use a consistent rupture plane for all stations which recorded an earthquake rather than use distances from a number of different studies.

C. REALISTIC STRUCTURAL PARAMETERS

In the past vertical strong ground motions have not been thought to be as important as horizontal motions in the design and analysis of structures. Consequently few measurements or estimates of realistic vertical structural parameters (for example natural period and damping) have been published. Table C.1 summarises those estimates for these parameters which could be found.

C.1 Simple method of estimating vertical natural period

To get a rough estimate of the ratio of vertical to horizontal natural periods for a SDOF structure consider a column with Young's modulus E, moment of inertia, I, cross-sectional area, A, and length, L. The horizontal stiffness of the column, k_h, is given by:

$$k_h = \frac{BEI}{L^3};$$

where $B = 3$ for columns fixed at one end and free at the other, and for columns pinned at one end and fixed at the other, and $B = 12$ for columns fixed at both ends. Vertical stiffness, k_v, is given by:

$$k_v = \frac{EA}{L}.$$

Thus the ratio of vertical to horizontal stiffness is:

$$\frac{k_v}{k_h} = \frac{AL^2}{BI}.$$

Then since the mass on the column, m, is the same, the ratio of natural periods from $T = 2\pi\sqrt{m/k}$ is:

$$\frac{T_v}{T_h} = \frac{1}{L}\sqrt{\frac{BI}{A}}.$$

For $I = 8 \times 10^{-6}\,\mathrm{m}^4$, $A = 1\,\mathrm{m}^2$ and $L = 2\,\mathrm{m}$ the ratio of T_v/T_h is 0.002 for $B = 3$ and T_v/T_h is 0.005 for $B = 12$, showing the natural period vertically is much smaller than that horizontally.

Tab. C.1: Published estimates of natural period (T_h and T_v) and damping (ξ) in horizontal and vertical directions for different types of structures.

Reference	Structure	T_h (s)	T_v (s)	ξ (%)
Anderson & Bertero (1973)	Unbraced, single bay ten storey frame	2.0	0.18 (floor mode) 0.15 (column mode)	5
		They state that due to the way damping is implemented, damping in the vertical direction is negligible		
Papadopoulou (1989)	RC moment resisting frames			
	1 storey	0.1	0.040	
	2 storeys	0.2	0.064	
	3 storeys	0.3	0.082	
	4 storeys	0.4	0.091	
	5 storeys	0.5	0.099	
	6 storeys	0.6	0.106	
	7 storeys	0.7	0.114	
	8 storeys	0.8	0.120	

continued on next page

Tab. C.1: *continued*

Reference	Structure	T_h (s)	T_v (s)	ξ (%)
Papaleontiou & Roesset (1993)	Bare steel three span frames			
	4 storeys	1.00	0.16	5
	10 storeys	2.22	0.20	5
	16 storeys	1.54	0.19	5
	20 storeys	2.27	0.25	5
		They state that other resisting elements in the vertical direction such as walls and strong partitions could substantially decrease vertical period.		
Papazoglou & Elnashai (1996)	Eight storey, three bay coupled wall frame RC structure	0.534	≤ 0.075	
Elnashai & Papazoglou (1997)	RC frames with less than ten storeys		$T_v = 0.022 + 0.22T_h - 0.13T_h^2$	≤ 2
		They state that, in the absence of detailed information, it is considered that the use of equivalent viscous damping larger than 2% is not justified although further studies are required to define this value accurately.		
Chouw & Hirose (1999)	Three storey one bay frame	0.80	0.16	1 (Kelvin chain model)
Yamazaki *et al.* (2000)	Ordinary high-rise building		$0.1T_h \leq T_v \leq 0.2T_h$	

continued on next page

Tab. C.1: *continued*

Reference	Structure	T_h (s)	T_v (s)	ξ (%)
Diotallevi & Landi (2000)	Five storey, three bay moment resisting RC frame	0.9	0.074	
Hu *et al.* (1984)	Unreinforced brick smokestacks			
	20 m high	0.85	0.07	
	24 m high	1.01	0.08	
	30 m high	1.30	0.10	
	36 m high	1.52	0.12	
	40 m high	1.66	0.13	
	45 m high	1.69	0.15	

D. DATA USED IN THIS STUDY

D.1 Near-field records in construction set

The two letter country abbreviations used are: AR for Armenia, CA for Canada, GR for Greece, IR for Iran, IT for Italy, JA for Japan, ME for Mexico, NI for Nicaragua, TA for Taiwan, TU for Turkey, US for United States of America, UZ for Uzbekistan and YU for Yugoslavia/former Yugoslavia.

Tab. D.1: Near-field records in construction set

Date			Time	Lat.	Long.	Depth	M_s	$\log M_0$	F	C
			d	a_h	a_v	v_h	v_v	S	Station	
1940	5	19	0436	32.73	-115.45	7	7.14	26.49	S	US
			6	3.39	2.49	32.0	8.6	S	El Centro Array-Station 9[1]	
1954	12	21	1956	40.82	-124.08	15	6.67	25.48	S	US
			1	2.67	0.43	28.58	8.3	S	Eureka-Myrtle & West	
1966	6	28	0426	35.90	-120.90	7	6.13	25.36	S	US
			0	4.85	2.72	73.5	14.1	S	Cholame Shandon Array 2W[2]	
			6	4.19	1.28	23.7	7.0	S	Cholame Shandon Array 5W	
			10	2.63	1.23	11.8	4.8	S	Cholame Shandon Array 8W	
			11	3.64	1.24	20.4	4.2	A	Parkfield-Temblor	
			15	0.64	0.59	5.5	4.6	A	Cholame Shandon Array 12W	
1971	2	9	1401	34.40	-118.40	8	6.61	26.00	T	US
			15	3.50	1.62	16.6	3.8	A	Lake Hughes Array-Station 12	
1972	12	23	0629	12.33	-86.13	5	6.16	26.52[3]	S	NI
			4	3.60	3.18	29.8	15.2	S	Esso	
1976	5	17	0258	40.28	63.39	13	7.04	26.26	T	UZ
			3	6.78	13.17	65.1	66.1	L	Gazli	
1976	9	15	0315	46.29	13.20	15	6.06	24.80	S	IT
			9	1.06	0.63	11.4	7.1	S	Buia	
			12	1.19	0.57	7.6	5.6	A	San Rocco	
			12	2.59	0.92	10.1	6.7	A	Forgaria-Cornio	
			14	4.87	1.81	27.7	9.8	A	Breginj-Fabrika IGLI	
1976	9	15	0921	46.32	13.16	12	5.98	25.11	T	IT
			6	1.32	0.58	6.9	3.3	S	Tarcento	
			7	4.15	1.26	11.7	4.9	A	Breginj-Fabrika IGLI	
			8	0.91	0.84	8.0	4.7	S	Buia	
			9	3.45	1.82	23.2	10.5	A	Forgaria-Cornio	
			9	2.33	0.82	18.7	13.9	A	San Rocco	
			12	0.87	0.45	2.3	1.5	R	Robic	

continued on next page

[1] The instrument was in a building with massive foundations which could have affected high frequencies (Brune & Anooshehpoor, 1991).
[2] Only one horizontal and one vertical component.
[3] This seismic moment estimate comes from Wells & Coppersmith (1994) using an estimate of the rupture area and the slip which occurred along the fault. It is an overestimate.

Tab. D.1: *continued*

Date			Time	Lat.	Long.	Depth	M_s	$\log M_0$	F	C
			d	a_h	a_v	v_h	v_v	S	Station	
1977	4	6	1336	31.90	50.76	10	6.02	25.11	T	IR
			4	10.28		57.8		R	Naghan 1[4]	
1978	4	15	2333	38.27	14.86	15	5.83	25.08	T	IT
			11	1.59	0.47	15.5	2.4	S	Patti-Cabina Prima	
1978	9	16	1535	33.36	57.42	5	7.33	27.11	T	IR
			3	9.34	7.27	84.5	36.9	A	Tabas	
			11	3.92	1.86	24.8	10.6	R	Dayhook	
1979	4	15	0619	41.98	18.98	12	7.04	26.49	T	YU
			9	2.75	4.25	48.1	16.2	A	Ulcinj-Hotel Olimpic	
			9	2.22	2.19	26.1	11.9	R	Ulcinj-Hotel Albatros	
			12	4.52	2.03	39.0	13.3	A	Petrovac-Hotel Oliva	
			12	3.66	2.35	51.7	15.1	A	Bar-Skupstina Opstine	
1979	5	24	1723	42.23	18.76	5	6.34	25.34	T	YU
			7	2.91	1.21	16.8	9.0	A	Petrovac-Hotel Rivijera	
			9	2.67	1.78	27.3	7.1	A	Budva-PTT	
			12	2.62	0.98	16.4	7.5	A	Bar-Skupstina Opstine	
			15	1.69	0.94	8.5	5.3	A	Tivat-Aerodrom	
1979	9	19	2135	42.76	13.02	4	5.84	24.84	N	IT
			6	1.87	1.76	14.0	5.6	R	Cascia-Cabina Petrucci	
1979	10	15	2316	32.64	-115.31	10	6.87	25.70	S	US
			0	3.03	1.42	42.0	5.1	S	Mexicali-Aeropuerto	
			0	4.84	5.39	71.8	30.0	S	El Centro Array-Station 5	
			1	4.19	15.46	88.1	49.7	S	El Centro Array-Station 6	
			1	2.90	2.45	84.4	28.4	S	Meloland Overpass-Free Field	
			2	3.33	8.84	38.9	13.6	A	Agrarias (Mexicali Valley)[5]	
			2	7.45	3.58	40.8	13.9	S	Bonds Corner-Maintenance Shop	
			3	4.86	2.46	66.7	11.7	S	El Centro Array-Station 4	
			3	4.41	6.11	90.6	22.6	S	El Centro Array-Station 7	
			5	2.32	2.32	38.4	7.9	S	Holtville-Post Office	

continued on next page

[4] Only one horizontal component and no vertical component.
[5] Vertical component's recording may be erroneous due to a loose mounting bolt (Brune *et al.*, 1982).

Tab. D.1: *continued*

Date			Time	Lat.	Long.	Depth	M_s	$\log M_0$	F	C
			d	a_h	a_v	v_h	v_v	S	Station	
			6	2.19	1.52	31.3	7.0	S	Brawley-Airport Hangar	
			6	5.92	4.47	48.0	19.6	S	El Centro Array-Station 8	
			7	4.71	6.06	54.7	17.8	S	El Centro Differential Array	
			9	2.61	1.26	42.5	8.1	L	El Centro Array-Station 3	
			9	4.26	3.81	28.9	8.2	S	Mexicali-Casa Flores	
			10	2.37	2.31	52.8	13.0	S	Imperial County Centre (Lot)	
			11	2.65	1.94	14.7	4.7	S	Calexico-Fire Station	
			11	4.09	1.15	28.6	6.3	S	El Centro Array-Station 2	
			11	2.18	0.95	39.5	8.8	S	El Centro Array-Station 10	
			12	2.94	1.24	34.7	3.1	S	Cucapah (Mexicali Valley)[6]	
			13	1.06	0.84	17.9	6.0	S	Westmorland-Fire Station	
			15	3.88	1.34	33.1	10.8	S	El Centro Array-Station 11	
			15	1.97	1.59	15.8	4.7	A	El Centro-Parachute Test Site	
1979	10	16	0658	33.02	-115.58	5	5.86	24.51	S	US
			5	1.53	1.03	10.8	2.3	S	Westmorland-Fire Station	
1980	5	25	1633	37.61	-118.85	9	6.15	25.26	N	US
			1	4.42	3.73	23.8	19.8	S	Convict	
			12	3.02	2.22	15.7	10.8	A	High School-Gym (Centre)	
			12	2.44		15.8		A	High School-Gym (West Wall)[7]	
1980	5	25	1944	37.56	-118.84	16	5.99	24.92	N	US
			5	2.25	1.70	18.0	7.9	S	Convict	
1980	6	9	0328	32.19	-115.08	5	6.49	25.79	S	ME
			2	8.48	14.66	65.2	62.2	S	Victoria (Mexicali Valley)	
			10	5.83	2.64	31.7	11.1	A	Cerro Prieto (Mexicali Valley)	
1980	11	23	1834	40.78	15.33	16	6.87	26.40	N	IT
			6	1.80	0.97	30.8	14.4	R	Bagnoli-Irpino	
			10	0.58	0.35	5.9	3.5	A	Auletta	
			14	2.99	1.67	57.2	20.1	R	Sturno	
			14	1.70	1.58	27.8	17.1	A	Calitri-Cabina Pittoli	

continued on next page

[6] Only one horizontal and one vertical component.
[7] Only one horizontal and no vertical component.

Tab. D.1: *continued*

Date			Time	Lat.	Long.	Depth	M_s	$\log M_0$	F	C
			d	a_h	a_v	v_h	v_v	S	Station	
1981	2	24	2053	38.10	22.84	10	6.69	25.95	N	GR
			4	2.88	1.28	23.1	8.2	S	Xilokastro-OTE Building	
			13	2.97	1.13	22.5	6.8	S	Korinthos-OTE Building	
1981	4	26	1209	33.13	-115.65	8	6.04	24.72	S	US
			6	1.85	2.02	13.7	5.6	L	Salton Sea-Wildlife Refuge	
			7	4.51	6.12	43.7	14.7	S	Westmorland-Fire Station	
			15	1.73	1.12	7.3	3.3	S	Niland-Fire Station	
1983	5	2	2342	36.24	-120.27	7	6.57	25.66	T	US
			7	5.77	3.51	62.3	17.9	S	Pleasant Valley-Pumping Yard	
			7	2.92	2.07	39.7	12.5	S	Pleasant Valley-Pumping (Base.)	
1984	4	24	2115	37.31	-121.68	9	6.20	25.84	S	US
			0	3.05	1.08	39.6	11.8	S	Halls Valley-Grant Park	
			10	1.68	0.77	11.2	6.4	R	San Jose-IBM Building 12	
			13	2.87	4.15	36.7	15.1	A	Gilroy Array-Station 6	
			14	3.53	3.96	18.5	11.5	S	Gilroy Array-Station 4	
			15	0.89	0.91	2.8	2.9	R	Gilroy Array-Station 1	
			15	2.03	5.61	12.0	9.3	S	Gilroy Array-Station 2	
			15	1.97	3.81	11.3	8.6	S	Gilroy Array-Station 3	
			15	1.15	1.08	3.4	3.0	A	Gilroy-Gavilan College	
			15	1.50	0.59	12.6	3.2		IBM Almaden	
1985	12	23	0516	62.19	-124.24	6	6.79	26.28	T	CA
			0	10.41	19.41	45.7	37.1	R	Nahanni-Station 1	
			4	3.48		30.9		R	Nahanni-Station 2 [8]	
1986	7	8	0920	34.00	-116.61	12	6.13	24.84	S	US
			0	6.05	4.31	37.7	15.7	R	White Water Canyon-Trout Farm	
			1	8.91	4.09	88.8	18.1	S	Devers Substation	
			5	6.48	6.82	61.9	12.5	A	North Palm Springs-Post Office	
			6	3.22	4.37	32.0	19.1	A	Desert Hot Springs-Fire Station	
			7	2.15	2.95	36.8	8.5	A	Morongo Valley-Fire Station	
			11	2.04	2.99	14.0	7.2	S	Cabazon-Post Office	

continued on next page

[8] No vertical component.

Tab. D.1: *continued*

Date			Time	Lat.	Long.	Depth	M_s	$\log M_0$	F	C
			d	a_h	a_v	v_h	v_v	S	Station	
			15	1.96	1.80	12.1	6.4	S	Palm Springs-Airport	
1987	10	1	1442	34.07	-118.08	14	5.94	24.92	T	US
			2	2.43	1.65	16.8	4.7	S	El Monte-11338 Fairview Ave.	
			2	2.63	2.61	23.5	6.0	A	San Gabriel-600 E. Grand Ave.	
			4	2.86	2.23	18.3	6.1	A	Arcadia-180 Campus Drive	
			4	3.70	1.76	21.2	6.3	A	Alhambra-Fremont School	
			4	4.21	1.40	21.6	5.3	A	Obregon Park	
			5	4.63	2.40	31.8	7.3	S	11500 E. Joslin St.	
			6	2.17	1.17	26.2	2.7	S	Bell Gardens-7420 Jaboneria	
			6	1.30	0.90	7.4	2.7	A	Baldwin-3699 N. Hollywood Ave.	
			6	1.71	1.19	13.1	6.2	A	San Marino-S.W. Academy	
			6	4.48	4.38	38.4	7.1	S	Bell-Bulk Mail Facility	
			8	3.39	2.55	37.9	4.6	S	Downey-12500 Birchdale	
			8	2.32	1.58	10.2	5.9	S	1488 Old House Rd	
			9	1.65	1.01	10.6	2.5	S	2369 E. Vernon Ave.	
			9	2.91	1.33	11.1	3.2	S	Altadena-Eaton Canyon	
			10	1.34	0.85	10.0	2.9	S	Covina-1271 W. Badillo	
			10	1.81	1.70	12.9	5.5	A	5921 N. Figueroa St.	
			10	2.02	1.49	30.1	3.1	S	Downey-Co. Maintenance Build.	
			13	2.23	1.19	19.9	6.2	S	3036 Fletcher Drive	
			14	0.78	0.68	7.0	3.4	S	Covina-656 S. Grand Ave.	
			14	3.12	1.69	29.1	3.7	S	Compton-14637 Castlegate St.	
			14	2.20	1.56	30.9	3.0	S	Long Beach-6979 Orange Ave.	
			14	1.74	0.69	12.9	3.3	S	La Habra-950 Briarcliff Drive	
			14	1.59	1.11	4.5	2.5	R	Mt. Wilson-Caltech Seism. Stat.	
			15	1.15	0.83	5.4	2.8	A	Glendora-120 North Oakbank	
			15	1.73	0.79	17.7	3.0	S	924 W. 70th St.	
1988	12	7	0745	40.96	44.27	11	5.8		T	AR
			10	1.45	0.39	11.0	3.0	S	Gukasian	
1989	10	18	0004	37.04	-121.88	18	7.17	26.66	T	US
			1	6.37	4.32	55.2	16.8	A	Corralitos-Eureka Canyon Rd.	

continued on next page

Tab. D.1: *continued*

Date			Time	Lat.	Long.	Depth	M_s	$\log M_0$	F	C
			d	a_h	a_v	v_h	v_v	S	Station	
			7	4.99	3.55	39.0	19.8	A	Saratoga-Aloha Avenue	
			9	5.01	5.31	38.9	17.8	S	Capitola-Fire Station	
			12	4.43	2.00	35.4	10.1	R	Gilroy Array-Station 1	
			12	3.68	1.89	26.0	8.1	A	Gilroy-Gavilan College	
			14	3.65	2.79	40.0	10.9	S	Gilroy Array-Station 2	
			15	4.48	3.65	18.8	10.8	A	USCS Santa Cruz-Lick Obs.	
			15	5.24	2.89	42.7	12.4	S	Gilroy Array-Station 3	
			15	2.81	1.46	43.2	7.7	A	Gilroy-2 Storey Hist. Com. Build.	
1992	3	13	1718	39.72	39.63	10	6.75	26.40	S	TU
			1	5.03	2.44	102.4	15.7	A	Erzincan-Meteorologij Mudurlugu	
1992	4	23	0450	33.96	-116.32	12	6.20	25.26	S	US
			15	2.00	1.83	12.9	6.2	S	Thousand Palms-Post Office	
1992	4	25	1806	40.37	-124.32	15	7.10	26.92	T	US
			0	14.68	7.39	126.1	60.3	R	Cape Mendocino (C)	
			9	2.07	0.83	43.5	10.9	R	Eel River Valley-Bunker Hill	
			14	4.67	1.11	52.1	16.5	A	Eel River Valley-Centreville Beach	
1992	6	28	1157	34.19	-116.53	1	7.55	27.04	S	US
			3	7.74	8.07	146.5	41.1	R	Lucerne Valley (C)	
			11	2.78	1.78	42.7	14.8	A	Joshua Tree-Fire Station(C)	
1992	6	28	1505	34.27	-116.78	15	6.52	25.83	S	US
			13	5.34	1.90	34.4	11.3	A	Big Bear Lake-Civic Center(C)	
1994	1	17	1230	34.16	-118.57	14	6.81	26.08	T	US
			0	3.80	4.98	60.7	13.5	S	7769 Topanga Canyon Boulevard	
			0	4.02	2.72	96.3	30.4	A	Newhall-26835 W. Pico Canyon Rd	
			0	8.90	3.84	52.3	14.0	A	Simi Valley-6334 Katherine Rd	
			0	3.17	2.52	12.8	11.4	R	Santa Susana-6633 Canoga Ave.[9]	
			0	6.21	3.85	92.1	30.9	A	Jensen Filtration-Admin. Build.	
			0	9.79	7.30	66.9	27.2	A	Jensen Filtration-Filter Gen. Room	
			0	5.78	5.37	94.7	30.7	S	Newhall-Fire Station (C)	
			0	8.27	5.25	128.9	18.6	S	Sylmar-Co. Hosp. (Parking Lot) (C)	

continued on next page

[9] Only one horizontal and one vertical component.

Tab. D.1: *continued*

Date			Time	Lat.	Long.	Depth	M_s	$\log M_0$	F	C
			d	a_h	a_v	v_h	v_v	S	Station	
			0	4.44	7.85	61.2	35.4	S	Northridge-17645 Saticoy Street (C)	
			0	8.16	8.19	147.5	35.6	S	Rinaldi Receiving Station	
			0	9.25	4.52	75.8	22.0	S	Sepulveda VA Hospital	
			1	17.45	10.28	110.2	72.3	S	Tarzana-Cedar Hill Nursey A (C)	
			5	4.59	2.89	46.2	18.3	S	16628 W. Lost Canyon Rd	
			5	3.37	5.41	40.4	17.5	S	Arleta-Nordhoff Ave. Fire Stat. (C)	
			6	3.23	1.77	15.7	5.1	A	Topanga Fire Station	
			7	4.40	2.92	41.9	12.3	S	Sun Valley-13248 Roscoe Boulevard	
			8	4.24	1.77	50.9	14.2	A	Pacoima Dam-Kagel Canyon(C)	
			9	2.06	1.58	30.4	7.0	A	12001 Chalon Road	
			9	3.02	2.70	28.6	11.4	A	6850 Coldwater Canyon Ave.	
			10	4.62	1.65	32.6	13.5	S	17291 Sunset Boulevard	
			10	4.74	3.09	65.6	19.5	S	14145 Mulholland Drive	
			10	3.70	1.40	37.1	5.9	A	Stone Canyon Reservoir	
			12	1.81	1.21	8.3	3.6	A	Monte Nido Fire Station	
			12	1.78	1.37	23.6	9.3	A	Brentwood V.A. Hospital	
			13	6.15	2.91	30.2	10.2	A	12520 Mulholland Drive	
			13	2.77	1.89	26.1	6.8	A	700 North Faring Road	
			13	3.67	1.30	31.9	10.8	A	Wadsworth V.A. Hosp. (GS South)	
			13	2.51	1.60	33.0	8.8	A	Wadsworth V.A. Hosp. (GS North)	
			14	2.53	1.15	11.7	4.5	A	Lake Hughes Array-Station 12 (C)	
			14	1.51	1.90	16.6	12.4	A	Sunland-10965 Mt Gleason Ave.	
			15	4.36	1.50	63.9	12.3		1955 Purdue Ave. (Base.)	
			15	8.66	2.28	41.8	14.0	S	Santa Monica-City Hall (C)	
			15	5.57	2.13	52.6	12.2	A	Castaic-Ridge Route (C)	
			15	2.51	1.13	25.1	6.2	S	Century City-LACC North (C)	
1995	1	16	2046	34.55	135.04	19	6.95	26.80	S	JA
			0	8.21	3.34	90.4	40.1	R	Kobe-Kaiyo (C)	
			1	3.01	4.23	55.4	19.7	R	Kobe-University (C)	
			1	3.42	5.58	91.1	62.0	S	Kobe-Port Island Array (Surface) (C)	
			3	7.62	3.62	54.3	35.5	R	Kobe-Motoyama (C)	

continued on next page

Tab. D.1: *continued*

Date			Time	Lat.	Long.	Depth	M_s	$\log M_0$	F	C
			d	a_h	a_v	v_h	v_v	S	Station	
			6	5.05	4.49	91.7	32.6		Kobe-Port	
			11	4.95	2.93	60.9	24.6	L	Amagasaki-G	
			12	6.92	3.40	174.1	32.6		Kobe-8G	
			12	2.87	1.23	24.2	5.9		Tadaoka (C)	
1995	6	15	0015	38.37	22.15	3	6.35	25.78	N	GR
			0	5.17	1.92	49.7	14.2	A	Aigio-OTE Building	
			11	0.47	0.29	3.5	2.3	A	Nafpaktos-OTE Building	
1995	10	1	1557	38.06	30.15	5	6.07	25.73	N	TU
			1	3.18	1.33	41.1	14.9	S	Dinar-Meteoroloji Mudurlugu	
1997	9	26	0940	43.01	12.84	8	5.9	25.06	N	IT
			3	2.56	1.81	17.6	7.7	A	Colfiorito	
			4	5.35	3.62	32.5	28.5	R	Nocera Umbra	
1999	8	17	0001	40.70	29.99	17	7.8	27.15	S	TU
			3	3.46	2.41	34.6	32.7	A	Sakarya[10]	
			14	2.18	1.32	27.5	11.2	R	Izmit-Meteoroloji Istasyonu	
1999	9	20	1747	23.86	120.81	11	7.6	27.53	T	TA
			0	4.16	2.98	36.0	28.6		CWB station code: T078	
			3	9.73	5.91	62.2	36.7		CWB station code: T129	
1999	11	12	1657	40.77	31.15	14	7.3	26.65	S	TU
			9 [11]	5.00	3.33	66.5	13.0		Duzce-Meteoroloji Mudurlugu	

[10] Only one horizontal and one vertical component.
[11] This is the epicentral distance since fault location unknown at present.

D.2 Near-field records in validation set

The two letter country abbreviations used are the same as for the near-field records in the construction set (see Section D.1). The 'Type' column gives where the record was recorded: S means structural-related free-field (ground floor or basement of buildings greater than two storeys high), D means dam-related free-field (not on dam but close enough so that possibly affected by dam) and F means true free-field using definition of Joyner & Boore (1981).

Tab. D.2: Near-field records in validation set

Date			Time	Lat.	Long.	Depth	M_s	$\log M_0$	F	C
			d	a_h	a_v	v_h	v_v	S	Station	Type
1933	3	11	0154	33.62	-117.97	16	6.41	25.79	S	US
			8	2.09	2.04	19.1	17.9	S	Long Beach-City Hall	S
1971	2	9	1401	34.40	-118.40	8	6.61	26.00	T	US
			0	11.4	6.79	94.9	43.5	R	Pacoima Dam (Upper L. Abut.)	D
			10	2.47	1.78	25.0	31.6	S	8244 Orion Boulevard	S
1976	5	6	2000	46.32	13.32	6	6.50	25.53	T	IT
			6	3.58	2.35	32.6	9.8	R	Tolmezzo-Diga Ambiesta	D
1976	9	15	0315	46.29	13.20	15	6.06	24.80	S	IT
			10	6.79		69.7		R	Gemona del Friuli[12]	S
1979	10	15	2316	32.64	-115.31	10	6.87	25.70	S	US
			1	3.67	2.27	89.4	26.9	S	Meloland Overpass-N	S
1980	5	25	1633	37.61	-118.85	9	6.15	25.26	N	US
			11	1.00	0.77	14.6	4.2	R	Long Valley Dam-Downstream	D
1980	5	25	1944	37.56	-118.84	16	5.99	24.92	N	US
			9	1.06	0.72	5.5	4.6	R	Long Valley Dam-Downstream	D
1980	6	9	0328	32.19	-115.08	5	6.49	25.79	S	ME
			12	1.82	1.32	26.1	5.3	S	Chihuahua (Mexicali Valley)	F
1984	4	24	2115	37.31	-121.68	9	6.20	25.84	S	US
			0	4.17	1.66	27.2	9.7	A	Anderson Dam-Downstream	D
			10	1.05	0.38	12.8	4.9		San Jose-Overpass (Free Field)	S
			13	0.57	0.37	11.6	2.8		San Jose — Town Park (Ground Floor S. Wall)	S
			13		0.44		3.1		San Jose — Town Park (Ground Floor SE Wall)[13]	S
			13	0.60		7.2			San Jose — Town Park (Ground Floor N Wall)[14]	S
			13		0.42		3.00		San Jose — Town Park (Ground Floor SW Wall)[15]	S
			14		0.30		3.8	S	San Jose — G.W. Savings (Basement SE)[16]	S

continued on next page

[12] No vertical component.
[13] No horizontal components.
[14] Only one horizontal component and no vertical component.
[15] No horizontal components.
[16] No horizontal components.

Tab. D.2: *continued*

Date			Time	Lat.	Long.	Depth	M_s	$\log M_0$	F	C
			d	a_h	a_v	v_h	v_v	S	Station	Type
			14		0.30		4.1	S	San Jose — G.W. Savings (Basement SW)[17]	S
			14	0.59		9.8		S	San Jose — G.W. Savings (Basement N)[18]	S
			14	0.57		11.9		S	San Jose — G.W. Savings (Basement S)[19]	S
			15	0.38	0.21	8.6	3.5		San Jose — Com. Bldg Gardens (Lower Level NW)[20]	S
			15		0.25		3.0		San Jose — Com. Bldg Gardens (Lower Level SE)[21]	S
			15	0.39	0.21	8.8	3.4		San Jose — Com. Bldg Gardens (Lower Level SW)	S
1987	10	1	1442	34.07	-118.08	14	5.94	24.92	T	US
			0	3.03	3.82	14.3	7.0	S	Whittier Narrows Dam-Baseyard Upstream	D
			5	2.74	1.72	20.6	5.0	A	Alhambra-900 South Fremont (Basement)	S
			6	4.48	4.38	38.4	7.1	S	Bell Postal Facility	S
			6	6.10	2.24	27.6	7.5	S	Whittier-7215 Bright Avenue (Basement)	S
			9	2.42	0.85	25.6	3.2	S	Norwalk-12400 Imp. Highway (S. Ground Site)	S
			9	2.03	0.63	25.0	2.5	S	Norwalk-12400 Imp. Highway (N. Ground Site)	S
1987	11	24	1315	33.08	-115.97	8	6.50	25.79	S	US
			5	8.14	6.21	41.7	16.3	R	Superstition Mountain-Camera Site 8	F
1989	10	18	0004	37.04	-121.88	18	7.17	26.66	T	US
			7		5.46		14.5	S	Watsonville-Station 1[22]	S
			7		5.19		16.6	S	Watsonville-Station 2[23]	S
			7	2.74	4.80	28.5	16.6	S	Watsonville-Station 3[24]	S
			7	2.51	6.35	29.1	22.8	S	Watsonville-Station 4[25]	S
			7	3.48		53.6		S	Watsonville-Station 13[26]	S

continued on next page

[17] No horizontal components.
[18] Only one horizontal component and no vertical component.
[19] No vertical component.
[20] Only one horizontal component.
[21] No horizontal components.
[22] No horizontal components.
[23] No horizontal components.
[24] Only one horizontal component.
[25] Only one horizontal component.
[26] Only one horizontal component and no vertical component.

Tab. D.2: *continued*

Date			Time	Lat.	Long.	Depth	M_s	$\log M_0$	F	C
			d	a_h	a_v	v_h	v_v	S	Station	Type
1994	1	17	1230	34.16	-118.57	14	6.81	26.08	T	US
			0	5.61	5.87	111.3	31.7		Sylmar Conv. Stat.-Valve Group 1-6 (Bsmt.)	S
			0	9.79	7.3	66.9	27.2	A	Jensen Filtration Plant-Filter Gen. Room	S
			0	3.16	1.79	16.8	11.1		6633 Canoga Ave. (Bldg 462 Ground)	S
			3	4.26	1.80	44.7	16.1	R	Pacoima Dam (Upper L. Abut.)	D
			8	4.55	1.49	26.4	6.8	S	Sepulveda Canyon	S
			12	2.30	1.14	26.0	6.8		Energy Control Cen.-Comm. Room (Ground)	S
			14	4.71	3.13	32.6	10.4		Receiving Station-E. (Ground Level)	S
1999	9	20	1747	23.86	120.81	11	7.6	27.53	T	TA
			0	5.76	3.75	70.1	17.7		CWB station code: TCU079	F
			0	6.14	4.28	51.8	26.8		CWB station code: TCU071	F
			0	4.58	2.68	65.4	26.1		CWB station code: TCU072	F
			0	3.34	1.66	32.6	18.2		CWB station code: TCU089	F
			0	8.42	6.86	105.2	40.3		CWB station code: CHY080	F
			0	2.26	0.97	29.8	14.6		CWB station code: CHY074	F
			0	9.81	3.12	128.2	25.8		CWB station code: TCU084	F
			1	4.15	1.91	123.8	41.7		CWB station code: TCU052	F
			1	7.49	2.33	75.2	75.0		CWB station code: TCU065	F
			2	5.01	2.33	85.1	38.1		CWB station code: TCU067	F
			3	2.56	1.49	66.8	47.5		CWB station code: TCU102	F
			3	3.99	2.32	50.2	31.3		CWB station code: TCU076	F
			3	2.85	2.26	60.6	48.0		CWB station code: TCU075	F
			4	7.63	2.93	80.7	27.0		CWB station code: CHY028	F
			4	2.36	1.23	38.8	31.5		CWB station code: TCU101	F
			4	5.89	2.67	69.7	20.7		CWB station code: TCU074	F
			6	2.64	1.66	38.1	11.4		CWB station code: TCU049	F
			7	1.48	1.32	27.8	32.3		CWB station code: TCU103	F
			8	2.05	1.16	25.6	22.3		CWB station code: TCU053	F
			8	1.69	1.18	32.5	17.4		CWB station code: TCU054	F
			8	1.86	1.12	37.1	21.8		CWB station code: TCU082	F
			9	2.02	1.51	42.7	33.5		CWB station code: TCU120	F

continued on next page

Tab. D.2: *continued*

Date	Time	Lat.	Long.	Depth	M_s	$\log M_0$	F	C
	d	a_h	a_v	v_h	v_v	S	Station	Type
	9	2.31	1.42	31.8	35.5		CWB station code: TCU055	F
	9	1.24	0.89	28.6	29.7		CWB station code: TCU087	F
	10	2.41	2.42	29.7	32.7		CWB station code: TCU122	F
	10	2.78	1.49	49.0	28.3		CWB station code: CHY024	F
	10	2.21	1.15	26.5	18.3		CWB station code: TCU051	F
	10	1.95	0.84	17.1	15.7		CWB station code: TCU060	F
	10	1.64	1.14	27.0	21.5		CWB station code: TCU136	F
	11	1.72	1.13	51.1	43.3		CWB station code: TCU063	F
	11	4.04	1.50	74.9	22.1		CWB station code: CHY101	F
	11	3.46	2.12	62.7	17.8		CWB station code: CHY006	F
	12	2.88	1.57	35.7	13.2		CWB station code: CHY029	F
	12	1.35	0.87	23.2	25.1		CWB station code: TCU050	F
	13	1.55	0.95	21.1	26.9		CWB station code: TCU056	F
	13	1.89	1.19	47.9	23.8		CWB station code: TCU110	F
	13	1.10	0.74	23.0	25.8		CWB station code: TCU100	F
	13	1.63	1.22	36.3	26.7		CWB station code: TCU116	F
	13	2.50	1.02	47.6	15.1		CWB station code: CHY035	F
	14	1.49	1.37	41.1	15.4		CWB station code: TCU109	F
	14	1.16	0.66	24.9	19.4		CWB station code: TCU057	F
	14	1.13	0.85	18.8	19.3		CWB station code: TCU104	F
	15	2.96	0.84	43.4	13.7		CWB station code: CHY034	F

D.3 Records used for pure error analysis

The two letter country abbreviations used are the same as for the near-field records (see Section D.1) with the addition of AL for Algeria, CO for Colombia, CR for Costa Rica, EL for El Salvador, FR for France, GE for Georgia, GY for Germany, LI for Liechtenstein, NI for Nicaragua, NZ for New Zealand, PO for Portugal and SP for Spain.

Tab. D.3: Records used for pure error analysis

Date			Time	Lat.	Long.	Depth	M_s	$\log M_0$	F					C
			d	a_h	$\mathrm{SA}_h(0.2)$	$\mathrm{SA}_h(0.5)$	$\mathrm{S}_h(1.0)$	a_v	$\mathrm{SA}_v(0.2)$	$\mathrm{SA}_v(0.5)$	$\mathrm{SA}_v(1.0)$	S	Station	
1933	3	11	0154	33.62	-117.97	16	6.41	18.79	S					US
			29	0.6887	2.1500	1.9600	1.5300	0.5304	1.4800	1.0700	0.5440	A	Subway Terminal	
			23	1.7068	3.2500	2.8600	2.1100	1.1468	2.5100	1.3600	0.4400	S	2369 East Vernon Avenue	
1938	9	12	0610	40.30	-124.80		5.64							US
			55	1.5943	3.4200	2.7800	0.9550	0.3242	0.8990	0.5000	0.1340	S	Ferndale Fire Station	
1940	5	19	0436	32.73	-115.45	7	7.14	19.49	S					US
			6	3.4750	6.4400	8.2300	5.0200	2.4320	3.2800	1.4700	0.5590	S	El Centro Array-Station 9 (Irr District)	
1952	7	21	0453	35.00	-119.03		7.20		T					US
			31	1.8492	4.4100	3.7200	1.8400	1.1065	2.3500	1.8200	0.6420	A	Taft-Lincoln	
1954	12	21	1956	40.82	-124.08	15	6.67	18.48	S					US
			1	2.4601	6.7600	5.2500	2.8300	0.4211	0.5570	1.1000	0.6840	S	Eureka-Myrtle & West	
			29	1.9293	3.4800	3.2100	3.6900	0.4211	0.5570	1.1000	0.6840	S	Ferndale Fire Station	
1966	6	28	0426	35.90	-120.90	7	6.13	18.36	S					US
			0	4.7924	5.1800	13.9000	5.1500	2.6946	4.0000	2.2600	1.9900	S	Cholame Shandon Array 2W[27]	
			6	4.3044	8.7900	7.7800	1.8400	1.2908	2.6000	2.0000	0.6580	S	Cholame Shandon Array 5W	
			10	2.5641	8.9100	3.6300	1.5800	1.2181	1.5700	0.5700	0.6800	S	Cholame Shandon Array 8W	
			11	3.6004	8.2000	4.7700	2.0500	1.2637	2.3200	0.9270	0.3490	A	Parkfield-Temblor	
			15	0.6089	1.3800	0.9520	0.5470	0.5802	1.3100	0.5600	0.4230	A	Cholame Shandon Array 12W	
			99	0.1119	0.2660	0.2630	0.1830	0.0550	0.1190	0.1400	0.1250	A	Taft-Lincoln	
1971	2	9	1401	34.40	-118.39	8	6.61	19.00	T					US
			15	3.4818	12.6000	2.0400	1.5500	1.6253	2.9700	0.6170	0.6820	A	Lake Hughes Array-Station 12A	
			24	2.0462	4.3100	3.5400	1.8600	1.0007	2.8200	2.5300	0.8380	S	CIT (Milikan Library)	
			25	0.9015	1.6700	1.6000	1.2400	0.3838	0.6610	1.1100	0.4810	S	Beverly Hills-435 N Oakhurst	
			25	1.6111	3.8900	3.5200	1.2300	0.4212	1.1900	0.8770	0.4020	S	Beverly Hills-9100 Wilshire Boulevard	
			26	1.8446	5.3300	2.5100	1.2800	0.3730	1.0800	0.6730	0.8060	S	Beverly Hills-450 N Roxbury	
			27	1.5772	2.3100	2.2000	1.7100	0.6729	1.1600	1.1800	0.7400		Water and Power Building	
			29	1.1911	2.7400	2.5500	2.0500	0.7657	2.0700	1.0100	1.3600	A	Alhambra-Fremont School	
			91	0.3698	0.8740	0.6340	0.1990	0.2508	0.5290	0.3520	0.1120	S	Colton-Edison College	
			168	0.3399	1.5600	0.9960	0.2040	0.1289	0.4230	0.2300	0.0683		Anza-Post Office	
1972	1	25	2322	43.70	13.41	10	4.02		N					IT
			8	0.6018	0.9900	0.5150	0.0893	0.3192	0.3960	0.1890	0.0356		Genio-Civile	
1972	2	4	0242	43.63	13.56	8	4.40							IT

continued on next page

[27] Only one horizontal component.

Tab. D.3: *continued*

Date			Time d	Lat. a_h	Long. $\mathrm{SA}_h(0.2)$	Depth $\mathrm{SA}_h(0.5)$	M_s $\mathrm{S}_h(1.0)$	$\log M_0$ a_v	F $\mathrm{SA}_v(0.2)$	$\mathrm{SA}_v(0.5)$	$\mathrm{SA}_v(1.0)$	S	Station	C
			2	1.1744	2.5800	0.9170	0.2120	0.7382	2.3000	0.6570	0.1420		Genio-Civile	
1972	2	4	0918	43.73	13.38	8	4.32							IT
			5	1.1968	1.7900	0.7480	0.0762	0.4720	1.0300	0.2670	0.0277		Genio-Civile	
1972	2	4	1817	43.70	13.40	10	3.96		N					IT
			6	0.8692	1.0300	0.7080	0.1030	0.4119	0.9620	0.1410	0.0674		Genio-Civile	
1972	2	5	0126	43.72	13.40	10	4.17							IT
			3	1.9436	3.8400	1.0200	0.1840	0.7055	1.9700	0.2970	0.1270		Genio-Civile	
1972	2	6	0134	43.70	13.43	5	4.12							IT
			2	1.6921	2.3800	1.2200	0.1570	0.6709	1.4200	0.6520	0.1110		Genio-Civile	
1972	2	6	2144	43.70	13.40	10	3.56		N					IT
			13	0.4343	0.7640	0.3160	0.0609	0.1148	0.2070	0.1100	0.0272		Ancona-Palombina	
1972	2	8	1219	43.68	13.40	12	3.97		N					IT
			4	1.1465	2.1200	0.5330	0.1220	0.4711	0.7610	0.1790	0.0866		Ancona-Palombina	
1972	3	14	2303	43.63	13.42	10	3.27		N					IT
			5	0.5329	0.7650	0.1730	0.0402	0.2714	0.2320	0.0551	0.0193		Ancona-Palombina	
1972	4	4	0826	43.70	13.50	5	3.31		N					IT
			11	0.5882	1.3200	0.2880	0.0911	0.3357	0.3440	0.0899	0.0484		Ancona-Palombina	
1972	6	14	1855	43.65	13.61	8	4.55							IT
			4	1.5874	3.4800	0.8130	0.2420	0.5028	1.0200	0.2660	0.1180		Ancona-Palombina	
			10	3.9435	8.4500	6.7500	0.6850	1.4234	1.9500	1.5100	0.2990		Genio-Civile	
			10	5.0803	9.2800	1.8500	0.5860	2.5061	2.5700	0.4960	0.2470		Ancona-Rocca	
1972	6	14	2101	43.63	13.50	8	4.02		N					IT
			0	4.9632	8.1700	0.8660	0.1390	2.0729	1.4600	0.1930	0.0676		Ancona-Rocca	
			3	2.2112	6.3400	1.2900	0.2560	1.1561	2.0900	0.2470	0.0819		Ancona-Palombina	
1972	6	15	0913	43.65	13.60		2.55		N					IT
			11	0.2159	0.4290	0.0995	0.0492	0.1252	0.1210	0.0470	0.0292		Ancona-Palombina	
1972	6	21	1506	43.60	13.50	4	3.66		N					IT
			2	4.0335	11.2000	1.2600	0.2410	1.2359	4.0100	0.2850	0.0613		Ancona-Palombina	
			2	1.8427	1.0100	0.2510	0.1080	0.7692	0.4560	0.1050	0.0660		Ancona-Rocca	
			3	0.6723	0.7340	0.3420	0.0610	0.3998	0.4610	0.1070	0.0310		Genio-Civile	
1972	12	23	0629	12.33	-86.13	5	6.16		S					NI
			4	3.6812	10.9000	10.3000	3.2000	3.1407	8.6700	2.4100	1.5000	S	Esso	
1973	11	4	1552	38.78	20.55	7	5.78		T					GR
			11	4.9308	8.2000	13.2000	6.4400	1.0334	1.8900	1.1400	1.4900	S	Lefkada-OTE Building	
1973	11	4	1611	38.76	20.65	15	4.64		T					GR

continued on next page

Tab. D.3: *continued*

Date			Time	Lat.	Long.	Depth	M_s	$\log M_0$	F					C
			d	a_h	$\mathrm{SA}_h(0.2)$	$\mathrm{SA}_h(0.5)$	$\mathrm{S}_h(1.0)$	a_v	$\mathrm{SA}_v(0.2)$	$\mathrm{SA}_v(0.5)$	$\mathrm{SA}_v(1.0)$	S	Station	
			14	0.7299	2.0400	1.3900	0.3360	0.2022	0.5110	0.2730	0.3450	S	Lefkada-OTE Building	
1973	11	23	1336	38.42	28.31	5	5.31		S					PO
			2	2.7187	5.7900	3.9800	1.3300						San Mateus[28]	
1974	11	28	2301	36.78	-121.60	9	4.50		S					US
			9	1.1500	3.5800	1.5400	0.5900	0.5126	1.4000	0.3450	0.1060	A	San Juan Bautista-24 Polk Street	
			19	1.6487	4.9600	4.1600	0.9270	0.7213	1.1900	0.6830	0.1720	S	Hollister-City Hall Annex	
			22	1.3826	2.2100	0.8230	0.1770	0.3761	0.5160	0.1450	0.0672	R	Gilroy Array-Station 1	
1976	5	6	2000	46.32	13.32	6	6.50	18.53	T					IT
			26	0.8304	1.6100	1.4900	1.2500	0.3480	0.4800	0.6650	0.7160	A	Codroipo	
			40	0.3175	1.1600	0.4250	0.3570	0.1391	0.3520	0.2070	0.2450	S	Barcis	
			91	0.3967	0.8540	0.5000	0.1600	0.2717	0.5530	0.2540	0.1960	R	Feltre	
			128	0.2868	0.4650	0.4360	0.3130	0.1280	0.2790	0.3180	0.1110	R	Asiago	
1976	5	11	2244	46.25	13.01	12	4.72	16.49	T					IT
			2	2.9184	7.1600	4.9400	0.7730	1.2182	3.2000	1.3900	0.2570	A	Forgaria-Cornio	
1976	5	13	1304	46.20	13.00	10	3.36	15.92	T					IT
			2	0.6542	1.3600	0.6950	0.1170	0.4763	0.8650	0.3040	0.0657	A	Forgaria-Cornio	
1976	5	15	0426	46.24	13.27	10	3.62		T					IT
			21	0.2618	0.5340	0.1260	0.0515	0.0943	0.3450	0.0745	0.0511	A	Forgaria-Cornio	
1976	5	17	0258	40.28	63.39	13	7.05	19.26	T					UZ
			3	6.3131	12.7000	14.1000	7.5100	13.6290	25.2000	10.5000	4.9500	L	Gazli	
1976	5	18	0130	46.27	13.03	7	3.47	15.83	T					IT
			6	0.5923	1.5700	0.9330	0.1720	0.3640	1.2600	0.4090	0.0844	A	Forgaria-Cornio	
			6	0.4346	0.7840	0.3900	0.1780	0.2480	0.4560	0.4320	0.0811	A	San Rocco	
1976	5	18	0239	46.32	12.95	10	3.00		T					IT
			12	0.2188	0.7590	0.2180	0.0981	0.1988	0.4630	0.1030	0.0642	A	Forgaria-Cornio	
1976	6	9	1848	46.26	13.01	13	3.63	15.91	T					IT
			5	0.7149	1.1400	0.3830	0.0854	0.4024	0.7300	0.1540	0.0692	A	Forgaria-Cornio	
1976	6	11	1716	46.27	12.97	9	4.00	16.11	T					IT
			6	0.8550	1.5600	0.5180	0.0958	0.4651	0.9490	0.3790	0.0818	A	Forgaria-Cornio	
			6	0.6290	0.8170	0.5810	0.1760	0.2862	0.4080	0.3630	0.1410	A	San Rocco	
1976	6	17	1428	46.18	12.80	15	4.23	16.34	T					IT
			16	0.5242	1.9900	0.8970	0.1230	0.2716	1.0900	0.1750	0.0705	A	Forgaria-Cornio	
1976	7	14	0539	46.37	13.27	16	4.00		T					IT

continued on next page

[28] No vertical component.

Tab. D.3: *continued*

Date			Time	Lat.	Long.	Depth	M_s	$\log M_0$	F					C
			d	a_h	$\mathrm{SA}_h(0.2)$	$\mathrm{SA}_h(0.5)$	$\mathrm{S}_h(1.0)$	a_v	$\mathrm{SA}_v(0.2)$	$\mathrm{SA}_v(0.5)$	$\mathrm{SA}_v(1.0)$	S	Station	
			16	0.0972	0.1050	0.0373	0.0182	0.0677	0.1120	0.0298	0.0155	R	Somplago-Cunicolo Pompe	
1976	8	19	0112	37.71	29.00	5	5.11		N					TU
			3	3.4684	6.0200	9.2400	1.7500	1.5784	2.6200	1.5600	0.3640	A	Denizli-Bayindirlik ve Iskan Mudurlugu	
1976	9	11	1631	46.30	13.23	6	5.48	17.00	T					IT
			8	1.8946	3.4700	1.8800	0.6110	0.6538	0.7420	0.6630	0.3280	S	Tarcento	
			14	0.4585	1.5900	1.0200	0.3070	0.2050	0.4120	0.3930	0.1480	S	Buia	
			14	0.3272	0.6820	0.2580	0.1330	0.2623	0.3880	0.2550	0.1130	R	Somplago-Cunicolo Pompe	
			15	1.6626	2.9900	0.8500	0.3020	0.5091	1.2200	0.3340	0.3270	A	Breginj-Fabrika IGLI	
			20	0.9793	2.7200	1.0100	0.2070	0.4799	1.7000	0.2450	0.0629	A	Forgaria-Cornio	
			27	1.0017	2.6400	1.2600	0.2370	0.5315	1.1800	0.2390	0.1820		Kobarid-Osn.Skola	
1976	9	11	1635	46.29	13.18	16	5.52	17.40	T					IT
			7	2.2777	3.2800	6.1800	2.1800	0.8603	1.2100	3.1300	1.0400	S	Buia	
			11	0.6058	1.2900	0.4630	0.4710	0.3107	0.8220	0.3990	0.2050	R	Somplago-Cunicolo Pompe	
			17	0.8910	2.7300	0.8610	0.4740	0.4308	0.6180	0.5210	0.5990	A	San Rocco	
			17	2.2726	6.8700	3.3800	0.5800	1.1723	3.8000	0.7060	0.1930	A	Forgaria-Cornio	
			31	0.8667	4.5700	0.7570	0.2000	0.5523	1.7600	0.2440	0.1670		Kobarid-Osn.Skola	
			83	0.1246	0.3690	0.3770	0.1010	0.0792	0.2640	0.1360	0.0731	A	Conegliano-Veneto	
1976	9	13	1854	46.25	13.19	14	3.90	16.30	T					IT
			8	0.6269	0.8550	0.4650	0.1830	0.5678	0.6540	0.1770	0.0856	S	Buia	
1976	9	15	0315	46.29	13.20	15	6.06	17.80						IT
			9	1.0495	3.0000	2.1200	1.5100	0.5969	1.2000	0.6960	0.6450	S	Buia	
			12	1.2444	2.6900	1.0900	0.6200	0.6028	1.4900	0.8910	0.4020	A	San Rocco	
			12	2.5944	6.0600	2.6300	0.5760	0.8426	2.1500	0.8080	0.2460	A	Forgaria-Cornio	
			14	4.8448	11.9000	6.0000	2.5600	1.8124	3.6100	1.9800	1.3600	A	Breginj-Fabrika IGLI	
			19	1.0131	2.0300	0.9490	0.2850	0.4000	0.6890	0.5310	0.2780	R	Robic	
			25	1.2418	3.0400	2.3500	0.6480	0.8655	1.7700	1.1400	0.5550		Kobarid-Osn.Skola	
			77	0.2035	0.5750	0.3220	0.0868	0.0580	0.2560	0.0796	0.0548	A	Conegliano-Veneto	
1976	9	15	0438	46.28	13.19	18	4.30	16.45	T					IT
			10	0.3314	0.8380	0.3300	0.0755	0.1449	0.2750	0.1340	0.0453	S	Buia	
1976	9	15	0921	46.32	13.16	12	5.98	18.11	T					IT
			6	1.3271	3.1200	1.0800	0.7960	0.5607	0.7720	0.5620	1.0400	S	Tarcento	
			7	4.1667	6.9400	2.9500	0.7420	1.2496	1.0400	0.8690	0.4740	A	Breginj-Fabrika IGLI	
			8	0.8604	3.5100	1.6100	1.0200	0.8300	1.3000	0.7540	0.3020	S	Buia	
			9	3.4707	9.6500	11.1000	1.4500	1.8975	6.7700	2.6900	0.8800	A	Forgaria-Cornio	
			9	2.4225	7.0000	3.5900	1.4400	0.8111	1.7500	2.3900	1.9500	A	San Rocco	

continued on next page

Tab. D.3: *continued*

Date			Time	Lat.	Long.	Depth	M_s	$\log M_0$	F					C
			d	a_h	$SA_h(0.2)$	$SA_h(0.5)$	$S_h(1.0)$	a_v	$SA_v(0.2)$	$SA_v(0.5)$	$SA_v(1.0)$	S	Station	
			12	0.8712	1.9600	0.4690	0.1770	0.4582	1.4800	0.1870	0.1250	R	Robic	
			19	1.4012	3.3100	2.1100	0.3530	0.5293	1.4900	0.4230	0.1070		Kobarid-Osn.Skola	
			88	0.2000	0.2910	0.1030	0.0746	0.0892	0.1390	0.0589	0.0535	R	Feltre	
1976	11	24	1222	39.05	44.04	10	7.26	19.94	S					TU
			44	1.0097	2.0800	1.2400	0.3860	0.5680	0.9700	0.3100	0.2930	A	Maku	
1977	2	11	1833	48.30	9.07	5	3.30		S					GY
			4	0.5724	0.5360	0.0481	0.0221	0.1503	0.0367	0.0133	0.0076	R	Jungingen	
1977	4	6	1336	31.90	50.76	10	5.89	18.11	T					IR
			4	10.5680	14.7000	11.2000	3.2700					R	Naghan 1[29]	
1977	9	16	2348	46.26	12.98	15	5.22	17.15	T					IT
			6	2.2587	5.1800	2.6700	0.4140	1.0976	3.2000	1.2000	0.2510	A	Forgaria-Cornio	
			7	0.9041	2.0900	0.8360	0.3360	0.4795	0.9740	0.5120	0.2200	A	San Rocco	
			11	1.8234	4.4100	2.3500	0.5390	0.5920	1.0300	0.4570	0.1220	R	Somplago-Uscita Galleria	
			11	1.0883	2.1800	0.7400	0.4750	0.4893	1.8800	0.4650	0.1510	R	Somplago-Cunicolo Pompe	
			11	0.7546	1.3600	1.5500	0.5090	0.5610	1.0600	0.8710	0.1390	R	Somplago-Galleria Cavi	
1977	12	16	0737	38.41	27.19	5	5.02		N					TU
			3	2.0782	6.6200	0.6660	0.1050	0.4793	0.6680	0.2480	0.1460	A	Izmir-Bayindirlik ve Iskan Mudurlugu	
1978	1	16	1431	48.29	9.03	6	3.30	14.72	S					GY
			5	0.4892	1.1800	0.4630	0.0908	0.2157	0.4230	0.0974	0.0231	R	Jungingen	
1978	3	11	1920	38.02	16.03	15	5.02	16.92	T					IT
			10	0.7578	1.7700	1.9300	0.2390	0.3320	0.7380	0.3510	0.1130	R	Ferruzzano	
1978	4	15	2333	38.27	14.86	15	5.83	18.08	T					IT
			11	1.5570	4.2400	2.5800	2.2000	0.4701	1.2100	0.6480	0.3360	S	Patti-Cabina Prima	
			16	1.4416	4.6400	1.9200	0.7870	0.8030	2.7500	0.6310	0.3630	A	Naso	
			30	0.7208	2.0000	0.5140	0.3990	0.7328	0.8660	0.2460	0.1950	R	Milazzo	
			52	0.3709	1.0500	0.5670	0.2090	0.2460	0.5580	0.1900	0.0743	R	Messina 1	
1978	8	13	2254	34.40	-119.68	13	5.70	17.76	S					US
			0	2.3079	3.9300	4.4500	2.0400	0.5943	1.4200	0.8330	0.3050	A	Santa Barbara-Freitas Building	
			0	2.0332	3.0100	4.1600	1.5700	0.7302	1.2500	1.2200	0.3300	A	Santa Barbara-Court House	
			6	4.0771	10.1000	6.1500	3.4500	1.0251	2.5100	1.6700	1.1100		Santa Barbara-UCSB North Gardens (C)	
			6	3.3802	6.5700	7.5300	6.2300	1.3485	1.9000	2.3300	2.3900	S	Santa Barbara-UCSB Goleta	
			10	2.7384	9.1600	4.1600	1.2400	1.0284	2.1500	1.7600	0.5450	A	Santa Barbara-SCE Substation Goleta	
			39	0.1259	0.2750	0.3150	0.2390	0.0524	0.1140	0.1290	0.0875		Harbour & California (Holiday Inn)	

continued on next page

[29] Only one horizontal and no vertical component.

Tab. D.3: *continued*

Date			Time	Lat.	Long.	Depth	M_s	$\log M_0$	F					C
			d	a_h	$\mathrm{SA}_h(0.2)$	$\mathrm{SA}_h(0.5)$	$\mathrm{S}_h(1.0)$	a_v	$\mathrm{SA}_v(0.2)$	$\mathrm{SA}_v(0.5)$	$\mathrm{SA}_v(1.0)$	S	Station	
1978	9	16	1535	33.36	57.42	5	7.41	20.11	T					IR
			3	9.9496	33.7000	18.7000	8.5000	7.3725	15.9000	4.8300	2.8500	A	Tabas	
1978	9	21	1937	37.97	38.59	22	4.20							TU
			48	0.2592	0.3010	0.0671	0.0226	0.1402	0.1250	0.0399	0.0254	R	Malatya-Bayindirlik ve Iskan Mudurlugu	
1979	1	24	1058	42.77	13.01	11	3.50							IT
			23	0.8567	0.9060	0.4270	0.1060	0.3816	0.4860	0.1160	0.0383	R	Arquata del Tronto	
1979	4	9	0210	42.07	19.02	3	5.23	17.18	T					YU
			16	0.4838	1.3100	0.7660	0.0809	0.1850	0.6210	0.1290	0.0536	A	Petrovac-Hotel Oliva	
			26	0.7358	2.1800	0.7700	0.5750	0.3575	0.6250	0.3740	0.1120	A	Ulcinj-Hotel Olimpic	
1979	4	15	0619	41.98	18.98	12	7.03	19.49	T					YU
			9	2.7623	4.2000	6.1800	5.1300	4.2328	5.0900	2.3800	2.0100	A	Ulcinj-Hotel Olimpic	
			12	4.5812	9.5300	14.4000	6.0600	2.0256	5.0900	3.7700	1.3400	A	Petrovac-Hotel Oliva	
			29	2.5034	8.2800	5.9500	1.7300	2.0611	2.9700	2.0500	0.7420	R	Hercegnovi Novi-O.S.D. Pavicic School	
			46	0.3014	0.9200	0.5060	0.4450	0.3821	0.6450	0.7190	0.4800	R	Titograd-Seismoloska Stanica	
			46	0.4736	1.0600	0.8440	0.4570	0.3023	0.5590	0.5840	0.3840	R	Titograd-Geoloski Zavod	
			65	0.7443	1.9100	1.9300	0.3230	0.2601	0.5200	0.4320	0.3160	R	Dubrovnik-Pomorska Skola	
			105	2.6067	4.1800	5.2200	0.6560	0.4670	1.0100	0.5000	0.1970		Veliki Ston-F-Ka Soli	
			108	0.5808	2.0200	0.7490	0.3160	0.2577	0.7340	0.3700	0.2070		Debar-Skupstina Opstine	
			110	0.5502	1.3600	1.1000	0.4000	0.3739	0.8950	0.4550	0.5300		Gacko-Zemlj. Zadruga	
1979	4	15	0631	42.17	18.72	10	4.80							YU
			52	0.5384	1.2100	0.5730	0.1810	0.8421	0.5680	0.1770	0.0549	A	Ulcinj-Hotel Olimpic	
1979	4	15	0808	42.30	18.57	10	3.60							YU
			33	0.6896	2.1000	1.4300	0.1900	0.2682	1.1400	0.2820	0.0695	A	Petrovac-Hotel Oliva	
1979	4	15	1243	41.91	19.16	6	4.00							YU
			7	0.5809	1.3700	0.7500	0.4040	0.2384	0.7320	0.2680	0.0938	A	Ulcinj-Hotel Olimpic	
1979	4	15	1443	42.29	18.68	7	5.77	17.78	T					YU
			22	0.9224	1.7700	1.0600	0.1630	0.4647	1.0000	0.3100	0.0564	R	Hercegnovi Novi-O.S.D. Pavicic School	
			24	0.9855	3.8400	2.6500	0.3810	0.4002	1.8600	0.4680	0.1140	A	Petrovac-Hotel Oliva	
			63	0.5358	0.8690	0.3420	0.1100	0.3214	0.2560	0.0782	0.0746	A	Ulcinj-Hotel Olimpic	
1979	4	15	1524	43.39	18.87	10	3.50							YU
			167	0.5533	1.3300	0.5170	0.0914	0.2094	0.5470	0.1180	0.0530	A	Ulcinj-Hotel Olimpic	
1979	4	16	1004	41.93	19.22	11	4.86							YU
			3	1.3732	3.4900	0.5720	0.2400	0.4979	0.9460	0.1650	0.0547	A	Ulcinj-Hotel Olimpic	
			82	0.5502	1.8800	0.6410	0.3970	0.3121	1.2300	0.3800	0.1590	R	Hercegnovi Novi-O.S.D. Pavicic School	
1979	4	28	0338	42.20	18.90	15	4.16		T					YU

continued on next page

Tab. D.3: *continued*

Date			Time	Lat.	Long.	Depth	M_s	log M_0	F					C
			d	a_h	SA$_h(0.2)$	SA$_h(0.5)$	S$_h(1.0)$	a_v	SA$_v(0.2)$	SA$_v(0.5)$	SA$_v(1.0)$	S	Station	
			11	0.4699	1.2700	1.1000	0.1100	0.4387	0.4100	0.1730	0.0458		Budva-PTT	
1979	5	12	0330	42.25	18.96	7	4.68		T					YU
			4	1.3822	1.9600	4.0000	1.3600	0.6813	1.2600	0.9900	0.2180		Budva-PTT	
			20	0.8595	1.8600	0.9020	0.1800	0.3225	0.6870	0.6690	0.1190		Kotor-Zovod za Biologiju Mora	
1979	5	14	0953	41.93	19.23	5	4.23							YU
			7	0.8211	1.1800	2.1200	0.3520	0.5298	0.7700	0.2620	0.1370	A	Ulcinj-Hotel Olimpic	
1979	5	20	0845	42.22	18.68	5	4.01							YU
			9	0.7695	1.5000	1.1000	0.2030	0.4895	0.4950	0.2860	0.0722		Budva-PTT	
1979	5	21	1434	43.09	12.75	4	3.20							IT
			4	1.2860	2.2700	0.3380	0.1210	0.7632	0.3280	0.1340	0.0224	R	Nocera Umbra	
1979	5	24	1723	42.23	18.76	5	6.31	18.34	T					YU
			7	2.8267	4.2900	1.6100	0.9550	1.1647	1.7800	2.5800	0.5580		Petrovac-Hotel Rivijera	
			9	2.7482	4.7000	8.0700	3.4900	1.7215	2.6200	1.6000	0.2850		Budva-PTT	
			15	1.6567	3.7300	1.7500	0.7590	0.9113	1.3200	1.1600	0.5380		Tivat-Aerodrom	
			18	0.7948	2.2400	1.6100	0.4330	0.4359	0.8980	0.8250	0.2500	R	Hercegnovi Novi-O.S.D. Pavicic School	
			19	0.5921	1.7900	1.4200	0.7060	0.3115	0.6380	0.6760	0.4890	R	Kotor Nas Rakit	
			19	1.5640	3.6100	3.8300	0.4360	0.7895	1.9200	1.0400	0.3870		Kotor-Zovod za Biologiju Mora	
			30	0.3323	0.8880	0.6790	0.5690	0.1223	0.2630	0.1340	0.1490	A	Ulcinj-Hotel Olimpic	
1979	7	14	1129	42.26	18.76	5	3.63							YU
			56	0.9419	2.1500	0.3580	0.0788	0.3817	0.9690	0.1140	0.0476	A	Ulcinj-Hotel Olimpic	
1979	7	18	1312	39.66	28.65	7	4.99	17.04	N					TU
			6	2.8959	6.4800	2.7600	0.6060	1.5636	3.2100	1.6500	0.4090	A	Dursunbey-Kandilli Gozlem Istasyonu	
1979	8	2	1441	41.90	19.05	5	3.94							YU
			17	1.4615	2.6300	2.1400	0.7840	1.6431	1.3400	0.3930	0.2010	A	Ulcinj-Hotel Olimpic	
1979	8	6	1705	37.13	-121.51	9	5.70	17.70						US
			2	4.1489	7.7600	7.0000	5.6100	1.4599	3.2600	1.2200	1.7500	A	Gilroy Array-Station 6	
			6	2.3967	4.9300	5.9400	3.7900	4.0951	4.8100	0.9120	1.0200	S	Gilroy Array-Station 4	
			8	2.4347	5.5300	3.2600	4.1700	1.4535	1.5300	0.5360	0.6200	S	Gilroy Array-Station 3	
			10	2.5206	7.1600	3.8100	3.0800	1.6135	4.4900	1.0500	0.6860	S	Gilroy Array-Station 2	
			11	1.0923	3.1000	0.7240	0.8680	0.6244	0.9730	0.4870	0.2250	R	Gilroy Array-Station 1	
			21	1.1125	3.5200	3.0700	0.8650	1.0857	2.5500	1.3800	0.3860	A	San Juan Bautista-24 Polk Street	
1979	9	19	2135	42.76	13.02	4	5.84	17.84	N					IT
			6	1.8426	5.3900	1.9000	1.4000	1.7932	2.7500	0.9710	0.4220	R	Cascia	
			21	0.8750	2.0600	1.2400	0.4590	0.5222	1.0900	0.6070	0.2090	R	Arquata del Tronto	
			21	0.4201	1.3000	0.4550	0.2050	0.3983	0.5080	0.3120	0.2570	A	Spoleto	

continued on next page

Tab. D.3: *continued*

Date			Time	Lat.	Long.	Depth	M_s	$\log M_0$	F					C
			d	a_h	$\mathrm{SA}_h(0.2)$	$\mathrm{SA}_h(0.5)$	$\mathrm{S}_h(1.0)$	a_v	$\mathrm{SA}_v(0.2)$	$\mathrm{SA}_v(0.5)$	$\mathrm{SA}_v(1.0)$	S	Station	
			33	0.3613	0.5610	0.6610	0.3250	0.2290	0.3640	0.4610	0.0761	A	Bevagna	
1979	9	21	0052	42.80	12.99	10	3.40							IT
			5	0.9806	2.9200	0.4670	0.0999	0.4286	1.2500	0.1990	0.0424	R	Cascia-Cabina Petrucci	
1979	9	24	0507	42.65	12.88	5	3.10							IT
			5	1.0159	2.3700	0.6250	0.1330	0.5575	0.9460	0.1500	0.0686	A	Norcia	
1979	9	28	0441	42.75	13.10	5	3.10							IT
			4	0.1909	0.6710	0.2350	0.0945	0.2042	0.3570	0.0957	0.0489	A	Norcia	
1979	10	15	2316	32.64	-115.31	10	6.87	18.70	S					US
			0	3.1507	5.2400	5.1600	3.8100	1.4306	1.7000	0.7740	0.4130	S	Mexicali-Aeropuerto	
			0	4.2030	10.4000	9.5000	6.6200	5.1549	7.2300	3.9400	1.4800	S	El Centro Array-Station 5	
			1	4.2734	6.1200	6.3300	5.3800	15.9200	20.3000	5.0900	4.2500	S	El Centro Array-Station 6	
			1	2.4554	3.9800	5.3400	3.7800	2.1367	4.5200	2.4300	2.3300	S	Meloland Overpass-Free Field	
			2	3.1619	3.3700	5.7500	2.7700	8.8214	4.1900	1.3800	0.7370	A	Agrarias (Mexicali Valley)	
			2	7.3025	22.8000	13.7000	4.3200	3.5919	5.4500	1.5300	1.9400	S	Bonds Corner-Maintenance Shop	
			3	4.4602	9.8600	6.8500	5.1500	2.4280	3.2400	1.9900	0.8910	S	El Centro Array-Station 4	
			3	3.6363	6.0600	7.8900	6.0600	6.0315	3.8600	2.9200	2.7100	S	El Centro Array-Station 7	
			5	2.4105	7.9400	5.2400	3.1900	2.3498	3.9700	1.3500	0.5200	S	Holtville-Post Office	
			6	5.5289	9.8900	6.8200	3.2000	4.3948	5.2800	2.0500	1.7400	S	El Centro Array-Station 8	
			6	2.2231	5.0100	4.4400	2.7100	1.4847	2.7500	0.7290	0.9020	S	Brawley-Airport Hangar	
			7	4.5625	9.8000	10.3000	4.8800	6.1281	4.5500	1.4000	1.2600	S	El Centro Differential Array	
			9	2.7507	8.1000	5.6000	2.3200	1.2610	1.7100	1.1300	0.5050	L	El Centro Array-Station 3	
			9	4.2565	14.4000	9.6600	2.9000	3.8266	5.2700	1.3700	0.9100	S	Mexicali-Casa Flores	
			10	2.2169	5.6700	7.5400	4.0500	2.1705	2.7000	1.9000	1.1700	S	El Centro-Imperial County Centre	
			11	2.5625	5.8700	6.0400	1.7600	1.9286	2.4800	0.8610	0.3290	S	Calexico-Fire Station	
			11	3.9599	9.7500	7.4500	2.8000	1.1203	1.4700	0.8970	0.6290	S	El Centro Array-Station 2	
			11	1.8015	5.6500	5.6700	2.8100	0.9641	2.5900	1.1600	0.8950	S	El Centro Array-Station 10	
			12	3.0563	10.1000	5.1500	3.4800	1.2313	1.7800	0.5310	0.3210	S	Cucapah (Mexicali Valley)[30]	
			14	1.0366	1.5400	2.1700	0.8500	0.8210	1.2200	1.0800	1.0400	S	Westmorland-Fire Station	
			15	3.8348	11.9000	7.4800	2.3200	1.3170	4.1400	0.8070	0.6440	S	El Centro Array-Station 11	
			15	1.8407	4.5300	3.3500	1.2800	1.5681	4.4600	0.9260	0.4850	A	El Centro-Parachute Test Site (Base)	
			17	2.6631	5.5600	5.5700	4.1400	2.1330	3.1700	0.9920	0.4970	S	Chihuahua (Mexicali Valley)	
			18	1.5908	3.9400	1.9500	1.8800	0.7214	0.9830	0.5270	0.3060	S	El Centro Array-Station 12	
			20	1.1643	2.9300	1.0900	1.0900	0.5153	1.9700	0.6970	0.4960	S	Calipatria-Fire Station	

continued on next page

[30] Only one horizontal component.

Tab. D.3: *continued*

Date			Time	Lat.	Long.	Depth	M_s	$\log M_0$	F					C
			d	a_h	$\mathrm{SA}_h(0.2)$	$\mathrm{SA}_h(0.5)$	$\mathrm{S}_h(1.0)$	a_v	$\mathrm{SA}_v(0.2)$	$\mathrm{SA}_v(0.5)$	$\mathrm{SA}_v(1.0)$	S	Station	
			22	1.6383	4.7500	4.6500	2.7100	1.6079	4.8100	0.9980	0.6230	A	Cerro Prieto (Mexicali Valley)	
			22	1.3827	3.8900	2.2700	1.3300	0.4373	1.0900	0.6120	0.4070	S	El Centro Array-Station 13	
			22	1.4301	2.5800	2.0800	1.0400	0.6129	1.2500	0.5050	0.2990	S	El Centro Array-Station 1	
			23	1.8123	3.5300	2.8100	0.9310	0.7060	1.0500	0.7530	0.2990	S	Compuertas (Mexicali Valley)	
			26	1.8529	5.7300	1.2800	0.4410	0.7335	1.3500	0.2940	0.1990	R	Superstition Mountain-Camera Site 8	
			32	3.3392	6.4900	6.6500	4.6200	1.4876	2.2200	1.2600	0.7020	S	Delta (Mexicali Valley)	
			32	1.1220	2.4100	2.1200	1.3900	0.3215	1.0200	0.7010	0.4040	S	Niland-Fire Station	
			34	0.5689	2.0400	0.8020	0.5850	0.2507	0.8950	0.3360	0.2310	S	Plaster City-Storehouse	
			40	1.2742	2.4800	4.5900	1.0500	0.3766	1.2100	1.0000	0.6360	S	Coachella	
			43	1.5194	6.1000	1.5100	0.6870	0.4747	0.6870	0.2530	0.1680	S	Victoria (Mexicali Valley)	
1979	10	16	0658	33.02	-115.58	5	5.86	17.51	S					US
			5	1.4683	3.2900	1.6900	0.8610	1.0408	1.0300	0.4050	0.1790	S	Westmorland-Fire Station	
1980	1	1	1642	38.75	27.75	5	7.02	19.45	S					PO
			80	0.5370	0.9550	1.0800	0.4650	0.3249	0.9920	0.3060	0.2120		Horta	
1980	2	20	0240	39.28	16.15	14	3.30							IT
			9	1.2043	2.4900	0.3570	0.1090	0.5050	0.5840	0.0906	0.0253	A	Cosenza	
1980	4	21	1808	48.28	9.03	6	3.00		S					GY
			6	0.2232	0.1610	0.0315	0.0101	0.0811	0.0428	0.0272	0.0081	R	Jungingen	
1980	5	25	1633	37.61	-118.85	9	6.15	18.26	N					US
			1	4.6126	12.6000	4.8000	1.7300	3.5584	7.9700	3.1700	1.2900		Convict Creek	
			12	2.9656	6.0900	3.6100	1.1400	2.1993	3.7500	1.5900	0.8850	A	High School (Gym, Center)	
			12	2.4439	6.8300	3.7500	1.1300					A	High School (Gym, W. Wall)[31]	
1980	5	25	1944	37.56	-118.84	16	5.99	17.92	N					US
			5	2.1070	5.8000	5.0700	2.0000	1.6937	2.8300	3.0200	0.7110		Convict Creek	
1980	5	25	2035	37.51	-118.91	5	5.70							US
			14	4.3355	10.7000	2.7800	1.5400	3.1351	3.6700	1.8100	0.7370		Convict Creek	
1980	5	27	1451	37.49	-118.78	22	6.00		N					US
			9	1.9007	3.1500	3.6300	3.0900	0.9304	2.1800	1.8400	0.3360		Long Valley-Fire Station	
			11	3.1627	7.6100	8.4800	2.6600						Mc Gee Creek Inn[32]	
			13	6.7424	22.0000	3.9500	2.2400	3.6710	5.8000	3.8900	0.7500		Convict Lake	
			14	3.2026	7.7400	5.6200	1.7400	1.6738	2.5600	3.0200	0.9240		Convict Creek	
			14	3.6429	9.6500	6.5600	1.8800	1.5532	2.3100	3.4300	0.9480		FIS	

continued on next page

[31] Only one horizontal and no vertical component.
[32] No vertical component.

Tab. D.3: *continued*

Date			Time	Lat.	Long.	Depth	M_s	$\log M_0$	F					C
			d	a_h	SA$_h(0.2)$	SA$_h(0.5)$	S$_h(1.0)$	a_v	SA$_v(0.2)$	SA$_v(0.5)$	SA$_v(1.0)$	S	Station	
			15	3.5650	6.2800	7.0800	2.3900	1.3910	1.8200	1.5200	0.7240		Green Church	
			16	1.0995	1.5700	0.5860	0.5000	0.6023	1.8500	0.6370	0.2820	R	Bishop-Paradise Lodge	
			18	3.8444	15.4000	4.7200	1.1500	2.4401	3.8000	0.9830	1.1500		Elementary School	
			21	1.8405	4.3500	3.8900	4.2500	1.8447	2.0300	2.9700	0.8410		Cash Baugh Ranch	
			45	1.7157	5.3200	2.1400	0.9780	0.6436	1.2000	0.6860	0.7770	S	Benton	
1980	5	27	1901	37.55	-118.84	6	3.40		N					US
			7	0.9966	1.8600	1.3500	0.7930	0.3826	0.7010	0.8090	0.2420		FIS	
			7	2.9499	5.9400	1.6200	0.4410						Mc Gee Creek Inn[33]	
			8	1.7764	3.3400	2.9800	0.8930	0.7395	0.7120	0.5050	0.1910		Green Church	
			8	0.3141	0.6190	0.3860	0.3010	0.3040	0.4100	0.2700	0.1180		Long Valley-Fire Station	
			10	0.8215	1.8400	1.1800	0.3040	0.1740	0.4520	0.2690	0.2450		Elementary School	
			14	0.3969	0.7810	0.6730	0.7740	0.2430	0.4050	0.8510	0.2100		Cash Baugh Ranch	
1980	6	7	1835	44.08	10.65	30	4.33							IT
			15	0.6074	1.4000	0.4130	0.1170	0.3517	0.7400	0.1630	0.0707	A	Barga	
1980	6	9	0328	32.19	-115.08	5	6.49	18.79	S					ME
			3	7.9818	28.3000	7.8400	3.9800	14.4860	28.7000	15.8000	6.0300	S	Victoria (Mexicali Valley)	
			8	5.8050	10.6000	9.4900	5.8600	2.6940	7.9200	2.5100	1.3300	A	Cerro Prieto (Mexicali Valley)	
			12	1.8812	4.4300	3.2900	1.9500	1.3365	2.0200	1.1400	0.6350	S	Chihuahua (Mexicali Valley)	
			19	0.7232	1.7200	1.7400	0.9230	1.1058	1.7700	0.9920	0.6670	S	Cucapah (Mexicali Valley)[34]	
			33	1.0335	3.0500	1.8000	0.7540	0.4577	0.7710	0.5600	0.4300	S	Mexicali-Casa Flores	
			37	0.4267	0.6600	0.8530	0.8180	0.2364	0.4400	0.5200	0.3140		Victoria-Hospital (Mexicali Valley)	
1980	8	11	0916	39.24	22.75	27	4.76							GR
			6	0.7060	1.7500	1.0800	1.1900	0.7412	0.7850	0.6690	0.6530	A	Almiros Volos-Town Hall	
1980	10	22	0246	36.33	1.64	7	3.40		T					AL
			7	0.3595	0.7340	0.3230	0.0778	0.1368	0.2820	0.1080	0.0488	R	El Safsaf	
1980	10	22	1623	36.42	1.65	6	4.26		T					AL
			8	0.6146	1.1400	1.9200	0.3570	0.5449	0.7340	0.6180	0.2530	R	El Safsaf	
1980	10	23	0957	36.44	1.74	12	4.38		T					AL
			4	1.4829	4.0700	2.7400	0.4190	0.6559	2.0300	0.4650	0.0913	R	El Safsaf	
			28	0.2421	0.6010	0.5080	0.2430	0.2180	0.3840	0.2020	0.0808	R	Beni Rashid	
1980	10	26	0228	36.54	1.60	10	3.71		T					AL
			21	0.1422	0.3680	0.4880	0.0735	0.1423	0.2390	0.3810	0.1190	R	El Safsaf	

continued on next page

[33] No vertical component.
[34] Only one horizontal component.

Tab. D.3: *continued*

Date			Time d	Lat. a_h	Long. $\mathrm{SA}_h(0.2)$	Depth $\mathrm{SA}_h(0.5)$	M_s $\mathrm{S}_h(1.0)$	$\log M_0$ a_v	F $\mathrm{SA}_v(0.2)$	$\mathrm{SA}_v(0.5)$	$\mathrm{SA}_v(1.0)$	S	Station	C
1980	10	30	0835	36.33	1.70	3	3.70		T					AL
			6	0.3424	0.3780	0.1740	0.0605	0.2045	0.4470	0.2230	0.0382	R	El Safsaf	
1980	11	8	0206	36.45	1.62	2	4.64		T					AL
			22	0.2509	0.6510	0.5960	0.2580	0.1995	0.2720	0.4310	0.2770	R	Beni Rashid[35]	
1980	11	8	0754	36.14	1.40	8	4.90		T					AL
			18	0.9232	2.0500	1.4500	0.3010	0.5398	1.2500	0.8710	0.2690	R	Beni Rashid[36]	
1980	11	10	0001	36.49	1.48	3	4.18		T					AL
			24	0.4206	0.8240	0.5050	0.2380	0.1310	0.3530	0.3080	0.3440	R	Beni Rashid[37]	
1980	11	12	2356	36.13	1.41	5	3.00		T					AL
			18	0.1800	0.2530	0.0790	0.0284	0.0952	0.1290	0.0583	0.0234	R	Beni Rashid	
1980	11	23	1834	40.78	15.33	16	6.87	19.40	N					IT
			6	1.9580	3.4300	4.0700	2.7100	0.9239	2.2000	1.9800	1.4800	R	Bagnoli-Irpino	
			10	0.5823	1.4700	1.1000	0.6260	0.3097	0.5390	0.5970	0.3370	R	Auletta	
			14	3.5594	11.8000	5.9000	3.7000	1.7338	3.4900	2.2100	1.6500	R	Sturno	
			14	1.6715	3.8100	4.5200	3.8400	1.5180	4.1400	2.0300	2.5100	A	Calitri	
			22	1.0027	1.5500	2.4600	2.3300	0.5296	1.0200	1.3900	1.5700	A	Bisaccia	
			30	1.0056	3.4400	2.5900	1.3000	0.6822	1.9200	1.1500	1.0100	R	Rionero in Vulture	
			33	2.1261	7.1700	2.9000	1.2800	1.5153	2.8800	1.6400	0.4460	A	Brienza	
			33	1.3423	4.6100	2.8700	2.0000	0.5008	1.5400	0.6310	0.2830	S	Mercato San Severino	
			41	0.5431	1.8400	0.8940	0.9130	0.2739	0.4910	0.4480	0.4870	A	Benevento	
			46	0.4638	1.5100	0.6860	0.4730	0.2784	0.5730	0.4230	0.3360	A	Bovino	
			48	0.1834	0.3030	0.4370	0.3440	0.1024	0.2020	0.1550	0.1340	R	San Giorgio la Molara	
			60	0.3548	1.1900	1.0500	0.3320	0.2105	0.3430	0.3650	0.3450	R	Arienzo	
			63	0.4468	0.9440	0.7730	0.7310	0.2307	0.4750	0.3230	0.4690	R	Tricarico	
			65	0.5964	1.1700	1.5900	0.6450	0.2872	0.7600	0.5650	0.3720	R	Torre del Greco	
			77	0.2814	0.5690	0.5100	0.4710	0.1842	0.3510	0.3520	0.5330	S	Gioia-Sannitica	
			88	0.2349	0.5880	0.5150	0.4040	0.1090	0.2480	0.1960	0.1490	A	San Severo	
			119	0.3302	0.5110	0.9140	0.8200	0.2190	0.2820	0.2850	0.6950	L	Garigliano-Centrale Nucleare 1	
			119	0.3163	0.4770	0.8860	0.7890	0.2052	0.2510	0.2790	0.6700	L	Garigliano-Centrale Nucleare 2	
1980	11	24	0024	40.83	15.28	18	4.70		N					IT
			18	0.3313	0.8560	0.8270	0.2660	0.1570	0.3250	0.4310	0.0825	R	Bagnoli-Irpino	

continued on next page

[35] Only one horizontal component.
[36] Only one horizontal component.
[37] Only one horizontal component.

Tab. D.3: *continued*

Date			Time	Lat.	Long.	Depth	M_s	$\log M_0$	F					C
			d	a_h	$\mathrm{SA}_h(0.2)$	$\mathrm{SA}_h(0.5)$	$\mathrm{S}_h(1.0)$	a_v	$\mathrm{SA}_v(0.2)$	$\mathrm{SA}_v(0.5)$	$\mathrm{SA}_v(1.0)$	S	Station	
			25	0.3164	1.0500	0.1810	0.0604	0.1275	0.3550	0.0866	0.0269	R	Sturno	
1980	11	24	0303	40.89	15.31	21	4.70		N					IT
			26	0.3719	0.7720	0.8720	0.2880	0.2082	0.4770	0.1910	0.2520	A	Calitri	
1980	11	26	1455	40.95	15.33	24	4.10		N					IT
			10	0.8423	2.4100	0.6940	0.1360	0.3155	0.5820	0.1760	0.0760	A	Contrada Fiumicella-Teora	
			15	0.6417	1.5000	0.5000	0.1610	0.2036	0.9340	0.1940	0.0378	A	Procisa Nuova	
			59	0.3526	0.6280	0.1310	0.0387	0.1471	0.2600	0.1590	0.0231	A	Brienza	
1980	12	1	1904	40.83	15.23	9	4.50		N					IT
			4	1.8457	6.2900	2.0700	0.5190	0.7202	2.3300	0.5380	0.1790	A	Contrada Fiumicella-Teora	
			5	1.5104	3.9100	1.8000	0.4690	0.5297	1.2900	0.5490	0.2210	A	Selva Piana-Morra	
			5	0.8153	2.0600	1.8600	0.5670	0.4264	1.0300	0.5550	0.2820	R	Oppido-Balzata	
1981	1	16	0037	40.85	15.28	15	5.01	16.93	N					IT
			4	1.5094	5.8800	0.9040	0.2590	0.5146	1.8500	0.3390	0.1330	A	Cairano 3	
			5	0.9361	2.2700	0.7500	0.3170	0.3471	0.6530	0.3580	0.1070	S	Conza-Base	
			5	1.0324	3.0900	0.4220	0.3850	0.3507	1.0300	0.2200	0.1100	A	Contrada Fiumicella-Teora	
			5	0.8572	3.6500	1.0900	0.7110	0.6798	1.1900	0.4930	0.2530	A	Conza-Vetta	
			5	1.5355	3.8600	1.3300	0.4880	0.3546	1.0000	0.6380	0.1130	A	Cairano 1	
			6	1.7174	5.3900	0.9620	0.3330	0.4484	1.5800	0.4400	0.1160	A	Cairano 2	
			7	0.6803	1.9500	0.5080	0.1800	0.2807	1.0900	0.2560	0.1420	A	Cairano 4	
			8	0.6296	1.6600	1.0300	0.2940	0.2597	0.6020	0.4100	0.1180	R	Lioni-Macello	
			15	0.2008	0.5720	0.4620	0.2430	0.1276	0.2730	0.2420	0.1620	A	Calitri-Cabina Pittoli	
1981	1	16	0436	40.98	15.23	5	3.70		N					IT
			8	0.4012	0.8560	0.4920	0.2070	0.2455	0.3040	0.2050	0.0447	A	Conza-Vetta	
			9	0.3689	0.7050	0.2810	0.0693	0.2005	0.3280	0.1230	0.0458	S	Conza-Base	
			9	0.5802	1.2000	0.3010	0.0676	0.2445	0.5110	0.1300	0.0326	A	Cairano 2	
			11	0.4520	1.3300	0.2640	0.0961	0.1595	0.5500	0.1620	0.0579	A	Cairano 4	
1981	1	16	0631	40.87	15.27	4	3.10		N					IT
			4	0.5202	1.0600	0.4640	0.1450	0.1769	0.5310	0.1960	0.0364	A	Cairano 2	
1981	2	14	1727	41.00	14.67	10	4.52		N					IT
			17	0.2636	0.9440	0.1900	0.0862	0.1639	0.2810	0.0812	0.0710	R	Arienzo	
			33	0.1657	0.4500	0.2620	0.0676	0.1282	0.2370	0.1110	0.0341	R	Torre del Greco	
1981	3	10	1516	39.20	20.80	10	5.10	17.65						GR
			7	1.3751	3.1600	3.5200	0.5630	0.7633	1.3600	0.7770	0.2230	A	Preveza-OTE Building	
			21	0.9544	1.8300	1.2800	0.5690	0.2066	0.5590	0.5240	0.3200	S	Lefkada-OTE Building	
1981	4	10	0833	38.91	21.02	10	4.30							GR

continued on next page

Tab. D.3: *continued*

Date			Time	Lat.	Long.	Depth	M_s	$\log M_0$	F					C
			d	a_h	$SA_h(0.2)$	$SA_h(0.5)$	$S_h(1.0)$	a_v	$SA_v(0.2)$	$SA_v(0.5)$	$SA_v(1.0)$	S	Station	
			15	0.3738	0.5840	0.3790	0.0631	0.0959	0.1620	0.0989	0.0515	S	Lefkada-OTE Building	
1981	4	26	1209	33.13	-115.65	8	6.04	17.72	S					US
			6	1.8842	4.9800	3.1100	2.0200	1.9823	1.8900	0.5940	0.4150	L	Salton Sea-Wildlife Refuge	
			7	4.4258	9.1500	9.3600	7.4100	6.1421	4.3100	1.5200	0.9560	S	Westmorland-Fire Station	
			15	1.7151	5.1300	2.0300	0.5260	1.1276	2.1900	0.5290	0.1840	S	Niland-Fire Station	
			16	2.1516	6.5700	5.4900	3.2300	1.4039	2.8000	3.7700	1.1000	A	El Centro-Parachute Test Site	
			17	1.5467	3.2900	2.3100	0.9640	0.9163	1.2800	0.7120	0.1630	S	Brawley-Airport Hangar	
			18	1.0590	2.9600	1.7500	0.6860	0.5147	0.5790	0.2740	0.1220	R	Superstition Mountain-Camera Site 8	
1981	5	25	2304	38.71	20.95	15	4.00							GR
			7	0.5588	1.9100	0.2980	0.0553	0.2315	0.4970	0.0575	0.0858	S	Lefkada-OTE Building	
1981	5	27	1504	38.79	21.01	15	4.94							GR
			11	1.1705	2.7700	1.4700	0.2080	0.4799	0.9580	0.2240	0.0823	S	Lefkada-OTE Building	
1981	9	20	2040	42.72	12.95	6	5.80							IT
			18	0.4375	0.5740	0.0603	0.0178	0.3180	0.2190	0.0356	0.0166	A	Spoleto	
1982	3	21	0944	39.85	15.72	17	5.10							IT
			24	0.3959	0.7560	0.3560	0.0713	0.2071	0.2320	0.1780	0.0525	R	Lauria-Galdo	
			47	0.3700	1.6200	0.1680	0.0893	0.1697	0.7560	0.1190	0.0450	A	Roggiano-Gravina	
1983	1	17	1241	38.07	20.25	14	6.98	19.36	T					GR
			23	1.4586	3.5700	3.1300	0.6990	0.6018	1.1500	0.9610	0.3290	A	Argostoli-OTE Building	
			87	0.6467	1.4800	2.3200	0.9260	0.1605	0.3850	0.5380	0.5380	S	Lefkada-Hospital	
1983	1	17	1653	38.06	20.30	28	5.01							GR
			20	0.7508	0.7750	0.4300	0.1430	0.2523	0.2950	0.1270	0.0786	A	Argostoli-OTE Building	
1983	1	19	0002	38.12	20.31	13	5.52							GR
			16	0.7712	1.6900	1.3600	0.2280	0.3661	0.6710	0.2390	0.1240	A	Argostoli-OTE Building	
1983	2	20	0545	37.69	21.26	28	4.34							GR
			86	0.6447	1.0700	0.2700	0.0592	0.2064	0.2600	0.0638	0.0662	A	Argostoli-OTE Building[38]	
1983	3	16	2119	38.81	20.89	25	4.77							GR
			16	0.2585	0.6140	0.3980	0.1560	0.0633	0.1610	0.0725	0.0046	S	Lefkada-Hospital	
1983	3	23	1904	38.78	20.81	25	5.01		T					GR
			26	0.5035	1.3700	0.6500	0.7350	0.1393	0.3410	0.2460	0.6220	S	Lefkada-Hospital	
1983	3	23	2351	38.23	20.29	3	6.10	18.34	S					GR
			17	2.3213	8.3400	1.5600	1.0700	1.0537	2.0700	0.7220	0.4050	A	Argostoli-OTE Building	
			70	0.2570	0.7730	0.6210	0.2810	0.1052	0.5050	0.2000	0.1170	A	Zakinthos-OTE Building	

continued on next page

[38] Only one horizontal component.

Tab. D.3: *continued*

Date			Time	Lat.	Long.	Depth	M_s	log M_0	F					C
			d	a_h	$\mathrm{SA}_h(0.2)$	$\mathrm{SA}_h(0.5)$	$\mathrm{S}_h(1.0)$	a_v	$\mathrm{SA}_v(0.2)$	$\mathrm{SA}_v(0.5)$	$\mathrm{SA}_v(1.0)$	S	Station	
1983	3	24	0417	38.10	20.37	22	5.09							GR
			12	2.8425	8.0800	2.2000	0.2420	0.6705	1.2000	0.2110	0.1530	A	Argostoli-OTE Building	
1983	5	2	2342	36.24	-120.27	7	6.57	18.66	T					US
			7	5.6089	12.8000	20.4000	9.6500	3.5011	7.8700	4.2200	2.5000	S	Pleasant Valley-Pumping Plant (Switchyard)	
			7	2.8557	6.4900	11.4000	5.7500	2.0629	5.3700	3.5400	2.0600	S	Pleasant Valley-Pump Plant (Basement)	
			22	2.8461	6.8700	10.0000	4.0500	1.1247	2.1300	2.4200	0.5800		Cantua Creek School	
			28	1.6931	4.7300	5.1800	2.0300	0.6658	1.4000	1.3100	1.3900	A	Parkfield-Vineyard Canyon 2E	
			28	1.7639	3.4100	2.7600	2.7200	0.4709	1.1800	1.0300	0.8680		Coalinga-Slack Canyon	
			31	2.2490	2.8400	3.7300	5.4200	0.7595	1.4500	1.5600	2.4300	A	Parkfield-Vineyard Canyon 1E	
			32	1.8196	5.0200	3.2100	3.1900	0.6069	2.1900	0.8720	0.8400	A	Parkfield-Fault Zone 16	
			33	0.6358	1.4700	1.2500	0.9840	0.2702	0.6920	0.9940	0.4110	R	Parkfield-Stone Corral 4E	
			33	0.8319	2.0300	2.6600	1.1300	0.4214	0.8720	0.6710	0.6650	A	Parkfield-Fault Zone 11	
			34	2.6550	4.1000	5.5600	9.9500	0.9149	1.6600	2.3200	1.8800	A	Parkfield-Fault Zone 14	
			34	1.7297	2.8200	5.7600	5.0600	0.8366	1.5100	1.4000	1.6000	A	Parkfield-Fault Zone 15	
			34	0.8883	1.7400	1.6600	1.1300	0.5604	0.6720	0.9240	1.0600	A	Parkfield-Gold Hill 3E	
			34	1.1448	2.1800	2.7500	3.4500	0.6771	1.0700	1.7400	1.2500	S	Parkfield-Fault Zone 12	
			34	0.8494	2.2100	2.2200	2.8200	0.6383	2.0400	0.8260	0.7420	A	Parkfield-Vineyard Canyon 1W	
			34	1.2483	2.3200	3.4200	2.5400	0.5093	1.2600	1.2000	0.5590	A	Parkfield-Fault Zone 8	
			35	0.8211	1.9800	1.4700	1.0300	0.5601	1.6200	0.6730	0.7360	A	Parkfield-Vineyard Canyon 2W	
			35	1.1589	1.8600	2.9500	2.0400	0.5315	0.9420	1.3100	0.9180	A	Parkfield-Fault Zone 7	
			36	0.5315	1.0100	1.4000	1.5100	0.2794	0.3600	0.4310	0.6530	A	Parkfield-Fault Zone 9	
			36	1.2931	1.8300	2.4700	3.0200	0.3873	0.8160	0.9300	1.5800	A	Parkfield-Fault Zone 10	
			37	0.7821	1.3500	2.3500	1.2300	0.3258	1.1400	0.7980	0.4220	A	Parkfield-Gold Hill 2E	
			37	1.4460	2.8000	2.7100	0.8280	0.3403	0.7150	0.9400	0.4230	A	Parkfield-Stone Corral 3E	
			37	1.3220	1.9400	3.2500	3.1300	0.5590	1.2500	1.3000	1.1700	A	Parkfield-Vineyard Canyon 3W	
			37	0.5350	1.1700	1.2500	1.5800	0.2596	0.7670	0.8440	0.5530	A	Parkfield-Fault Zone 6	
			39	0.5676	1.0100	1.3200	1.3100	0.2640	0.4610	0.5650	0.4940	A	Parkfield-Vineyard Canyon 4W	
			39	1.0980	1.5000	3.2500	2.1300	0.4702	0.9040	1.3500	0.8870	A	Parkfield-Fault Zone 4	
			40	1.1833	1.4900	2.4100	2.4400	0.3532	0.8550	0.8200	0.5920	S	Parkfield-Gold Hill 1W	
			40	0.8856	1.1700	1.8900	0.8770	0.3345	0.4940	0.8690	0.6410	A	Parkfield-Stone Corral 2E	
			41	0.8665	1.2600	1.8700	1.5800	0.3507	0.5700	0.6090	0.6170	A	Parkfield-Gold Hill 2W	
			41	1.6806	2.5000	4.7200	3.9800	0.4618	0.8300	0.9680	0.9680	S	Parkfield-Fault Zone 3	
			42	1.2648	3.3400	2.0100	1.4400	0.6555	2.0100	0.7110	0.5480	A	Parkfield-Stone Corral 1E	
			42	0.5957	1.3400	1.9400	1.5500	0.4653	0.7240	0.8730	1.4000	A	Parkfield-Vineyard Canyon 5W	
			43	1.3786	3.0400	2.1700	1.8300	0.6216	1.3400	0.9610	0.9150	R	Parkfield-Gold Hill 3W	

continued on next page

Tab. D.3: *continued*

Date			Time	Lat.	Long.	Depth	M_s	$\log M_0$	F					C
			d	a_h	$\mathrm{SA}_h(0.2)$	$\mathrm{SA}_h(0.5)$	$\mathrm{S}_h(1.0)$	a_v	$\mathrm{SA}_v(0.2)$	$\mathrm{SA}_v(0.5)$	$\mathrm{SA}_v(1.0)$	S	Station	
			43	1.2505	2.3300	4.0400	2.9500	0.3649	0.8070	0.5610	0.5600	S	Parkfield-Fault Zone 2	
			44	0.4657	1.1800	1.1300	0.5160	0.2551	0.4230	0.5870	0.5340	A	Cholame Shandon Array 3E	
			46	1.4605	2.4100	3.1700	4.6200	0.3821	0.6850	0.6990	1.1800	S	Parkfield-Fault Zone 1	
			46	0.9519	2.5000	1.2000	0.9450	0.2890	0.8840	0.6360	0.5140	A	Parkfield-Gold Hill 4W	
			46	0.3931	0.8370	0.7140	0.4450	0.1695	0.3660	0.3440	0.4220	A	Cholame Shandon Array 2E	
			46	0.7365	1.7500	1.4400	1.2400	0.3599	0.6410	0.7850	0.9390	A	Parkfield-Vineyard Canyon 6W[39]	
			47	0.9028	1.6200	2.9600	1.7000	0.5814	0.6520	1.5700	0.7620	S	Cholame Shandon Array 1E	
			48	0.6972	1.4600	1.2700	1.4200	0.3367	0.6520	0.7510	0.6620	A	Parkfield-Gold Hill 5W	
			49	1.1386	2.4000	3.3500	1.4300	0.4199	0.6590	0.7370	0.5740	S	Cholame Shandon Array 2WA	
			50	0.9853	2.0600	2.2600	1.1600	0.3233	0.6960	0.9200	0.5080	A	Cholame Shandon Array 3W	
			50	1.3362	2.6900	4.8200	0.9780	0.3997	0.8980	0.8140	0.3830	A	Cholame Shandon Array 4W	
			52	0.6784	1.5400	2.1800	0.7840	0.2409	0.5130	0.8540	0.2330	A	Cholame Shandon Array 4AW	
			53	1.3525	2.7600	4.1100	1.3100	0.3306	0.8390	0.6020	0.2690	S	Cholame Shandon Array 5W	
			53	0.6527	1.5200	1.4700	1.1600	0.3495	0.9890	0.5200	0.5600	A	Parkfield-Gold Hill 6W	
			54	1.2929	2.2800	4.0200	1.1800	0.3223	0.7140	0.5830	0.2580	A	Cholame Shandon Array 6W	
			56	1.0063	1.2100	3.1200	0.8350	0.2471	0.5330	0.4910	0.4120	S	Cholame Shandon Array 8W	
			60	0.4702	1.2100	1.3300	0.8750	0.2274	0.9170	0.5130	0.5070	A	Cholame Shandon Array 12W	
1983	6	14	0440	40.45	23.95	12	3.50							GR
			9	1.0002	1.7100	0.3110	0.0930	0.4269	0.4190	0.1880	0.0475	A	Ierissos-Police Station	
1983	7	9	0740	36.19	-120.38	12	5.20	16.80						US
			5	1.7861	4.0100	1.3100	0.3400	0.7229	1.2900	0.4990	0.1720		Coalinga-14th & Elm	
			5	3.6254	7.3600	3.1200	1.0400	1.8740	2.5200	1.0900	0.2440		Oil City	
			6	3.7033	12.5000	3.2300	0.7400	1.0754	2.4600	1.6300	0.2820		Anticline Ridge-Free-Field	
			6	4.0708	12.9000	2.8300	0.7400	1.1135	2.7600	1.6000	0.2450		Anticline Ridge-Pad	
			6	1.3713	4.0400	1.9700	0.3780	0.7468	1.2600	1.2700	0.2020		Coalinga-Burnett Construction Company	
			7	1.8840	4.5300	3.6800	0.8650	1.0281	1.5600	0.7550	0.3070		Transmitter Hill	
			8	1.9010	4.1500	1.1700	0.2990	0.7630	1.2500	0.3760	0.1540		Palmer Avenue	
			9	0.9447	2.8100	1.3400	0.4080	0.5720	0.7210	0.3870	0.1830		Oil Fields-Fire Station (Free-Field)	
			9	1.0171	2.9800	1.3400	0.4020	0.6464	0.7000	0.3860	0.2280		Oil Fields-Fire Station (Pad)	
			12	1.7460	3.9200	1.7200	0.3700	1.5628	2.3800	0.4730	0.1490		Skunk Hollow	
1983	7	22	0239	36.21	-120.37	9	5.80	17.72	T					US
			2	8.1263	28.1000	15.6000	3.8600	4.8732	9.2500	2.8200	1.1300		Oil City	
			5	8.7928	12.0000	12.1000	6.6500	2.6759	3.7900	2.9200	1.4800		Transmitter Hill	

continued on next page

[39] Only one horizontal component.

Tab. D.3: *continued*

Date			Time	Lat.	Long.	Depth	M_s	$\log M_0$	F					C
			d	a_h	$\mathrm{SA}_h(0.2)$	$\mathrm{SA}_h(0.5)$	$\mathrm{S}_h(1.0)$	a_v	$\mathrm{SA}_v(0.2)$	$\mathrm{SA}_v(0.5)$	$\mathrm{SA}_v(1.0)$	S	Station	
			7	4.9741	10.5000	4.2100	1.3700	1.6730	2.5600	1.3100	1.0200		Coalinga-14th & Elm	
			7	2.0533	5.5500	2.1200	2.7500	1.2836	3.3900	1.0800	1.3800		Oil Fields-Fire Station (Free-Field)	
			7	2.0534	5.8500	2.1100	2.7300	1.4010	3.6000	1.1800	1.4800		Oil Fields-Fire Station (Pad)	
			7	2.9565	5.2400	4.2600	1.8400	2.2544	3.2900	1.9000	1.0000		Palmer Avenue	
			8	3.3056	9.6100	6.4000	2.1500	2.0294	3.3900	2.5000	0.9760		Coalinga-Burnett Construction Company	
			9	3.7199	8.7100	2.8700	1.7700	2.3356	4.7000	1.4100	0.8890		Skunk Hollow	
			10	1.2781	3.9200	1.0500	0.5980	0.8238	2.4200	0.6310	0.3810		Coalinga-Sulphur Bath	
			15	3.6836	6.8800	3.8800	1.0300	1.2592	2.4500	3.0900	0.5270	S	Pleasant Valley-Pump Plant	
			15	4.2010	8.2600	4.3600	0.9520	0.7336	3.2300	2.2900	0.4850	S	Pleasant Valley-Pump Plant (Base.)	
			15	5.5921	12.5000	6.7200	1.5900	2.8630	8.2800	3.7900	0.5600	S	Pleasant Valley-Pump. Plant (Switchyard)	
1983	7	25	2231	36.14	-120.42	9	5.30	16.97						US
			3	1.8642	7.2700	2.2100	0.7830	1.6035	3.6200	0.8000	0.4170		Coalinga-Sulphur Bath	
			6	7.0132	15.4000	8.4900	1.8200	2.8576	3.5900	1.1400	0.5050		Coalinga-14th & Elm	
1983	8	6	1543	40.11	24.78	2	7.06	19.08	S					GR
			83	0.3010	0.5930	0.5850	0.1860	0.0962	0.2350	0.1570	0.0677	A	Ierissos-Police Station	
1983	8	26	1252	40.45	23.95	3	4.86							GR
			9	1.6496	5.4400	1.9800	0.5190	1.1602	1.0100	0.5710	0.2160	A	Ierissos-Police Station	
			14	1.2364	4.8400	1.3900	0.3370	0.3829	0.7960	0.3560	0.1110	R	Ouranoupolis-Seismograph Station	
1983	10	30	0412	40.35	42.18	14	6.74	18.94	S					TU
			17	1.4216	4.1600	3.0600	1.2400	0.6784	1.5800	0.6320	0.5980	A	Horasan-Meteoroloji Mudurlugu	
1984	3	29	0006	39.64	27.87	15	4.12							TU
			0	1.9631	9.0200	0.9580	0.2860	2.5054	1.5200	0.2540	0.1540	A	Balikesir-Bayindirlik ve Iskan Mudurlugu	
1984	4	24	2115	37.31	-121.68	9	6.20	18.84	S					US
			0	3.1172	5.0100	6.4500	4.2200	1.0831	2.0100	2.9300	1.1900	S	Halls Valley-Grant Park	
			10	1.5736	2.9900	3.0600	0.7130	0.7804	1.3200	0.9790	0.5310	R	San Jose-IBM Building 12	
			13	2.8505	10.3000	4.8000	5.5700	4.1363	8.6500	2.4600	1.2600	A	Gilroy Array-Station 6	
			14	3.5642	7.8300	5.7800	2.6300	3.9563	6.3000	1.9100	0.5890	S	Gilroy Array-Station 4	
			15	1.4670	2.4200	4.9300	0.9680	0.5926	0.7790	1.5500	0.2860		IBM Almaden	
			15	0.8919	2.6600	0.7850	0.2380	0.9090	1.1000	0.3660	0.2390	R	Gilroy Array-Station 1	
			15	2.0829	3.7500	2.2700	0.9370	5.5911	5.0500	0.6870	0.4890	S	Gilroy Array-Station 2	
			15	1.9381	3.9700	3.5600	1.6700	3.7951	4.2500	1.0400	0.5460	S	Gilroy Array-Station 3	
			15	1.1354	2.2200	0.5680	0.2930	1.0765	0.8980	0.3040	0.2320	A	Gilroy-Gavilan College	
			16	1.7468	3.3000	2.0300	0.5000	4.3280	2.1700	0.8230	0.2330	S	Gilroy Array-Station 7	
			20	0.3534	0.9320	1.0600	1.2400	0.1422	0.4700	0.3790	0.3260	S	Santa Clara-Agnew State Hospital	
			20	1.0804	2.4800	2.6300	1.8000	0.4308	1.3000	1.2000	0.8150	A	Corralitos-Eureka Canyon Road	

continued on next page

Tab. D.3: *continued*

Date			Time	Lat.	Long.	Depth	M_s	$\log M_0$	F					C
			d	a_h	$\mathrm{SA}_h(0.2)$	$\mathrm{SA}_h(0.5)$	$\mathrm{S}_h(1.0)$	a_v	$\mathrm{SA}_v(0.2)$	$\mathrm{SA}_v(0.5)$	$\mathrm{SA}_v(1.0)$	S	Station	
			26	0.2529	0.4670	0.6820	0.4030	0.2001	0.4840	0.3370	0.3040	A	Fremont-Mission San Jose	
			30	0.9759	4.0800	1.6500	1.5500	2.1670	4.8300	1.7500	0.3710	S	Hollister-Differential Array (Airport)	
			32	0.3897	1.4200	0.7750	0.8210	0.5252	0.8400	0.4360	0.2210	A	San Juan Bautista-24 Polk Street	
			36	1.3675	4.4500	2.8400	0.8940	0.4270	0.7840	0.6290	0.3490	S	Capitola-Fire Station	
			44	0.7432	2.4500	1.2000	0.4070	0.2751	0.6370	0.2970	0.1140	A	USCS Santa Cruz-Lick Observatory	
			47	0.3959	0.7970	0.5560	0.5150	0.1330	0.3230	0.1580	0.3960	L	Hayward-Apeel 1E	
			48	0.6240	1.3100	1.3700	0.8530	0.1529	0.4790	0.2220	0.1360	L	Foster City-Redwood Shores	
			66	0.5357	0.8110	1.6200	0.8000	0.1038	0.2420	0.2630	0.1680	S	Los Banos	
			66	0.4846	1.4300	0.8740	0.7010	0.1550	0.3850	0.2700	0.1390	S	San Francisco-Airport (Engrg. Building)	
1984	4	29	0502	43.25	12.47	7	5.38	17.53	N					IT
			13	0.6401	1.7800	0.7180	0.3560	0.3579	0.7530	0.4040	0.2770	R	Gubbio	
			16	1.9051	5.0000	1.3400	0.9180	0.5228	1.1200	0.5710	1.0800	R	Pietralunga	
			17	0.3282	0.5190	0.3920	0.0896	0.1484	0.4170	0.1900	0.0897	R	Umbertide	
			19	2.1244	5.8100	0.7010	0.2460	0.4966	0.9110	0.2390	0.0946	R	Nocera Umbra	
			30	0.4997	1.6100	0.8870	0.5910	0.1477	0.4620	0.3880	0.2430	S	Citta di Castello-Regnano	
1984	5	7	1749	41.73	13.90	8	5.79	17.89	N					IT
			12	1.0745	3.1000	1.5800	0.4870	0.5847	2.1800	0.4650	0.3190	R	Atina	
			17	1.3931	3.7600	2.6500	1.9400	0.9586	2.6100	0.8330	0.4540	S	Cassino-Sant' Elia	
			31	0.6581	1.7000	0.8370	0.5560	0.2463	0.5330	0.4350	0.2380	R	Ponte Corvo	
			33	0.6543	3.2600	0.9740	0.6830	0.3593	0.9280	0.8030	0.2550	A	San Agapito	
			50	0.4274	0.9420	0.9810	0.5470	0.2622	0.7480	0.6180	0.4730	R	Roccamonfina	
			53	0.5953	1.5800	2.2300	1.4900	0.1596	0.3280	0.4220	0.1860	L	Garigliano-Centrale Nucleare 1	
			53	0.6009	1.6100	2.3300	1.5600	0.1598	0.3000	0.4080	0.1720	L	Garigliano-Centrale Nucleare 2	
1984	5	11	1041	41.77	13.91	8	5.27	17.30	N					IT
			2	2.0843	4.4500	1.5700	0.8110	1.4061	1.3600	0.8220	0.4760	R	Villetta-Barrea	
			19	0.2567	0.5290	0.3190	0.1150	0.1509	0.4200	0.2260	0.0959	R	Atina	
			28	0.3655	1.2500	0.7480	0.3960	0.1966	0.4330	0.3300	0.1860	S	Cassino-Sant' Elia	
			35	0.2616	0.8880	0.4690	0.1550	0.1413	0.2850	0.3950	0.1030	A	San Agapito	
1984	5	11	1314	41.78	13.93	12	4.27	16.32	N					IT
			0	1.3537	2.6400	1.5200	0.2640	0.4722	0.7340	0.3230	0.1210	R	Villetta-Barrea	
1984	6	24	1430	36.84	3.74	5	4.54	16.38						SP
			29	0.1501	0.3300	0.1080	0.0301	0.1037	0.2370	0.0641	0.0193	R	Alhama de Granada-Escuela Taller	
			39	0.3360	0.9360	0.5320	0.0625	0.2263	0.5340	0.1590	0.0203	S	Ayuantamiento de Santa Fe	
1984	10	25	0949	37.07	21.82	5	4.65							GR
			4	1.7753	3.8500	1.4600	0.6830	0.9102	2.2500	0.6940	0.1040	R	Pelekanada-Town Hall	

continued on next page

Tab. D.3: *continued*

Date			Time	Lat.	Long.	Depth	M_s	$\log M_0$	F					C
			d	a_h	$SA_h(0.2)$	$SA_h(0.5)$	$S_h(1.0)$	a_v	$SA_v(0.2)$	$SA_v(0.5)$	$SA_v(1.0)$	S	Station	
			24	0.2481	0.4450	0.1420	0.0313	0.1202	0.2230	0.0762	0.0425	R	Kyparrisia-Agriculture Bank	
1985	3	22	2038	38.96	21.12	25	3.96							GR
			12	0.3625	1.5800	0.0823	0.0302	0.2542	0.2510	0.0509	0.0254	R	Amfilochia-OTE Building	
1985	5	20	1000	42.23	13.33		4.50							IT
			20	0.5028	1.6100	0.5350	0.0763	0.2547	0.7320	0.1060	0.0262	A	Poggio-Picenze	
			26	0.4841	1.1300	0.1290	0.0567	0.1766	0.4080	0.0974	0.0393	A	Castelnuovo	
1985	8	12	0254	39.95	39.77	29	4.31							TU
			86	1.4118	3.6100	0.5500	0.1310	0.4204	1.2600	0.2210	0.0468		Kigi-Meteoroloji Mudurlugu	
1985	8	31	0603	39.00	20.61	15	4.91							GR
			13	0.8205	1.8600	0.6170	0.2660	0.3377	0.9760	0.1690	0.0760	A	Preveza-OTE Building	
			21	0.7134	1.5500	0.9630	0.1610	0.1964	0.4020	0.3410	0.0383	S	Lefkada-Hospital	
1985	9	19	1317	18.54	-102.32	29	7.90	21.04	T					ME
			0	1.7899	5.0100	3.8100	2.4300	1.1483	2.5800	1.7800	1.3800	R	La Union	
			0	1.1689	2.0100	3.6000	1.8700	0.5692	1.8200	0.8660	0.6930	R	La Villita	
			0	1.3330	3.9500	3.3400	2.0300	0.8800	1.7600	1.8000	0.6910	R	Caleta de Campos	
			0	3.8589	13.5000	4.7700	1.5600	2.9957	11.0000	2.6400	0.6430		Infiernillo N-120	
			0	1.2074	2.6400	1.2900	1.1000	0.8437	2.3700	1.5900	0.5740		Infiernillo Margen Der.-INMDA	
			0	1.3757	2.4800	1.3900	1.2000	0.7873	2.4600	1.6100	0.6520		Infiernillo Margen Der.-INMSS	
			0	2.6749	7.5600	6.4100	4.4600	1.5181	3.7600	1.9500	1.2400		Zacatula	
			16	1.4850	3.1000	2.8400	1.9000	1.0252	2.5300	1.3300	1.0100	R	Zihuatanejo-Airport	
			18	0.8263	2.1200	1.4200	1.6400	0.4672	0.7900	0.8180	0.5810		Apatzingan de la Constitucion	
			68	1.5091	3.0700	2.0700	0.7150	0.7741	2.1600	1.1700	0.8590	R	Papanoa	
			111	0.9320	1.8100	2.9500	1.2700	0.4770	1.0200	0.8080	0.4750	R	Suchil	
			133	0.5870	1.4800	0.9350	0.7800	0.6037	1.6600	1.1200	0.7750	R	Atoyac de Alvarez	
			147	1.0972	1.8800	0.9980	0.5170	0.5890	0.7570	0.6510	0.6960	R	Paraiso	
			156	0.4685	1.0300	0.6030	0.6710	0.2054	0.3450	0.4370	0.4410	A	Cayaco	
			175	0.4624	1.1900	0.7670	0.8480	0.1973	0.4550	0.4850	0.3490	R	Coyuca de Benitez	
			177	0.8848	2.7200	0.9800	0.4000	0.3787	0.8480	0.6250	0.5540		Caracol Margen Izq.	
			190	0.4758	0.8030	0.9700	0.9510	0.3037	0.4440	1.0000	0.5380	R	Teacalco	
			200	0.2702	0.4430	0.6980	0.5480	0.2284	0.5080	0.5110	0.4040		Acapulco-Pellandini[40]	
			201	0.2638	0.6090	0.6360	0.3350	0.1794	0.3840	0.3800	0.3640		Acapulco-Sop.	
			206	0.1672	0.2730	0.5050	0.4910	0.1723	0.2910	0.3350	0.5260	R	La Venta	
			207	0.2793	0.4170	0.5810	0.3800	0.2039	0.4000	0.3790	0.4410	R	Xaltianguis	

continued on next page

[40] Only one horizontal component.

Tab. D.3: *continued*

Date			Time	Lat.	Long.	Depth	M_s	$\log M_0$	F					C
			d	a_h	$\mathrm{SA}_h(0.2)$	$\mathrm{SA}_h(0.5)$	$\mathrm{S}_h(1.0)$	a_v	$\mathrm{SA}_v(0.2)$	$\mathrm{SA}_v(0.5)$	$\mathrm{SA}_v(1.0)$	S	Station	
			208	0.4647	0.6360	1.1300	1.8500	0.2223	0.2860	0.4700	0.7310		Chilpancingo de los Bravos	
			209	0.1746	0.4210	0.5930	0.2700	0.0764	0.1630	0.1600	0.1140	R	Fica de Caballo	
			226	0.3004	0.3470	0.6130	0.7700	0.0983	0.1990	0.2090	0.2530	A	Mexico City-Tacubaya D.F.	
			230	0.2348	0.2490	0.4520	0.5470	0.1161	0.1560	0.2740	0.3820	R	Cerro de Piedra	
			233	0.2249	0.2850	0.4760	0.4210	0.1335	0.1970	0.3220	0.2990	R	Las Mesas	
			240	0.3191	0.3760	0.5500	0.9460	0.1061	0.1400	0.2980	0.3110	A	Ciudad Universitaria DF	
			240	0.3343	0.4100	0.5620	0.9510	0.1177	0.1600	0.2440	0.3330	A	Instituto de Ingeominas Patio	
			240	0.2801	0.3270	0.8550	1.0300	0.1448	0.1850	0.2900	0.4010	A	Mexico City-Mesa Vibradora	
			243	0.4170	0.4580	1.3300	1.1400	0.0950	0.1590	0.2410	0.2620	S	Mexico City-Sismex Viveros	
			246	0.8686	0.9410	2.5100	1.5200	0.3308	0.4140	0.6880	0.6080	L	Mexico City-Sec. Com. y Transportes	
			250	0.7201	0.8770	0.9270	1.5300	0.1667	0.2280	0.4210	0.4650	L	Tlahuac-Bomba	
			250	0.7121	0.7310	1.1700	1.6000	0.6466	0.6800	1.2600	1.6700	L	Tlahuac-Deportivo	
			251	0.7514	0.5600	0.8330	1.0400	0.2307	0.2820	0.3300	0.6400	L	Mexico City-Cdaf	
			251	0.5586	0.6000	0.8960	1.6200	0.2042	0.2540	0.4380	0.5840	L	Mexico City-Cdaf de Abastos Oficia	
			268	0.7595	0.7950	1.2400	2.3700	0.1738	0.2030	0.2930	0.5740	L	Texcoco-Sosa	
			326	0.3514	0.4320	0.5410	1.2000	0.1319	0.1610	0.2610	0.3490	A	Puebla-Sismex	
1985	11	9	2330	41.22	24.02	18	5.16	16.88	N					GR
			45	0.5415	0.8490	0.7140	0.0660	0.3816	0.4780	0.3500	0.0727	R	Kavala-Prefecture	
1985	12	6	2235	36.97	28.85	9	4.58							TU
			14	1.5525	2.4100	1.5600	0.6670	0.6323	0.5120	0.2870	0.2950	A	Koycegiz-Meteorological Station	
1985	12	23	0516	62.19	-124.24	6	6.79	19.28	T					CA
			0	10.4900	27.1000	8.3200	4.9200	19.1940	22.4000	7.5100	3.8000	R	Nahanni-Station 1 (Inverson)	
			4	3.5335	4.8300	7.1600	2.5900					R	Nahanni-Station 2 (Slide Mountain)[41]	
			18	1.3493	1.6500	0.7500	0.3290	1.3525	2.1100	0.5430	0.3510	R	Nahanni-Station 3 (Battlement Creek)	
1986	2	13	2036	62.10	-124.21	10	4.90							CA
			14	0.5988	1.0000	0.4170	0.1710	0.4036	0.5670	0.3720	0.1880	R	Nahanni-Station 1 (Inverson)	
			15	1.8525	1.3700	0.3840	0.1960	0.4420	0.5060	0.2910	0.0742	R	Nahanni-Station 2 (Slide Mountain)	
1986	3	31	1155	37.52	-121.59	11	5.60							US
			23	1.3339	3.4200	4.2600	2.0500	0.6401	1.5900	1.5300	0.2970	S	Halls Valley-Grant Park	
1986	5	5	0335	38.02	37.79	4	5.86	18.15	T					TU
			27	0.5977	0.8860	0.9210	0.9750	0.2806	0.3810	0.3310	0.1960	R	Golbasi-Devlet Hastanesi	
1986	7	8	0920	34.00	-116.61	12	6.13	17.84	S					US
			0	5.9932	16.5000	11.5000	3.1100	4.3295	8.1400	4.8900	0.9390	A	White Water Canyon-Trout Farm	

continued on next page

[41] No vertical component.

Tab. D.3: *continued*

Date			Time	Lat.	Long.	Depth	M_s	$\log M_0$	F					C
			d	a_h	$\mathrm{SA}_h(0.2)$	$\mathrm{SA}_h(0.5)$	$\mathrm{S}_h(1.0)$	a_v	$\mathrm{SA}_v(0.2)$	$\mathrm{SA}_v(0.5)$	$\mathrm{SA}_v(1.0)$	S	Station	
			1	9.2812	17.4000	9.9300	11.1000	4.1014	6.2500	3.7500	1.2700	S	Devers Substation	
			5	6.2195	17.5000	6.0700	8.2800	6.8346	5.5600	2.9500	1.7000	S	North Palm Springs-Post Office	
			6	3.4423	9.3500	5.2900	3.3600	4.3096	8.3000	3.5300	1.7200	S	Desert Hot Springs-Fire Station	
			7	2.2005	4.7500	3.5300	5.3600	2.9249	4.0800	1.2600	1.8600	S	Morongo Valley-Fire Station	
			11	2.0727	9.6300	2.0200	1.0800	2.9719	3.9700	1.5400	0.5940	S	Cabazon-Post Office	
			15	1.9477	4.2000	2.0200	1.8400	1.7613	2.0400	1.1500	0.8080	S	Palm Springs-Airport	
			18	1.2654	2.0300	2.4000	1.1500	0.6488	1.2500	0.8870	0.3080	A	Fun Valley-Reservoir 361	
			21	1.3709	1.8400	0.7980	0.3660	0.9494	2.2600	0.7200	0.1860	R	Banning-Silent Valley (Poppet Flat)	
			27	2.3663	8.4100	3.1300	1.5900	1.7893	3.2500	1.5000	0.7920	A	San Jacinto-Soboba	
			29	0.6453	1.5600	1.5700	0.5910	0.3683	1.0100	0.8370	0.4800	A	Joshua Tree-Fire Station	
			30	1.6095	2.6400	3.0400	1.2200	1.1955	1.2800	0.9740	0.8500	A	Cranston Forest Service (Fire Station)	
			30	2.2469	5.8800	3.2100	0.7270	0.7489	1.7300	0.5000	0.2800	A	Hurkey Creek County Park	
			35	0.6650	1.6600	1.0500	0.4700	0.5389	0.8210	0.5740	0.1440	S	San Jacinto-Valley Cemetery	
			36	0.9246	2.5300	1.4200	0.3550	0.5131	1.2800	0.4360	0.1310	S	Landers	
			38	1.4747	4.5900	1.2400	1.1900	0.9072	2.9500	0.6900	0.0977	S	Hemet-Stetson Avenue Fire Station	
			40	1.1522	2.4900	1.4900	0.3900	0.6326	1.0400	0.4920	0.2110	R	Red Mountains	
			41	1.1388	3.0200	1.2200	2.1000	0.8053	0.7650	0.3660	0.5790	S	Indio-Jackson Road	
			42	1.1113	1.9100	0.3570	0.3190	0.4569	1.1000	0.3860	0.0756	A	Santa Rosa Mountains	
			42	1.0853	3.1400	1.6400	0.7470	0.7121	2.0100	0.9490	0.2040	S	Winchester-Page Brothers Ranch	
			43	1.1257	2.7200	1.1000	0.3980	0.5277	1.6800	0.4800	0.3380	R	Anza Fire Station	
			44	1.2157	2.5200	2.0800	0.6450	0.5574	1.3700	0.4010	0.2310		Sunny Meadow	
			47	0.8756	1.1000	0.2980	0.1490	0.3636	0.6990	0.1660	0.0661	R	Winchester-Hidden Valley	
			47	0.5209	1.0900	0.8740	0.6880	0.5449	0.4300	0.4340	0.2480	S	Indio-Coachella Canal	
			52	0.9933	1.4900	2.0400	0.6860	0.3668	0.6370	0.6110	0.3310	A	Tule Canyon	
			53	0.9527	0.9650	0.3580	0.1810	0.7295	0.8990	0.2460	0.1360	R	Winchester-Bergman Ranch	
			59	0.4947	1.4600	0.2340	0.1570	0.3150	0.6190	0.1810	0.1070	R	Murrieta Hot Springs	
			68	1.0425	3.1900	1.2000	0.9510	0.2882	0.4860	0.3290	0.3140	S	Temecula-CDF Fire Station	
			69	0.6920	2.6300	0.4790	0.1540	0.3055	0.4680	0.4210	0.1550	A	Lake Henshaw-Puerta la Cruz	
			71	0.4911	1.8700	0.1640	0.0898	0.2176	0.3450	0.0928	0.0340	A	Riverside-Airport	
			83	0.3871	0.9950	0.4180	0.2430	0.3266	0.7510	0.4260	0.1110	S	Hesperia	
1986	7	21	1442	37.54	-118.45	9	6.30	18.42						US
			30	0.8375	1.7300	0.6050	0.1410	0.5757	0.6240	0.1970	0.1090	A	Mc Gee Creek Downhole Array (0m)	
1986	9	15	1141	37.03	22.13	12	4.74	16.52	N					GR
			6	0.4646	1.4900	0.5200	0.3620	0.1876	0.3290	0.1640	0.3350	A	Messinia-Town Hall	
1986	10	10	1749	13.67	-89.20	8	5.40	17.67						EL

continued on next page

Tab. D.3: *continued*

Date			Time	Lat.	Long.	Depth	M_s	$\log M_0$	F					C
			d	a_h	$\mathrm{SA}_h(0.2)$	$\mathrm{SA}_h(0.5)$	$\mathrm{S}_h(1.0)$	a_v	$\mathrm{SA}_v(0.2)$	$\mathrm{SA}_v(0.5)$	$\mathrm{SA}_v(1.0)$	S	Station	
			0	5.2412	7.5900	14.4000	9.0500	4.0344	6.6000	3.0100	1.2000	S	National Geographical Institut	
			1	6.5917	16.7000	12.4000	6.3900	3.8192	9.1800	3.2100	1.8600	A	Geotechnical Investigation Centre	
1987	3	2	0142	-37.93	176.78	20	6.49	18.81						NZ
			135	0.2071	0.2470	0.3580	0.8590	0.0628	0.0672	0.1420	0.1620		Wairoa Telephone Exchange	
1987	5	2	2043	44.81	10.72	2	4.60							IT
			4	0.7524	1.1600	1.6500	0.4820	0.1640	0.4160	0.1220	0.0175	A	Novellara	
1987	5	14	0629	38.17	22.06	9	4.23							GR
			9	0.2956	0.9820	0.1950	0.2360	0.3143	0.3170	0.1320	0.1370	A	Aigio-OTE Building	
1987	10	1	1442	34.07	-118.08	14	5.94	17.92	T					US
			2	2.5084	6.1500	5.6000	2.0300	1.6496	3.1500	1.1000	0.3280	S	11338 Fairview Avenue	
			2	2.5833	6.5900	8.5000	2.8200	2.6119	2.8500	1.4100	0.3490	A	600 East Grand Avenue	
			4	2.9159	7.5200	5.4700	1.9500	2.2352	3.0900	1.6100	0.4810	A	180 Campus Drive	
			4	3.7109	8.2400	4.5800	3.3800	1.7763	3.1600	1.1100	0.8540	A	Alhambra-Fremont School	
			4	4.1849	15.2000	5.3200	2.4800	1.3990	4.0600	1.0400	0.6710	A	Obregon Park	
			5	4.5542	10.2000	11.3000	3.0900	2.3832	5.1900	1.5200	0.3710	S	11500 East Joslin Street	
			6	2.1708	5.3300	6.1100	3.1400	1.1634	1.5600	0.9300	0.3040	S	7420 Jaboneria	
			6	1.2463	2.6100	1.2300	0.9210	0.8976	2.6600	0.5620	0.4290	A	3699 North Hollywood Avenue	
			6	1.7658	3.6500	2.4500	2.0000	1.1833	2.4400	1.4300	0.6760	A	San Marino-Southwestern Academy	
			8	3.2565	7.6500	6.3500	4.3400	2.5325	5.2000	0.7960	0.3630	S	12500 Birchdale	
			8	2.3073	8.3300	3.2200	1.1300	1.4870	2.7600	0.9180	0.4160	S	1488 Old House Road	
			9	1.6300	4.1500	2.8600	1.4500	0.9981	1.7900	0.5600	0.3800	S	2369 East Vernon Avenue	
			9	2.8940	6.0600	4.6100	1.2300	1.3151	2.3600	0.8920	0.5380	R	Altadena-Eaton Canyon Park	
			10	1.3011	3.0100	2.1500	0.8370	0.8595	1.9800	0.4590	0.2730	S	1271 West Badillo	
			10	1.7866	3.0300	8.1100	1.8600	1.6858	3.6100	1.3300	0.3490	A	5921 North Figueroa Street	
			10	1.9261	4.0200	4.8700	3.8600	1.5086	2.0000	0.7460	0.1640	S	Downey-County Maintenance Building	
			13	2.2446	6.2400	6.0500	2.4300	1.1804	2.6600	2.4000	0.9660	S	3036 Fletcher Drive	
			14	0.7591	1.3100	1.9100	0.9250	0.6766	1.1100	0.8370	0.4180	S	656 South Grand Avenue	
			14	3.0427	5.8100	5.8500	4.0300	1.6886	3.0500	0.4980	0.2250	S	14637 Castlegate Street	
			14	2.2487	5.5000	4.9300	4.3600	1.5635	2.6400	0.4460	0.2150	S	6979 Orange Avenue	
			14	1.6914	4.2000	2.5200	1.0400	0.6812	1.2500	0.4470	0.2620	S	950 Briarcliff Drive	
			14	1.6020	4.5900	0.6430	0.4580	1.1151	1.8300	0.5150	0.2290	R	Mt. Wilson-Caltech Seismograph Station	
			15	1.1627	2.7200	1.8500	0.7610	0.8272	1.4900	0.8600	0.2940	A	120 North Oakbank	
			15	1.7209	5.6100	6.6000	2.7700	0.7894	2.8700	0.8810	0.4600	S	924 West 70th Street	
			16	3.8742	13.6000	4.3400	2.2900	0.9241	2.4000	0.5450	0.3040	S	116th Street School	
			19	2.5892	6.3800	3.4300	2.3400	0.6616	1.6000	0.4340	0.2540	A	Inglewood-Union Oil Yard	

continued on next page

Tab. D.3: *continued*

Date			Time	Lat.	Long.	Depth	M_s	$\log M_0$	F					C
			d	a_h	$SA_h(0.2)$	$SA_h(0.5)$	$S_h(1.0)$	a_v	$SA_v(0.2)$	$SA_v(0.5)$	$SA_v(1.0)$	S	Station	
			19	2.2689	4.6500	5.0500	2.3500	0.8501	2.6000	0.7240	0.2490	S	Long Beach-Rancho los Cerritos	
			20	1.9685	5.2100	2.2100	1.1400	0.6669	1.1000	0.9140	0.3800	S	Hollywood Storage	
			21	1.5814	5.4900	2.1500	0.9740	1.1019	4.8900	0.6540	0.3190	S	Baldwin Hills	
			24	0.4604	1.0700	0.6130	0.1310	0.2975	0.2910	0.2130	0.0987	R	8510 Wonderland Avenue	
			32	0.9573	2.7000	2.4000	0.4050	0.6814	0.6480	0.3100	0.0975	S	Pacifico Mountain-Mill Creek Station	
			39	5.9914	10.7000	6.5000	0.9320	2.4128	3.3700	1.5700	0.2310	S	Tarzana-Cedar Hill Nursery A	
			46	0.6646	1.5900	0.5150	0.1330	0.1503	0.3330	0.2400	0.1510		Malibu Beach-3504 Las Flores Canyon	
1987	11	24	1315	33.08	-115.97	8	6.50	18.79	S					US
			5	8.1674	17.1000	11.7000	6.5600	6.2358	7.5200	3.7100	1.6500	R	Superstition Mountain-Camera Site 8	
1988	4	3	0356	38.13	22.84	28	4.00							GR
			23	0.5927	1.4900	0.4190	0.0763	0.1799	0.3210	0.0975	0.0382	A	Korinthos-Town Hall	
1988	4	24	1010	38.83	20.56	20	4.20							GR
			14	2.0462	4.9200	4.8000	0.7280	0.5332	1.4400	0.2990	0.0852	S	Lefkada-OTE Building	
1988	5	18	0517	38.35	20.47	26	5.00	17.04						GR
			23	1.6498	2.8100	2.7200	0.6840	0.7828	2.0400	1.1700	0.3850	R	Valsamata-Seismograph Station	
1988	5	22	0344	38.35	20.54	15	4.69							GR
			11	0.7644	1.4700	0.3260	0.2030	0.3197	0.7820	0.2240	0.0896	R	Valsamata-Seismograph Station	
1988	7	5	2034	38.10	22.86	10	5.08							GR
			19	0.6949	1.9600	0.5440	0.1270	0.2399	0.6930	0.0907	0.0581	A	Korinthos-Town Hall	
1988	10	16	1234	37.90	21.06	12	5.75	17.88	T					GR
			11	1.4546	4.4600	3.6200	1.2300	0.7453	2.1700	1.1600	0.3710	A	Zakinthos-OTE Building	
1988	10	19	0027	37.81	20.92	10	4.00							GR
			16	0.6623	1.0800	1.0300	0.1800	0.2012	0.2650	0.2090	0.0570	A	Vartolomio-I.Th. Residence[42]	
1988	10	22	0934	37.80	20.93	10	3.70							GR
			23	0.3857	0.4730	0.1860	0.0982	0.1205	0.2190	0.0935	0.0351	A	Kyllini-Police Station	
			24	0.7710	1.3600	0.8410	0.1540	0.3148	0.2530	0.0684	0.0734	A	Vartolomio-I.Th. Residence	
1988	10	23	0317	37.31	20.94	10	3.10							GR
			71	0.3620	0.6800	0.1080	0.0722	0.1509	0.1810	0.0734	0.0615	A	Kyllini-Police Station	
1988	10	31	0259	37.85	21.01	10	3.75							GR
			8	0.5462	1.1900	0.4900	0.2020	0.2638	0.1840	0.0797	0.0719	A	Vartolomio-I.Th. Residence	
			8	0.5867	1.4300	0.4340	0.1340	0.1824	0.5160	0.0905	0.0650	A	Kyllini-Police Station	
1988	12	7	0741	40.91	44.25	6	6.76	19.20	T					AR
			20	1.7883	4.3600	4.1300	3.3200	1.2660	1.8700	0.7380	1.1200	S	Gukasian	

continued on next page

[42] Only one horizontal component.

Tab. D.3: *continued*

Date			Time d	Lat. a_h	Long. $\mathrm{SA}_h(0.2)$	Depth $\mathrm{SA}_h(0.5)$	M_s $\mathrm{S}_h(1.0)$	$\log M_0$ a_v	F $\mathrm{SA}_v(0.2)$	$\mathrm{SA}_v(0.5)$	$\mathrm{SA}_v(1.0)$	S	Station	C
1988	12	7	0745	40.96	44.27	11	5.80		T					AR
			10	1.3551	3.5600	2.4200	1.2200	0.3842	1.0100	0.5690	0.2090	S	Gukasian	
1988	12	19	1729	40.80	44.22	10	4.20							AR
			3	0.9083	1.9700	0.6460	0.1150	0.2501	0.6070	0.1250	0.0396		Dzhrashen	
			8	0.4336	0.8310	0.1930	0.0424	0.1972	0.2080	0.0790	0.0262	A	Nalband	
			26	0.1613	0.3290	0.0846	0.0258	0.0469	0.1850	0.0600	0.0361	A	Stepanavan	
1988	12	22	0956	38.37	21.78	10	4.10							GR
			5	1.0779	3.2500	1.9000	0.8870	0.4922	0.9680	0.7310	0.2010	A	Nafpaktos-OTE Building	
1988	12	30	1328	40.92	43.98	10	3.90							AR
			9	0.2676	0.7300	0.1110	0.0464	0.1033	0.0838	0.0375	0.0175	R	Toros	
			16	0.1088	0.3110	0.0509	0.0177	0.0409	0.0887	0.0241	0.0111	S	Leninakan	
			17	0.7046	1.6200	0.1480	0.0624	0.2748	0.5220	0.1030	0.0174	A	Nalband	
1988	12	31	0407	40.95	43.99	5	4.17							AR
			10	1.6652	4.4900	0.2920	0.1020	0.5151	0.5670	0.0905	0.0236	R	Toros	
			18	1.2298	4.7700	0.4750	0.1710	0.3812	1.1000	0.2250	0.0827	A	Nalband	
			21	0.2920	0.8060	0.1360	0.1030	0.0902	0.1180	0.0617	0.0502	S	Leninakan	
			24	0.4753	1.1800	0.3690	0.0689	0.1725	0.3690	0.1060	0.0243		Dzhrashen	
			35	0.2510	0.6220	0.2570	0.0411	0.0667	0.1530	0.0430	0.0206	A	Stepanavan	
1989	1	4	0729	40.90	44.28	5	4.10							AR
			12	0.7449	0.9830	0.3890	0.0767	0.2832	0.3450	0.1350	0.0413	A	Nalband	
			15	0.2710	0.2560	0.0763	0.0652	0.1679	0.1160	0.0909	0.0590	A	Stepanavan	
1989	1	8	1309	40.88	44.27	10	3.70							AR
			10	1.8912	5.7100	0.6660	0.2810	0.6741	0.7890	0.1350	0.0242	A	Nalband	
			12	0.9234	1.4200	0.2040	0.0640	0.3532	0.3930	0.0458	0.0388		Dzhrashen	
			14	0.4832	0.6090	0.3380	0.0553	0.2593	0.4640	0.0876	0.0314		Metz-Parni	
1989	3	30	1636	40.98	44.03	3	4.34							AR
			14	1.7755	5.1100	1.0400	0.2690	1.1195	1.2800	0.2620	0.1820	R	Toros	
1989	10	18	0004	37.04	-121.88	18	7.17	19.66	T					US
			1	6.2756	9.8800	13.9000	5.4600	4.3069	13.1000	4.3400	1.7300	A	Corralitos-Eureka Canyon Road	
			7	5.0290	10.9000	6.0300	4.1900	3.6796	4.3500	2.6900	2.2600	A	Saratoga-Aloha Avenue	
			9	5.1588	12.9000	8.3000	4.7000	5.3398	17.8000	2.2500	1.5200	S	Capitola-Fire Station	
			12	3.7316	10.9000	6.3800	2.5100	1.8967	2.8300	1.4200	0.4760	A	Gilroy-Gavilan College	
			12	4.5297	12.8000	11.7000	3.1700	2.0885	3.5900	2.0100	0.6980	R	Gilroy Array-Station 1	
			14	3.5516	8.6800	7.4700	3.9400	2.8745	4.5200	1.7300	0.8750	S	Gilroy Array-Station 2	
			15	5.2072	19.6000	10.5000	3.2500	2.8602	3.0100	2.2000	1.4200	S	Gilroy Array-Station 3	

continued on next page

Tab. D.3: *continued*

Date			Time	Lat.	Long.	Depth	M_s	$\log M_0$	F					C
			d	a_h	$\mathrm{SA}_h(0.2)$	$\mathrm{SA}_h(0.5)$	$\mathrm{S}_h(1.0)$	a_v	$\mathrm{SA}_v(0.2)$	$\mathrm{SA}_v(0.5)$	$\mathrm{SA}_v(1.0)$	S	Station	
			15	4.4822	13.4000	4.9300	2.7600	3.6121	5.3700	1.1900	0.4930	A	USCS Santa Cruz-Lick Observatory	
			15	2.9014	4.6400	6.2500	4.3600	1.5038	3.4300	1.6900	1.2500	A	Gilroy-2 Story Hist. Com. Building	
			20	4.0089	6.1300	9.4300	3.4900	1.5740	3.3600	1.0500	0.9880	S	Gilroy Array-Station 4	
			24	1.7079	4.7400	2.6400	2.0100	0.9160	2.0600	1.1300	0.5500	A	Gilroy Array-Station 6	
			24	2.4833	2.9600	6.3900	6.6500	2.0813	4.2800	1.2800	1.6200	S	Hollister-City Hall Annex	
			25	2.6686	4.4700	9.0200	5.2400	1.5551	4.8900	1.1900	0.9220	S	Hollister-Differential Array (Airport)	
			25	3.4908	5.3600	11.3000	9.6100	1.9444	4.8000	1.6400	1.0200		Hollister-South Street & Pine Drive	
			25	1.6742	4.5500	2.7600	1.8100	0.9484	1.7200	1.6800	1.0300	S	Santa Clara-Agnew State Hospital	
			27	2.2358	7.9100	4.1900	2.7300	1.0336	1.2600	1.1400	0.7980	S	Sunnyvale-1058 Colton Avenue	
			28	3.1539	6.7600	7.0700	0.9820	1.1220	2.4700	0.5060	0.2850	S	Gilroy Array-Station 7	
			31	2.7847	5.8200	7.1400	5.4300	0.9374	2.7300	1.9800	1.0300	S	Stanford University-Ground (Test Lab)	
			35	2.3075	5.5100	7.3500	3.2800	1.4408	2.8900	1.0500	1.6400		Stanford University-Amphitheatre	
			36	2.5618	5.7100	4.6700	4.1500	1.0091	2.2400	0.8490	1.0700	S	Menlo Park-Veterans Hospital	
			42	1.8903	4.2500	2.7400	1.8100	0.6528	1.8700	1.1300	0.5870	S	Calaveras Array-Emerson	
			44	3.1295	5.1500	7.7900	4.3800	1.0547	2.4500	1.4100	0.6130	L	Foster City-Redwood Shores	
			47	2.5994	2.7400	4.9600	11.3000	0.7861	1.9500	1.1200	1.1500	L	Redwood City-Apeel 2	
			60	3.2094	4.5600	7.1100	3.6100	0.6460	1.0700	1.1700	0.9280	S	San Francisco-Airport (Engrg. Building)	
			72	1.1134	1.8500	2.3300	1.3200	0.4088	0.7880	1.0000	0.7600	A	Diamond Heights Fire Station	
			72	2.2471	4.1100	5.3400	5.3400	1.2460	2.1400	1.0800	0.7180	S	Oakland-Two Story Office Building	
			74	2.7681	5.6600	5.8300	6.7600	0.7637	1.7900	1.3500	0.8860	S	Oakland-Outer Harbour Wharf	
			74	0.8038	1.3800	1.7600	1.1800	0.2795	0.4940	0.8290	0.4670	R	Rincon Hill	
			76	0.5255	0.9660	1.0000	1.5000	0.2502	0.4450	0.7290	0.6360	R	Pacific Heights Fire Station	
			77	0.6609	0.9710	1.5400	0.7800	0.2642	0.4840	0.6700	0.5870	R	Yerba Buena Island	
			78	1.9315	3.5900	5.2400	2.9300	0.5796	1.0600	1.2200	1.4700	A	Presidio	
			79	1.0756	1.8200	2.4700	2.8100	0.5718	0.7340	1.4400	1.0400	A	Cliff House	
			79	1.3795	2.2400	3.6600	3.1000	0.1429	0.4000	0.1760	0.1200	L	Treasure Island (Naval Fire Station)	
			81	2.3881	4.7700	5.7900	6.5400	0.5609	1.3300	0.5810	0.9760	S	Emeryville-Pacific Park Plaza Building	
1989	10	29	1909	36.78	2.44	6	5.67	18.00	T					AL
			61	0.3759	0.9280	0.6720	0.1610	0.2261	0.6610	0.2490	0.1050	R	Alger-Bouzareah	
1990	5	5	0721	40.65	15.92	12	5.60	17.75						IT
			31	0.9270	2.8200	1.2100	0.7600	0.3109	0.7560	0.6550	0.2350	A	Brienza	
			37	0.8657	1.8600	1.2600	0.8210	0.7120	1.4900	1.2300	0.4820	R	Rionero in Vulture	
1990	5	17	0844	38.39	22.22	26	4.77							GR
			4	1.9604	6.6900	1.6600	0.3220	0.7219	1.1100	0.6340	0.1680	A	Aigio-OTE Building	
1990	6	20	2100	36.96	49.41	19	7.46	20.04						IR

continued on next page

Tab. D.3: *continued*

Date			Time	Lat.	Long.	Depth	M_s	$\log M_0$	F					C
			d	a_h	$\mathrm{SA}_h(0.2)$	$\mathrm{SA}_h(0.5)$	$\mathrm{S}_h(1.0)$	a_v	$\mathrm{SA}_v(0.2)$	$\mathrm{SA}_v(0.5)$	$\mathrm{SA}_v(1.0)$	S	Station	
			51	1.8880	4.4900	2.2800	1.1000	0.8562	2.2200	0.9360	0.6810	A	Qazvin	
			65	0.9261	2.7200	1.8700	1.3300	0.7382	1.2700	1.0200	0.6820	S	Rudsar	
			67	1.9191	5.0100	7.4100	2.1800	0.7597	1.2100	0.9660	0.8420	S	Abhar	
			78	1.1813	1.6200	2.8100	2.5500	0.3502	0.6420	0.6640	0.5150	S	Tonekabun	
			151	1.0465	2.8500	0.7150	0.4700	0.4003	0.9140	0.8010	0.2530	A	Gachsar	
1990	8	3	1525	36.87	49.54	10	3.90							IR
			20	0.4233	0.6290	0.0975	0.0185	0.1666	0.2230	0.0243	0.0129		Zietune	
1990	8	6	1124	36.94	49.36		4.40							IR
			14	0.4630	0.3960	0.0996	0.0322	0.2542	0.2190	0.0388	0.0179	S	Rudbar	
			24	0.1823	0.3460	0.1310	0.0217	0.1064	0.1760	0.0410	0.0087		Zietune	
1990	8	11	0845	36.86	49.42	6	3.40							IR
			15	0.6336	0.2880	0.0355	0.0126	0.1342	0.0549	0.0087	0.0101		Zietune	
1990	8	20	1220	36.81	49.88	11	5.00							IR
			17	1.3528	3.0100	0.8670	0.1300	0.7312	0.8710	0.2500	0.0503		Barorud	
			33	0.8998	1.1400	0.4090	0.1010	0.4849	0.2720	0.1770	0.0545		Ilja Tube	
1990	8	21	0347	37.09	49.59	8	5.00							IR
			23	1.4805	0.6750	0.2340	0.1070	0.6362	0.2280	0.3070	0.0449		Ilja Tube	
			33	1.1328	2.7300	0.7280	0.1430	0.5449	0.8180	0.2770	0.0434	S	Rudbar	
1990	8	23	0650	36.91	49.41	8	4.40							IR
			10	0.4198	0.3930	0.0588	0.0238	0.2885	0.2090	0.0586	0.0193		Ilja Tube	
1990	8	26	0941	36.85	49.44	6	3.30							IR
			3	0.4645	0.3540	0.0638	0.0169	0.1571	0.1350	0.0228	0.0162	S	Rudbar	
1990	8	27	1736	36.75	49.70	9	3.90							IR
			4	0.3228	0.1870	0.0243	0.0125	0.2021	0.0588	0.0103	0.0060		Barorud	
1990	8	30	0341	36.90	49.44		3.40							IR
			8	0.3127	0.1620	0.0267	0.0097	0.1128	0.1300	0.0221	0.0053		Ilja Tube	
1990	9	14	0411	36.83	49.72	7	4.30							IR
			5	1.2992	1.2700	0.1840	0.0345	0.3015	0.3340	0.0477	0.0084		Barorud	
1990	9	14	2244	36.90	49.55	3	3.10							IR
			2	0.2172	0.0535	0.0230	0.0079	0.4437	0.0441	0.0171	0.0103		Ilja Tube	
1990	9	15	1354	36.87	49.45	9	3.90							IR
			2	0.7617	0.8510	0.1190	0.0410	0.4909	0.4640	0.0547	0.0226		Gandja	
			7	0.4135	0.6670	0.1260	0.0478	0.2873	0.2730	0.0732	0.0269		Ilja Tube	
1990	9	18	1538	36.87	49.65	3	3.80							IR
			10	0.4075	0.3800	0.0243	0.0081	0.1161	0.1070	0.0097	0.0077		Barorud	

continued on next page

Tab. D.3: *continued*

Date			Time d	Lat. a_h	Long. $\mathrm{SA}_h(0.2)$	Depth $\mathrm{SA}_h(0.5)$	M_s $\mathrm{S}_h(1.0)$	$\log M_0$ a_v	F $\mathrm{SA}_v(0.2)$	$\mathrm{SA}_v(0.5)$	$\mathrm{SA}_v(1.0)$	S	Station	C
1990	9	20	0342	36.86	49.46	3	3.30							IR
			1	0.8931	0.1030	0.0305	0.0121	0.3291	0.0538	0.0314	0.0155		Gandja	
1990	12	13	0024	37.53	15.47	5	5.20	17.52						IT
			35	0.3710	0.7380	0.6830	0.1880	0.1361	0.3750	0.3640	0.0585	S	Giarre	
			39	2.3907	6.1800	2.0000	0.7430	0.6208	1.5300	0.3870	0.2520	S	Catania-Piana	
			56	1.0048	1.5600	1.4300	1.0000	0.3829	0.7390	0.8990	0.1850	R	Sortino	
			75	0.6761	2.0200	1.2100	0.6850	0.3738	0.6180	0.6590	0.1540	R	Vizzini	
			79	0.8377	1.3100	0.7530	1.0100	0.3450	0.3780	0.4660	0.3740	R	Noto	
			97	0.6196	0.7320	0.3460	0.1470	0.1519	0.3490	0.1000	0.0854	A	Pachino	
1990	12	15	1038	40.86	44.29	5	3.10							AR
			3	0.3952	0.5540	0.0686	0.0141	0.2605	0.1460	0.0364	0.0115	A	Spitak-Karadzor	
1990	12	16	1545	41.37	43.72	28	5.25	17.23						AR
			15	0.4074	1.2700	0.6490	0.2090	0.5879	0.9570	0.2040	0.1690	A	Bogdanovka	
			20	0.3319	0.6590	0.2750	0.1140	0.1170	0.3140	0.0773	0.0448	R	Akhalkalaki	
			29	1.0623	2.4100	0.8710	0.5040	0.6645	1.4500	0.3520	0.0960	A	Bavra	
			44	0.4063	1.2200	0.2660	0.0844	0.1167	0.3610	0.0752	0.0410	R	Bakuriani	
			51	0.5887	1.7500	0.2250	0.1630	0.2376	0.4820	0.0601	0.0273	R	Toros	
			70	0.2223	0.3320	0.1230	0.0799	0.0866	0.1200	0.0669	0.0495	A	Stepanavan	
			77	0.1108	0.2700	0.1300	0.0598	0.1101	0.1220	0.0537	0.0301	A	Spitak-Karadzor	
1990	12	22	1727	9.96	84.24	7	5.70	18.00	S					CR
			7	4.3854	9.8900	8.3800	3.2800	1.9910	3.4400	6.0300	0.5370		Alajuela	
1990	12	23	2128	41.65	44.30	5	4.10							GE
			73	0.1164	0.0601	0.0234	0.0120	0.0377	0.0414	0.0217	0.0089	A	Stepanavan	
1991	1	11	0604	40.90	44.33	5	3.30							AR
			6	1.3068	1.6000	0.1910	0.0340	1.3902	0.4400	0.0503	0.0164	A	Spitak-Karadzor	
1991	3	19	1209	34.92	26.36	7	5.36	17.40						GR
			40	0.5632	1.8800	0.7630	0.1790	0.1703	0.4640	0.1370	0.0395	A	Sitia-OTE Building	
1991	4	29	0912	42.39	43.68	6	6.97	19.52	T					GE
			108	0.1072	0.2190	0.3130	0.1240	0.0618	0.2390	0.1570	0.0509	R	Akhalkalaki	
			163	0.1058	0.4050	0.1070	0.0376	0.0405	0.0701	0.0460	0.0241	R	Toros	
1991	5	3	2019	42.60	43.15	6	5.36	17.49						GE
			9	4.9223	14.2000	8.9700	1.8500	1.3609	1.8000	1.5200	1.0300	S	Ambrolauri	
			24	0.4681	1.8400	0.3900	0.1050	0.1569	0.6480	0.1470	0.1390	S	Oni-Base Camp	
			24	0.7682	3.6700	0.4610	0.1520	0.3293	0.5140	0.1240	0.0530	A	Oni	
			34	0.2331	0.5580	0.5840	0.1070	0.1366	0.3450	0.3110	0.0546	A	Iri	

continued on next page

Tab. D.3: *continued*

Date			Time d	Lat. a_h	Long. $SA_h(0.2)$	Depth $SA_h(0.5)$	M_s $S_h(1.0)$	$\log M_0$ a_v	F $SA_v(0.2)$	$SA_v(0.5)$	$SA_v(1.0)$	S	Station	C
1991	5	3	2341	42.58	43.29	6	4.43							GE
			12	0.3544	1.2500	0.3030	0.0971	0.1052	0.2320	0.1180	0.0307	S	Oni-Base Camp	
			12	0.4516	1.5400	0.3100	0.0624	0.1945	0.2720	0.1950	0.0380	A	Oni	
			13	2.0290	4.8700	4.5600	0.8760	0.5436	1.6300	0.9630	0.3190	S	Ambrolauri	
			23	0.1952	0.5980	0.4780	0.0733	0.1053	0.3490	0.1290	0.0392	A	Iri	
1991	5	10	0125	42.58	43.22	8	4.40							GE
			8	0.3733	1.0400	0.4250	0.1510	0.2095	0.5960	0.2010	0.0870	S	Ambrolauri	
			10	0.6429	1.8400	0.8620	0.1240	0.1824	0.6710	0.2770	0.0524	A	Zemo Bari	
			30	0.1289	0.3120	0.2440	0.1550	0.0778	0.2420	0.1140	0.0256		Sackhere	
1991	5	10	2030	42.46	43.48	4	4.50							GE
			9	0.5023	1.5300	0.3200	0.0759	0.3259	0.5740	0.1560	0.0264	A	Iri	
			13	0.7558	1.7700	0.3730	0.0730	0.1360	0.2530	0.0510	0.0265	S	Oni-Base Camp	
			14	0.1146	0.2050	0.1580	0.1040	0.0631	0.1360	0.0722	0.0111		Sackhere	
			16	0.2701	0.8310	0.9160	0.0645	0.1468	0.6760	0.3150	0.0283	A	Zemo Bari	
			28	0.0619	0.2180	0.1050	0.0407	0.0316	0.0627	0.0480	0.0262	S	Ambrolauri	
1991	5	14	0936	42.47	43.46	5	3.80							GE
			9	1.0438	2.0400	0.5820	0.1120	0.4942	0.9440	0.2640	0.0386	A	Iri	
			13	0.6285	2.2300	0.1260	0.0309	0.1789	0.2640	0.0535	0.0194	A	Oni	
			14	0.0869	0.2140	0.1760	0.0308	0.0489	0.1490	0.0444	0.0183	A	Zemo Bari	
1991	5	15	1428	42.54	43.35	6	4.23							GE
			4	1.6345	3.6600	3.7900	0.4660	1.1058	3.4300	1.1100	0.1410	A	Zemo Bari	
			8	0.6501	1.9500	0.4560	0.1000	0.1502	0.2620	0.1090	0.0782	S	Oni-Base Camp	
			9	0.5280	1.2400	0.2110	0.0913	0.2178	0.2040	0.0854	0.0412	A	Oni	
			16	0.4814	0.7250	0.6530	0.1010	0.0817	0.2530	0.1330	0.1010	S	Ambrolauri	
			17	0.4075	0.8500	0.4980	0.1460	0.1846	0.5370	0.2070	0.0465	A	Iri	
1991	6	2	0610	42.48	43.54	10	3.70							GE
			14	0.4055	0.5630	0.0629	0.0255	0.1704	0.0615	0.0234	0.0124	A	Oni	
			20	0.1187	0.3030	0.1340	0.0229	0.0993	0.3460	0.0415	0.0127	A	Zemo Bari	
1991	6	15	0059	42.44	44.03	6	6.24	18.45	T					GE
			36	1.1009	1.8600	3.0600	0.7310	0.4173	0.6790	1.0300	0.5160	A	Iri	
			47	0.3484	1.0200	0.5890	0.3410	0.1530	0.3690	0.2750	0.1750	S	Oni-Base Camp	
			47	0.6921	2.9200	0.7440	0.3320	0.1566	0.3500	0.4860	0.1280	A	Oni	
			54	0.6069	1.1200	1.4300	0.5580	0.2393	0.8450	0.3770	0.2900	A	Zemo Bari	
1991	6	17	0026	34.87	24.42	21	3.07							GR
			21	0.3158	1.4200	0.3030	0.0686	0.2197	0.5260	0.2280	0.0352		Rethimno-OTE Building	

continued on next page

Tab. D.3: *continued*

Date			Time d	Lat. a_h	Long. $SA_h(0.2)$	Depth $SA_h(0.5)$	M_s $S_h(1.0)$	$\log M_0$ a_v	F $SA_v(0.2)$	$SA_v(0.5)$	$SA_v(1.0)$	S	Station	C
1991	6	28	1443	34.24	-118.01	9	5.33	17.55	S					US
			15	2.7911	5.3200	3.5700	1.5400	1.3784	1.8000	3.2700	0.6640	R	Pasadena-Old Seismic Laboratory	
1991	10	6	0146	41.07	43.44	2	4.85	16.73						TU
			40	0.1349	0.5090	0.0684	0.0346	0.0650	0.1200	0.0395	0.0218	R	Toros	
1992	3	13	1718	39.72	39.63	10	6.89	19.40	S					TU
			1	5.6544	12.0000	8.3300	7.1000	2.4963	4.0800	2.7600	1.6700	A	Erzincan-Meteorologij Mudurlugu	
			62	0.6987	2.4100	0.9000	0.7960	0.3461	0.9880	0.3510	0.2490	A	Refahiye-Kaymakamlik Binasi	
1992	3	15	1616	39.53	39.93	10	5.48	17.88	S					TU
			45	0.3800	0.7300	1.4400	0.4170	0.1783	0.5600	0.3140	0.1500	A	Erzincan-Meteorologij Mudurlugu	
1992	3	25	0358	39.59	39.62	18	3.00							TU
			20	0.9543	0.3640	0.1790	0.1110	0.5564	0.3370	0.1050	0.0717	A	Erzincan 1 (Esentepe)	
1992	4	23	0450	33.96	-116.32	12	6.20	18.26	S					US
			15	1.9323	7.9300	3.1600	1.5600	1.8237	4.0000	1.2800	1.0600	S	Thousand Palms-Post Office	
			21	1.6648	4.8700	3.0700	1.0800	0.9126	1.7600	0.8260	0.3030	S	North Palm Springs-Post Office	
			23	1.2391	2.3300	1.8900	1.1500	0.8410	1.0600	1.1900	0.8190	S	Morongo Valley-Fire Station	
			24	3.9622	5.5100	6.0700	7.3900	0.9731	1.4900	1.0300	1.5700	S	Indio-Jackson Road	
			30	2.0003	6.9300	3.1700	0.8380	1.4375	4.9900	1.4300	0.2900	A	White Water Canyon-Trout Farm	
1992	4	25	1806	40.37	-124.32	15	7.10	19.92	T					US
			0	14.6830	26.4000	15.4000	7.3500	7.3891	10.3000	6.3800	3.6700	R	Cape Mendocino (C)	
			9	2.2497	3.8600	6.7800	3.8000	0.7997	1.8400	1.8700	0.8950	R	Bunker Hill	
			14	4.2350	11.0000	9.7100	5.5800	1.1103	1.8200	2.7100	1.0200	A	Centreville Beach	
			18	3.4151	6.5400	8.7700	7.3200	0.7062	1.2900	1.0200	0.9750	S	Ferndale Fire Station	
			24	3.4656	6.1600	13.9000	3.4400	0.7952	2.7700	1.2800	0.8810	A	Fortuna Fire Station	
			27	2.4578	7.6000	3.9500	2.6300	1.2550	3.9000	2.0700	0.7200		Loleta Fire Station	
			33	1.4409	3.4400	6.2300	2.5800	0.7036	1.4600	0.9560	1.1300	A	College of the Redwoods	
			36	2.2199	9.0200	0.7690	0.2410	0.4945	0.9380	0.3980	0.1290	A	Shelter Cove-Airport (C)	
			37	1.9711	3.4700	6.9100	3.0800	0.5135	0.8810	1.1500	0.5480	A	South Bay Union School	
			54	1.4790	3.0400	4.4700	2.3800	0.7099	1.2500	1.5800	1.0200	A	Butler Valley (ERVA)	
1992	4	26	0741	40.55	-124.25	20	6.50	18.78	S					US
			22	4.1645	8.3100	9.5000	3.7100	0.9821	1.2900	2.2600	0.9870	A	Centreville Beach	
			22	1.5149	2.6100	4.7300	2.9800	0.5973	0.7950	1.5700	0.3770	R	Bunker Hill	
			29	2.7901	5.4800	10.7000	5.3000	0.5801	1.5700	1.4400	0.7890	S	Ferndale Fire Station	
			36	2.3840	4.9100	3.4700	2.7400	1.3810	2.8400	0.8980	0.5430		Loleta Fire Station	
			37	3.9249	7.5000	9.6400	5.4800	0.5491	1.2700	0.8330	0.9070	A	Fortuna Fire Station	
			42	1.9451	2.1800	3.7000	2.8900	0.4657	1.0600	0.9490	1.0700	A	College of the Redwoods	

continued on next page

Tab. D.3: *continued*

Date			Time	Lat.	Long.	Depth	M_s	$\log M_0$	F					C
			d	a_h	$SA_h(0.2)$	$SA_h(0.5)$	$S_h(1.0)$	a_v	$SA_v(0.2)$	$SA_v(0.5)$	$SA_v(1.0)$	S	Station	
			45	1.5121	5.8300	2.2300	1.2800	0.2702	0.5590	0.6040	0.3790	A	South Bay Union School	
			68	0.9308	2.2500	2.3400	1.3100	0.2424	0.5520	0.6670	0.2900	A	Butler Valley (ERVA)	
1992	4	26	1118	40.42	-124.41	22	6.50	19.00	S					US
			26	2.3782	2.7100	4.3100	8.6000	0.3813	0.9180	1.0600	0.7090	R	Bunker Hill	
			27	2.1981	9.5500	4.3700	1.6900	1.0554	1.9600	2.0400	0.5810	A	Centreville Beach	
			33	2.9598	3.5800	6.9000	7.0900	0.8099	1.5100	0.8190	1.3300	S	Ferndale Fire Station	
			41	1.1193	2.1200	2.7800	1.6700	1.0215	1.7300	0.7800	0.5400		Loleta Fire Station	
			42	2.1884	3.5700	4.1700	3.6000	0.6661	1.5100	0.8640	0.8720	A	Fortuna Fire Station	
			47	1.4847	2.5400	3.5800	0.7920	0.3827	0.6360	0.8070	0.4700	A	College of the Redwoods	
			50	1.1621	4.7600	2.2700	0.5860	0.3444	0.7770	0.6830	0.2060	A	South Bay Union School	
1992	5	15	0043	47.16	9.53	11	3.50							LI
			2	0.7411	0.5800	0.1900	0.0665	0.3264	0.2540	0.1480	0.0505	A	Schaan-Hilti	
			4	0.2011	0.3190	0.0636	0.0242	0.2452	0.1570	0.0447	0.0210	A	Buchs-Gewerbestrasse	
			4	0.1436	0.3050	0.1390	0.0791	0.2743	0.2530	0.0483	0.0184	S	Buchs-Werdenberg	
1992	5	30	1855	38.04	21.45	12	4.77							GR
			33	0.4500	1.0600	0.7910	0.4080	0.2609	0.3850	0.1980	0.1430	A	Patra-San Dimitrios Church	
1992	6	28	1157	34.19	-116.53	1	7.55	20.04	S					US
			3	7.7389	12.5000	5.9600	4.6900	8.0696	5.8200	3.8400	3.3100	R	Lucerne Valley (C)	
			11	2.7838	4.8100	6.7300	5.2200	1.7773	5.0300	4.6800	1.7200	A	Joshua Tree-Fire Station (C)	
			20	2.1670	4.0300	7.6500	2.5400	1.6060	2.6000	1.3600	1.2900	S	Morongo Valley-Fire Station	
			24	2.4002	4.2800	5.3700	4.9200	1.3324	4.7200	1.4200	1.5200	S	Yermo-Fire Station (C)	
			24	1.6745	5.2000	3.0200	3.3500	1.6373	2.2200	1.2800	1.5900	S	Desert Hot Springs-Fire Station (C)	
			27	2.1026	6.9800	4.7000	2.3900	1.0085	2.2700	1.8000	0.4530	A	Fun Valley-Reservoir 361	
			30	1.2586	3.2000	2.5300	2.2100	0.9827	2.2400	1.3100	0.8930	A	North Palm Springs-Fire Station	
			30	1.2320	3.3900	1.8400	1.4800	0.9898	2.5200	1.0000	0.5020	A	White Water Canyon-Trout Farm	
			36	1.3263	2.2200	2.8600	2.2100	0.6438	1.9500	0.6480	0.6770	A	Barstow-Vineyard (C)	
			39	0.9991	3.4200	2.3300	2.0700	0.7958	1.7600	0.8760	0.9700	S	Thousand Palms-Post Office	
			39	0.8721	1.8900	2.1600	2.2100	1.0618	1.1000	0.8340	0.8400	S	Palm Springs-Airport (C)	
			41	0.7867	2.1200	0.5230	0.2660	0.3879	0.7360	0.2470	0.2070	R	Joshua Tree-29 Palms (C)	
			47	1.1091	2.8900	1.8400	1.6900	0.8020	1.2000	0.9950	0.5210	A	Forest Falls-Post Office	
			51	2.9145	3.8200	6.8600	4.5400	0.8180	1.0400	0.7090	1.5500	S	Indio-Jackson Road	
			53	0.4892	0.9900	0.8740	0.2860	0.3730	0.6170	0.4340	0.2300	R	Banning-Silent Valley (Poppet Flat) (C)	
			56	1.0730	2.6000	3.0300	1.6900	0.4095	0.7870	0.6440	1.1800	S	Indio-Coachella Canal (C)	
			68	1.4322	3.7700	3.0000	2.1900	0.8805	2.0900	1.2600	0.7910	R	Amboy (C)	
			71	0.9517	1.9900	1.4200	1.0200	0.6139	1.0900	0.7320	0.1540	S	Hemet-Stetson Avenue Fire Station (C)	

continued on next page

Tab. D.3: *continued*

Date			Time	Lat.	Long.	Depth	M_s	$\log M_0$	F					C
			d	a_h	$SA_h(0.2)$	$SA_h(0.5)$	$S_h(1.0)$	a_v	$SA_v(0.2)$	$SA_v(0.5)$	$SA_v(1.0)$	S	Station	
			98	0.4179	1.7100	0.3980	0.3730	0.3934	0.4500	0.2350	0.1450	A	Riverside-Airport (C)	
1992	6	28	1505	34.27	-116.78	15	6.52	18.83	S					US
			13	5.3423	11.4000	5.8900	1.9700	1.9027	4.2200	0.9920	0.6190	A	Big Bear Lake-Civic Center (C)	
			26	1.4971	3.7800	3.5300	2.4200	1.9261	4.2800	1.4700	0.7500	S	Morongo Valley-Fire Station	
			31	1.5296	5.5500	1.5400	0.8840	0.7652	1.2200	0.7030	0.2500	A	San Bernardino-Highland Fire Station	
			38	1.4218	4.9800	3.3100	1.4800	1.1987	1.8400	1.0100	0.8730	A	North Palm Springs-Fire Station	
			39	0.9878	2.2400	2.3100	2.0200	0.7128	1.5300	0.7940	0.7780	S	San Bernardino-Hospital (C)	
			48	1.1170	2.8200	2.2700	0.9220	0.5902	1.1300	1.0400	0.2180	A	Fun Valley-Reservoir 361	
1992	11	6	1908	38.16	27.00	17	5.97	18.11						TU
			58	0.3017	0.9780	0.6480	0.2270	0.1261	0.4010	0.1480	0.0666		Ilica-Meteoroloji Mudurlugu	
1992	11	18	2110	38.26	22.37	15	5.72	17.93						GR
			25	0.3599	1.2400	0.3010	0.1100	0.2594	0.4870	0.2370	0.0703	A	Aigio-OTE Building	
			30	1.0612	2.0800	1.5800	0.2430	0.3011	0.7520	0.2030	0.1340		Amfissa-OTE Building	
1993	1	7	0447	38.35	21.84	5	3.20							GR
			6	0.4529	0.9730	0.6250	0.1470	0.1813	0.4740	0.3450	0.0556	A	Nafpaktos-OTE Building	
1993	3	26	1145	37.68	21.44	10	4.64							GR
			1	1.7574	3.2000	1.0900	0.3800	0.7713	0.8570	0.2090	0.0719	S	Pirgos-Agriculture Bank	
1993	3	26	1156	37.71	21.38	10	5.15							GR
			7	1.0997	3.9300	0.6830	0.2230	0.5033	0.7690	0.1080	0.0716	S	Pirgos-Agriculture Bank	
1993	3	26	1158	37.59	21.39	10	5.08	17.21						GR
			10	4.2847	6.7700	4.5100	1.1500	1.1949	0.9770	0.5300	0.1710	S	Pirgos-Agriculture Bank	
1993	6	4	0324	38.70	20.45	27	3.60							GR
			16	0.5492	1.1800	0.7860	0.1700	0.5861	0.7240	0.3540	0.0928	A	Vasiliki-Town Hall	
1993	6	13	2326	39.26	20.58	15	4.99	17.02						GR
			33	1.4392	3.2200	1.9700	0.2960	0.8133	1.2300	0.1450	0.0408	S	Lefkada-OTE Building	
			37	0.1845	0.2980	0.5670	0.3970	0.1159	0.2410	0.2420	0.1360	A	Preveza-OTE Building	
1993	7	14	1231	38.18	21.76	15	5.39	17.51						GR
			7	3.2725	5.0200	2.3800	0.9690	1.1574	1.1300	0.5350	0.2980	A	Patra-San Dimitrios Church	
			25	0.4971	1.3300	1.1900	0.3490	0.3689	0.8230	0.7150	0.1300	A	Nafpaktos-OTE Building	
			29	0.4833	1.7200	0.6520	0.2370	0.2540	0.5570	0.1670	0.0829	A	Aigio-OTE Building	
1993	9	26	0753	37.68	20.79	10	4.20							GR
			15	0.5883	1.0100	0.2620	0.1150	0.1310	0.3340	0.1250	0.0335	A	Zakinthos-Town Hall[43]	
1993	11	4	0518	38.34	21.91	10	5.09							GR

continued on next page

[43] Only one horizontal component.

Tab. D.3: *continued*

Date			Time	Lat.	Long.	Depth	M_s	$\log M_0$	F					C
			d	a_h	$SA_h(0.2)$	$SA_h(0.5)$	$S_h(1.0)$	a_v	$SA_v(0.2)$	$SA_v(0.5)$	$SA_v(1.0)$	S	Station	
			10	1.0115	2.8900	2.6700	0.8540	0.5306	1.3600	1.1700	0.1710	A	Nafpaktos-OTE Building	
			18	0.2723	0.6860	0.3250	0.0646	0.2020	0.2270	0.1000	0.0651	A	Aigio-OTE Building	
1993	12	23	1422	36.80	2.98	18	5.10	16.93	N					SP
			6	0.2523	0.8950	0.3150	0.0571	0.1363	0.1970	0.0870	0.0370	R	Adra-Refugio de la Plaza	
			71	0.0089	0.0197	0.0197	0.0118	0.0044	0.0103	0.0087	0.0090	S	Granada-Facultad de Ciencias	
			110	0.0173	0.0597	0.0282	0.0329	0.0104	0.0214	0.0155	0.0106		Vera-Local Ayto	
1994	1	4	0803	36.61	2.80	16	4.80							SP
			25	0.5932	1.4100	0.5370	0.2140	0.4356	1.0400	0.5120	0.0722	R	Adra-Refugio de la Plaza	
			41	0.1996	0.5090	0.1790	0.0773	0.1652	0.3280	0.0561	0.0439	A	Almeria	
			96	0.0122	0.0187	0.0277	0.0231	0.0047	0.0101	0.0108	0.0104	S	Granada-Facultad de Ciencias	
			109	0.0117	0.0392	0.0128	0.0117	0.0085	0.0211	0.0066	0.0051		Vera-Local Ayto	
1994	1	14	0607	37.61	20.88	10	4.54							GR
			19	0.8326	1.1500	0.6090	0.2200	0.1926	0.3220	0.1840	0.0588	A	Zakinthos-Town Hall[44]	
1994	1	17	1230	34.16	-118.57	14	6.81	19.08						US
			0	3.8533	10.9000	9.1300	4.8500	5.0020	5.4600	2.8500	2.2600	S	7769 Topanga Canyon Boulevard	
			0	2.8350	4.5600	8.4700	7.6800	2.8322	6.0100	5.0900	3.5400	S	26835 West Pico Canyon Road	
			0	8.9668	11.8000	18.7000	7.0900	3.8491	7.5100	4.7000	1.3800	A	6334 Katherine Road	
			0	3.0993	8.6000	3.6600	0.9200	2.5070	4.8400	1.8400	1.1800	R	6633 Canoga Avenue (Building 026)[45]	
			0	5.7819	13.7000	16.1000	11.5000	5.3734	11.1000	8.2100	2.4700	S	Newhall-Fire Station (C)	
			0	8.2676	12.1000	19.7000	8.5200	5.2498	8.6800	2.2500	1.7500	S	Sylmar-County Hospital (Parking Lot) (C)	
			0	4.4400	10.3000	13.5000	8.0500	7.8500	11.8000	6.2200	3.1000	S	Northridge-17645 Saticoy Street (C)	
			0	7.5722	14.1000	16.8000	17.9000	8.1488	20.0000	7.3400	3.9700	S	Rinaldi Receiving Station	
			1	17.4450	26.4000	29.5000	7.7800	10.2750	33.3000	7.7900	2.4400	S	Tarzana-Cedar Hill Nursery A (C)	
			5	4.5687	14.0000	11.2000	6.2800	2.8255	5.3900	2.8200	1.2200	S	16628 West Lost Canyon Road	
			5	3.3732	7.9100	5.9800	5.1700	5.4137	7.9200	3.0800	1.5500	S	Arleta-Nordhoff Avenue Fire Station (C)	
			6	3.2842	8.3800	5.3000	1.1700	1.7743	3.9400	1.2200	0.5450	A	Topanga-Topanga Fire Station	
			7	4.3253	9.4800	7.2500	6.0300	2.9401	3.7400	3.3300	2.6100	S	Sun Valley-13248 Roscoe Boulevard	
			8	4.2421	7.4400	11.5000	5.2300	1.7664	2.8300	2.5700	1.6200	A	Pacoima Dam-Kagel Canyon (C)	
			9	1.9317	4.1900	7.0600	3.0100	1.6027	2.5700	2.8600	0.8950	A	12001 Chalon Road	
			9	2.9773	11.9000	4.9900	3.8600	2.7318	3.9400	2.4700	0.8010	A	6850 Coldwater Canyon Avenue	
			10	4.5648	16.3000	6.1700	1.7300	1.7503	6.9000	1.4300	1.3300	S	17291 Sunset Boulevard	
			10	4.6565	11.1000	21.6000	10.4000	3.1158	10.3000	5.8900	2.6100	S	14145 Mulholland Drive	

continued on next page

[44] Only one horizontal component.
[45] Only one horizontal component.

Tab. D.3: *continued*

Date	Time	Lat.	Long.	Depth	M_s	$\log M_0$	F					C
	d	a_h	$\mathrm{SA}_h(0.2)$	$\mathrm{SA}_h(0.5)$	$\mathrm{S}_h(1.0)$	a_v	$\mathrm{SA}_v(0.2)$	$\mathrm{SA}_v(0.5)$	$\mathrm{SA}_v(1.0)$	S	Station	
	10	3.6395	6.4900	6.9400	2.9900	1.3969	1.5600	1.5100	0.5490	A	Stone Canyon Reservoir	
	12	1.8189	3.4000	2.2800	1.1500	1.2070	1.5900	1.0100	0.4280	A	Monte Nido Fire Station	
	12	1.6093	4.0600	6.2700	2.5000	1.3381	4.3500	1.4100	0.7020	A	Brentwood V.A. Hospital (Bldg 259)	
	13	6.1784	15.7000	6.7900	3.4400	2.9500	13.5000	1.9700	1.2700	A	12520 Mulholland Drive	
	13	2.7551	7.4900	4.0600	3.3400	1.8861	4.1400	1.4300	0.7850	A	700 North Faring Road	
	13	4.6455	8.7900	4.6700	2.3500	2.6060	8.0600	1.8400	1.1400	A	UCLA Grounds (C)	
	14	2.5274	7.6900	1.9700	0.7850	1.1506	1.4800	1.0900	0.3370	A	Lake Hughes Array-Station 12A (C)	
	14	1.4766	3.9900	4.4000	4.2700	1.9026	5.5000	2.4300	1.3600	A	Sunland-10965 Mt Gleason Avenue	
	15	8.6596	26.3000	6.9800	3.3600	2.2767	3.7600	1.2000	1.1200	S	Santa Monica-City Hall (C)	
	15	5.5710	12.2000	13.0000	9.5200	2.1299	5.4200	3.1500	0.6330	A	Castaic-Ridge Route (C)	
	15	2.5067	8.6000	4.8600	4.1800	1.1323	1.6400	1.2800	1.0600	S	Century City-LACC North (C)	
	16	1.4855	2.8300	2.8800	1.7400	1.0933	1.8200	1.4500	0.5020	R	8510 Wonderland Avenue	
	16	2.8618	6.2000	4.1700	2.2800	1.4318	5.3200	1.9800	0.9650	S	Moorpark-Fire Station (C)	
	17	1.4804	5.0900	3.5000	2.0100	0.8400	1.7300	1.3800	0.7220	A	Vasquez-Rocks Park (C)	
	18	2.3968	3.9300	4.6500	5.5200	1.3926	2.2300	1.2200	1.2500	A	Hollywood-8023 Willoughby Avenue	
	18	2.4736	6.2400	2.8800	1.6900	1.9117	1.9300	0.7460	0.8830	A	Angeles Nat. Forest-Big Tujunga Stat.	
	18	1.5272	6.1400	2.8900	0.8570	0.8456	1.3900	1.0100	0.4480	R	Burbank-1250 Howard Road	
	18	2.2121	7.4500	1.9000	0.3200	0.7831	1.3800	0.7630	0.2540		Leona Valley Array-Station 9A (C)	
	19	4.4223	8.5700	4.6000	3.4000	0.9907	2.6300	0.9280	0.7000	S	3960 Centinela Street	
	20	2.1938	4.9300	5.6600	1.3600	1.0130	2.4400	1.5400	0.3560	S	La Crescneta-4747 New York Avenue	
	20	3.8139	9.7500	6.2400	4.4800	1.3942	2.5700	1.1300	1.4600	S	Hollywood Storage (C)	
	21	4.5503	13.4000	11.6000	4.7200	0.9969	2.5200	1.9100	0.7320	S	5360 Saturn Street	
	22	2.7917	8.9900	11.4000	3.5700	1.3045	2.7300	2.2200	0.6630	R	Griffith Observatory	
	22	1.3199	2.2200	3.8400	1.8200	0.4906	1.7200	1.0100	0.6260	S	Playa del Rey-8505 Saran Drive	
	22	1.1197	3.1200	3.2600	1.6200	0.8253	1.6100	1.1000	0.5280	A	28211 West Coast Highway	
	23	2.3418	4.2900	3.9200	1.6200	0.8900	2.5700	2.2600	0.9750	S	Baldwin Hills (C)	
	24	0.6174	1.7600	1.1600	0.5030	0.4082	0.9100	0.5380	0.3770	A	Lake Hughes 4B (C)	
	24	0.8244	2.1700	1.3200	0.8280	0.5205	1.5000	0.6660	0.4480	S	Lake Hughes 4 (C)	
	24	4.2573	12.3000	6.4400	1.8900	0.9933	2.3100	1.2900	0.6400		607 North Westmoreland Avenue	
	24	3.6743	11.8000	5.4800	0.6260	1.3567	3.8000	1.0200	0.3170	S	Glendale-3320 Las Palmas Avenue	
	24	1.2720	2.5700	2.0800	0.9940	0.8517	2.8700	0.9170	0.5450	A	Malibu-Point Dume (C)	
	26	1.6646	2.6400	2.8900	1.7500	0.5120	1.2200	0.8650	0.5770	S	2628 West 15th Street	
	27	2.4120	5.3600	7.5800	2.1300	1.1523	3.0500	1.2400	1.2100	S	3036 Fletcher Drive	
	28	1.2916	3.7100	2.6900	1.4100	2.2756	3.7500	2.9900	2.5500	S	3620 South Vermont Avenue	
	28	0.8488	2.1700	2.2900	2.3000	0.9694	1.6400	0.9670	1.1400	A	Lake Hughes Array-Station 1 (C)	

continued on next page

Tab. D.3: *continued*

Date	Time	Lat.	Long.	Depth	M_s	$\log M_0$	F					C
	d	a_h	$SA_h(0.2)$	$SA_h(0.5)$	$S_h(1.0)$	a_v	$SA_v(0.2)$	$SA_v(0.5)$	$SA_v(1.0)$	S	Station	
	29	1.5183	3.4600	2.6600	1.1100	0.4774	0.7690	0.6770	0.5650	A	Elizabeth Lake (C)	
	30	2.7065	6.5600	6.9800	2.1900	0.9592	2.3500	1.3200	0.5610	S	4312 South Grand Avenue	
	30	2.0992	5.0500	5.9900	1.5900	0.7724	2.0400	0.7060	0.4520	A	624 Cypress Avenue	
	31	0.8717	1.7400	1.7100	1.4800	0.4883	0.6010	0.9610	1.1900	A	Leona Valley Array-Station 1 (C)	
	31	1.0382	1.8800	1.7300	1.7600	0.5047	0.9490	1.0200	1.2000	R	Leona Valley Array-Station 3 (C)	
	31	1.4944	4.2600	3.3400	1.4300	0.8060	2.3800	0.8890	0.3870	S	1400 Manhattan Beach Boulevard	
	31	0.5913	1.1500	1.4600	1.4700	0.4288	0.8480	0.8690	0.9730	S	Anaverde Valley (C)	
	31	0.8930	1.9100	1.3000	1.5300	0.5667	0.9800	1.0000	1.1700	A	Leona Valley Array-Station 2 (C)	
	31	0.7756	2.0800	1.5300	2.6100	0.4657	0.6750	0.8240	1.5000	A	Leona Valley Array-Station 4 (C)	
	31	1.4365	3.5500	2.0900	3.5600	0.9501	1.3000	1.6600	2.2300	A	Leona Valley Array-Station 5 (C)	
	32	1.5877	5.4600	3.2800	1.1000	0.9488	2.3200	0.6780	0.4750	A	5921 North Figueroa Street	
	32	1.7413	7.0100	3.3600	1.5800	0.6114	1.3000	1.1100	1.1700	A	Leona Valley Array-Station 6 (C)	
	33	1.2226	2.5100	4.3600	1.8900	0.4757	1.2500	0.7440	0.6000	S	Camarillo (C)	
	34	2.1870	4.1000	5.4400	1.1000	0.6603	1.8400	1.3000	0.3680	A	Point Mugu-Laguna Park (C)	
	34	4.8333	10.6000	10.8000	2.1900	1.1686	3.1500	2.5200	0.4240	S	University Hospital (C)	
	34	1.3801	5.2300	2.6800	1.1900	0.6462	1.8400	0.7340	0.3390	S	2369 East Vernon Avenue	
	35	2.2850	8.2900	1.1600	0.5570	0.8714	2.6600	0.6170	0.3500	R	Mt. Wilson-Caltech Seismograph Station (C)	
	35	0.6548	1.9400	1.5000	1.6000	0.3965	0.9860	0.7210	0.8630	S	Palmdale-Highway 14 & Palm (C)	
	36	1.5538	6.3400	4.4600	1.0600	0.9626	3.2600	1.2000	0.6550	S	535 South Wilson Avenue	
	36	3.1011	9.0600	5.3600	1.6500	1.3194	2.7200	2.8200	0.3950	A	City Terrace (C)	
	36	2.5559	5.8300	4.0100	0.9630	1.4680	4.1500	2.5500	0.3620	S	1150 North Sierra Madre Villa Avenue	
	36	0.9920	2.1300	2.2800	1.2600	0.5352	1.7200	0.6140	0.2510	A	Inglewood-Union Oil Yard (C)	
	36	1.9413	4.3300	3.7900	1.5000	0.5602	1.3700	0.7090	0.3720	S	116th Street School (C)	
	36	0.9651	1.8800	2.8600	1.9700	0.4338	0.8350	0.7710	0.9840	A	Sandberg-Bald Mountain (C)	
	37	0.9907	2.7800	2.1900	1.3200	0.4484	1.4100	1.3300	0.5550	A	Alhambra-Fremont School (C)	
	37	4.0263	13.7000	4.6500	2.8200	0.9995	2.0100	1.1700	0.4110	A	Obregon Park	
	37	1.4818	5.1400	2.4800	1.2100	0.8845	2.1300	1.6100	0.3160	A	San Marino-Southwestern Academy (C)	
	39	0.6695	1.2900	0.7180	0.5040	0.2849	0.5560	0.3980	0.2940		Lancaster-Antelope (C)	
	39	1.7410	5.4100	4.7600	3.4000	0.6300	1.2600	0.6720	0.8270	S	Point Mugu-Naval Air Station (C)	
	41	0.7061	2.1800	1.2900	1.4500	0.3484	0.7760	0.4090	0.3620	R	Littlerock-Brainard Canyon (C)	
	41	2.4917	5.9300	3.9300	1.4900	0.7349	1.9100	0.8970	0.3720	A	San Gabriel-600 East Grand Avenue	
	42	1.5908	5.0900	2.3600	2.1100	0.7000	1.3900	0.7810	0.2660	A	Littlerock-Post Office	
	42	1.1346	2.2800	2.9900	0.7500	0.3975	1.1800	0.4160	0.2060	R	Rolling Hills Estates-Rancho Vista Sch. (C)	
	42	0.9740	2.3900	2.0600	1.5900	0.5061	1.4800	0.5070	0.3300	S	Bell Gardens-7420 Jaboneria	
	42	0.9058	3.2700	2.4700	1.5300	0.8445	1.7600	1.7700	0.4910	S	Arcadia-855 Arcadia Avenue	

continued on next page

Tab. D.3: *continued*

Date	Time	Lat.	Long.	Depth	M_s	$\log M_0$	F					C
	d	a_h	$\mathrm{SA}_h(0.2)$	$\mathrm{SA}_h(0.5)$	$\mathrm{S}_h(1.0)$	a_v	$\mathrm{SA}_v(0.2)$	$\mathrm{SA}_v(0.5)$	$\mathrm{SA}_v(1.0)$	S	Station	
	42	1.2848	3.5200	2.1800	0.9700	0.4414	1.5000	0.4930	0.2590	S	Compton-14637 Castlegate Street	
	43	2.1844	6.5300	3.3500	1.5100	1.2911	3.5200	0.6570	0.2610	S	Downey-County Maintenance Building (C)	
	44	1.6872	5.5600	2.7500	1.1400	0.7777	1.9700	0.7420	0.2680		Montebello-1105 Bluff Road	
	44	0.9015	1.7000	1.7600	0.5330	0.4769	1.2800	0.4710	0.2570	S	Carson-23536 Catskill Avenue	
	44	1.1644	3.1600	2.2600	1.2800	0.5659	1.5900	1.0700	0.5340	A	Arcadia-180 Campus Drive	
	44	0.8551	2.7200	2.5300	1.1900	0.4490	0.7040	0.6820	0.2410	S	Carson-21288 Water Street	
	45	0.6780	1.2400	1.5900	1.1700	0.4580	0.9850	0.9350	0.5410	S	Neenach-Sacatara Creek (C)	
	45	0.7111	1.9400	1.3800	0.6090	0.4222	0.9670	0.4740	0.2410	R	Rancho Palos Verdes-Hawthorne Boul. (C)	
	46	1.6026	3.3700	3.0600	1.1600	0.5607	1.7200	0.6210	0.4030	S	Downey-12500 Birchdale	
	46	0.7980	2.2200	1.8000	1.2100	0.4709	1.7600	0.4760	0.5040	S	Lancaster-Fox Airfield (C)	
	46	1.0114	1.6400	2.5800	1.5100	0.3635	0.7610	0.5280	0.2670	S	Oxnard-Port Hueneme (C)	
	47	1.5528	5.9600	3.3800	1.0500	0.5902	1.6600	0.6320	0.3520	S	El Monte-11338 Fairview Avenue	
	47	0.6795	2.1200	1.2000	1.1300	0.3836	1.6900	0.6200	0.2590	S	Long Beach-Rancho los Cerritos (C)	
	48	1.5090	3.0000	2.6800	0.9750	0.7234	1.8100	1.2200	0.4100	S	30511 Luconia Drive	
	48	0.7891	1.9300	1.0800	0.3970	0.4682	1.5000	0.8350	0.2740	A	Duarte-237 Mel Canyon Road	
	48	1.3251	3.6200	2.6200	0.5570	0.4567	2.2200	0.4660	0.2350	A	3699 North Hollywood Avenue	
	49	1.2883	4.8900	2.5700	0.7210	0.4796	1.2300	0.6640	0.3400	S	11500 East Joslin Street	
	50	0.7555	1.3700	1.4800	1.2800	0.2189	0.5140	0.7100	0.1660	A	Whittier-6302 South Alta Drive	
	51	1.8002	3.1600	4.8800	1.2000	0.5019	1.1800	1.1700	0.3560	S	954 South Seaside Avenue	
	51	0.9886	2.0800	2.6900	0.8940	0.6905	1.1200	1.0600	0.2730	A	San Pedro-Palos Verdes (C)	
	53	0.7367	1.5400	2.0400	1.9300	0.2467	0.5500	0.5090	0.5490		Harbour & California (Holiday Inn) (C)	
	53	0.8813	2.4200	1.4500	0.6110	0.4551	1.7300	1.1500	0.5030	A	Glendora-120 North Oakbank	
	53	1.0252	2.6200	2.9100	0.8560	0.4357	1.5100	0.6830	0.3480	S	Covina-1271 West Badillo	
	53	1.3412	3.7900	2.1500	1.3800	0.7100	0.9110	0.5260	0.1980	S	Lakewood-6701 Del Amo Boulevard	
	54	0.6333	1.9200	1.2300	0.9170	0.4801	1.7300	0.6760	0.2960	S	West Covina-1307 South Orange	
	57	0.6826	1.1900	2.0400	0.8180	0.5472	1.3500	0.9880	0.4230	S	Covina-656 South Grand Avenue	
	58	0.7364	1.2500	0.9980	0.4870	0.2271	0.5910	0.3910	0.1520	S	Rosamond-Airport (C)	
	59	1.1171	2.8000	3.2100	0.8830	0.4750	1.9400	1.2500	0.2170	S	La Puente-504 Rimgrove Avenue	
	59	0.7190	2.5100	1.4500	0.6820	0.3962	0.9290	0.3890	0.3150	S	Hacienda Heights-16750 Colima Road	
	60	2.0290	4.6400	3.0600	1.2600	0.5596	1.4900	0.7520	0.2910	S	La Habra-950 Briarcliff Drive	
	60	1.4219	3.8100	4.5300	1.2500	0.3160	0.7320	0.3460	0.1990	S	Buena Park-6625 La Palma Avenue	
	60	0.8235	2.3700	2.5000	0.8030	0.3599	0.8160	0.4200	0.2330	S	Seal Beach-Office Building (Parking Lot) (C)	
	61	0.5536	1.0000	1.6000	0.9480	0.3341	0.7990	0.6370	0.2850	R	Wrightwood-Jackson Flat (C)	
	63	1.0707	2.7000	3.2200	1.2300	0.1733	0.3000	0.0816	0.0444	S	Garden Grove-6861 Santa Rita	
	64	0.6594	2.3400	0.5320	0.3390	0.1377	0.3910	0.1910	0.0942	A	Anacapa Island (C)	

continued on next page

Tab. D.3: *continued*

Date			Time	Lat.	Long.	Depth	M_s	$\log M_0$	F					C
			d	a_h	$\mathrm{SA}_h(0.2)$	$\mathrm{SA}_h(0.5)$	$\mathrm{S}_h(1.0)$	a_v	$\mathrm{SA}_v(0.2)$	$\mathrm{SA}_v(0.5)$	$\mathrm{SA}_v(1.0)$	S	Station	
			65	0.8743	2.0400	2.4100	0.6480	0.2008	0.3630	0.4590	0.2030	S	Huntington Beach-16081 Waikiki Lane	
			66	0.9735	2.5300	2.8700	1.2700	0.3779	1.2000	0.7160	0.2320	S	Brea-200 South Flower	
			67	0.7382	1.6800	1.9000	1.0600	0.4137	1.2000	0.4910	0.2080	S	Anaheim-2000 West Ball Road	
			68	0.5850	1.3500	1.5000	0.5350	0.3295	0.8260	0.8050	0.2140	A	Wrightwood-Swarthout Valley (C)	
			68	0.5823	1.7800	0.7680	0.4020	0.2480	0.6730	0.2630	0.1500	A	Mojave-Oak Creek Canyon (C)	
			69	1.1876	2.6700	5.2300	1.1200	0.1845	0.5410	0.5910	0.1880	S	18401 Springdale	
			69	0.7797	2.0500	1.3200	0.4620	0.3622	0.6440	0.4780	0.3320	R	Mount Baldy-Elementary School (C)	
			74	0.8889	1.8900	2.0200	0.8680	0.1817	0.5870	0.3710	0.2450	A	Lake Street (Fire Station) (C)	
			78	0.7008	3.0200	1.2200	0.4710	0.2486	1.0100	0.2860	0.2400	R	Rancho Cucamonga-Deer Canyon (C)	
			78	0.5172	1.0400	0.7080	1.2900	0.2609	0.7740	0.4920	0.2680	S	Mojave-Highways 14 & 58 (C)	
			79	0.4125	0.8510	0.7260	0.3560	0.2066	0.5070	0.4150	0.1350	A	Wrightwood-Nielson (C)	
			81	1.0347	1.9100	1.8800	0.6770	0.1902	0.6710	0.4820	0.4670	A	Newport Boulevard & Coastal Highway (C)	
			82	0.5952	1.8200	1.5400	0.5530	0.1694	0.3090	0.6640	0.2790		Newport Beach-Irvin Avenue (C)	
			82	0.5600	1.5500	0.9330	0.9240	0.3510	1.1800	0.9280	0.2500	A	Phelan-Wilson Ranch (C)	
			84	1.0217	2.9100	2.5800	0.9520	0.2379	0.9550	0.3340	0.1860	S	Featherly Park (C)	
			98	0.6234	2.3800	0.4710	0.2380	0.2142	0.5870	0.3370	0.2620	A	Riverside-Airport (C)	
			106	0.7607	1.9000	2.0600	0.9980	0.3819	1.1800	0.7840	0.3300	S	Santa Barbara-UCSB Goleta (C)	
			107	0.9395	1.8800	2.8100	0.7200	0.4327	1.2300	0.8440	0.3400	S	San Bernardino-Hospital (C)	
			144	0.6256	1.0300	1.2700	0.3970	0.2666	0.5890	0.6010	0.2770	S	Hemet-Ryan Airfield (C)	
			147	0.9709	2.3400	2.3200	1.2500	0.2185	0.4360	0.7510	0.3920	S	San Jacinto-CDF Fire Station (C)	
1994	1	29	1120	34.17	-118.83	1	5.30							US
			26	7.4654	16.7000	12.7000	4.2000	3.7962	7.3100	3.4700	0.9540		Browns Canyon	
1994	2	25	0230	38.73	20.58	10	5.08	17.14						GR
			12	0.5747	1.8000	1.3000	0.4930	0.9672	0.9190	0.5570	0.1320	A	Vasiliki-Town Hall	
			15	1.2912	3.7000	3.6700	1.3500	0.5226	1.0200	0.8630	1.1500	S	Lefkada-Hospital	
			16	1.9676	3.3100	3.9500	1.3100	0.5241	1.3400	0.8070	1.2200	S	Lefkada-OTE Building	
			29	0.3385	0.7700	0.7780	1.0800	0.1683	0.5660	0.3320	0.3340	A	Preveza-OTE Building	
1994	2	27	2234	38.69	20.46	10	4.00							GR
			27	0.8141	2.3900	0.5260	0.1710	0.3183	0.6960	0.0923	0.0647	S	Lefkada-OTE Building	
1994	4	10	1946	39.98	23.64	18	4.60							GR
			6	0.6643	0.7780	0.8980	0.2030	0.3323	0.4890	0.4030	0.1040	A	Paliouri-Seismograph Station	
1994	7	18	1544	38.60	20.58	10	4.20							GR
			4	0.6257	1.6500	0.9850	0.2360	0.1923	0.5140	0.2460	0.0707	A	Vasiliki-Town Hall	
1994	9	1	1515	40.38	-125.78	10	6.90	19.59						US
			121	0.2326	0.7970	0.2380	0.2920	0.0839	0.2060	0.1320	0.1750	R	Cape Mendocino (C)	

continued on next page

Tab. D.3: *continued*

Date			Time	Lat.	Long.	Depth	M_s	$\log M_0$	F					C
			d	a_h	$\mathrm{SA}_h(0.2)$	$\mathrm{SA}_h(0.5)$	$\mathrm{S}_h(1.0)$	a_v	$\mathrm{SA}_v(0.2)$	$\mathrm{SA}_v(0.5)$	$\mathrm{SA}_v(1.0)$	S	Station	
			151	0.7046	1.4200	0.5410	0.1340	0.2218	0.2770	0.3120	0.0808	A	Shelter Cove-Airport (C)	
1994	10	12	0106	38.24	21.87	18	4.30							GR
			18	0.1731	0.4870	0.3790	0.0935	0.1446	0.1260	0.1980	0.0425	A	Nafpaktos-OTE Building	
1994	11	29	1430	38.66	20.46	21	4.80	16.68						GR
			28	0.7488	1.3700	1.5600	0.6390	0.2675	0.6610	0.3050	0.2870	S	Lefkada-Hospital	
			29	1.0120	2.4300	1.4300	0.5100	0.5106	1.1500	0.3340	0.2900	S	Lefkada-OTE Building	
1994	12	1	0717	38.69	20.55	5	4.80							GR
			21	0.3206	0.6110	0.6460	0.2750	0.2341	0.4160	0.3360	0.1160	S	Lefkada-OTE Building	
1995	1	16	2046	34.55	135.04	19	6.95	19.80	S					JA
			0	8.2121	10.5000	21.1000	15.1000	3.3401	10.1000	6.4400	5.5000	R	Kobe-Kaiyo (C)	
			1	3.4176	4.6300	6.4200	9.5600	5.5819	12.6000	5.4000	3.4300	S	Kobe-Port Island Array (Surface) (C)	
			1	3.0130	4.4900	4.8800	5.7400	4.2258	5.4200	2.0200	2.5800	R	Kobe-University (C)	
			3	7.6204	12.2000	6.2900	9.4300	3.6214	6.0100	3.9700	5.8600	R	Kobe-Motoyama (C)	
			6	4.4661	7.7300	11.0000	6.1200	4.7101	8.2000	7.6700	3.9100		Kobe-Port	
			11	4.3028	6.1700	5.2400	7.7400	2.8805	6.3700	3.3400	1.8800	L	Amagasaki-G	
			12	7.0809	7.2800	14.4000	19.5000	3.5117	8.1600	6.6100	3.9000		Kobe-8G	
			12	2.8677	12.2000	5.6300	2.3700	1.2349	2.9000	0.8090	0.4910		Tadaoka (C)	
			17	1.4810	4.5900	3.7000	1.8700	0.8976	1.7400	1.0400	0.6230		Sakai (C)	
			18	2.0986	2.7300	4.9900	8.7300	1.8520	3.5700	2.1300	0.8190	S	Osaka-Fukushima (C)	
			22	0.8120	1.6600	1.9300	2.4100	0.6472	1.7200	1.2400	0.6480		Osaka (C)	
			24	2.2003	3.6800	3.4900	3.5100	1.0697	2.2700	0.8140	0.4110	S	Osaka-Abeno (C)	
			25	2.0973	3.0200	5.2500	6.3400	1.5320	3.4400	1.2500	0.7600		Osaka-Morigawachi (C)	
			28	1.5488	2.0100	5.5900	4.5100	1.2081	2.3900	1.0900	0.6250		Higashi Osaka-Yae (C)	
			36	1.0656	3.1900	0.9580	0.5600	0.6608	2.1400	0.3440	0.1790	R	Chihaya (C)	
			56	0.6708	1.9300	2.5700	0.5300	0.3962	1.4700	0.4090	0.1640		Maizuru (C)	
			93	0.7767	1.7800	1.5200	0.4410	0.3609	0.6170	0.3890	0.2750	R	Okayama (C)	
1995	6	15	0015	38.36	22.20	10	6.34	18.78	N					GR
			6	5.0493	11.5000	14.2000	4.0600	1.9437	4.7600	4.0000	1.4500	A	Aigio-OTE Building	
			22	1.8416	3.0900	3.9700	0.5550	0.5975	3.0300	0.5790	0.2620		Amfissa-OTE Building	
1995	6	15	0031	38.30	22.03	5	5.77							GR
			7	0.6832	1.2500	1.3800	0.2590	0.3567	0.5350	0.2770	0.1350	A	Aigio-OTE Building	
1995	6	15	0451	38.26	22.15	25	3.90							GR
			6	0.4705	0.7770	0.1840	0.0596	0.2747	0.7080	0.2210	0.0639	A	Aigio-OTE Building	
1995	6	15	0701	38.35	22.09	9	3.60							GR
			11	0.5077	0.3860	0.0768	0.0342	0.3145	0.2300	0.0631	0.0640	A	Aigio-OTE Building	

continued on next page

Tab. D.3: *continued*

Date			Time	Lat.	Long.	Depth	M_s	$\log M_0$	F					C
			d	a_h	$\mathrm{SA}_h(0.2)$	$\mathrm{SA}_h(0.5)$	$\mathrm{S}_h(1.0)$	a_v	$\mathrm{SA}_v(0.2)$	$\mathrm{SA}_v(0.5)$	$\mathrm{SA}_v(1.0)$	S	Station	
1995	7	5	1825	38.38	22.10	12	4.90							GR
			15	0.1915	0.5200	0.0872	0.0556	0.1505	0.3110	0.0870	0.0778	A	Aigio-OTE Building	
1995	10	1	1557	38.06	30.15	5	6.04	18.73	N					TU
			1	3.1449	7.2300	6.1500	5.3700	1.3286	3.2200	1.8100	2.2800	S	Dinar-Meteoroloji Mudurlugu	
			37	0.4079	1.4600	0.9500	0.6080	0.3495	1.3000	0.5180	0.3870		Burdur-Meteoroloji Mudurgulu	
			47	0.6176	2.2500	1.5200	0.4300	0.9251	1.5800	0.8260	0.2090		Cardak-Saglik Ocagi	
			87	0.1440	0.2590	0.4580	0.4250	0.0911	0.2430	0.2750	0.2130	A	Denizli-Bayindirlik ve Iskan Mudurlugu	
1995	10	5	0821	38.13	20.30	26	4.30							GR
			15	0.6700	1.3400	0.4290	0.1150	0.3838	0.4510	0.2080	0.0651		Lixouri-OTE Building	
1995	12	5	1852	39.48	40.32	10	5.70							TU
			75	0.2730	1.1400	0.5400	0.1900	0.1698	0.4540	0.1520	0.1320		Erzincan-Bayindirlik Mudurlugu	
1995	12	5	1849	39.35	40.22	26	5.63	17.74						TU
			75	0.2820	0.9790	0.5300	0.2310	0.2272	0.3970	0.1910	0.1550		Erzincan-Bayindirlik Mudurlugu	
1996	4	2	0759	37.78	26.64	11	5.11	17.20	N					GR
			57	0.2927	0.6270	0.2160	0.0655	0.1185	0.2910	0.1040	0.0489	A	Kusadasi-Meteoroloji Mudurlugu	
1996	7	4	2157	38.20	20.39	6	4.10							GR
			4	1.2413	1.8900	1.4500	0.3100	0.3503	0.5840	0.2020	0.1610		Lixouri-OTE Building	
1996	7	15	0013	45.93	6.09	2	4.50							FR
			30	0.0789	0.2050	0.0667	0.0166	0.0715	0.1450	0.0278	0.0149	A	Genf-Marziano	
1996	8	14	0155	40.74	35.29	12	5.30	17.66						TU
			47	0.5257	1.5900	0.2970	0.1770	0.2460	0.6080	0.0807	0.0492	R	Amasya-Bayindirlik Mudurlugu	
1996	8	14	0259	40.79	35.23	3	5.31	17.54						TU
			24	0.9082	1.8700	1.3000	0.5560	0.2891	0.7430	0.3230	0.1330	S	Merzifon-Meteoroloji Mudurlugu	
			53	0.3219	0.9490	0.3230	0.1660	0.1581	0.3340	0.1290	0.0344	R	Amasya-Bayindirlik Mudurlugu	
1996	10	11	0948	38.20	20.35	8	4.30							GR
			8	0.1861	0.1910	0.1070	0.0560	0.0985	0.1430	0.1550	0.0777		Lixouri-OTE Building	
1997	7	2	1253	36.49	3.19	25	3.60							SP
			33	0.0785	0.1230	0.0234	0.0086	0.0543	0.0708	0.0164	0.0062	R	Adra-Refugio de la Plaza	
1997	9	26	0033	43.02	12.89	7	5.50	17.58	N					IT
			3	3.9437	8.3100	4.0000	3.9200	3.6413	5.5200	3.2800	1.2000	A	Colfiorito	
			13	5.7034	11.9000	2.3600	0.7930	1.3813	3.1900	0.8210	0.2940	R	Nocera Umbra	
			17	1.7776	3.2200	1.2200	0.3270	1.0575	1.4100	1.0200	0.2850	R	Borgo-Cerreto Torre	
			23	0.2484	1.0600	0.2900	0.0931	0.1869	0.5210	0.2530	0.1140	R	Monte Fiegni	
			24	0.9733	2.0000	1.4900	1.4500	0.3215	0.9850	0.4900	0.4190	S	Castelnuovo-Assisi	
			24	1.4868	5.3500	1.1800	0.3030	0.3913	1.2200	0.2920	0.1160		Assisi-Stallone	

continued on next page

Tab. D.3: *continued*

Date			Time	Lat.	Long.	Depth	M_s	$\log M_0$	F					C
			d	a_h	$\mathrm{SA}_h(0.2)$	$\mathrm{SA}_h(0.5)$	$\mathrm{S}_h(1.0)$	a_v	$\mathrm{SA}_v(0.2)$	$\mathrm{SA}_v(0.5)$	$\mathrm{SA}_v(1.0)$	S	Station	
			25	0.5198	0.8850	1.5200	0.6370	0.4396	1.0100	0.7030	0.1760	A	Bevagna	
			26	0.4128	1.1000	0.5500	0.5060	0.3005	0.8900	0.6370	0.4940		Norcia-Zona Industriale	
			27	0.4723	0.8550	0.5530	0.2110	0.2098	0.2620	0.1930	0.1390	A	Matelica	
			41	0.3275	0.9630	0.7270	0.5190	0.1611	0.4560	0.3470	0.2610	R	Gubbio-Piana	
			61	0.2530	1.0100	0.3740	0.3310	0.0843	0.3520	0.1020	0.1130	S	Rieti	
			79	0.0662	0.0834	0.1070	0.1120	0.0336	0.0653	0.0937	0.1550		Aquilpark-Citta	
			79	0.0648	0.0798	0.0964	0.1150	0.0380	0.0691	0.0865	0.1700		Aquilpark-Galleria	
			79	0.0568	0.1040	0.1180	0.1090	0.0400	0.0924	0.1020	0.1640		Aquilpark-Parcheggio	
			119	0.0755	0.0901	0.1670	0.1750	0.0302	0.0486	0.0413	0.1210	S	Borgo-Ottomila	
1997	9	26	0940	43.03	12.86	6	5.90	18.06	N					IT
			3	2.6427	5.9900	2.5200	4.4400	1.7602	3.6500	1.8900	1.3200	A	Colfiorito	
			4	5.2992	17.0000	6.4500	3.0100	3.5505	5.7400	3.2300	2.0000	R	Nocera Umbra	
			19	1.8408	6.0700	2.9800	0.4950	0.7555	1.9100	0.5720	0.1440		Assisi-Stallone	
			21	1.1647	2.0400	1.3500	1.2800	0.4436	0.8060	0.8150	0.3990	A	Matelica	
			23	1.6774	2.5500	4.1400	2.1000	0.4560	1.0200	1.1700	0.4790	S	Castelnuovo-Assisi	
			23	1.0446	2.1000	0.9080	0.1960	0.4263	0.7310	0.3460	0.1460	R	Borgo-Cerreto Torre	
			25	0.3041	0.8900	0.2750	0.1490	0.1959	0.4550	0.1540	0.1110	R	Monte Fiegni	
			26	0.7645	1.3900	3.5900	1.1000	0.3681	0.9880	1.1300	0.5160	A	Bevagna	
			30	0.9320	2.6400	1.8400	1.1600	0.6106	1.9400	0.8140	0.9450	R	Gubbio-Piana	
			30	0.5770	1.6400	1.0500	0.5050	0.2293	0.6110	0.3430	0.1430		Norcia-Altavilla	
			47	0.6694	1.2400	0.5280	0.3130	0.1933	0.4750	0.3200	0.1920	R	Pietralunga	
			66	0.1839	0.5720	0.3100	0.4390	0.0861	0.2170	0.1560	0.0786	S	Rieti	
			71	0.6908	2.7600	0.7810	0.2030	0.2628	0.7370	0.1830	0.0893	R	Peglio	
			86	0.0420	0.0800	0.1020	0.0947	0.0399	0.0483	0.0958	0.1000		Aquilpark-Citta	
			86	0.0386	0.0481	0.1100	0.1170	0.0402	0.0508	0.1080	0.1080		Aquilpark-Galleria	
			86	0.0393	0.0703	0.0978	0.1140	0.0459	0.0762	0.0922	0.1040		Aquilpark-Parcheggio	
			126	0.0658	0.0767	0.1370	0.2330	0.0338	0.0350	0.0490	0.1340	S	Borgo-Ottomila	
1997	10	3	0855	43.03	12.84	6	4.90	16.99	N					IT
			5	1.8139	5.2600	2.4100	0.3280	2.0290	2.1800	0.7870	0.2010	S	Colfiorito-Casermette	
			7	1.1560	1.6400	1.6900	1.8800	0.9846	1.2300	1.9600	0.4680	A	Colfiorito	
			8	2.6043	2.8700	0.6250	0.1850	0.8879	1.4800	0.6940	0.5080	R	Nocera Umbra-Biscontini	
			10	2.8711	7.0100	0.5130	0.2330	0.8913	1.8900	0.3190	0.1140	R	Nocera Umbra	
			13	0.5914	0.6960	0.3180	0.1600	0.3904	0.4470	0.2860	0.0845	S	Nocera Umbra-Salmata	
			37	0.4866	2.2700	0.6020	0.2820	0.2349	0.8710	0.2170	0.1390	R	Gubbio-Piana	
1997	10	6	2324	43.02	12.84	7	5.20	17.37	N					IT

continued on next page

Tab. D.3: *continued*

Date			Time	Lat.	Long.	Depth	M_s	$\log M_0$	F					C
			d	a_h	SA$_h(0.2)$	SA$_h(0.5)$	S$_h(1.0)$	a_v	SA$_v(0.2)$	SA$_v(0.5)$	SA$_v(1.0)$	S	Station	
			5	2.2477	6.6200	2.1400	1.1800	1.7991	2.7100	1.4100	0.2060	S	Colfiorito-Casermette	
			7	1.2880	2.2000	1.3300	2.5500	0.8107	1.7400	0.9420	0.2950	A	Colfiorito	
			10	3.3726	7.4700	1.5700	0.8150	1.1105	1.4900	1.0300	0.8490	R	Nocera Umbra-Biscontini	
			11	4.9763	12.4000	2.7400	1.0900	1.1599	3.9500	1.0600	0.5780	R	Nocera Umbra	
			15	1.7057	4.4700	2.6300	0.7490	0.7685	1.6800	0.8240	0.8150	S	Nocera Umbra-Salmata	
			20	1.0452	2.3300	1.6900	1.3400	0.2451	0.8900	0.3070	0.2830	S	Castelnuovo-Assisi	
			20	1.7759	6.4900	1.3300	0.4630	0.4461	1.4300	0.2200	0.1050		Assisi-Stallone	
			21	0.5112	0.8850	1.8900	0.5480	0.2606	0.7110	0.5440	0.2130	A	Bevagna	
			33	0.3035	0.6990	0.2990	0.2280	0.1914	0.2460	0.2270	0.1280	A	Norcia	
			38	0.6973	3.3500	0.9620	0.8210	0.2316	0.8520	0.3740	0.4560	R	Gubbio-Piana	
			42	0.3923	1.4900	0.2390	0.0935	0.1072	0.3840	0.1270	0.0573	R	Gubbio	
			42	0.3536	0.9960	0.1510	0.0758	0.1831	0.2430	0.0818	0.0262	R	Forca Canapine	
			65	0.1689	0.7460	0.2290	0.1960	0.0730	0.2110	0.0888	0.0628	S	Rieti	
			88	0.0376	0.0748	0.0887	0.0589	0.0234	0.0399	0.0655	0.0469		Aquilpark-Citta	
			88	0.0255	0.0421	0.0591	0.0545	0.0221	0.0363	0.0647	0.0573		Aquilpark-Galleria	
			88	0.0311	0.0630	0.0743	0.0482	0.0247	0.0605	0.0756	0.0478		Aquilpark-Parcheggio	
1997	10	12	1108	42.91	12.95	6	5.20	16.95	N					IT
			11	1.5920	2.6300	1.1800	0.3590	0.7328	1.3600	0.5270	0.2060	R	Borgo-Cerreto Torre	
			14	0.2817	0.4810	0.2670	0.0613	0.2780	0.2260	0.1690	0.0506	S	Colfiorito-Casermette	
			14	0.4393	0.8710	0.6150	0.4630	0.2209	0.5420	0.7430	0.0976	A	Colfiorito	
			18	0.6744	1.3000	0.9240	0.5130	0.3295	0.6930	0.9870	0.1250	A	Norcia	
			24	0.3410	0.6170	0.1530	0.0490	0.1311	0.2920	0.1380	0.0429	R	Nocera Umbra-Biscontini	
			26	0.7492	0.7830	0.1800	0.0457	0.1528	0.2200	0.0690	0.0328	R	Nocera Umbra	
			54	0.1061	0.2590	0.1640	0.1920	0.0351	0.1020	0.0635	0.0479	S	Rieti	
1997	10	14	1523	42.92	12.93	7	5.60	17.53	N					IT
			9	1.6130	4.5800	1.6000	0.5440	0.3934	1.0400	0.5780	0.2280		Cesi-Monte	
			12	0.7058	2.2800	0.5620	0.1310	0.5242	0.6120	0.2680	0.1440	S	Colfiorito-Casermette	
			12	3.2189	6.8100	2.7800	1.0300	1.4361	3.0700	1.6000	0.4940	R	Borgo-Cerreto Torre	
			13	0.9037	1.5500	1.0300	2.1000	0.5472	1.2400	1.0500	0.3750	A	Colfiorito	
			16	0.5866	0.6850	0.4650	0.1290	0.4948	0.6450	0.1450	0.1380		Annifo	
			17	0.7297	1.0100	0.4420	0.1120	0.3381	0.7700	0.3290	0.1890	R	Cassignano	
			17	0.3183	1.6000	0.3540	0.1290	0.2315	0.6640	0.2920	0.1230	R	Serravalle di Chienti	
			19	2.3536	7.6300	3.1000	1.4900	0.8150	1.1500	1.4100	0.6590		Norcia-Altavilla	
			20	1.3030	4.0300	2.5600	1.4400	0.7514	1.5700	0.9270	0.4100	A	Norcia	
			21	0.9919	2.5600	1.8800	0.9790	0.5915	1.3600	1.1700	0.8420		Norcia-Zona Industriale	

continued on next page

Tab. D.3: *continued*

Date			Time	Lat.	Long.	Depth	M_s	$\log M_0$	F					C
			d	a_h	$\mathrm{SA}_h(0.2)$	$\mathrm{SA}_h(0.5)$	$\mathrm{S}_h(1.0)$	a_v	$\mathrm{SA}_v(0.2)$	$\mathrm{SA}_v(0.5)$	$\mathrm{SA}_v(1.0)$	S	Station	
			23	0.6486	1.4800	1.7100	0.4590	0.5850	1.2700	1.2300	0.3560	R	Cascia	
			23	0.5084	1.2100	0.2960	0.0799	0.1545	0.3190	0.2530	0.1020	R	Nocera Umbra-Biscontini	
			24	1.3272	3.2500	0.3190	0.0768	0.2971	0.4090	0.2220	0.0611	R	Nocera Umbra	
			26	0.4061	1.6900	0.3850	0.1610	0.1815	0.3960	0.1700	0.1180	R	Spoleto Monteluco	
			26	0.4101	0.7430	1.0700	0.7100	0.2266	0.5430	0.3810	0.1900	A	Bevagna	
			26	0.1595	0.4210	0.1660	0.0751	0.1453	0.5320	0.1360	0.0993	R	Monte Fiegni	
			31	0.2525	0.8430	0.1280	0.0721	0.1093	0.2070	0.0476	0.0468		Assisi-Stallone	
			52	0.1380	0.3900	0.3290	0.2270	0.0735	0.1460	0.1130	0.1420	R	Gubbio-Piana	
			55	0.3399	1.5900	0.5000	0.6020	0.1192	0.3160	0.2130	0.1600	S	Rieti	
			69	0.0579	0.1220	0.0799	0.0469	0.0341	0.0689	0.0575	0.0396		Valle Aterno-Moro	
			69	0.1666	0.2360	0.3980	0.0761	0.0369	0.1350	0.1010	0.0393		Valle Aterno-Valle	
			69	0.1083	0.1810	0.2980	0.0742	0.0261	0.0552	0.0627	0.0394		Valle Aterno-Fiume	
			75	0.0822	0.1580	0.2100	0.1730	0.0497	0.0696	0.1210	0.1810		Aquilpark-Citta	
			75	0.0833	0.1120	0.1570	0.1890	0.0556	0.0763	0.1470	0.1940		Aquilpark-Galleria	
			75	0.0841	0.1720	0.1700	0.1720	0.0635	0.0958	0.1410	0.2100		Aquilpark-Parcheggio	
			114	0.1010	0.1180	0.2290	0.2060	0.0445	0.0449	0.0610	0.2040	S	Borgo-Ottomila	
1997	11	9	1907	42.90	12.95	10	4.80							IT
			2	0.6396	1.1300	0.6710	0.2510	0.2610	0.8010	0.3570	0.1690	R	Sellano	
			14	0.1508	0.3560	0.1660	0.0422	0.0684	0.1170	0.0722	0.0315	S	Colfiorito-Casermette	
			15	0.2184	0.6380	0.5300	0.4290	0.1354	0.3750	0.4920	0.1080	A	Colfiorito	
			17	0.6622	1.9300	0.4260	0.1970	0.3065	0.4920	0.3730	0.0743	A	Norcia	
			25	0.1292	0.1750	0.0488	0.0394	0.0398	0.1030	0.0790	0.0329	R	Nocera Umbra-Biscontini	
			27	0.1833	0.5250	0.0854	0.0327	0.0637	0.1250	0.0852	0.0277	R	Nocera Umbra	
			31	0.0559	0.1720	0.0976	0.1620	0.0197	0.0596	0.0410	0.0567	S	Castelnuovo-Assisi	
1997	11	14	2138	38.86	25.74	12	5.70	17.87						GR
			280	0.0188	0.0352	0.0449	0.0361	0.0067	0.0153	0.0192	0.0193		Tekirdag-Bayindirlik Mudurlugu	
1998	4	3	0726	43.20	12.79	6	4.80							IT
			10	3.4280	9.5900	1.5000	0.2660	1.2634	2.4300	0.2610	0.0819	R	Nocera Umbra	
			11	3.0414	7.5600	1.1200	0.1810	0.6967	1.4400	0.3360	0.1010	R	Nocera Umbra-Biscontini	
			17	0.7907	1.4300	0.2830	0.1080	0.2881	0.3840	0.1750	0.0589	R	Cassignano	
			21	0.4651	1.5400	1.1400	0.5790	0.2517	0.6170	0.5860	0.1560	R	Gubbio-Piana	
			27	0.7575	2.4100	0.7220	0.6370	0.1613	0.4840	0.1590	0.2250	S	Castelnuovo-Assisi	
			33	0.2574	1.2400	0.7700	0.3910	0.2142	0.7910	0.2280	0.0876	A	Bevagna	
			36	0.1999	0.3340	0.2610	0.0368	0.1164	0.2620	0.1480	0.0351	R	Sellano	
1998	4	5	1552	43.19	12.72	10	4.40							IT

continued on next page

Tab. D.3: *continued*

Date			Time	Lat.	Long.	Depth	M_s	$\log M_0$	F					C
			d	a_h	$\mathrm{SA}_h(0.2)$	$\mathrm{SA}_h(0.5)$	$\mathrm{S}_h(1.0)$	a_v	$\mathrm{SA}_v(0.2)$	$\mathrm{SA}_v(0.5)$	$\mathrm{SA}_v(1.0)$	S	Station	
			8	0.9470	2.6600	0.2850	0.1750	0.6605	1.1700	0.1780	0.0608	S	Nocera Umbra-Salmata	
			10	1.6011	3.6700	0.3620	0.0992	0.6889	0.7670	0.0960	0.0384	R	Nocera Umbra	
			11	2.1657	5.5800	0.6450	0.1110	0.4495	0.9080	0.2730	0.1470	R	Nocera Umbra-Biscontini	
			18	0.2839	0.6900	0.5800	0.3090	0.1484	0.3610	0.3910	0.1260	R	Gubbio-Piana	
			37	0.1121	0.1700	0.0785	0.0157	0.0356	0.0809	0.0462	0.0096	R	Sellano	
1998	4	13	1514	39.27	41.05	9	4.80	16.96						TU
			73	0.0815	0.1290	0.2170	0.0787	0.0396	0.1030	0.0949	0.0265		Erzurum-Bayindirlik ve Iskan Mudurlugu	
			80	0.0344	0.0761	0.0974	0.0442	0.0133	0.0263	0.0377	0.0165	A	Tercan-Meteoroji Mudurlugu	
1999	4	6	0008	39.34	38.32	7	4.70	17.13						TU
			106	0.1158	0.2260	0.2840	0.1710	0.0356	0.0922	0.0949	0.0995		Elazig-Bayindirlik ve Iskan Mudurlugu	
			110	0.0383	0.1150	0.0601	0.0732	0.0276	0.0970	0.0247	0.0063	R	Malatya-Bayindirlik ve Iskan Mudurlugu	
1999	8	17	0001	40.70	29.99	17	7.80	20.36	S					TU
			3	3.5058	8.3400	4.3500	3.7100	2.4528	4.1600	3.4800	4.1100	A	Sakarya-Bayindirlik ve Iskan Mudurlugu[46]	
			14	2.1104	6.0800	4.0800	2.8700	1.3274	2.7100	1.2700	0.7960	R	Izmit-Meteoroloji Istasyonu	
			29	3.8204	5.7000	6.3100	6.2400	3.3595	3.7800	1.9100	1.2100	A	Duzce-Meteoroloji Mudurlugu	
			31	1.3007	5.8000	2.3400	1.5100	1.2847	1.8200	1.2200	0.7280		Goynuk-Devlet Hastanesi	
			45	1.1522	2.4500	3.2500	2.6400	0.6107	2.2300	0.8560	1.1200		Iznik-Karayollari Sefligi Muracaati	
			55	2.0356	4.6500	4.8500	1.9100	1.7381	3.4300	2.5700	0.9010		Gebze	
			60	2.0619	6.4100	2.0700	1.0900	0.7545	2.0400	1.1300	0.5470	A	Arcelik	
			60	0.9743	2.4400	2.5800	2.0500	0.4901	1.0100	0.8430	1.1600	S	Bursa-Tofa Fabrikasi	
			93	0.5157	1.3900	0.7740	0.5610	0.3159	0.8400	0.5150	0.3370	A	Istanbul-Bayindirlik ve Iskan Mudurlugu	
			100	0.5452	0.9720	1.2200	1.4400	0.2281	0.7930	0.5100	0.7560		Bursa-Sivil Savunma Mudurluga	
			103	1.8400	4.4800	8.9000	1.1600	1.2653	1.7900	0.8690	0.3210	S	Fatih	
			111	0.9284	1.7100	3.4000	1.9300	0.4703	0.7450	1.0600	0.5940	A	Yesilkoy-Havaalani	
			117	1.6805	9.2800	1.8400	1.1200	0.5669	1.6600	0.7820	0.3140	A	Kucuk-Cekmece	
			120	1.1805	2.8300	2.4100	1.4600	0.4981	1.4200	1.2200	0.4890		Istanbul-Nukleer Santrali	
			121	2.5575	4.1700	6.6700	5.6600	0.7476	1.7900	0.8590	1.2200	S	Ambarli-Termik Santrali	
			143	0.5652	0.7820	1.3100	2.2100	0.2130	0.3160	0.5090	0.5280		Kutahya-Sivil Savunma Mudurlugu	
			179	0.9206	1.6300	1.9500	1.2800	0.2048	0.3970	0.3330	0.2110	A	Botas-Gas Terminal	
			195	1.0127	1.3300	2.6300	2.4500	0.5336	0.9810	1.6900	0.3020		Eregli-Kaymakamlik Binasi	
			208	0.1421	0.1670	0.3620	0.5950	0.0510	0.0619	0.1470	0.2370		Afyon-Bayindirlik ve Iskan Mudurlugu	
			221	0.1454	0.3320	0.4380	0.2370	0.0756	0.1550	0.1860	0.0999	A	Balikesir-Bayindirlik ve Iskan Mudurlugu	
			234	0.1078	0.1360	0.4760	0.3370	0.0343	0.0796	0.1070	0.0707		Usak-Meteorologji Mudurlugu	

continued on next page

[46] Only one horizontal component.

Tab. D.3: *continued*

Date			Time	Lat.	Long.	Depth	M_s	$\log M_0$	F					C
			d	a_h	$\mathrm{SA}_h(0.2)$	$\mathrm{SA}_h(0.5)$	$\mathrm{S}_h(1.0)$	a_v	$\mathrm{SA}_v(0.2)$	$\mathrm{SA}_v(0.5)$	$\mathrm{SA}_v(1.0)$	S	Station	
			269	0.0833	0.0925	0.1980	0.2350	0.0283	0.0548	0.0820	0.0830		Tosya-Meteoroloji Mudurlugu	
			319	0.2171	0.2780	0.7530	0.7250	0.0597	0.1210	0.2400	0.1070		Canakkale-Meteoroloji Istasyonu	
			350	0.0913	0.1020	0.2190	0.2530	0.0295	0.0344	0.1090	0.0826		Bornova-Eylul Universite Ziraat Fakultesi	
			373	0.0456	0.0496	0.0903	0.1110	0.0149	0.0189	0.0436	0.0489	S	Aydin-Hayvan Hastanesi	
			485	0.0102	0.0122	0.0374	0.0148	0.0036	0.0076	0.0058	0.0077	R	Tokat-DSI Misafirhanesi	
1999	9	7	1156	38.08	23.58	17	5.90	17.89	N					GR
			15	3.1849	9.6600	5.1400	1.5300	1.9361	2.3000	0.8810	0.8250		Athens-Sepolia (Garage)	
			15	5.0240	12.5000	4.6400	1.0200	2.1675	1.1600	0.5160	0.2520		Athens-Monastiraki	
			16	2.9917	9.5800	3.8000	1.2400	1.2439	2.1800	1.1300	0.3880	R	Athens 3 (Kallithea District)	
			19	1.5661	5.8300	0.9720	0.4100	0.8821	1.7400	0.5420	0.6290	A	Athens 2 (Chalandri District)	
			23	0.6243	1.0900	0.5020	0.3280	0.3955	0.5430	0.3950	0.3450		Athens-Ayia Paraskevi (Demokritos)	
1999	9	20	1747	23.86	120.81	11	7.60	20.53	T					TA
			0	4.2167	10.4000	8.4700	5.5200	1.5712	3.4300	2.5200	1.9100		Taiwan-CWB station: TCU078	
			0	6.0813	20.9000	11.2000	7.5100	4.1037	8.6000	2.2600	2.4500		Taiwan-CWB station: TCU071	
			0	5.6846	18.7000	11.7000	6.6200	3.7708	5.8600	4.3500	2.2100		Taiwan-CWB station: TCU079	
			0	4.8968	11.0000	11.1000	9.6400	2.4207	4.6800	3.5400	3.0200		Taiwan-CWB station: TCU072	
			0	3.3881	9.0700	5.7700	4.0600	1.5328	3.5000	2.3200	1.7500		Taiwan-CWB station: TCU089	
			0	8.1471	15.4000	17.5000	21.7000	7.2123	10.3000	13.6000	5.5200		Taiwan-CWB station: CHY080	
			0	2.0038	4.4200	5.3700	2.4300	0.9322	1.1700	1.5300	1.2500		Taiwan-CWB station: CHY074	
			0	10.1140	16.0000	17.9000	25.6000	3.2474	6.5600	7.7400	2.7300		Taiwan-CWB station: TCU084	
			1	3.4237	6.3100	5.8500	9.7600	1.5246	2.3000	3.4600	1.8700		Taiwan-CWB station: TCU052	
			1	6.6151	8.0900	12.7000	7.4000	2.7347	4.4000	2.5200	4.1400		Taiwan-CWB station: TCU068	
			1	6.9449	9.5600	9.4200	12.1000	1.8117	5.0800	3.4200	2.8400		Taiwan-CWB station: TCU065	
			2	9.7779	16.8000	14.5000	5.6200	3.4421	3.6500	8.3000	6.1600		Taiwan-CWB station: TCU129	
			2	4.7264	8.0300	11.0000	9.1100	2.0972	5.2000	3.6900	2.6600		Taiwan-CWB station: TCU067	
			3	2.1379	2.7800	6.3200	5.7600	0.9643	1.3900	2.0100	2.7000		Taiwan-CWB station: TCU102	
			3	3.5484	10.1000	9.8900	7.0000	2.3344	2.9600	2.7600	2.9100		Taiwan-CWB station: TCU076	
			3	2.5028	7.0000	5.2600	3.2300	1.6286	3.7400	2.8900	1.8000		Taiwan-CWB station: TCU075	
			4	7.4480	15.7000	18.7000	10.5000	2.8444	5.2400	2.5500	1.9000		Taiwan-CWB station: CHY028	
			4	2.2911	5.8700	5.3400	3.4700	1.2974	2.3800	2.2500	2.7600		Taiwan-CWB station: TCU101	
			4	5.7203	8.3500	13.8000	13.7000	2.5874	4.2200	3.5900	1.4100		Taiwan-CWB station: TCU074	
			6	2.7827	6.7600	5.2400	3.6600	1.6335	2.7500	2.0300	1.9900		Taiwan-CWB station: TCU049	
			7	1.3612	2.4900	4.2100	3.4800	1.4849	2.5200	1.4100	1.2700		Taiwan-CWB station: TCU103	
			8	2.0210	3.9200	6.5100	2.8900	1.4132	3.4200	3.3000	2.3800		Taiwan-CWB station: TCU053	
			8	1.7400	2.7100	4.1500	3.2500	1.2164	2.0600	1.9900	1.7600		Taiwan-CWB station: TCU054	

continued on next page

Tab. D.3: *continued*

Date	Time	Lat.	Long.	Depth	M_s	$\log M_0$	F					C
	d	a_h	$SA_h(0.2)$	$SA_h(0.5)$	$S_h(1.0)$	a_v	$SA_v(0.2)$	$SA_v(0.5)$	$SA_v(1.0)$	S	Station	
	8	1.9144	3.6700	6.2700	3.4400	1.1507	2.5300	1.7900	2.2100		Taiwan-CWB station: TCU082	
	9	1.7552	5.3100	4.2900	4.6100	1.4861	3.8300	3.0200	1.7700		Taiwan-CWB station: TCU120	
	9	2.2545	5.5400	7.4000	3.3500	1.3478	2.0100	1.4600	1.9800		Taiwan-CWB station: TCU055	
	9	1.1085	2.2400	4.0700	2.3900	0.7346	1.2900	0.9330	1.4100		Taiwan-CWB station: TCU087	
	10	2.2773	5.4400	4.9900	3.8100	2.2664	4.9300	0.9740	1.2100		Taiwan-CWB station: TCU122	
	10	2.6016	5.3600	6.1100	4.3500	1.6150	4.0200	1.9500	1.7300		Taiwan-CWB station: CHY024	
	10	2.0028	5.4500	4.4800	3.6100	1.1538	1.4400	1.8700	1.8800		Taiwan-CWB station: TCU051	
	10	1.8673	3.2100	4.6100	2.1500	0.7809	1.9900	1.7300	1.2000		Taiwan-CWB station: TCU060	
	10	1.6382	2.6800	4.0000	5.4400	1.2211	2.9200	1.5700	2.9900		Taiwan-CWB station: TCU136	
	11	1.8438	4.2700	5.1000	4.5700	0.9393	1.8900	1.6100	1.2900		Taiwan-CWB station: TCU063	
	11	3.8445	6.6900	9.9200	7.9600	1.3803	3.5800	2.2800	1.4200		Taiwan-CWB station: CHY101	
	11	3.7498	5.8100	9.9200	8.4800	1.9549	2.8100	3.1100	2.4700		Taiwan-CWB station: CHY006	
	12	2.8425	4.1200	7.4700	3.7500	1.5005	3.1100	2.3500	1.5200		Taiwan-CWB station: CHY029	
	12	1.3185	3.2800	3.5700	2.6000	0.7690	1.5000	1.6400	1.0100		Taiwan-CWB station: TCU050	
	13	1.2985	3.1600	4.8100	2.9200	0.6401	1.2900	1.3200	0.8910		Taiwan-CWB station: TCU056	
	13	1.8062	2.3200	4.0100	5.4400	1.0640	2.0500	1.9700	1.4100		Taiwan-CWB station: TCU110	
	13	1.2051	2.8900	2.9400	2.2700	0.7024	1.4200	1.1400	1.4500		Taiwan-CWB station: TCU100	
	13	1.7070	4.0000	4.4000	5.8600	1.0028	1.8100	1.0900	1.3400		Taiwan-CWB station: TCU116	
	13	2.4359	4.2100	6.5700	6.0500	0.9476	1.9300	1.9100	1.2000		Taiwan-CWB station: CHY035	
	14	1.5376	2.4400	5.3100	3.7500	1.3062	2.3500	1.4200	0.8460		Taiwan-CWB station: TCU109	
	14	1.1276	2.1900	2.9600	2.6800	0.6094	1.4100	1.2100	1.5500		Taiwan-CWB station: TCU057	
	14	1.0041	1.8900	2.4700	2.6900	0.7188	1.5400	1.0500	1.1700		Taiwan-CWB station: TCU104	
	15	3.0054	4.1400	7.6600	11.0000	0.8548	1.7500	1.9200	1.7600		Taiwan-CWB station: CHY034	
	16	1.5313	2.2100	3.2200	2.0400	0.7887	1.8000	1.2000	1.2300		Taiwan-CWB station: TCU048	
	16	1.3434	2.2500	3.7200	3.7100	0.6991	1.6800	0.9140	1.3600		Taiwan-CWB station: TCU123	
	16	1.5426	3.6300	6.2500	3.2600	1.0184	1.6500	1.3700	1.2700		Taiwan-CWB station: TCU106	
	16	1.4362	2.2700	5.4600	2.5100	0.8305	1.5100	1.4100	1.6400		Taiwan-CWB station: TCU128	
	17	2.6762	5.9700	8.6900	6.0800	0.9521	1.7100	1.2400	0.6450		Taiwan-CWB station: CHY036	
	18	1.1552	2.1700	4.1000	1.8300	0.5290	1.1200	1.1100	0.9180		Taiwan-CWB station: TCU105	
	18	1.4046	2.6300	4.8900	2.1800	0.7493	1.7600	1.1100	0.9820		Taiwan-CWB station: TCU061	
	19	5.9979	8.0300	15.1000	3.5600	1.2134	2.7300	3.5900	0.8520		Taiwan-CWB station: CHY041	
	19	1.4803	2.2200	3.7300	4.8700	0.4170	0.9960	0.9130	1.6400		Taiwan-CWB station: TCU059	
	19	0.8709	1.5000	2.1700	1.8200	0.5938	1.4100	1.4400	0.9990		Taiwan-CWB station: TCU064	
	20	1.4950	2.8700	4.6900	3.3500	1.1676	2.8600	1.6300	1.0800		Taiwan-CWB station: CHY025	
	20	2.3509	2.9700	8.4700	3.7700	0.6046	1.4200	1.6300	1.0200		Taiwan-CWB station: TCU070	

continued on next page

Tab. D.3: *continued*

Date	Time	Lat.	Long.	Depth	M_s	$\log M_0$	F					C
	d	a_h	$\mathrm{SA}_h(0.2)$	$\mathrm{SA}_h(0.5)$	$\mathrm{S}_h(1.0)$	a_v	$\mathrm{SA}_v(0.2)$	$\mathrm{SA}_v(0.5)$	$\mathrm{SA}_v(1.0)$	S	Station	
	20	2.1775	4.5100	5.2700	1.8000	1.1130	1.8800	2.1900	0.6300		Taiwan-CWB station: CHY010	
	21	1.2092	4.7700	2.3100	1.4600	0.7870	2.1300	2.1800	1.0100		Taiwan-CWB station: TCU046	
	21	1.1526	2.1600	3.9100	3.4400	0.6518	1.6100	1.1900	1.1600		Taiwan-CWB station: TCU107	
	22	1.3967	2.9000	3.3300	2.8300	0.6010	1.6000	1.3800	0.9750		Taiwan-CWB station: TCU036	
	23	1.1999	1.5000	3.0200	2.8200	0.8277	1.2900	1.0600	0.7070		Taiwan-CWB station: TCU111	
	24	1.3386	3.5300	4.6500	2.9900	0.9585	1.5000	1.4200	0.9590		Taiwan-CWB station: TCU039	
	24	0.8157	1.8700	2.7200	1.6100	0.6884	1.1600	1.2000	0.7140		Taiwan-CWB station: TCU115	
	25	1.7832	5.5200	3.4100	3.0000	0.7318	1.6300	0.8350	0.5780		Taiwan-CWB station: CHY046	
	25	1.4234	2.4000	4.0300	2.2600	0.6310	1.4700	1.0400	0.5630		Taiwan-CWB station: TCU040	
	26	1.0885	1.7200	2.3700	2.8100	0.7461	1.4700	0.9130	1.0700		Taiwan-CWB station: TCU117	
	26	0.8420	1.9800	1.8500	0.6980	0.3142	0.8750	0.7330	0.5110		Taiwan-CWB station: KAU054	
	27	0.8801	1.9000	2.2100	1.8800	0.5551	0.9050	1.5700	0.6290		Taiwan-CWB station: CHY042	
	27	1.4303	3.0200	3.8900	3.2100	0.6072	1.8000	1.1300	0.4850		Taiwan-CWB station: TCU038	
	27	1.9641	2.6000	9.7900	2.9500	0.4902	0.9660	2.1900	0.7760		Taiwan-CWB station: CHY086	
	28	0.6983	2.1000	1.7700	1.2900	0.5208	1.2600	0.9500	0.7990		Taiwan-CWB station: TCU112	
	28	0.9515	1.6800	2.2800	1.4700	1.0130	1.4500	1.6100	0.6690		Taiwan-CWB station: TCU118	
	29	1.3426	4.3900	3.8000	1.0100	0.5571	1.2300	1.3500	0.5310		Taiwan-CWB station: CHY087	
	30	0.7686	1.2900	1.3300	1.8200	0.6501	1.3100	1.0700	0.8190		Taiwan-CWB station: CHY026	
	30	4.9346	9.5900	12.3000	4.4700	2.8922	4.0300	4.6300	2.5700		Taiwan-CWB station: TCU045	
	31	2.3485	4.8100	4.0400	2.9700	0.7397	1.2900	1.6600	1.7800		Taiwan-CWB station: TCU042	
	32	0.7175	1.6700	1.8900	1.0400	0.7273	1.0300	0.6930	0.5300		Taiwan-CWB station: TCU113	
	32	2.1899	5.6500	3.7800	2.9400	0.5485	1.0500	0.8200	0.9050		Taiwan-CWB station: TCU029	
	32	2.4879	4.0400	13.6000	2.3500	0.9686	1.7800	3.9800	1.3400		Taiwan-CWB station: CHY014	
	33	1.0646	2.0800	2.7900	2.2700	0.3624	0.6280	0.8730	0.3280		Taiwan-CWB station: CHY039	
	33	1.3278	2.5800	2.3100	2.2900	0.5951	1.1800	0.9410	0.6330		Taiwan-CWB station: TCU031	
	34	0.4800	0.9910	1.2600	0.7660	0.2279	0.3840	0.7640	0.3430		Taiwan-CWB station: CHY102	
	37	0.7854	1.6900	1.9500	1.6500	0.4899	0.7140	0.6590	0.4560		Taiwan-CWB station: CHY032	
	37	0.3786	1.1100	0.9610	0.8370	0.2058	0.3790	0.5120	0.5430		Taiwan-CWB station: KAU050	
	38	2.1354	4.4700	7.0300	2.6900	0.3830	0.8350	0.9710	0.6780		Taiwan-CWB station: CHY088	
	38	3.9707	9.3200	7.7400	8.4000	2.4424	2.4900	3.0500	1.6300		Taiwan-CWB station: TCU047	
	38	1.4883	2.4800	4.6900	1.3300	0.3652	0.8500	0.7590	0.5490		Taiwan-CWB station: CHY052	
	39	0.3246	1.0900	0.7600	0.4460	0.2108	0.6860	0.3270	0.4260		Taiwan-CWB station: TTN051	
	39	0.4657	0.6530	1.8100	1.3500	0.2666	0.3790	0.7650	0.4120		Taiwan-CWB station: CHY109	
	40	2.4985	3.5700	9.1700	2.3300	0.7218	1.0600	1.2800	0.6380		Taiwan-CWB station: TCU034	
	40	3.7168	8.7900	5.2700	3.0200	0.8004	2.2000	1.6100	1.8900		Taiwan-CWB station: NST	

continued on next page

Tab. D.3: *continued*

Date	Time	Lat.	Long.	Depth	M_s	$\log M_0$	F					C
	d	a_h	$\mathrm{SA}_h(0.2)$	$\mathrm{SA}_h(0.5)$	$\mathrm{S}_h(1.0)$	a_v	$\mathrm{SA}_v(0.2)$	$\mathrm{SA}_v(0.5)$	$\mathrm{SA}_v(1.0)$	S	Station	
	41	0.5160	1.1000	1.8600	0.9270	0.2651	0.4690	0.6030	0.4530		Taiwan-CWB station: CHY081	
	41	0.4028	0.7900	0.9380	0.5040	0.3933	0.9460	0.9550	0.9040		Taiwan-CWB station: KAU001	
	44	0.5244	1.3500	1.3800	0.8380	0.4389	1.0400	0.5790	0.4410		Taiwan-CWB station: CHY027	
	45	1.0377	1.4900	2.3700	0.5340	0.2691	0.5140	0.5740	0.2620		Taiwan-CWB station: CHY050	
	45	1.5813	5.1300	4.1800	2.1800	0.5752	1.4100	0.7740	0.8180		Taiwan-CWB station: TCU033	
	45	0.5015	1.2600	1.5300	0.7710	0.2698	0.6830	0.4980	0.3480		Taiwan-CWB station: CHY079	
	47	6.8420	15.2000	9.7500	3.6900	2.1821	3.0000	1.7500	1.4900		Taiwan-CWB station: TCU095	
	47	1.3811	2.4000	4.0800	1.3700	0.6691	1.2300	1.7300	0.6580		Taiwan-CWB station: HWA034	
	47	1.8807	4.6200	3.6200	2.5500	0.9308	1.7200	1.0100	0.4370		Taiwan-CWB station: ILA067	
	48	0.2425	0.6890	0.3400	0.2850	0.2224	0.4080	0.5830	0.2690		Taiwan-CWB station: HWA053	
	49	0.9427	1.5100	2.6900	1.6800	0.3215	0.8670	0.6820	0.3230		Taiwan-CWB station: CHY054	
	49	0.2576	0.6470	0.5420	0.4850	0.2487	0.5520	0.3810	0.4670		Taiwan-CWB station: HWA024	
	49	0.5270	1.3500	1.1000	0.7000	0.3590	1.1400	0.7780	0.3720		Taiwan-CWB station: HWA038	
	49	0.6068	1.4600	1.4400	0.8840	0.2057	0.5610	0.5490	0.4110		Taiwan-CWB station: CHY019	
	50	1.3472	2.4800	2.3600	1.2200	0.8353	1.1100	1.1300	0.6460		Taiwan-CWB station: HWA032	
	50	0.6052	1.0800	1.4600	1.6200	0.2873	0.8560	0.6660	0.5860		Taiwan-CWB station: HWA036	
	50	0.5271	1.1200	1.2600	0.9580	0.0031	0.0049	0.0031	0.0017		Taiwan-CWB station: HWA054	
	50	0.8832	2.1700	2.5800	0.8020	0.6003	1.5400	0.9900	0.5220		Taiwan-CWB station: HWA006	
	50	0.7910	1.9900	1.6200	0.6770	0.3502	1.4100	0.5720	0.5270		Taiwan-CWB station: TTN041	
	50	1.4380	3.4400	5.1500	2.3300	0.4546	0.8790	1.0200	0.6880		Taiwan-CWB station: HWA005	
	51	0.3796	0.7260	0.9720	0.6630	0.1933	0.3030	0.4170	0.4730		Taiwan-CWB station: KAU047	
	52	0.9795	3.1400	2.0900	1.4400	0.4524	0.9580	0.9300	0.6320		Taiwan-CWB station: TCU098	
	52	0.6845	1.7000	1.6700	1.1600	0.5501	1.2700	1.2700	0.5830		Taiwan-CWB station: HWA020	
	53	0.6791	2.4100	1.2200	0.8920	0.3499	0.5830	0.6860	0.5810		Taiwan-CWB station: TCU025	
	53	0.9799	2.3500	3.0500	2.0600	0.6515	1.4200	0.8970	0.5000		Taiwan-CWB station: TCU015	
	53	0.7423	1.5600	2.8500	2.2500	0.4294	0.6570	1.0000	0.8650		Taiwan-CWB station: HWA039	
	53	0.7453	1.7000	1.3000	0.8310	0.5082	1.1000	0.8450	0.8220		Taiwan-CWB station: HWA035	
	54	0.7815	1.1400	1.5800	2.0400	0.4411	0.9280	0.8260	0.9330		Taiwan-CWB station: HWA030	
	54	1.1788	2.3000	2.6900	2.9700	0.6894	1.4000	1.8600	2.2600		Taiwan-CWB station: HWA037	
	54	0.7753	1.2900	2.6300	2.6400	0.4165	0.8260	1.2700	1.0100		Taiwan-CWB station: HWA041	
	54	0.3175	0.6080	0.7980	0.3650	0.2016	0.4440	0.5720	0.2320		Taiwan-CWB station: TTN040	
	54	0.8828	1.5000	3.6500	3.0300	0.5808	0.7740	1.6500	1.6900		Taiwan-CWB station: HWA055	
	54	0.6163	2.0700	1.8000	1.2000	0.2146	0.5360	0.4190	0.6400		Taiwan-CWB station: CHY100	
	55	0.4176	1.2900	0.6150	0.4390	0.1822	0.4610	0.4020	0.4180		Taiwan-CWB station: CHY061	
	55	0.5732	1.2500	0.9750	0.4840	0.1899	0.5120	0.3370	0.3920		Taiwan-CWB station: CHY062	

continued on next page

Tab. D.3: *continued*

Date	Time d	Lat. a_h	Long. $\mathrm{SA}_h(0.2)$	Depth $\mathrm{SA}_h(0.5)$	M_s $\mathrm{S}_h(1.0)$	$\log M_0$ a_v	F $\mathrm{SA}_v(0.2)$	$\mathrm{SA}_v(0.5)$	$\mathrm{SA}_v(1.0)$	S	Station	C
	55	1.0785	2.8900	1.4700	0.6040	0.6046	1.7300	0.5380	0.3080		Taiwan-CWB station: HWA056	
	55	1.0729	2.7400	2.2700	1.1200	0.5027	1.2500	0.7880	0.6540		Taiwan-CWB station: HWA058	
	56	0.9154	1.3700	1.4900	1.7400	0.3315	0.6820	0.6120	0.8950		Taiwan-CWB station: TCU094	
	56	1.0730	1.3200	2.3200	2.3300	0.4994	0.9020	0.7810	0.5820		Taiwan-CWB station: TCU017	
	56	0.7283	1.2300	1.4300	1.6400	0.2321	0.5780	0.3910	0.2790		Taiwan-CWB station: CHY044	
	56	0.5111	1.1800	1.0100	0.6280	0.1999	0.4310	0.4800	0.3860		Taiwan-CWB station: CHY057	
	56	1.6155	3.2500	4.9400	2.6000	0.4871	1.0900	1.0100	0.6700		Taiwan-CWB station: HWA033	
	57	1.1720	2.5600	2.2700	1.4400	0.4813	1.4700	0.9270	0.5810		Taiwan-CWB station: TCU026	
	57	0.3306	0.6780	1.3900	0.7230	0.2095	0.3230	0.3850	0.6770		Taiwan-CWB station: TTN020	
	58	0.7588	1.7500	1.6200	1.2600	0.2949	0.6020	0.5170	0.6210		Taiwan-CWB station: TCU096	
	58	0.8292	1.3200	3.1200	1.9000	0.2597	0.6090	0.5450	0.4630		Taiwan-CWB station: TCU081	
	58	1.0494	2.0900	1.9100	3.0900	0.6530	0.8480	1.0700	1.3800		Taiwan-CWB station: HWA031	
	59	1.3698	2.5400	4.0600	1.7800	0.5650	0.6790	1.6500	0.8420		Taiwan-CWB station: HWA059	
	59	0.4848	1.1000	1.3900	1.2200	0.2724	0.8730	0.5350	0.3440		Taiwan-CWB station: CHY017	
	60	0.4878	1.3800	1.7300	1.4100	0.2483	0.4600	0.4910	0.4010		Taiwan-CWB station: CHY058	
	60	0.7531	0.9790	2.5500	1.4200	0.3973	0.5810	1.0900	0.9640		Taiwan-CWB station: TTN022	
	60	0.6525	1.0500	1.2500	1.5600	0.2628	0.3990	0.6610	0.8450		Taiwan-CWB station: TTN023	
	61	0.8302	1.7000	1.8000	1.2400	0.4456	1.1000	0.7430	0.7110		Taiwan-CWB station: HWA017	
	61	0.6212	1.1000	2.0900	1.1700	0.3759	0.5890	0.7700	0.5110		Taiwan-CWB station: TCU085	
	61	0.8839	1.6000	1.5200	1.1000	0.3194	1.0800	0.8440	0.3590		Taiwan-CWB station: HWA002	
	61	1.0008	1.8100	4.1200	2.8900	0.3865	0.8430	0.5340	1.1100		Taiwan-CWB station: HWA049	
	61	0.6238	1.5000	2.0500	0.4400	0.2244	0.8550	0.5410	0.3470		Taiwan-CWB station: CHY022	
	62	0.9561	1.6200	1.7400	1.9200	0.4678	0.8160	0.9200	1.1500		Taiwan-CWB station: HWA016	
	62	0.7272	1.1900	2.2800	0.9010	0.2739	0.4420	0.7110	0.4980		Taiwan-CWB station: HWA044	
	62	1.0481	1.3300	1.9200	3.1400	0.4844	0.9960	0.9210	0.8540		Taiwan-CWB station: HWA015	
	62	1.6311	2.4500	4.8100	3.4100	0.4980	1.1200	1.3100	0.5720		Taiwan-CWB station: HWA048	
	63	0.6750	1.7500	1.4400	0.9070	0.2896	0.5660	0.7640	0.4330		Taiwan-CWB station: HWA043	
	63	1.1560	2.1500	2.9800	2.1500	0.3552	0.8630	1.0100	0.5160		Taiwan-CWB station: HWA027	
	63	1.1615	1.3200	2.4800	2.6100	0.4509	0.7140	1.1800	0.7240		Taiwan-CWB station: HWA003	
	63	1.6348	2.8000	4.3500	3.0200	0.4199	1.0200	0.6360	0.5980		Taiwan-CWB station: HWA051	
	64	0.9195	1.5700	2.4900	2.7100	0.3433	0.8410	0.6490	1.2500		Taiwan-CWB station: HWA011	
	64	0.8603	1.3600	1.6700	1.1900	0.3891	0.8070	0.6110	0.9220		Taiwan-CWB station: TTN031	
	64	0.8652	1.2900	1.8300	2.4800	0.2731	0.6160	0.6120	0.4840		Taiwan-CWB station: HWA029	
	64	0.3663	0.9540	0.9500	0.5390	0.2595	0.5240	0.6860	0.4280		Taiwan-CWB station: HWA023	
	64	0.8467	2.2200	1.8600	2.5000	0.5066	1.4600	0.9280	1.3300		Taiwan-CWB station: HWA050	

continued on next page

Tab. D.3: *continued*

Date	Time	Lat.	Long.	Depth	M_s	$\log M_0$	F					C
	d	a_h	$\mathrm{SA}_h(0.2)$	$\mathrm{SA}_h(0.5)$	$\mathrm{S}_h(1.0)$	a_v	$\mathrm{SA}_v(0.2)$	$\mathrm{SA}_v(0.5)$	$\mathrm{SA}_v(1.0)$	S	Station	
	64	0.8121	1.1900	2.6900	1.8700	0.3307	0.5650	1.1300	0.6920		Taiwan-CWB station: TTN001	
	65	1.1888	2.1000	2.3000	3.2800	0.5203	1.3300	0.6340	0.8610		Taiwan-CWB station: HWA013	
	65	0.2749	0.6110	0.6530	0.3200	0.1986	0.5330	0.4330	0.2290		Taiwan-CWB station: TTN024	
	65	0.9926	2.2800	2.9500	2.4300	0.4970	0.9460	1.0700	0.6880		Taiwan-CWB station: HWA028	
	65	0.7014	0.9870	1.7900	2.4000	0.2693	0.5430	1.1000	0.6550		Taiwan-CWB station: TTN032	
	65	1.2106	3.2300	1.2400	0.7130	0.5049	1.7800	0.6500	0.4600		Taiwan-CWB station: HWA057	
	65	0.4578	0.6610	1.7600	1.3600	0.2831	0.3540	0.7730	0.9120		Taiwan-CWB station: TTN044	
	65	0.5739	1.3800	1.5400	1.0600	0.2067	0.4610	0.5760	0.4590		Taiwan-CWB station: CHY099	
	66	1.3237	2.8200	4.8700	3.6700	0.4583	1.0300	1.2300	0.5700		Taiwan-CWB station: HWA2	
	66	0.9849	1.2900	3.6200	3.1800	0.3814	0.9670	0.7520	0.7150		Taiwan-CWB station: HWA014	
	66	0.6969	1.5900	1.7000	1.5400	0.3091	0.9720	0.6540	0.5100		Taiwan-CWB station: HWA026	
	67	0.9015	1.0700	1.8600	1.9700	0.3205	0.6550	0.5920	0.5310		Taiwan-CWB station: HWA007	
	67	1.1063	2.6600	1.9000	1.4300	0.3235	0.7300	0.5670	0.5710		Taiwan-CWB station: HWA009	
	67	0.3655	0.6580	0.9490	0.7800	0.1633	0.3990	0.3740	0.4880		Taiwan-CWB station: TTN033	
	67	0.8180	2.8300	2.7600	1.6600	0.4646	0.8310	0.6410	0.3780		Taiwan-CWB station: HWA046	
	67	0.3427	0.4680	0.7560	0.8250	0.1649	0.3320	0.4930	0.4440		Taiwan-CWB station: TTN045	
	68	0.4288	0.8270	1.4600	0.9850	0.2437	0.3330	0.5420	0.3750		Taiwan-CWB station: TCU018	
	68	0.7100	1.4200	1.5800	2.1200	0.2765	0.5170	0.4320	0.6970		Taiwan-CWB station: HWA012	
	68	0.3945	1.0600	0.8250	0.5780	0.2363	0.5220	0.4580	0.4910		Taiwan-CWB station: HWA060	
	69	0.3817	1.4700	0.5390	0.2910	0.1757	0.3190	0.3020	0.2130		Taiwan-CWB station: KAU069	
	69	0.6690	1.8100	1.5300	1.2900	0.3199	0.7360	0.7760	0.2240		Taiwan-CWB station: HWA025	
	69	0.8250	1.9300	0.5980	0.4190	0.3234	0.4730	0.4540	0.2870		Taiwan-CWB station: ILA063	
	71	0.5943	1.0400	2.3400	1.2200	0.2251	0.5620	0.7410	0.5940		Taiwan-CWB station: CHY063	
	71	0.4837	0.9690	1.2900	1.3200	0.2404	0.4710	0.8160	0.5060		Taiwan-CWB station: TTN014	
	72	0.7359	0.8310	1.9300	2.7200	0.1961	0.2740	0.3430	0.6680		Taiwan-CWB station: KAU020	
	72	1.1382	1.4800	2.4500	2.4800	0.5033	0.9230	1.1100	1.5200		Taiwan-CWB station: TCU147	
	72	1.1051	1.5600	5.1600	0.7240	0.1672	0.4440	0.3960	0.2890		Taiwan-CWB station: TTN046	
	72	0.5802	1.6200	1.4400	0.8040	0.1763	0.4880	0.5690	0.3430		Taiwan-CWB station: TTN042	
	72	0.4175	0.6940	1.2200	1.0200	0.2496	0.5290	0.6100	0.4230		Taiwan-CWB station: TTN004	
	73	0.8487	1.7700	1.9300	1.6500	0.2605	0.6630	0.7800	0.7230		Taiwan-CWB station: TCU006	
	74	0.4448	1.1100	1.2700	1.0500	0.1295	0.2410	0.3310	0.3080		Taiwan-CWB station: CHY059	
	75	0.3468	0.4720	0.8360	0.7710	0.1457	0.2140	0.5020	0.3940		Taiwan-CWB station: KAU018	
	75	0.3914	0.6520	1.0200	0.5390	0.1355	0.2880	0.3680	0.2310		Taiwan-CWB station: TTN026	
	76	0.6422	1.1700	1.4600	2.1500	0.2895	0.4950	0.5250	0.3810		Taiwan-CWB station: TCU011	
	76	0.2364	0.5310	0.8810	0.4610	0.1048	0.2070	0.3870	0.2970		Taiwan-CWB station: TTN002	

continued on next page

Tab. D.3: *continued*

Date	Time	Lat.	Long.	Depth	M_s	$\log M_0$	F					C
	d	a_h	$\mathrm{SA}_h(0.2)$	$\mathrm{SA}_h(0.5)$	$\mathrm{S}_h(1.0)$	a_v	$\mathrm{SA}_v(0.2)$	$\mathrm{SA}_v(0.5)$	$\mathrm{SA}_v(1.0)$	S	Station	
	77	0.8862	1.0200	1.8300	1.7700	0.1941	0.7590	0.3860	0.2520		Taiwan-CWB station: CHY078	
	77	0.3498	0.8040	0.8850	0.6420	0.2152	0.3880	0.5530	0.4490		Taiwan-CWB station: ILA024	
	78	1.1460	1.6300	4.5700	1.1100	0.3721	0.6010	0.7500	0.3390		Taiwan-CWB station: HWA022	
	79	0.7907	1.2500	1.8900	1.5200	0.1228	0.4120	0.2170	0.2130		Taiwan-CWB station: CHY071	
	79	0.3559	0.4850	1.2300	0.4690	0.1373	0.3150	0.5050	0.1310		Taiwan-CWB station: TTN018	
	79	1.8141	2.6600	4.4300	5.0400	0.6945	0.9610	1.7200	0.8830		Taiwan-CWB station: HWA045	
	79	0.2416	0.6270	0.6030	0.7850	0.0078	0.0258	0.0141	0.0071		Taiwan-CWB station: TTN047	
	80	0.4921	1.2700	1.1300	0.4190	0.1913	0.7170	0.5380	0.5020		Taiwan-CWB station: TTN025	
	80	0.5211	1.1000	1.6200	1.0800	0.1685	0.5360	0.2990	0.3320		Taiwan-CWB station: CHY023	
	81	0.6650	0.8010	1.7200	1.8800	0.2373	0.5350	0.4620	0.5270		Taiwan-CWB station: TCU009	
	81	0.8337	0.9350	2.4500	1.3600	0.2056	0.3430	0.5750	0.6200		Taiwan-CWB station: KAU012	
	81	1.1053	1.4400	3.7500	2.7200	0.3061	0.5120	0.8300	0.3800		Taiwan-CWB station: CHY065	
	81	0.3678	0.5860	1.2700	0.6170	0.1601	0.3240	0.5090	0.3290		Taiwan-CWB station: TTN027	
	81	0.9968	1.2500	2.2800	2.0900	0.3501	0.7410	0.6670	0.6010		Taiwan-CWB station: TCU083	
	82	0.6460	1.6800	1.3700	0.5990	0.5101	1.0600	0.6200	0.6590		Taiwan-CWB station: ILA050	
	82	0.3374	0.4880	1.2300	1.1700	0.1487	0.3290	0.3660	0.2180		Taiwan-CWB station: CHY096	
	83	0.4180	0.6540	1.0800	1.4200	0.1486	0.3910	0.3200	0.2170		Taiwan-CWB station: CHY070	
	83	0.8978	1.4800	2.1100	1.8300	0.2170	0.3960	0.4290	0.4340		Taiwan-CWB station: TCU010	
	83	0.2200	0.7150	0.3980	0.3160	0.1223	0.2970	0.2500	0.1810		Taiwan-CWB station: KAU077	
	83	0.1838	0.3950	0.5430	0.2820	0.1381	0.4800	0.3590	0.1530		Taiwan-CWB station: TTN028	
	83	0.2323	0.4440	0.8360	0.7230	0.1779	0.4030	0.3460	0.4500		Taiwan-CWB station: TTN048	
	84	0.5138	0.7860	1.6600	1.8400	0.2011	0.3880	0.6760	0.7140		Taiwan-CWB station: KAU085	
	85	0.6059	1.0500	1.5800	1.2700	0.2416	0.6580	0.7620	0.6900		Taiwan-CWB station: TAP047	
	85	0.7437	1.5900	1.7600	1.6700	0.2411	0.6130	0.6660	0.3250		Taiwan-CWB station: TCU008	
	85	0.9940	2.1900	2.3700	1.3200	0.5125	0.9170	1.5000	0.4000		Taiwan-CWB station: ILA066	
	85	0.2478	0.5240	0.4630	0.2290	0.1668	0.4140	0.2990	0.2110		Taiwan-CWB station: SSD	
	86	0.4212	0.9300	0.9530	1.4500	0.2071	0.3490	0.3640	0.3850		Taiwan-CWB station: CHY069	
	86	0.2369	0.2730	0.5170	0.9790	0.1350	0.1630	0.4200	0.3650		Taiwan-CWB station: TTN006	
	86	0.1466	0.1800	0.3280	0.4660	0.0612	0.0894	0.1420	0.1910		Taiwan-CWB station: TTN013	
	86	0.2624	0.3560	0.7200	0.7750	0.1505	0.1930	0.3690	0.4890		Taiwan-CWB station: TTN036	
	86	0.6716	0.9790	1.9000	1.4400	0.2673	0.9380	0.5210	0.3780		Taiwan-CWB station: ILA021	
	87	0.2178	0.2510	0.4020	0.8300	0.1449	0.1780	0.3110	0.5110		Taiwan-CWB station: TTN007	
	87	0.2267	0.3270	0.5930	0.7550	0.1224	0.1360	0.2360	0.3260		Taiwan-CWB station: TTN012	
	87	0.7042	1.4500	1.5500	1.1300	0.4322	0.7230	0.9440	0.5140		Taiwan-CWB station: ILA064	
	88	0.2728	0.3850	0.7730	0.8310	0.1166	0.1410	0.3330	0.3620		Taiwan-CWB station: TTN009	

continued on next page

Tab. D.3: *continued*

Date	Time	Lat.	Long.	Depth	M_s	$\log M_0$	F				C
	d	a_h	$\mathrm{SA}_h(0.2)$	$\mathrm{SA}_h(0.5)$	$\mathrm{S}_h(1.0)$	a_v	$\mathrm{SA}_v(0.2)$	$\mathrm{SA}_v(0.5)$	$\mathrm{SA}_v(1.0)$	S	Station
	88	0.6140	0.9180	1.5600	1.5800	0.2821	0.6430	0.6370	0.7470		Taiwan-CWB station: TCU007
	88	0.7002	0.9020	1.6200	1.3400	0.2124	0.3710	0.4790	0.5240		Taiwan-CWB station: TCU003
	88	0.2470	0.3530	0.6420	0.9410	0.1396	0.1790	0.3200	0.3850		Taiwan-CWB station: TTN005
	88	0.3033	0.3110	0.5090	0.9090	0.1358	0.1460	0.2470	0.3550		Taiwan-CWB station: TTN008
	88	0.4488	1.6800	0.4870	0.2980	0.1371	0.5970	0.3980	0.2990		Taiwan-CWB station: KAU078
	88	0.2370	0.2800	0.4300	0.9050	0.1422	0.1730	0.3340	0.6060		Taiwan-CWB station: TTN015
	88	0.7804	1.2700	2.4600	1.2000	0.2352	0.5260	0.8230	0.3440		Taiwan-CWB station: ILA051
	88	0.7909	2.0700	1.7000	1.2400	0.4876	1.3400	1.2400	0.4550		Taiwan-CWB station: ILA062
	89	0.2880	0.3780	0.8080	1.0200	0.0990	0.2100	0.2070	0.2880		Taiwan-CWB station: TTN010
	89	0.5873	1.3100	1.9100	0.7060	0.3584	0.8900	1.0500	0.3330		Taiwan-CWB station: ILA043
	91	0.5774	1.3400	1.3700	1.0200	0.2354	0.4010	0.5900	0.3220		Taiwan-CWB station: ILA046
	91	0.3983	0.4910	0.7550	1.0800	0.0915	0.1250	0.2100	0.2680		Taiwan-CWB station: KAU048
	91	0.6189	1.3500	2.0600	1.5800	0.2136	0.3840	0.5750	0.3580		Taiwan-CWB station: ILA014
	91	0.7238	0.9840	1.8400	2.0500	0.3799	0.4320	0.9580	0.5700		Taiwan-CWB station: ILA016
	92	0.7478	1.0000	1.9700	1.2500	0.2341	0.5850	0.4890	0.3820		Taiwan-CWB station: TAP043
	92	0.3741	0.5880	0.5090	0.6310	0.1396	0.2140	0.2350	0.3730		Taiwan-CWB station: TAP036
	92	0.3779	0.6020	0.7890	1.4600	0.0815	0.1670	0.2380	0.1860		Taiwan-CWB station: KAU063
	92	0.8322	1.1900	1.9600	2.4800	0.3135	0.6370	0.5010	0.5300		Taiwan-CWB station: ILA044
	93	0.6628	1.6600	1.6600	1.2300	0.1861	0.3740	0.4620	0.3640		Taiwan-CWB station: TCU014
	93	0.2652	0.4500	0.9790	0.2390	0.0865	0.1920	0.2030	0.1530		Taiwan-CWB station: TTN050
	93	0.5762	1.4100	1.4000	0.6550	0.2202	0.6730	0.8210	0.4150		Taiwan-CWB station: ILA010
	93	0.5299	0.6920	1.2400	1.5100	0.2355	0.4880	0.5480	0.4850		Taiwan-CWB station: ILA061
	94	0.8546	1.5300	2.0800	1.2400	0.2457	0.5640	0.7930	0.3900		Taiwan-CWB station: TAP035
	94	0.7156	0.8290	1.9800	1.8200	0.2577	0.6090	0.7370	0.4250		Taiwan-CWB station: ILA037
	94	1.3787	2.2400	4.6800	3.4700	0.3801	0.8190	0.7770	0.3920		Taiwan-CWB station: ILA013
	94	0.4438	0.8530	1.3500	0.9810	0.1994	0.3330	0.3290	0.3310		Taiwan-CWB station: ILA015
	94	0.3889	0.5670	0.9200	1.2900	0.1293	0.3590	0.2880	0.3670		Taiwan-CWB station: KAU086
	94	1.0264	1.5800	2.3200	1.2400	0.1979	0.4740	0.4330	0.2870		Taiwan-CWB station: ILA027
	95	0.8417	1.3600	2.3900	1.3400	0.3475	0.9540	1.0200	0.5750		Taiwan-CWB station: TAP053
	95	0.4860	0.9480	1.0600	2.1800	0.1852	0.4040	0.5960	0.4410		Taiwan-CWB station: ILA039
	96	0.9687	1.5000	2.5900	2.1400	0.2752	1.1200	0.4300	0.4000		Taiwan-CWB station: ILA030
	96	0.6257	1.2500	2.3700	0.6350	0.2257	0.5600	0.4790	0.7180		Taiwan-CWB station: TAP034
	96	0.8269	1.3900	1.9400	1.7200	0.3083	0.6770	0.5310	0.3790		Taiwan-CWB station: ILA008
	97	0.7402	1.3500	2.3700	1.2400	0.1852	0.4800	0.4380	0.2600		Taiwan-CWB station: ILA042
	97	0.4067	0.4040	0.6780	1.2200	0.0959	0.1560	0.1980	0.2080		Taiwan-CWB station: KAU022

continued on next page

Tab. D.3: *continued*

Date	Time	Lat.	Long.	Depth	M_s	$\log M_0$	F					C
	d	a_h	$\mathrm{SA}_h(0.2)$	$\mathrm{SA}_h(0.5)$	$\mathrm{S}_h(1.0)$	a_v	$\mathrm{SA}_v(0.2)$	$\mathrm{SA}_v(0.5)$	$\mathrm{SA}_v(1.0)$	S	Station	
	97	1.1064	1.6900	2.1900	3.4300	0.5503	0.7600	0.9020	1.1700		Taiwan-CWB station: TAP032	
	97	0.7538	1.9100	2.1100	0.6360	0.2763	0.6170	0.7690	0.5210		Taiwan-CWB station: ILA031	
	97	0.7128	1.2600	2.1000	2.1800	0.2569	0.5530	0.6470	0.7630		Taiwan-CWB station: ILA012	
	97	0.5396	0.8430	1.2200	2.1100	0.2422	0.4380	0.6880	0.3840		Taiwan-CWB station: ILA032	
	98	0.4623	0.7850	1.1600	0.7380	0.3082	0.3400	0.5370	0.6680		Taiwan-CWB station: TAP086	
	98	0.7480	1.2700	3.0000	1.4400	0.2649	0.6040	0.6440	0.4500		Taiwan-CWB station: TCU092	
	98	0.7329	0.8240	1.4100	2.2700	0.2171	0.3440	0.4820	0.3870		Taiwan-CWB station: ILA049	
	98	0.3937	0.5810	0.7180	1.3100	0.0822	0.2560	0.1660	0.1990		Taiwan-CWB station: KAU064	
	98	0.8390	1.6100	2.1800	1.4700	0.3449	0.8050	1.2800	0.7080		Taiwan-CWB station: ILA007	
	98	0.8644	1.4100	3.1600	2.0500	0.3469	0.5570	0.7680	1.3200		Taiwan-CWB station: ILA006	
	98	0.6742	1.3600	1.7300	1.1900	0.2900	0.6190	0.7520	0.3150		Taiwan-CWB station: ILA059	
	99	0.6711	1.1400	1.5900	1.2600	0.2128	0.4270	0.3890	0.6840		Taiwan-CWB station: ILA036	
	99	0.5821	0.9420	1.3100	1.6100	0.1218	0.3300	0.2110	0.2550		Taiwan-CWB station: KAU011	
	99	0.3727	0.9090	0.8040	0.5530	0.1699	0.2880	0.4070	0.3630		Taiwan-CWB station: ILA052	
	99	0.8749	1.1300	2.3600	2.8300	0.2121	0.4770	0.5250	0.2520		Taiwan-CWB station: ILA041	
	99	0.2180	0.5580	0.6140	0.4670	0.1223	0.4090	0.3320	0.1960		Taiwan-CWB station: TTN003	
	99	0.9199	1.2300	2.5000	2.6400	0.2508	1.0500	0.5250	0.3710		Taiwan-CWB station: ILA048	
	99	0.6738	0.9310	1.8100	1.9600	0.2468	0.7050	0.3660	0.3080		Taiwan-CWB station: ILA004	
	99	0.7805	1.2400	1.7200	1.6300	0.2647	0.4430	0.6700	0.4330		Taiwan-CWB station: ILA005	
	100	1.1235	3.1000	1.6800	2.0100	0.3424	0.7050	0.5400	0.5780		Taiwan-CWB station: TAP052	
	101	0.4111	0.4480	0.6200	1.1500	0.1048	0.1390	0.3020	0.2210		Taiwan-CWB station: KAU030	
	101	0.3806	0.5810	1.0800	0.9260	0.3488	0.4260	0.7180	0.8640		Taiwan-CWB station: TAP067	
	101	0.7619	0.9180	1.9200	2.6200	0.1893	0.4260	0.6510	0.5320		Taiwan-CWB station: TAP097	
	102	0.6295	0.8340	2.3900	1.3900	0.1530	0.3400	0.3900	0.3480		Taiwan-CWB station: ILA003	
	102	0.6351	1.0600	1.9500	1.7500	0.2234	0.5500	0.4470	0.2530		Taiwan-CWB station: ILA056	
	102	0.6158	0.6830	1.8400	2.2200	0.1103	0.1440	0.1870	0.3620		Taiwan-CWB station: ILA035	
	103	0.8386	0.9650	1.2100	2.0200	0.3299	0.4010	0.7870	0.8500		Taiwan-CWB station: TAP087	
	103	0.4320	0.6120	1.0800	1.6700	0.1379	0.3460	0.4600	0.2220		Taiwan-CWB station: TAP	
	104	1.0753	2.1100	1.3500	1.8000	0.3533	0.8350	0.5200	0.7450		Taiwan-CWB station: TAP051	
	104	0.2816	0.3910	1.0300	0.9310	0.1230	0.1960	0.3010	0.3550		Taiwan-CWB station: KAU015	
	105	0.2313	0.3340	0.7130	0.6340	0.1043	0.2210	0.2860	0.2190		Taiwan-CWB station: KAU007	
	105	0.2907	0.3730	0.5980	0.8740	0.1236	0.2270	0.2550	0.3870		Taiwan-CWB station: KAU074	
	107	0.8122	1.8200	2.0000	1.8800	0.2342	0.7640	0.4990	0.7620		Taiwan-CWB station: TAP042	
	107	0.6781	0.8330	2.4400	1.8100	0.2002	0.3580	0.8020	0.6140		Taiwan-CWB station: ILA002	
	107	0.5152	0.7260	1.1900	1.1800	0.1814	0.2930	0.5180	0.4140		Taiwan-CWB station: TAP072	

continued on next page

Tab. D.3: *continued*

Date	Time	Lat.	Long.	Depth	M_s	$\log M_0$	F					C
	d	a_h	$\mathrm{SA}_h(0.2)$	$\mathrm{SA}_h(0.5)$	$\mathrm{S}_h(1.0)$	a_v	$\mathrm{SA}_v(0.2)$	$\mathrm{SA}_v(0.5)$	$\mathrm{SA}_v(1.0)$	S	Station	
	107	0.2536	0.5250	0.6690	0.9070	0.1060	0.3410	0.2000	0.2360		Taiwan-CWB station: KAU088	
	109	1.0926	1.3800	3.3000	2.0400	0.3432	0.5770	1.2400	0.8350		Taiwan-CWB station: TAP049	
	109	0.2134	0.2590	0.6140	0.6370	0.1043	0.1360	0.2500	0.2670		Taiwan-CWB station: KAU083	
	110	0.1607	0.3290	0.3140	0.3400	0.0882	0.1550	0.1990	0.1660		Taiwan-CWB station: KAU057	
	110	0.2855	0.4080	0.4960	1.0200	0.1161	0.2740	0.2430	0.3480		Taiwan-CWB station: KAU087	
	111	0.7411	1.6400	2.0500	2.0200	0.1911	0.3950	0.3500	0.4470		Taiwan-CWB station: TAP041	
	111	0.1859	0.3650	0.5710	0.4130	0.0862	0.1750	0.2290	0.2290		Taiwan-CWB station: K003	
	112	0.2404	0.3630	0.8640	0.5220	0.1077	0.2490	0.3040	0.1760		Taiwan-CWB station: ILA001	
	115	0.3167	0.4490	0.9630	0.8850	0.0986	0.1800	0.2490	0.1420		Taiwan-CWB station: KAU075	
	115	0.7021	1.1500	1.3400	1.7100	0.2201	0.6120	0.5840	0.7540		Taiwan-CWB station: TAP075	
	116	0.6717	1.0500	0.9220	1.8000	0.1834	0.2100	0.3500	0.6100		Taiwan-CWB station: TAP066	
	119	0.1868	0.2420	0.5410	0.6090	0.0807	0.1670	0.1400	0.1380		Taiwan-CWB station: KAU033	
	121	0.3987	0.4250	0.7790	0.8940	0.0845	0.1740	0.1770	0.1600		Taiwan-CWB station: KAU044	
	122	1.7958	2.3100	4.2200	4.4400	0.2543	0.4140	0.5890	0.3360		Taiwan-CWB station: TAP103	
	122	0.4261	0.6870	0.7420	1.1300	0.1622	0.2230	0.3750	0.5890		Taiwan-CWB station: TAP083	
	123	0.3639	0.5450	0.8030	0.6380	0.1615	0.2740	0.2980	0.2290		Taiwan-CWB station: TAP059	
	124	0.7456	1.2100	0.8980	1.3000	0.1615	0.3810	0.2720	0.2790		Taiwan-CWB station: TAP046	
	125	0.3555	0.5550	0.5220	0.6940	0.1019	0.3110	0.2600	0.3010		Taiwan-CWB station: TAP060	
	125	0.0948	0.1490	0.3130	0.2650	0.0534	0.1040	0.2300	0.1110		Taiwan-CWB station: KAU051	
	125	0.2748	0.4850	0.8310	0.7580	0.1004	0.1810	0.2400	0.2230		Taiwan-CWB station: ILA054	
	126	0.0762	0.0978	0.1790	0.2430	0.0566	0.0720	0.0967	0.1340		Taiwan-CWB station: TTN016	
	126	0.3724	0.5430	0.7890	1.2500	0.2549	0.3070	0.4900	0.6660		Taiwan-CWB station: TAP077	
	126	0.3351	0.5840	0.7530	1.2900	0.1133	0.2610	0.2390	0.2970		Taiwan-CWB station: TAP084	
	128	0.3267	0.4770	0.6210	0.7540	0.1141	0.2290	0.3150	0.3760		Taiwan-CWB station: TAP065	
	128	0.2370	0.3570	0.6120	0.6240	0.1504	0.1780	0.3070	0.3380		Taiwan-CWB station: TAP079	
	128	0.3801	0.7470	0.8850	0.9630	0.1678	0.2670	0.4630	0.5020		Taiwan-CWB station: TAP078	
	133	0.2597	0.3170	0.7510	1.0200	0.1012	0.1080	0.2290	0.2810		Taiwan-CWB station: KAU037	
	133	0.3254	0.4600	0.5300	0.8810	0.0962	0.1360	0.2330	0.2690		Taiwan-CWB station: TAP069	
	133	0.3210	0.3950	0.8360	0.6080	0.1001	0.1820	0.2050	0.2760		Taiwan-CWB station: TAP081	
	144	0.0951	0.1460	0.2430	0.2130	0.0588	0.0751	0.1200	0.1570		Taiwan-CWB station: KAU038	
	144	0.0801	0.0967	0.1250	0.3150	0.0544	0.0692	0.1280	0.1780		Taiwan-CWB station: KAU040	
	154	0.1006	0.1200	0.2050	0.3980	0.0538	0.0589	0.1240	0.1590		Taiwan-CWB station: KAU039	
	163	0.0913	0.1250	0.2240	0.3270	0.0567	0.0582	0.1090	0.1320		Taiwan-CWB station: KAU042	
	164	0.1895	0.2050	0.4900	0.6530	0.0847	0.0920	0.1470	0.1920		Taiwan-CWB station: KAU081	
	165	0.2179	0.2220	0.4430	0.6370	0.0713	0.0740	0.1540	0.1760		Taiwan-CWB station: KAU046	

continued on next page

Tab. D.3: *continued*

Date			Time	Lat.	Long.	Depth	M_s	$\log M_0$	F					C
			d	a_h	$\mathrm{SA}_h(0.2)$	$\mathrm{SA}_h(0.5)$	$\mathrm{S}_h(1.0)$	a_v	$\mathrm{SA}_v(0.2)$	$\mathrm{SA}_v(0.5)$	$\mathrm{SA}_v(1.0)$	S	Station	
			171	0.0725	0.0764	0.1340	0.2200	0.0483	0.0520	0.0901	0.1260		Taiwan-CWB station: KAU052	
			172	0.1518	0.1720	0.3340	0.4260	0.0705	0.0779	0.1650	0.2470		Taiwan-CWB station: KAU082	
			175	0.1526	0.1920	0.3930	0.4760	0.0676	0.0734	0.1350	0.2130		Taiwan-CWB station: KAU043	
1999	11	12	1657	40.77	31.15	14	7.30	19.65						TU
			0	4.8975	12.0000	10.4000	6.9100	3.2901	6.1700	1.6500	1.2600	A	Duzce-Meteoroloji Mudurlugu	
			18	7.7262	15.5000	15.8000	10.8000	1.7922	5.7600	1.7800	1.9800	A	Bolu-Bayindirlik ve Iskan Mudurlugu	
			34	1.1974	2.7900	1.3400	0.5400	0.5762	1.8700	0.5900	0.4400		Mudurnu-Kaymakamlik Binasi	
			47	0.2156	0.5660	0.3400	0.2480	0.1028	0.2490	0.1830	0.1410	A	Sakarya-Bayindirlik ve Iskan Mudurlugu	
			157	0.0725	0.1230	0.1700	0.1190	0.0699	0.0917	0.1480	0.1510	A	Istanbul-Bayindirlik ve Iskan Mudurlugu	
			164	0.1393	0.2000	0.3430	0.3250	0.0860	0.1360	0.2900	0.1780		Sirkeci	
			168	0.3331	0.4720	1.6100	0.4160	0.0708	0.1680	0.1990	0.0817	S	Fatih	
			170	0.1744	0.2540	0.3800	0.7140	0.0700	0.1260	0.2670	0.1370		Istanbul-K.M.Pasa	
			170	0.1739	0.2040	0.3980	0.5970	0.1010	0.1100	0.1710	0.3850	S	Bursa-Tofa Fabrikasi	
			171	0.1427	0.1670	0.3110	0.5500	0.0885	0.1030	0.1550	0.3170		Kutahya-Sivil Savunma Mudurlugu	
			178	0.1505	0.1860	0.3530	0.4370	0.0674	0.0808	0.1510	0.2380	A	Yesilkoy-Havaalani	
			184	0.1535	0.2870	0.3920	0.4870	0.0674	0.0864	0.1850	0.1220	A	Kucuk-Cekmece	
			189	0.3114	0.4000	0.5580	0.9240	0.0683	0.1490	0.2410	0.1200	S	Ambarli-Termik Santrali	
			222	0.0978	0.1070	0.2270	0.3830	0.0285	0.0301	0.0837	0.0944		Afyon-Bayindirlik ve Iskan Mudurlugu	
			288	0.0467	0.0612	0.0795	0.1450	0.0160	0.0179	0.0291	0.0373		Tekirdag-Bayindirlik Mudurlugu	
			365	0.0171	0.0174	0.0215	0.0447	0.0077	0.0089	0.0175	0.0235	A	Denizli-Bayindirlik ve Iskan Mudurlugu	

Tab. E.1: Coefficients of horizontal spectral acceleration relations. T is natural period. Soil coefficients labelled with (*) are significant at the 5% level.

T	b_1	b_2	b_3	b_A	b_S	σ
0.10	0.028	0.143	−0.0238	−0.042	−0.014	0.240
0.11	0.008	0.144	−0.0221	−0.020	0.010	0.246
0.12	0.132	0.127	−0.0215	−0.016	0.016	0.245
0.13	0.114	0.131	−0.0202	−0.009	0.010	0.247
0.14	0.100	0.135	−0.0191	−0.011	0.000	0.250
0.15	0.110	0.135	−0.0189	0.001	0.001	0.251
0.16	0.008	0.149	−0.0175	0.004	0.005	0.249
0.17	−0.036	0.155	−0.0169	0.004	0.025	0.250
0.18	−0.083	0.160	−0.0157	0.004	0.035	0.250
0.19	−0.101	0.163	−0.0151	0.006	0.034	0.250
0.20	−0.182	0.175	−0.0164	0.006	0.049	0.251
0.22	−0.289	0.189	−0.0175	0.033	0.066	0.248
0.24	−0.570	0.226	−0.0176	0.081	0.114(*)	0.243
0.26	−0.652	0.241	−0.0196	0.084	0.103	0.238
0.28	−0.587	0.235	−0.0226	0.064	0.107	0.247
0.30	−0.554	0.231	−0.0251	0.057	0.117(*)	0.251
0.32	−0.584	0.235	−0.0259	0.048	0.120(*)	0.258
0.34	−0.559	0.232	−0.0271	0.039	0.108	0.252
0.36	−0.543	0.230	−0.0272	0.043	0.094	0.252
0.38	−0.610	0.236	−0.0265	0.059	0.095	0.255
0.40	−0.714	0.246	−0.0263	0.086	0.119(*)	0.256
0.42	−0.812	0.257	−0.0262	0.107	0.134(*)	0.252
0.44	−0.903	0.268	−0.0262	0.114	0.148(*)	0.252
0.46	−0.971	0.278	−0.0258	0.103	0.150(*)	0.252
0.48	−0.955	0.273	−0.0257	0.102	0.162(*)	0.251
0.50	−0.992	0.275	−0.0252	0.110	0.178(*)	0.253
0.55	−1.113	0.289	−0.0275	0.126	0.202(*)	0.255
0.60	−1.100	0.285	−0.0311	0.133	0.226(*)	0.257
0.65	−1.054	0.275	−0.0331	0.129	0.241(*)	0.263
0.70	−1.088	0.280	−0.0352	0.118	0.234(*)	0.266
0.75	−1.182	0.291	−0.0352	0.113	0.220(*)	0.264
0.80	−1.236	0.293	−0.0342	0.123	0.222(*)	0.268
0.85	−1.318	0.301	−0.0350	0.142(*)	0.221(*)	0.268
0.90	−1.406	0.310	−0.0335	0.145(*)	0.216(*)	0.267
0.95	−1.540	0.325	−0.0321	0.142(*)	0.208(*)	0.268
1.00	−1.726	0.347	−0.0307	0.153(*)	0.220(*)	0.272
1.10	−1.980	0.372	−0.0293	0.186(*)	0.268(*)	0.275
1.20	−2.265	0.412	−0.0307	0.173(*)	0.252(*)	0.271
1.30	−2.505	0.442	−0.0311	0.158(*)	0.242(*)	0.271
1.40	−2.725	0.470	−0.0297	0.139	0.229(*)	0.274

continued on next page

Tab. E.1: *continued*

T	b_1	b_2	b_3	b_A	b_S	σ
1.50	−2.904	0.492	−0.0298	0.128	0.225(*)	0.276
1.60	−3.052	0.510	−0.0304	0.123	0.221(*)	0.271
1.70	−3.127	0.517	−0.0306	0.114	0.213(*)	0.265
1.80	−3.206	0.525	−0.0316	0.107	0.213(*)	0.264
1.90	−3.300	0.534	−0.0319	0.102	0.215(*)	0.264
2.00	−3.380	0.543	−0.0326	0.098	0.215(*)	0.262

Tab. E.2: Coefficients of vertical spectral acceleration relations. T is natural period. Soil coefficients labelled with (*) are significant at the 5% level.

T	b_1	b_2	b_3	b_A	b_S	σ
0.10	−0.513	0.209	−0.0287	0.025	0.113	0.308
0.11	−0.479	0.202	−0.0297	0.033	0.132	0.308
0.12	−0.596	0.218	−0.0291	0.036	0.136	0.303
0.13	−0.576	0.213	−0.0270	0.032	0.109	0.296
0.14	−0.630	0.218	−0.0271	0.053	0.116	0.295
0.15	−0.706	0.226	−0.0268	0.070	0.118	0.287
0.16	−0.725	0.231	−0.0278	0.052	0.087	0.291
0.17	−0.696	0.227	−0.0297	0.047	0.082	0.290
0.18	−0.784	0.236	−0.0296	0.058	0.090	0.288
0.19	−0.819	0.240	−0.0288	0.053	0.068	0.286
0.20	−0.858	0.241	−0.0275	0.056	0.066	0.282
0.22	−0.866	0.238	−0.0269	0.051	0.041	0.275
0.24	−0.958	0.245	−0.0282	0.092	0.070	0.264
0.26	−0.946	0.239	−0.0273	0.096	0.041	0.265
0.28	−1.002	0.244	−0.0261	0.080	0.033	0.264
0.30	−1.106	0.261	−0.0265	0.050	0.012	0.256
0.32	−1.239	0.277	−0.0265	0.043	0.019	0.256
0.34	−1.388	0.298	−0.0274	0.040	0.025	0.258
0.36	−1.440	0.303	−0.0286	0.061	0.034	0.255
0.38	−1.489	0.303	−0.0291	0.105	0.053	0.255
0.40	−1.547	0.309	−0.0292	0.108(*)	0.043	0.255
0.42	−1.586	0.312	−0.0289	0.109(*)	0.047	0.253
0.44	−1.594	0.312	−0.0289	0.098	0.038	0.255
0.46	−1.563	0.305	−0.0296	0.099	0.037	0.252
0.48	−1.521	0.299	−0.0308	0.097	0.030	0.248
0.50	−1.524	0.302	−0.0325	0.081	0.015	0.243
0.55	−1.621	0.316	−0.0359	0.074	0.001	0.244
0.60	−1.700	0.324	−0.0364	0.061	0.005	0.253
0.65	−1.675	0.317	−0.0385	0.068	0.023	0.253
0.70	−1.700	0.318	−0.0380	0.065	−0.002	0.263
0.75	−1.855	0.337	−0.0364	0.057	−0.006	0.258
0.80	−1.973	0.348	−0.0358	0.064	0.012	0.252
0.85	−2.006	0.349	−0.0352	0.043	0.009	0.256
0.90	−2.040	0.352	−0.0346	0.031	0.013	0.257
0.95	−2.185	0.370	−0.0338	0.032	0.018	0.259
1.00	−2.294	0.384	−0.0335	0.028	0.021	0.259
1.10	−2.482	0.406	−0.0333	0.029	0.020	0.259
1.20	−2.544	0.411	−0.0334	0.011	−0.007	0.272

continued on next page

Tab. E.2: *continued*

T	b_1	b_2	b_3	b_A	b_S	σ
1.30	−2.580	0.412	−0.0324	−0.010	−0.023	0.271
1.40	−2.758	0.435	−0.0309	−0.044	−0.036	0.280
1.50	−2.981	0.466	−0.0292	−0.072	−0.055	0.285
1.60	−3.120	0.481	−0.0285	−0.076	−0.054	0.290
1.70	−3.227	0.492	−0.0301	−0.062	−0.034	0.288
1.80	−3.368	0.509	−0.0315	−0.060	−0.019	0.287
1.90	−3.537	0.529	−0.0310	−0.057	−0.011	0.287
2.00	−3.680	0.543	−0.0304	−0.042	0.004	0.290

Tab. E.3: Coefficients of horizontal spectral acceleration (buckling model) relations. T is natural period. Soil coefficients labelled with (*) are significant at the 5% level.

T	b_1	b_2	b_3	b_A	b_S	σ
0.10	−0.078	0.155	−0.0240	−0.013	0.016	0.235
0.11	−0.118	0.158	−0.0214	0.004	0.040	0.241
0.12	0.015	0.141	−0.0212	0.006	0.043	0.242
0.13	0.004	0.146	−0.0199	0.000	0.022	0.247
0.14	0.008	0.148	−0.0190	−0.006	0.008	0.250
0.15	0.030	0.147	−0.0189	0.002	0.004	0.255
0.16	−0.058	0.161	−0.0183	−0.004	0.000	0.252
0.17	−0.084	0.166	−0.0177	−0.017	0.007	0.254
0.18	−0.149	0.173	−0.0161	−0.007	0.023	0.253
0.19	−0.179	0.175	−0.0156	0.008	0.040	0.252
0.20	−0.247	0.186	−0.0169	0.010	0.056	0.254
0.22	−0.355	0.202	−0.0186	0.030	0.067	0.253
0.24	−0.627	0.237	−0.0188	0.079	0.117(*)	0.248
0.26	−0.712	0.250	−0.0204	0.090	0.111(*)	0.242
0.28	−0.641	0.244	−0.0233	0.061	0.108	0.251
0.30	−0.632	0.243	−0.0260	0.063	0.130(*)	0.254
0.32	−0.662	0.246	−0.0264	0.058	0.137(*)	0.259
0.34	−0.645	0.245	−0.0278	0.049	0.124(*)	0.256
0.36	−0.639	0.244	−0.0282	0.054	0.111	0.259
0.38	−0.709	0.251	−0.0275	0.069	0.109	0.258
0.40	−0.815	0.261	−0.0266	0.098	0.132(*)	0.257
0.42	−0.913	0.272	−0.0272	0.120	0.154(*)	0.255
0.44	−1.013	0.284	−0.0271	0.128	0.171(*)	0.255
0.46	−1.078	0.293	−0.0265	0.118	0.173(*)	0.254
0.48	−1.053	0.286	−0.0267	0.125	0.189(*)	0.253
0.50	−1.086	0.287	−0.0261	0.142(*)	0.214(*)	0.254
0.55	−1.219	0.302	−0.0281	0.155(*)	0.234(*)	0.256
0.60	−1.189	0.297	−0.0320	0.155(*)	0.251(*)	0.260
0.65	−1.149	0.289	−0.0342	0.149(*)	0.265(*)	0.267
0.70	−1.175	0.293	−0.0363	0.138	0.256(*)	0.270
0.75	−1.237	0.299	−0.0361	0.134	0.244(*)	0.266
0.80	−1.300	0.301	−0.0349	0.143	0.244(*)	0.271
0.85	−1.349	0.305	−0.0357	0.160(*)	0.241(*)	0.272
0.90	−1.438	0.314	−0.0344	0.162(*)	0.237(*)	0.270
0.95	−1.586	0.333	−0.0330	0.151(*)	0.222(*)	0.271
1.00	−1.769	0.354	−0.0317	0.163(*)	0.232(*)	0.276

continued on next page

Tab. E.3: *continued*

T	b_1	b_2	b_3	b_A	b_S	σ
1.10	−2.002	0.377	−0.0305	0.191(*)	0.271(*)	0.279
1.20	−2.277	0.416	−0.0321	0.172(*)	0.250(*)	0.275
1.30	−2.540	0.451	−0.0323	0.158(*)	0.243(*)	0.274
1.40	−2.759	0.478	−0.0310	0.135	0.224(*)	0.277
1.50	−2.933	0.499	−0.0308	0.128	0.224(*)	0.279
1.60	−3.100	0.519	−0.0312	0.125	0.221(*)	0.274
1.70	−3.185	0.527	−0.0317	0.121	0.221(*)	0.268
1.80	−3.262	0.534	−0.0327	0.115	0.223(*)	0.268
1.90	−3.349	0.544	−0.0332	0.109	0.225(*)	0.268
2.00	−3.432	0.552	−0.0338	0.108	0.228(*)	0.266

Tab. E.4: Coefficients of horizontal spectral acceleration (hinging model) relations. T is natural period. Soil coefficients labelled with (*) are significant at the 5% level.

T	b_1	b_2	b_3	b_A	b_S	σ
0.10	−0.086	0.155	−0.0234	−0.018	0.014	0.236
0.11	−0.119	0.157	−0.0216	0.008	0.044	0.239
0.12	0.032	0.138	−0.0212	0.005	0.043	0.242
0.13	0.024	0.142	−0.0199	0.009	0.032	0.246
0.14	0.026	0.144	−0.0189	0.000	0.016	0.249
0.15	0.037	0.144	−0.0187	0.013	0.016	0.250
0.16	−0.040	0.156	−0.0176	0.005	0.009	0.248
0.17	−0.083	0.163	−0.0171	0.001	0.024	0.250
0.18	−0.129	0.167	−0.0157	0.007	0.039	0.249
0.19	−0.158	0.170	−0.0151	0.012	0.043	0.250
0.20	−0.232	0.182	−0.0164	0.011	0.057	0.250
0.22	−0.336	0.196	−0.0176	0.036	0.071	0.248
0.24	−0.618	0.232	−0.0176	0.090	0.124(*)	0.243
0.26	−0.704	0.246	−0.0196	0.098	0.120(*)	0.239
0.28	−0.641	0.241	−0.0227	0.074	0.121(*)	0.247
0.30	−0.617	0.238	−0.0251	0.068	0.132(*)	0.251
0.32	−0.645	0.242	−0.0258	0.061	0.136(*)	0.257
0.34	−0.615	0.239	−0.0271	0.049	0.121(*)	0.251
0.36	−0.593	0.235	−0.0271	0.054	0.107	0.252
0.38	−0.671	0.243	−0.0265	0.070	0.108	0.254
0.40	−0.782	0.255	−0.0262	0.098	0.133(*)	0.254
0.42	−0.887	0.266	−0.0262	0.122	0.154(*)	0.250
0.44	−0.984	0.277	−0.0262	0.130	0.169(*)	0.250
0.46	−1.043	0.285	−0.0258	0.121	0.173(*)	0.250
0.48	−1.026	0.280	−0.0255	0.125	0.189(*)	0.250
0.50	−1.059	0.281	−0.0250	0.138	0.208(*)	0.252
0.55	−1.183	0.295	−0.0272	0.154(*)	0.231(*)	0.254
0.60	−1.162	0.290	−0.0309	0.159(*)	0.253(*)	0.257
0.65	−1.111	0.280	−0.0329	0.152(*)	0.265(*)	0.263
0.70	−1.136	0.284	−0.0351	0.137	0.255(*)	0.266
0.75	−1.221	0.294	−0.0352	0.133	0.240(*)	0.264
0.80	−1.270	0.295	−0.0341	0.143	0.241(*)	0.268
0.85	−1.343	0.303	−0.0349	0.162(*)	0.239(*)	0.269
0.90	−1.428	0.311	−0.0335	0.161(*)	0.231(*)	0.268

continued on next page

Tab. E.4: *continued*

T	b_1	b_2	b_3	b_A	b_S	σ
0.95	−1.565	0.328	−0.0322	0.154(*)	0.220(*)	0.269
1.00	−1.752	0.349	−0.0309	0.166(*)	0.232(*)	0.273
1.10	−1.999	0.374	−0.0296	0.198(*)	0.278(*)	0.276
1.20	−2.272	0.413	−0.0313	0.175(*)	0.253(*)	0.273
1.30	−2.523	0.446	−0.0316	0.160(*)	0.243(*)	0.273
1.40	−2.745	0.474	−0.0304	0.139	0.227(*)	0.276
1.50	−2.925	0.496	−0.0304	0.131	0.227(*)	0.278
1.60	−3.093	0.517	−0.0311	0.127	0.224(*)	0.273
1.70	−3.180	0.526	−0.0315	0.121	0.222(*)	0.267
1.80	−3.261	0.534	−0.0328	0.116	0.225(*)	0.268
1.90	−3.351	0.544	−0.0334	0.109	0.226(*)	0.269
2.00	−3.441	0.554	−0.0343	0.109	0.230(*)	0.267

Tab. E.5: Coefficients of horizontal maximum absolute input energy relations. T is natural period. Soil coefficients labelled with (*) are significant at the 5% level.

T	b_1	b_2	b_3	b_A	b_S	σ
0.10	−0.874	0.613	−0.0593	0.041	0.169	0.397
0.11	−0.774	0.598	−0.0569	0.070	0.186(*)	0.392
0.12	−0.637	0.582	−0.0559	0.088	0.180(*)	0.402
0.13	−0.416	0.556	−0.0528	0.066	0.138	0.408
0.14	−0.267	0.538	−0.0512	0.069	0.132	0.405
0.15	−0.181	0.529	−0.0492	0.082	0.133	0.413
0.16	−0.153	0.531	−0.0485	0.056	0.116	0.420
0.17	−0.187	0.538	−0.0458	0.046	0.129	0.420
0.18	−0.097	0.526	−0.0442	0.048	0.149	0.416
0.19	−0.085	0.527	−0.0436	0.055	0.159	0.412
0.20	−0.156	0.539	−0.0426	0.052	0.171	0.412
0.22	−0.381	0.579	−0.0429	0.060	0.166	0.423
0.24	−0.514	0.598	−0.0430	0.122	0.233(*)	0.424
0.26	−0.583	0.614	−0.0437	0.142	0.242(*)	0.412
0.28	−0.490	0.605	−0.0459	0.143	0.268(*)	0.425
0.30	−0.381	0.600	−0.0504	0.120	0.271(*)	0.435
0.32	−0.412	0.609	−0.0511	0.106	0.272(*)	0.434
0.34	−0.369	0.608	−0.0500	0.102	0.233(*)	0.441
0.36	−0.327	0.604	−0.0500	0.128	0.216(*)	0.444
0.38	−0.317	0.604	−0.0515	0.155	0.223(*)	0.453
0.40	−0.429	0.617	−0.0512	0.195	0.257(*)	0.458
0.42	−0.477	0.622	−0.0516	0.221	0.286(*)	0.461
0.44	−0.620	0.645	−0.0502	0.208	0.286(*)	0.465
0.46	−0.662	0.652	−0.0491	0.208	0.296(*)	0.470
0.48	−0.674	0.652	−0.0476	0.213	0.320(*)	0.473
0.50	−0.743	0.662	−0.0471	0.215	0.344(*)	0.478
0.55	−0.787	0.667	−0.0497	0.265(*)	0.414(*)	0.473
0.60	−0.808	0.675	−0.0554	0.240	0.432(*)	0.480
0.65	−0.623	0.651	−0.0616	0.263(*)	0.476(*)	0.489
0.70	−0.500	0.640	−0.0645	0.241	0.451(*)	0.499
0.75	−0.519	0.639	−0.0640	0.243	0.460(*)	0.499
0.80	−0.565	0.640	−0.0625	0.274(*)	0.456(*)	0.487

continued on next page

Tab. E.5: *continued*

T	b_1	b_2	b_3	b_A	b_S	σ
0.85	−0.605	0.648	−0.0629	0.276(*)	0.435(*)	0.499
0.90	−0.758	0.672	−0.0605	0.266(*)	0.413(*)	0.501
0.95	−0.977	0.699	−0.0582	0.281(*)	0.424(*)	0.507
1.00	−1.291	0.740	−0.0560	0.296(*)	0.440(*)	0.523
1.10	−1.793	0.805	−0.0550	0.337(*)	0.521(*)	0.527
1.20	−2.139	0.855	−0.0568	0.349(*)	0.545(*)	0.530
1.30	−2.449	0.900	−0.0559	0.312(*)	0.504(*)	0.517
1.40	−2.780	0.945	−0.0541	0.293(*)	0.504(*)	0.510
1.50	−3.198	1.005	−0.0509	0.262	0.487(*)	0.502
1.60	−3.554	1.055	−0.0501	0.243	0.485(*)	0.497
1.70	−3.613	1.062	−0.0530	0.239	0.479(*)	0.496
1.80	−3.589	1.059	−0.0562	0.219	0.470(*)	0.491
1.90	−3.641	1.066	−0.0575	0.209	0.460(*)	0.492
2.00	−3.700	1.074	−0.0593	0.206	0.464(*)	0.487

Tab. E.6: Coefficients of vertical maximum absolute input energy relations. T is natural period. Soil coefficients labelled with (*) are significant at the 5% level.

T	b_1	b_2	b_3	b_A	b_S	σ
0.10	−0.986	0.572	−0.0585	−0.009	0.177	0.477
0.11	−1.045	0.584	−0.0592	0.034	0.225	0.494
0.12	−1.007	0.584	−0.0578	0.038	0.219	0.501
0.13	−0.899	0.569	−0.0549	0.047	0.202	0.502
0.14	−0.905	0.571	−0.0534	0.084	0.204	0.505
0.15	−0.928	0.576	−0.0522	0.093	0.194	0.505
0.16	−0.939	0.580	−0.0528	0.112	0.191	0.512
0.17	−1.019	0.594	−0.0542	0.108	0.193	0.509
0.18	−1.046	0.599	−0.0544	0.110	0.189	0.509
0.19	−1.060	0.599	−0.0536	0.141	0.198	0.505
0.20	−1.096	0.606	−0.0508	0.112	0.154	0.499
0.22	−1.067	0.604	−0.0512	0.106	0.118	0.485
0.24	−0.987	0.590	−0.0528	0.143	0.120	0.475
0.26	−1.074	0.601	−0.0510	0.152	0.105	0.462
0.28	−1.192	0.619	−0.0506	0.127	0.102	0.461
0.30	−1.327	0.644	−0.0497	0.088	0.064	0.457
0.32	−1.505	0.668	−0.0489	0.083	0.072	0.462
0.34	−1.587	0.679	−0.0500	0.105	0.102	0.470
0.36	−1.586	0.678	−0.0512	0.148	0.123	0.473
0.38	−1.613	0.680	−0.0520	0.174	0.127	0.469
0.40	−1.673	0.689	−0.0528	0.184	0.122	0.465
0.42	−1.711	0.697	−0.0530	0.177	0.116	0.458
0.44	−1.676	0.692	−0.0533	0.184	0.114	0.460
0.46	−1.598	0.680	−0.0550	0.200(*)	0.124	0.463
0.48	−1.539	0.672	−0.0554	0.198	0.121	0.458
0.50	−1.532	0.675	−0.0571	0.177	0.098	0.457
0.55	−1.526	0.687	−0.0628	0.109	0.044	0.457
0.60	−1.615	0.705	−0.0643	0.082	0.035	0.466
0.65	−1.526	0.688	−0.0664	0.151	0.078	0.472
0.70	−1.497	0.689	−0.0676	0.151	0.055	0.474

continued on next page

Tab. E.6: *continued*

T	b_1	b_2	b_3	b_A	b_S	σ
0.75	−1.589	0.699	−0.0652	0.144	0.067	0.476
0.80	−1.719	0.716	−0.0634	0.115	0.061	0.469
0.85	−1.679	0.710	−0.0619	0.076	0.045	0.460
0.90	−1.739	0.720	−0.0606	0.065	0.041	0.471
0.95	−1.935	0.747	−0.0602	0.085	0.082	0.486
1.00	−2.044	0.762	−0.0600	0.090	0.105	0.488
1.10	−2.161	0.773	−0.0586	0.098	0.131	0.491
1.20	−2.321	0.803	−0.0598	0.045	0.072	0.506
1.30	−2.553	0.838	−0.0571	−0.004	0.032	0.501
1.40	−2.847	0.881	−0.0536	−0.054	−0.001	0.506
1.50	−3.177	0.932	−0.0516	−0.079	−0.010	0.521
1.60	−3.437	0.970	−0.0543	−0.070	0.006	0.535
1.70	−3.515	0.980	−0.0573	−0.079	0.038	0.542
1.80	−3.644	0.996	−0.0583	−0.081	0.067	0.537
1.90	−3.816	1.020	−0.0593	−0.085	0.075	0.531
2.00	−3.997	1.042	−0.0582	−0.070	0.077	0.528

Tab. E.7: Coefficients of vertical to horizontal spectral ratio, q_s, relations. T is natural period.

	All		Normal		Thrust		Strike-slip		European	
T	b_1	σ	b_1	σ	b_1	σ	b_1	σ	b_1	σ
0.10	−0.052	0.261	−0.152	0.157	−0.063	0.245	−0.017	0.292	−0.150	0.264
0.11	−0.080	0.262	−0.121	0.141	−0.106	0.243	−0.038	0.300	−0.168	0.251
0.12	−0.110	0.266	−0.162	0.178	−0.140	0.252	−0.061	0.293	−0.210	0.272
0.13	−0.140	0.258	−0.194	0.182	−0.165	0.231	−0.096	0.299	−0.231	0.261
0.14	−0.160	0.258	−0.229	0.189	−0.181	0.232	−0.118	0.298	−0.254	0.254
0.15	−0.193	0.258	−0.260	0.187	−0.213	0.240	−0.152	0.289	−0.285	0.243
0.16	−0.215	0.267	−0.274	0.198	−0.233	0.255	−0.178	0.292	−0.304	0.243
0.17	−0.246	0.263	−0.268	0.182	−0.266	0.251	−0.215	0.290	−0.324	0.234
0.18	−0.264	0.261	−0.267	0.165	−0.279	0.256	−0.243	0.285	−0.335	0.229
0.19	−0.285	0.256	−0.285	0.157	−0.296	0.252	−0.270	0.279	−0.350	0.220
0.20	−0.300	0.250	−0.303	0.156	−0.305	0.248	−0.293	0.269	−0.351	0.211
0.22	−0.337	0.242	−0.336	0.151	−0.341	0.243	−0.334	0.258	−0.343	0.184
0.24	−0.364	0.239	−0.326	0.191	−0.366	0.243	−0.368	0.246	−0.357	0.190
0.26	−0.385	0.233	−0.311	0.212	−0.388	0.230	−0.396	0.242	−0.368	0.191
0.28	−0.412	0.229	−0.363	0.217	−0.415	0.215	−0.419	0.250	−0.387	0.180
0.30	−0.421	0.229	−0.363	0.224	−0.419	0.214	−0.435	0.249	−0.365	0.180
0.32	−0.430	0.228	−0.372	0.218	−0.438	0.207	−0.431	0.257	−0.365	0.180
0.34	−0.439	0.233	−0.378	0.215	−0.449	0.201	−0.438	0.274	−0.374	0.185
0.36	−0.446	0.239	−0.387	0.214	−0.451	0.206	−0.451	0.283	−0.387	0.193
0.38	−0.459	0.243	−0.397	0.216	−0.464	0.215	−0.465	0.281	−0.400	0.193
0.40	−0.474	0.250	−0.414	0.205	−0.479	0.226	−0.480	0.288	−0.408	0.201

continued on next page

Tab. E.7: *continued*

	All		Normal		Thrust		Strike-slip		European	
T	b_1	σ	b_1	σ	b_1	σ	b_1	σ	b_1	σ
0.42	−0.478	0.248	−0.405	0.174	−0.486	0.227	−0.482	0.285	−0.399	0.207
0.44	−0.485	0.242	−0.371	0.167	−0.503	0.220	−0.484	0.277	−0.395	0.205
0.46	−0.492	0.239	−0.354	0.174	−0.513	0.218	−0.494	0.268	−0.389	0.208
0.48	−0.498	0.240	−0.327	0.154	−0.526	0.224	−0.496	0.263	−0.383	0.203
0.50	−0.502	0.240	−0.334	0.141	−0.529	0.226	−0.500	0.262	−0.394	0.203
0.55	−0.514	0.250	−0.364	0.167	−0.537	0.233	−0.516	0.277	−0.423	0.223
0.60	−0.527	0.253	−0.426	0.194	−0.544	0.248	−0.525	0.267	−0.443	0.242
0.65	−0.525	0.249	−0.430	0.176	−0.535	0.254	−0.533	0.253	−0.456	0.244
0.70	−0.520	0.271	−0.385	0.153	−0.540	0.281	−0.523	0.271	−0.428	0.237
0.75	−0.511	0.267	−0.359	0.150	−0.538	0.277	−0.507	0.265	−0.405	0.236
0.80	−0.513	0.260	−0.379	0.125	−0.545	0.274	−0.499	0.253	−0.407	0.235
0.85	−0.518	0.264	−0.397	0.138	−0.554	0.280	−0.495	0.254	−0.423	0.247
0.90	−0.511	0.266	−0.391	0.153	−0.546	0.283	−0.489	0.255	−0.427	0.269
0.95	−0.499	0.267	−0.347	0.153	−0.538	0.279	−0.479	0.257	−0.404	0.266
1.00	−0.496	0.270	−0.335	0.161	−0.540	0.284	−0.470	0.255	−0.394	0.267
1.10	−0.494	0.274	−0.347	0.188	−0.533	0.289	−0.473	0.258	−0.383	0.250
1.20	−0.499	0.285	−0.338	0.212	−0.540	0.285	−0.479	0.287	−0.383	0.252
1.30	−0.485	0.285	−0.310	0.209	−0.523	0.282	−0.472	0.292	−0.370	0.252
1.40	−0.476	0.290	−0.255	0.221	−0.517	0.279	−0.468	0.298	−0.351	0.252
1.50	−0.465	0.295	−0.235	0.199	−0.503	0.281	−0.462	0.312	−0.343	0.261
1.60	−0.461	0.292	−0.229	0.196	−0.488	0.272	−0.473	0.315	−0.348	0.277
1.70	−0.452	0.280	−0.227	0.197	−0.472	0.260	−0.473	0.302	−0.355	0.278

continued on next page

Tab. E.7: *continued*

	All		Normal		Thrust		Strike-slip		European	
T	b_1	σ	b_1	σ	b_1	σ	b_1	σ	b_1	σ
1.80	−0.447	0.272	−0.229	0.204	−0.463	0.251	−0.471	0.293	−0.363	0.265
1.90	−0.443	0.259	−0.247	0.207	−0.450	0.241	−0.474	0.276	−0.373	0.258
2.00	−0.444	0.254	−0.257	0.193	−0.450	0.234	−0.475	0.277	−0.378	0.259

Tab. E.8: Coefficients of vertical to horizontal simultaneous spectral ratio, q_i, relations. T is natural period.

	All		Normal		Thrust		Strike-slip		European	
T	b_1	σ	b_1	σ	b_1	σ	b_1	σ	b_1	σ
0.10	−0.860	0.512	−1.067	0.656	−0.836	0.518	−0.849	0.467	−0.966	0.618
0.11	−0.863	0.577	−0.919	0.684	−0.893	0.581	−0.810	0.553	−0.810	0.530
0.12	−0.955	1.236	−1.124	0.904	−0.843	0.521	−1.069	1.832	−0.962	0.699
0.13	−0.891	0.576	−0.858	0.486	−0.848	0.497	−0.955	0.684	−0.880	0.489
0.14	−0.823	0.483	−0.755	0.422	−0.861	0.482	−0.786	0.497	−0.949	0.548
0.15	−0.921	0.594	−0.951	0.416	−0.924	0.606	−0.910	0.616	−0.913	0.506
0.16	−0.912	0.561	−0.864	0.455	−0.928	0.628	−0.900	0.485	−0.950	0.541
0.17	−0.997	0.533	−1.029	0.670	−1.012	0.553	−0.972	0.479	−1.019	0.561
0.18	−0.921	0.491	−1.072	0.776	−0.921	0.488	−0.888	0.417	−0.937	0.370
0.19	−0.928	0.502	−1.100	0.793	−0.882	0.431	−0.953	0.514	−1.047	0.626
0.20	−0.960	0.555	−0.950	0.521	−0.896	0.505	−1.047	0.618	−0.962	0.553
0.22	−0.944	0.517	−0.957	0.355	−0.920	0.575	−0.974	0.465	−1.011	0.641
0.24	−1.029	0.482	−0.863	0.336	−1.023	0.499	−1.070	0.482	−0.943	0.420

continued on next page

Tab. E.8: *continued*

	All		Normal		Thrust		Strike-slip		European	
T	b_1	σ	b_1	σ	b_1	σ	b_1	σ	b_1	σ
0.26	−1.008	0.506	−1.108	0.435	−0.934	0.574	−1.084	0.404	−0.989	0.495
0.28	−0.983	0.473	−1.111	0.681	−0.913	0.468	−1.048	0.417	−0.986	0.530
0.30	−1.079	0.542	−1.152	0.494	−1.055	0.598	−1.096	0.473	−1.123	0.537
0.32	−1.104	0.540	−1.092	0.500	−1.063	0.526	−1.162	0.569	−1.031	0.513
0.34	−1.118	0.568	−1.151	0.615	−1.096	0.542	−1.140	0.600	−0.940	0.407
0.36	−1.051	0.529	−1.025	0.433	−0.998	0.530	−1.126	0.542	−1.000	0.438
0.38	−1.067	0.564	−0.866	0.409	−1.061	0.554	−1.117	0.602	−0.929	0.467
0.40	−1.117	0.585	−1.131	0.642	−1.090	0.572	−1.149	0.596	−0.979	0.568
0.42	−1.047	0.554	−1.099	0.630	−1.051	0.555	−1.030	0.544	−0.948	0.520
0.44	−1.041	0.569	−0.938	0.314	−1.006	0.563	−1.109	0.614	−0.866	0.389
0.46	−1.125	0.550	−1.249	0.598	−1.053	0.529	−1.195	0.561	−0.960	0.414
0.48	−1.089	0.552	−0.932	0.424	−1.069	0.598	−1.149	0.508	−0.911	0.464
0.50	−1.137	0.527	−1.067	0.482	−1.157	0.555	−1.125	0.503	−0.917	0.401
0.55	−1.123	0.526	−1.095	0.575	−1.047	0.475	−1.231	0.567	−0.936	0.483
0.60	−1.154	0.542	−1.060	0.493	−1.135	0.541	−1.199	0.556	−0.973	0.527
0.65	−1.189	0.511	−1.091	0.431	−1.171	0.523	−1.234	0.511	−1.154	0.528
0.70	−1.129	0.562	−0.958	0.403	−1.075	0.521	−1.237	0.625	−1.113	0.658
0.75	−1.123	0.499	−1.015	0.382	−1.141	0.553	−1.123	0.445	−0.975	0.478
0.80	−1.095	0.528	−1.038	0.617	−1.102	0.561	−1.096	0.467	−0.952	0.562
0.85	−1.140	0.574	−0.953	0.443	−1.133	0.601	−1.188	0.558	−0.964	0.491
0.90	−1.164	1.190	−0.962	0.460	−1.092	0.496	−1.302	1.796	−0.916	0.431
0.95	−1.067	0.539	−0.946	0.524	−1.085	0.541	−1.069	0.544	−0.832	0.407

continued on next page

Tab. E.8: *continued*

	All		Normal		Thrust		Strike-slip		European	
T	b_1	σ	b_1	σ	b_1	σ	b_1	σ	b_1	σ
1.00	−1.099	0.590	−0.893	0.600	−1.104	0.569	−1.134	0.616	−0.933	0.544
1.10	−1.063	0.508	−0.805	0.367	−1.084	0.521	−1.088	0.506	−0.867	0.447
1.20	−1.078	0.560	−0.851	0.548	−1.113	0.494	−1.077	0.636	−0.906	0.512
1.30	−1.053	0.549	−0.903	0.680	−1.135	0.568	−0.975	0.480	−0.856	0.539
1.40	−1.036	0.563	−0.775	0.499	−1.067	0.541	−1.049	0.596	−0.812	0.483
1.50	−1.076	0.569	−0.919	0.599	−1.094	0.521	−1.085	0.624	−0.911	0.611
1.60	−1.049	0.573	−0.721	0.365	−1.098	0.527	−1.052	0.646	−0.800	0.391
1.70	−0.962	0.509	−0.767	0.444	−1.002	0.522	−0.948	0.501	−0.811	0.644
1.80	−0.966	0.539	−0.614	0.345	−0.999	0.505	−0.994	0.592	−0.764	0.458
1.90	−0.990	0.541	−0.635	0.456	−1.053	0.557	−0.979	0.512	−0.809	0.471
2.00	−0.973	0.497	−0.777	0.429	−1.025	0.522	−0.945	0.469	−0.896	0.480

Tab. E.9: Coefficients of vertical to horizontal maximum absolute input energy ratio, q_e, relations. T is natural period.

	All		Normal		Thrust		Strike-slip		European	
T	b_1	σ	b_1	σ	b_1	σ	b_1	σ	b_1	σ
0.10	−0.385	0.365	−0.401	0.261	−0.403	0.337	−0.358	0.419	−0.442	0.323
0.11	−0.372	0.375	−0.400	0.269	−0.392	0.352	−0.339	0.423	−0.452	0.338
0.12	−0.369	0.378	−0.435	0.277	−0.378	0.355	−0.343	0.426	−0.453	0.352
0.13	−0.392	0.369	−0.461	0.318	−0.391	0.345	−0.379	0.412	−0.472	0.370
0.14	−0.395	0.363	−0.469	0.286	−0.388	0.347	−0.390	0.400	−0.490	0.351

continued on next page

Tab. E.9: *continued*

	All		Normal		Thrust		Strike-slip		European	
T	b_1	σ	b_1	σ	b_1	σ	b_1	σ	b_1	σ
0.15	−0.421	0.371	−0.492	0.281	−0.421	0.363	−0.406	0.399	−0.514	0.357
0.16	−0.439	0.377	−0.475	0.304	−0.431	0.367	−0.444	0.406	−0.510	0.353
0.17	−0.476	0.373	−0.480	0.312	−0.454	0.371	−0.505	0.389	−0.554	0.347
0.18	−0.505	0.375	−0.509	0.271	−0.476	0.393	−0.543	0.370	−0.575	0.365
0.19	−0.525	0.378	−0.513	0.260	−0.494	0.395	−0.568	0.375	−0.580	0.370
0.20	−0.550	0.374	−0.517	0.252	−0.514	0.385	−0.606	0.377	−0.562	0.346
0.22	−0.598	0.353	−0.563	0.228	−0.567	0.372	−0.646	0.348	−0.544	0.282
0.24	−0.652	0.364	−0.597	0.250	−0.603	0.375	−0.729	0.360	−0.612	0.268
0.26	−0.691	0.343	−0.580	0.251	−0.649	0.343	−0.769	0.348	−0.631	0.253
0.28	−0.733	0.348	−0.654	0.367	−0.705	0.340	−0.785	0.351	−0.637	0.280
0.30	−0.761	0.357	−0.686	0.356	−0.736	0.354	−0.808	0.360	−0.634	0.302
0.32	−0.793	0.357	−0.678	0.301	−0.774	0.347	−0.843	0.376	−0.638	0.276
0.34	−0.810	0.374	−0.714	0.318	−0.791	0.347	−0.854	0.415	−0.685	0.302
0.36	−0.818	0.391	−0.761	0.306	−0.784	0.360	−0.875	0.442	−0.744	0.305
0.38	−0.835	0.401	−0.787	0.277	−0.802	0.366	−0.888	0.462	−0.743	0.292
0.40	−0.852	0.405	−0.755	0.311	−0.824	0.372	−0.909	0.457	−0.719	0.312
0.42	−0.853	0.408	−0.710	0.349	−0.836	0.380	−0.905	0.450	−0.702	0.345
0.44	−0.861	0.403	−0.673	0.347	−0.860	0.376	−0.901	0.440	−0.699	0.348
0.46	−0.879	0.403	−0.665	0.337	−0.889	0.377	−0.910	0.439	−0.705	0.368
0.48	−0.891	0.408	−0.637	0.310	−0.908	0.385	−0.922	0.441	−0.707	0.373
0.50	−0.908	0.419	−0.615	0.314	−0.928	0.398	−0.941	0.445	−0.711	0.395
0.55	−0.950	0.434	−0.666	0.345	−0.964	0.406	−0.990	0.469	−0.773	0.409

continued on next page

Tab. E.9: *continued*

	All		Normal		Thrust		Strike-slip		European	
T	b_1	σ	b_1	σ	b_1	σ	b_1	σ	b_1	σ
0.60	−0.936	0.429	−0.714	0.349	−0.941	0.425	−0.975	0.440	−0.780	0.443
0.65	−0.935	0.442	−0.744	0.336	−0.932	0.434	−0.979	0.466	−0.803	0.475
0.70	−0.928	0.460	−0.704	0.302	−0.939	0.459	−0.959	0.480	−0.793	0.443
0.75	−0.919	0.459	−0.685	0.305	−0.938	0.458	−0.943	0.479	−0.792	0.443
0.80	−0.916	0.450	−0.725	0.292	−0.938	0.456	−0.926	0.463	−0.799	0.429
0.85	−0.923	0.450	−0.761	0.316	−0.942	0.460	−0.931	0.458	−0.809	0.457
0.90	−0.922	0.462	−0.768	0.332	−0.941	0.471	−0.928	0.471	−0.821	0.505
0.95	−0.899	0.462	−0.724	0.313	−0.933	0.478	−0.891	0.463	−0.788	0.509
1.00	−0.884	0.458	−0.696	0.346	−0.923	0.473	−0.871	0.453	−0.766	0.510
1.10	−0.892	0.463	−0.627	0.307	−0.932	0.466	−0.895	0.472	−0.725	0.455
1.20	−0.897	0.496	−0.621	0.315	−0.926	0.499	−0.915	0.511	−0.736	0.438
1.30	−0.881	0.481	−0.584	0.326	−0.919	0.485	−0.892	0.486	−0.718	0.424
1.40	−0.871	0.502	−0.509	0.372	−0.910	0.486	−0.894	0.522	−0.676	0.428
1.50	−0.847	0.503	−0.448	0.408	−0.871	0.476	−0.898	0.524	−0.662	0.465
1.60	−0.839	0.499	−0.415	0.423	−0.858	0.455	−0.902	0.532	−0.663	0.504
1.70	−0.825	0.485	−0.422	0.442	−0.853	0.429	−0.871	0.530	−0.667	0.485
1.80	−0.800	0.471	−0.428	0.385	−0.823	0.425	−0.848	0.515	−0.653	0.464
1.90	−0.795	0.463	−0.451	0.357	−0.818	0.427	−0.837	0.503	−0.654	0.470
2.00	−0.797	0.453	−0.463	0.374	−0.810	0.417	−0.848	0.491	−0.655	0.475